UNIVERSITÀ DELLA CALABRIA

UNIVERSITÀ DELLA CALABRIA

DIPARTIMENTO DI FISICA

DOTTORATO DI RICERCA IN

SCIENZE E TECNOLOGIE FISICHE, CHIMICHE E DEI MATERIALI

CICLO

XXXI

MEASUREMENTS OF TOP QUARK PAIR PRODUCTION DIFFERENTIAL CROSS SECTIONS IN THE ALL-HADRONIC DECAY CHANNEL IN pp COLLISIONS AT $\sqrt{s}$=13 TEV USING THE ATLAS DETECTOR

SETTORE SCIENTIFICO DISCIPLINARE FIS/01

COORDINATORE: PROF. VINCENZO CARBONE

SUPERVISORE: PROF. ENRICO TASSI

DOTTORANDO: DOTT. MATTEO SCORNAJENGHI

Abstract

In this thesis, the measurements of the differential cross sections of top quark pair production in proton - proton collisions at a center of mass energy of $\sqrt{s} = 13$ TeV are presented. Data are collected at the LHC by the ATLAS detector during the 2015 and 2016 data-taking periods, corresponding to an integrated luminosity of $\mathscr{L} = 36.1$ fb^{-1}. The top quark pair events are selected in the fully hadronic decay channel, resolved regime. The measurements are presented for several kinematics spectra and for observables sensitive to Initial and Final State Radiation. The measured spectra are corrected for detector effects and are compared to several theoretical Monte Carlo simulations. The measured spectra provide stringent tests of perturbative QCD, gives a better understanding of the top quark pair production mechanism and can be used to tune the Monte Carlo simulations. In addition, the expected performance of the Inner Tracker and the High Granularity Timing Detector, which will be installed during the Phase II upgrade of the ATLAS detector, will be presented.

Abstract

In questa tesi verrà presentata la misura delle sezioni d'urto differenziali di produzione di coppie di quark top-antitop in collisioni protone - protone ad un'energia nel centro di massa di $\sqrt{s} = 13$ TeV. I dati sono stati raccolti ad LHC dal detector ATLAS durante il 2015 e il 2016 e corrispondono ad una luminosità integrata di $\mathscr{L} = 36.1$ fb^{-1}. I candidati eventi $t\bar{t}$ sono stati selezionati nel canale di decadimento completamente adronico, in regime risolto. La misura viene presentata in funzione di diverse osservabili; sia relative alla cinematica del sistema $t\bar{t}$ che osservabii particolarmente sensibili all'emissione di gluoni da parte dei quark top nello stato iniziale e finale. Gli spettri misurati sono poi corretti per tenere conto degli effetti indotti dal detector e sono poi confrontati con diverse predizioni Monte Carlo. Tali misure consentono di effettuare dei test stringenti della QCD perturbativa, garantiscono una migliore comprensione dei meccanismi di produzione delle coppie di quark top-antitop e possono essere usati per la calibrazione dei parametri caratteristici delle simulazioni Monte Carlo. Inoltre, verranno presentate le performance attese dell'Inner Tracker e dell'High Granularity Timing Detector, i quali saranno installati durante l'upgrade di Fase II del rilevatore ATLAS.

Contents

Abstract **i**

Introduction **xxxvi**

1 Theory foundations **1**
1.1 The Standard Model of Particle Interactions . . . 1
1.2 Quantum Electrodynamics . . . 3
1.3 Quantum Chromodynamics . . . 4
1.4 Weak Interactions . . . 7
1.5 Electroweak theory . . . 7
1.6 Spontaneous symmetry breaking mechanism . . . 9
1.7 Principles of collider physics . . . 11
1.7.1 Factorization Theorem . . . 11
1.7.2 Parton Density Functions . . . 12
1.7.3 Luminosity at proton-proton colliders . . . 14
1.8 The top quark at the LHC . . . 15
1.8.1 Top quark properties . . . 15
1.8.2 Top quark decay modes . . . 18
1.8.3 Top quark pair production . . . 20
1.8.4 Charge asymmetry in $t\bar{t}$ quark pair production . . . 23
1.8.5 Single top quark production . . . 23

2 The ATLAS Detector at the LHC **25**
2.1 The Large Hadron Collider . . . 25
2.1.1 The LHC experiments . . . 29
2.1.2 The Worldwide LHC Computing Grid . . . 30
2.2 The ATLAS Detector . . . 32
2.2.1 Coordinate system . . . 34
2.2.2 Magnet system . . . 35
2.2.3 Inner Detector . . . 36
Silicon pixel tracker and the Insertable B-Layer (IBL) . 38
SemiConductor Tracker (SCT) . . . 38
Transition Radiation Tracker (TRT) . . . 38
2.2.4 Calorimetry . . . 38
Electromagnetic calorimetry . . . 40
Hadronic calorimeter . . . 40
Forwards calorimeter . . . 41
2.2.5 Muon Spectrometer . . . 41
Monitored Drift Tubes . . . 42

Catode Strip Chambers . . . 42
Resistive Plate Chambers . . . 43
Thin Gap Chambers . . . 43
2.2.6 Forward detectors . . . 43
2.2.7 Trigger and data acquisition . . . 44
Level 1 trigger . . . 45
The High Level Trigger . . . 45
Data Acquisition . . . 45
2.2.8 Trigger strategy in the cross section measurement . . . 46

3 The ATLAS Detector at the HL-LHC 50
3.1 From the LHC to the HL-LHC . . . 50
3.2 The Inner Tracker . . . 53
3.2.1 The ITk layout . . . 54
3.2.2 Tracking and physics performance . . . 55
Tracking and vertexing performance . . . 55
Physics object performance . . . 59
3.3 The High Granularity Timing Detector . . . 62
3.3.1 HGTD layout . . . 63
3.3.2 Performance studies . . . 63
Track extrapolation to the HGTD . . . 64
Track-to-vertex association . . . 65
Jet performance . . . 66

4 Event reconstruction at the ATLAS experiment 68
4.1 Monte Carlo event generation . . . 68
4.1.1 Hard processes . . . 70
4.1.2 Parton showers . . . 71
4.1.3 Hadronization . . . 74
String model . . . 76
Cluster model . . . 77
4.1.4 Hadron decays . . . 78
4.1.5 Underlying event . . . 78
4.1.6 Generator filtering . . . 79
4.2 ATLAS detector simulation . . . 80
4.2.1 ATLAS simulation overview . . . 80
4.2.2 Simulated ATLAS detector geometry . . . 81
4.2.3 Digitalization . . . 82
4.2.4 Fast simulations . . . 82
4.3 Object reconstruction . . . 84
4.4 Samples adopted for the cross section measurement . . . 85
4.4.1 Data samples . . . 85
4.4.2 Monte Carlo samples . . . 85

5 Object reconstruction performance of the ATLAS detector 88
5.1 Tracking performance . . . 88
5.1.1 Track reconstruction . . . 89
5.1.2 Track reconstruction performance . . . 90

5.2 Vertexing performance . . . 94
5.2.1 Primary vertex reconstruction . . . 94
5.2.2 Vertices truth classification . . . 95
5.2.3 Vertex performance . . . 97
5.3 Photon performance . . . 99
5.3.1 Photon reconstruction . . . 99
5.3.2 Photon identification . . . 100
5.3.3 Photon isolation . . . 101
5.3.4 Photon identification efficiency . . . 102
5.4 Electron performance . . . 105
5.4.1 Electron reconstruction . . . 105
5.4.2 Electron identification . . . 106
5.4.3 Electron isolation . . . 106
5.4.4 Electron efficiency . . . 107
5.5 Muon performance . . . 108
5.5.1 Muon reconstruction . . . 108
5.5.2 Muon identification . . . 109
5.5.3 Muon isolation . . . 110
5.5.4 Muon efficiency . . . 111
5.6 Tau performance . . . 112
5.6.1 Tau reconstruction . . . 112
5.6.2 Tau identification . . . 113
5.6.3 Tau identification efficiency . . . 113
5.7 Jet performance . . . 114
5.7.1 Jet reconstruction . . . 115
5.7.2 Jet energy scale calibration . . . 115
5.7.3 Pile up corrections . . . 116
5.7.4 Jet energy scale and η calibration . . . 117
5.7.5 Global sequential calibration . . . 117
5.7.6 In situ calibration . . . 118
5.7.7 Systematic uncertainties . . . 118
5.8 B-tagged jet performance . . . 120
5.8.1 MV2c10 b-tagging algorithm . . . 120
5.8.2 Calibration methods . . . 121
T&P method . . . 122
LH method . . . 123
5.8.3 b-jet tagging efficiencies . . . 123
5.9 E_T^{miss} performance . . . 125
5.9.1 E_T^{miss} reconstruction . . . 126
E_T^{miss} hard term . . . 126
E_T^{miss} soft term . . . 129
5.9.2 Systematic uncertainties . . . 130
5.9.3 E_T^{miss} resolution . . . 131

6 Analysis strategy and techniques **135**
6.1 The fully hadronic $t\bar{t}$ decay channel in the resolved topology . 135
6.2 Measured observables . . . 137

6.2.1 $t\bar{t}$ system kinematics . . . 137
6.2.2 ISFR-sensitive $t\bar{t}$ system spectra . . . 137
6.3 Objects definitions . . . 139
6.3.1 Jets . . . 139
6.3.2 Electrons . . . 140
6.3.3 Muons . . . 140
6.3.4 τ jets . . . 140
6.3.5 B-Tagging . . . 141
6.3.6 Overlap removal . . . 141
6.3.7 Event cleaning . . . 142
Good Run List . . . 142
Corrupted data . . . 142
Vertex Requirement . . . 142
6.3.8 Particle level objects definition . . . 142
6.3.9 Parton level objects definition . . . 143
6.4 Topology-based event preselection . . . 143
6.5 $t\bar{t}$ system reconstruction . . . 144
6.6 Event selection . . . 146
6.7 Background determination . . . 148
6.7.1 Monte Carlo-based background estimation . . . 149
6.7.2 Data-driven multi-jet QCD background estimation . . . 150
6.8 Reconstructed level results . . . 153

7 Unfolding strategy **162**
7.1 The unfolding problem . . . 162
7.2 The iterative D'Agostini unfolding technique . . . 163
7.3 Unfolding procedure . . . 165
7.4 Unfolding validation . . . 168
7.4.1 Closure tests . . . 168
7.4.2 Stress tests . . . 168
7.4.3 Test on the number of iterations . . . 170

8 Systematic uncertainties **172**
8.1 Detector uncertainties . . . 172
8.1.1 Jet reconstruction . . . 173
8.1.2 b-tagging . . . 173
8.1.3 Lepton reconstruction . . . 173
8.1.4 τ reconstruction . . . 174
8.1.5 E_T^{miss} reconstruction . . . 174
8.2 Modelling uncertainties . . . 174
8.2.1 Matrix element and parton shower models . . . 174
8.2.2 Initial and Final State Radiation . . . 175
8.2.3 PDF . . . 175
8.2.4 MC sample finite statistics . . . 176
8.3 Background uncertainties . . . 176
8.3.1 $t\bar{t}$ normalization . . . 176
8.3.2 Data-driven multi-jet estimation . . . 176
8.4 Luminosity uncertainties . . . 177

8.5 Uncertainties affecting the measurement . . . 177
8.5.1 Systematics breakdown, particle level . . . 177
8.5.2 Systematics breakdown, parton level . . . 188

9 Results **192**
9.1 Unfolded distributions . . . 192
9.1.1 Particle level unfolded distributions . . . 192
9.1.2 Parton level unfolded distributions . . . 203
9.2 χ^2 evaluation . . . 203

Conclusions **210**

A Stability of the $t\bar{t}$ reconstruction method **212**

B Implementation of the χ^2 minimization algorithm **217**

C Cutflows for data and MC-estimated processes **226**

D Systematic uncertainties breakdown tables **232**
D.1 Absolute cross sections, unfolded to particle level . . . 232
D.2 Relative cross sections, unfolded to particle level . . . 252
D.3 Absolute cross sections, unfolded to parton level . . . 252
D.4 Relative cross sections, unfolded to parton level . . . 260

E Unfolding corrections **268**
E.1 Corrections at particle level . . . 268
E.2 Corrections at parton level . . . 288

F Unfolding stability tests **294**
F.1 Closure tests . . . 294
F.1.1 Closure, particle level . . . 294
F.1.2 Closure, parton level . . . 300
F.2 Stress tests . . . 301
F.2.1 Stress test, particle level . . . 301
F.2.2 Stress test, parton level . . . 321
F.3 Unfolding iterations stability checks . . . 329

G Covariance matrices **339**

Bibliography **347**

List of Figures

1.1 Properties of fundamental particles in the SM framework. Values are taken from [9] . . . 3
1.2 Comparison of the values of $\alpha_s(Q)$ obtained from fits to the TEEC [15] functions (red star points) with the uncertainty band from the global fit (orange full band) and the 2016 world average (green hatched band). Determinations from other measurements from DØ and CMS experiments are also shown. The error bars include all experimental and theoretical sources of uncertainty. . . . 6
1.3 The Higgs potential $\mu^2\Phi^\dagger\Phi - \lambda[\Phi^\dagger\Phi]^2$ for $\lambda > 0$. In case (a), no degeneration of the ground state occurs; in case (b), a degenerate circle of minimum potential exists and an arbitrary choice for the ground state can be made. . . . 10
1.4 Schematic representation of the Factorization Theorem for hadron-hadron cross section. . . . 11
1.5 NNLO PDFs from the MMHT14 set evaluated at $Q^2 = 10$ GeV (a) and $Q^2 = 10^4$ GeV (b). The associated solid bands represent the 68% confidence-level uncertainties. The Figures has been taken from [28] . . . 13
1.6 Summary of the ATLAS and CMS direct m_t measurements. The results are compared with the LHC and Tevatron+LHC m_t combinations. For each measurement, the statistical uncertainty and the sum in quadrature of the statistical and systematic uncertainties are shown. The results below the solid black line have been produced after the LHC and Tevatron+LHC combinations were performed. Figure taken from [41]. . . . 16
1.7 Summary of measured W helicity fractions by ATLAS and CMS at 7 and 8 TeV, compared to the respective theory predictions. The uncertainty on the theory predictions is shown by a green band, the total experimental uncetainties are given by the sum in quadrature of the statisical and systematic ones. Figure taken from [41] . . . 18
1.8 Pie charts showing the Branching Ratios of the single top quark (a) and top-antitop quark pair production (b). Data is taken from [9]. 19
1.9 Feynman diagrams for the single top quark decay modes (a), $t\bar{t}$ completely hadronic (b), semileptonic (c) and dileptonic (d). 19

1.10 Feynman diagrams for the top-antitop quark pair production at Leding Order of perturbation expansion: gluon-gluon fusion (a) in the t (left), u (center) and s (right) channels and quark-antiquark annihilation (b). 20
1.11 Selection of feynman diagrams for the top-antitop quark pair production at NLO of perturbation expansion: real quark emission (a), virtual loop correction (b), qg interaction (c) and $\bar{q}g$ interaction (d). 21
1.12 Summary of LHC and Tevatron measurements of the top-pair production cross section as a function of the center of mass energy compared to the NNLO+NNLL QCD calculations at $m_t = 172.5$ GeV. The theory band represents uncertainties due to renormalisation and factorisation scale, parton density functions and the strong coupling. Figure taken from [41]. 22
1.13 Summary of the charge asymmetry measurements on ATLAS and CMS at 8 TeV showing both the inclusive measurements and the measurement using boosted events, compared to the respective theory predictions. Figure taken from [41]. 22
1.14 Feynman diagrams for the single top quark production at LO of perturbation expansion: association production with a real W (a), t-channel (b) and s-channel (c). 24
1.15 Summary of ATLAS and CMS measurements of the single top quark production cross sections in various channels as a function of the center of mass energy. The measurements are compared to theoretical calculations based on: NLO QCD, NLO QCD complemented with NNLL resummation and NNLO QCD (t-channel only). Figure taken from [41] 24

2.1 Bird's-eye view of the LHC accelerator complex and its experiments. 25
2.2 Cumulative luminosity versus time delivered to (green) and recorded by ATLAS (yellow) during stable beams for *pp* collisions at 7 TeV center of mass energy in 2010 (a) and 2011 (b), at 8 TeV center of mass energy in 2012 (c) and at $\sqrt{s} = 13$ TeV in 2015 (d), 2016 (e), 2017 (f) and 2018 (g). The delivered luminosity accounts for luminosity delivered from the start of stable beams until the LHC requests ATLAS to put the detector in a safe standby mode to allow for a beam dump or beam studies. Figures taken from [53, 54]. 27
2.3 Scheme of a cryodipole superconducting magnet at the LHC. Figure taken from [8]. 28
2.4 Scheme of a four-cavity cryomodule at the LHC. Figure taken from [8]. 28
2.5 The CERN accelerator complex. The four yellow dots along the LHC rings correspond to the four interacting points where the major experiments are collocated. Figure taken from [55]. . 29

2.6 Schematic representation of the WLCG tiers. Dedicated "dark-fiber" connections between CERN and each of the Tier 1 sites were implemented to ensure the necessary data rates. These connections are supplemented with secondary connections to ensure reliability of the network. Connectivity between Tier 1 and Tier 2 sites is provided by national and international academic and research network infrastructures. Figure taken from [65]. 31
2.7 Schematic overview of the ATLAS detector and its subdetectors. Figure taken from [66]. 34
2.8 Illustration of the ATLAS Detector oriented in the global coordinate system. Figure taken from [67]. 35
2.9 Layout of the ATLAS magnet system. Figure extracted and adapted from [68]. 36
2.10 Cut-away view of the ATLAS ID during Run 1. The IBL is not shown since it has been installed during Run 2. Figure taken from [57]. 37
2.11 Sketch of the ATLAS inner detector showing all its components, including the new insertable B-layer (IBL). The distances to the interaction point are also shown. Figure taken from [69]. 37
2.12 Cut-away view of the ATLAS calorimeter system. Figure taken from [57]. 39
2.13 Photograph of a partly stacked barrel electromagnetic LAr module. The acccordion structure is clearly visible. Photograph taken from [57]. 40
2.14 Cut-away view of the ATLAS muon spectrometer. Figure taken from [57]. 41
2.15 Schematic view of the forward ATLAS detectors. Their placement along the beam-line around the ATLAS IP in also shown. Figure taken from [57]. 43
2.16 Diagram of the ATLAS Trigger and Data Acquisition system in Run 2 showing expected peak rates and bandwidths through each component. Figure taken from [71]. 44
2.17 Trigger efficiency curves as a function of the 6th jet transverse momentum, for different values of the maximum allowed η of the jets. In particular, the η_{cut} values are 2.0 (a), 2.1 (b), 2.2 (c), 2.3 (d) and 2.4 (e). These are computed in data and for a ttbar MC sample, selecting events with two b-tagged jets. 48
2.18 Trigger efficiency curves as a function of the 6th jet transverse momentum, for different values of the maximum allowed η of the jets. In particular, the η_{cut} values are 2.0 (a), 2.1 (b), 2.2 (c), 2.3 (d) and 2.4 (e). These are computed in data and for a ttbar MC sample, selecting events with zero b-tagged jets. 49

3.1 Timeline for planned LHC upgrades. Figure taken from [73]. . 51

3.2 (a): Schematic representation of the ITk *Inclined Duals* layout. Only one quadrant and only active detector elements are shown. The active elements of the barrel and end-cap Strip Detector are shown in blue, for the Pixel Detector the sensors are shown in red for the barrel layers and in dark red for the end-cap rings. The horizontal axis is along the beam line with zero being the interaction point. (b): Cut-away view of the ITk *Inclined Layout* Geant4 [86] geometry model. The Figures have been taken from [80]. 54
3.3 Radiation lenght X_0 versus η for the current ID (a) and *Inclined Duals* ITk (b), . Only positive η are shown due to detector symmetry. The Figures have been taken from [80]. 55
3.4 (a): Track reconstruction efficiency for a top-pair sample with an average of 200 pile up events. Overlaid are the results for the current Run 2 detector. (b): Fake rate for reconstructed tracks in $t\bar{t}$ events with $< \mu >= 200$ using the truth particle matching criterion P_{match}. ITk is compared to the Run 2 detector results for two different levels of track selection. The Figures have been taken from [80]. 56
3.5 Track parameter resolution in d_0 (a), z_0 (b) and p_T (c) as a function of η for the *Inclined Duals* ITk layout. Results are shown for single muons with p_T of 1, 10 and 100 GeV. Performance results from Run 2 ID are shown for comparison. The Figures have been taken from [80]. 57
3.6 The primary vertex reconstruction (a) and identification (b) efficiency for $t\bar{t}$ and vector boson fusion $H \rightarrow \nu\nu\nu\nu$ interactions as a function of local pile up density in events with an average pile up of 200. The vertex identification is done using the Σp_T^2 criterion. The dotted lines on the right plot indicate the rate of events for the ITk where the true primary interaction vertex actually has the highest true Σp_T^2. Shown as well are results for a Run 2 simulation sample using the Run 2 primary vertex reconstruction code. The Figures have been taken from [80]. . 58
3.7 z_0 resolution as a function of η for different p_T values. Figure taken from [83]. 59
3.8 The rejection of pile up jets as a function of the efficiency for hard-scatter jets with $20 < p_T < 40$ GeV (a) and $p_T > 40$ GeV (b) using the R_{p_T} discriminant in di-jet events with an average of 200 pile up events. The Figures have been taken from [80]. . . 60
3.9 The resolutions of E_T^{miss} in Monte Carlo $t\bar{t}$ events with an average of 200 pile up events. The resolutions are shown as a function of the local pile up vertex density around the hard-scatter vertex, for three different ETmiss definitions. The first (blue) considers only tracks in the region $|\eta| < 2.5$ for both pile up jet rejection and ETmiss soft term. The second (red) uses hard tracks up $|\eta|$ of 4. The third (black) uses tracks up to $|\eta| < 4.0$. Figure taken from [80]. 62

3.10 Exploded view of the various components of the HGTD, excluding the cooling plates. Figure taken from [83]. 63
3.11 Efficiencies for matching tracks to at least one pixel in the HGTD in single pion events (a) and for correctly reconstructing the time of a track in simulated VBF events with $< \mu >= 200$ (b). An exponential fit is performed on the points and the parameters of the fit are shown. The Figures have been taken from [83]. 64
3.12 (a): View in the Rz plane of the tracks associated to the primary vertices in a simulated VBF event at $< \mu >= 200$. The distribution of tracks associated to the hard-scatter vertex as a function of reconstructed times and z position is shown in (b). For convenience, the projections on z and t are presented in (c) and (d), respectively. The Figures have been taken from [83]. . 65
3.13 Pile up jet rejection as a function of hard-scatter jet efficiency in the $2.4 < |\eta| < 4.0$ region for jets with $30 < p_T < 50$ GeV (a) and $p_T > 50$ GeV (b) and hard-scatter jet efficiency versus $|\eta|$ for a 2% pile up jet efficiency rejection for jets with $30 < p_T < 50$ GeV (c) and $p_T > 50$ GeV (d). The curves refer to the ITk-only and ITk + HGTD scenarios with different time resolutions. The results have been obtained for di-jet simulated Monte Carlo events. The Figures have been taken from [83]. . 67

4.1 Schematic representation of a hadron-hadron collision as simulated by a MC event generator. The red blob in the center represents the hard collision, surrounded by a tree-like structure representing Bremsstrahlung as simulated by parton showers. The purple blob indicates a secondary hard scattering event. Parton-to-hadron transitions are represented by light green blobs, dark green blobs indicate hadron decays, while yellow lines signal soft photon radiation. Figure taken from [93]. 69
4.2 Schematic representation of parton shower. Figure extracted from Figure 4.1. 72
4.3 Schematic representation of parton shower in the dipole approach. Figure taken from [94]. 73
4.4 Schematic representation of string (a) and cluster (b) hadronization models. The Figures has been taken from [4]. 75
4.5 (a): Graphical representation of a colour flux tube between a quark and an antiquark. (b): Example of motion and breakup of a monodimensional string system. Diagonal lines represent (anti)quarks, horizontal lines are instantaneous representations of the string fiels. The Figures have been taken from [94]. 75
4.6 Invariant mass distribution of colour-singlet clusters at different center of mass energy Q obtained with the Herwig event generator. The Figure has been taken from [94]. 77

4.7 Overview of the ATLAS simulation software, from event generators (top left) through reconstruction (top right). Algorithms are placed in square-cornered boxes and persistent data objects are placed in rounded boxes. The optional pile up portion of the chain, used only when events are overlaid, is dashed. Generators are used to produce data in HepMC format. Monte Carlo truth is saved in addition to energy depositions in the detector (hits). This truth is merged into Simulated Data Objects (SDOs) during the digitization. Also, during the digitization stage, Read Out Driver (ROD) electronics are simulated. The Figure has been taken from [117]. 81
4.8 Geant4 models of the ATLAS detector showing a cut-away view of the ID and the calorimetry system (a) and the outer muon chambers (b). The Figures have been taken from [120] and [117], respectively. 82
4.9 Distributions of CPU time for 250 $t\bar{t}$ events in full, Fast G4, and ATLFAST-II simulations. Vertical dotted lines denote the averages of the distributions. The Figure has been taken from [117]. 83
4.10 Fast simulations (color) and full simulation (black) comparison of missing transverse energy along the x-axis in di-jet events with a leading parton pT between 560 and 1120 GeV (a) and of jet p_T resolution as a function of pseudorapidity in $t\bar{t}$ events for jets with $20 < p_T^{true} < 40$ GeV (b). The Figures have been taken from [117]. 84

5.1 Sketch of the flow of tracks through the ambiguity solver. Figure taken from [138]. 90
5.2 The average number of primary tracks per unit of angular area as a function of the angular distance from the jet axis. Data (dashed lines) and dijet MC (solid lines) samples are compared in bins of jet pT showing the high density in the cores of energetic jets. Figure taken from [138]. 91
5.3 The average number of shared pixel (a) and SCT (b) clusters on primary tracks are shown as a function of the angular distance of the track from the jet axis. Data (dashed lines) and dijet MC (solid lines) samples are compared in bins of jet pT. The rise in both populations at small distances from the jet axis is expected due to the increasingly dense environment. The Figures have been taken from [138]. 92
5.4 Single-track reconstruction efficiency is shown as (a) a function of the initial particle's p_T when it is required that the parent particle decays before the IBL for the decay products of a ρ, three- and five-prong τ and a B^0 and (b) versus the production radius for the decay products of a three- and five-prong τ as well as a B^0, where no requirement in imposed on the production radius of stable charged particles. The Figures have been taken from [138]. 92

5.5 The efficiency to reconstruct charged primary particles in jets with (a) $|\eta| < 1.2$ and (b) $|\eta| > 1.2$ is shown as a function of the angular distance of the particle from the jet axis for various jet p_T for simulated dijet MC events. The Figures have been taken from [138]. 93
5.6 Contributions to the predicted primary vertex reconstruction efficiency as a function of the average number of interactions per bunch crossing, μ for the Higgs-boson decay into $\gamma\gamma$ (a), $t\bar{t}$ pair production leptonically decaying (b) and Z-boson to $\mu\mu$ decay (c). The black circles show the contribution to the efficiency from events categorised as clean, and the blue and red circles show the contributions from events with low and high pile-up contamination respectively. The open crosses show the sum of the contributions from events that are clean and those with low pile-up contamination; the filled crosses show the sum of the contributions from all categories and represent the overall efficiency, as shown in (d). The Figures have been taken from [144]. 96
5.7 (a): the distributions of the sum of the squared transverse momentum for tracks from primary vertices, shown for simulated hard-scatter processes and a minimum-bias sample. (b): efficiency to reconstruct and then select the hard-scatter primary vertex as a function of μ, for different physics processes. The Figures have been taken from [144]. 97
5.8 Distribution of the average number of reconstructed vertices as a function of μ. (a): MC simulation of minimum-bias events (triangles) and the analytical function in Equation 5.2 fit to the simulation (solid line). The dashed curve shows the average estimated number of vertices lost to merging. (b): minimum-bias data (black points). The curve represents the result of the fit to the simulation after applying the μ-rescaling correction. The inner dark (blue) band shows the systematic uncertainty in the fit from the beam-spot length, while the outer light (green) band shows the total uncertainty in the fit. The panels at the bottom of each figure represent the respective ratios of simulation or data to the fits described in the text. The Figures have been taken from [144]. 98
5.9 Schematic representation of the photon identification discriminating variables. $E_C^{S_N}$ identifies the electromagnetic energy collected in the N-th longitudinal layer of the electromagnetic calorimeter in a cluster of properties C, identifying the number and/or properties of selected cells. E_i is the energy in the i-th cell, η_i the pseudorapidity center of that cell. Figure taken from [156]. 101

5.10 Comparison of the data-driven measurements of the identification efficiency for converted (a) and unconverted (b) photons as a function of E_T, for the $|\eta| < 0.6$ pseudorapidity interval. The error bars represent the sum in quadrature of the statistical and systematic uncertainties estimated in each method. The shaded areas correspond to the statistical uncertainties. The Figures have been taken from [149]. 103
5.11 Comparison of the measurements of the data-driven identification efficiency for converted (a) and unconverted (b) photons measurements obtained using the radiative Z method with the predictions from $Z \to ll\gamma$ simulation as a function of photon E_T, for the $|\eta| < 0.6$ pseudorapidity interval. Predictions are shown for both the nominal simulation and with the corrections applied. The bottom panels show the ratio of the data-driven values to the MC predictions. The Figures have been taken from [149]. 104
5.12 Comparison of the measurements of the data-driven identification efficiency for converted (a) and unconverted (b) photons obtained using the electron extrapolation and inclusive photon methods with the predictions from prompt-photon+jet simulation as a function of photon E_T, for the $|\eta| < 0.6$ pseudorapidity interval. Predictions are shown for both the nominal simulation and with the corrections applied. The bottom panels show the ratio of the data-driven values to the MC predictions. The Figures have been taken from [149]. 104
5.13 Efficiency scale factors (SF) for each method and their combination for converted (a) and unconverted (b) photons, for the $|\eta| < 0.6$ pseudorapidity interval. The Figures have been taken from [149]. 105
5.14 The efficiency to identify electrons from $Z \to ee$ decays (a) and the efficiency to identify hadrons as electrons (background rejection) (b) estimated using simulated di-jet samples. The efficiencies are obtained using Monte Carlo simulations, and are measured with respect to reconstructed electrons. The Figures have been taken from [161]. 106
5.15 Combined electron reconstruction and identification efficiencies in $Z \to ee$ events as a function of E_T, integrated over the full pseudorapidity range (a), and as a function of η, integrated over the full E_T range (b). Two sets of uncertainties are shown: the inner error bars show the statistical uncertainty, the outer error bars show the combined statistical and systematic uncertainty. The Figures have been taken from [161]. 108

5.16 Muon reconstruction efficiency as a function of η measured in $Z \to \mu\mu$ events for muons with $p_T > 10$ GeV shown for the *Medium* muon selection for the *Loose* selection (squares) in the region $|\eta| < 0.1$, where the *Loose* and *Medium* selections differ significantly (a), for the *Tight* muon selection (b) and for the *High-*p_T uon selection (c). The error bars on the efficiencies indicate the statistical uncertainty. Panels at the bottom show the ratio of the measured to predicted efficiencies, with statistical and systematic uncertainties. The Figures have been taken from [164]. 111
5.17 Tau identification efficiency scale factors for one track and three track τ had-vis candidates with $p_T > 20$ GeV. The combined systematic and statistical uncertainties are shown. Figure taken from [167]. 114
5.18 Calibration stages for EM-scale jets. Other than the origin correction, each stage of the calibration is applied to the four-momentum of the jet. Figure taken from [174]. 115
5.19 Combined uncertainty in the JES of fully calibrated jets as a function of jet p_T at $\eta = 0$ (a) and η at $p_T = 80$ GeV (b). The Figures have been taken from [177]. 119
5.20 (a): The MV2c10 output for b-jets (solid line), c-jets (dashed line) and light-flavour jets (dotted line) in simulated $t\bar{t}$ events. (b): The light-flavour jet (dashed line) and c-jet rejection factors (solid line) as a function of the b-jet tagging efficiency of the MV2c10 b-tagging algorithm. The Figures have been taken from [179]. 121
5.21 The light-flavour jet (squares) and c-jet rejection factors (triangles) at a b-tagging efficiency of 70% single-cut OP (a) and flat-efficiency OP (b) as a function of the jet p_T for the MV2c10 b-tagging algorithms in $t\bar{t}$ events. The Figures have been taken from [179]. 122
5.22 The b-jet tagging efficiency measured in data (full circles) and simulation (open circles), corresponding to the 70% b-jet tagging efficiency single-cut OP, as a function of the jet p_T using the T&P (a) and the LH method (b), for R=0.4 calorimeter-jets. The error bars correspond to the total statistical and systematic uncertainties. The Figures have been taken from [179]. 124
5.23 Data-to-simulation scale factors, corresponding to the 70% b-jet tagging efficiency single-cut OP, as a function of the jet $|\eta|$ using the T&P (a) and the LH method (b) for R=0.4 calorimeter-jets. Both the statistical uncertainties (error bars) and total uncertainties (shaded region) are shown. The Figures have been taken from [179]. 124
5.24 Fake rate from pile up jets versus hard-scatter jet efficiency curves for JVF, corrJVF, R_{pT}, and JVT. The widely used JVF working points with cut values 0.25 and 0.5 are indicated with gold and green stars. Figure taken from [183]. 128

5.25 Distributions of the E_T^{miss} resolution versus N_{PV} for E_T^{miss} built with three different forward jet selections in a $Z \to \mu\mu$ (a) and VBF $H \to WW$ (b) simulation. The Figures have been taken from [187]. 130
5.26 Sketch of the track-based soft term projections with respect to p_T^{hard} for the calculation of the TST systematic uncertainties. Figure taken from [187]. 131
5.27 Parallel resolution plots for the EMTopo TST for the jet-inclusive (a) and jet-veto (b) selections. Analougously, the resoluton plots for the PFlow TST are shown in (c) and (d), respectively. The pink band, centered on data, represents the resulting systematic uncertainty applied to the $Z \to ee$ MC simulation. The Figures have been taken from [187]. 132
5.28 The RMS obtained from the combined distributions of EMTopo E_x^{miss} and E_y^{miss} for data with EMTopo jets (circular marker) and PFlow jets (triangular marker) and MC simulation with EMTopo jets (square marker) in a $Z \to ee$ event selection. The resolutions are shown using the Loose E_T^{miss} WP are shown versus $< \mu >$ (a) and N_{PV} (b). The same distributions for the Tight E_T^{miss} WP are shown in (c) and (d), respectively. The pink band indicates the size of the detector level systematic uncertainties. The Figures have been taken from [187]. 133

6.1 Pictorical representation of a top-antitop quark pair decaying into the *fully hadronic* channel. The red blob in the center represents the hard-scatter collision. Light-quark (b-quark) initiated jets are represented by purple (yellow) cones. 136
6.2 Mass spectra at detector level of the W boson (a) and top quark (c), determined from parton-matched jets. The particle level results are shown in (b) and (d), respectively. The fitted gaussian is shown in red, with the peak and width parameters shown. . 146
6.3 Distributions of observables used for background rejection, shown in data, non all hadronic $t\bar{t}$ and signal for events preselected as in Section 6.4. The variables shown are the χ^2 discriminant 6.3a, ΔR_{bb} (b), ΔR_{bW}^{max} (c) and m_{top} (d), filled for both top quark candidates in each event. Cut values are indicated by red dashed lines. 147
6.4 Distributions of observables used for background rejection, shown in data, non all hadronic $t\bar{t}$ and signal with all selection cuts applied with the exception of the cut on the variable being shown. The variables shown are the χ^2 discriminant (a), ΔR_{bb} (b), ΔR_{bW}^{max} (c) and m_{top} (d), filled for both top quark candidates in each event. Cut values are indicated by red dashed lines. . . . 148
6.5 MC-subtracted data distribution of m_t in exclusive n_{b-jets} regions. All other selection criteria are applied. 151

6.6 Reconstructed level distribution in the signal regions as a function of $\sigma_{t\bar{t}}$. The signal prediction (open histogram) is based on the Powheg+Pythia8 generator. The background is the sum of the data-driven multijet estimate (purple histogram) and the MC-based expectation for the contributions of non all-hadronic $t\bar{t}$ production process (light blue histogram). The shaded area represents the total statistical and systematic uncertainties. 154
6.7 Reconstructed level distributions in the signal regions as a function of p_T^{top1} for particle (a) and parton level (b) optimized binning and as a function of p_T^{top2} for particle (c) and parton level (d) optimized binning. The signal prediction (open histogram) is based on the Powheg+Pythia8 generator. The background is the sum of the data-driven multijet estimate (purple histogram) and the MC-based expectation for the contributions of non all-hadronic $t\bar{t}$ production process (light blue histogram). The shaded area represents the total statistical and systematic uncertainties. 155
6.8 Reconstructed level distributions in the signal regions as a function of y_{top1} for particle (a) and parton level (b) optimized binning and as a function of y_{top2} for particle (c) and parton level (d) optimized binning. The signal prediction (open histogram) is based on the Powheg+Pythia8 generator. The background is the sum of the data-driven multijet estimate (purple histogram) and the MC-based expectation for the contributions of non all-hadronic $t\bar{t}$ production process (light blue histogram). The shaded area represents the total statistical and systematic uncertainties. 156
6.9 Reconstructed level distributions in the signal regions as a function of $p_T^{t\bar{t}}$ for particle (a) and parton level (b) optimized binning and as a function of $y_{t\bar{t}}$ for particle (c) and parton level (d) optimized binning. The signal prediction (open histogram) is based on the Powheg+Pythia8 generator. The background is the sum of the data-driven multijet estimate (purple histogram) and the MC-based expectation for the contributions of non all-hadronic $t\bar{t}$ production process (light blue histogram). The shaded area represents the total statistical and systematic uncertainties. 157
6.10 Reconstructed level distributions in the signal regions as a function of $m_{t\bar{t}}$ for particle (a) and parton level (b) optimized binning. The signal prediction (open histogram) is based on the Powheg+Pythia8 generator. The background is the sum of the data-driven multijet estimate (purple histogram) and the MC-based expectation for the contributions of non all-hadronic $t\bar{t}$ production process (light blue histogram). The shaded area represents the total statistical and systematic uncertainties. 158

6.11 Reconstructed level distributions in the signal regions as a function of N_{jets} (a), $\Delta\phi_{t\bar{t}}$ (b), $|P_{\text{out}}^{t\bar{t}}|$ (c) and $H_{\text{T}}^{t\bar{t}}$ (d). The signal prediction (open histogram) is based on the Powheg+Pythia8 generator. The background is the sum of the data-driven multijet estimate (purple histogram) and the MC-based expectation for the contributions of non all-hadronic $t\bar{t}$ production process (light blue histogram). The shaded area represents the total statistical and systematic uncertainties. 159

6.12 Reconstructed level distributions in the signal regions as a function of R_{b1}^{W} (a), R_{b2}^{W} (b), R_{t1}^{W} (c) and R_{t2}^{W} (d). The signal prediction (open histogram) is based on the Powheg+Pythia8 generator. The background is the sum of the data-driven multijet estimate (purple histogram) and the MC-based expectation for the contributions of non all-hadronic $t\bar{t}$ production process (light blue histogram). The shaded area represents the total statistical and systematic uncertainties. . . 160

6.13 Reconstructed level distributions in the signal regions as a function of $\Delta R_{\text{top}}^{\text{extra1}}$ (a), $\Delta R_{\text{jet1}}^{\text{extra1}}$ (b), $R_{\text{top1}}^{\text{extra1}}$ (c) and $R_{\text{jet1}}^{\text{extra1}}$ (d). The signal prediction (open histogram) is based on the Powheg+Pythia8 generator. The background is the sum of the data-driven multijet estimate (purple histogram) and the MC-based expectation for the contributions of non all-hadronic $t\bar{t}$ production process (light blue histogram). The shaded area represents the total statistical and systematic uncertainties. 161

7.1 The acceptance and efficiency corrections for the p_T^{top1} spectrum at particle ((a) and (b), respectively) and parton level ((c) and (d), respectively). The corrections are obtained from the nominal fully hadronic $t\bar{t}$ MC sample. 166

7.2 The migration matrices from reconstruction to particle (a) and reconstruction to parton levels (b) for the p_T^{top1} spectrum. The corrections are obtained from the nominal fully hadronic $t\bar{t}$ MC sample. 167

7.3 Unfolding to particle (a) and parton (b) level closure test of the differential cross section as a function of p_T^{top1}; the observable is normalised in the fiducial phase-space. The shaded area represents the statistical uncertainty. 168

7.4 Linearity stress test using for the normalised cross section as a function of p_T^{top1}. The stress is achieve by re-weigthing the input distribution (red line) by a factor proportional to the data/MC difference. The particle level results have used a factor of 1 (a) or 5 (b). The corresponding parton level results are shown in (c) and (d), respectively. 169

7.5 χ^2 (a) between the unfolded result and the prior of the $i-th$ iteration of unfolding to particle level as a function of the N_{iter} for p_T^{top1}. Figures (b), (c) and (d) show the statistical error, the residuals (w.r.t. previous iteration) and their ratio for the fifth bin of p_T^{top1}, respectively. 171

8.1 Fractional uncertainties in the fiducial phase space as a function of $|P_{\text{out}}^{t\bar{t}}|$: absolute (a) and normalised (b). The shaded area represents the total statistical and systematic uncertainties. 178

8.2 Fractional uncertainties in the fiducial phase space as a function of $\Delta\phi_{t\bar{t}}$: absolute (a) and normalised (b). The shaded area represents the total statistical and systematic uncertainties. 178
8.3 Fractional uncertainties in the fiducial phase space as a function of $\Delta R_{\mathrm{jet1}}^{\mathrm{extra1}}$: absolute (a) and normalised (b). The shaded area represents the total statistical and systematic uncertainties. 179
8.4 Fractional uncertainties in the fiducial phase space as a function of $\Delta R_{\mathrm{topclose}}^{\mathrm{extra1}}$: absolute (a) and normalised (b). The shaded area represents the total statistical and systematic uncertainties. 179
8.5 Fractional uncertainties in the fiducial phase space as a function of $H_{\mathrm{T}}^{t\bar{t}}$: absolute (a) and normalised (b). The shaded area represents the total statistical and systematic uncertainties. 180
8.6 Fractional uncertainties in the fiducial phase space as a function of number of jets: absolute (a) and normalised (b). The shaded area represents the total statistical and systematic uncertainties. 180
8.7 Fractional uncertainties in the fiducial phase space as a function of $R_{\mathrm{jet1}}^{\mathrm{extra1}}$: absolute (a) and normalised (b). The shaded area represents the total statistical and systematic uncertainties. 181
8.8 Fractional uncertainties in the fiducial phase space as a function of $R_{\mathrm{top1}}^{\mathrm{extra1}}$: absolute (a) and normalised (b). The shaded area represents the total statistical and systematic uncertainties. 181
8.9 Fractional uncertainties in the fiducial phase space as a function of $R_{Wb}^{leading}$: absolute (a) and normalised (b). The shaded area represents the total statistical and systematic uncertainties. 182
8.10 Fractional uncertainties in the fiducial phase space as a function of $R_{Wb}^{subleading}$: absolute (a) and normalised (b). The shaded area represents the total statistical and systematic uncertainties. 182
8.11 Fractional uncertainties in the fiducial phase space as a function of $R_{Wt}^{leading}$: absolute (a) and normalised (b). The shaded area represents the total statistical and systematic uncertainties. 183
8.12 Fractional uncertainties in the fiducial phase space as a function of $R_{Wt}^{subleading}$: absolute (a) and normalised (b). The shaded area represents the total statistical and systematic uncertainties. 183
8.13 Fractional uncertainties in the fiducial phase space as a function of p_T^{top1}: absolute (a) and normalised (b). The shaded area represents the total statistical and systematic uncertainties. 184
8.14 Fractional uncertainties in the fiducial phase space as a function of y_{top1}: absolute (a) and normalised (b). The shaded area represents the total statistical and systematic uncertainties. 184
8.15 Fractional uncertainties in the fiducial phase space as a function of p_T^{top2}: absolute (a) and normalised (b). The shaded area represents the total statistical and systematic uncertainties. 185
8.16 Fractional uncertainties in the fiducial phase space as a function of y_{top2}: absolute (a) and normalised (b). The shaded area represents the total statistical and systematic uncertainties. 185

8.17 Fractional uncertainties in the fiducial phase space as a function of $m_{t\bar{t}}$: absolute (a) and normalised (b). The shaded area represents the total statistical and systematic uncertainties. 186
8.18 Fractional uncertainties in the fiducial phase space as a function of $p_T^{t\bar{t}}$: absolute (a) and normalised (b). The shaded area represents the total statistical and systematic uncertainties. 186
8.19 Fractional uncertainties in the fiducial phase space as a function of $y_{t\bar{t}}$: absolute (a) and normalised (b). The shaded area represents the total statistical and systematic uncertainties. 187
8.20 Fractional uncertainties in the full phase space as a function of p_T^{top1}: absolute (a) and normalised (b). The shaded area represents the total statistical and systematic uncertainties. 188
8.21 Fractional uncertainties in the full phase space as a function of y_{top1}: absolute (a) and normalised (b). The shaded area represents the total statistical and systematic uncertainties. 188
8.22 Fractional uncertainties in the full phase space as a function of p_T^{top2}: absolute (a) and normalised (b). The shaded area represents the total statistical and systematic uncertainties. 189
8.23 Fractional uncertainties in the full phase space as a function of y_{top2}: absolute (a) and normalised (b). The shaded area represents the total statistical and systematic uncertainties. 189
8.24 Fractional uncertainties in the full phase space as a function of $m_{t\bar{t}}$: absolute (a) and normalised (b). The shaded area represents the total statistical and systematic uncertainties. 190
8.25 Fractional uncertainties in the full phase space as a function of $p_T^{t\bar{t}}$: absolute (a) and normalised (b). The shaded area represents the total statistical and systematic uncertainties. 190
8.26 Fractional uncertainties in the full phase space as a function of $y_{t\bar{t}}$: absolute (a) and normalised (b). The shaded area represents the total statistical and systematic uncertainties. 191

9.1 Differential cross sections in the fiducial phase space as a function of $|P_{\mathrm{out}}^{t\bar{t}}|$: absolute (a) and normalised (b). The shaded area represents the total statistical and systematic uncertainties. 193
9.2 Differential cross sections in the fiducial phase space as a function of $\Delta\phi_{t\bar{t}}$: absolute (a) and normalised (b). The shaded area represents the total statistical and systematic uncertainties. 193
9.3 Differential cross sections in the fiducial phase space as a function of $\Delta R_{\mathrm{jet1}}^{\mathrm{extra1}}$: absolute (a) and normalised (b). The shaded area represents the total statistical and systematic uncertainties. 194
9.4 Differential cross sections in the fiducial phase space as a function of $\Delta R_{\mathrm{topclose}}^{\mathrm{extra1}}$: absolute (a) and normalised (b). The shaded area represents the total statistical and systematic uncertainties. 194
9.5 Differential cross sections in the fiducial phase space as a function of $H_{\mathrm{T}}^{t\bar{t}}$: absolute (a) and normalised (b). The shaded area represents the total statistical and systematic uncertainties. 195

9.6 Differential cross sections in the fiducial phase space as a function of number of jets: absolute (a) and normalised (b). The shaded area represents the total statistical and systematic uncertainties. 195
9.7 Differential cross sections in the fiducial phase space as a function of $R_{\mathrm{jet1}}^{\mathrm{extra1}}$: absolute (a) and normalised (b). The shaded area represents the total statistical and systematic uncertainties. 196
9.8 Differential cross sections in the fiducial phase space as a function of $R_{\mathrm{top1}}^{\mathrm{extra1}}$: absolute (a) and normalised (b). The shaded area represents the total statistical and systematic uncertainties. 196
9.9 Differential cross sections in the fiducial phase space as a function of $R_{Wb}^{leading}$: absolute (a) and normalised (b). The shaded area represents the total statistical and systematic uncertainties. 197
9.10 Differential cross sections in the fiducial phase space as a function of $R_{Wb}^{subleading}$: absolute (a) and normalised (b). The shaded area represents the total statistical and systematic uncertainties. 197
9.11 Differential cross sections in the fiducial phase space as a function of $R_{Wt}^{leading}$: absolute (a) and normalised (b). The shaded area represents the total statistical and systematic uncertainties. 198
9.12 Differential cross sections in the fiducial phase space as a function of $R_{Wt}^{subleading}$: absolute (a) and normalised (b). The shaded area represents the total statistical and systematic uncertainties. 198
9.13 Differential cross sections in the fiducial phase space as a function of p_T^{top1}: absolute (a) and normalised (b). The shaded area represents the total statistical and systematic uncertainties. 199
9.14 Differential cross sections in the fiducial phase space as a function of y_{top1}: absolute (a) and normalised (b). The shaded area represents the total statistical and systematic uncertainties. 199
9.15 Differential cross sections in the fiducial phase space as a function of p_T^{top2}: absolute (a) and normalised (b). The shaded area represents the total statistical and systematic uncertainties. 200
9.16 Differential cross sections in the fiducial phase space as a function of y_{top2}: absolute (a) and normalised (b). The shaded area represents the total statistical and systematic uncertainties. 200
9.17 Differential cross sections in the fiducial phase space as a function of $m_{t\bar{t}}$: absolute (a) and normalised (b). The shaded area represents the total statistical and systematic uncertainties. 201
9.18 Differential cross sections in the fiducial phase space as a function of $p_T^{t\bar{t}}$: absolute (a) and normalised (b). The shaded area represents the total statistical and systematic uncertainties. 201
9.19 Differential cross sections in the fiducial phase space as a function of $y_{t\bar{t}}$: absolute (a) and normalised (b). The shaded area represents the total statistical and systematic uncertainties. 202
9.20 Differential cross sections in the full phase space as a function of p_T^{top1}: absolute (a) and normalised (b). The shaded area represents the total statistical and systematic uncertainties. 203

9.21 Differential cross sections in the full phase space as a function of y_{top1}: absolute (a) and normalised (b). The shaded area represents the total statistical and systematic uncertainties. 203
9.22 Differential cross sections in the full phase space as a function of p_T^{top2}: absolute (a) and normalised (b). The shaded area represents the total statistical and systematic uncertainties. 204
9.23 Differential cross sections in the full phase space as a function of y_{top2}: absolute (a) and normalised (b). The shaded area represents the total statistical and systematic uncertainties. 205
9.24 Differential cross sections in the full phase space as a function of $m_{t\bar{t}}$: absolute (a) and normalised (b). The shaded area represents the total statistical and systematic uncertainties. 206
9.25 Differential cross sections in the full phase space as a function of $p_T^{t\bar{t}}$: absolute (a) and normalised (b). The shaded area represents the total statistical and systematic uncertainties. 208
9.26 Differential cross sections in the full phase space as a function of $y_{t\bar{t}}$: absolute (a) and normalised (b). The shaded area represents the total statistical and systematic uncertainties. 209

A.1 Detector- to particle-level migration matrices for the $H_{t\bar{t}}^T$ spectrum in 4 different configuration: using the fitted resolutions at detector and particle level and a fixed χ^2 cut (a), imposing the detector level resolution at particle level with a fixed χ^2 cut (b), using the fitted resolutions at detector and particle level and a flat efficiency χ^2 cut (c), and imposing the detector level resolution at particle level with a flat efficiency χ^2 cut (d). The relative differences are at 1% level. 213
A.2 Detector- to particle-level migration matrices for the $|P_{out}|$ spectrum in 4 different configuration: using the fitted resolutions at detector and particle level and a fixed χ^2 cut (a), imposing the detector level resolution at particle level with a fixed χ^2 cut (b), using the fitted resolutions at detector and particle level and a flat efficiency χ^2 cut (c), and imposing the detector level resolution at particle level with a flat efficiency χ^2 cut (d). The relative differences are at 1% level. 214
A.3 Detector- to particle-level migration matrices for the $p_T^{t\bar{t}}$ spectrum in 4 different configuration: using the fitted resolutions at detector and particle level and a fixed χ^2 cut (a), imposing the detector level resolution at particle level with a fixed χ^2 cut (b), using the fitted resolutions at detector and particle level and a flat efficiency χ^2 cut (c), and imposing the detector level resolution at particle level with a flat efficiency χ^2 cut (d). The relative differences are at 1% level. 215
A.4 Detector- to particle-level migration matrices for the $|y_T^{t\bar{t}}|$ spectrum in 4 different configuration: using the fitted resolutions at detector and particle level and a fixed χ^2 cut (a), imposing the detector level resolution at particle level with a fixed χ^2 cut (b), using the fitted resolutions at detector and particle level and a flat efficiency χ^2 cut (c), and imposing the detector level resolution at particle level with a flat efficiency χ^2 cut (d). The relative differences are at 1% level. 216

E.1 (a) Acceptance correction,(b) efficiency and (c) reconstruction-to-particle-level migration matrix for $|P_{\text{out}}^{t\bar{t}}|$ observable. 269
E.2 (a) Acceptance correction,(b) efficiency and (c) reconstruction-to-particle-level migration matrix for $\Delta\phi_{t\bar{t}}$ observable. 270
E.3 (a) Acceptance correction,(b) efficiency and (c) reconstruction-to-particle-level migration matrix for $\Delta R_{\text{jet1}}^{\text{extra1}}$ observable. 271
E.4 (a) Acceptance correction,(b) efficiency and (c) reconstruction-to-particle-level migration matrix for $\Delta R_{\text{topclose}}^{\text{extra1}}$ observable. 272
E.5 (a) Acceptance correction,(b) efficiency and (c) reconstruction-to-particle-level migration matrix for $H_{\text{T}}^{t\bar{t}}$ observable. 273
E.6 (a) Acceptance correction,(b) efficiency and (c) reconstruction-to-particle-level migration matrix for N. jets observable. 274
E.7 (a) Acceptance correction,(b) efficiency and (c) reconstruction-to-particle-level migration matrix for $R_{\text{jet1}}^{\text{extra1}}$ observable. 275
E.8 (a) Acceptance correction,(b) efficiency and (c) reconstruction-to-particle-level migration matrix for $R_{\text{top1}}^{\text{extra1}}$ observable. 276
E.9 (a) Acceptance correction,(b) efficiency and (c) reconstruction-to-particle-level migration matrix for $R_{Wb}^{leading}$ observable. 277
E.10 (a) Acceptance correction,(b) efficiency and (c) reconstruction-to-particle-level migration matrix for $R_{Wb}^{subleading}$ observable. 278
E.11 (a) Acceptance correction,(b) efficiency and (c) reconstruction-to-particle-level migration matrix for $R_{Wt}^{leading}$ observable. 279
E.12 (a) Acceptance correction,(b) efficiency and (c) reconstruction-to-particle-level migration matrix for $R_{Wt}^{subleading}$ observable. 280
E.13 (a) Acceptance correction,(b) efficiency and (c) reconstruction-to-particle-level migration matrix for p_T^{top1} observable. 281
E.14 (a) Acceptance correction,(b) efficiency and (c) reconstruction-to-particle-level migration matrix for y_{top1} observable. 282
E.15 (a) Acceptance correction,(b) efficiency and (c) reconstruction-to-particle-level migration matrix for p_T^{top2} observable. 283
E.16 (a) Acceptance correction,(b) efficiency and (c) reconstruction-to-particle-level migration matrix for y_{top2} observable. 284
E.17 (a) Acceptance correction,(b) efficiency and (c) reconstruction-to-particle-level migration matrix for $m_{t\bar{t}}$ observable. 285
E.18 (a) Acceptance correction,(b) efficiency and (c) reconstruction-to-particle-level migration matrix for $p_T^{t\bar{t}}$ observable. 286
E.19 (a) Acceptance correction,(b) efficiency and (c) reconstruction-to-particle-level migration matrix for $y_{t\bar{t}}$ observable. 287
E.20 (a) Acceptance correction,(b) efficiency and (c) reconstruction-to-parton-level migration matrix for p_T^{top1} observable. 288
E.21 (a) Acceptance correction,(b) efficiency and (c) reconstruction-to-parton-level migration matrix for y_{top1} observable. 289
E.22 (a) Acceptance correction,(b) efficiency and (c) reconstruction-to-parton-level migration matrix for p_T^{top2} observable. 290
E.23 (a) Acceptance correction,(b) efficiency and (c) reconstruction-to-parton-level migration matrix for y_{top2} observable. 291

E.24 (a) Acceptance correction,(b) efficiency and (c) reconstruction-to-parton-level migration matrix for $p_T^{t\bar{t}}$ observable. 292
E.25 (a) Acceptance correction,(b) efficiency and (c) reconstruction-to-parton-level migration matrix for $y_{t\bar{t}}$ observable. 293

F.1 Unfolding closure of a differential cross-section as a function of p_T^{top1} (a), y_{top1} (b), p_T^{top2} (c) and y_{top2} (d) observables normalised in the fiducial phase-space. The shaded area represents the statistical uncertainty. . 295
F.2 Unfolding closure of a differential cross-section as a function of $p_T^{t\bar{t}}$ (a), $y_{t\bar{t}}$ (b) and $m_{t\bar{t}}$ (c) observables normalised in the fiducial phase-space. The shaded area represents the statistical uncertainty. 296
F.3 Unfolding closure of a differential cross-section as a function of $|P_{\mathrm{out}}^{t\bar{t}}|$ (a), $\Delta\phi_{t\bar{t}}$ (b), $H_{\mathrm{T}}^{t\bar{t}}$ (c) and N_{jets} (d) observables normalised in the fiducial phase-space. The shaded area represents the statistical uncertainty. . 297
F.4 Unfolding closure of a differential cross-section as a function of $\Delta R_{\mathrm{jet1}}^{\mathrm{extra1}}$ (b), $\Delta R_{\mathrm{topclose}}^{\mathrm{extra1}}$ (c), $R_{\mathrm{jet1}}^{\mathrm{extra1}}$ (a) and $R_{\mathrm{top1}}^{\mathrm{extra1}}$ (d) observables normalised in the fiducial phase-space. The shaded area represents the statistical uncertainty. 298
F.5 Unfolding closure of a differential cross-section as a function of $R_{Wb}^{leading}$ (a), $R_{Wb}^{subleading}$ (b), $R_{Wt}^{leading}$ (c) and $R_{Wt}^{subleading}$ (d) observables normalised in the fiducial phase-space. The shaded area represents the statistical uncertainty. 299
F.6 Unfolding closure of a differential cross-section as a function of the $p_T^{t,1}$ (a), $y^{t,1}$ (b), $p_T^{t,2}$ (c) and $y^{t,2}$ (d) observables normalised in the full phase-space. The shaded area represents the statistical uncertainty. . 300
F.7 Unfolding closure of a differential cross-section as a function of the $m^{t\bar{t}}$ (a), $p_T^{t\bar{t}}$ (b) and $y^{t\bar{t}}$ (c) observable normalised in the full phase-space. The shaded area represents the statistical uncertainty. 301
F.8 Linearity stress test using for the normalised cross section as a function of $|P_{\mathrm{out}}^{t\bar{t}}|$. The stress is achieve by re-weigthing the input distribution (red line) by a factor proportional to the data/MC difference. The factors are 1 (top left), 2 (top right), 3 (center left), 4 (center right), 5 (bottom). The efficiency correction has been applied. 302
F.9 Linearity stress test using for the normalised cross section as a function of $\Delta\phi_{t\bar{t}}$. The stress is achieve by re-weigthing the input distribution (red line) by a factor proportional to the data/MC difference. The factors are 1 (top left), 2 (top right), 3 (center left), 4 (center right), 5 (bottom). The efficiency correction has been applied. 303
F.10 Linearity stress test using for the normalised cross section as a function of $\Delta R_{\mathrm{jet1}}^{\mathrm{extra1}}$. The stress is achieve by re-weigthing the input distribution (red line) by a factor proportional to the data/MC difference. The factors are 1 (top left), 2 (top right), 3 (center left), 4 (center right), 5 (bottom). The efficiency correction has been applied. 304
F.11 Linearity stress test using for the normalised cross section as a function of $\Delta R_{\mathrm{topclose}}^{\mathrm{extra1}}$. The stress is achieve by re-weigthing the input distribution (red line) by a factor proportional to the data/MC difference. The factors are 1 (top left), 2 (top right), 3 (center left), 4 (center right), 5 (bottom). The efficiency correction has been applied. 305

F.12 Linearity stress test using for the normalised cross section as a function of $H_{\mathrm{T}}^{t\bar{t}}$. The stress is achieve by re-weigthing the input distribution (red line) by a factor proportional to the data/MC difference. The factors are 1 (top left), 2 (top right), 3 (center left), 4 (center right), 5 (bottom). The efficiency correction has been applied. 306
F.13 Linearity stress test using for the normalised cross section as a function of number of jets. The stress is achieve by re-weigthing the input distribution (red line) by a factor proportional to the data/MC difference. The factors are 1 (top left), 2 (top right), 3 (center left), 4 (center right), 5 (bottom). The efficiency correction has been applied. 307
F.14 Linearity stress test using for the normalised cross section as a function of $R_{\mathrm{jet1}}^{\mathrm{extra1}}$. The stress is achieve by re-weigthing the input distribution (red line) by a factor proportional to the data/MC difference. The factors are 1 (top left), 2 (top right), 3 (center left), 4 (center right), 5 (bottom). The efficiency correction has been applied. 308
F.15 Linearity stress test using for the normalised cross section as a function of $R_{\mathrm{top1}}^{\mathrm{extra1}}$. The stress is achieve by re-weigthing the input distribution (red line) by a factor proportional to the data/MC difference. The factors are 1 (top left), 2 (top right), 3 (center left), 4 (center right), 5 (bottom). The efficiency correction has been applied. 309
F.16 Linearity stress test using for the normalised cross section as a function of $R_{Wb}^{leading}$. The stress is achieve by re-weigthing the input distribution (red line) by a factor proportional to the data/MC difference. The factors are 1 (top left), 2 (top right), 3 (center left), 4 (center right), 5 (bottom). The efficiency correction has been applied. 310
F.17 Linearity stress test using for the normalised cross section as a function of $R_{Wb}^{subleading}$. The stress is achieve by re-weigthing the input distribution (red line) by a factor proportional to the data/MC difference. The factors are 1 (top left), 2 (top right), 3 (center left), 4 (center right), 5 (bottom). The efficiency correction has been applied. 311
F.18 Linearity stress test using for the normalised cross section as a function of $R_{Wt}^{leading}$. The stress is achieve by re-weigthing the input distribution (red line) by a factor proportional to the data/MC difference. The factors are 1 (top left), 2 (top right), 3 (center left), 4 (center right), 5 (bottom). The efficiency correction has been applied. 312
F.19 Linearity stress test using for the normalised cross section as a function of $R_{Wt}^{subleading}$. The stress is achieve by re-weigthing the input distribution (red line) by a factor proportional to the data/MC difference. The factors are 1 (top left), 2 (top right), 3 (center left), 4 (center right), 5 (bottom). The efficiency correction has been applied. 313
F.20 Linearity stress test using for the normalised cross section as a function of p_T^{top1}. The stress is achieve by re-weigthing the input distribution (red line) by a factor proportional to the data/MC difference. The factors are 1 (top left), 2 (top right), 3 (center left), 4 (center right), 5 (bottom). The efficiency correction has been applied. 314

F.21 Linearity stress test using for the normalised cross section as a function of y_{top1}. The stress is achieve by re-weigthing the input distribution (red line) by a factor proportional to the data/MC difference. The factors are 1 (top left), 2 (top right), 3 (center left), 4 (center right), 5 (bottom). The efficiency correction has been applied. 315
F.22 Linearity stress test using for the normalised cross section as a function of p_T^{top2}. The stress is achieve by re-weigthing the input distribution (red line) by a factor proportional to the data/MC difference. The factors are 1 (top left), 2 (top right), 3 (center left), 4 (center right), 5 (bottom). The efficiency correction has been applied. 316
F.23 Linearity stress test using for the normalised cross section as a function of y_{top2}. The stress is achieve by re-weigthing the input distribution (red line) by a factor proportional to the data/MC difference. The factors are 1 (top left), 2 (top right), 3 (center left), 4 (center right), 5 (bottom). The efficiency correction has been applied. 317
F.24 Linearity stress test using for the normalised cross section as a function of $m_{t\bar{t}}$. The stress is achieve by re-weigthing the input distribution (red line) by a factor proportional to the data/MC difference. The factors are 1 (top left), 2 (top right), 3 (center left), 4 (center right), 5 (bottom). The efficiency correction has been applied. 318
F.25 Linearity stress test using for the normalised cross section as a function of $p_T^{t\bar{t}}$. The stress is achieve by re-weigthing the input distribution (red line) by a factor proportional to the data/MC difference. The factors are 1 (top left), 2 (top right), 3 (center left), 4 (center right), 5 (bottom). The efficiency correction has been applied. 319
F.26 Linearity stress test using for the normalised cross section as a function of $y_{t\bar{t}}$. The stress is achieve by re-weigthing the input distribution (red line) by a factor proportional to the data/MC difference. The factors are 1 (top left), 2 (top right), 3 (center left), 4 (center right), 5 (bottom). The efficiency correction has been applied. 320
F.27 Linearity stress test using for the normalised cross section as a function of p_T^{top1}. The stress is achieve by re-weigthing the input distribution (red line) by a factor proportional to the data/MC difference. The factors are 1 (top left), 2 (top right), 3 (center left), 4 (center right), 5 (bottom). The efficiency correction has been applied. 322
F.28 Linearity stress test using for the normalised cross section as a function of y_{top1}. The stress is achieve by re-weigthing the input distribution (red line) by a factor proportional to the data/MC difference. The factors are 1 (top left), 2 (top right), 3 (center left), 4 (center right), 5 (bottom). The efficiency correction has been applied. 323
F.29 Linearity stress test using for the normalised cross section as a function of p_T^{top2}. The stress is achieve by re-weigthing the input distribution (red line) by a factor proportional to the data/MC difference. The factors are 1 (top left), 2 (top right), 3 (center left), 4 (center right), 5 (bottom). The efficiency correction has been applied. 324

F.30 Linearity stress test using for the normalised cross section as a function of y_{top2}. The stress is achieve by re-weigthing the input distribution (red line) by a factor proportional to the data/MC difference. The factors are 1 (top left), 2 (top right), 3 (center left), 4 (center right), 5 (bottom). The efficiency correction has been applied. 325
F.31 Linearity stress test using for the normalised cross section as a function of $m_{t\bar{t}}$. The stress is achieve by re-weigthing the input distribution (red line) by a factor proportional to the data/MC difference. The factors are 1 (top left), 2 (top right), 3 (center left), 4 (center right), 5 (bottom). The efficiency correction has been applied. 326
F.32 Linearity stress test using for the normalised cross section as a function of $p_T^{t\bar{t}}$. The stress is achieve by re-weigthing the input distribution (red line) by a factor proportional to the data/MC difference. The factors are 1 (top left), 2 (top right), 3 (center left), 4 (center right), 5 (bottom). The efficiency correction has been applied. 327
F.33 Linearity stress test using for the normalised cross section as a function of $y_{t\bar{t}}$. The stress is achieve by re-weigthing the input distribution (red line) by a factor proportional to the data/MC difference. The factors are 1 (top left), 2 (top right), 3 (center left), 4 (center right), 5 (bottom). The efficiency correction has been applied. 328
F.34 χ^2 F.34a, statistical error F.34b, residuals (w.r.t. previous iteration) F.34c and statistical error over residuals ratio F.34d as a function of the N_{iter} in $|P_{\text{out}}^{t\bar{t}}|$bins in the fiducial phase-space. 329
F.35 χ^2 (a), statistical error (b), residuals (w.r.t. previous iteration) (c) and statistical error over residuals ratio (d) as a function of the N_{iter} in $\Delta\phi_{t\bar{t}}$bins in the fiducial phase-space. 330
F.36 χ^2 (a), statistical error (b), residuals (w.r.t. previous iteration) (c) and statistical error over residuals ratio (d) as a function of the N_{iter} in $\Delta R_{\text{jet1}}^{\text{extra1}}$bins in the fiducial phase-space. 330
F.37 χ^2 (a), statistical error (b), residuals (w.r.t. previous iteration) (c) and statistical error over residuals ratio (d) as a function of the N_{iter} in $\Delta R_{\text{topclose}}^{\text{extra1}}$bins in the fiducial phase-space. 331
F.38 χ^2 (a), statistical error (b), residuals (w.r.t. previous iteration) (c) and statistical error over residuals ratio (d) as a function of the N_{iter} in $H_{\text{T}}^{t\bar{t}}$bins in the fiducial phase-space. 331
F.39 χ^2 (a), statistical error (b), residuals (w.r.t. previous iteration) (c) and statistical error over residuals ratio (d) as a function of the N_{iter} in N_{jets} bins in the fiducial phase-space. 332
F.40 χ^2 (a), statistical error (b), residuals (w.r.t. previous iteration) (c) and statistical error over residuals ratio (d) as a function of the N_{iter} in $R_{\text{jet1}}^{\text{extra1}}$bins in the fiducial phase-space. 332
F.41 χ^2 (a), statistical error (b), residuals (w.r.t. previous iteration) (c) and statistical error over residuals ratio (d) as a function of the N_{iter} in $R_{\text{top1}}^{\text{extra1}}$bins in the fiducial phase-space. 333
F.42 χ^2 (a), statistical error (b), residuals (w.r.t. previous iteration) (c) and statistical error over residuals ratio (d) as a function of the N_{iter} in $R_{Wb}^{leading}$bins in the fiducial phase-space. 333

F.43 χ^2 (a), statistical error (b), residuals (w.r.t. previous iteration) (c) and statistical error over residuals ratio (d) as a function of the N_{iter} in $R_{Wb}^{subleading}$bins in the fiducial phase-space. 334
F.44 χ^2 (a), statistical error (b), residuals (w.r.t. previous iteration) (c) and statistical error over residuals ratio (d) as a function of the N_{iter} in $R_{Wt}^{leading}$bins in the fiducial phase-space. 334
F.45 χ^2 (a), statistical error (b), residuals (w.r.t. previous iteration) (c) and statistical error over residuals ratio (d) as a function of the N_{iter} in $R_{Wt}^{subleading}$bins in the fiducial phase-space. 335
F.46 χ^2 (a), statistical error (b), residuals (w.r.t. previous iteration) (c) and statistical error over residuals ratio (d) as a function of the N_{iter} in p_T^{top1}bins in the fiducial phase-space. 335
F.47 χ^2 (a), statistical error (b), residuals (w.r.t. previous iteration) (c) and statistical error over residuals ratio (d) as a function of the N_{iter} in y_{top1}bins in the fiducial phase-space. 336
F.48 χ^2 (a), statistical error (b), residuals (w.r.t. previous iteration) (c) and statistical error over residuals ratio (d) as a function of the N_{iter} in p_T^{top2}bins in the fiducial phase-space. 336
F.49 χ^2 (a), statistical error (b), residuals (w.r.t. previous iteration) (c) and statistical error over residuals ratio (d) as a function of the N_{iter} in y_{top2}bins in the fiducial phase-space. 337
F.50 χ^2 (a), statistical error (b), residuals (w.r.t. previous iteration) (c) and statistical error over residuals ratio (d) as a function of the N_{iter} in $m_{t\bar{t}}$bins in the fiducial phase-space. 337
F.51 χ^2 (a), statistical error (b), residuals (w.r.t. previous iteration) (c) and statistical error over residuals ratio (d) as a function of the N_{iter} in $p_T^{t\bar{t}}$bins in the fiducial phase-space. 338
F.52 χ^2 (a), statistical error (b), residuals (w.r.t. previous iteration) (c) and statistical error over residuals ratio (d) as a function of the N_{iter} in $y_{t\bar{t}}$bins in the fiducial phase-space. 338

List of Tables

1.1 Quantitative comparison of the four fundamental interactions between two test particles with unit charges and $m_1 = m_2 \approx 1$ GeV at a transfer momentum $Q = 1$ GeV. 2

2.1 Achieved $\mathscr{L}$ and $\mathscr{L}_{peak}$ by the ATLAS detector, broken down by year of operation. 26
2.2 Performance goals of the ATLAS detector. The units of E and p_T are in GeV. Table taken from [57]. 33

3.1 Table showing the Phase-II upgrade plans for the ATLAS experiment. 52
3.2 Cuts applied during the track reconstruction depending on the $|\eta|$ interval. Holes are defined when track candidates cross active sensors on which no hit was found, double holes are two consecutive active sensors crossed without a hit found. d_0 and z_0 are defined with respect to the mean position of the beam spot. 56

4.1 Summary of MC samples adopted for the cross section measurement. Complementary information on their configuration are also included. 86

6.1 Summary of selection requirements for events entering the $t\bar{t}$ reconstruction. 143
6.2 Parameters of Equation 6.2 extracted from nominal $t\bar{t}$ MC sample at reconstructed and particle level. 145
6.3 Summary of selection requirements for the analysis. 149
6.4 Event yields for data, signal and background processes estimated with MC-techniques after the signal region selection. The ratio of each background yields to the signal $t\bar{t}$ and to data yields are shown for convenience. Only statistical uncertainties are given. 149
6.5 Basic division of data into four regions according to the values assumed by parameters i and j. 150
6.6 Phase-space division into orthogonal regions according to the values assumed by parameters n_{b-jets} and m_{top}. 152
6.7 Signal and $t\bar{t}$-like background contamination in the different regions, defined by the values assumed by n_{b-jets} and m_{top}. . . 152

6.8 Event yields for data, signal and background processes after the signal region selection. The ratio of each yield to data yields is shown for convenience. Only statistical uncertainties are given. 153

9.1 Comparison of the measured fiducial phase space absolute differential cross sections respect the predictions from several MC generators. For each prediction the χ^2 and the resulting *p-value* are presented. The NDF is equal to the number of bins in the distribution. 207
9.2 Comparison of the measured fiducial phase space relative differential cross sections respect the predictions from several MC generators. For each prediction the χ^2 and the resulting *p-value* are presented. The NDF is equal to the number of bins in the distribution minus one. 207

A.1 χ^2_{min} cuts leading to ~57% efficiency. The first column shows the cut applied at detector-level while the last two columns show the cut that needs to be applied at particle level to obtain the same efficiency on the signal for two scenarios; when the σ values used in the χ^2 are those obtained at detector-level and when their are evaluated from the particle level distributions. See Table 6.2 for the values. 214
A.2 Efficiencies in the different χ^2_{min} cut scenarios. The first column shows the efficiency obtained by applying the nominal cut (10) at detector-level and particle-level for two scenarios; when the σ values used in the χ^2 are those obtained at detector-level and when their are evaluated from the particle level distributions. See Table 6.2 for the values. 214

C.1 Complete cutflow for data. Only statistical uncertainties are given. Selection criteria are those stated in Table 6.3. 227
C.2 Complete cutflow for $t\bar{t}$ fully hadronic process. Only statistical uncertainties are given. Selection criteria are those stated in Table 6.3. 228
C.3 Complete cutflow for $t\bar{t}$ non-all hadronic process. Only statistical uncertainties are given. Selection criteria are those stated in Table 6.3. 229
C.4 Complete cutflow for Wt process. Only statistical uncertainties are given. Selection criteria are those stated in Table 6.3. . 230
C.5 Complete cutflow for $t - channel$ single top process. Only statistical uncertainties are given. Selection criteria are those stated in Table 6.3. 231

D.1 Table of systematics for the absolute differential cross-section at the particle level for the $|P^{t\bar{t}}_{\text{out}}|$ observable. 233
D.2 Table of systematics for the absolute differential cross-section at the particle level for the $\Delta\phi_{t\bar{t}}$ observable. 234

D.3 Table of systematics for the absolute differential cross-section at the particle level for the $\Delta R_{\mathrm{jet1}}^{\mathrm{extra1}}$ observable. 235
D.4 Table of systematics for the absolute differential cross-section at the particle level for the $\Delta R_{\mathrm{topclose}}^{\mathrm{extra1}}$ observable. 236
D.5 Table of systematics for the absolute differential cross-section at the particle level for the $H_{\mathrm{T}}^{t\bar{t}}$ observable. 237
D.6 Table of systematics for the absolute differential cross-section at the particle level for the jet multiplicity observable. 238
D.7 Table of systematics for the absolute differential cross-section at the particle level for the $Rptxone J$ observable. 239
D.8 Table of systematics for the absolute differential cross-section at the particle level for the $Rptxonetl$ observable. 240
D.9 Table of systematics for the absolute differential cross-section at the particle level for the $R_{Wb}^{leading}$ observable. 241
D.10 Table of systematics for the absolute differential cross-section at the particle level for the $R_{Wb}^{subleading}$ observable. 242
D.11 Table of systematics for the absolute differential cross-section at the particle level for the $R_{Wt}^{leading}$ observable. 243
D.12 Table of systematics for the absolute differential cross-section at the particle level for the $R_{Wt}^{subleading}$ observable. 244
D.13 Table of systematics for the absolute differential cross-section at the particle level for the p_T^{top1} observable. 245
D.14 Table of systematics for the absolute differential cross-section at the particle level for the y_{top1} observable. 246
D.15 Table of systematics for the absolute differential cross-section at the particle level for the p_T^{top2} observable. 247
D.16 Table of systematics for the absolute differential cross-section at the particle level for the y_{top2} observable. 248
D.17 Table of systematics for the absolute differential cross-section at the particle level for the $m_{t\bar{t}}$ observable. 249
D.18 Table of systematics for the absolute differential cross-section at the particle level for the $p_T^{t\bar{t}}$ observable. 250
D.19 Table of systematics for the absolute differential cross-section at the particle level for the $y_{t\bar{t}}$ observable. 251
D.20 Table of systematics for the absolute differential cross-section at the parton level for the p_T^{top1} observable. 253
D.21 Table of systematics for the absolute differential cross-section at the parton level for the y_{top1} observable. 254
D.22 Table of systematics for the absolute differential cross-section at the parton level for the p_T^{top2} observable. 255
D.23 Table of systematics for the absolute differential cross-section at the parton level for the y_{top2} observable. 256
D.24 Table of systematics for the absolute differential cross-section at the parton level for the $m_{t\bar{t}}$ observable. 257
D.25 Table of systematics for the absolute differential cross-section at the parton level for the $p_T^{t\bar{t}}$ observable. 258

D.26 Table of systematics for the absolute differential cross-section at the parton level for the $y_{t\bar{t}}$ observable. 259
D.27 Table of systematics for the normalised differential cross-section at the parton level for the p_T^{top1} observable. 261
D.28 Table of systematics for the normalised differential cross-section at the parton level for the y_{top1} observable. 262
D.29 Table of systematics for the normalised differential cross-section at the parton level for the p_T^{top2} observable. 263
D.30 Table of systematics for the normalised differential cross-section at the parton level for the y_{top2} observable. 264
D.31 Table of systematics for the normalised differential cross-section at the parton level for the $m_{t\bar{t}}$ observable. 265
D.32 Table of systematics for the normalised differential cross-section at the parton level for the $p_T^{t\bar{t}}$ observable. 266
D.33 Table of systematics for the normalised differential cross-section at the parton level for the $y_{t\bar{t}}$ observable. 267

G.1 Covariance matrix of the absolute cross section as function of $|P_{\mathrm{out}}^{t\bar{t}}|$, accounting for the statistical and systematic uncertainties. 339
G.2 Covariance matrix of the absolute cross section as function of $\Delta\phi_{t\bar{t}}$, accounting for the statistical and systematic uncertainties. 340
G.3 Covariance matrix of the absolute cross section as function of $R_{Wt}^{leading}$, accounting for the statistical and systematic uncertainties. 340
G.4 Covariance matrix of the absolute cross section as function of $R_{Wt}^{subleading}$, accounting for the statistical and systematic uncertainties. 340
G.5 Covariance matrix of the absolute cross section as function of $R_{Wb}^{leading}$, accounting for the statistical and systematic uncertainties. 340
G.6 Covariance matrix of the absolute cross section as function of $R_{Wb}^{subleading}$, accounting for the statistical and systematic uncertainties. 340
G.7 Covariance matrix of the absolute cross section as function of $H_{\mathrm{T}}^{t\bar{t}}$, accounting for the statistical and systematic uncertainties. 340
G.8 Covariance matrix of the absolute cross section as function of N_{jets}, accounting for the statistical and systematic uncertainties. 341
G.9 Covariance matrix of the absolute cross section as function of $\Delta R_{\mathrm{jet1}}^{\mathrm{extra1}}$, accounting for the statistical and systematic uncertainties. 341
G.10 Covariance matrix of the absolute cross section as function of $\Delta R_{\mathrm{topclose}}^{\mathrm{extra1}}$, accounting for the statistical and systematic uncertainties. 341
G.11 Covariance matrix of the absolute cross section as function of $R_{\mathrm{jet1}}^{\mathrm{extra1}}$, accounting for the statistical and systematic uncertainties. 341

G.12 Covariance matrix of the absolute cross section as function of $R_{\mathrm{top1}}^{\mathrm{extra1}}$, accounting for the statistical and systematic uncertainties. . . . 341
G.13 Covariance matrix of the absolute cross section as function of p_T^{top1}, accounting for the statistical and systematic uncertainties. 341
G.14 Covariance matrix of the absolute cross section as function of y_{top1}, accounting for the statistical and systematic uncertainties. 342
G.15 Covariance matrix of the absolute cross section as function of p_T^{top2}, accounting for the statistical and systematic uncertainties. 342
G.16 Covariance matrix of the absolute cross section as function of $p_T^{t\bar{t}}$, accounting for the statistical and systematic uncertainties. 342
G.17 Covariance matrix of the absolute cross section as function of $y_{t\bar{t}}$, accounting for the statistical and systematic uncertainties. 342
G.18 Covariance matrix of the absolute cross section as function of y_{top2}, accounting for the statistical and systematic uncertainties. 342
G.19 Covariance matrix of the absolute cross section as function of $m_{t\bar{t}}$, accounting for the statistical and systematic uncertainties. 342
G.20 Covariance matrix of the relative cross section as function of $|P_{\mathrm{out}}^{t\bar{t}}|$, accounting for the statistical and systematic uncertainties. 343
G.21 Covariance matrix of the relative cross section as function of $\Delta\phi_{t\bar{t}}$, accounting for the statistical and systematic uncertainties. 343
G.22 Covariance matrix of the relative cross section as function of $R_{Wt}^{leading}$, accounting for the statistical and systematic uncertainties. . . . 343
G.23 Covariance matrix of the relative cross section as function of $R_{Wt}^{subleading}$, accounting for the statistical and systematic uncertainties. . . . 343
G.24 Covariance matrix of the relative cross section as function of $R_{Wb}^{leading}$, accounting for the statistical and systematic uncertainties. . . . 343
G.25 Covariance matrix of the relative cross section as function of $R_{Wb}^{subleading}$, accounting for the statistical and systematic uncertainties. . . . 343
G.26 Covariance matrix of the relative cross section as function of $H_{\mathrm{T}}^{t\bar{t}}$, accounting for the statistical and systematic uncertainties. 344
G.27 Covariance matrix of the relative cross section as function of N_{jets}, accounting for the statistical and systematic uncertainties. 344
G.28 Covariance matrix of the relative cross section as function of $\Delta R_{\mathrm{jet1}}^{\mathrm{extra1}}$, accounting for the statistical and systematic uncertainties. . . . 344
G.29 Covariance matrix of the relative cross section as function of $\Delta R_{\mathrm{topclose}}^{\mathrm{extra1}}$, accounting for the statistical and systematic uncertainties. . . . 344
G.30 Covariance matrix of the relative cross section as function of $R_{\mathrm{jet1}}^{\mathrm{extra1}}$, accounting for the statistical and systematic uncertainties. . . . 344

G.31 Covariance matrix of the relative cross section as function of $R_{\mathrm{top1}}^{\mathrm{extra1}}$, accounting for the statistical and systematic uncertainties. 344
G.32 Covariance matrix of the relative cross section as function of p_T^{top1}, accounting for the statistical and systematic uncertainties. 345
G.33 Covariance matrix of the relative cross section as function of y_{top1}, accounting for the statistical and systematic uncertainties. 345
G.34 Covariance matrix of the relative cross section as function of p_T^{top2}, accounting for the statistical and systematic uncertainties. 345
G.35 Covariance matrix of the relative cross section as function of $p_T^{t\bar{t}}$, accounting for the statistical and systematic uncertainties. 345
G.36 Covariance matrix of the relative cross section as function of $y_{t\bar{t}}$, accounting for the statistical and systematic uncertainties. 345
G.37 Covariance matrix of the relative cross section as function of y_{top2}, accounting for the statistical and systematic uncertainties. 345
G.38 Covariance matrix of the relative cross section as function of $m_{t\bar{t}}$, accounting for the statistical and systematic uncertainties. 346

Introduction

The top quark was discovered at Fermilab in 1995. It is the heaviest known elementary particle and the only quark decaying before hadronizing, thus allowing access to the properties of a *bare* quark through its decay products. Furthermore, thanks to its unique properties, it has a Yukawa coupling with the Higgs boson close to one and plays a central role in electroweak symmetry breaking mechanism and Beyound Standard Model searches. In addition, the measurement of the $t\bar{t}$ production differential cross sections represents a stringent test of perturbative QCD.

The large number of top quark pair events produced at the LHC allows detailed studies of the characteristics of the $t\bar{t}$ system as a function of several kinematic variables. In this thesis, the measurement of the differential cross sections in the hadronic decay mode of the $t\bar{t}$ system, where both the intermediate W-bosons decay hadronically, are presented. This channel is the one with the highest branching ratio and, unlike the other decay modes, the four-momenta of the top quarks can be fully reconstructed from their products, leading to a better top quark reconstruction, as the kinematic ambiguities arising from the presence of one or two neutrinos in the final state are avoided. Data used in the analysis were collected by the ATLAS detector during the full 2015 and 2016 data-taking periods at a center of mass energy of 13 TeV.

After several years of successful operations, the LHC and the ATLAS detector will undergo several upgrades, culminating in the High Luminosity LHC, characterized by a peak luminosity of $\mathscr{L}_{peak} = 7.5 \cdot 10^{34}$ cm^{-s}s^{-1}, a factor of five respect to the actual Run 2 luminosity. In order to guarantee similar or better performance, the ATLAS detector will be subjected to substantial upgrades, such as the all-silicon Inner Tracker (ITk) and the High Granularity Timing Detector (HGTD), whose expected performance and main features will be discussed in this thesis.

The present thesis is organized as follows:

- in Chapter 1 an overview of the Standard Model of the particle physics, with particular focus on the top quark sector, including the latest results from the ATLAS Collaboration, will be presented;

- an overview of the LHC and the ATLAS detector will be given in Chapter 2;
- the upgrade plans of the LHC and the ATLAS detector, together with the expected performance of the ITk and HGTD will be presented in Chapter 3;
- in Chapter 4 all the steps of the Monte Carlo production and the detector simulation are described;
- in Chapter 5 the object reconstruction and the performance of the ATLAS detector will be presented;
- the measurement of the differential cross sections of the $t\bar{t}$ system in the fully hadronic channel will be presented in Chapter 6, with particular emphasis on the event selection, the $t\bar{t}$ system reconstruction and background determination;
- in Chapter 7 the unfolding method adopted in the analysis, as well as the validation tests to assess the robustness and stability of the method, are presented;
- the different sources of uncertainties affecting the measurement will be discussed in Chapter 8;
- in Chapter 9, the results of the measurement will be presented.

Finally, the final conclusions of this work will be presented. Furthermore, additional material will be presented in the Appendices:

- Appendix A will provide additional studies to assess the stability of the $t\bar{t}$ system reconstruction;
- Appendix B will present the code implementation of the C++ class used to reconstruct the $t\bar{t}$ system;
- Appendix C will present the complete cutflows for data and Monte Carlo estimated processes;
- in Appendix D, the uncertainties tables, broken down into the different sources, are reported;
- Appendix E will present the corrections to the unfolding;
- Appendix F will present the results of the validation tests of the unfolding method;
- in Appendix G the covariance matrices, used to evaluate the χ^2 to assess the compatibility between the measured spectra and the theoretical predictions, are reported.

Chapter 1

Theory foundations

In this Chapter, a concise overview of the Standard Model (SM) of Particle Interactions will be given. The SM is a renormalizable, Lorentz-invariant gauge theory [1–4] formulated in the 60s and 70s [5]. During the last 50 years, its predictions have been tested with increasing precision at several High Energy Physics (HEP) experiments in a wide range of center of mass energies, $\sqrt{s}$ and up to $\sqrt{s} = 13$ TeV[1] (see e.g. [7]) at the Large Hadron Collider (LHC) [8]. After a brief description of the SM, given in Sections 1.1–1.6, the basic principles of hadron collider physics will be discussed in Section 1.7. A more focused overview of the top quark physics, from its discovery to the most recent measurements, is given in Section 1.8.

1.1 The Standard Model of Particle Interactions

The Standard Model of Particle Interactions is a gauge field theory based on the $SU(3) \otimes SU(2) \otimes U(1)$ Lie group which successfully describes the interaction between the fundamental building blocks of nature, spin-$1/2$ fermions, in terms of the exchange of spin-1 gauge bosons. The SM is able to include, in a coherent scheme, three of the four fundamental forces known to exist in nature:

- **electromagnetic**: it occurs between electrically charged particles, it is mediated by the massless *photon* (γ);
- **weak interaction**: it is the force responsible of radioactive decays, it is mediated by the charged $W^{\pm}$ and the neutral Z^0 bosons, which interact to left-handed fermions;
- **strong interaction**: this force is responsible of keeping coloured spin-$1/2$ fermions, quarks, bounded inside hadrons and nucleons in atoms. It is mediated by the coulored, massless *gluons* (g).

The current formulation of the SM does not include the gravitational force. However, the gravitational interaction is negligible at typical HEP energy

[1] In HEP, the natural units [6] are adopted, in which $c = \hbar = \epsilon_0 = 1$ and energies are measured in (multiple of) electron-volts, eV, defined as the energy gained by an electron moving across an electrical potential field of one Volt.

Interaction	Approximate potential	Parameters values	Relative strenght
strong	$\frac{12\cdot\pi/23}{Q^2\cdot\log(Q^2/\Lambda^2)}$	$\Lambda \sim 0.2$ GeV	1
electromagnetic	$\frac{\alpha_{em}}{Q^2}$	$\alpha_{em} \sim \frac{1}{137}$	$1.4 \cdot 10^{-2}$
weak	$\frac{\alpha_{em}}{Q^2 - M_W^2}$	$M_W \sim 80$ GeV	$2.2 \cdot 10^{-6}$
gravity	$\frac{G_N \cdot m_1 \cdot m_2}{Q^2}$	$G_N \sim \frac{6.7\cdot 10^{-39}}{GeV}$, $m_1 \sim m_2 \sim 1$ GeV	$1.2 \cdot 10^{-38}$

TABLE 1.1: Quantitative comparison of the four fundamental interactions between two test particles with unit charges and $m_1 = m_2 \approx 1$ GeV at a transfer momentum $Q = 1$ GeV.

scales, as it is shown in Table 1.1, which compares the potentials which mediate all the fundamental forces, expressed in the momentum space, at a reference scale (momentum transfer) of $Q = 1$ GeV and considering the unit charges of each interaction; for the gravitational one, the proton mass is used.

Figure 1.1 shows the leptons and bosons included in the SM framework, as well as their interactions and fundamental properties (mass, electric charge and spin), taken from the Review of Particle Physics by the Particle Data Group, PDG [9]. For each fermion, a correspondent charge-conjugated antifermion exists. Quarks and lepton are both divided into three doublets, called *families* or *generations*. The electrically charged leptons are, in order of increasing mass, the electron, e, the muon, μ, and the tau, τ. All of them carry an electric charge equal to -1. The other three leptons are called neutrinos and they match the flavour of their charged counterparts: electron neutrino, ν_e, muon neutrino, ν_μ, and tau neutrino, ν_τ. Neutrinos interact only through the weak force and are supposed to be massless in the SM. However, several measurements observed the phenomenon of neutrino oscillation [10], implying that neutrinos have not vanishing mass.

Each of the three quark doublets carry electric charge, $+2/3$ for up-like quarks (up, u, charm, c, and top, t) and $-1/3$ for down-like ones (down, d, strange, s, and bottom b). They also carry strong charge (red, r, green, g, and blue, b). The strong interaction, as will be discussed in Section 1.3, is responsible for the *confinement* of quarks, which can not be observed as free particles in nature. Quarks always come in bound colourless states, called hadrons. Hadrons can be constituted of a quark-antiquark pair (mesons) or a quark triplet (barions).

As shown in Figure 1.1, electroweak (EW) gauge bosons have a very high mass, being $m_W = 80.385 \pm 0.015$ GeV and $m_Z = 91.1876 \pm 0.0021$ GeV the masses of the $W^\pm$ and Z^0 bosons, respectively. As will be further discussed in Sections 1.5 and 1.6, the observed masses of the EW mediators would require a mass term in the corresponding lagrangian. This requirement would break the $SU(2) \otimes U(1)$ symmetry. Therefore, a spontaneous symmetry breaking mechanism was introduced in 1964 by Brout, Englert and Higgs [11, 12]; a scalar field permeates the vacuum and interacts with other particles through the Higgs boson. The strenght of interaction is proportional to the mass acquired by the particle.

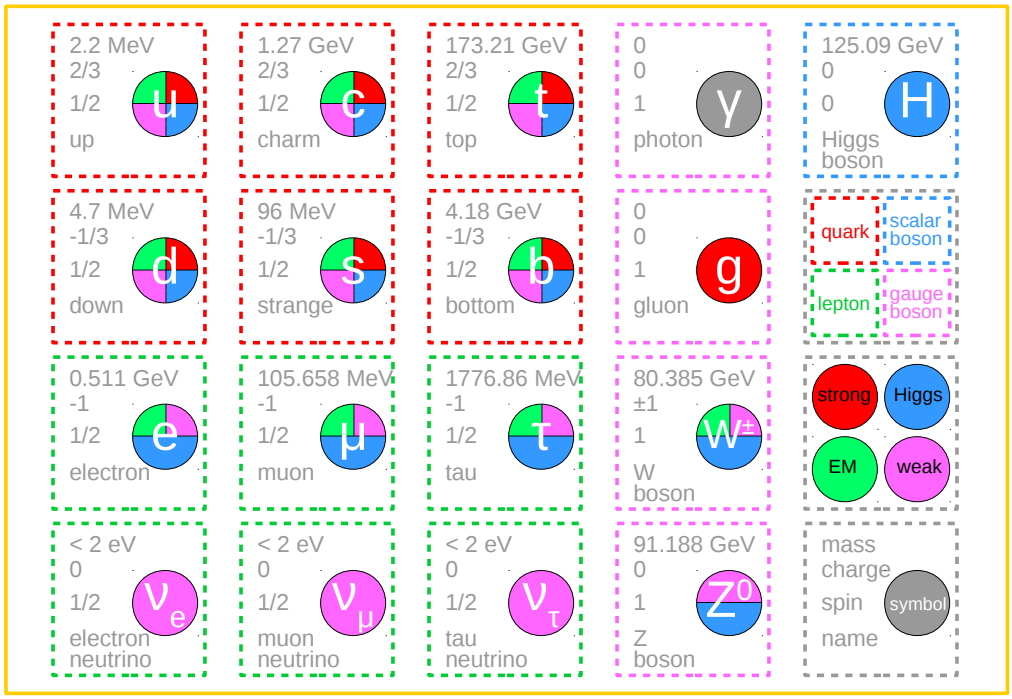

FIGURE 1.1: Properties of fundamental particles in the SM framework. Values are taken from [9]

1.2 Quantum Electrodynamics

Quantum Electrodynamics (QED) was the first relativistic quantum field theory ever introduced. It is an Abelian gauge theory with $U(1)$ symmetry in which the interactions between electrically charged $1/2$-spin fermions are mediated through the massless photon. To satisfy the local $U(1)$ gauge invariance principle, the Lagrangian density of the QED has to be invariant under the local gauge transformations:

$$\begin{cases} \psi(x) \rightarrow U\psi(x) = e^{ie\alpha(x)}\psi(x) \\ A_\mu(x) \rightarrow A_\mu(x) + \frac{1}{e}\partial_\mu\alpha(x) \end{cases}, \tag{1.1}$$

where $\alpha(x)$ is an arbitrary gauge-field depending on the space-time coordinates and e is the elementary electric charge. The Lagrangian density for the interaction between a charged particle ψ of mass m and the electromagnetic field A_μ can be written as:

$$\mathcal{L}_{QED} = -\frac{1}{4}F^{\mu\nu}F_{\mu\nu} + \bar{\psi}(i\gamma^\mu D_\mu - m)\psi, \tag{1.2}$$

where $F^{\mu\nu} = \partial_\mu A_\nu - \partial_\nu A_\mu$ is the electromagnetic field tensor, γ^μ are the 4×4 Dirac matrices and $D_\mu = \partial_\mu - ieA_\mu$ is the covariant derivative, which transforms as $D_\mu\psi \rightarrow e^{i\alpha(x)}D_\mu\psi$, thus ensuring the local gauge invariance. The

physical interpretation of the Lagrangian density is immediate if the covariant derivative is explicited:

$$\mathcal{L}_{QED} = -\frac{1}{4}F^{\mu\nu}F_{\mu\nu} + \bar{\psi}(i\gamma^{\mu}\partial_{\mu} - m)\psi + e\bar{\psi}A_{\mu}\gamma^{\mu}\psi, \tag{1.3}$$

where the first term describes the propagation of a free photon (A_μ field), the second one is the free Dirac field for the lepton and the last is the interaction term between a photon and a lepton.

1.3 Quantum Chromodynamics

Quantum Chromodynamics (QCD) is described in terms of an SU(3) non-Abelian gauge theory. Similar to the QED, a conserved charge exists; the colour charge, which can assume three different values: red, green and blue (r,g,b). The conservation of the colour charge explains the observed phenomemon of *confinement*, i.e. quarks are never observed as free particles, but always in bounded colourless states, called hadrons. The Lagrangian density describing the free quarks is:

$$\mathcal{L}_q = \bar{\Psi}^f(i\gamma^{\mu}\partial_{\mu} - m_f)\Psi^f, \tag{1.4}$$

where the sum over the flavour index f=u, d, s, c, t, b is implicit. Here Ψ^f is a three-component field; each component being a Dirac field ψ^f_c with defined colour c=r, g, b. The $\mathcal{L}_q$ is not invariant under local phase $SU(3)$ transformations, which are defined as:

$$\begin{cases} \Psi^f(x) = \exp\left[ig_s\lambda_j\omega(x)/2\right]\Psi^f(x) \\ \bar{\Psi}^f(x) = \bar{\Psi}^f(x)\exp\left[-ig_s\lambda_j\omega(x)/2\right] \end{cases}, \tag{1.5}$$

where g_s is the strong coupling constant, λ_j are the Gell-Mann matrices [13], eight linearly independant traceless 3×3 matrices, closely related to the generators of the $SU(3)$ Lie group, $T_j = \lambda_j/2$, with $j = 0, \cdots, 8$. Finally, $\omega(x)$ is a generic real, differentiable function.

In order for the QCD Lagrangian density to be gauge-invariant, a covariant derivative, D^μ, is introduced:

$$D^{\mu} = \partial^{\mu} + ig_s\lambda_j A^{\mu}_j(x)/2, \tag{1.6}$$

where A^μ_j are eight gauge fields, whose quanta correspond to the eight mediators of the strong interaction, the gluons. In order not to break gauge-invariance, the fields obey the following transformation rule, strictly valid only for infinitesimal ω_i:

$$A^{\mu}_i(x) \rightarrow A^{\mu}_i(x) - \partial^{\mu}\omega_i(x) - g_s f_{ijk}\omega_j(x)A^{\mu}_k(x), \tag{1.7}$$

where f_{ijk} are the structure constants, defined by the commutation relations of the group generators, T_i:

$$[T_i, T_j] = i f_{ijk} T_k. \tag{1.8}$$

The complete Lagrangian density of the QCD is:

$$\mathcal{L}_{QCD} = \bar{\Psi}^f (i\gamma^\mu D_\mu - m_f)\Psi^f - \frac{1}{4} G_{f\mu\nu} G_f^{\mu\nu}, \tag{1.9}$$

where $G_f^{\mu\nu}$ is the gauge-invariant gluon field tensor, defined as:

$$G_f^{\mu\nu} = F_f^{\mu\nu} + g_s f_{ijk} A_j^\mu A_k^\nu. \tag{1.10}$$

The physics interpretation of $\mathcal{L}_{QCD}$ is made clear if expressed in the terms of the fields:

$$\begin{aligned} \mathcal{L}_{QCD} &= \mathcal{L}_q - \frac{1}{4} F_{i\mu\nu} F_i^{\mu\nu} \\ &- \frac{1}{2} g_s \bar{\Psi}^f \gamma_\mu \Psi^f A_j^\mu + g_s f_{ijk} A_{i\mu} A j \nu \partial^\mu A_k^\nu \\ &- \frac{1}{4} g_s^2 f_{ijk} f_{ilm} A_j^\mu A_k^\nu A_{lmu} A_{m\nu} \\ &= \mathcal{L}_q^0 + \mathcal{L}_g^0 + \mathcal{L}_{qqg}^I + \mathcal{L}_{ggg}^I + \mathcal{L}_{gggg}^I, \end{aligned} \tag{1.11}$$

where $\mathcal{L}_q^0$ describes the free quarks lagrangian, $\mathcal{L}_g^0$ is the free gluon lagrangian term, $\mathcal{L}_{qqg}^I$ describes the three-point quark-gluon interaction vertex, $\mathcal{L}_{ggg}^I$ and $\mathcal{L}_{gggg}^I$ are the three and four point gluon vertices, respectively.

Contrary to the QED, the gluons are colour-charged spin-1 bosons, that are also self-interacting. Furthermore, due to the non-diagonality of the Gell-Mann matrices, the gluon-quark interaction changes the colour charge of the quark.

The gluon self-interaction is responsible of a peculiar property of QCD, the *aymptotic freedom*. It can be proved [14] that, in absence of the gluon self-interaction term, and analogously to the QED case, the fermionic self-interaction term would lead to a *screening* effect, i.e. the decrease of the coupling strength $\alpha_s(Q)$ with the energy scale Q; but the gluon self-interaction, with no counterpart in QED, induces an *anti-screening* effect, which is the dominating one, leading to an overall increase of $\alpha_s(Q)$ with Q. In the leading log approximation, $\alpha_s(Q)$ *runs* as:

$$\alpha_s(Q) = \frac{\alpha_s(Q_0)}{1 + [\beta_0/4\pi]\alpha_s(Q_0)\ln(Q^2/Q_0^2)}, \tag{1.12}$$

where $\alpha_s(Q_0)$ is a value arbitrarily taken at a reference scale Q_0 and $\beta_0 = 11 - 2/3 n_f$, n_f being the number of quark flavours. Equation 1.12 shows that

at very high energies or, equivalently, at very short distances, α_s tends to zero, so that quarks inside hadrons are essentially free, given that the typical hadron radius is of the order of 1 fm.

Equation 1.12 is often expressed in terms of a scale parameter $\Lambda \sim 200$ MeV, measured in experiments, at which α_s becomes large as Q decreases:

$$\alpha_s(Q) = \frac{4\pi}{\beta_0 \ln\left(Q^2/\Lambda\right)}, \tag{1.13}$$

Taking into account Equation 1.12, a common choice for the reference scale is $Q_0 = m_Z = 91.1876$ GeV. The latest world average for $\alpha_s(m_Z)$ is [9]:

$$\alpha_s(m_Z^2) = 0.1181 \pm 0.0011, \tag{1.14}$$

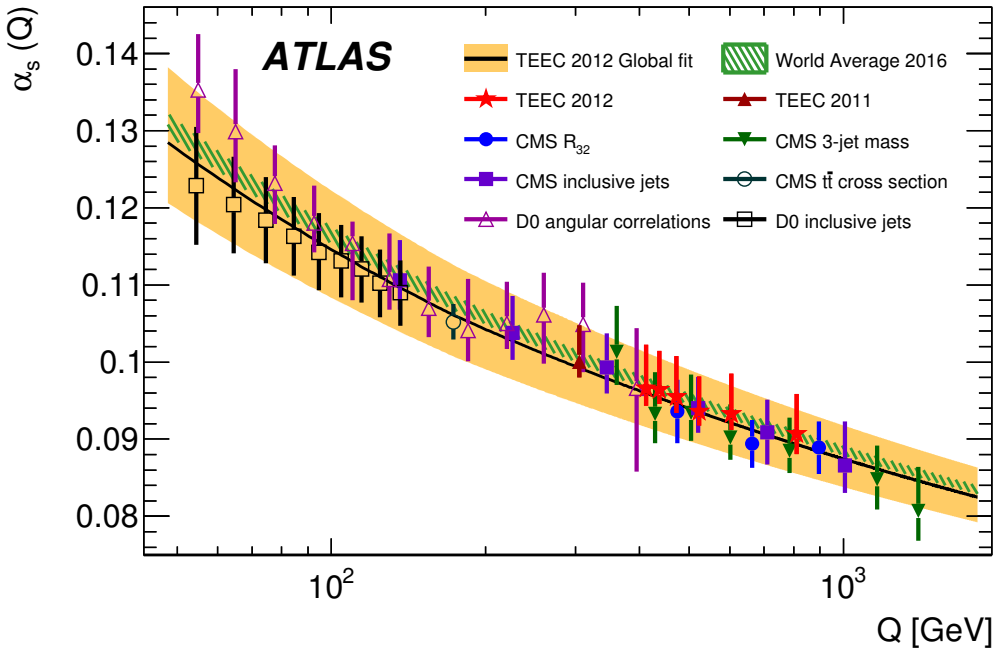

FIGURE 1.2: Comparison of the values of $\alpha_s(Q)$ obtained from fits to the TEEC [15] functions (red star points) with the uncertainty band from the global fit (orange full band) and the 2016 world average (green hatched band). Determinations from other measurements from DØ and CMS experiments are also shown. The error bars include all experimental and theoretical sources of uncertainty.

Figure 1.2 shows a recent ATLAS measurement [16] of α_s at different values of Q obtained by fitting to the Transverse Energy-Energy Correlation (TEEC) functions [15] and several measurements from DØ and CMS Collaborations. The *running* behaviour of α_s as a function of Q is evident.

1.4 Weak Interactions

The weak interactions are described in terms of a non-Abelian gauge theory invariant under the $SU(2)$ symmetry group. Like QED and QCD, the force is mediated through spin-1 bosons, namely the massive charged $W^{\pm}$ and neutral Z^0 bosons. Given their large masses ($m_W = 80.385 \pm 0.015$ GeV and $m_Z = 91.1876 \pm 0.0021$ GeV), the interaction range of the force is of the order of 10^{-3} fm, since it is given by the Compton wavelength of the mediator. The $SU(2)_L \otimes U(1)$ gauge-invariant theory describing, at the same time, both the weak and electromagnetic interactions, referred as *electroweak* theory, was developed by Glashow, Salam and Weinberg in the 60s [17–19]. The L subscript is to remark that the weak force only acts on left-handed fermions. Two remarkable aspect of the electroweak theory are:

1. the unification of the electromagnetic and weak interactions, which can be considered a major breakthrough just as the unification of the electric and magnetic forces by Faraday and Maxwell;
2. in addition to the description of the already observed charged currents (mediated by the $W^{\pm}$ bosons), responsible, among others, of the radioactive decays of nucleons, a third, neutral current, mediated by the Z^0 boson, naturally arose in theory. It was only observed at CERN in 1973 by the Gargamelle Collaboration [20], several years after its prediction.

In the next Section, a brief overview of the electroweak theory is presented.

1.5 Electroweak theory

The Lagrangian density of free fermions can be expressed in terms of the helicity-defined left and right-handed Dirac field $\psi_l^{L,R}$:

$$\psi_l^{L,R} = \frac{1}{2}(1 \mp \gamma^5)\psi_l, \tag{1.15}$$

where $\gamma^5 = i\gamma^0\gamma^1\gamma^2\gamma^3$. Since the $SU(2)_L$ only acts on left-handed fields, a weak isospinor, Ψ_l^L, is defined:

$$\Psi_l^L = \begin{pmatrix} \psi_{\nu_l}^L \\ \phi_l^L \end{pmatrix}, \tag{1.16}$$

where ν_l is the neutrino belonging to the leptonic family l. It is named after the conserved charge of the $SU(2)_L$ group, the weak isospin charge. The Lagrangian density of free leptons reads:

$$\mathcal{L}_l = i\left[\bar{\Psi}_l^L \gamma^\mu \partial_\mu \Psi_l^L + \bar{\psi}_l^R \gamma^\mu \partial_\mu \psi_l^R + \bar{\psi}_{\nu_l}^R \gamma^\mu \partial_\mu \psi_{\nu_l}^R\right], \tag{1.17}$$

where no mass term is present in order to preserve gauge-invariance. Section 1.6 will show how the masses are restored through the electroweak spontaneous symmetry breaking mechanism.

Equation 1.17 is required to be invariant under the following transformations:

$$\begin{cases} \Psi_l^L(x) \to \exp\left[ig\tau_j\omega_j(x)/2\right]\Psi_l^L(x) \\ \psi_{l,\nu_l}^R \to \psi_{l,\nu_l}^R(x) \\ \psi_{l,\nu_L}(x) \to \exp\left[ig'Yf(x)\right]\psi_{l,\nu_L}(x) \end{cases}, \tag{1.18}$$

where g and g' are coupling constants, τ_j are the 2×2 Pauli matrices, $\omega_j(x)$ and $f(x)$ are arbitrary, differentiable functions and $Y = -1/2, -1, 0$ is the weak hypercharge associated with the Ψ_l^L, ψ_l^R and $\psi_{\nu_l}^L$ fields, respectively. The coupling constants are linked to the elementary charge e by the following relation:

$$g\sin\left(\theta_W\right) = g'\cos\left(\theta_W\right) = e, \tag{1.19}$$

where $\theta_W = 0.2232 \pm 0.0003$ [21] is the *Weinberg angle*.

The invariance of the lagrangian (Equation 1.17) under the gauge transformation (Equation 1.18) is assured through the introduction of the covariant derivatives:

$$\begin{cases} D^\mu\Psi_l^L = \left[\partial^\mu + ig\tau_j W_j^\mu/2\right]\Psi_l^L \\ D^\mu\psi = \left[\partial^\mu + ig'YB^\mu\right]\psi \end{cases}, \tag{1.20}$$

where W_j^μ is an isotriplet of gauge fields, associated to $SU(2)_L$, and B^μ is a singlet gauge field, associated to $U(1)$. They transform (for infinitesimal ω_i and f) as:

$$\begin{cases} W_i^\mu \to W_i^\mu - \partial^\mu\omega_i - g\epsilon_{ijk}\omega_j W_k^\mu \\ B^\mu \to B^\mu - \partial^\mu f \end{cases}, \tag{1.21}$$

where ϵ_{ijk} are the structure constants of the $SU(2)_L$ group. The four gauge fields can be linearly combined to represent the W_μ, $W_\mu^\dagger$, Z_μ^0 and A_μ vector fields, associated to the $W^\pm$, Z^0 and γ bosons:

$$\begin{cases} W_\mu = \frac{1}{\sqrt{2}}(W_\mu^{(1)} + iW_\mu^{(2)}) \\ W_\mu^\dagger = \frac{1}{\sqrt{2}}(W_\mu^{(1)} - iW_\mu^{(2)}) \\ W_\mu^{(3)} = \cos\left(\theta_W\right)Z_\mu + \sin\left(\theta_W\right)A_\mu \\ B_\mu = \sin\left(\theta_W\right)Z_\mu + \cos\left(\theta_W\right)A_\mu \end{cases}. \tag{1.22}$$

The resulting Lagrangian density for the resulting electroweak interaction is:

$$\begin{aligned} \mathcal{L}_I =& -\bar{\psi}_l\gamma^\mu A_\mu\psi_l - g_W[\bar{\psi}_{\nu_l}\gamma^\mu(1-\gamma^5)W_\mu\psi_l + \bar{\psi}_l\gamma^\mu(1-\gamma^5)W_\mu^\dagger\psi_{\nu_l}] \\ & - g_Z\{\bar{\psi}_{\nu_l}\gamma^\mu(1-\gamma^5)\psi_{\nu_l} - \bar{\psi}_l\gamma^\mu[(1-4\sin^2\left(\theta_W\right)-\gamma^5]\psi_l\}Z_\mu \\ =& \mathcal{L}_I^\gamma + \mathcal{L}_I^W + \mathcal{L}_I^Z, \end{aligned} \tag{1.23}$$

where $g_W = g/[4\cos(\theta_W)]$ and $g_Z = g/[4\cos(\theta_W)]$, while $\mathcal{L}_I^\gamma$, $\mathcal{L}_I^W$ and $\mathcal{L}_I^Z$ describe the electromagnetic current, the charged weak current and the neutral weak current, respectively. Finally, the Lagrangian density for the boson fields is:

$$\begin{aligned}\mathcal{L}_B &= -\frac{1}{4}F_{\mu\nu}F^{\mu\nu} - \frac{1}{2}F^\dagger_{W,\mu\nu}F_W^{\mu\nu} - \frac{1}{4}Z_{\mu\nu}Z^{\mu\nu} \\ &= \mathcal{L}_\gamma + \mathcal{L}_W + \mathcal{L}_Z,\end{aligned} \tag{1.24}$$

where the terms $\mathcal{L}_\gamma$, $\mathcal{L}_W$ and $\mathcal{L}_Z$, expressed in terms of the tensor fields $F^{\mu\nu}$, $F_W^{\mu\nu}$ and $Z^{\mu\nu}$, describe the free γ, W bosons and Z boson fields, respectively.

The EW theory can be easily extended to also take into account quarks by defining a *quark* weak isospin doublet $\Psi^L_{q_i}$:

$$\Psi^L_{q_i} = \begin{pmatrix}\psi^L_{u_i} \\ \phi^L_{d'_i}\end{pmatrix}, \tag{1.25}$$

where u_i is a quark with flavour i and $d'_i = \sum_j V_{ij}d_j$, where V is the Cabibbo-Kobayashi-Maskawa (CKM) mixing matrix. It explains all the CP-violating phenomena in flavour-changing processes in the SM. A recent determination of the CKM matrix elements [9] is:

$$\begin{aligned}V &= \begin{bmatrix}V_{ud} & V_{us} & V_{ub} \\ V_{cd} & V_{cs} & V_{cb} \\ V_{td} & V_{ts} & V_{tb}\end{bmatrix} \\ &= \begin{bmatrix}0.97417 \pm 0.00021 & 0.2248 \pm 0.0006 & (4.09 \pm 0.39)\cdot 10^{-3} \\ 0.220 \pm 0.005 & 0.995 \pm 0.016 & (40.5 \pm 1.5)\cdot 10^{-3} \\ (8.2 \pm 0.6)\cdot 10^{-3} & (40.0 \pm 2.7)\cdot 10^{-3} & 1.009 \pm 0.031\end{bmatrix},\end{aligned} \tag{1.26}$$

by substituting $\Psi_l \to \Psi_f$, where f indicates a generic fermion, the final Lagrangian density for the EW interaction is:

$$\mathcal{L}_{EW} = \mathcal{L}_g + \mathcal{L}_I + \mathcal{L}_B + \mathcal{L}_{Higgs}, \tag{1.27}$$

where the additional term $\mathcal{L}_{Higgs}$, which will be further discussed in the next Section, accounts for the non-vanishing masses of the elementary particles.

1.6 Spontaneous symmetry breaking mechanism

In order to preserve the $SU(2)_L$ symmetry in the weak interactions and provide mass to the $W^\pm$ and Z^0 bosons, the spontaneous $SU(2)_L$ symmetry breaking mechanism can be exploited. A new weak isospin doublet, Φ, composed of two scalar fields, ϕ_a and ϕ_b, transforming as Ψ^L_l, under the $SU(2)_L$ transformations, and $\psi_{l\,\nu_l}$ under $U(1)$ ones (cfr. Equation 1.18) is introduced. The value of ipercharge is $Y = 1/2$. This ensures invariance of the field under

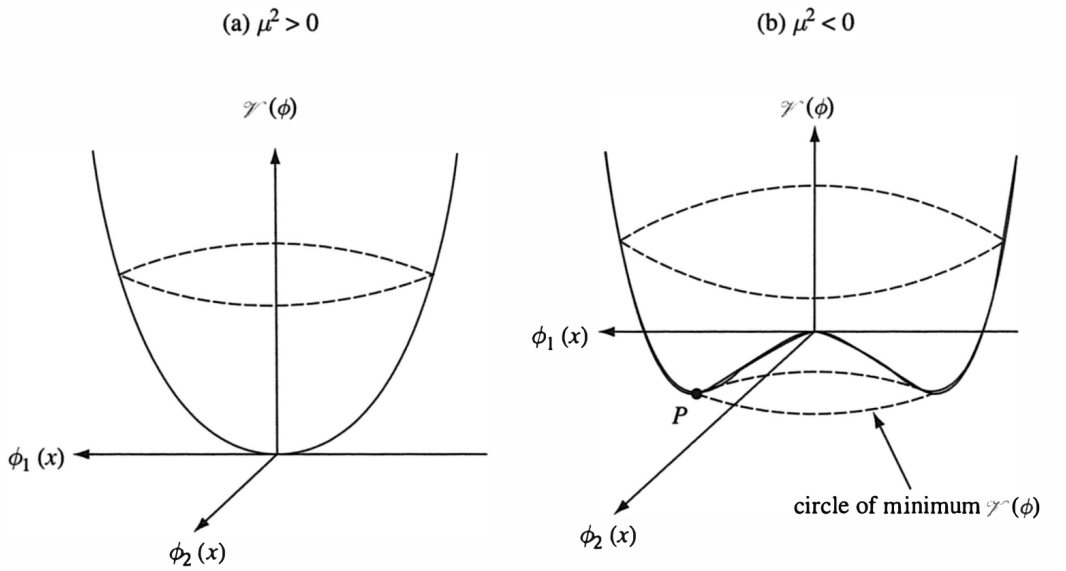

FIGURE 1.3: The Higgs potential $\mu^2\Phi^\dagger\Phi - \lambda[\Phi^\dagger\Phi]^2$ for $\lambda > 0$. In case (a), no degeneration of the ground state occurs; in case (b), a degenerate circle of minimum potential exists and an arbitrary choice for the ground state can be made.

$U(1)$ transformations. The Lagrangian density for Φ, the Higgs field, is:

$$\mathcal{L}_{Higgs} = [D^\mu\Phi]^\dagger[D_\mu\Phi] - \mu^2\Phi^\dagger\Phi - \lambda[\Phi^\dagger\Phi]^2, \tag{1.28}$$

where λ is a positive real parameter and $\mu^2 < 0$. As usual, the covariant derivative is introduced:

$$D^\mu\Phi = [\partial^\mu + ig\tau_j W_j^\mu/2 + ig'YB^\mu]\Phi. \tag{1.29}$$

As Figure 1.3 shows, when $\mu^2 < 0$, the state of lowest energy for Φ, the vacuum state, is not unique. The vacuum expectation state is $\Phi_0^2 = -\frac{\mu^2}{2\lambda} = \frac{\nu^2}{2}$, corresponding to a circumference with radius Φ_0^2 in the complex plane. Among all possible ground states, one can be arbitrarly chosen. A common choice is:

$$\Phi_0 = \frac{1}{\sqrt{2}}\begin{pmatrix}0\\ \nu\end{pmatrix}. \tag{1.30}$$

The choice of the ground state is what *breaks* the symmetry, leading to the weak bosons to acquire mass. According to the Goldstone theorem [11], breaking the symmetry produces one physical scalar field that gives rise to a spin-0, electrically neutral particle, the Higgs boson, with mass $m_H = \sqrt{2\lambda\nu}$ and three unphysical fields that can be gauged away (i.e. removed), so that the weak bosons acquire mass. In July 2012, the ATLAS [22] and CMS [23] announced the discovery of the Higgs boson. The combination of the ATLAS and CMS mass measurements [24] gives:

$$m_H = 125.09 \pm 0.21\,(\text{stat.}) \pm 0.11\,(\text{scale}) \pm 0.01\,(\text{theory})\ \text{GeV}. \tag{1.31}$$

1.7 Principles of collider physics

In an hadron collider experiment, such as the LHC, hadron beams are accelerated up to very high energies and then let them interact. The interaction takes place between constituents of the hadrons, which carry different fractions of their momentum. Although the hard-scattering processes (i.e. between the point-like constituents of hadrons) can be successfully described in the framework of the SM, some new concepts need to be introduced in order to allow a fair comparison between observed quantities and theoretical predictions. In particular, the basic ingredients of the cross section will be presented. The cross section is defined as the probability that a given reaction between interacting particles occurs. It is expressed in terms of area, since its geometrical meaning is the area of the scattering centers in a fixed target exposed to the incident particle beam. It is measured in barns, b, where $1\ \text{b} = 10^{-24}\ \text{cm}^{-1}$. Its theoretical counterpart, the transition rate, is described by Fermi's Golden Rule [25]. Subsection 1.7.1 will introduce the factorization theorem, widely employed to express the cross section for a process initiated by at least one hadron in terms of a perturbative term, the hard-scattering cross section, and a non-perturbative one describing the internal structure of the hadrons, the Parton Density Functions (PDFs), discussed in Subsection 1.7.2. From an experimental point of view, the cross section can be defined independently of the machine design by means of the luminosity ($\mathscr{L}$), introduced in Subsection 1.7.3.

1.7.1 Factorization Theorem

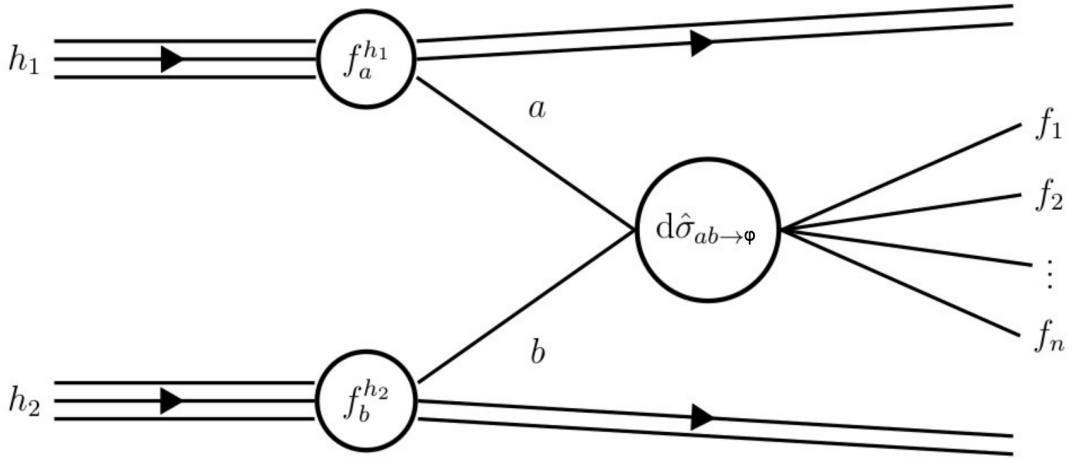

FIGURE 1.4: Schematic representation of the Factorization Theorem for hadron-hadron cross section.

As already observed in Section 1.3, the $\Lambda \sim 200$ MeV parameter present in Equation 1.13 sets the scale above which partons inside hadrons can be considered *free*. It is then possible to separate the total cross section σ into two components:

- short distance factor: the hard-scattering process in which perturbative QCD (pQCD) can be applied;
- long distance factor: the description of the internal structure of the hadron. This term is intrinsically non perturbative and pQCD is not applicable.

The two terms are independant of each other, in the sense that the non perturbative one does not depend on the specific hard-scattering process considered. This separation is justified by the Factorization Theorems [4, 26], depicted in Figure 1.4 for an hadron-hadron initiated process. The total cross section σ^{h_1,h_2} can be expressed as:

$$\sigma^{h_1,h_2} = \sum_{a,b} \iint_0^1 dx_a dx_b \int_\phi f_a(x_a,\, \mu_F) f_b(x_b,\, \mu_F) d\hat{\sigma}_{ab\to\phi}(x_a p_1,\, x_b p_2,\, Q^2,\, \mu_F,\, \mu_R), \tag{1.32}$$

where h_1 and h_2 are the incoming hadrons (protons at the LHC), a and b are the parton flavours, μ_F is the factorization scale, separating the long and short scales, μ_R is the renormalization scale, introduced to regularize UV divergences appearing at higher perturbative orders in pQCD, $f_{a,b}$ are the PDFs, further discussed in the following Subsection 1.7.2, and $d\hat{\sigma}_{ab\to\phi}$ is the hard-scattering cross section, calculated with pQCD methods, for the production of the final state ϕ from partons a and b.

1.7.2 Parton Density Functions

The proton is a composite particle made of three valence quarks, (u, u, d), and a *sea* of virtual quark-antiquark pairs and gluons continuously absorbed and emitted. One would then have to consider all the interactions occurring between the proton constituents, called partons. But since the energy of the colliding protons is generally more than one order of magnitude larger than the Λ scale, introduced in Equation 1.13 of Section 1.3, the proton can be seen as a composite system made of *almost free* costituents, each of them carrying a fraction x of its total momentum p_i. The Parton density functions (PDFs) are a set of funtions which allow to understand the internal proton structure by describing the momentum distributions of its constituent partons. The PDFs are universal, in the sense that they do not depend on the particular physics process considered, and are usually expressed as:

$$f_i(x, Q^2), \quad i \in \{u,\, d,\, c,\, s,\, g\}\,, \tag{1.33}$$

where $f_i(x, Q^2)$ gives the probability of finding a parton of type i carrying a fraction of momentum x at a definite energy scale Q. The dependance of the Q scale is given by the Dokshitzer-Gribov-Lipatov-Altarelli-Parisi, DGLAP, evolution functions. Their complete formulation can be found in [27]. Their

simplified form, in which only one quark flavour is assumed, reads:

$$\frac{d}{d\ln Q^2}\begin{pmatrix} q \\ g \end{pmatrix} = \frac{\alpha_s(Q^2)}{2\pi}\begin{pmatrix} P_{qq} & P_{qg} \\ P_{gq} & P_{gg} \end{pmatrix} \otimes \begin{pmatrix} q \\ g \end{pmatrix}, \tag{1.34}$$

where $\otimes$ indicates the Mellin convolution:

$$P_{ij} \otimes q = \int_x^i P_{ij}(z)\frac{q(x/z, Q^2)}{z}dz, \tag{1.35}$$

between the PDF of the quark (gluon) and the splitting functions P_{ij}, which gives the probability that a parton j converts into a parton i carrying a fraction z of the momentum of j. These function can be calculated with perturbative methods. With the DGLAP equations, the PDFs can be evolved to any scale Q, provided that they have been extracted from data at a certain initial scale. The extraction is performed from a selection of hard-scattering processes, measured at different experiments.

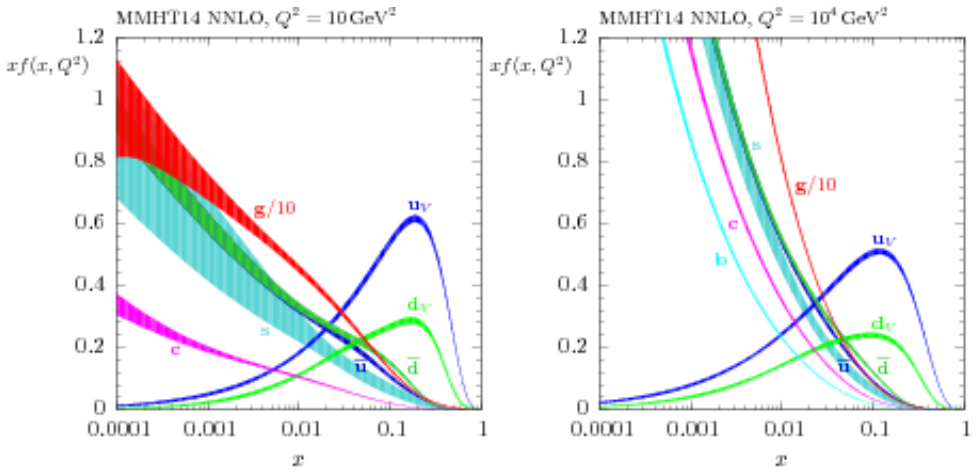

(A) (B)

FIGURE 1.5: NNLO PDFs from the MMHT14 set evaluated at $Q^2 = 10$ GeV (a) and $Q^2 = 10^4$ GeV (b). The associated solid bands represent the 68% confidence-level uncertainties. The Figures has been taken from [28]

The particular choice of the fitting models, the data used in the extraction, the number of quark flavours taken into account and the perturbative order the DGLAP evolution is calculated define a PDF set. Many PDF sets exist, they are provided by different groups. The most up-to-date are the CT14 [29], MMHT14 [28], NNPDF3.0 [30], HERAPDF2.0 [31], ABM12 [32], JR14 [33] and CJ12 [34]. They are available at leading order (LO), next-to-leading order (NLO) and, in some cases, next-to-next-to-leading order (NNLO) in pQCD. Figure 1.5 shows the MMHT14 NNLO PDF set evaluated $Q^2 = 10$ GeV and $Q^2 = 100$ GeV. As it will become clear in next Section and in Chapter 4, where Monte Carlo simulations will be introduced, PDFs play a fundamental role at hadron colliders. There are three main contexts in which PDFs are used at the LHC:

1. comparison between data and theory for SM measurements;
2. searches for Beyond the SM (BSM) phenomena;
3. calculation of PDF uncertainties in precision observables.

In the first case, precision measurements of SM processes can contribute in constraining the PDFs, so a comparison between different PDF sets is advisable. In the other cases, the choice of the PDF sets may have a strong impact on the measurement, because BSM searches often require the knowledge of PDF in the $x \sim 1$ region, where data constraints are limited (second case) or because the PDF uncertainties can affect the extraction of the physics parameter of interest (third case). To overcome those issues, at the LHC, the PDF4LHC Working Group has provided a recommended PDF set, PDF4LHC15 [35], suitable for application at the LHC Run II[2], which contains, among others, information from experimental data from Run I. The set is derived from a statistical combination of PDF sets provided by other groups, namely the CT14, MMHT14 and NNPDF3.0 sets.

1.7.3 Luminosity at proton-proton colliders

At hadron colliders, the event rate $\dot{N}_r$, i.e. the number of events per second generated in the collisions, is determined by the instantaneous luminosity $\mathscr{L}$ of the machine and the cross section σ for the relevant physic process taken into account:

$$\dot{N}_r = \mathscr{L}\sigma, \tag{1.36}$$

The machine luminosity only depends on beam parameters. At proton-proton (pp) colliders, like the LHC, it can be written, assuming a Gaussian beam distribution, as:

$$\mathscr{L} = \frac{N_b^2 n_b f_{rev} \gamma_r}{4\pi\epsilon_n \beta^*} F, \tag{1.37}$$

where N_b is the number of particles per bunch, n_b is the number of bunches per beam, f_{rev} is the revolution frequency, $\gamma_r = 1/\sqrt{1-\beta_r^2}$ is the relativistic gamma-factor, with $\beta_r = v/c$. $\epsilon_n = \epsilon\gamma_r\beta_r$ is the normalized transverse beam emittance, where ϵ is the transverse emittance, defined as the average of the areas enclosed by the single particle phase space ellipsoids, divided by π, componing the beam. The normalized transverse emittance at the LHC is [36] $\epsilon_n = 3.75$ μm. β^* is the wavelenght of the betatron oscillations of the beams at the interaction point (IP), i.e. where the beams intersect, and F is the geometric luminosity reduction factor due to the crossing angles at the IP:

[2]More information on LHC Runs will be given in Chapter 2

$$F = 1/\sqrt{1 + \left(\frac{\theta_c \sigma_z}{2\sigma^*}\right)}, \tag{1.38}$$

where θ_c is the crossing angle between the beams, σ_z is the RMS of the bunch lenght and σ^* is RMS of the transverse beam size. Each quantity is measured at the IP. In actual measurements, Equation 1.36 is integrated over the operating time of the machine (T_{op}) to give the number of observed events, N:

$$N = \int_{T_{op}} \dot{N}_r(t)dt = \left(\int_{T_{op}} \mathscr{L}(t)dt\right)\sigma = L\sigma, \tag{1.39}$$

where L, measured in inverse barns, is the integrated luminosity.

1.8 The top quark at the LHC

More than 20 years ago, in 1995, the CDF and D$\emptyset$ Collaboration announced the discovery of the top quark [37, 38] at the Tevatron proton-antiproton collider at Fermilab. Top quark existence was predicted long before its actual discovery. Kobayashi and Maskawa realized in 1973 that the CP-violation due to flavour mixing, presented in Section 1.5, can only be explained if at least three quarks isospin doublets exists. The weak isospin partner of the top quark, the bottom quark, was discovered at the Tevatron in 1977 [39]. Initially, the top mass was supposed to be close to the bottom ones, of the order of 10 GeV, so measurements focused on the process $W^+ \to t\bar{b}$. When in 1992 the CDF collaboration set the lower limit for the top mass to 91 GeV [40], the decay $t \to W^+b$ was now kinematically allowed, leading to different search strategies at Tevatron and its discovery.

The top quark is now being extensively studied at the LHC, which is also referred as a *top quark factory*, because of its high rate of top quarks production. There are two possible production modes; the top-antitop quark pair production, via strong interactions, and the subdominant electroweak production of single top quarks. In the last part of this Chapter, the foundamental properties of the top quark will be reviewed.

1.8.1 Top quark properties

The top quark is the heaviest particle of the SM. Its mass, m_t is a fundamental parameter of the SM, directly related, through quantum corrections, to other parameters, such as the masses of the W and the Higgs bosons. Furthermore, the mass of the top quark plays a central role in the stability of the electroweak vacuum up to very high energy scales [42]. This is why a precise measure of m_t is a very important ingredient of precision tests of the SM. In the SM, fermion masses are generated by their Yukawa coupling to the Higgs

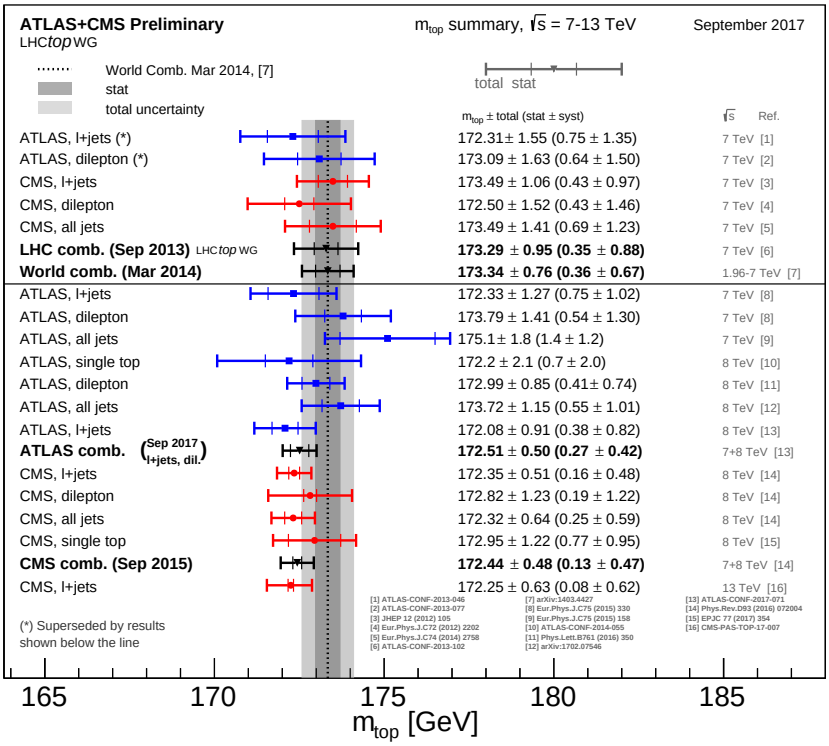

FIGURE 1.6: Summary of the ATLAS and CMS direct m_t measurements. The results are compared with the LHC and Tevatron+LHC m_t combinations. For each measurement, the statistical uncertainty and the sum in quadrature of the statistical and systematic uncertainties are shown. The results below the solid black line have been produced after the LHC and Tevatron+LHC combinations were performed. Figure taken from [41].

boson. The Lagrangian density relative to the top-Higgs Yukawa interaction is:

$$\mathcal{L}_{Yukawa,\,top} = -y_t \frac{\nu}{\sqrt{2}}(\bar{\Psi}_t^L \Psi_t^R + \bar{\Psi}_t^R \Psi_t^L), \quad m_t = y_t \frac{\nu}{\sqrt{2}}, \tag{1.40}$$

where $\Psi_t^{R,\,L}$ is the right (left)-handed three-component field for the top quark and y_t is the top-Yukawa coupling constant. Figure 1.6 shows a summary of the top mass measurement at the Tevatron and at the LHC, it includes the reference value for the top mass value, the 2014 Tevatron + LHC world combination [43]:

$$m_t = 173.34 \pm 0.27\,(stat.) \pm 0.71\,(syst.)\,\text{GeV}, \tag{1.41}$$

Due to the large mass of the top quark and since $\nu = \sqrt{\sqrt{2}G_F} \sim 246$ GeV, with G_F the Fermi constant, the y_t value is very close to one. This can be an hint that the top quark may play a special role in BSM physics. The top quark decay via the electroweak charged-current process $t \to W^+q$, where q is a down-type quark. At LO, the total decay width of the top quark reads:

$$\Gamma_t^{LO} = \frac{G_F}{8\pi\sqrt{2}} \left(1 - \frac{m_W^2}{m_t^2}\right)\left(1 + 2\frac{m_W^2}{m_t^2}\right) \sim 1.5\,\text{GeV}. \tag{1.42}$$

IF NNLO QCD corrections and NLO EW corrections are included, the decay width results smaller by approximately 10% [44]. The partial decay width $\Gamma(t \to W^+q)$ is proportional to the CKM matrix element $|V_{tq}|$. It was shown in Section 1.5 that $|V_{tb}| >> |V_{ts}| > |V_{td}|$, this implies that the $t \to W^+b$ is the leading process, with a branching ratio $BR(t \to W^+b) = 0.998$ [9]. The inverse of the decay width is the top quark mean lifetime, $\tau_t = 5 \cdot 10^{-25}$ s. This value is an order of magnitude smaller than the time of hadronization, $\tau_\Lambda = \Lambda^{-1} \sim 3 \cdot 10^{-24}$ s. This implies that the top quark decays before hadronizing. This gives an unique opportunity to study the properties of a free quark, since top quark properties are transferred to its decay products. Furthermore, because the top quark decay is an EW process, the W bosons are polarized. This is the only source of polarized W bosons in the SM. At LO, the fraction of left-handed (F_L), longitudinal (F_0) and right-handed (F_R) polarization are:

$$\begin{cases} F_L = \frac{2m_W^2}{m_t^2+2m_W^2} \\ F_0 = \frac{m_t^2}{m_t^2+2m_W^2} \\ F_R = \frac{m_b^2}{m_t^2}\frac{2m_W^2}{(1-m_t^2/m_W^2)^2(m_t^2+2m_W^2)} \end{cases}, \tag{1.43}$$

whilst the most recent NNLO predictions [45] gives $F_L = 0.3108$, $F_0 = 0.688$ and $F_R = 0.00126$). The predicted values are in good agreement with the measured quantities at the LHC, as shown in Figure 1.7.

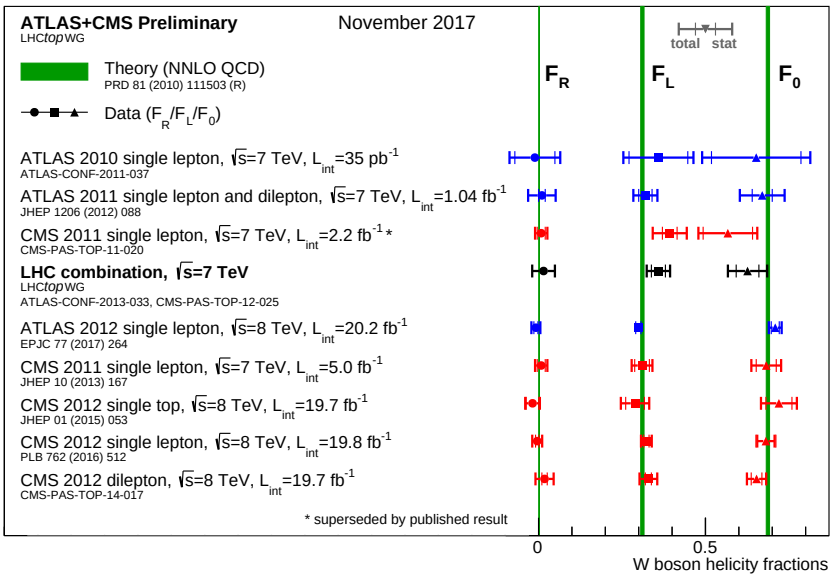

FIGURE 1.7: Summary of measured W helicity fractions by ATLAS and CMS at 7 and 8 TeV, compared to the respective theory predictions. The uncertainty on the theory predictions is shown by a green band, the total experimental uncetainties are given by the sum in quadrature of the statisical and systematic ones. Figure taken from [41]

1.8.2 Top quark decay modes

As already mentioned in Section 1.8, top quarks can be produced in $t\bar{t}$ pairs, via strong interaction, or as single particles in EW processes. Since the top quark decays almost exclusively to a W boson and a b quark, its decay signatures can be categorized according to the decay mode of the W boson (Figure 1.8). In the leptonic decay mode ($BR(W^+ \to l^-\bar{\nu}_l) \sim 33\%$), the W boson decays to a lepton (antilepton) and its associated antineutrino (neutrino), while in the hadronic decay mode ($BR(W^+ \to q\bar{q}') \sim 67\%$), the W boson decays to an up-type quark (antiquark) and a down-type antiquark (quark).

The top-antitop quark pairs are classified according to the decay modes of W^+W^- associated bosons in the following three *channels*:

- **completely hadronic or all jets**, Figure 1.9b: this is the channel where both W bosons decay hadronically. This channel has the largest Branching Ratio (BR$\sim 45\%$) but it is the most background contaminated, mostly from QCD Multijet processes, as it will be shown in Chapter 6;
- **semileptonic or ℓ+jets**, Figure 1.9c: in this channel, one of the W bosons decays hadronically, the other leptonically. This channel has an high BR ($\sim 44\%$), although several measurements exclude the τ+jets channel, reducing the BR by approximately $1/3$ ($\sim 29\%$); the background contamination is also moderate, this is why this channel is often referred as *the golden channel*;

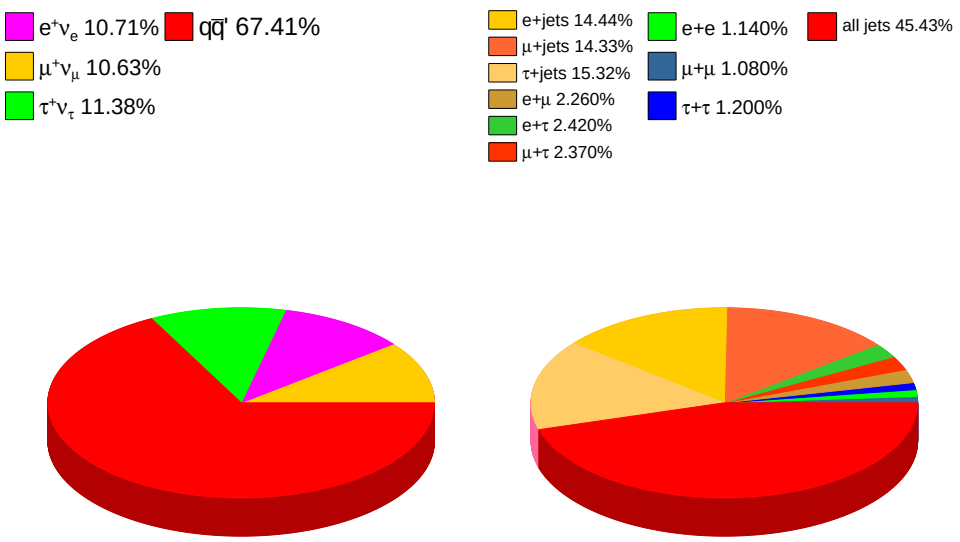

(A) (B)

FIGURE 1.8: Pie charts showing the Branching Ratios of the single top quark (a) and top-antitop quark pair production (b). Data is taken from [9].

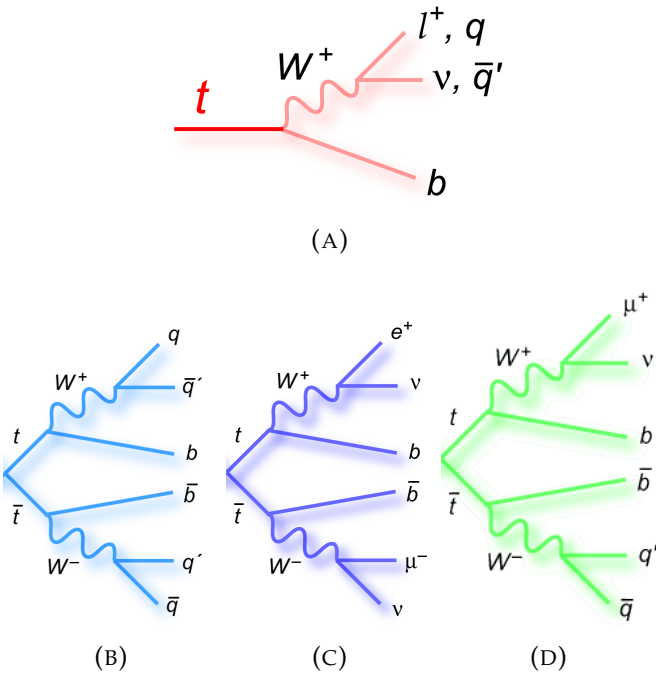

(A)

(B) (C) (D)

FIGURE 1.9: Feynman diagrams for the single top quark decay modes (a), $t\bar{t}$ completely hadronic (b), semileptonic (c) and dileptonic (d).

- **dileptonic**, Figure 1.9d: the background purest channel is the one in which both W bosons decay leptonically. It has the lowest BR ($\sim 11\%$), which is further reduced if the τ final states are excluded ($\sim 5\%$).

1.8.3 Top quark pair production

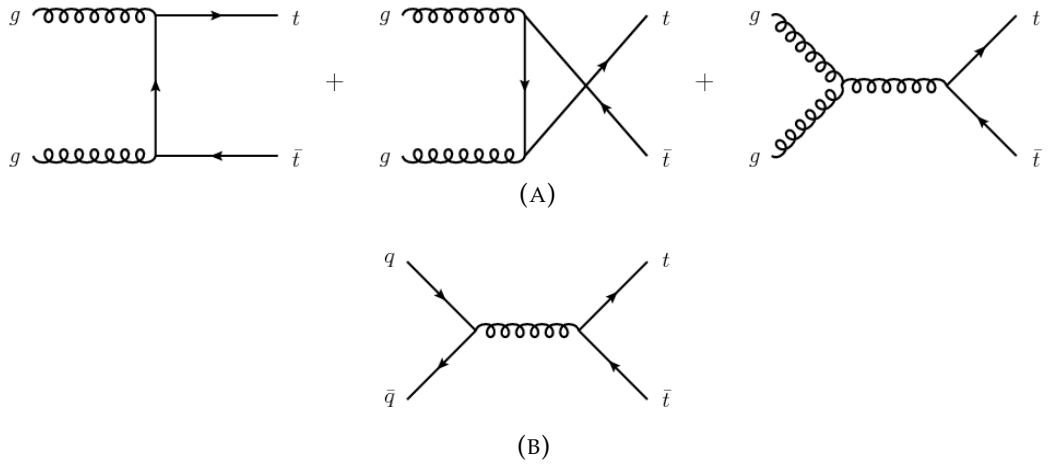

FIGURE 1.10: Feynman diagrams for the top-antitop quark pair production at Leading Order of perturbation expansion: gluon-gluon fusion (a) in the t (left), u (center) and s (right) channels and quark-antiquark annihilation (b).

Top-antitop quark pair production is the top production mode with the largest cross section at hadron colliders. At LO, $t\bar{t}$ pairs can be produced via gluon-gluon fusion (Figure 1.10a) in the s, t and u channels and quark-antiquark annihilation (Figure 1.10b). The relative weight of the two processes depends on the interacting particles and the center of mass energy $\sqrt{s}$ of the collision. In pp collisions at the LHC, with $\sqrt{s}$ spanning from 7 TeV to 14 TeV, the dominant $t\bar{t}$ production mechanism is the gg fusion (occurring $\sim 90\%$ of the times), since also at small parton momentum fraction x_i, the condition $\sqrt{x_a x_b s} \geq 2m_t$ is met and, at small x, the probability of probing a gluon increases. Furthermore, in pp collisions a large x is required to probe a sea antiquark (cfr. Figure 1.5), so $q\bar{q}$ initiated $t\bar{t}$ production is suppressed. At NLO, in addition to real additional emission (Figure 1.11a), and virtual corrections (Figure 1.11b), new production channels are allowed, namely quark-gluon (Figure 1.11c) and antiquark-gluon (Figure 1.11d) interactions. It is worth mentioning here that, when going at higher orders of the perturbative expansion, different kind of divergences start to appear. Loop diagrams introduce UV divergences, which are renormalized through the introduction of a renormalization scale, μ_R. Starting at NLO, two different additional divergencies appear:

- **collinear**, when a parton is emitted at low angles with respect to another parton;
- **soft**, when low-p_T partons are emitted.

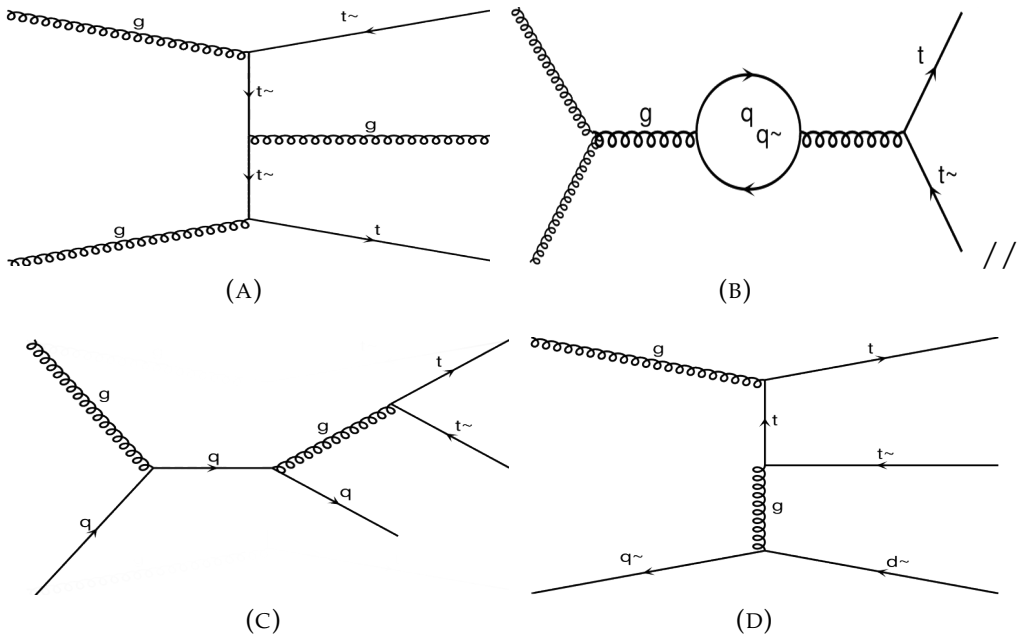

FIGURE 1.11: Selection of feynman diagrams for the top-antitop quark pair production at NLO of perturbation expansion: real quark emission (a), virtual loop correction (b), qg interaction (c) and $\bar{q}g$ interaction (d).

Those are treated by introducing a factorization scale, μ_F in the PDFs and the perturbative cross section. The introduction of μ_F effectively imposes cut on the phase-space, which spoils the pQCD calculation with large logarithmic contributions. Leading logarithm (LL) are proportional to $\alpha_s^n \ln(\dots)^{2n}$; next-to-leading logarithm (NLL) are proportional to $\alpha_s^n \ln(\dots)^{2n-1}$ and so on. We are now able to calculate resummed soft gluons contributions up to NNLL accuracy.

Figure 1.12 shows the total cross sections measured at different $\sqrt{s}$ both at the Tevatron and the LHC. The NNLO+NNLL calculations [46] are in very good agreement with data. At $\sqrt{s} = 13$ TeV, the expected total cross section is:

$$\sigma^{NNLO+NNLL}(13\text{ TeV}) = 831.76^{+19.77}_{-29.20}\,(\text{scale})\,^{+35.06}_{-35.06}\,(\text{PDFs}+\alpha_s)\,\text{pb}, \tag{1.44}$$

while the latest ATLAS [47] and CMS [48] measurements in the dilepton channel give:

$$\sigma^{ATLAS}(13\text{ TeV}) = 818 \pm 8\,(\text{stat}) \pm 27\,(\text{syst}) \pm 19\,(\text{lumi})\,\text{pb}, \tag{1.45}$$

$$\sigma^{CMS}(13\text{ TeV}) = 815 \pm 9\,(\text{stat}) \pm 38\,(\text{syst}) \pm 19\,(\text{lumi})\,\text{pb}, \tag{1.46}$$

both measurements are in very good agreement with the theory predictions.

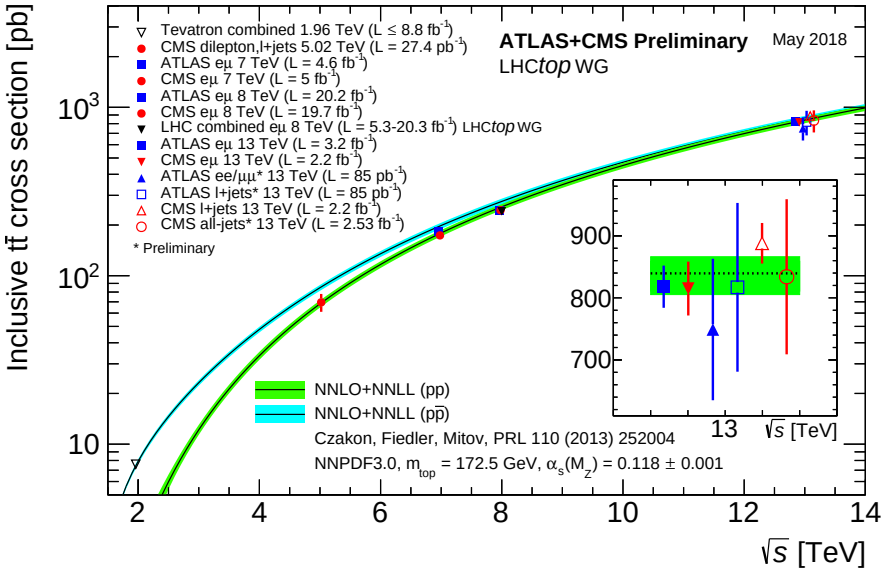

FIGURE 1.12: Summary of LHC and Tevatron measurements of the top-pair production cross section as a function of the center of mass energy compared to the NNLO+NNLL QCD calculations at $m_t = 172.5$ GeV. The theory band represents uncertainties due to renormalisation and factorisation scale, parton density functions and the strong coupling. Figure taken from [41].

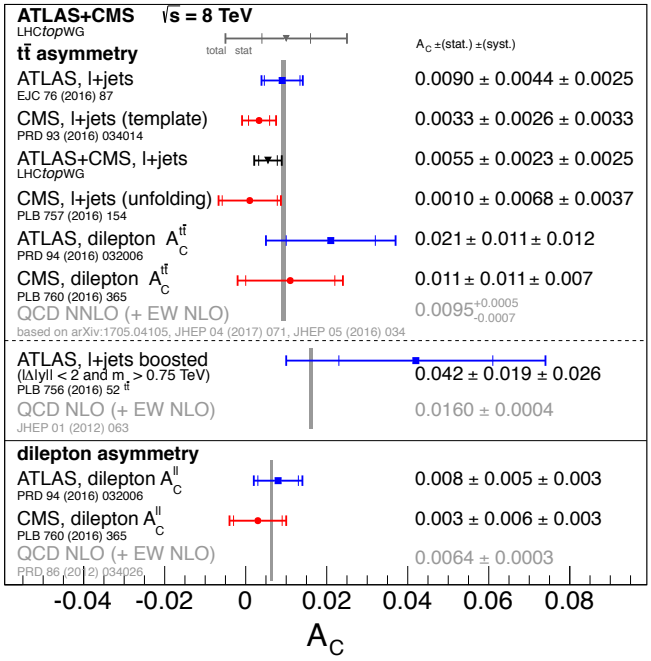

FIGURE 1.13: Summary of the charge asymmetry measurements on ATLAS and CMS at 8 TeV showing both the inclusive measurements and the measurement using boosted events, compared to the respective theory predictions. Figure taken from [41].

1.8.4 Charge asymmetry in $t\bar{t}$ quark pair production

At LO, $t\bar{t}$ pair production is symmetric under the exchange of t and $\bar{t}$, the symmetry for $q\bar{q}$ annihilation processes is broken at NLO, where a small asymmetry is predicted. Another source of asymmetry comes from EW corrections to $t\bar{t}$ pair production. A large observed asymmetry could represent a clear signal of BSM physics. At the LHC, the observable in which the asymmetry is more clearly manifested is the charge asymmetry, A_C, defined as:

$$A_C = \frac{N^{\Delta|y|>0} - N^{\Delta|y|<0}}{N^{\Delta|y|>0} + N^{\Delta|y|<0}}, \tag{1.47}$$

where $\Delta|y| = |y_t| - |y_{\bar{t}}|$ is the difference of the absolute values of the rapidity between the top and antitop quarks.

In pp collision at $\sqrt{8}$ TeV, the NLO+NLO EW correction predicted value [49] for the dilepton channel is very small; $A_C = 0.0064 \pm 0.0003$. This is in good agreement with latest ATLAS [50] and CMS [51] measurements:

$$A_C^{ATLAS} = 0.008 \pm 0.005\,(\text{stat.}) \pm 0.003\,(\text{syst.}), \tag{1.48}$$

$$A_C^{CMS} = 0.003 \pm 0.006\,(\text{stat.}) \pm 0.003\,(\text{syst.}). \tag{1.49}$$

Figure 1.13 shows a summary of the A_C measurements of the ATLAS and CMS experiments at 8 TeV in different channels, compared to (N)NLO+NLO EW theoretical predictions. No significant deviation from the SM is observed.

1.8.5 Single top quark production

The inclusive cross section for the EW single top quark production is about three times smaller with respect to the $t\bar{t}$ one. The production processes are classified according to the virtuality of the exchanged W boson. At the LHC, the dominant process is the t-channel production ($\sim 70\%$) (Figure 1.14b), followed by the associated production with a real W (Wt) (Figure 1.14a) ($\sim 25\%$). The less abundant process is the s-channel one (Figure 1.14c) ($\sim 5\%$). In Wt associated production, a set of NLO diagrams, the *double resonant*, in which the top (anti)quark is produced on-shell and the W boson is produced, in association with a b quark, from an off-shell (anti)top quark, share the same final state as the $t\bar{t}$ pair production. In MC simulation, those overlapping diagrams are addressed by removing all double-risonant contributions (diagram-removal approach) or by introducing subtraction-terms (diagram subtraction approach).

Figure 1.15 shows a comprehensive comparison between LHC measurements and NNLO or NLO+NLL predictions for the total cross section in the three single top quark channels. A good agreement between data and theory is observed in all channels.

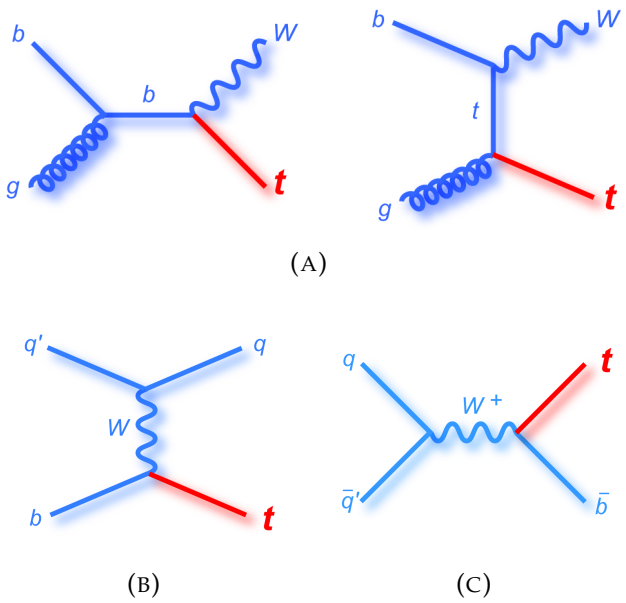

FIGURE 1.14: Feynman diagrams for the single top quark production at LO of perturbation expansion: association production with a real W (a), t-channel (b) and s-channel (c).

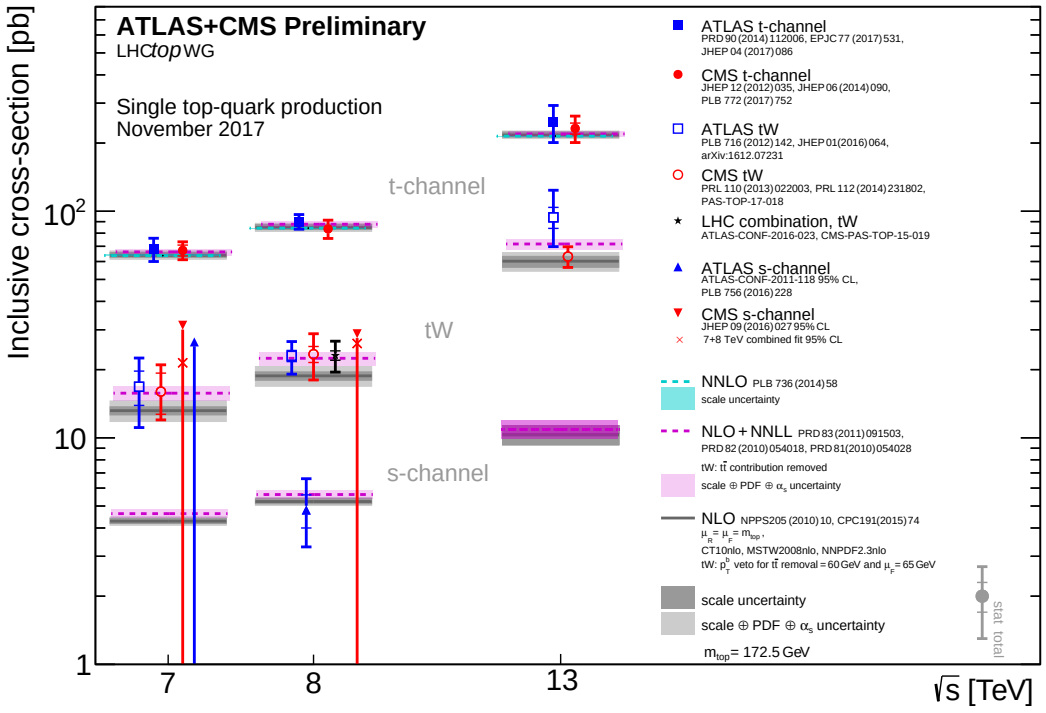

FIGURE 1.15: Summary of ATLAS and CMS measurements of the single top quark production cross sections in various channels as a function of the center of mass energy. The measurements are compared to theoretical calculations based on: NLO QCD, NLO QCD complemented with NNLL resummation and NNLO QCD (t-channel only). Figure taken from [41]

Chapter 2

The ATLAS Detector at the LHC

The *Conseil Européen pour la Recherche Nucléaire* (European Council for Nuclear Research, CERN) was one of the first Europe's joint projects. It was founded the 29^{th} September 1954 by 12 State Members, including Italy, to create an European scientific center of excellence. It now has 22 State Members and operates the largest particle physics experiment in the world. The CERN Laboratories are located on the Franco-Swiss border, between Geneva and Saint-Genis-Pouilly. The main activity at CERN is the study of the fundamental constituents of matter and the forces acting between them. To achieve this, CERN operates several accelerators and detectors. Accelerators are responsible of producing collisions between particles (protons or lead ions) at very high energy, while detectors record the products of these collisions. In Section 2.1 of this Chapter, the LHC accelerator and its experiments will be presented; while in Section 2.2 a complete description of the ATLAS experiment and its subdetectors will be given.

2.1 The Large Hadron Collider

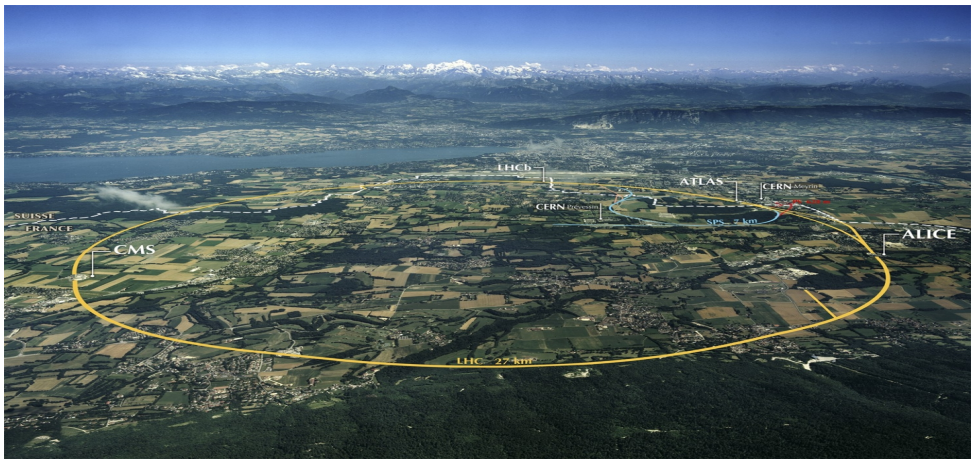

FIGURE 2.1: Bird's-eye view of the LHC accelerator complex and its experiments.

The LHC [8] at CERN is the most powerful and largest collider ever built. It is made of two superconducting rings installed in the existing 26.7 tunnel that was excavated between 1984 and 1989 for the Large Electron Positron

Collider [52] (LEP) at a depth between 45 m and 170 m below the surface. The tunnel has an internal diameter of 3.7 m and crosses the Franco-Swiss border, as shown in Figure 2.1.

The main goal of the LHC is to allow precise measurements of the SM and reveal BSM physics through *pp* collisions at a design center of mass energy of $\sqrt{s} = 14$ TeV and a peak luminosity of $\mathscr{L} = 10^{34}$ cm^{2}s. In addition to protons, the LHC is able to provide lead ions collisions (p-Pb and Pb-Pb) at $\sqrt{2.76}$ TeV and $\mathscr{L} = 10^{27}$ cm^{2}s. A complete overview of the LHC machine design has already been given in Section 1.7.3. The cumulative luminosity as a function of time delivered by the LHC, as well as the one collected by the ATLAS detector, from 2010 to 2018 is shown in Figure 2.2. The LHC began operation in November 2009 at a center of mass energy of 900 GeV, which reached $\sqrt{s} = 2.36$ TeV by the end of the year. In 2010 $\sqrt{s}$ was increased to 7 TeV and the first data, to be used by analizers, were recorded by the LHC experiments under stable beam conditions. In 2012, the center of mass energy was further increased up to 8 TeV and, after a long shutdown, the second phase of the LHC, called Run2, started to produce *pp* collisions again in 2015 at $\sqrt{s} = 13$ TeV. The achieved instantaneous peak luminosity ($\mathscr{L}_{peak}$) and collected $\mathscr{L}$, broken down by year, are shown in Table 2.1

Year	$\mathscr{L}$ fb^{-1}	$\mathscr{L}_{peak}$ cm^{-2}s^{-1}
2010	45.00	$2.1 \cdot 10^{32}$
2011	5.08	$3.6 \cdot 10^{33}$
2012	21.30	$7.7 \cdot 10^{33}$
2015	3.90	$5.1 \cdot 10^{33}$
2016	35.60	$1.5 \cdot 10^{34}$
2017	46.90	$2.1 \cdot 10^{34}$
2018	62.20	$2.2 \cdot 10^{34}$

TABLE 2.1: Achieved $\mathscr{L}$ and $\mathscr{L}_{peak}$ by the ATLAS detector, broken down by year of operation.

The two main elements of the LHC are the superconductive magnets and the Resonant Frequency cavities (RF), which bend and accelerate the beams, respectively.

The LHC superconductive magnets are made NbTi Rutherford cables, cooled down to a temperature below 2 K using superfluid helium, and operate at fields above 8 T. To reduce costs and due to tunnel space limitations, the magnets adopt a *twin-bore* design; the windings for the two beam channels are accomodated in a common cryostat. The magnetic flux circulates in opposite directions in the two beam pipes, thus allowing the circulation of two proton beams in opposite directions. The LHC ring accomodates 1232 main dipoles (Figure 2.3) to bend the particle beams, and more than 4800 higher-order multipole (quadrupole, sextupole, octupole, decapole) to correct the

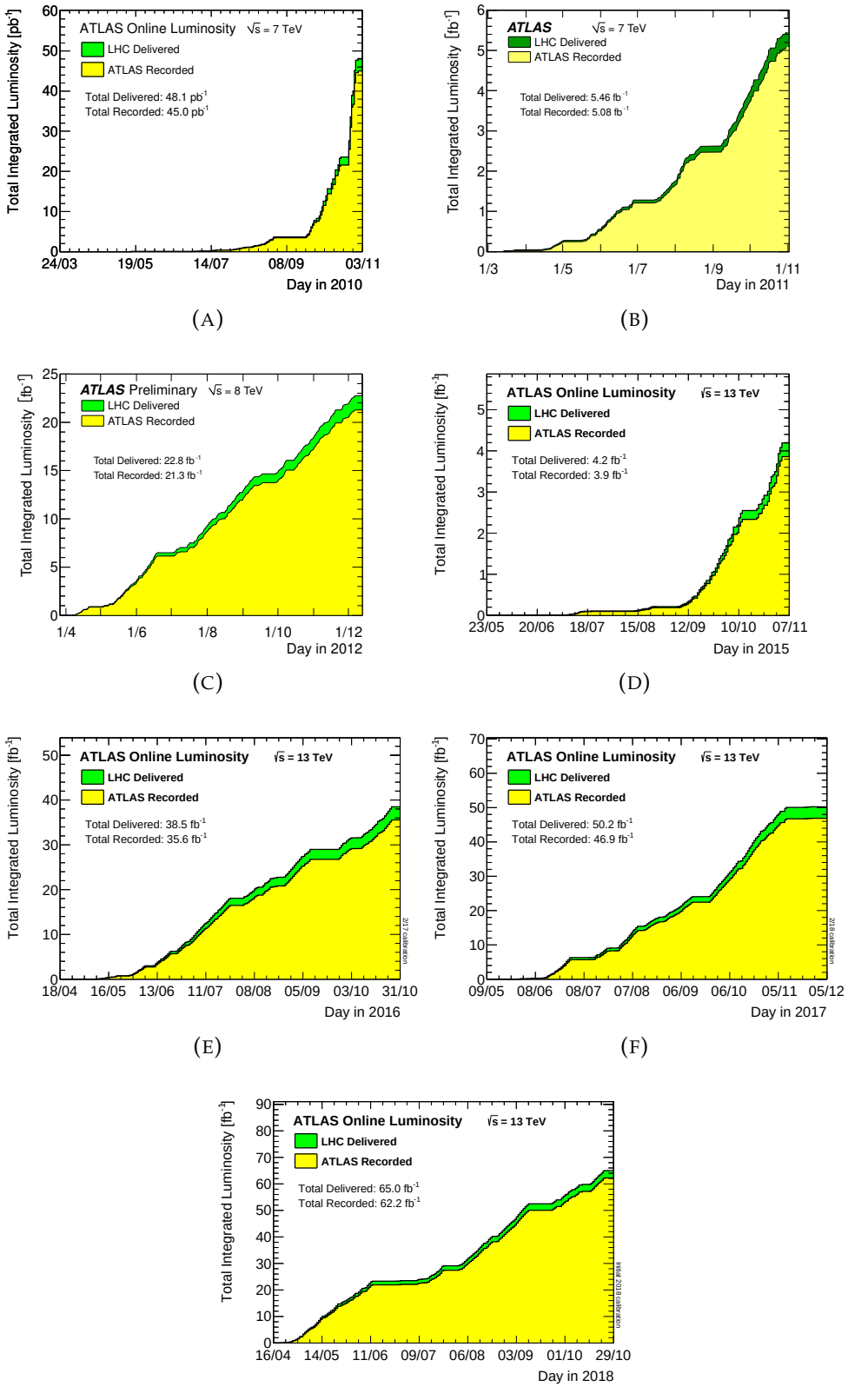

FIGURE 2.2: Cumulative luminosity versus time delivered to (green) and recorded by ATLAS (yellow) during stable beams for *pp* collisions at 7 TeV center of mass energy in 2010 (a) and 2011 (b), at 8 TeV center of mass energy in 2012 (c) and at $\sqrt{s} = 13$ TeV in 2015 (d), 2016 (e), 2017 (f) and 2018 (g). The delivered luminosity accounts for luminosity delivered from the start of stable beams until the LHC requests ATLAS to put the detector in a safe standby mode to allow for a beam dump or beam studies. Figures taken from [53, 54].

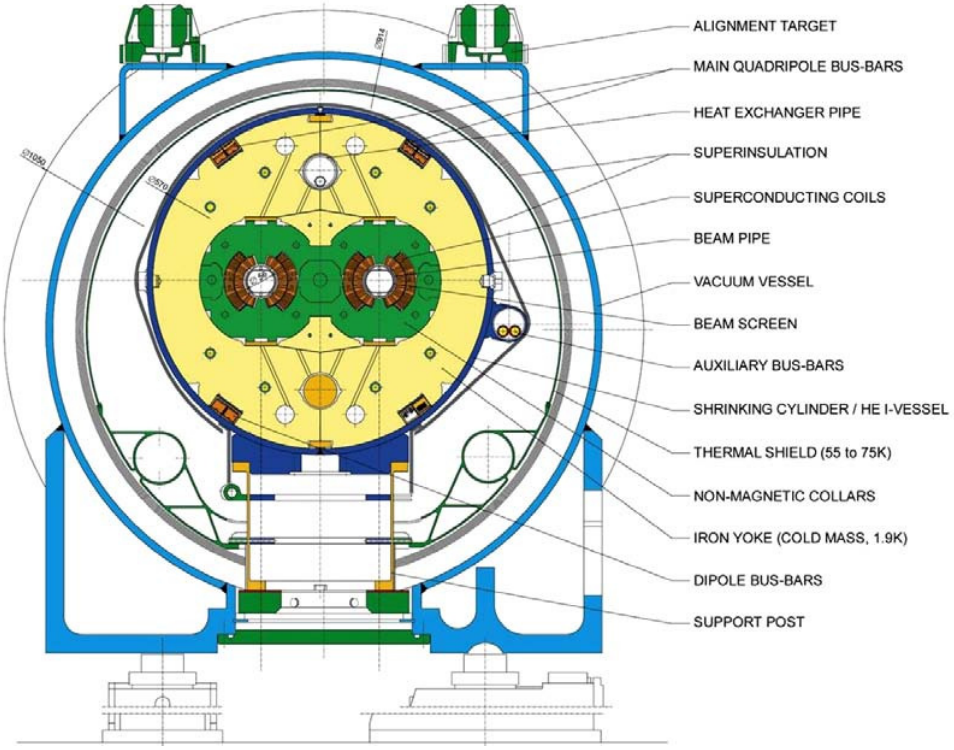

FIGURE 2.3: Scheme of a cryodipole superconducting magnet at the LHC. Figure taken from [8].

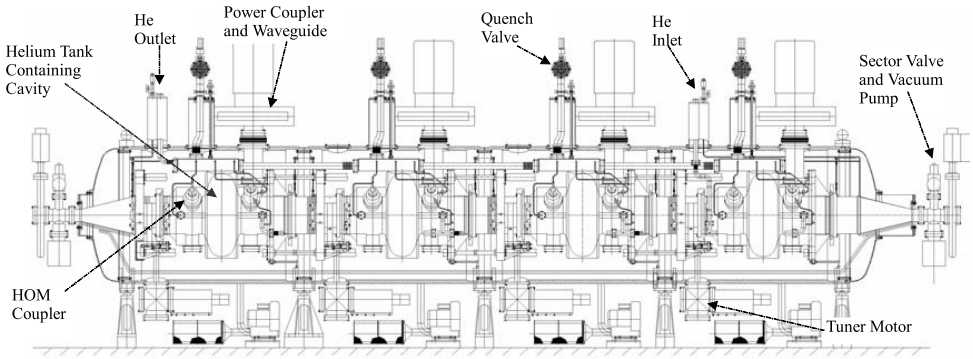

FIGURE 2.4: Scheme of a four-cavity cryomodule at the LHC. Figure taken from [8].

beam trajectory and shrink the particle bunches into a small area where they interact.

The two independent LHC RF systems are 400 MHz superconducting cavity systems able to capture, accelerate and store the beams. They are constituted of single cell with 2 MV accelerating voltage, corresponding to a conservative field strenght of 5.5 MV/m. Each RF system (Figure 2.4) has eight cavities, with a geometry cavity parameter R/Q of 45 Ω and sharing a common cryostat.

2.1.1 The LHC experiments

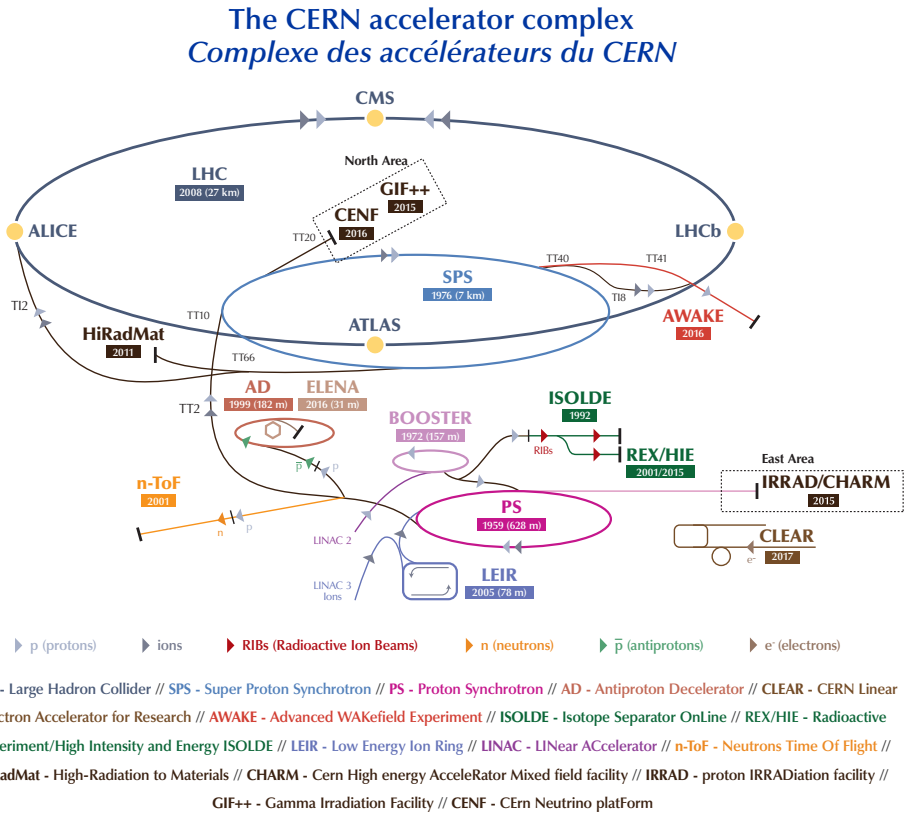

FIGURE 2.5: The CERN accelerator complex. The four yellow dots along the LHC rings correspond to the four interacting points where the major experiments are collocated. Figure taken from [55].

The LHC is the last step of a long accelerator complex, as shown in Figure 2.5. The source of protons is a bottle of hydrogen gas. Hydrogen atoms are stripped of their electrons by means of an electric field and the resulting protons are accelerated up to 50 MeV by a linear accelerator, *Linac2*. Then the beam is injected into the *Proton Synchrotron Booster* (PSB), which accelerates the protons up to 1.4 GeV. After this stage, the *Proton Synchroton* (PS) pushes the protons to an energy of 25 GeV, then they are injected to the *Super Proton Synchroton* (SPS), where they reach an energy of 450 GeV. The proton beams

can now be finally injected to the two LHC beams and reach their final energy. The four yellow dots along the LHC rings shown in Figure 2.5 represent the nominal interacting point (IP) where four large caverns, holding the main experiments, are present. The four experiments are:

- **ALICE** *(A Large Ion Collider Experiment)* **[56]**: it is a 10000-tonne, 26 m long, 16 m wide and 16 m high heavy-ion detector designed to study the quark-gluon plasma phase of matter, which is formed due to the strong interaction of matter at very high energy densities;
- **ATLAS** *A Toroidal Large ApparatuS* [57]: it is a general-purpose experiment, built to investigate a wide range of physics; from high precision SM measurements and Higgs sector to search for dark matter, exotic particles and BSM searches. The ATLAS 7000-tonne detector is the largest LHC experiment, being 46 long, 25 m high and 25 m wide. The remainder of this Chapter and Chapter 3 will give a complete overview of the ATLAS experiment;
- **CMS** *Compact Muon Solenoid* [58]: like ATLAS, it is a general-purpose experiment with the same scientific goals. It employes different technical solutions and a different magnet-system design, able to generate a 4 T field. The detector is 21 m long, 15 m high and 15 m wide and, with its 14000-tonne, it's the heaviest LHC experiment;
- **LHCb** *LHC beauty* [59]: this 5600-tonne detector is specialized in the physics of the beauty and the study of CP violation. Is was built to work at low luminosities (1–2 interactions per bunch crossing) and to detect very forward particles, being made of a a forward spectrometer and planar detectors. It is 21 m long, 10 m high and 13 m wide.

beside these four major experiments, three minor experiments exists. **LHCf** *(LHC forward)* **[60]** shares the IP with ATLAS, **TOTEM***(TOTal Elastic and diffractive cross section Measurement)* **[61]** uses detectors positioned on either side of the CMS detector, while **MoEDAL** *(Monopole and Exotics Detector At the LHC)* **[62]** is placed near the LHCb experiment.

2.1.2 The Worldwide LHC Computing Grid

The Worldwide LHC Computing Grid (WLCG) [63] is a global collaboration of computer centers launched in 2002. This collaboration is managed through a memorandum of understanding [64] (MoU) between CERN and the various national funding agencies providing resources for the partecipating computing centers. The basic requirement of the collaboration is to be able to manage very large data volumes at very high data rates, to provide the CPU and storage computing requisites, to allow thousands of users to access the data and to provide robust and long-term data archiving.

The main elements of the WLCG infrastructure are the tiers of computer centers, schematically represented in Figure 2.6. They have different roles and responsabilities:

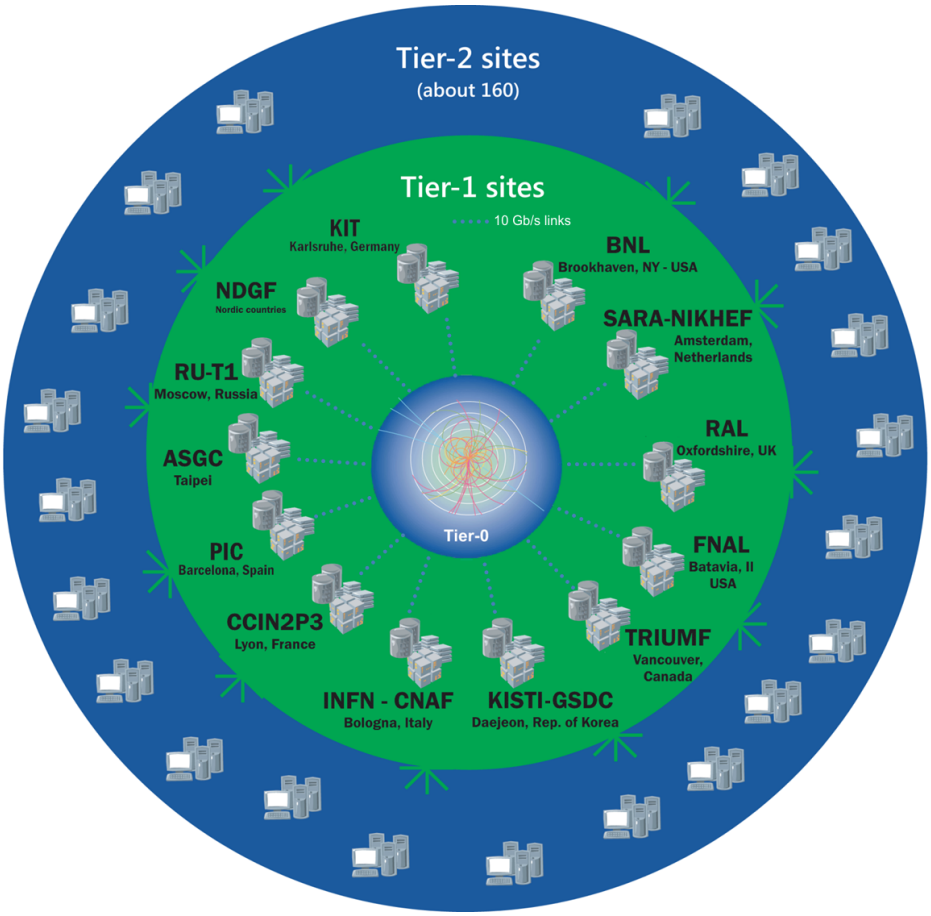

FIGURE 2.6: Schematic representation of the WLCG tiers. Dedicated "dark-fiber" connections between CERN and each of the Tier 1 sites were implemented to ensure the necessary data rates. These connections are supplemented with secondary connections to ensure reliability of the network. Connectivity between Tier 1 and Tier 2 sites is provided by national and international academic and research network infrastructures. Figure taken from [65].

- **Tier 0**: It is located at CERN and it is responsible for accepting the full data stream from the LHC experiments and recording it to tape. The Tier 0 is also responsible for distributing a copy of the raw data among the different Tier 1 sites by means of a dedicated 10 GBs^{-1} *dark-fiber* network. The Tier 0 provides a large computing farm with more than 50000 CPU cores available. Raw data are then preprocessed and distributed processed data out of CERN to Tier 1 sites. Finally, Tier 0 is for coordinating the operations on the WLCG;
- **Tier 1**: there are 11 Tier 1 sites; 1 in Canada (ATLAS), 2 in the USA (one for ATLAS, the other for CMS), 1 in the Asia-Pacific region (for both CMS and ATLAS) and 7 in Europe, four of those support all the 4 experiments, the others only three. The Tier 1 centers store on the long term a share of the raw and reconstructed data from Tier 0 and are responsible for reprocessing data with improved calibrations and providing data-intensive analysis facilities. They also support several Tier 2 sites. The association is usually on a geographical-base. Tier 1 sites provide data and support to the Tier 2 centers and, furthermore, they run a a number of grid services as defined in the MoU.
- **Tier 2**: The about 160 Tier 2 sites are essentially analysis facilities for the use of an entire experiment. They provide computing power for MC simulations, which are sent to Tier 1 centers for long-term archiving. The connection between the Tier 1 and Tier 2 sites rely on national and international academic and research networks. The Tier 2 can either support one or all the experiments. They provide disk space to analysers, but they are not required to archive data. The grid services run on Tier 2 sites are usually those needed to access their resources, as defined in the MoU. Finally, Tier 2 sites must be able to distribute data sets to Tier 3 for end-user analysis;
- **Tier 3**: Tier 3 sites are local computing resources directly accesible to scientists. They largely vary in scale: from a few CPUs to large national farms.

2.2 The ATLAS Detector

The ATLAS experiment is one of the two general purpose detectors at the LHC. It was built to perform serveral type of precise measurements and searches at the TeV scale:

- precise measurements of the SM parameters;
- measurements of the Higgs boson properties;
- high precision tests of QCD, electroweak interactions and flavour physics;
- searches for the Higgs boson beyond the SM;
- searches for exotic particles, such as new heavy gauge bosons and extra dimensions;

- searches for supersymmetric particles.

Many of the processes aforementioned are expected to have a very small cross section. Hence, the high luminosity and resulting interaction rate are needed. The drawback is that every candidate event will be accompanied by several additional inelastic events. At $\sqrt{s} = 13$ TeV, the mean number of interactions per crossing, usually referred as *pile-up*, was ∼37. The detector must then be able to cope with this harsh pile-up conditions and the high radiation envoronment. Furthermore, the nature of *pp* collisions leads to a dominant QCD multijet production cross section over the other processes of physics interest. This translated in high demands for the detector in distinguishing interesting events, going from precise vertices reconstruction to reliable particle identification. In order to deal with these challenges, the ATLAS detector was designed with the following goals in mind:

- fast and radiation-hard electronic and sensors to deal with the LHC environment. High detector granularity to handle the particle fluxes and the high pile-up conditions;
- large acceptance in pseudorapidity with almost full azimuthal angle coverage;
- in order to achieve good offline tagging of τ leptons and b-tagged jets, a very good particle momentum resolution and reconstruction efficiency in the inner tracker is essential to precisely reconstruct secondary vertices;
- good electromagnetic (EM) calorimetry for e and γ identification and full coverage hadronic calorimetry for accurate jet and missing transverse energy measurements;
- precise muon identification and momentum resolution over a wide range of muon p_T and unambiguously determination of its electric charge;
- in order to achieve an acceptable trigger rate for all the physics processes of interest, an efficient triggering on low p_T objets with good background rejection is required.

Detector component	Required resolution	η coverage	
		Measurement	Trigger
Tracking	$\sigma_{p_T}/p_T = 0.05\% \cdot p_T \oplus 1\%$	$\pm$2.5	
EM calorimetry	$\sigma_E/E = 10\%/\sqrt{E} \oplus 0.7\%$	$\pm$3.2	$\pm$2.5
Hadronic calorimetry			
barrel and end-cap	$\sigma_E/E = 50\%/\sqrt{E} \oplus 3\%$	$\pm$3.2	$\pm$3.2
forward	$\sigma_E/E = 100\%/\sqrt{E} \oplus 3\%$	$3.1 < \|\eta\| < 4.9$	$3.1 < \|\eta\| < 4.9$
Muon spectrometer	$\sigma_{p_T}/p_T = 10\%$ at $p_T = 1$ TeV	$\pm$2.7	$\pm$2.4

TABLE 2.2: Performance goals of the ATLAS detector. The units of E and p_T are in GeV. Table taken from [57].

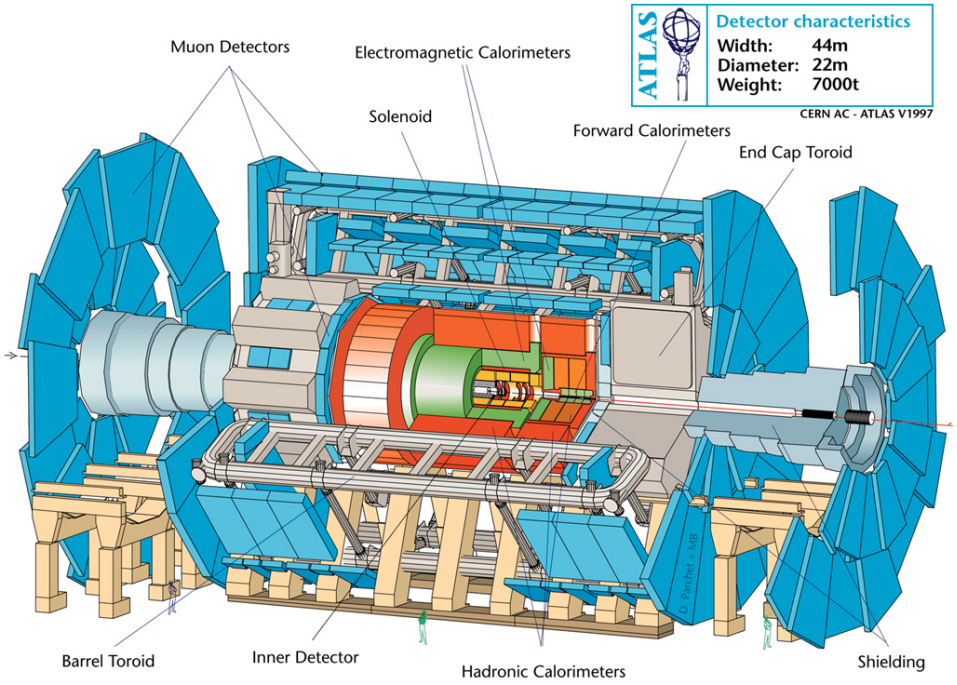

FIGURE 2.7: Schematic overview of the ATLAS detector and its subdetectors. Figure taken from [66].

The performance goals of the ATLAS detector are listed in Table 2.2. Figure 2.7 shows a scheme of the ATLAS detector. It is forward-backward symmetric with respect to the IP and consists of several subdetectors. Closer to the beam pipe is the Inner Detector (ID), surrounded by the electromagnetic calorimeter, the hadron calorimeter and the muon spectrometer (MS), respectively. The ID is immersed in a 2 T solenoidal magnetic field to allow precise momentum measurement. The MS is also immersed in a magnetic field, provided by an air-core toroidal system which maximize the bending power over a large volume over the amount of material used, thus minimizing multiple-scattering effects. The online selection of interesting physics events is performed by means of a three-level trigger system. Given its cylindrical symmetry, The following subsections will describe in details the various components of the ATLAS detector.

2.2.1 Coordinate system

The ATLAS coordinate system, shown in Figure 2.8, is a right-handed cartesian system with origin in the IP. The beam direction defines the z-axis, while the x-y plane is transverse to the beam line. The x-axis points from the IP to the center of the LHC ring and the y-axis points upward. Given the cylindrical symmetry of the detector, a polar coordinate system (r, θ, ϕ) is usually employed to describe physical objects. r denotes the radius, while θ and ϕ are the polar and azimuthal angle, respectively; they are measured, in order, from the positive z- and x-axis. The θ angle is usually expressed in terms of the pseudorapidity $\eta = -\ln\tan(\theta/2)$, which approaches the rapidity $y = 1/2 \cdot \ln[(E + p_z)/(E - p_z)]$ in the limit of massless particles. The

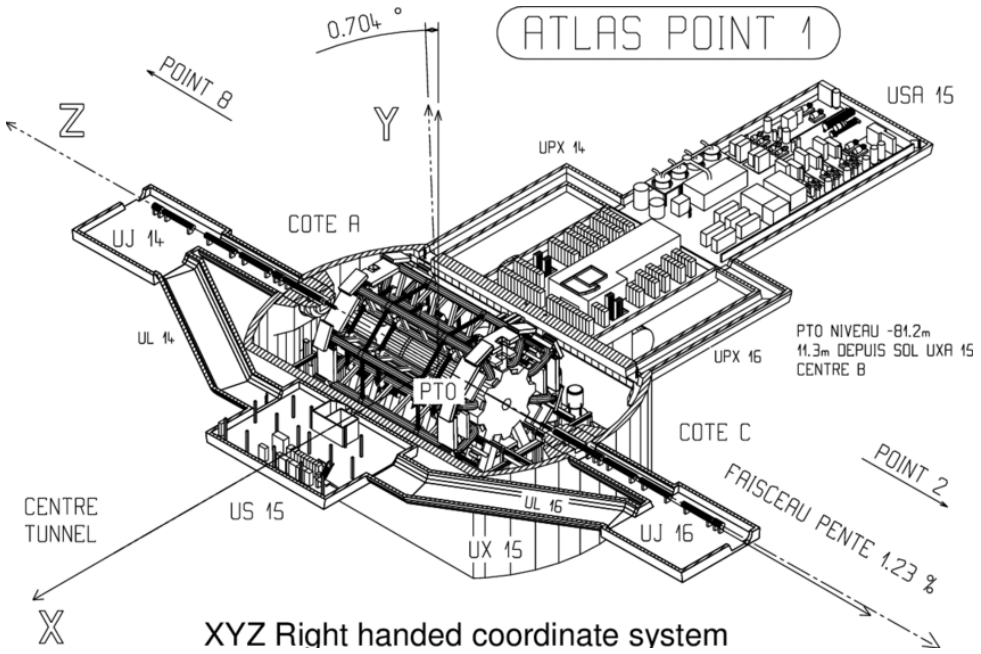

FIGURE 2.8: Illustration of the ATLAS Detector oriented in the global coordinate system. Figure taken from [67].

rapidity and pseudorapidity are commonly used in systems where the initial z-momentum can not be observed, since the difference in (pseudo)rapidity between two particles is invariant under Lorentz boosts. The most used quantity to express distances in the (η, ϕ) plane is $\Delta R = \sqrt{\Delta\eta^2 + \Delta\phi^2}$. Since the initial z-momentum is not exactly known, E and p are often projected to the transverse x-y plane, where conservation laws apply. The transverse energy and momentum are defined as $E_T = E \sin\theta$ and $p_T = \sqrt{p_x^2 + p_y^2}$, respectively.

Finally, trajectories of charged particles in a magnetic field can be described by five helix, or nuisance, parameters: $(r, z, \phi, \theta, q/p)$, where q is the charge and p is the momentum of the particle. Another commonly employed parametrization is $(1/p_T, \phi, d_0, \cot\theta, z_0)$, where d_0 is the transverse impact parameter, defined as the transverse distance to the beam axis at the point of closest approach, $\cot\theta$ is the cotangent of the polar angle and d_0 is the longitudinal impact parameter, defined as the z position of the track at the point of closest approach.

2.2.2 Magnet system

The ATLAS magnet system is made of four superconducting magnet, used to generate a magnetic field for bending charged tracks and measuring their momenta. The 2 T magnetic field in the ID is directed along the z-direction and produced by a single solenoid. The magnetic field in the MS, instead, is generated by three air-core toroids able to produce fields in a range from 0.5

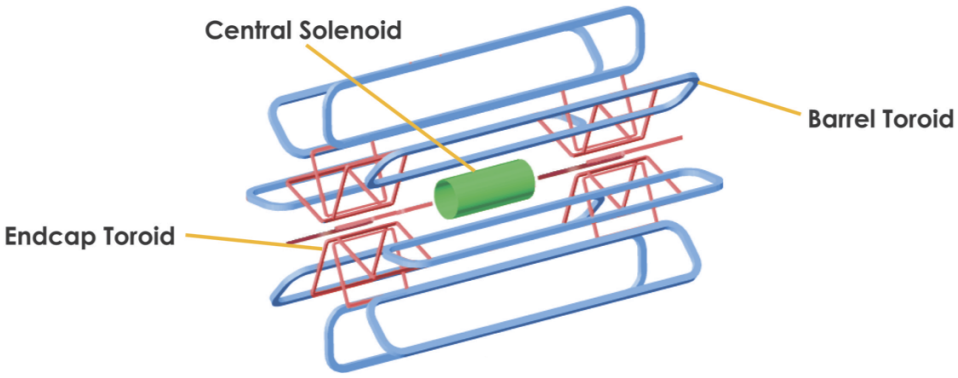

FIGURE 2.9: Layout of the ATLAS magnet system. Figure extracted and adapted from [68].

to 4 T in the ϕ direction. The final result is that the field in the ID bends particles in the ϕ direction, and in the η direction in the MS. The superconducting magnets, cooled down to 4.5 K, are made of aluminium (Al) stabilised niobium-titanium (NbTi) cables. In order to minimize the energy losses of the passing particles, the central solenoid is 0.66 radiation lenghts, corresponding to 10 cm and shares the same cryostat as the electromagnetic calorimeter. Similarly, the air-cored toroid structures allow muons to travel through the magnetic field without crossing the superconducting coils. The size of the toroid maximise the bending volume over the crossed material ratio, resulting in very good tracking performance. Figure 2.9 shows the layout of the magnet system; the green cylinder is the central solenoid, the blue and red structures are the three air-core toroids for the barrel and the end-cap regions, respectively.

2.2.3 Inner Detector

The ID is the innermost detector of the ATLAS experiment. It is designed to provide robust pattern recognition, good momentum resolution and discriminating power between primary and secondary vertex measurements for tracks above a p_T threshold of 0.5 GeV. Its acceptance is in the pseudorapidity range of $|\eta| < 2.5$. It is also able to provide reliable electron identification for $|\eta| < 2.0$ in a wide range of energies, from 0.5 to 150 GeV. The ID layout is shown in Figure 2.10. It is contained in a cylindrical envelope of lenght ± 3.51 m and radius of 1.15 m; it is immersed in a solenoidal magnetic field of 2 T and consists of three complementary subdetectors, shown in Figure 2.11: an innermost silicon pixel detector capable of high-resolution patter recognition, an intermediate silicon strip detector (SCT) and, at larger radii, the transition radiation tracker (TRT), composed of several layers of gaseous straw tube elements interleaved with transition radiation material. In the following, a brief overview of the different components of the ID will be outlined.

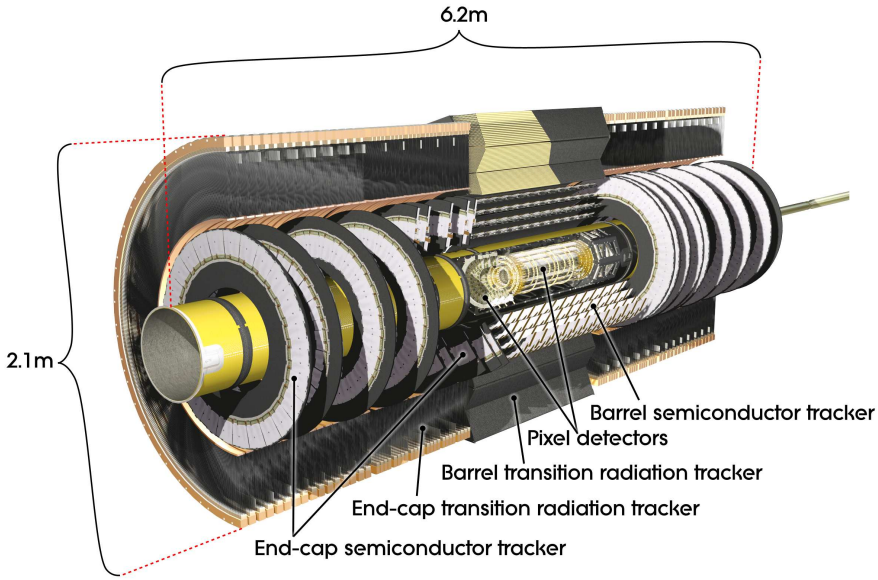

FIGURE 2.10: Cut-away view of the ATLAS ID during Run 1. The IBL is not shown since it has been installed during Run 2. Figure taken from [57].

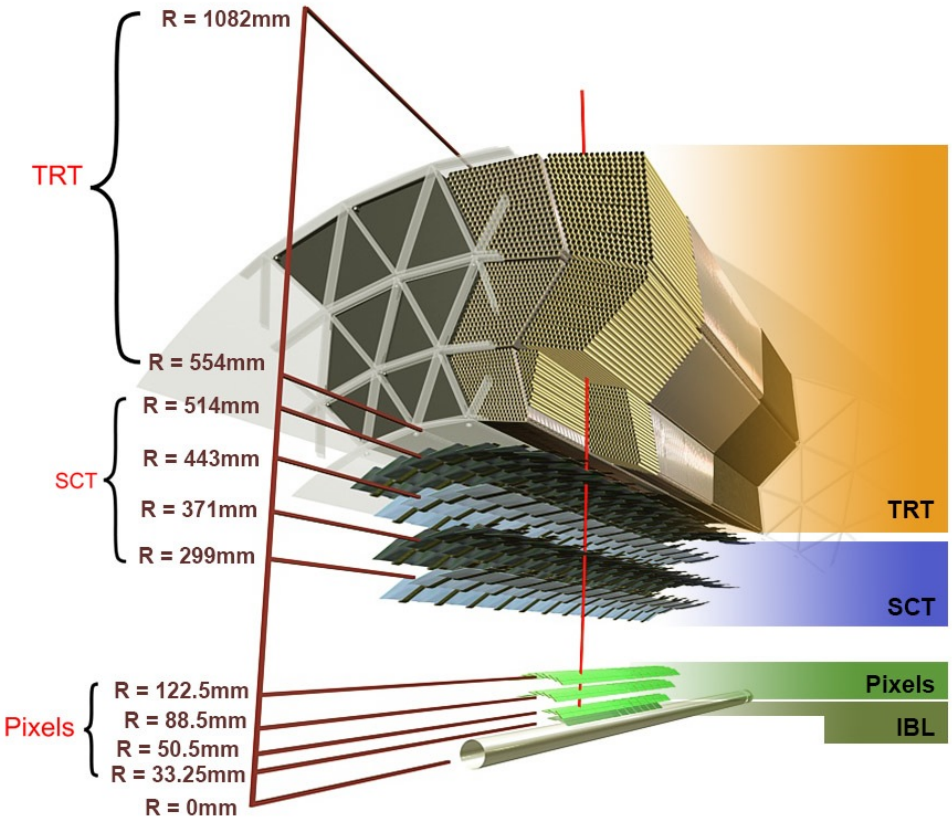

FIGURE 2.11: Sketch of the ATLAS inner detector showing all its components, including the new insertable B-layer (IBL). The distances to the interaction point are also shown. Figure taken from [69].

Silicon pixel tracker and the Insertable B-Layer (IBL)

The pixel detector is the closest component of the ID to the beampipe. It is made of several layers of silicon pixel with a very high granularity, allowing to resolve primary and secondary interaction vertices. It is composed of three cylindrical layers in the barrel region and three disks per side in the endcap. The innermost layer during Run 1 was the B-layer, placed at a radius of 50.5 mm. It was expected to be replaced after three years of operation, given the high radiation dose under the LHC environment. Given the technical difficulties of performing such an operation, it was decided to install a fourth pixel layer, the IBL [70], inserted at a radius of 3.3 cm during the LHC long shutdown in 2013, before the Run 2 data-taking period. The fourth pixel layer provides an additional track hit, thus mitigating the possible loss of of track space points in the outermost three layers due to radiation damage.

SemiConductor Tracker (SCT)

The SCT is designed to provide track precision measurements in the radial region between 299 and 514 mm. It also contributes to measure the momentum and track parameters of charged particles and to the vertex reconstruction. It is composed of four barrel layers and two endcaps formed by nine disks each. The barrel layers are formed by 2112 modules, while each endcap consists of 988 modules. The modules are arranged such that each particle passes through four layers of the detector. Each module consists of four rectangular silicon-strip sensors with a constant pitch of 80 μm.

Transition Radiation Tracker (TRT)

The TRT is the outermost component of the ATLAS ID. It is a straw drift tube tracker which also allows electron identification capability from transition identification of X-Ray photons. It consists of 4 mm diameter Kapton and carbon fibers drift tubes (straws). Each straw is filled with a gas mixture consisting of 70% Xe, 27% CO_2 and 3% O_2 and present at its center a 31 μm diameter tungsten wire. The TRT barrel is made of three cylindrical layers of 52544 straws of 1.5 m lenght, parallel to the beampipe. The barrel pseudorapidity coverage is $|\eta| < 1$. Each endcap consists of 122880 radially disposed tubes covering the $1 < |\eta| < 2$ region. Charged particles with $p_T > 0.5$ GeV and $|\eta| < 2$ will traverse at least 36 tubes, except in the endcap transition region ($0.8 < |\eta| < 1$), where the number goes down to 22. Despite the lower resolution compared to the silicon trackers and the lack of measurement in the z direction, the TRT contributes to a precise pattern recognition and momentum measurement given the large number of hits.

2.2.4 Calorimetry

The ATLAS calorimetry system, presented in Figure 2.12, is placed outside the ID and its magnetic field. It provides a destructive measure of the energy and position of particles, both electrically charged and neutral. A particle

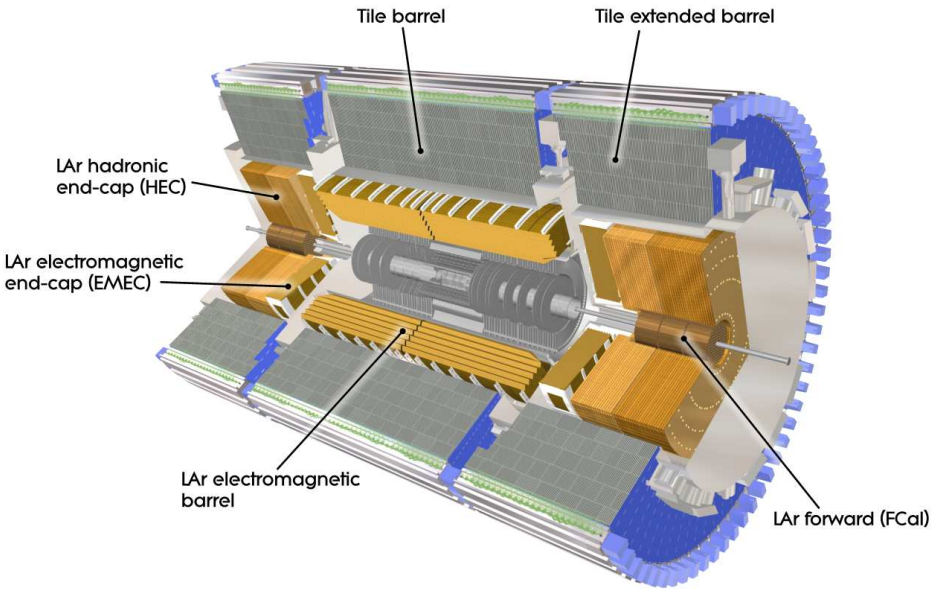

FIGURE 2.12: Cut-away view of the ATLAS calorimeter system. Figure taken from [57].

entering the calorimeter interacts with the material and starts a decay chain, called *shower*, which stops inside the calorimetry system (except for muons and neutrinos), thus allowing the determination of its energy. The position measurement is performed by segmenting the detector in the z and ϕ directions. The ATLAS calorimeters consist of a number of sampling detectors with full ϕ coverage and symmetric around the beam line. The calorimeters closer to the beam pipe are housed in three cryostats, one barrel and two endcaps. The barrel cryostat contains the electromagnetic barrel calorimeter; each of the two endcaps contain an electromagnetic endcap calorimeter (EMEC) and a forward calorimeter (FCal). Those calorimeters use liquid argon as active material. In particular, the precision electromagnetic calorimeters use lead-liquid argon detectors with accordion-shape abosorbers to maximize the number of layers a particle traverse (three in the $0.0 < |\eta| < 2.5$ region, two in the forward $2.5 < |\eta| < 3.2$ region). The FCal provide electromagnetic coverage at very high pseudorapidity ($3.1 < |\eta| < 4.9$). Furthermore, single instrumented argon layer electromagnetic presamplers are placed in the $|\eta| < 1.8$ region to measure the energy lost in front of the electromagnetic calorimeters. The tile outer hadronic calorimeter uses steel as absorber medium and scintillator tiles as sampling detectors. It is composed of one central and two external barrels, providing a coverage of $|\eta| < 1.7$. Its acceptance is further extended up to $|\eta| < 4.9$ by the liquid argon hadronic endcap (HEC), which uses copper as absorbing material, and the hadronic FCal, a copper-tungsten and liquid argon detector. In the following, further details of the ATLAS calorimeters will be given.

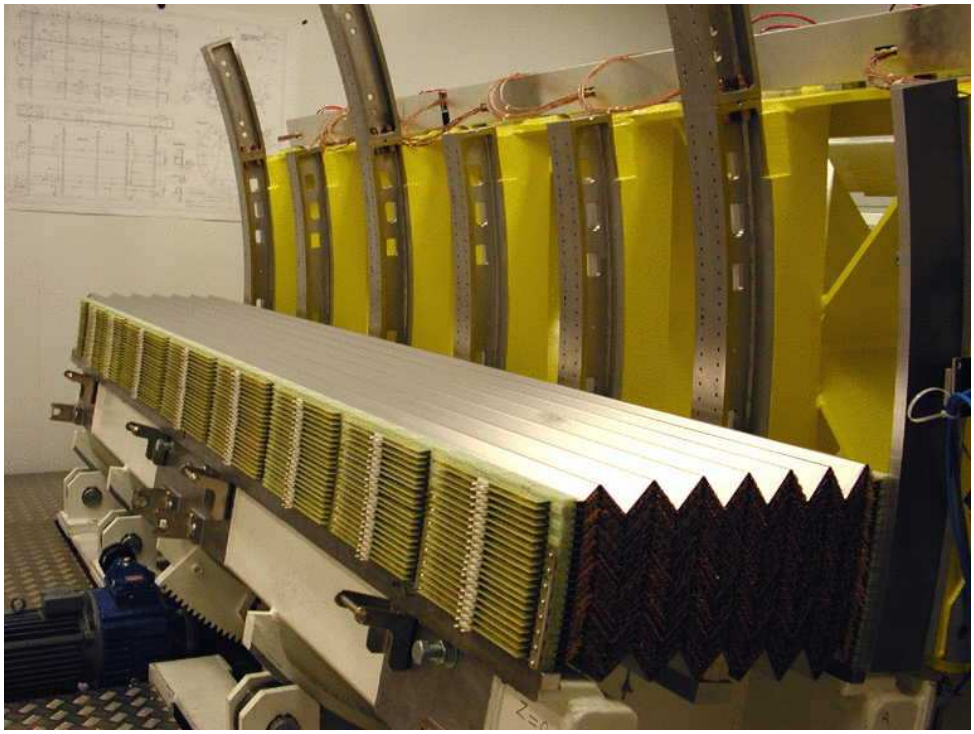

FIGURE 2.13: Photograph of a partly stacked barrel electromagnetic LAr module. The acccordion structure is clearly visible. Photograph taken from [57].

Electromagnetic calorimetry

The electromagnetic calorimeter use liquid argon as active material and lead as absorber. Charged particles belonging to the shower ionise the liquid argon, whose electrons drift to the copper electrodes due to the electric field in which the active material is immersed. The electromagnetic calorimeter is composed of two half barrels, covering the $|\eta| < 1.475$ region, with a 4 mm gap at $z = 0$, and two half wheels per side, the EMEC. The first has an acceptance of $1.375 < |\eta| < 2.5$, the second covers the $2.5 < |\eta| < 3.2$ region. The presence of additional service material creates a *crack* in the $1.375 < |\eta| < 1.52$, where the energy resolution is significantly degraded. As explained in the previous Subsection, the barrel calorimeter has an accordion structure, made by the lead absorbers, as Figure 2.13 shows. The 2.1 mm gaps between them are filled with liquid argon. This geometrical shape prevents azimuthal gaps and guarantees a ϕ-symmetry.

Hadronic calorimeter

The hadronic calorimeter consists of an iron-scintillating tile calorimeter and the liquid argon HEC. The tile calorimeter is located behind the liquid argon EM calorimeter and it is subdivided into a barrel covering $|\eta| < 0.8$ and two extended barrels with acceptance $0.8 < |\eta| < 1.7$. The active material consists of 3 mm thick layer of scintillators perpendicular to the beam axis; iron is used as absorber. The region between the barrel and the extended barrel is instrumented with special modules allowing a partial recover of the energy

lost in the *crack* regions. The HEC consists of two wheels per endcap placed directly behind the EMEC and sharing the same cryostat. The wheels consist of two layers each. The closest to the IP is built using 25 mm parallel copper plates, the other uses 50 mm copper plates as absorber, while liquid argon is used as active material. The pseudorapidity coverage is of $1.5 < |\eta| < 3.2$. The overlap with the tile calorimeter from one side and the FCal on the other avoids cracks in the transition regions.

Forwards calorimeter

The FCal covers the $3.1 < |\eta| < 4.9$ forward region. Given its closeness to the beam axis, it is exposed to very high particle fluxes. Although the neutron flux is reduced by placing the modules 1.2 m away from the EM calorimeter maximum extension on the z-axis, the radiation and the particle energy are so high that a very dense calorimeter is needed to contain the particle showers. The FCal is divided into three compartments. The one closest to the IP is designed for EM measurements. The active material is liquid argon, the passive one is copper. The other two compartments, designed for hadronic measurements, present small diameter tungsten rods as absorbers. The small gaps between rods are filled with liquid argon. This results in a very dense design which minimize the lateral development of hadronic showers.

2.2.5 Muon Spectrometer

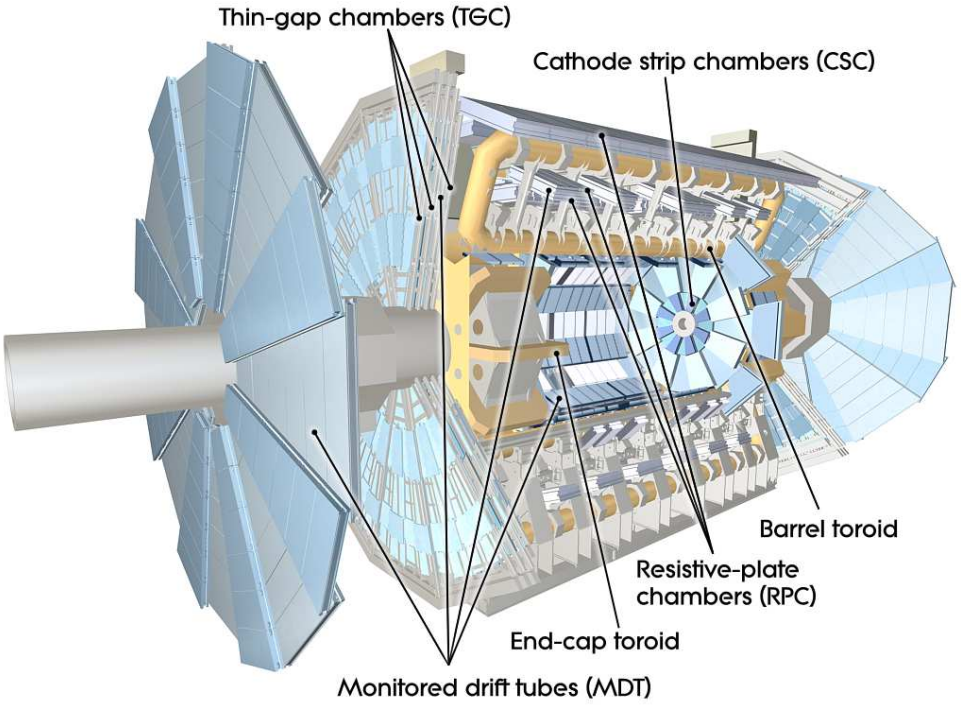

FIGURE 2.14: Cut-away view of the ATLAS muon spectrometer. Figure taken from [57].

The ATLAS MS is the outer part of the ATLAS detector. It adopts different detector technologies: tracking chamnbers for precise momentum and spatial measurements of muons in a wide range of energy (from approximately 6 GeV up to 2 TeV) and trigger chambers to provide, in the same energy range, excellent triggering performance. As Figure 2.14 shows, the MS fully envelopes the calorimetry system and occupies the most part of the detector volume. It is immersed in the magnetic field generated by the toroid magnets, located in the barrel and endcap sides. The magnetic field is mostly orthogonal to the muon trajectories, thus minimizing the resolution deterioration due to multiple scattering. The pseudorapidity acceptance of the MS is $|\eta| < 2.7$. In the barrel region ($|\eta| < 1.0$), muon tracks are measured in chambers arranged in stations composed of three concentrical cylindrical layers, centered around the beam axis, the inner, medium and outer stations, with radii of 5 m, 7.5 m and 10 m, respectively. In each of the two endcaps ($1.0 < |\eta| < 2.7$), the chambers are installed on four large wheels perpendicular to the z-axis, positioned at 7.4 m, 10.8 m, 14 m and 21.5 m from the nominal IP. The ATLAS MS employes four different detector technologies. Two of them, the Resistive Plate Chambers (RPC) in the barrel region and the Thin Gap Chambers (TGC) in the endcaps, provide trigger signals. The Monitored Drift Tubes (MDT) provide high precision measurements in most of the detector acceptance. In the very forward region, however, to cope with the high particle flux, Cathode Strip Chambers (CST) are employed. A complete overview of the four different types of muon chambers is given in the following.

Monitored Drift Tubes

The MDT chambers provide high precision momentum mesurement. Their acceptance is $|\eta| < 2.7$ and each chamber is made of three to eight layers of drift tubes. Each tube is made of aluminium with diameter of 3 cm and an anodic high voltage 50 μm central wire made of gold plated tungsten-rhenium. They operate using a gas mixture of Ar and CO_2 (93%, 7%) at a pressure of 3 bar. Each MDT chamber consists of two multilayers of tubes fixed to a mechanical support structure. Each multilayer is composed either of three or four layers, depending on the spatial position of the chamber. The particular geometrical assembly is robust against failure of single tubes. The chambers are present both in the barrel and the endcaps of the MS. In the barrel, rectangular MDT chambers are arranged into three concentrical cylinders (inner, middle and outer) of two differend types: large and small, according to the lenght of the tubes; 1.8 m and 5.2 m, respectively. The endcap MDT are arranged in trapezoidal structures on three coaxial disks, perpendicular to the z-axis. The MDT chambers have a spatial resolution of 80 μm and a typical drift time of 700 ns.

Catode Strip Chambers

The CSC chambers are used in the first station of the endcap MS. They cover a pseudorapidity range of $2.0 < |\eta| < 2.7$. The CSC system is composed of two

disks with eight chambers each (four small and four large chambers, for a total of sixteen). Each chamber is made of four CSC planes. The CSCs employ multiwire proportional technology and are arranged in arrays of positively charged wires (anode) crossed with negatively charged copper strips (cathode) within a gas volume. Since the strips and the wires are perpendicular, each passing particle leaves two hits.

Resistive Plate Chambers

The RPC trigger chambers are located in the barrel region. They are gaseous detectors consisting of two parallel plates with opposite electrical charge made of high resistivity plastic material, separated by a gas volume. Each RPC consists of two rectangular detector layers with two orthogonal series of pick-up strips as readout. The η strips are parallel to the MDT wires, while the ϕ strips are orthogonal to them and provide the second coordinate measurement.

Thin Gap Chambers

The TGC chambers are used for the muon trigger system of the endcap ATLAS MS. Each TGC chamber consists of a plane of closely spaced wires maintained at positive high voltage, sandwiched between resistive grounded cathode planes. The spacing between the wires is 1.8 mm, while the spacing between anode and cathode is 1.4 mm. The operational gas is a mixture of 55% CO_2 and 45% $n-C_5H_{12}$ (n-pentane). The anode wires are arranged parallelly to the MDT wires and provide trigger signal using readout strips arranged orthogonal to the wires. The TGC spatial resolution is of the order of 100 μm.

2.2.6 Forward detectors

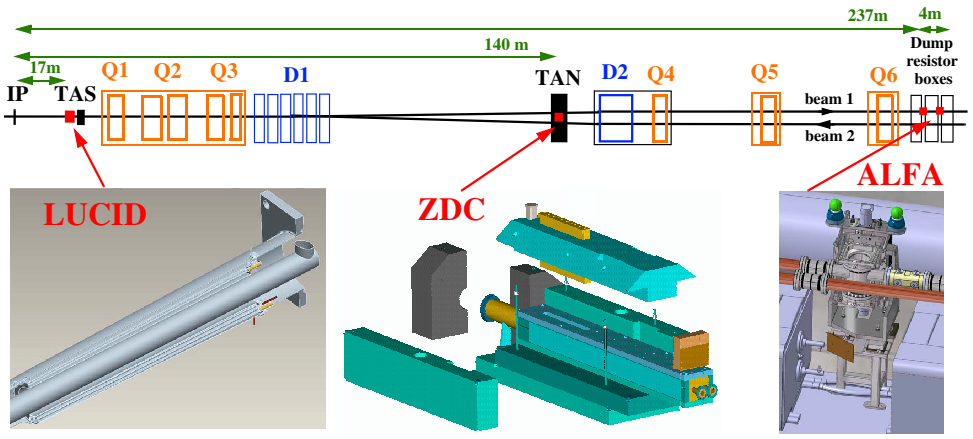

FIGURE 2.15: Schematic view of the forward ATLAS detectors. Their placement along the beam-line around the ATLAS IP in also shown. Figure taken from [57].

In addition to the main ATLAS detector systems, three smaller set of detectors complement the experiment and provide good coverage in the very forward region. As shown in Figure 2.15, from the closer to the further with respect to the IP, the three detectors are:

- **LUCID** (LUminosity measurement using Cerenkov Integrating Detector): this Cerenkov detector is placed at a distance of ± 17 m from the IP. The LUCID main purpose is to detect inelastic pp scattering in the forward direction, thus accomplishing the dual goal of measuring the integrated luminosity and providing online monitoring of the instantaneous luminosity. It cover the pseudorapidity range of $5.6 < |\eta| < 6.0$.
- **ZDC** (Zero Degree Calorimeter): this detector is located at a distance of ± 140 m, where the LHC beam pipe is divided into two separate pipes. Its primary purpose is to detect forward neutrons in heavy-ion collisions.
- **ALFA** (Absolute Luminosity For ATLAS): the ALFA detector, consisting of scintillating-fibre trackers located inside Roman pots at a distance of ± 240 m from the IP, allows to measure the absolute luminosity via elastic scattering at small angles.

2.2.7 Trigger and data acquisition

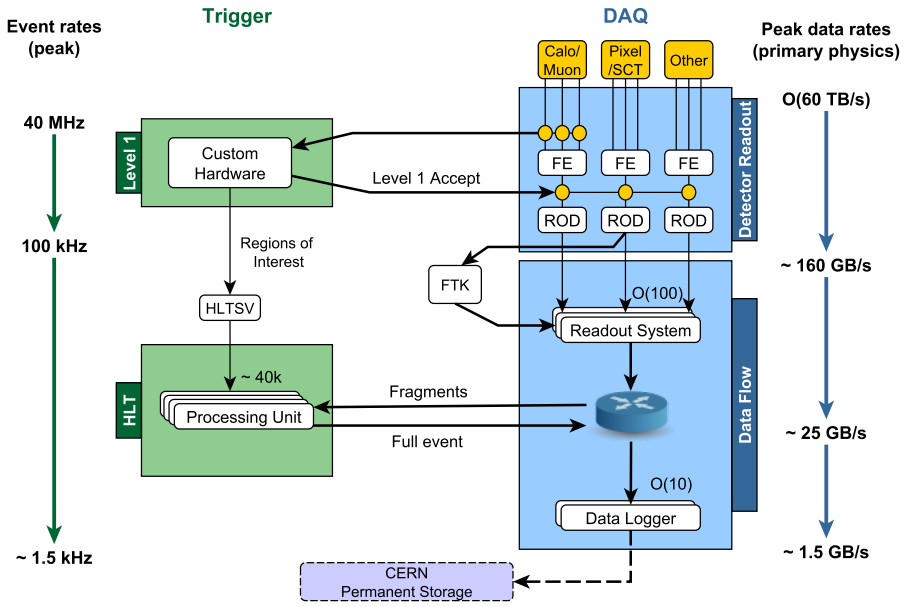

FIGURE 2.16: Diagram of the ATLAS Trigger and Data Acquisition system in Run 2 showing expected peak rates and bandwidths through each component. Figure taken from [71].

The ATLAS Trigger and Data AcQuisition (TDAQ) system provides the identification and selection of interesting physical events for the offline analyses. As Figure 2.16 shows, the TDAQ system comprises a hardware-based first level trigger (Level 1), implemented using custom electronics, and a software-based High Level Trigger (HLT). The HLT can be further broken down to two steps of increasing complexity: the second level trigger (Level 2), which further processes the Region of Interest (RoI) identified by the Level 1, and the Event Filter (EF), which performs more sophisticated online calculations. Figure 2.16 also shows the expected event rates during Run 2; from an initial peak of 40 MHz, only 1.5 kHz are recorded to disk. The remaining part of this Subsection will provide some further details on the TDAQ system. Further details can be found in [72].

Level 1 trigger

The Level 1 trigger looks for large p_T objects (electrons, photons, muons, jets and hadronically decaying τ leptons) or events with high missing transverse energy or total transverse energy. In order to cope with the high rate of LHC collisions, the Level 1 trigger must be able to take decisions in less than 2.5 μs. To achieve this, it can only access information from calorimeters and the muon systems with reduced granularity. No information from the ID can be used, given the time-intensive track reconstruction process. The Level 1 calorimeter trigger receives data from both the electromagnetic and hadronic calorimeters, while the Level 1 muon trigger can access information from the muon trigger chambers (RPCs in the barrel region, $|\eta| < 1.05$ and TGCs in the endcaps, $1.05 < |\eta| < 2.4$). The Level 1 trigger determines RoI passed down to the Level 2 trigger at a rate of 100 kHz.

The High Level Trigger

The HLT system is able to process multiple events in parallel to achieve an high I/O event rate. It accesses high granularity information from the whole detector and is software-based. The first component of the HLT, the Level 2 trigger, performs decisions within 40 ms using information from the RoI only, passed down to the EF at a rate of 3.5 kHz. The EF, on the other hand, can access information from the full detector. The final output rate is of 1.5 kHz.

Data Acquisition

The Data AcQuisition (DAQ) system is responsible for monitoring and recording data on the storage disks. Whenever the Level 1 system triggers an event, the DAQ moves the event data from the detector electronics to Read Out Drivers (ROD), specific for the detector component. If the event both passes the Level 2 trigger and EF, the DAQ collect the information from the ROD, which are then merged together and recorded to disk.

2.2.8 Trigger strategy in the cross section measurement

This Subsection will present the trigger strategy adopted for the cross section measurement presented in Chapter 6. Since the signature of $t\bar{t}$ events decaying into the fully hadronic channel is characterized by the presence of six jets (two of them coming from b-hadrons), the most natural choice is either adopting a b-tag or multi-jet trigger. The latter has been preferred over the former for two main reasons:

- the ATLAS 2015+2016 trigger menu does not feature any unprescaled b-jet trigger, hence (in)efficiency scale factors would have been introduced;
- as it will be evident from Chapter 6, the definition of a 0 b-tagged jet control region is essential to the data-driven estimation of the QCD multi-jet background, and requiring a b-jet trigger would impossibilitate the definition of such a region.

Hence, events are required to fire the `HLT_6j45_0eta240` trigger. This is a multi-jet trigger requiring 6 jets with a p_T greater than 45 GeV in the HLT; all 6 jets must be in the central region of the detector ($|\eta| < 2.4$). The measurement of the trigger efficiency has been measured in data and MC through the production of turn-on curves of the `HLT_6j45_0eta240` trigger with different selections. This allows to estimate if any bias is introduced by using this trigger in the signal and control regions. The first test is performed changing the η requirement of the jets to monitor any dependence on this parameter as the trigger threshold is close to the offline object selection, as shown in Chapter 6. Different turn-on curves are produced using the following selection for both data and MC:

- pass the prescaled `HLT_5j45` trigger;
- pass the `HLT_6j45_0eta240` trigger;
- 5 jets with at least 55 GeV. This assures that we are on the plateau for the prescaled trigger;
- the sixth jet having at least 40 GeV;
- exactly 2 b-tagged jet with 70% single-cut operating point[1] are required;
- all jets are required to satisfy the $|\eta| < \eta_{cut}$ requirement, where η_{cut} is varied from 2.0 to 2.4.

The study is summarised in Figure 2.17. For events containing a 6 jets with $p_T > 55$ GeV, the trigger is highly efficient, with an efficiency of 96% measured in data. The MC efficiency is found to be higher in all bins, the difference being 4% at 55 GeV. The difference between the efficiency curves for different $|\eta|$ selections is negligible so using a selection of 2.4 is a safe option.

A second study, with a requirement of 0 instead of 2 b-tagged jets, has been performed. The turn-on curves are shown in Figure 2.18. The difference is

[1] The definition of b-tagging algorithms and operating points will be given in Chapter 5.

very small and therefore using the nominal trigger in the control region does not impact the background estimation.

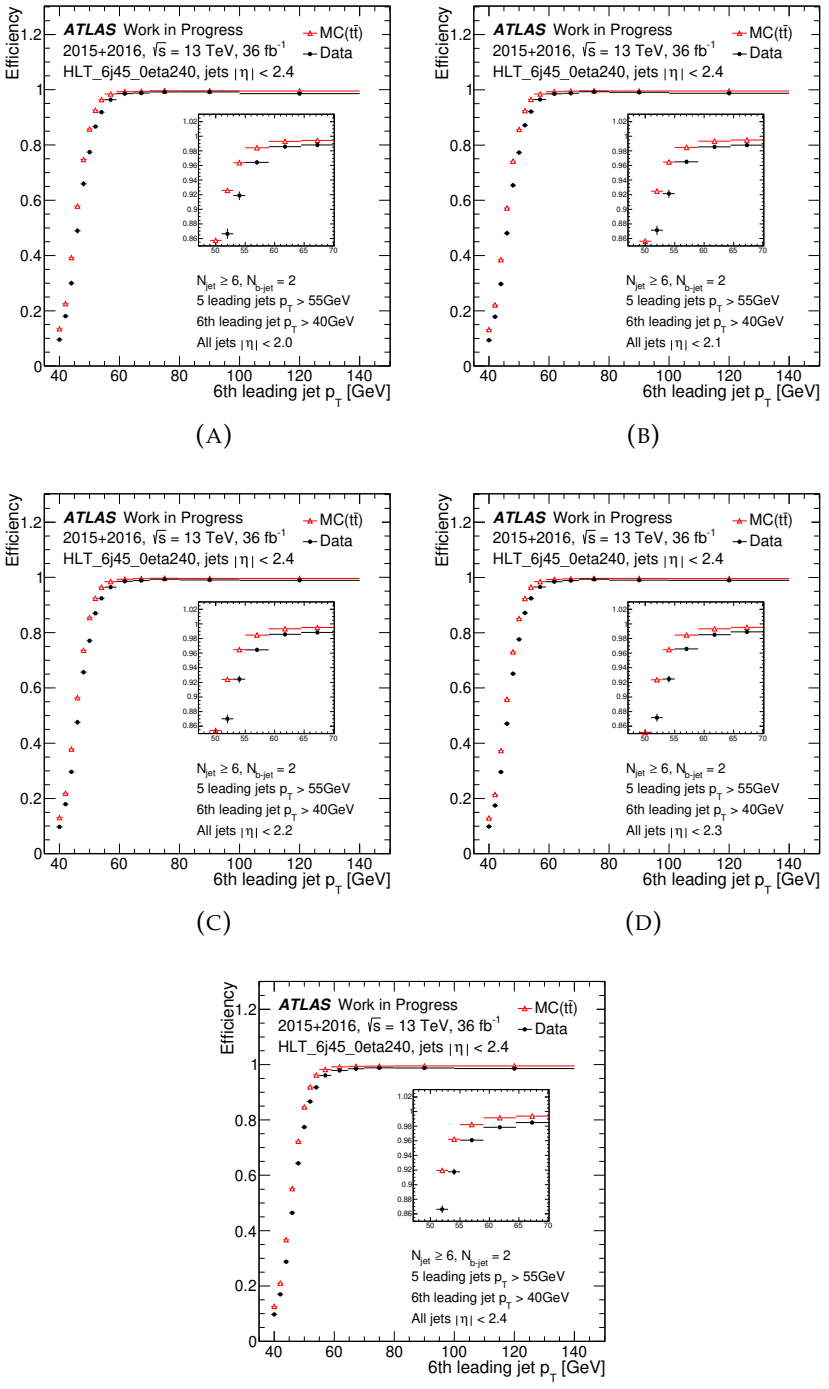

FIGURE 2.17: Trigger efficiency curves as a function of the 6th jet transverse momentum, for different values of the maximum allowed η of the jets. In particular, the η_{cut} values are 2.0 (a), 2.1 (b), 2.2 (c), 2.3 (d) and 2.4 (e). These are computed in data and for a ttbar MC sample, selecting events with two b-tagged jets.

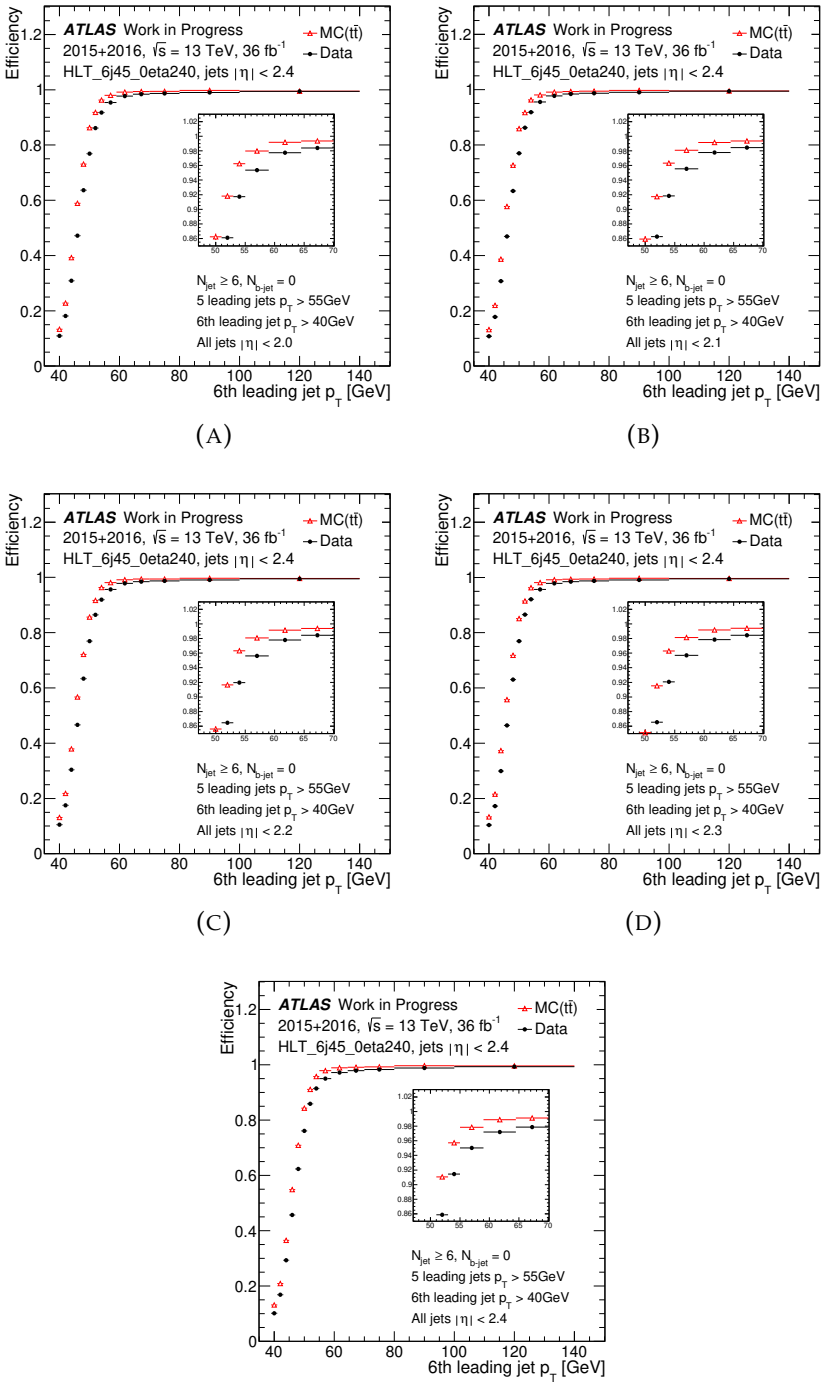

(A) (B) (C) (D) (E)

FIGURE 2.18: Trigger efficiency curves as a function of the 6th jet transverse momentum, for different values of the maximum allowed η of the jets. In particular, the η_{cut} values are 2.0 (a), 2.1 (b), 2.2 (c), 2.3 (d) and 2.4 (e). These are computed in data and for a ttbar MC sample, selecting events with zero b-tagged jets.

Chapter 3

The ATLAS Detector at the HL-LHC

After several years of successful operations, the LHC complex is planned to undergo a series of upgrades which will increase the peak luminosity by a roughly factor of five with respect to the current Run 2 conditions. The expected delivered instantaneous luminosity at the High Luminosity LHC (HL-LHC) will be in the range from $\mathscr{L} = 5 \cdot 10^{34}$ fb^{-1} to $\mathscr{L} = 7.5 \cdot 10^{34}$ fb^{-1}, corresponding to a number of mean interaction per bunch crossing, or pile up, from $< \mu >= 140$ to $< \mu >= 200$, more than three times with respect to the Run 2 $< \mu >= 37$. To cope with the high-density, high-radiation and high-occupancy environment, the LHC experiments will be subjected to substantial upgrades. After a brief overview of the upgrade schedule of the ATLAS detector at the HL-LHC, this Chapter will focus on the new Inner Tracker (ITk) and the High Granularity Timing Detector (HGTD), which will be installed during the Phase-II upgrade of the detector (2024 - 2026). Their expected performance under HL-LHC conditions will be presented. Particular attention will be given to the tracking, jet and E_T^{miss} performance of the ITk and HGTD detectors, since I was directly involved in those studies during my Qualification Task (QT)[1]. In Section 3.1, an overview of the HL-LHC will be presented, while the ITk and HGTD will be treated in detail in Section 3.2 and 3.3, respectively.

3.1 From the LHC to the HL-LHC

The main motivation for the HL-LHC is to extend and improve the LHC physics programme. The main topics that can be addressed involves the measurements of Higgs rare decay and Higgs self-coupling, performing precision SM tests of the top quark and EW sectors, searching for exotic and SUSY particles and probing an hypothetical structure of lepton and quarks.

[1]The policy for authorship in ATLAS require that an ATLAS author should have made a significant contribution to the experiment. In order to sign ATLAS papers, people are required to accomplish a so-called Qualification Task, usually consisting in technical work in the interest of the whole ATLAS Collaboration. The duration of the QT can not be less than one year and each qualifying author has to guarantee at least 0.5 FTE (full-time equivalent) to his QT.

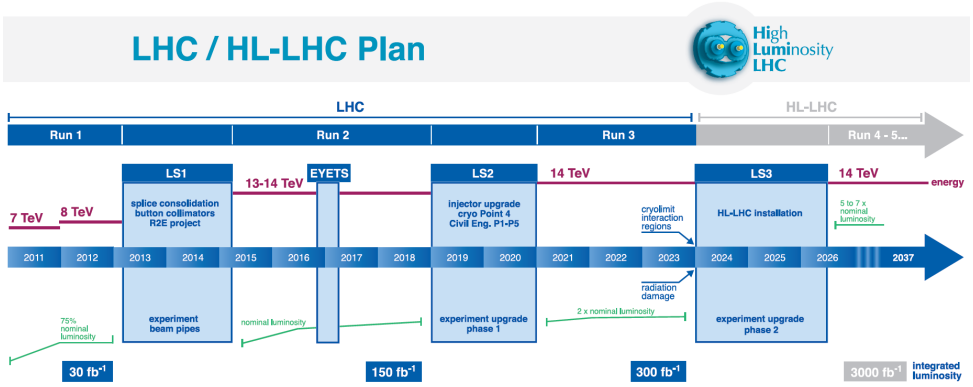

FIGURE 3.1: Timeline for planned LHC upgrades. Figure taken from [73].

Figure 3.1 shows the schedule for the upgrades of the LHC accelerator complex, leading to the HL-LHC. The accelerator and detector upgrades will be progressively installed during the anticipated next Long Shutdowns (LSs). The LS2 will start on December 2018 and will last for roughly two years, until February 2021, while the LS3 is scheduled to take place in 2024 and to last for 30 months. The Phase-0 upgrading process of the LHC complex has already been started in 2013 during the LS1, in which ATLAS installed the IBL, as discussed in Section 2.2.3. During the LS2, the Phase-I upgrade will see installed new LHC injectors and collimators. The current Linac2 will be replaced with the more powerful Linac4, the Proton Synchroton Booster will increase its output energy to reduce the beam emettance and the collider collimation system will be upgraded. The ATLAS Phase-I upgrade [74] will allow collection of an integrated luminosity of 300-400 fb^{-1} at $\sqrt{s} = 14$ TeV. Due to the increasing luminosity, most of the Phase-I ATLAS upgrades are related to trigger improvements, needed to keep an acceptable trigger rate without increasing threshold cuts. In particular, the New Small Wheels [75] (NSW) will be installed in the MS, the L1Calo [76] granularity will be improved, and a new online global track reconstruction electronic will be implemented, the Fast TracKer [77] (FTK). Furthermore, the TDAQ system [78] will be improved and revised.

The Phase-II upgrade will take place during the LS2. The LHC rings will be upgraded with new inner triplet magnets and crab cavities, allowing to reach the nominal HL-LHC luminosity of $\mathscr{L} = 7.5 \cdot 10^{34}$ fb^{-1}. During the expected 10 years of operation, approximately 300 fb^{-1} per year will be delivered, for a total of 3000 fb^{-1} integrated luminosity. To cope with the harsh HL-LHC environment and to provide similar or better physics performance with respect to the Run II, the whole ATLAS experiment will undergo several substantial upgrades, summarized in Table 3.1.

	Inner Tracker [79, 80]
Pixel detector	5 pixel barrel layers. 4, 11, 10, 8 and 9 pixel rings from the innermost to the outermost layer, $\|\eta\| < 4.0$ coverage.
Strip detector	4 strip barrel layers. 6 disk strips.
	Calorimeters [81–83]
Calorimeter electronics	Upgraded read-out electronics to extend the radiation tolerance limits and to operate with the L0 and L1 expected trigger rates.
Forward calorimeter	Upgraded 100 μm LAr small-gap Forward Calorimeter (sFCal) with high transverse granularity.
High Granularity Timing Detector (HGTD)	Finely segmented precision timing detector placed in the existing volume of the Minimum Bias Trigger Scintillator (MBTS), $2.4 < \|\eta\| < 4.3$ coverage.
	Muon Spectrometer [84]
Barrel detectors	new RPC and small tube diameter MDT (sMDT) chambers installed in the Barrel Inner Small chamber sectors (BIS) with higher throughput front-end electronic. New RPCs will also replace the current MDTs in the Barrel Inner Large chamber sectors (BIL)
Endcap detectors	Forward $2.0 < \|\eta\| < 2.4$ trigger chambers replaced with small Thin Gap Chambers (sTGC). Replacement of the MDT front-end readout and the L0 trigger electronics. Installation of a very-forward tagger.
	TDAQ [85]
Level 0 trigger system	Makes use of Field-Programmable Gate Array (FPGA) over Application-Specific Integrated Circuit (ASIC) as information feed. The calorimeter trigger has an acceptance of $\|\eta\| < 4.0$. The L0 trigger has access to the whole MS.
Level 1 trigger system	RoI-based tracking using tracks with $p_T > 4$ GeV and $\|\eta\| < 4.0$. Output rate of 400 MHz.
HLT	Upgraded Fast TracKer trigger (FTK++) using tracks with $p_T > 1$ GeV at maximum rate of 100 kHz. 10 kHz EF output rate.
DAQ	400 kHz L1 rate for both detector read-out and data writing.

TABLE 3.1: Table showing the Phase-II upgrade plans for the ATLAS experiment.

3.2 The Inner Tracker

One of the most substantial upgrades of the ATLAS detector at the HL-LHC consists of the replacement of the ID with the new all-silicon ITk with extended acceptance, from $|\eta| < 2.5$ to $|\eta| < 4.0$. The existing ID was designed for 10 years of operation at a constant instantaneous luminosity of $\mathscr{L} = 1.0 \cdot 10^{34}$ cm^{-2}s^{-1}, $\sqrt{s} = 14$ TeV, 25 ns between beam crossing and $< \mu >= 23$. Although the LHC exceeded, in 2016, these parameters, the ID performance was adequate for its physics programme. However, the ID does not meet the requirement for the Phase-II upgrade for several compelling reasons:

- Radiation damage: the ID was not designed to withstand the radiation damage at the HL-LHC. Its read-out electronics, the SCT modules and the IBL were constructed to cope with a radiation equivalent to an integrated luminosity of 400 fb^{-1}, 700 fb^{-1} and 850 fb^{-1}, respectively. Above those thresholds, the hit efficiency will be degraded and the leaking currents of the detector will exceed the limits of the power supplies and, due to the heating induced by the leaking currents, the capacities of the cooling system;
- Bandwidth saturation: the front-end electronics of the Pixel and SCT modules can accomodate up to 50 interactions per bunch crossing. With a $< \mu >= 200$ at the HL-LHC, the optical links between the front-end chips and the Read-Out Drivers (RODs) will saturate, leading to data loss;
- Detector occupancy: the higher pile up conditions at the HL-LHC will lead to an increasing number of tracks per event. Without a finer granularity of the tracker, the efficiency of the pattern recognition and track-finding would be compromised. The ID would not be able to resolve nearby tracks, thus prejudicing the physic reach of the HL-LHC programme;
- Track trigger: the current ID does not provide any tracking information to the L1 hardware trigger system. Adding tracking information to the L1 trigger could lower trigger thresholds, leading to better physic performance.

In general, the general requirement for the ITk is to deliver equal or better tracking performance to that provided by the ID during Run 2 conditions despite an average pile up of 200 events. Furthermore, the ITk design has to be robust enough to withstand a failure of 10% of its component without a significant degrade in performance, the track efficiency should be independent of ϕ and have a good track separation resolution in order to be able to measure tracks in the core of high-energy jets with high efficiency. Such an efficiency should not decrease more than 1% from low jet p_T to jets with a transverse momentum up to 1 TeV. In addition, high transverse momentum objects from a common vertex has to be correctly associated to the same

vertex with good efficiency, despite the mean separation between primary vertices under HL-LHC conditions is typically less than 1 mm.

3.2.1 The ITk layout

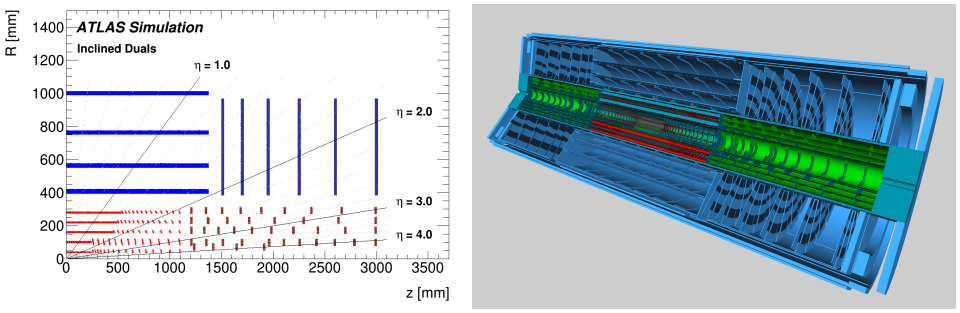

(A) (B)

FIGURE 3.2: (a): Schematic representation of the ITk *Inclined Duals* layout. Only one quadrant and only active detector elements are shown. The active elements of the barrel and end-cap Strip Detector are shown in blue, for the Pixel Detector the sensors are shown in red for the barrel layers and in dark red for the end-cap rings. The horizontal axis is along the beam line with zero being the interaction point. (b): Cut-away view of the ITk *Inclined Layout* Geant4 [86] geometry model. The Figures have been taken from [80].

The ITk *Inclined Duals* Layout is presented in Figure 3.2. It combines precision central tracking in the presence of an high pile up environment with the ability to extend the tracking converage up to $|\eta| < 4.0$ while mantaining excellent tracking efficiency and performance. The ITk comprises two subsystems: a Pixel detector surrounded by a Strip detector. The Strip detector has four barrel layers and six endcap petal-design disk, both having double modules each with a small stereo angle between them in order to allow the second coordinate measurement. The Pixel detector has a coverage of $|\eta| < 2.7$, which is extended up to 4.0 by the Strip detector. The two detectors are separated by the Pixel Support Tube (PST), while the two inner Pixel layers are separated by the outers by an Inner Support Tube (IST), thus facilitating the replacement of the innermost layers. The ITk is designed to provide at least 13 hits, with the exception of the transition region of the Strip detector, where the hit count is 11.

The ITk layout takes the name from the Pixel detector modules; they are, indeed, made of pixel read-out chips with active size of 19.2 mm$\times$20 mm combined into modules of *duals* (2) or *quads* (4) read-out chips. In addition, the barrel layers comprises a *flat*, i.e. parallel to the z-axis, section and an inclined one. This geometrical solution allows to keep the number of hits stable as a function of η. The distribution of material within the detector volume has a large impact on the overall tracking performance, electron and photon measurements, and the total ionising radiation doses. This is why particular attention was given to the location of the materials in the ITk volume. Figure 3.3 shows the material distribution of the radiation lenght X_0 as

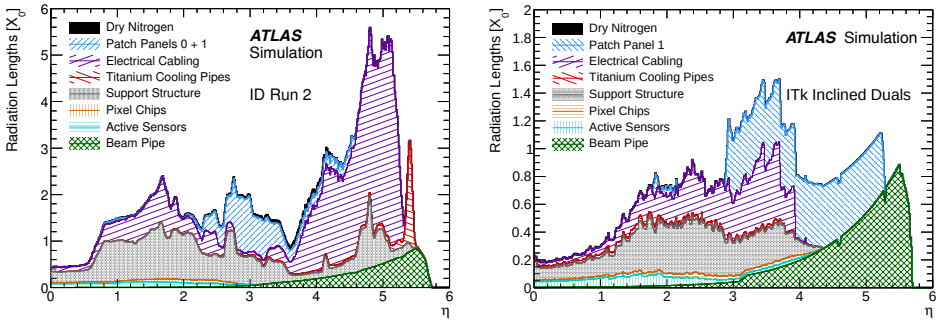

(A) (B)

FIGURE 3.3: Radiation lenght X_0 versus η for the current ID (a) and *Inclined Duals* ITk (b), . Only positive η are shown due to detector symmetry. The Figures have been taken from [80].

a function of the pseudorapidity for the Run 2 ID and the *Inclined Duals* ITk. It is shown that the improved ITk geometry model allows employing much less material with respect to the current ID.

3.2.2 Tracking and physics performance

In this Subsection, the tracking and physics performance of the simulated ITk with the *Inclined Duals* layout is presented. The full description of object definitions in ATLAS is given in Chapter 6. All performance studies here presented are done using Monte Carlo events based on a full Geant4 simulation of the ITk. The event generation is the same as the one used for Run 2 performance studies and measurements, as discussed in more detail in Chapter 4, while the reconstruction software is adapted from Run 2 to reflect the new detector geometry. For most studies, samples where an average of 200 pile up interactions are overlaid on the hard-scatter event are used.

Tracks have to fulfill the quality requirements reported in Table 3.2.

Tracking and vertexing performance

Two of the most significant figure of merit for a tracking detector are efficiency and the fake rate, i.e. the rate at which *fake* tracks are reconstructed. Fake tracks arise from random association of cluster from tracks and (to a smaller extent) noise hits. Those parameters are calculated from tracks passing the quality criteria of Table 3.2 and truth particles produced from primary interactions with $p_T > 1$ GeV and $|\eta| < 4.0$. Tracks are required to have an high matching probability, $P_{match} > 0.5$, a parameter which takes into account that a single track can have clusters generated by different particles. It is defined as

$$P_{match} = \frac{2N^{pix}_{common} + N^{strip}_{common}}{2N^{pix}_{track} + N^{strip}_{track}}, \tag{3.1}$$

Requirement	Pseudorapidity interval		
	$\lvert\eta\rvert < 2.0$	$2.0 < \lvert\eta\rvert < 2.6$	$2.6 < \lvert\eta\rvert < 4.0$
Pixel+Strip hits	≥ 9	≥ 8	≥ 7
Pixel hits	≥ 1	≥ 1	≥ 1
Holes	< 2	< 2	< 2
Double holes	≤ 1	≤ 1	≤ 1
Pixel holes	< 2	< 2	< 2
Strip holes	< 2	< 2	< 2
p_T [MeV]	> 900	> 400	> 400
$\lvert d_0\rvert$ [mm]	≤ 2	≤ 2	≤ 10
$\lvert z_0\rvert$ [cm]	≤ 20	≤ 20	≤ 20

TABLE 3.2: Cuts applied during the track reconstruction depending on the $|\eta|$ interval. Holes are defined when track candidates cross active sensors on which no hit was found, double holes are two consecutive active sensors crossed without a hit found. d_0 and z_0 are defined with respect to the mean position of the beam spot.

where $N_{common}^{pix(strip)}$ is the number of Pixel (Strip) detector clusters common to both the track and the particle being matched with and $N_{track}^{pix(strip)}$ is the number of Pixel(Strip) hits assigned to the track. The factor of 2 takes into account the fact each pixel layer provides a 2D measurement, whilst each double-sided strip gives two 1D measurements.

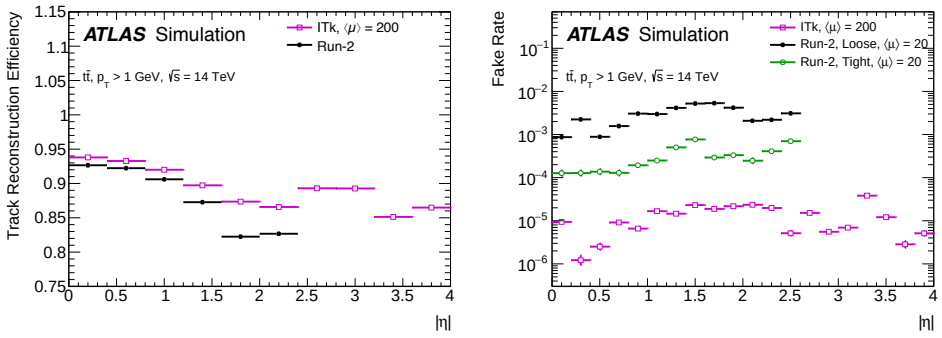

(A) (B)

FIGURE 3.4: (a): Track reconstruction efficiency for a top-pair sample with an average of 200 pile up events. Overlaid are the results for the current Run 2 detector. (b): Fake rate for reconstructed tracks in $t\bar{t}$ events with $< \mu >= 200$ using the truth particle matching criterion P_{match}. ITk is compared to the Run 2 detector results for two different levels of track selection. The Figures have been taken from [80].

The tracking efficiency, ϵ, defined as the ratio between the number of selected tracks matched to a selected truth particle, divided by the number of selected particles, has been evaluated from simulated $t\bar{t}$ events for an average number of interactions of 200 as a function of the pseudorapidity. Figure 3.4a shows the comparison of the tracking efficiency of the *Inclined Duals* ITk layout under HL-LHC condition and the Run 2 ID. Despite the high-luminosity environment, the ITk outperforms the actual ID. The better efficiency mostly

comes from the fact that a particle has to traverse significantly less material with the ITk, as Figure 3.3 shows. The rate of tracks without a matching truth particle using the P_{match} criterion is shown in Figures 3.4b. The ITk results are compared to the Run 2 detector performance with the *standard* and *loose* track selections, defined in Chapter 5. Despite a much higher pileup, the ITk shows better performance with respect to the ID. This is primarly due to the higher granularity of the Pixel and Strip detectors and the higher number of hit requirements.

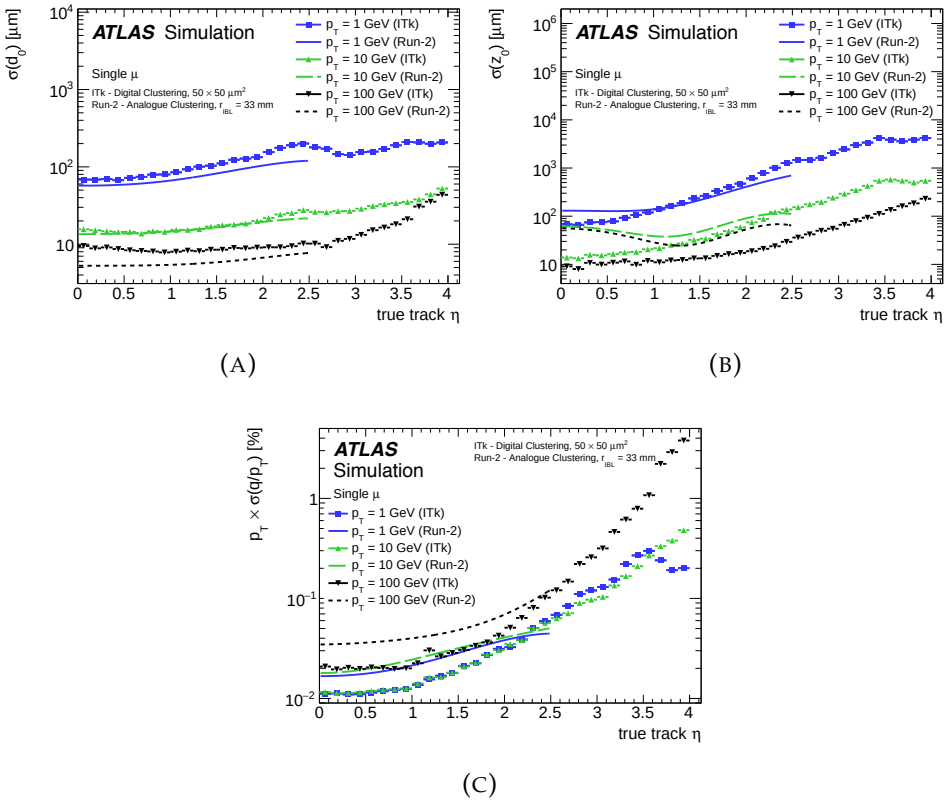

FIGURE 3.5: Track parameter resolution in d_0 (a), z_0 (b) and p_T (c) as a function of η for the *Inclined Duals* ITk layout. Results are shown for single muons with p_T of 1, 10 and 100 GeV. Performance results from Run 2 ID are shown for comparison. The Figures have been taken from [80].

As already stated in Subsection 2.2.1, the definition of the track parameters determines, through their resolutions, the performance of the detector in terms of object reconstruction (lepton and jet) and b-tagging capabilities. The resolutions are obtained from the RMS of the core of the distribution of the difference between the reconstructed and true value of the parameters of selected tracks. The selection is the same as for the efficiency studies. The resolutions for single muons with different p_T values are shown in Figure 3.5. At high muon p_T, the effect of multiple scattering is negligible, thus the intrinsic d_0 resolution dominates. It is worse than the Run 2 ID one since the latter has a smaller radius of the first pixel layer than the former, due to the harsh HL-LHC environment. For lower p_T values, multiple scattering is dominant and the performance achieved by the ITk are very similar to those of the ID.

The z_0 resolution is significantly better for the ITk. This is mainly due to the decreased pitch in the z direction. The p_T resolution is nearly a factor 2 better than the ID one. This is the result of the higher precision of the Strip tracker compared to the TRT and the reduced material of the ITk geometry.

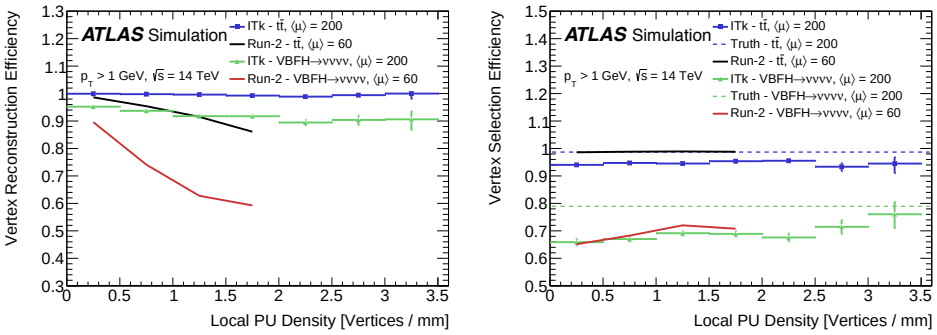

(A) (B)

FIGURE 3.6: The primary vertex reconstruction (a) and identification (b) efficiency for $t\bar{t}$ and vector boson fusion $H \rightarrow \nu\nu\nu\nu$ interactions as a function of local pile up density in events with an average pile up of 200. The vertex identification is done using the Σp_T^2 criterion. The dotted lines on the right plot indicate the rate of events for the ITk where the true primary interaction vertex actually has the highest true Σp_T^2. Shown as well are results for a Run 2 simulation sample using the Run 2 primary vertex reconstruction code. The Figures have been taken from [80].

The aim of the primary vertex reconstruction is the determintion of the positions of the hard-scatter and pile up vertices in a collision event. For Run 2, an Iterative Vertex Finder procedure through an Adaptive Vertex Fit [87] (AVF) is used. An improved version of the AVF algorithm is employed for ITk studies, the Adapative Multi-Vertex Finder [88] (AMVF). It shares the same fitting technique, but also fits for N vertices in parallel to allow for tracks being compatible with multiple vertices. Only a subset of reconstructed tracks enters the vertex reconstruction algorithm. In addition to the quality cuts described above, tracks have to meet the following requirements:

- the p_T of the track must be greater than 0.9 GeV;
- each track is required to have at least 3 pixel clusters;
- $\sigma(d_0) < 0.3$ mm and $\sigma(z_0) < 0.5$ mm.

Figure 3.6a shows that the vertex reconstruction efficiency as a function of the local pile up density in a 2 mm window around the primary interaction. For $t\bar{t}$ events with $< \mu >= 200$, the efficiency is close to 100% and no significant local pile up dependency is observed. For the vector boson fusion (VBF) $H \rightarrow \nu\nu\nu\nu$ case, there is a small pile up dependency and a few percent vertex reconstruction inefficiency. Run 2 results show a larger local pile up dependency. Figure 3.6b shows the identification efficiency for $t\bar{t}$ and $H \rightarrow \nu\nu\nu\nu$ events as a function of the local pile up density. In both topologies an high identification efficiency is achieved. For comparison, the rate of events for which the true primary interaction vertex has the highest Σp_T^2 is shown for

HL-LHC events. For Run 2, given its low level of pile up activity, the selection efficiency is higher. However, no effects due to a large density of pile up vertices is observed.

Physics object performance

Track to vertex association The ITk detector performance can be characterised in terms of physics object reconstruction. The remainder of this Section will present the pile up suppression for tracks in jets and for E_T^{miss}, given my direct involvment in those performance studies. The ITk performance for photon conversion efficiency and b-tagging are discussed in [80], the muon and electron reconstruction performance are described in [82, 84], respectively.

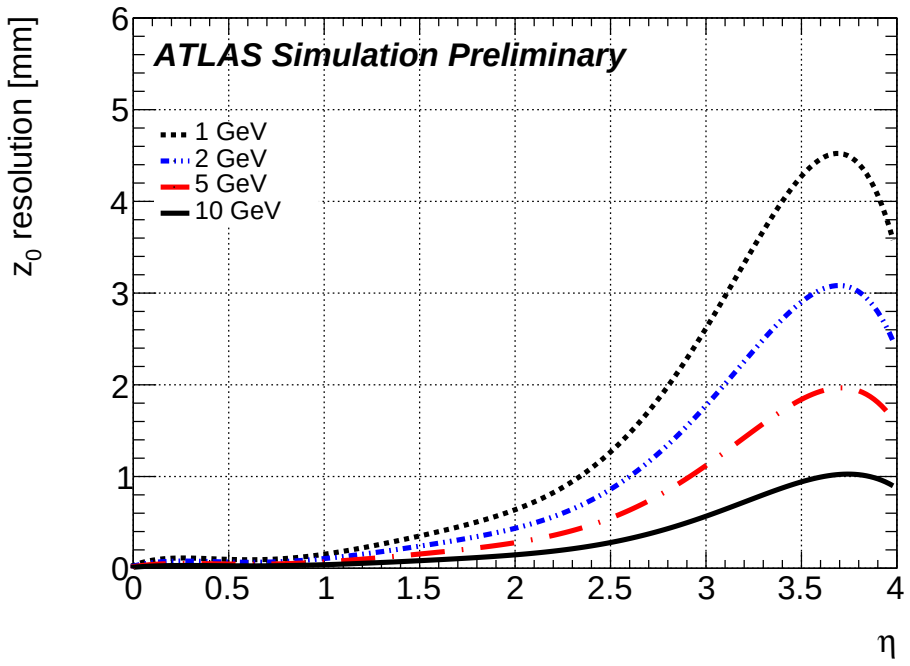

FIGURE 3.7: z_0 resolution as a function of η for different p_T values. Figure taken from [83].

To mitigate effects of pileup on the event reconstruction, one of the most fundamental elements is a precise track to vertex association. Jet reconstruction, pileup jet mitigation and E_T^{miss} reconstruction, among others, strongly depend on the correct assignment of tracks to primary vertices and jets. To improve the track to vertex association, the plain $\sigma(z_0) < 0.5$ mm is replaced with a more refined one. A track is associated to a vertex if its origin is geometrically compatible with the vertex position, in z. The compatibility is given by the following requirement on the resolution of the z_0 track parameter:

$$\frac{|z_0 - z_{vtx}|}{\sigma_{z_0}(\eta, p_T)} < 2. \tag{3.2}$$

z_{vtx} is the z position of the vertex and $\sigma_{z_0}(\eta, p_T)$ is the longitudinal impact parameter resolution, parametrized as a function of the track η and p_T, as shown in Figure 3.7. The factor of 2 is to ensure a track selection efficiency of 95% on the whole p_T and η spectra. The longitudinal impact parameter resolution is relatively small at low η, but grows fast in pseudorapidity, reaching very large values of several millimiters for $|\eta| > 2.5$; this makes the plain cut, also used during Run 2, inadequate at the HL-LHC. The degradation of the distribution at low p_T is primarly due to multiple scattering effects. Given the small resolution at very small η values, below $|\eta|$ of 2.2, a p_T-only dependant z_0 resolution is used, corresponding to $\sigma_{z_0}(\eta = 2.2, p_T)$.

Pile up jet tagging Among the several techniques developed during Run 1 and Run 2 to tag and suppress pile up jets, the simplest discriminant R_{p_T} [89] is considered. It is defined as the scalar p_T sum of the tracks ghost-associated[2] with the jet and originating from the hard-scatter vertex PV_0, divided by the fully-calibrated jet p_T:

$$R_{p_T} = \frac{\Sigma_k p_T^{trk}(PV_0)}{p_T^{jet}}. \tag{3.3}$$

Small values of R_{p_T} correspond to jets with a small fraction of tracks coming from the hard-scatter vertex; they are very likely to originate from a pile up vertex. Jets are reconstructed from three-dimensional topo-clusters [90] calibrated at the electromagnetic scale using the *anti-k_t* algorithm as implemented in the FastJet [91] package with a radius $R = 0.4$. The energy of the jets is corrected following the same calibration procedure used in ATLAS for Run 2, as described in Section 5.7.

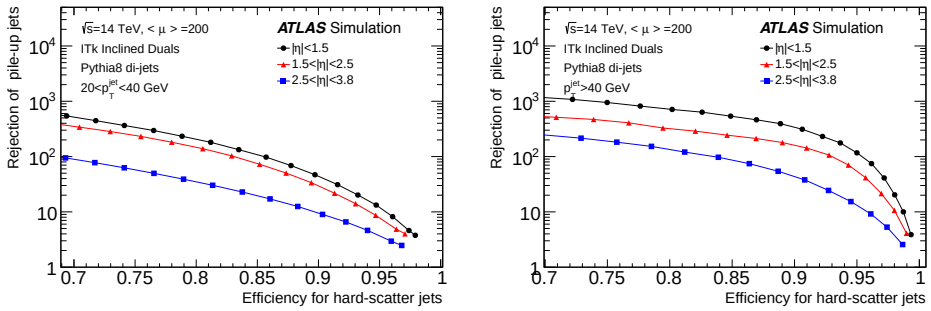

(A) (B)

FIGURE 3.8: The rejection of pile up jets as a function of the efficiency for hard-scatter jets with $20 < p_T < 40$ GeV (a) and $p_T > 40$ GeV (b) using the R_{p_T} discriminant in di-jet events with an average of 200 pile up events. The Figures have been taken from [80].

[2]The ghost-association technique consists of adding the tracks with vanishing transverse momentum to the input of the jet reclustering algorithm. If a *ghost* tracks belongs to the jet, then the original track is said to be ghost-associated.

Reconstructed jets are defined as hard-scatter jets if a truth jet associated with the primary hard-scatter vertex with $p_T > 10$ GeV is found within $\Delta R = 0.3$ of the reconstructed jet. Reconstructed jets which are separated by more than $\Delta R = 0.6$ from any truth hard-scatter jet with $p_T > 4$ GeV are labeled as pile up jets. The reconstructed hard-scatter vertex is required not to be separated from the truth hard-scatter vertex by more than 0.1 mm. Figure 3.8 shows the rejection of pile up jets as a function of the efficiency for hard-scatter jets for di-jet events in different jet p_T and η intervals. Each curve is obtained by varying the R_{p_T} cut to have a rejection factor of 50 for pile up jets independently of η and p_T. Very good efficiency is obtained at all η, even in the most forward bin.

E_T^{miss} performance In ATLAS, the E_T^{miss} is a global event quantity computed as the negative value of the vector momentum sum of high-p_T physics objects plus the soft-term from particles not belonging to any of high-p_T objects. The soft term is computed using charged tracks assigned to the hard-scatter vertex. The E_T^{miss} recommended for Run 2, described in Section 5.9, can not be applied to HL-LHC performance studies, given the larger pseudorapidity acceptance of the ITk with respect to the ID one. Therefore, a simplified E_T^{miss} definition is adopted. It is reconstructed using muons with $p_T > 2.5$ GeV or $p > 4$ GeV, electrons with $p_T > 10$ GeV and jets with $p_T > 20$ GeV. A working point of 50 pile up jet rejection is applied using the R_{p_T} discriminant to selected jets. Tracks with $p_T > 1$ GeV and $|\eta| < 4.0$ not associated to electron, muons or jets are used to reconstruct the soft-term of the E_T^{miss}.

Figure 3.9 shows the E_T^{miss} resolution, derived in $t\bar{t}$ Monte Carlo events with $< \mu >= 200$ as a function of the local pile up vertex density. Three different E_T^{miss} configuration are compared, according to the different use of forward tracking:

- tracks within $|\eta| < 2.5$ are used for both the pile up jet rejection through the R_{p_T} calculation and the track soft-term;
- full η coverage tracks are used in the R_{p_T} calculation, while only tracks within $|\eta| < 2.5$ are used to compute the soft-term;
- full pseudorapidity coverage track are used for both pile up jet rejection and the soft-term of the E_T^{miss}.

The E_T^{miss} reconstruction significantly benefits from the increased acceptance of the ITk, allowing to reject pile up jets in the forward region. The additional gain in the soft term using forward tracks is relatively small. In general, the E_T^{miss} strongly benefits from the new ITk even at the high pile up environment at the HL-LHC.

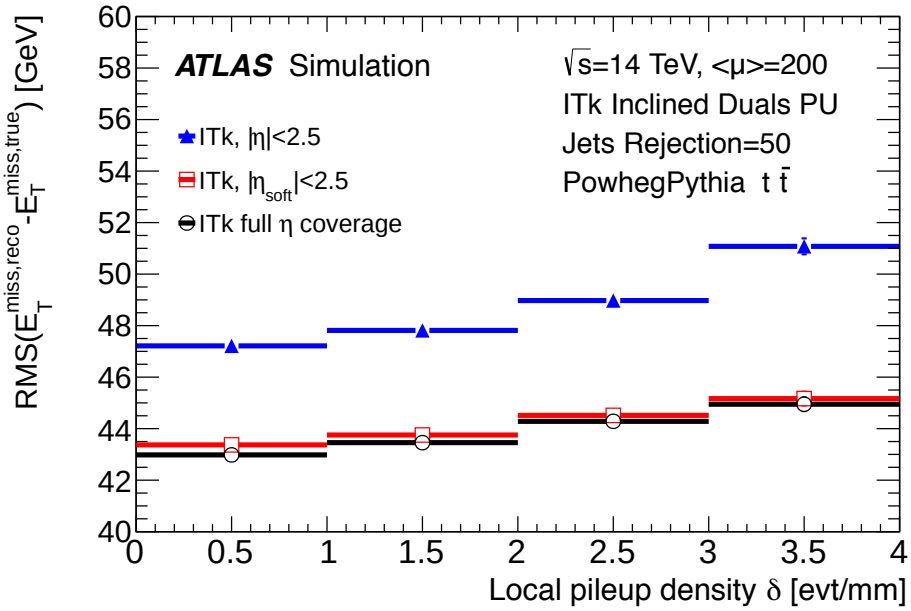

FIGURE 3.9: The resolutions of E_T^{miss} in Monte Carlo $t\bar{t}$ events with an average of 200 pile up events. The resolutions are shown as a function of the local pile up vertex density around the hard-scatter vertex, for three different ETmiss definitions. The first (blue) considers only tracks in the region $|\eta| < 2.5$ for both pile up jet rejection and ETmiss soft term. The second (red) uses hard tracks up $|\eta|$ of 4. The third (black) uses tracks up to $|\eta| < 4.0$. Figure taken from [80].

3.3 The High Granularity Timing Detector

One of the major challenges for the tracking detector is to efficiently reconstruct the charged particles and associate them to the correct production vertices. This requires the $\sigma(z_0)$ of the track to be much smaller than the inverse of the average pile up density. At the HL-LHC, with a $< \mu >= 200$, the average pile up density is of 1.8 collisions/mm. Tracks can therefore be efficiently assigned to the correct vertex if $\sigma(z_0) << 0.6$ mm. As already shown in Figure 3.7, the z_0 resolution is below this limit in the central region, but increases at large $|\eta|$, reaching up to 5 mm for low-p_T particles. The results is that a track can not be associated unambiguously to the correct vertex, leading to a degradation in performance. This limitation can be addressed by exploiting the time spread of the collisions in each bunch crossing to distinguish between tracks spatially close but well separated in time. Therefore, the ability to measure the time of individual tracks with a very high precision, much smaller than the typical collision time. At the HL-LHC, this is a Gaussian with a spread of 175 ps. The HGTD, with an expected timing resolution for Minimum Ionising Particles (MIPs) of 30 ps, will enhance the physic performance of the ATLAS detector in the forward regions by reducing the amount of pile by a factor of approximately $175/30 \sim 6$. Indeed, the HGTD, with a coverage of $2.4 < |\eta| < 4.0$, will provide timing information for nearly all parimary vertices and charged forward particles. Furthermore, the HGTD will supply online and offline luminosity measurement for each

bunch crossing and minimum-bias trigger capabilities.

3.3.1 HGTD layout

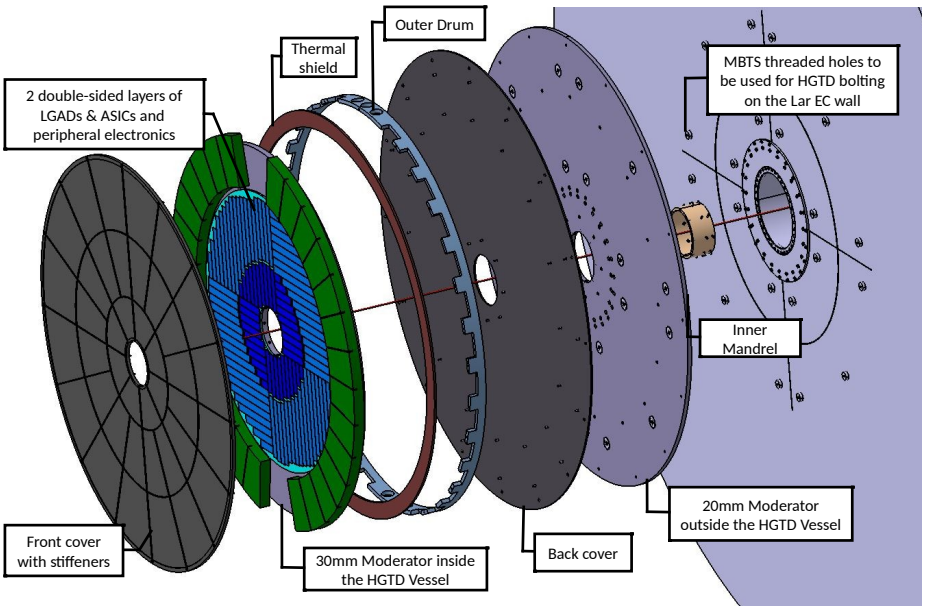

FIGURE 3.10: Exploded view of the various components of the HGTD, excluding the cooling plates. Figure taken from [83].

The HGTD will be located at $z = \pm 3.5$ m, in the volume currently occupied by the Minimum-Bias Trigger Scintillators (MBTS), between the ITk volume and the forward calorimeters. Due to space limitation and the necessity to install 50 cm of moderator material in order to protect the ITk and HGTD from back-scattered neutrons, the pseudorapidity acceptanceof the HGTD will be limited to $2.4 < |\eta| < 4.0$. The HGTD will be composed of array modules of silicon-based Low Gain Avalanche Detector (LGAD) pixel of 1.3×1.3 mm^2 with an active thickness of 50 μm. An expanded view of the HGTD is shown in Figure 3.10. The HGTD concept is based on individual planar layers of LGAD sensors to be fixed in front of both endcap calorimeter cryostats. Each layer is an independant object built on a cooling plate support disk. This modular design allow easy replacement of damaged modules during ATLAS Technical Stops.

3.3.2 Performance studies

The precise time resolution measurement capability introduced by the HGTD enhances the performance for track to vertex association, tagging jets and b-jets and calculating lepton isolation in the forward region. The results here presented focus on tracking, jet and E_T^{miss} performance; complete studies, as well as the application of the HGTD to measure luminosity and trigger

usage, are presented in [83]. In the performance studies, a simplified simulation of the HGTD, which smears the nominal track times with the expected per-track resolution, is adopted. Furthermore, in the jet performance studies, the time of the hard-scatter vertex (t_0) is assumed to be known with a precision much greater than 30 ps. Further studies are required to assess the t_0 reconstruction performance, which depends on how many tracks from the hard-scatter vertex are in the $2.4 < |\eta| < 4.0$ range and their p_T distribution. Four different HGTD scenarios are defined:

- **Initial**: corresponding to the expected performance at the beginning of the HL-LHC operation;
- **Intermediate**: considers the degradation in performance due to radiation damage after a collected integrated luminosity of 2000 fb^{-1};
- **Final**: represents the expected time resolution at the end of the HL-LHC programme, with 2000 fb^{-1} of integrated luminosity delivered. It is assumed the damaged sensors and read-out electronic have been replaced after half of the HL-LHC programme;
- **Worst case**: a resolution of 60 ps is considered. This resolution is worse than the expected one at the end of the HL-LHC programme, without sensor replacement.

Track extrapolation to the HGTD

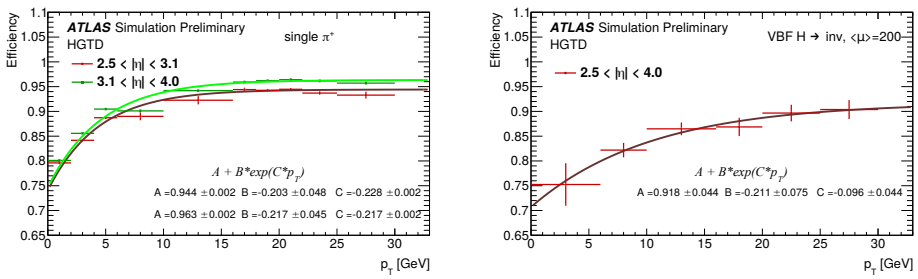

(A) (B)

FIGURE 3.11: Efficiencies for matching tracks to at least one pixel in the HGTD in single pion events (a) and for correctly reconstructing the time of a track in simulated VBF events with $< \mu >= 200$ (b). An exponential fit is performed on the points and the parameters of the fit are shown. The Figures have been taken from [83].

The matching of tracks reconstructed with the ITk to hits in the HGTD has been studied using single pions simulated samples. The matching is performed upon extrapolation of tracks to the HGTD; only tracks extrapolated to the HGTD acceptance are considered. A track is matched if the extrapolated position is within 5 mm radius a pixel hit in the HGTD. If multiple tracks match this requirement, the closest one is matched. Figure 3.11a shows the efficiency for matching a reconstructed track to at least one HGTD pixel hit as a function of the reconstructed track p_T in two different pseudorapidity regions; $2.5 < |\eta| < 3.1$ and $3.1 < |\eta| < 4.0$. An exponential fit of the points is

also presented. At high p_T, the efficiency reaches the 95% and it is limited by regions where no active material is present. At low p_T, the efficiency drops to 80% due to the interaction with the material in front of the HGTD. The comparison between the two curves show a small dependance on η. The higher $|\eta|$ region presents an efficiency 3% higher with respect to the lower one. The efficiency for correctly assigning a time to a track in an high-pile up environment is shown in Figure 3.11b for VBF $Z \rightarrow \nu\nu\nu\nu$ simulated samples as a function of the reconstructed track p_T. The p_T dependency of the efficiency is similar to the one observed in Figure 3.11a.

Track-to-vertex association

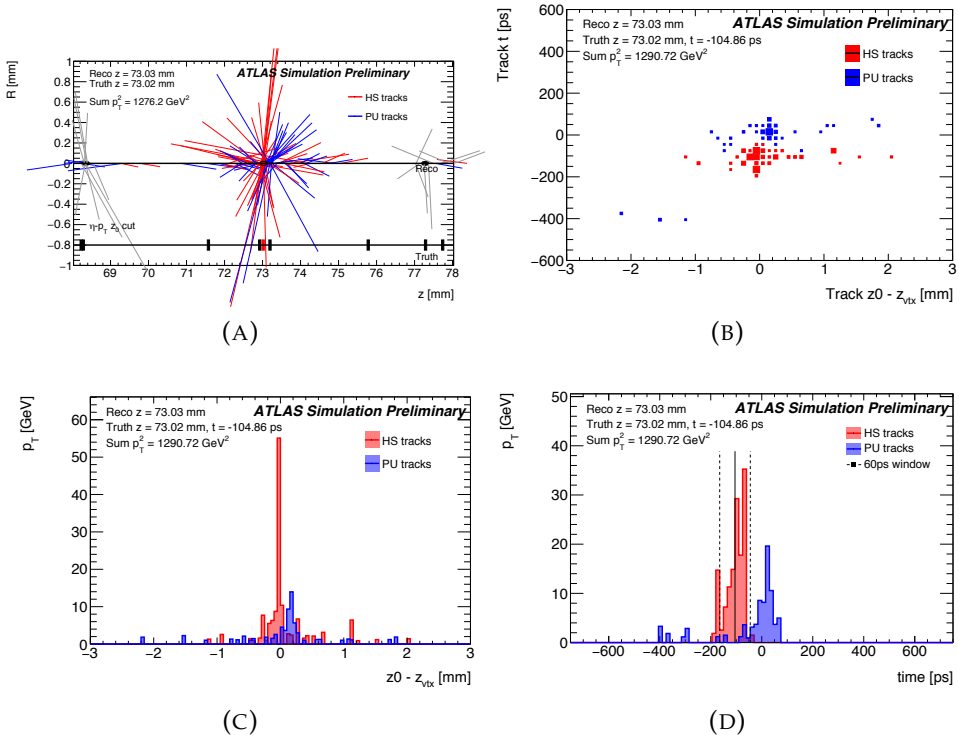

FIGURE 3.12: (a): View in the Rz plane of the tracks associated to the primary vertices in a simulated VBF event at $< \mu >= 200$. The distribution of tracks associated to the hard-scatter vertex as a function of reconstructed times and z position is shown in (b). For convenience, the projections on z and t are presented in (c) and (d), respectively. The Figures have been taken from [83].

Due to the high-pile up HL-LHC environment and the degradation of the z_0 resolution in the forward region, already discussed in Subsection 3.2.2 and shown in Figure 3.7, a non negligible contamination of pile up tracks around the hard-scatter vertex is expected. The effect is shown in Figure 3.12a, where tracks passing the quality criteria defined in Subsection 3.2.2 are displayed. Here, the lenght of each line is proportional to the track p_T, while the R position of the reconstructed and truth vertex are indicated at $R = 0$ and $R = -0.8$ mm, respectively and grey lines refers to tracks assigned to pile up

vertices. It is evident that the requirement on the z_0 track resolution of Equation 3.3 is not sufficient to unambiguously associate tracks to vertex when $\sigma(z_0)$ is large. Figure 3.12b shows the 2D distribution of the reconstructed times and z positions of the reconstructed tracks. Its projection in z, reported in Figure 3.12c, shows that the high-p_T hard-scatter and pile up tracks are well separated in space, while forward low-p_T tracks can not be resolved. On the contrary, the time projection in Figure 3.12d shows that both vertices can be resolved with a time resolution of 30 ps. The HGTD can therefore extend the track-to-vertex performance of the ITk also in the forward region by the use of the combined z-t criteria. In particular, in addition to Equation 3.3, the following requirement is introduced:

$$\frac{|t - t_0|}{\sigma_t} < 2, \tag{3.4}$$

where t is the time of the track and σ_t is its resolution, assumed to be 30 ps costant in p_T and η. The vertex time t_0 is computed as the average of high-p_T tracks associated to the hard-scatter vertex.

Jet performance

The overall jet performance of the ATLAS detector at the HL-LHC can be significantly degraded by the contamination of pile up particles to hard-scatter jets and misidentification of pile up jets as hard-scatter ones. These pile up jets can either come from hard QCD processes or from random recombination of particles coming from multiple vertices. The latter mechanism is dominant for low-p_T jets, while the former is more common for high-p_T jets. As seen in Subsection 3.2.2, the R_{p_T} is a simple but powerful discriminant for pile up jets suppression. At high pile up conditions the power of this discriminant is reduced, particularly in the forward region. The effect can be mitigated by the introduction of timing information by the HGTD to remove pile up tracks which are outside the $2\sigma_t$ window around the time of the hard-scatter vertex.

Figures 3.13a and 3.13b show the rejection of pile up jets as a function of the efficiency for selecting hard-scatter jets using the R_{p_T} discriminant for low 3.13a and high 3.13b p_T-jets in di-jet events with $< \mu >= 200$ with and without the HGTD for the different scenarios. An improvement in performance of up to a factor of 4 higher pile up rejection (at fixed hard-scatter efficiency) is achieved with the HGTD with respect to the ITk-only configuration. Furthermore, it is possible to use a p_T and $|\eta|$-dependant R_{p_T} cut to define different working point at fixed efficiency. Figures 3.13c and 3.13d show the hard-scatter jet efficiency for a fixed pile up jet efficiency of 2% as a function of the jet absolute pseudorapidity. In the forward region, the HGTD is able recover from 10 to 30% drop in efficiency observed only using tracking information from the ITk. This allows to mantain an efficiency for hard-scatter jets similar to the one in the barrel region of the detector also at large $|\eta|$. The effect is more evident for high-$|\eta|$ and low-p_T jets.

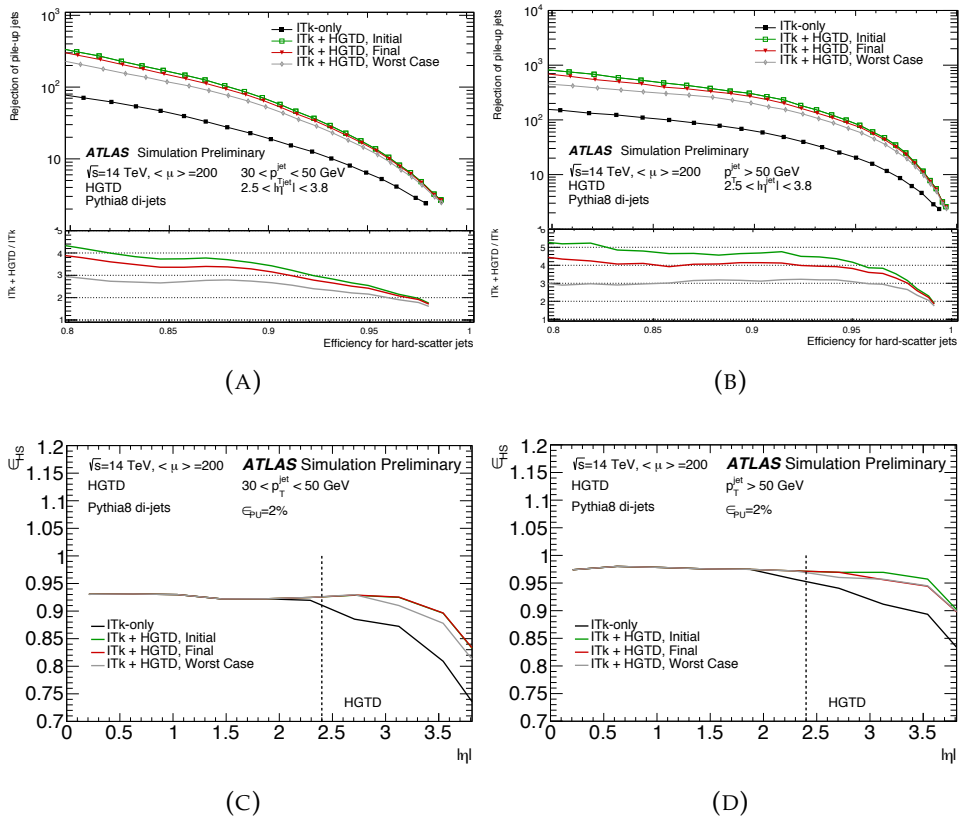

FIGURE 3.13: Pile up jet rejection as a function of hard-scatter jet efficiency in the $2.4 < |\eta| < 4.0$ region for jets with $30 < p_T < 50$ GeV (a) and $p_T > 50$ GeV (b) and hard-scatter jet efficiency versus $|\eta|$ for a 2% pile up jet efficiency rejection for jets with $30 < p_T < 50$ GeV (c) and $p_T > 50$ GeV (d). The curves refer to the ITk-only and ITk + HGTD scenarios with different time resolutions. The results have been obtained for di-jet simulated Monte Carlo events. The Figures have been taken from [83].

Chapter 4

Event reconstruction at the ATLAS experiment

In this chapter, the full chain to reconstruct the physic events, either from real data or Monte Carlo (MC) simulations, at the ATLAS experiment will be given. The basic principles of MC event generation are presented in Section 4.1, a brief overview of the simulation of the ATLAS detector is given in Section 4.2, while Section 4.3 presents a concise description of the object reconstruction and of the common dataset formats adpted by the ATLAS Collaboration. The dataset samples used in the analysis which will be presented in Chapter 6, are discussed in Section 4.4.

4.1 Monte Carlo event generation

In the broader sense of the term, MC is a technique for numerical integration based on numbers from pseudo-random number generator algorithms. MC methods find application in several different fields, from physics to biology, from medicine to finance. They are particularly suitable for event generations and perturbative calculation in HEP in terms of precision and CPU-time. Although, in one dimension, MC have a much slower convergence than numerical quadrature techniques, their associated error scale as the inverse of the square root of the number of generated points, independently on the dimension of the problem, unlike other integration techniques. This is one of the most compelling reasons they are largerly employed in HEP. Several different techniques have been developed through the years to improve MC precision and convergence time, such as importance sampling, stratified sampling, antithetic variates and adaptative MC methods. This Section will focus on the usage of MC methods at hadron colliders; a general overview on the MC techniques can be found in [92].

In a typical event at the LHC, hundreds of particles are produced and with their momenta ranging over many orders of magnitude, from a few MeV to several TeV. As discussed in Chapter 1, the matrix elements of the hard-scattering process are too laborious to be evaluated beyond the first few orders of perturbation theory. Furthermore, in order to obtain reliable predictions of experimental observables, it is necessary to deal with intrinsically

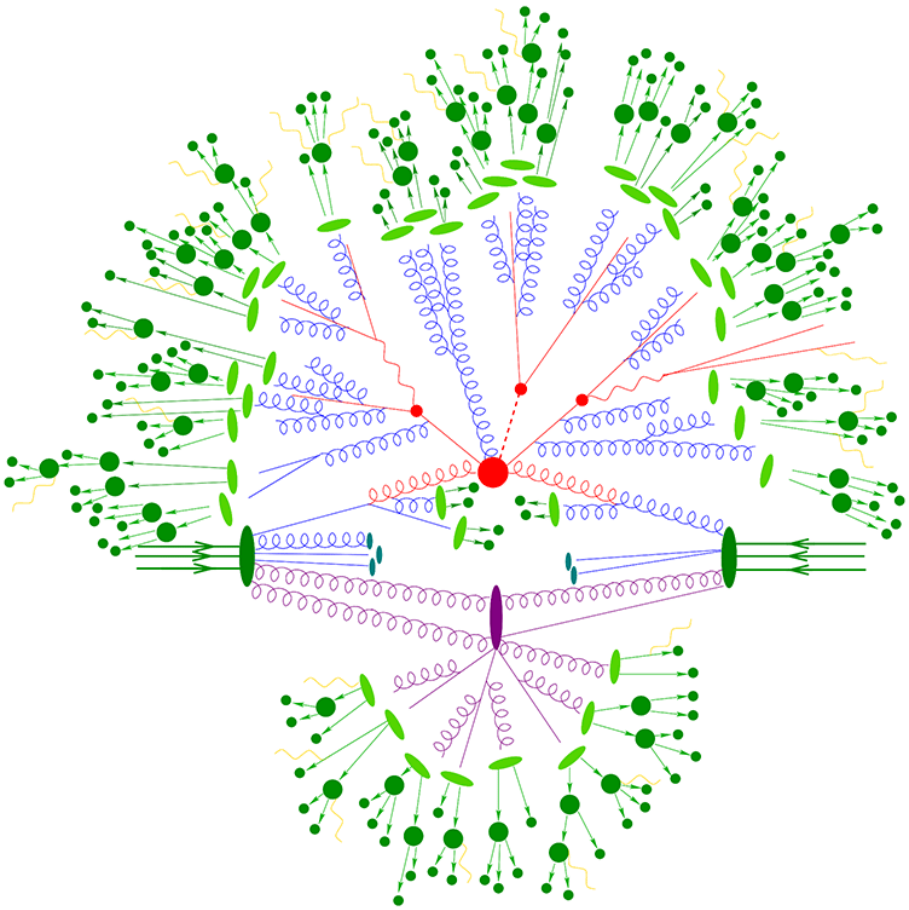

FIGURE 4.1: Schematic representation of a hadron-hadron collision as simulated by a MC event generator. The red blob in the center represents the hard collision, surrounded by a tree-like structure representing Bremsstrahlung as simulated by parton showers. The purple blob indicates a secondary hard scattering event. Parton-to-hadron transitions are represented by light green blobs, dark green blobs indicate hadron decays, while yellow lines signal soft photon radiation. Figure taken from [93].

non perturbative processes, characterized by low-momentum transfer Q^2, such as hadronization. Figure 4.1 gives a graphical representation of the several processes involved in a hadron-hadron collision simulated in MC generators. At high Q^2, the constituent partons of the incoming beams (dark-green open arrows) give rise to the hard interaction (red blob) to produce a small number of energetic outgoing particles. Involved partons can irradiate gluons, leading to the formation of parton showers (in blue). During this process, the interaction scale progressively decreases down to $Q^2 \sim 1$ GeV and the non-perturbative hadronization process takes place (light green blobs) during which coulorless hadrons are constituted from outgoing particles. Spectating particles, i.e. not partecipating in the hard-scattering process, undergo multiple interactions constituting the underlying event (purple blob). The majority of produced hadrons are not stable and their decay is taken into account by several phenomenological models (dark green blobs). A general purpose MC event generator has to be able to generate a wide range of physics processes within the same framework. The hard-scatter process is driven by fixed-order perturbative calculations, while the non-perturbative processes are modelled through a multitude of tunable parameters to well describe the data. A particular choice of parameters is referred as *tune*. The remains of this Section will give an overview of the implementation of the constituents of a general purpose MC event generator. A complete treatment can be found in [94].

4.1.1 Hard processes

Interesting processes at the LHC involve large momentum transfers. At high energies, QCD quanta are asymptotically free and it is possible to perform the calculation through perturbation theory. In most applications, one is interested in event of a particular type, so a specific process is generated rather than simulating typical events and waiting for one of them to be of the required type. As already shown in Equation 1.32, the factorization theorem allows to separate the total cross section into a short and a long distance factor, the former being the hard process, represented by the computation of the partonic cross section $d\hat{\sigma}_{ab\to\phi}$, which can be expressed as:

$$d\sigma_{ab\to\phi} = d\Phi_f \cdot \frac{1}{2\hat{s}} |\mathcal{M}_{ab\to\phi}|^2, \tag{4.1}$$

where Φ_f is the phase-space of the final state, $\frac{1}{2\hat{s}}$ is the partonic flux, $\hat{s}$ being the effective center of mass energy squared for the hard scattering process and $\mathcal{M}_{ab\to\phi}$ is the matrix element for the interested hard processes averaged over initial-state spin and colour degrees of freedom, which can be written in terms of a sum over Feynman diagrams:

$$\mathcal{M}_{ab\to\phi} = \sum_i \mathcal{F}^{(i)}_{ab\to\phi}. \tag{4.2}$$

Any general purpose event generator provides a comprehensive list of LO matrix elements and the correponding phase-space parametrizations for $2 \to 1$, $2 \to 2$ and $2 \to 3$ production channels. For higher multiplicity channels dedicated software is usually employed; these use recursive relations to compute Feynman diagrams and specific multi channel integration algorithms to properly build the phase-space [95]. The extension to NLO computation is less straightforward; a naive approach is constituted by the introduction of a K-factor, i.e. a multiplicative factor defined as the ratio of the total cross sections at NLO and LO:

$$K^{NLO}_{X\to Y} = \frac{\sigma^{NLO}_{X\to Y,}}{\sigma^{LO}_{X\to Y}}, \tag{4.3}$$

where X and Y represent the initial and final state, respectively. Therefore, the differential cross sections at NLO can be evaluated as

$$d\sigma^{NLO}_{X\to Y} = K^{NLO}_{X\to Y} \cdot d\sigma^{LO}_{X\to Y}. \tag{4.4}$$

This approach is now overcome by programs implementing an automated procedure to perform calculation natively at NLO, such as the MCFM[1] [96] fixed-order generator, MG5_aMC@NLO[2] [97] and Sherpa[3] [98] frameworks. The cross section is commonly factorized as

$$d\sigma^{NLO} = d\tilde{\Phi}_n \left[\mathcal{B} + \alpha_s \cdot \mathcal{V}\right] + d\tilde{\Phi}_{n+1} \cdot \mathcal{R} \tag{4.5}$$

where the tilde denotes integration over the n(+1)-particles final state and the Bjorken variables and the inclusion of the incoming partonic flux. $\mathcal{B}$, $\mathcal{V}$ and $\mathcal{R}$ stand for Born, virtual and real emission parts, respectively.

4.1.2 Parton showers

A fixed-order MC generator only simulates the hard scattering process (fixed-order MC). It is not sufficient to give a complete description of the process. Higher order corrections are simulated through a parton shower algorithm, depicted in Figure 4.2. It is typically formulated as an evolution from high Q^2 down to low scales of order $1\ GeV$, usually associated with the confinement of partons into hadrons. These algorithms are based upon the phenomena of QCD radiation, consisting of the emission of a gluon by a quark. If σ_0 refers to the cross section of any process having a parton of any flavour i, then the cross section for the same hard process accompanied by the collinead emission from parton i of a parton j with momentum fraction z can be expressed

[1] a Monte Carlo for FeMtobarn processes.

[2] Mad Graph 5: automation Monte Carlo parton shower at NLO.

[3] Simulation of High-Energy Reactions of PArticles in lepton-lepton, lepton-photon, photon-photon, lepton-hadron and hadron-hadron collisions.

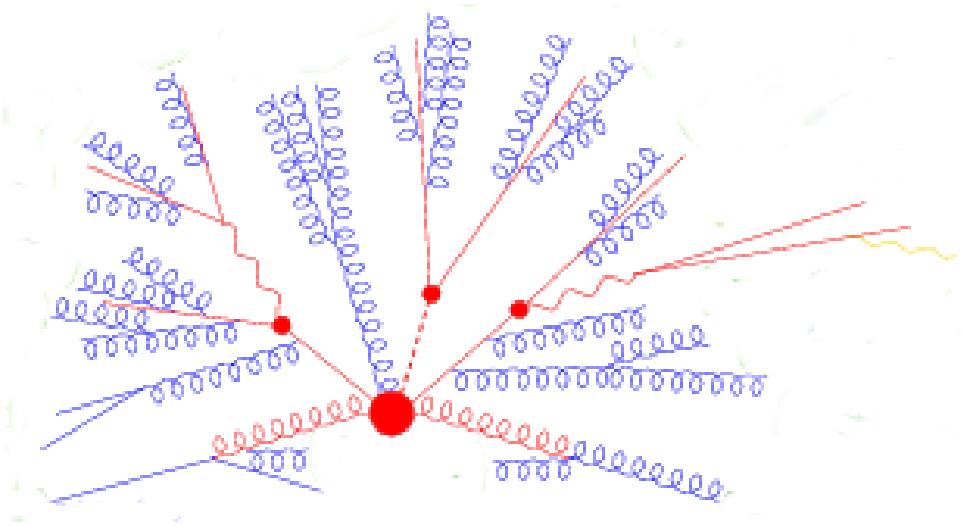

FIGURE 4.2: Schematic representation of parton shower. Figure extracted from Figure 4.1.

as:

$$d\sigma \approx \sigma_0 \cdot \sum_{i,j} \frac{\alpha_s}{2\pi} dz\, P_{ji}(z,\phi)\, d\phi, \tag{4.6}$$

where ϕ is the azimuthal angle between j and i and P_{ji} are the splitting functions already introduced in Section 1. The equation can be then iterated, treating the final state of the splitting process as an hard scattering event which generates a more collinear emission and so on. Each step must be vetoed by a probability distribution for one emission from an hard process; this is given by the Sudakov Form Factor [99], which represents the probability of not splitting during evolution at scales greater than q_1^2, given that the maximum possible scale is Q^2. It also includes quantum loop effects and can be expressed as:

$$\Delta_i(Q^2, q_1) = \exp\left\{ -\int_{q_1^2}^{Q^2} \frac{dq^2}{q^2} \frac{\alpha_s}{2\pi} \int_{Q_0^2/q^2}^{1-Q_0^2/q^2} dz P_{ji}(z) \right\}, \tag{4.7}$$

where $Q_0^2 \approx 1\, GeV^2$ is a cutoff under which further branchings are not resolvable and hadronization takes place. Equation 4.7 can be easily implemented within a MC approach: given a random number $\rho \in [0 \div 1]$, $\Delta_i(Q^2, q^2) = \rho$ is solved for q^2; if $q^2 > Q_0^2$ then a branching at a scale q^2 is generated, otherwise the evolution stops. If the condition is satisfied, then a z value is chosen according to $P_{ij}(z)$. However, the agorithm is not uniquely defined. Other than the energy fraction of the emitted parton, z can assume, in Equation 4.7, in the collinear limit, the meaning of any other momentum fraction. Furthermore, the momentum scale was chosen as the ordering evolution variable, but other choices are possible, since for the process considered the relation

$$\frac{dq^2}{q^2} = \frac{d\theta}{\theta} = \frac{dk_\perp^2}{k_\perp^2} \tag{4.8}$$

holds, as demonstated in [94]. Here θ is the polar angle between the emitting and the emitted partons and $k_\perp^2$ is the squared transverse momentum of the emitted parton with respect to the emitter one. If θ or, equivalently, $k_\perp^2$ is chosen, the very same collinear emission approach can also take into account for soft gluon emission [100]. Furthermore, only minor modifications are required for the algorithm to deal with Initial State Radiation (ISR), i.e. emission from incoming partons before the hard process. Given than the kinematic configuration of the partons produced in the hard-scattering interaction, the common approach used to simulate the initial state radiation is the implementation of a backward-evolution [101]; the generated probability density function now represents the probability a parton with a given momentum fraction z comes from one at a higher moment fraction x and lower scale. The Sudakov Form Factor is therefore replaced by the following non-emission probability:

$$\Delta_i(Q^2, q_1^2, x) = \exp\left\{ - \int_{q_1^2}^{Q^2} \frac{dq^2}{q^2} \frac{\alpha_s}{2\pi} \int_{Q_0^2/q^2}^{1-Q_0^2/q^2} dz\, P_{ij}(z) \frac{x/z f_j(x/z, q^2)}{x f_i(x, q^2)} \right\} \quad (4.9)$$

where $f_{i,j}$ are the PDFs for partons i and j. The process is iterated until the Q_0 scale is reached.

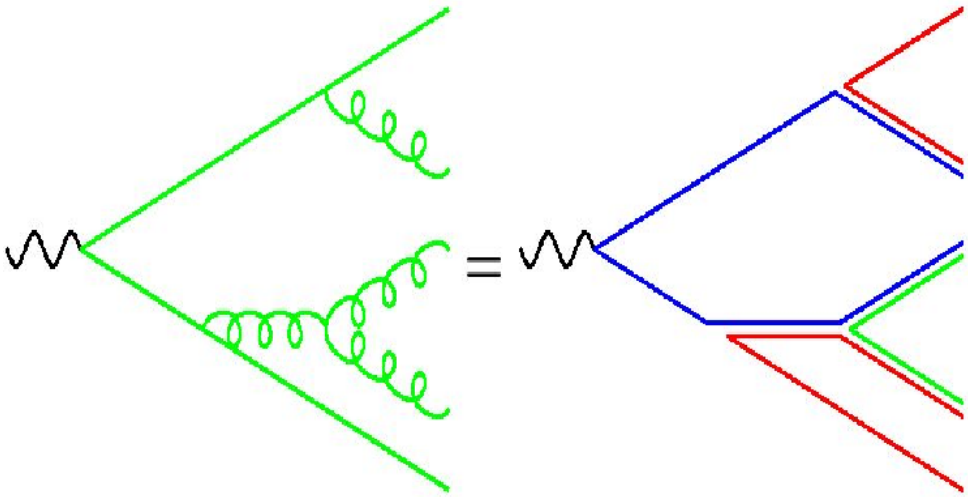

FIGURE 4.3: Schematic representation of parton shower in the dipole approach. Figure taken from [94].

An alternative to the parton showering algorithm is the dipole approach, shown in Figure 4.3; it is based on the observation that any system of partons may be decomposed as a color flows; each (anti)quark is uniquely connected to a colour partner and each gluon with 2 partners. Each colour line connecting a pair of partons represents a colour dipole which can emit independently. This approach can take account of both soft gluon and collinear

emission [102] and, being a $2 \to 3$ process rather than a $1 \to 2$, allow to conserve the momentum at each stage without relying on techniques such as momentum shuffling between partons to account for the virtuality introduced with the other algorithm. Another difference between the two approaches is that the former is θ ordered (first emission at higher angle), the latter is k_T ordered (first emission at higher transverse momentum). The different MC event generators on the market feature different parton shower implementation; Pythia[4] [103] adopts a k_T ordered one, while Herwig[5] [104] used a θ ordered parton shower algorithm.

The problem of interfacing the matrix elements of the hard-scatter process with parton showers is not trivial. Matrix elements are inclusive in the sense they give the probability of having at least n partons in a state computed exactly at a given order in α_s, while the same state generated with a parton shower is exclusive, i.e. it represents the probability that there are exactly n partons calculated approximately to all orders in α_s. Furthermore, some regions of the phase-space may be computed twice; a typical example is the emission of a single gluon. It may be seen both as a real correction to the hard process and as the result of an emission steered by a parton shower algorithm. There are several strategies for combining matrix elements and parton showers which can be grouped into 2 approaches:

- **matching:** high order correction to an inclusive process are included in the parton shower;
- **merging:** a merging scale is defined; any parton produced above that scale is generated with the computation of a matrix element and any parton produced below it is generated by the parton shower.

A more complete treatment of this topic can be found in [94].

4.1.3 Hadronization

After the parton shower, transition from the partonic state to the hadronic one is handled by the hadronization model. The process of hadronization is intrinsically non-perturbative and it can be only approached phenomenologically from general properties of QCD. Two main classes of hadronization models are currently used in HEP: the string and the cluster ones, shown in Figure 4.4. The main difference between the two is that the former transforms partonic systems directly into hadrons, the latter exploits an intermediate step in which clustered objects with a mass scale of a few GeV are formed.

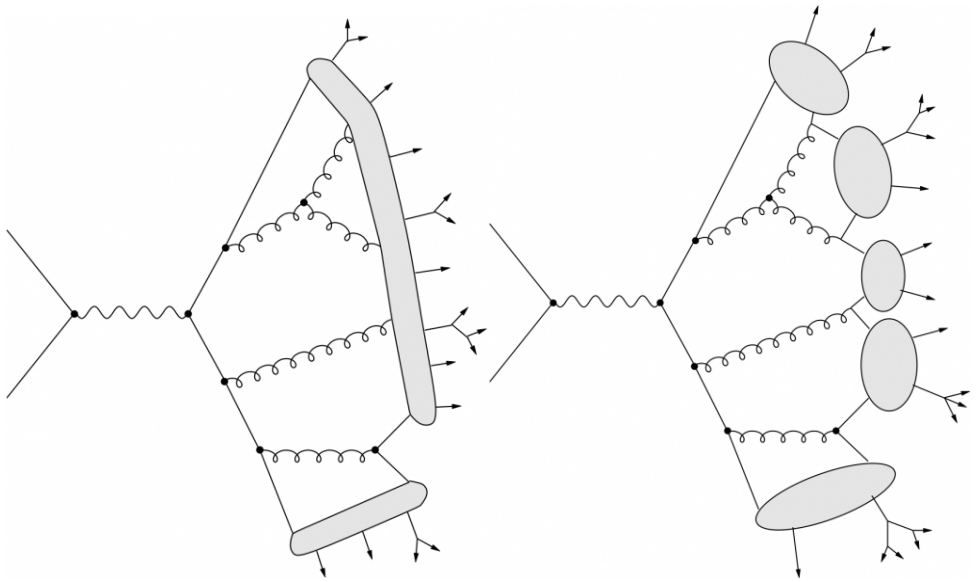

(A) (B)

FIGURE 4.4: Schematic representation of string (a) and cluster (b) hadronization models. The Figures has been taken from [4].

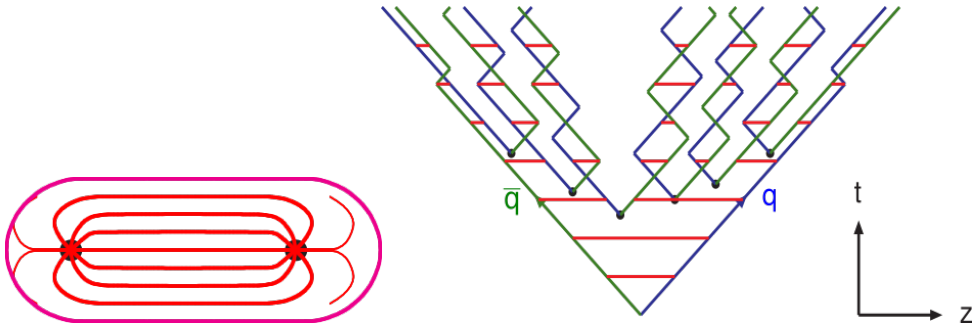

(A) (B)

FIGURE 4.5: (a): Graphical representation of a colour flux tube between a quark and an antiquark. (b): Example of motion and breakup of a monodimensional string system. Diagonal lines represent (anti)quarks, horizontal lines are instantaneous representations of the string fiels. The Figures have been taken from [94].

String model

Among the many different string hadronization models, the most sophisticated and used is the Lund one [105]. It is based on the propery of confinement at large distances in QCD. Given two partons moving apart, a colour flux tube is progressively stretched between them, as shown in figure 4.5a. The typical transverse dimension of the tube is of the order of $1\ fm$, comparable with the hadronic size. If the tube is assumed uniform, the confinement potential is linear, $V(r) = \kappa r$. From hadron mass spectroscopy the string constant κ, i.e. the amount of energy per unit lenght, is found to be $\kappa \approx 1\, GeV/fm$. The model is based on the fundamental assumption of massless strings with no transverse degrees of freedom or, in other words, of a cylindrical symmetric flux tube. A simple $q\bar{q}$ event is shown in Figure 4.5b; quarks are moving apart on the z axis, the potential stored in the string linearly increases until become energetically convenient for the string to break up by the production of a $q'\bar{q}'$ pair. The overall effect is the splitting of the original system into two independent ones with no field between them. Further breaks can occur if the invariant mass of any system is large enough and so on until a set of n ordinary hadrons are formed; each of them is made by the quark from one break and an antiquark from an adjacent break, i.e. $q\bar{q}_1,\ q_1\bar{q}_2,\ \ldots,\ q_{n-1}\bar{q}_n$.

Each break is independent from the others [106], but two adjacent breaks are constrained by the fact that the resulting string created has to be on the mass shell for the hadron being created. The relevant variable in this context is the transverse mass, defined as:

$$m_\perp^2 = m^2 + p_x^2 + p_y^2 = E^2 - p_z^2. \tag{4.10}$$

It is theregore possible to introduce a *left-right symmetry*; each string can be equivalently broken from left to right or the other way round. This argument leads to the derivation of a probability density function for a parton to fragment into a particular hadron carrying a certain fraction of its energy, called fragmentation function, $f(z)$ [107]:

$$f(z) \propto \frac{1}{z}(1-z)^a \exp\left(-\frac{bm_\perp^2}{z}\right), \tag{4.11}$$

where a and b are free parameters. This fragmentation process can only take place with a sufficiently massive string; if this is not the case, there is a small probability that the string collapses into a single hadron; this procedure is similar to the one employed within the cluster model, as discussed later. During fragmentation, production of heavy-quark pairs is highly suppressed, in fact they must be created in one point and then tunneled out at a distance so that the field energy between them can provide their masses.

[4] Its name comes from the Pythia, better known as the Oracle of Delphi, the most famous Greek oracle, whose **predictions** were directly inspired by Apollo.

[5] An event generator for Hadron Emission Reactions With Interfering Gluons.

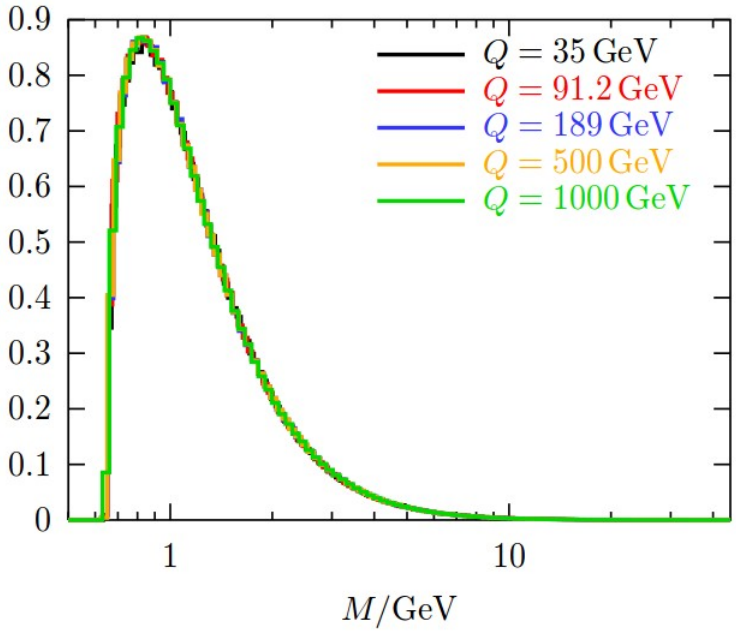

FIGURE 4.6: Invariant mass distribution of colour-singlet clusters at different center of mass energy Q obtained with the Herwig event generator. The Figure has been taken from [94].

This has a probability proportional to $\exp(-\pi m_T^2/\kappa)$. This implies a suppression of heavy quark production (top, bottom, charm quarks and often also strange quarks), so final state heavy quarks come from parton shower process. The string model can also deal with baryon production. They can come either allowing the production of diquark-antidiquark pair or adopting the *popcorn model*, where baryons arise from the successive production of quark-antiquark pairs. The model was presented assuming a simple case of a $q\bar{q}$ pair. The picture gets more complicated if more partons are taken into account. Gluons, carrying two colours, are connected to two partners and constitutes a *kink* on the string. The string model is collinear and infrared safe [108] but since the fragmentation of each string is treated independently, any possible scenario of collective phenomena is excluded. The Lund string model is implemented within the Pythia software framework.

Cluster model

The cluster model is based on the preconfinement property of parton showers, discovered by Amati and Veneziano [109]; at any scale Q_0 colour singlets of partons (clusters) can be formed with an asymptotically universal invariant mass distribution; universal in the sense it does not depend upon the nature of the hard scattering process, asymptotically implies that $Q^2 >> Q_0^2$. Furthermore, if the condition $Q_0 >> \Lambda$ holds, then the mass distribution can be computed perturbatively [110]. Cluster models enhances gluon splitting into quark-antiquark pairs at the shower cutoff scale Q_0 [111]; adjacent colour lines can form mesonic clusters. Since $Q_0 \approx 1\ GeV$, the effective gluon mass $m_g \approx Q_0$ is near the threshold for the production of light quark pairs, so

their momentum range is too small to influence the momenta and mass of the clusters. Like in the string model, heavy quark production, including strange flavour, is strongly suppressed. However, these flavours can be produced in cluster decays. Baryons can come from gluon splitting into diquark pairs or from cluster decays into baryon-antibaryon pairs. Most clusters undergo a 2 body decay into final hadron states, but a cluster can also produce a single hadron passing part of his momentum and energy to nearby clusters. Even if mass distribution of clusters is peaked around low values ($\approx 1\ GeV$), there is always an high-mass tail, as shown in Figure 4.6; similarly to the string model, these clusters undergo a chain of binary fissions until each sub-cluster has a mass below a certain threshold, typically $\approx 2 - 3\ GeV$. This hadronization model is implemented in the Herwig event generator.

4.1.4 Hadron decays

The hadronization phase of an event generator produces a final state in which many hadrons are not stable at collider time scales. The hadron decay model is not trivial. Usually a large number of mesons are included in the model, while only the lighest baryons are considered. As for the actual decay model, usually light hadrons decay via the weak interaction and their lifetime is long enough to not be considered in high energy collision simulations; the remaining electomagnetic and strong decays are simulated through simple matrix elements based on charge and parity invariance. Tau lepton decays are often included in the decay algorithm. They primarily ($\approx 65\%$) decays semileptonically into a tau neutrinos and light mesons. The process is simulated through a electroweak decay into a tau netrino and a virtual W boson, which will be eventually decayed. The simulation of decay modes of mesons containing a single charm or bottom quark are based on a combination of experimental fits and partonic decays of the heavy quarks followed by the hadronization of their products. A similar method is employed to deal with heavy baryons decays, even if it relies more on theorethical model of charmed-baryons decays rather than experimental fits.

4.1.5 Underlying event

In hadron collider events containing an hard subprocess, there is extra hadron production that can not be ascribed to showering from partons partecipating in the hard process. This production, referred as underlying event, arises from collisions between partons in the incoming hadrons not partecipating in the hard process. An event at the LHC is characterized by multiple interactions; the ones coming from the underlying event manifest the presence of back-to.back jets with low p_T, while jets arising from bremsstrahlung tend to be aligned with the direction of their parent partons. These *hard* events are less common than underlying soft QCD interactions, i.e. not experimentally resolvable, but affecting the final state activity in a more global way, increasing the multiplicity of hadrons, their transverse energy and contributing to the beam remnant breaking up in the forward direction. Several models of

Multiple Parton Interactions (MPI) exist [112]; they have in common the definition of *impact parameter* b (transverse distance between the centroids of the colliding hadrons, which are distributed over a transverse area of the order of $1\ fm$). With a large b, collisions are peripherical with a low probability of hard scattering and few MPI. On the other hand, a small b characterizes a central collision, with high probability of hard interaction and many MPI. There are three essential aspects in a MPI model, which also may be seen as corrections:

- parton shower of the MPI, currently included in any model [113], which leads to broader and more realistic jets;
- perturbative parton-rescattering effects, occurring if partons are allowed to undergo several distinct interactions, with showering activity taking place in between. This correction has not yet been fully studied, but some models has been proposes, i.e. [114];
- colour reconnections betweeen different MPI systems; this is the most poorly undestood part of the modelling and associated with significant uncertainties. However, several models have been developed both string-based [115] and cluster-based [116].

4.1.6 Generator filtering

As it will become clear in Sections 4.2 and 4.3, the MC event generation is much less CPU-expensive with respect to the other steps. For this reason, a much larger number of MC events is generated by the ATLAS Collaboration than the ones which go through the full ATLAS generation chain and are, therefore, available to analizers. The most common approach is to select the first N events from the generated sample such that the difference between the total cross section of the final, simulated sample and the one predicted by the complete one is under a certain threshold. This approach has one major drawback: the statistical significance of the final MC sample is reduced, especially in regions of phase-space with low-associated cross section, and this may be sub-optimal for analyses sensitive to such regions. The most common method used within the ATLAS Collaboration to address the problem is the application of a *filter*, i.e. to select, from the full-statistic sample, only events that pass some specific selection. Several different filters exist, such as E_T^{miss} filters, commonly used for SUSY or exotic searches, η filters, for analyses interested in forward activities and HT-filters, based on the value assumed by $H_T = \sum_{jet} p_T^{jet}$, employed in the measurements which will be presented in Chapter 6 to better populate high-p_T regions. In addition, *object-specific filters* exists. Those are mainly used to separate a physics process into several channels. For example, the inclusive $t\bar{t}$ sample is filtered, according the number of final-state leptons, in the *fully hadronic*, *semileptonic* and *dileptonic* channels. Each filter has an associated efficiency, corresponding to the ratio of the cross section relative to the *filtered* phase-space respect to the total cross section of the process taken into account,

$$\epsilon_{filter} = \frac{\sigma_{filtered}}{\sigma_{total}}, \tag{4.12}$$

which needs to be taken into account when using filtered samples in cross section measurements.

4.2 ATLAS detector simulation

Generated MC events can not be directly compared to real data collected at the ATLAS experiment. A detailed simulation of the detector is needed in order to carry events from the event generator to a format which is identical to that of the true detector, including its limited geometrical acceptance, response and resolution. The simulation program [117] is integrated within the ATLAS computing framework, Athena [118] and uses the Geant4 (G4) simulation toolkit [86]. After the simulation of the detector and physics interactions, the energy deposits in the sensitive regions of the detector are digitized into voltages and currents to be fully compatible to the ATLAS readout system. The ATLAS detector geometry used for simulation, digitalization and reconstruction is built starting from databases containing all the necessary information to simulate a complete data-taking of the detector; from the adopted materials to the temperature of its components, from the magnetic field description to the detector misalignement. Given the complexity of the simulation, large computing resources are needed. This has lead to the development of several kinds of simulation models with different complexity and taylored for specific user-cases.

4.2.1 ATLAS simulation overview

Figure 4.7 shows the ATLAS simulation data flow. A MC generator produces events in the HepMC format [119]. Only stable particles which are expected to interact with the detector are kept and processed by the simulation model of the ATLAS detector. The energies deposited in the active area of the detector are recorded as *hits*, containing the total energy deposition, time and position. The output *hit* file also contains the *truth record* of particles produced by the generator, whether those are passed through the detector simulation or not. The next step is the *digitalization*. Simulated Data Objects (SDOs) are created from the truth record. Those are maps from the hits in the detector to the particles. The digitalization takes hit output from different sources of generated events (hard-scattering process, beam halo, beam gas, cavern background and minimum bias events), which are *overlayed*, constituting the pile up, and detector noise is added. The resulting *digits* are passed to the simulated RODs to emulate the L1 trigger. At this stage, every trigger hypothesis is tested without discarding any event. The output is a *Raw Data Object* (ROD) file. The output from the real ATLAS detector is in *bytestream* format, which is easily converted to RDO. The ATLAS HLT and event reconstruction is therefore run on the RDO files (both data and simulation).

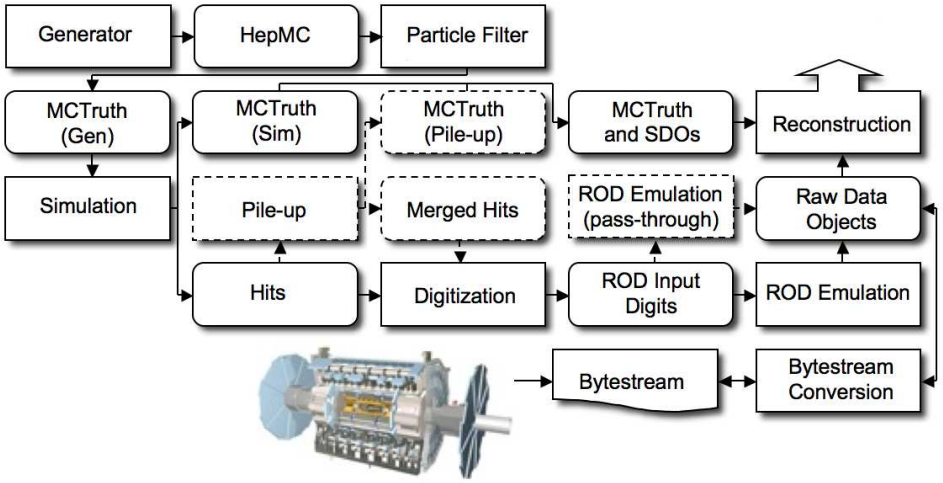

FIGURE 4.7: Overview of the ATLAS simulation software, from event generators (top left) through reconstruction (top right). Algorithms are placed in square-cornered boxes and persistent data objects are placed in rounded boxes. The optional pile up portion of the chain, used only when events are overlaid, is dashed. Generators are used to produce data in HepMC format. Monte Carlo truth is saved in addition to energy depositions in the detector (hits). This truth is merged into Simulated Data Objects (SDOs) during the digitization. Also, during the digitization stage, Read Out Driver (ROD) electronics are simulated. The Figure has been taken from [117].

4.2.2 Simulated ATLAS detector geometry

The complex geometry of the ATLAS detector has been simulaterd in great detail in order to allow an accurate modeling of, among others, missing transverse energy, track reconstruction efficiencies and calorimeter response. The basic units of the geometry structure of the detector are solids, logical volumes (solids with attributes, such as material and name) and physical volumes (logical volumes with a defined spatial position). The full geometry, shown in Figure 4.8, is constituted of hundreds of materials and hundreds of thousands of physical volumes. As stated above, only stable particles, with $c\tau > 10$ mm, are passed through the simulation step. Furthermore, to reduce the total CPU-time per event, particles with $|\eta| > 6$ are discarded; therefore, the forward detectors, like LUCID, are not included in the simulation. The resulting *hit* file is mostly (≈60%) constituted by hits from the ID, which are stored independently, although the highest number of hits are present in the calorimetry system. To reduce the global size of the output, nearby hits in the calorimeter are merged. Those hits constitute approximately the 25% of the *hit* file. Since the MS is mostly made of shielding material, the impact on the final output is negligible (at the 1% level). The remaining space is occupied by metadata (information on the simulation parameters) and the truth record.

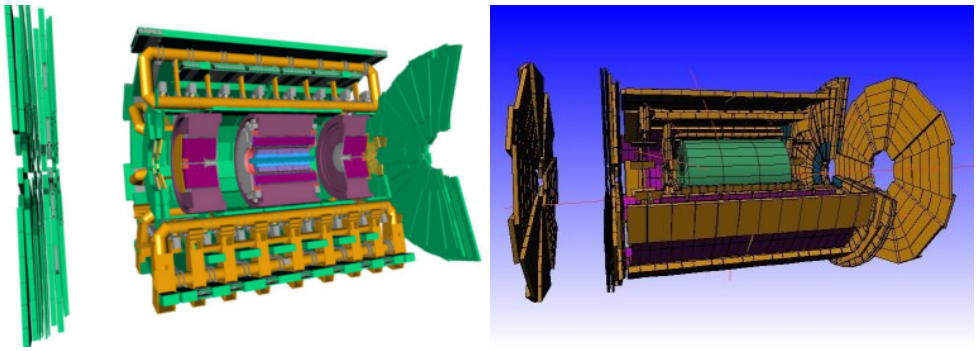

(A) (B)

FIGURE 4.8: Geant4 models of the ATLAS detector showing a cut-away view of the ID and the calorimetry system (a) and the outer muon chambers (b). The Figures have been taken from [120] and [117], respectively.

4.2.3 Digitalization

The ATLAS digitalization software converts the *hits* into detector responses, called *digits*, produced when the voltage or current of a ROD in a specified time-window rises above a certain threshold. The digits from each subdetector are written as RDOs. In addition, SDOs are produced; those contain information about all the particles and noise that contributed to the signal produced in a given sensor. RDOs and SDOs are closely related; for example, in the ID SCT, each RDO represents a group of consecutive strips which recorded a hit, while each SDO contains the information of a single strip where energy was deposited by a particle in the MC truth record. SDOs are not created in the calorimeter. The digitalization of a single hard-scattering process is not realistic; for this reason, within a digitalization job, hits from the hard-scatterring are overlaid with those of additional interaction, including multiple proton-proton scattering, beam gas effects, beam halo interactions, detector response for long-lived particles, cavern background and interactions from neighboring bunch crossing. Those events are usually referred as *pile up*. In addition, the effect of detector noise, detector conditions, including dead electronics and noisy channels, are considered.

4.2.4 Fast simulations

The ATLAS Geant4 simulation, or *full simulation* is so complex and detailed that the required CPU-time and computational resources are not compabile with the statistical needs of simulated samples. This is the main reason many different *fast simulations* techniques have been developed. Almost 80% of time of the full simulation is spent simulating particles traversing the calorimetry system, mostly electromagnetic ones (75% of total time). The Fast G4 simulation was developed to speed up the slowest part of the simulation step [121, 122]; low energy electromagnetic particles are removed from the calorimeter and replaced with pre-simulated EM showers retrieved from a database. This approach allows to reduce the total CPU-time by a factor of

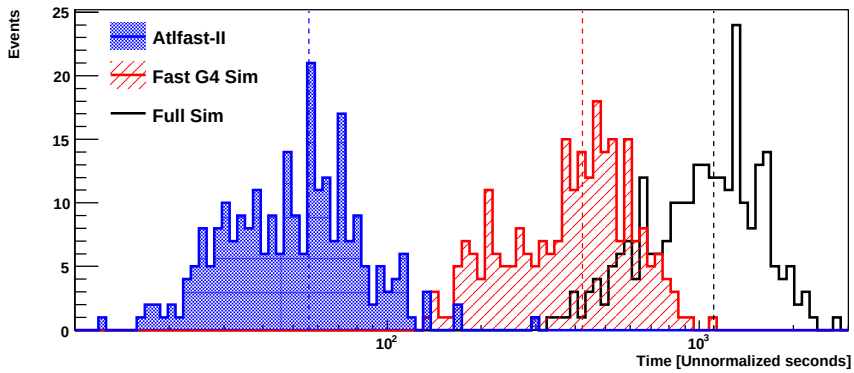

FIGURE 4.9: Distributions of CPU time for 250 $t\bar{t}$ events in full, Fast G4, and ATLFAST-II simulations. Vertical dotted lines denote the averages of the distributions. The Figure has been taken from [117].

three in hard-scattering events with negligible physics penalty. For physics parameter space scans and studies that require very large statistics without the high level of detail of the full simulation, the ATLFAST-I has been developed. Truth objects are smeared with predefined detector resolution functions to provide physics object that are similar to those obtained with the full reconstruction. No realistic detector description is present, so no simulation of reconstruction efficiency or misindefication rates are included. This is the faster and less precise ATLAS detector simulation, able to achieve a factor of 1000 speed increase with respect to the full simulation. ATLFAST-II (or AFII) is a fast simulation aiming to provide large statistics to complement the full simulation samples. This simulation allows a fast event simulation while still being able to run the standard ATLAS reconstruction algorithms. ATLFAST-II comprises two components: the Fast ATLAS tracking simulation (Fatras) to simulate the ID and MS [123] and the Fast Calorimeter Simulation (FastCaloSim) for the calorimeter simulation [124]. The employment of Fatras and FastCaloSim lead to a simulation faster by a factor of 100 than the full simulation. If the ID is simulated with the standard Geant4 framework, the achieved factor of speed reduced to 10 (ATLFAST-IIF). The CPU-time distribution for 50 simulated $t\bar{t}$ events with the different ATLAS detector simulation models are shown in Figure 4.9.

Figure 4.10 shows a comparison between the full simulation and the different fast simulations. The x-component of the E_T^{miss} for the full and fast simulations in di-jet events with a leading parton p_T between 560 and 1120 GeV is shown in Figure 4.10a. ATLFAST-II and the Fast G4 Simulation agree well with full simulation in the whole spectrum, while ATLFAST-I does not sufficiently populate the tails of the distribution and ATLFAST-IIF has too wide a distribution. Figure 4.10b shows the jet p_T resolution as a function of $|\eta|$ in $t\bar{t}$ events for jets with $20 < p_T^{true} < 40$ GeV. ATLFAST-I, ATLFAST-IIF, and ATLFAST-II show 10-20% deviations from full simulation. Fast G4 simulation is consistent with full simulation through the entire range in pseudorapidity.

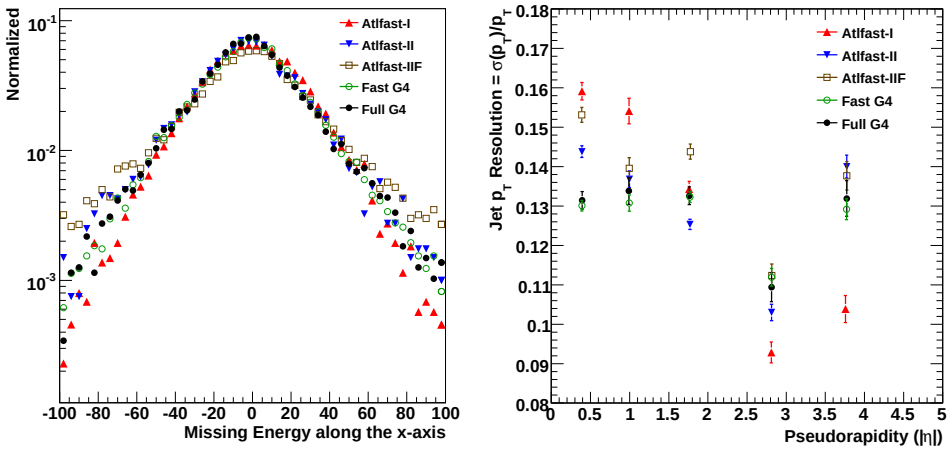

(A) (B)

FIGURE 4.10: Fast simulations (color) and full simulation (black) comparison of missing transverse energy along the x-axis in di-jet events with a leading parton pT between 560 and 1120 GeV (a) and of jet p_T resolution as a function of pseudorapidity in $t\bar{t}$ events for jets with $20 < p_T^{true} < 40$ GeV (b). The Figures have been taken from [117].

4.3 Object reconstruction

After the simulation step, simulated event and data have the very same structure. The only difference, apart the presence of truth information in MC samples, is that the HLT in data is applied on the *bytestream* directly, while the emulated HLT takes simulated ROD files as input. The reconstruction of events from the detector (data) and digitalization (MC) steps proceed in the same way. At first, specific reconstruction algorithms are run to reconstruct tracks and group calorimetric clusters of energy. Then objects candidates are built. Further details of the object reconstruction performance will be given in Chapter 5. The output of the reconstruction step is in the form of Analysis Object Data (AOD) files, containing sufficient information for common analyses. AOD files store information (tracks, candidate leptons, photons, jets, tracks) in a tree-like structure derived from ROOT [125]. Each AOD sample may have the size of several tens of TB. Furthermore, not all the information contained in the AOD is of interest for the specific physics analyses. To allow analysers to frequently perform studies using ATLAS datasets, each group (top, exotic, susy...) centrally provides to user a *refined* version of the AOD samples, called dAOD (derived AOD). The derivation process consist of four different operations:

- **skimming**: whole events are removed;
- **thinning**: whole objects within an event are removed, but the event is kept;
- **slimming**: part of object information are removed, but the object is kept;

- **augmentation**: new information, usually obtained through CPU-intensive operations, are added.

In addition, when bugs or detector misalignments that can be corrected offline are found, patching the AOD during at the derivation stage can speed up the propagation of the patch, since the derivation process is much faster than the simulation one. Analysers further process the xAOD sample into plain, small-sized ROOT n-tuples which can be easily managed on local clusters.

4.4 Samples adopted for the cross section measurement

This Section will briefly present an overview of the samples, both real data and simulated, adopted for the $t\bar{t}$ cross section measurement in the fully hadronic decay channel, which is the analysis work presented in this thesis.

4.4.1 Data samples

The data used in the analysis were recorded with the ATLAS detector at a center of mass energy of $\sqrt{s} = 13$ TeV during 2015 and 2016, corresponding to an integrated luminosity of $\mathscr{L} = 36.1$ fb^{-1}. The corresponding samples were collected in multiple data-taking periods characterized by different beam and detector conditions. Only data taken under stable beam conditions and with full operation of the ATLAS subdetectors are considered. The uncertainty in the combined 2015+2016 integrated luminosity is 2.1%. It is derived, following a methodology similar to that detailed in [126], and using the LUCID-2 detector for the baseline luminosity measurements [127], from calibration of the luminosity scale using x-y beam-separation scans.

4.4.2 Monte Carlo samples

In this Subsection a brief description of the MC samples used in the analysis to simulate the *signal* and *background* processes is given. In addition to the *nominal* signal sample, several alternative MC samples have been used to do a comparison with the latest theoretycal calculations and also to evaluate the uncertainties related to the *modelling* of the $t\bar{t}$ processes. Table 4.1 shows the complete list of MC samples used in the cross section measurement; each sample is characterized by a DataSet IDentifier (DSID), which uniquely identifies the generation step (physics process, generator, parton shower algorithm, MC tune, MC parameter configuration).

The signal samples simulates the $t\bar{t}$ production which decays into the fully hadronic channel. The nominal signal sample is generated using the NLO Powheg generator [128] with the NNPDF3.0 NLO PDF set [129]. The hard process renormalization μ_r and factorization μ_f scales are set to a common dynamic scale μ:

Process	DSID	HT-Slice [GeV]	Cross section normalization	Generator	PDF set	Tune
$t\bar{t}$ all-hadronic ($h_{damp} = 1.5m_t$)	410471 410428 410429 410444	inclusive 500-1000 1000-1500 1500-9000	NNLO+NNLL	Powheg-Box v2 Pythia8	NNPDF3.0 NLO (ME) NNPDF2.3 LO (PS)	A14
$t\bar{t}$ all-hadronic ($h_{damp} = 3.0m_t$)	410481 410430 410431 410445	inclusive 500-1000 1000-1500 1500-9000	NNLO+NNLL	Powheg-Box v2 Pythia8	NNPDF3.0 NLO (ME) NNPDF2.3 LO (PS)	A14
$t\bar{t}$ all-hadronic ($h_{damp} = 1.5m_t$)	410559 410432 410433 410446	inclusive 500-1000 1000-1500 1500-9000	NNLO+NNLL	Powheg-Box v2 Herwig7	NNPDF3.0 NLO (ME) MMHT2014 (PS)	H7UE
$t\bar{t}$ all-hadronic	410466 410434 410435 410447	inclusive 500-1000 1000-1500 1500-9000	NNLO+NNLL	MadGraph5_aMC@NLO Pythia8	NNPDF3.0 NLO (ME) NNPDF2.3 LO (PS)	A14
$t\bar{t}$ non all-hadronic ($h_{damp} = 1.5m_t$)	410470	inclusive	NNLO+NNLL	Powheg-Box v2 Pythia8	NNPDF3.0 NLO (ME) NNPDF2.3 LO (PS)	A14
Single top t-channel	410616	inclusive	NNLO+NNLL	Powheg-Box v2 Pythia8	CT10 NLO (ME) NNPDF2.3 LO (PS)	A14
Single antitop t-channel	410617	inclusive	NNLO+NNLL	Powheg-Box v2 Pythia8	CT10 NLO (ME) NNPDF2.3 LO (PS)	A14
Single top Wt-channel (DR) ($h_{damp} = 1.5m_t$)	410646	inclusive	NLO+NNLL	Powheg-Box v2 Pythia8	NNPDF3.0 NLO (ME) NNPDF2.3 LO (PS)	A14
Single antitop Wt-channel (DR) ($h_{damp} = 1.5m_t$)	410647	inclusive	NLO+NNLL	Powheg-Box v2 Pythia8	NNPDF3.0 NLO (ME) NNPDF2.3 LO (PS)	A14

TABLE 4.1: Summary of MC samples adopted for the cross section measurement. Complementary information on their configuration are also included.

$$\mu = \sqrt{m_{top}^2 + p_{T,\,top}^2}, \tag{4.13}$$

which depends, on an event-by-event basis, on the top quark mass m_{top} and its transverse momentum $p_{T,\,top}$, evaluated before any Initial/Final State Radiation (IFSR). The resummation damping factor, h_{damp} is set to 1.5 times the mass of the top quark. This parameter controls the Matrix Element (ME) and Parton Shower (PS) matching in Powheg and regulates the first, high-p_T emission. Parton shower and underlying events are simulated with Pythia8 [130] with the A14 MC tune [131] and the NNPDF2.3 LO PDFs [132].

To assess the effect of a lower IFSR, the same MC sample, after a reweighting procedure which coherently varies the dynamic scales μ by a factor 0.5 and the A14 tune to its *radLo* variation. On the other hand, to estimate the effect of additional IFSR on the $t\bar{t}$ system, a dedicated sample, with varied h_{damp} parameter, set to three times the top quark mass values, has been simulated. With an analougous reweighting procedure, the μ scales have been varied by a factor of 2 and the A14 tune has been set to its *radHigh* variation.

To estimate the effect of the parton shower algorithm, a $t\bar{t}$ signal sample, interfaced with the Herwig7 [133] parton shower algorithm, is used. The H7UE tune [104] and the MMHT2014 LO PDF set [28] are used. On the other hand, the impact on the choice of the ME generator is evaluated with a MC sample generated with MadGraph5_aMC@NLO [134] and matched to Pythia8 with the same configuration adopted for the nominal sample. The ME generator uses the NNPDF3.0 NLO PDFs. To each of the signal samples, a HT-generator filter 4.1.6 is applied; a total of four *slices* are available:

- inclusive sample. No HT-filter is applied. In performing the analysis, an offline filter given by $H_T < 500$ GeV is applied;

- $500 < H_T < 1000$ GeV;
- $1000 < H_T < 1500$ GeV;
- $1500 < H_T < 9000$ GeV.

In addition to the signal MC, several different processes that can contaminate data after selection are generated. Background events can be due to other physics processes that share a similar signature to the signal one, either cause by additional jets in the event or lepton misreconstructed as jets. The background processes here considered are the top-antitop quark pair production in the non all-hadronic channel (semileptonic and dileptonic), the single top in the t-channel and in association with a W boson. The s-channel is not considered given its low cross section production, as seen in Subsection 1.8.5. The single top quark samples are generated separately for the production of a top or an antitop.

The non all-hadronic $t\bar{t}$ sample is generated with the very same configuration of the signal sample, but at least one lepton in the final state is required.

The generation of t-channel single top quark samples are done with the Powheg generator using the CT10 [135] NLO PDF set and the A14 tune. It is interfaced with Pythia8 for the parton showering and underlying event generation. The PDFs used are the NNPDF2.3 LO. On the other hand, Wt samples are generated with Powheg using the NNPDF3.0 NLO PDFs and the H7UE tune. Herwig7 was chosen as PS algorithm along with the MMHT2014 LO set of PDFs.

Top quark pair production samples are normalized to the $t\bar{t}$ pair production total cross section evaluated at the NNLO+NNLL order (cfr. Equation 1.44), single top t-channel samples are normalized to their NNLO+NNLL theoretical cross section [136], while W-associated single top quark production are normalized to the fixed order NLO+NNLL calculations [137].

The multijet background, which represents the major source of background for this measurement, can not be estimated using a MC approach given the poor modelling of the process. As will be shown in Chapter 6, a data-driven method is preferred due to his robustness and reliability.

The nominal signal samples have been simulated both with the full simulation and the AFII one; the background samples have been simulated using the full simulation, while the alternative signal samples have been simulated using the AFII simulation.

Chapter 5

Object reconstruction performance of the ATLAS detector

As seen in Chapter 4, low-level detector signals, either from simulated MC events or real p-p collisions, are processed with complex algorithms to give the reconstructed objects commonly used in HEP measurements. This Chapter will focus on their performance obtained with the ATLAS detector. The tracking and vertexing performance will be described in Sections 5.1 and 5.2, respectively. The photon reconstruction efficiency will be presented in Section 5.3, while the electron and muon performance will be given in Sections 5.4 and 5.5. Finally, an overview of the tau and jet reconstruction performance will be presented in Sections 5.6 and 5.7, respectively. B-tagged jet performance are treated separately in Section 5.8. The Chapter will be closed by Section 5.9 by the description of the performance of the E_T^{miss} reconstruction. Although no genuine E_T^{miss} is present in the final state of the analysis presented in Chapter 6, its performance will be discussed in great detail, since I was directly involved, during my ATLAS QT, in E_T^{miss} performance studies.

5.1 Tracking performance

An high track reconstruction efficiency in a dense environment such as the Run 2 LHC is fundamental to identify long-lived b-hadrons and hadronic τ-decays or in calibrating the energy and mass of jets. The studies presented here are based on the data collected by the ATLAS detector during the full 2015 run at $\sqrt{s} = 13$ TeV, corresponding to $\mathscr{L} = 3.2$ fb^{-1}. Events are selected using triggers requiring a single jet above various p_T thresholds, the minimum one being 100 GeV. Furthermore, standard data-quality requirements are applied, ensuring all detectors were operational. Data are compared to several *full simulation* di-jet simulated events. In addition, four large single-particle MC samples have been used in the following studies: $\rho \to \pi^+\pi^-$, $\tau \to \nu_t 3\pi^\pm$, $B^0 \to X$ and $\tau \to \nu_t 5X^\pm$. Further details can be found in [138].

5.1.1 Track reconstruction

Charged-particle reconstruction in the pixel and SCT detectors begins by assembling clusters from the raw measurements. Pixels and strips in a given sensor with a common edge or corner are grouped by a connected component analysis [139] (CCA) if the deposited energy yields a charge above threshold. From these clusters, three-dimensional measurements, or *space-points* are created. They represent the points where the charged particle traversed the active material of the ID. In the pixel detector, each cluster equates to one space-point, while in the SCT, clusters from both sides of a strip layer must be combined to obtain a three-dimensional measurement. At MC generator level, several classes of cluster, identified using *truth information*, can be defined; cluster created by charge deposits from one particle are called *single-particle clusters*, while cluster created by charge deposits from multiple particles are referred as *merged clusters*. Based on the information provided by the track reconstruction algorithm, cluster can be *identified as merged*, if compatible with a merged cluster. Ideally, there is a one-to-one correspondence between *merged* and *identified as merged* clusters. A cluster used by multiple reconstructed tracks but not compatible with a merged cluster is referred as *shared cluster*. In general, a *multiply used* tracks can be either *identified as merged* or *shared*, but not both.

The next step is the formation of *track seeds* from sets of three space-points. Track seed impact parameter is estimated respect to the center of the interaction region, assuming an ideal helical trajectory in an uniform magnetic field. To increase the purity, or the fraction of seeds resulting in good-quality tracks, several criteria are placed: seed-type-dependant (SCT-only, TST-only or mixed-detector seeds) momentum and impact parameter requirements, suppression of use of the same space-point for multiple seeds and the requirement of a fourth space-point being compatible with the preliminary trajectory. Track candidates are built from the chosen seeds by incorporating additional space-points using an iterative combinatorial Kalman filter [140]. The filter can create multiple track candidates from the same seed. These criteria aim at achieving a very high reconstruction efficiency and strong suppression of tracks created from purely random collections of space-points.

To remove track candidates where space-points overlap or have been incorrectly assigned, an ambiguity-solving stage is then performed. Tracks candidates are processed individually in decreasing order of *track score*, which is a proxy of the track quality. Clusters assigned to a track increase the track score according to their weight fractions, reflecting the intrinsic resolutions and expected cluster multiplicities in the different subdetectors. Holes reduce the score. The χ^2 of the track fit is also considered to penalize candidates with a poor fit. Finally, the logarithm of the track momentum is considered to promote energetic tracks and suppress the larger number of tracks with incorrectly assigned clusters, which typically have a low-p_T. The ambiguity solver then deals with clusters assigned to multiple tracks candidates. Clusters can be shared by no more than two tracks. Priority is given based on the track score. Furthermore, a track can not have more than two shared clusters.

A cluster is removed from a track candidate if it is responsible for a track not to meet the shared-cluster criterion. The track candidate is then scored again and reinserted to the ordered list of track candidates. In addition, the ambiguity solver reject tracks if one of the following requirements is not met:

- $p_T > 400$ MeV;
- $|\eta| < 2.5$;
- at least seven pixel and SCT clusters;
- no more than one shared pixel cluster or two shared SCT clusters on the same layer;
- no more than two holes in the combined pixel and SCT detectors;
- no more than one hole in the pixel detector;
- $|d_O^{BL}| < 2.0$ mm;
- $|z_O^{BL} \sin\theta| < 3.0$ mm.

d_O^{BL} is the transverse impact parameter calculated with respect to the measured beam-line position, z_O^{BL} is the longitudinal difference along the beam line between the point where d_O^{BL} is measured and the primary vertex, and θ is the polar angle of the track.

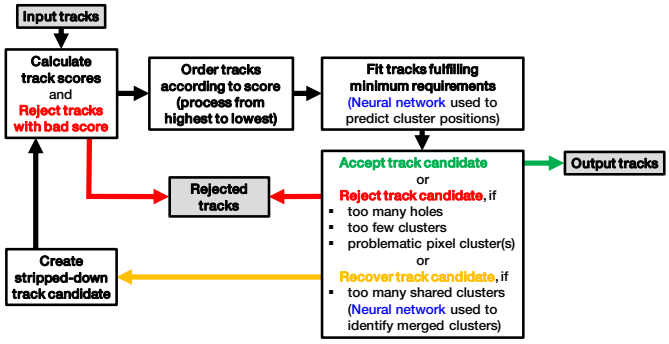

FIGURE 5.1: Sketch of the flow of tracks through the ambiguity solver. Figure taken from [138].

As shown in the simplified flows of track candidates through the ambiguity solver, Figure 5.1, an additional artificial Neural Network is used to identify shared clusters, determine the position where the charged particles intersected the sensor and predict the number of charged particles which created the cluster [141]. These information are used to perform an high-resolution fit. Fitted tracks which pass through the ambiguity solver without modification are added to the final track collection.

5.1.2 Track reconstruction performance

Tracks are classified based on a *truth-matching probability* determined by a truth-matching algorithm that associates truth-level particles to reconstructed

tracks [142]. A track can be matched either to the hard-scatter interaction or a pile up interaction. Furthermore, a track can be unmatched if reconstructed from a random combination of detector hits falsely identified as charged particle trajectories. Those tracks are also referred as *fake tracks*. Jets are reconstructed and calibrated as described in Section 5.7.

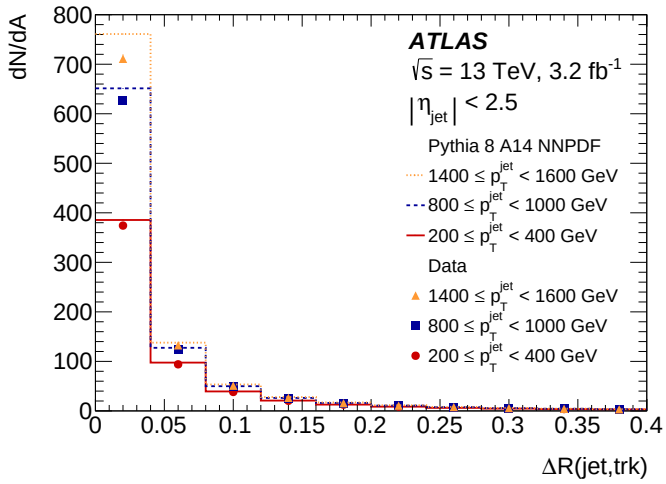

FIGURE 5.2: The average number of primary tracks per unit of angular area as a function of the angular distance from the jet axis. Data (dashed lines) and dijet MC (solid lines) samples are compared in bins of jet pT showing the high density in the cores of energetic jets. Figure taken from [138].

The average number of tracks per unit of angular area versus the angular distance from the jet axis in data and MC events is compared in Figure 5.2. The charged-particle density in jets increases linearly with the logarithm of the jet momentum, which reflects the average number of tracks inside the jet. Moreover, most tracks are located within an angular distance of 0.05 from the jet axis. Jets in data tend to have a slightly wider distribution of reconstructed charged particles than those in simulation.

Figure 5.3 shows the number of pixel and SCT clusters that are identified as shared on the track for data and MC simulation versus the angular distance from the jet axis.

The average number of shared pixel clusters remains low down to the smallest distances, because the reconstruction algorithm identifies merged clusters with high efficiency, and these consequently are not counted as shared. Although the SCT sensors are located at much higher radii than the pixel sensors, the expected number of shared clusters is considerably larger than for the pixels. This is due to the coarser segmentation of the SCT strips in one dimension and the lack of charge information hindering the identification of merged SCT clusters. The average number of shared SCT clusters decreases with the angular distance from the jet axis. MC simulation and data show reasonable agreement in the individual bins of jet p_T.

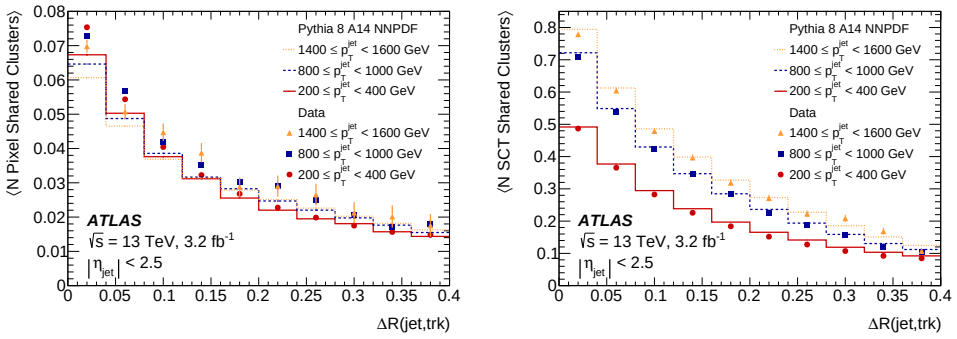

(A) (B)

FIGURE 5.3: The average number of shared pixel (a) and SCT (b) clusters on primary tracks are shown as a function of the angular distance of the track from the jet axis. Data (dashed lines) and dijet MC (solid lines) samples are compared in bins of jet pT. The rise in both populations at small distances from the jet axis is expected due to the increasingly dense environment. The Figures have been taken from [138].

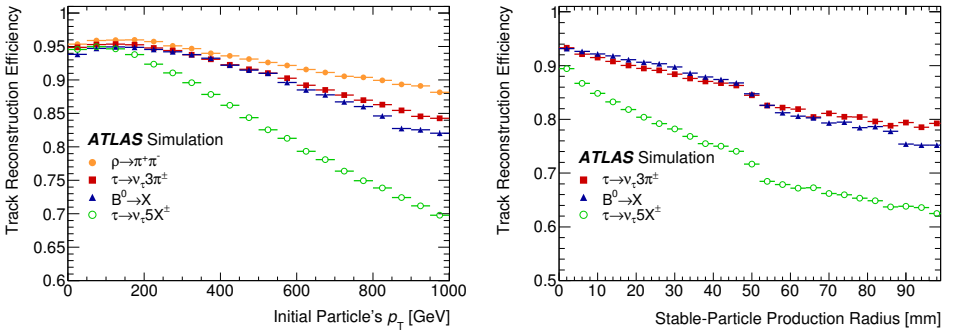

(A) (B)

FIGURE 5.4: Single-track reconstruction efficiency is shown as (a) a function of the initial particle's p_T when it is required that the parent particle decays before the IBL for the decay products of a ρ, three- and five-prong τ and a B^0 and (b) versus the production radius for the decay products of a three- and five-prong τ as well as a B^0, where no requirement in imposed on the production radius of stable charged particles. The Figures have been taken from [138].

The track reconstruction behaviour in the presence of highly collimated charged particles can be studied for many different physics processes using single-particle generated samples. The track reconstruction efficiency is shown in Figure 5.4 as a function of particle p_T and production radius, defined as the radial distance of the decay of the parent particle from the beam axis. Since the degradation of the track reconstruction performance is mainly driven by the distance between charged particles and the charged-particle multiplicity in their vicinity, the efficiency degrades with increased multiplicity of the decay products for the process taken into account. The visible inefficiency in all samples at low initial-particle p_T is due to inelastic interactions, such as hadronic interactions. At higher transverse momentum of the initial particle, a decrease in efficiency is driven by the increasingly collimated nature of the decay products. A decrease in efficiency is also seen with a increasing production radius as the charged particles arrive at each active layer with less average separation.

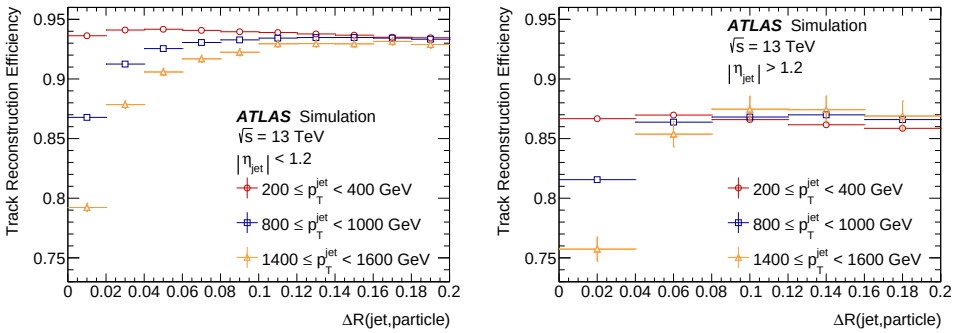

(A) (B)

FIGURE 5.5: The efficiency to reconstruct charged primary particles in jets with (a) $|\eta| < 1.2$ and (b) $|\eta| > 1.2$ is shown as a function of the angular distance of the particle from the jet axis for various jet p_T for simulated dijet MC events. The Figures have been taken from [138].

To quantify the expected tracking performance in a dense jet environment, the reconstructed tracking efficiencies has been evaluated using simulated di-jet samples. Figure 5.5 shows the charged-primary-particle reconstruction efficiency dependence on the angular distance of a particle to the jet axis for different jet η and p_T ranges. All charged particles studied are required to be created before the IBL. The efficiency drops rapidly towards the center of the jet, where the charged-particle density is maximal. A slight decrease in efficiency towards the edge of the jet is consistent with an isolated-track efficiency that rises with charged-particle p_T [143] and a decrease in the average charged-particle p_T with distance from the jet core.

5.2 Vertexing performance

An efficient and precise reconstruction of primary vertices is of primary importance to the reconstruction of hard-scatter interactions, given that the correct assignment of charged particle trajectories to the hard-scatter primary vertex is essential in the reconstruction of the full kinematics of the event. Furthermore, the primary vertex reconstruction is important in the determination of the luminous region, or beam spot, where collisions take place within the ATLAS detector. The studies presented here are based on the data collected by the ATLAS detector in 2012 at $\sqrt{s} = 8$ TeV with μ spanning a range from 0.01 to 72, with $< \mu > \approx 20$. In this Section, only a selection of results will be shown. The complete performance studies are available in [144]. Data is required to fire a single-arm trigger [145], i.e. one hit above threshold from either side of the ID MBSTs.

5.2.1 Primary vertex reconstruction

The input to the primary vertex reconstruction algorithm is constituted of tracks selected according to the following criteria:

- $p_T > 400$ MeV; $d_0 < 4$ mm; $\sigma(z_0) < 10$ mm;
- at least 4 SCT hits;
- at least 9 silicon (SCT+pixel) hits;
- no pixel holes.

The reconstruction procedure is divided in two steps: vertex finding and vertex fitting [146]. The first stage is the association of reconstructed tracks to vertex candidates, while the second reconstruct the actual vertex position and its covariance matrix. The procedure is outlined below:

- the seed position for the first vertex is selected according on the beam spot on the transverse plane. The x- and y-coordinates are those of the center of the beam spot, while the z-coordinate is the mode of the z-coordinates of tracks at their points of closest approach to the center of the beam spot. The mode is calculated using the Half-Sample Mode algorithm [147];
- the vertex position is determined using an adaptive vertex fitting algorithm with an annealing procedure [148]. The input of the algorithm are the seed position and the parameters of the reconstructed tracks. An iterative χ^2 minimization procedure finds the best vertex position. The procedure is iterated weighting the tracks with the following function:

$$\omega(\hat{\chi}^2) = \frac{1}{1 + \exp\left(\frac{\hat{\chi}^2 - \chi^2_{cutoff}}{2T}\right)}, \tag{5.1}$$

where $\hat{\chi}^2$ is the resulting χ^2 of the previous iteration step, χ^2_{cutoff} defines a threshold where the weight of an individual track is 0.5. It is set to nine, corresponding to three standard deviations. The temperature T controls the smoothness of the fit. It starts from very high values and it is lowered each step, converging to 1;

- after the vertex position and the final weights of the tracks are determined, tracks incompatible with the vertex position by more than seven standard deviations are added to the pool of *unused tracks*;
- rejected tracks are considered as input for a new vertex finding iteration;
- the procedure is repeated until no unused tracks are left or no additional vertex can be found in the remaining set of tracks.

A valid primary vertex candidate has at least two associated tracks. The output of the vertex reconstruction algorithm is a set of three dimensional vertex positions and their covariance matrices.

5.2.2 Vertices truth classification

Vertices can be classified using the same truth-matching algorithm used to associate generated particles to reconstructed tracks presented in Subsection 5.1.2. Tracks are then matched to their generated primary interaction, allowing the following exclusive classification of vertices:

- matched vertex: tracks coming from a single interaction contribute more than 70% of the total track weight of tracks fitted to the reconstructed vertex;
- merged vertex: two or more generated interactions contribute to the reconstructed vertex, but no interaction contributes more than 70% of track weight to the vertex;
- split vertex: the generated interaction with the largest contribution to the reconstructed vertex is also the largest contributor to at least one more reconstructed vertex. In this case, the vertex with the highest Σp_T of associated tracks is classified as *matched*, the other(s) as *split*;
- fake vertex: the highest contribution comes from fake tracks.

Furthermore, the whole event can be classified in one of those exclusive categories:

- clean: the event contains one matched vertex corresponding to the hard-scatter interaction. The contribution of the hard-scatter interaction to the other vertices is less than 50%;
- low pile up contamination: there is only one vertex in the event where the hard-scatter interaction contributes more than 50% of the weight tracks of the considered vertex;

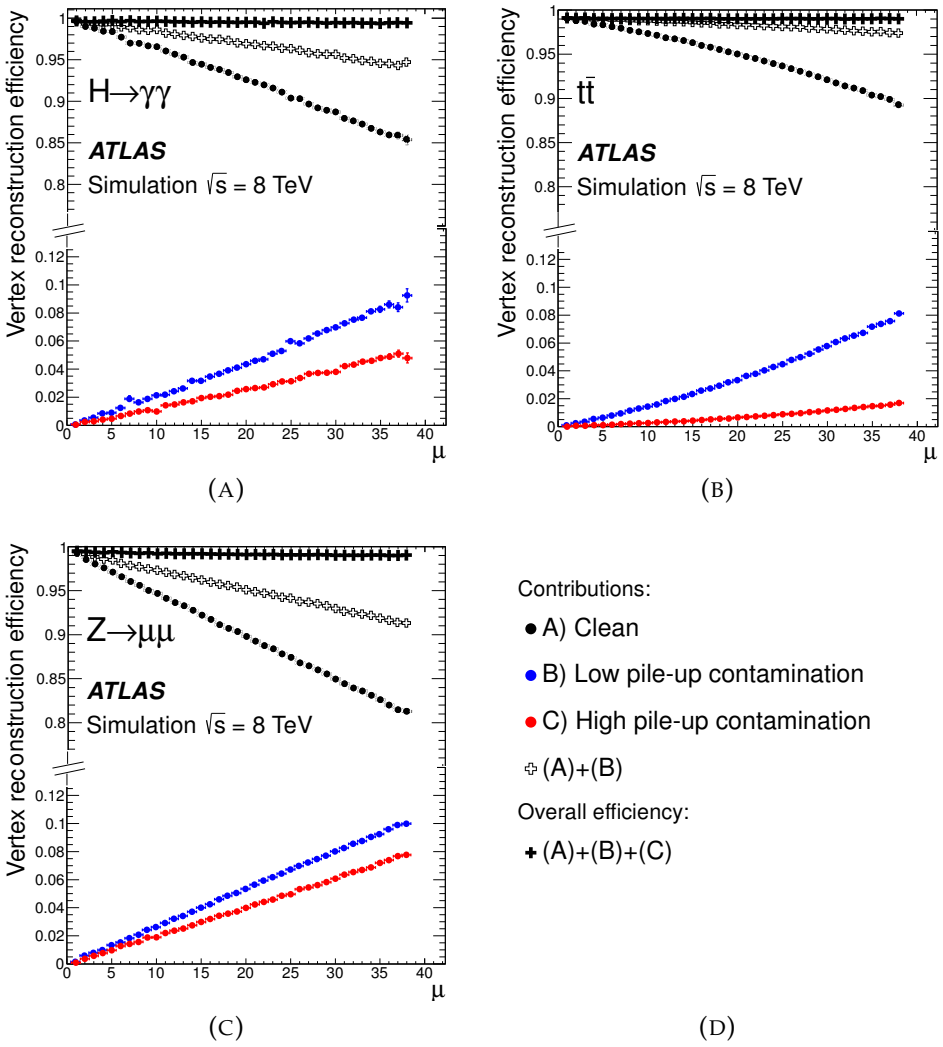

FIGURE 5.6: Contributions to the predicted primary vertex reconstruction efficiency as a function of the average number of interactions per bunch crossing, μ for the Higgs-boson decay into $\gamma\gamma$ (a), $t\bar{t}$ pair production leptonically decaying (b) and Z-boson to $\mu\mu$ decay (c). The black circles show the contribution to the efficiency from events categorised as clean, and the blue and red circles show the contributions from events with low and high pile-up contamination respectively. The open crosses show the sum of the contributions from events that are clean and those with low pile-up contamination; the filled crosses show the sum of the contributions from all categories and represent the overall efficiency, as shown in (d). The Figures have been taken from [144].

- high pile up contamination: there is no vertex where the hard-scatter interaction contributes more than 50% to the accumulated track weight. At least a vertex with a contribution from the hard interaction is in the range between 1 and 50% of the accumulated track weight;
- split: the event contains at least two merged vertices in which the hard-scatter interaction contributes more than 50% of the accumulated track weight;
- inefficient: the event does not contain any vertex where the hard-scatter interaction contributes more than 1% of the accumulated track weight.

Figure 5.6 shows the contributions to the vertex reconstruction efficiencies for the processes $H \to \gamma\gamma$, $t\bar{t} \to l + X$ and $Z \to \mu\mu$ as a function of μ. The fraction of clean events decreases with increasing μ, while the impact of the pile up contamination on the reconstruction efficiency is process-dependant. The hard-scatter interactions corresponding to Z-boson production leave on average fewer charged particles within the detector acceptance than those corresponding to $t\bar{t}$ production. This is reflected by the higher pile up contamination fraction for $Z \to \mu\mu$ events.

5.2.3 Vertex performance

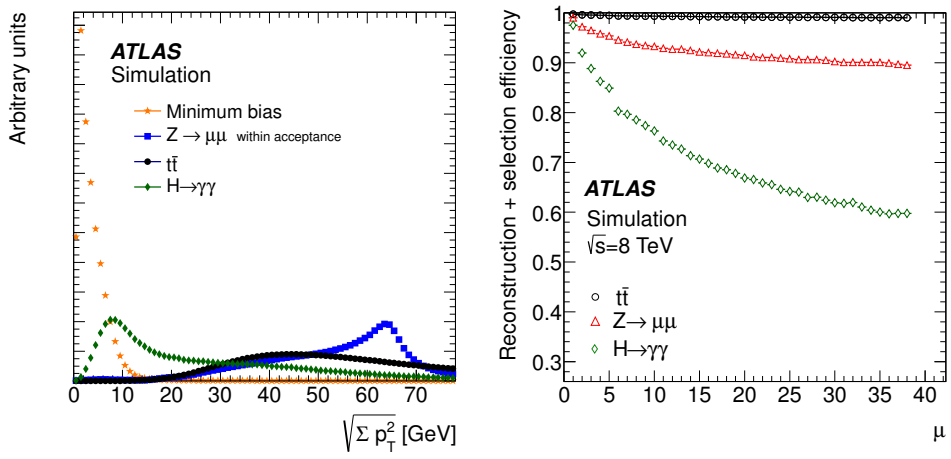

(A) (B)

FIGURE 5.7: (a): the distributions of the sum of the squared transverse momentum for tracks from primary vertices, shown for simulated hard-scatter processes and a minimum-bias sample. (b): efficiency to reconstruct and then select the hard-scatter primary vertex as a function of μ, for different physics processes. The Figures have been taken from [144].

The primary vertex selection efficiency can be defined as the fraction of events in which the highest Σp_T vertex is the MC hard vertex, i.e. the one with the highest weight of hard-scatter tracks. The selection is topology-dependant, since the Σp_T criteria is based on the assumption that most of the transverse momentum is carried by charged particles coming from the hard interaction,

and this does not hold if neutral particles are produced, as Figure 5.7a shows for $H \rightarrow \gamma\gamma$ events. This is reflected also on the vertex reconstruction efficiency, shown in Figure 5.7b for different hard-scatter processes. The highest efficiency is achieved for $t\bar{t}$ events for all values of μ. This observation is attributed to the high multiplicity of high transverse momentum tracks produced in top-quark decays.

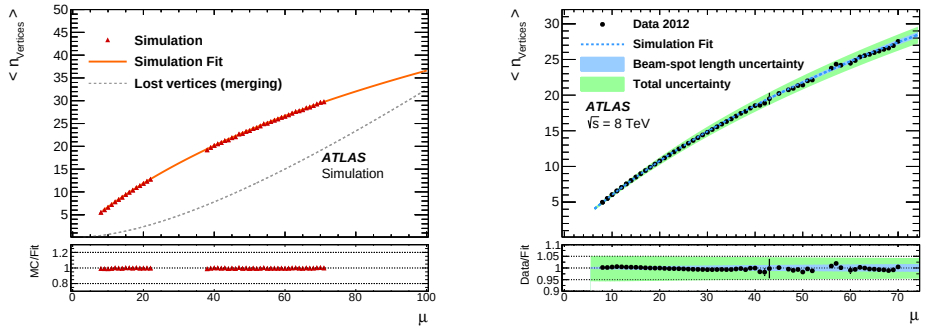

(A) (B)

FIGURE 5.8: Distribution of the average number of reconstructed vertices as a function of μ. (a): MC simulation of minimum-bias events (triangles) and the analytical function in Equation 5.2 fit to the simulation (solid line). The dashed curve shows the average estimated number of vertices lost to merging. (b): minimum-bias data (black points). The curve represents the result of the fit to the simulation after applying the μ-rescaling correction. The inner dark (blue) band shows the systematic uncertainty in the fit from the beam-spot length, while the outer light (green) band shows the total uncertainty in the fit. The panels at the bottom of each figure represent the respective ratios of simulation or data to the fits described in the text. The Figures have been taken from [144].

In the ideal case of perfect reconstruction efficiency, the number of reconstructed vertices would scale linearly with μ. Several effects cause the relation to be non-linear. The most important effect is the vertex merging. Other effects include reconstruction inefficiencies, limited detector acceptance and, to a smaller extent, non-collision background. On the other hand, the impact of split and fake vertices is negligible. The average number of reconstructed vertices, $< n_{Vertices} >$, can be parametrized as a function of μ:

$$< n_{Vertices} >= p_0 + \epsilon\mu - F(\epsilon\mu, p_{merge}). \tag{5.2}$$

ϵ is the efficiency of the vertex reconstruction, p_0 accounts for any offset arising from non-collisional background and the function $F(\epsilon\mu, p_{merge})$ represents the number of vertices lost due to merging effects as a function of the number of reconstructible vertices $\epsilon\mu$ and the vertex merging probability, p_{merge}. The complete derivation of the function is described in [144].

To allow a comparison with data, additional effects and systematic uncertainties need to be taken into account. The difference in the visible cross section in data and simulation is accounted for by rescaling ϵ by a factor of $1/1.11$,

corresponding to a μ-rescaling. The procedure comes with an associated uncertainty, primarly coming from the uncertainty in the determination of μ. Furthermore, a systematic uncertainty which takes into account possible discrepancies in longitudinal beam-spot size between data and MC has been introduced to account for variations in beam-spot size in data of ± 2 mm.

The result of the fit to MC simulation is shown in Figure 5.8a. Figure 5.8b shows the comparison between the result of the fit and data. The overall agreement is within 3%, with the largest observed discrepancies well within the systematic uncertainty band, computed as the sum in quadrature of the beam-spot size and the μ-rescaling uncertainty terms. This comparison shows that the simulation describes the primary vertex reconstruction efficiency dependence on μ accurately.

5.3 Photon performance

In this section, the performance of photon reconstruction with the ATLAS detector are only briefly discussed, since no *prompt* photon, i.e. produced directly in the hard-scattering process, are expected in the measurement discussed in this thesis. A detailed presentation of the photon reconstruction and identification performance can be found in [149]. The studies presented here are performed using the full dataset collected by ATLAS at $\sqrt{s} = 13$ TeV during 2015 and 2016, corresponding to an integrated luminosity of 36.1 fb^{-1}. Data has been collected requiring either lowest-unprescaled lepton triggers or a single-photon trigger with large prescaling factors and loose identification requirements. Generated MC samples include the LO $\gamma + jet$ events from $qg \to q\gamma$ and $q\bar{q} \to g\gamma$ processes and prompt-photons from quark fragmentation in QCD di-jet events. Furthermore, $Z \to ll\gamma$ and $Z(\to ll) + jets$ have been employed. Since the distributions of the photon transverse shower shapes in the ATLAS MC simulation do not perfectly describe those observed in data, data-driven methods have been used to correct simulated events. Further details can be found in [149].

5.3.1 Photon reconstruction

The interaction of photons and electrons with the ATLAS EMC produce similar EM showers, depositing a significant amount of energy deposits in few neighbouring calorimeter cells, therefore the reconstruction of photons and electrons in ATLAS proceeds in parallel. The electron reconstruction will be discussed in Section 5.4, while a detailed description of photon reconstruction is given in [150] and summarized as follows:

- a sliding 3×5 window in units of $\Delta\eta \times \Delta\phi = 0.025 \times 0.0245$ is used to search for EM clusters seeds as longitudinal towers with total transverse energy greater than 2.5 GeV. The cluster are formed around the seeds through a clustering algorithm [151] that allows for removal of duplicates. The cluster kinematics are reconstructed using an extended

windows with dimensions depending on the cluster position in the calorimeter;

- tracks reconstructed in the inner detector are loosely matched to seed clusters. Seed clusters that pass loose shower shape requirements, defined in [149] are used to create regions-of-interest (ROIs), within which standard track pattern reconstruction [152] is first performed. If it fails for a silicon track seed that is within an ROI, a modified pattern reconstruction algorithm is performed based on a Kalman filter formalism [140]. Track candidates are then fitted with the global χ^2 fitter [153]. Tracks with silicon hits loosely matched to EM clusters are re-fitted using a Gaussian-sum filter (GSF) fitter [154], a non-linear generalization of the Kalman filter, for improved track parameter estimation;
- the loosely-matched tracks serve as input to the conversion vertex reconstruction. Tracks with silicon hits, *Si tracks*, and tracks reconstructed only in the TRT, *TRT tracks*, are used for the conversion reconstruction. Two-track conversion vertices are reconstructed from two tracks forming a vertex consistent with that of a massless particle, while single-track vertices are built from tracks without hits in the innermost layers of the ID. If there are multiple conversion vertices matched to a cluster, double-track conversions with two silicon tracks are preferred over other double-track conversions, followed by single-track conversions. Within each category, the vertex with the smallest conversion radius is preferred;
- an object is reconstructed as an electron, a photon, or both, according to the properties of the tracks and conversion vertices matched to a given electromagnetic cluster.

The photon energy measurement is performed using information from the calorimeter. The photon energy calibration, which accounts for upstream energy loss and both lateral and longitudinal leakage, is described in [155]. The energy of the electromagnetic clusters associated with the photon candidates is corrected in subsequent steps using a combination of simulation-based and data-driven correction factors, with the calibration procedure being separately optimised for converted and unconverted photons. The photon E_T is computed from the photon cluster's calibrated energy E and the pseudo-rapidity η of the barycenter of the cluster in the second layer of the EMC as $E_T = E/\cosh(\eta)$.

5.3.2 Photon identification

The identification of photon candidates in ATLAS relies on rectangular cuts using calorimetric variables which deliver good separation between prompt-photons and fake signatures from non-prompt-photons originating from the decay of neutral hadrons in jets, or QCD jets depositing a large energy fraction in the EMC. Such variables are depicted and defined in Figure 5.9. They

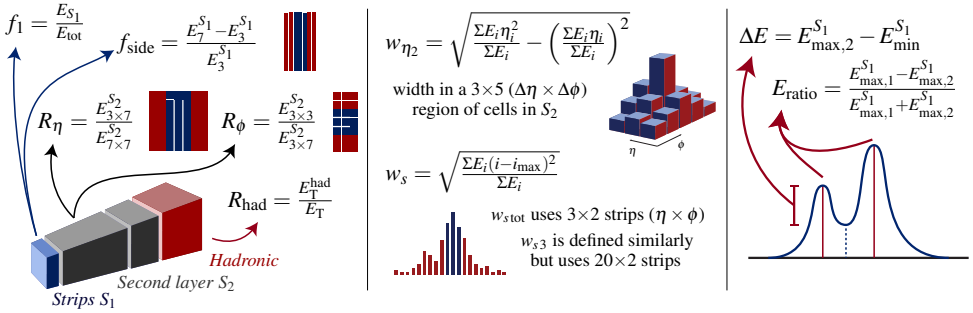

FIGURE 5.9: Schematic representation of the photon identification discriminating variables. $E_C^{S_N}$ identifies the electromagnetic energy collected in the N-th longitudinal layer of the electromagnetic calorimeter in a cluster of properties C, identifying the number and/or properties of selected cells. E_i is the energy in the i-th cell, η_i the pseudorapidity center of that cell. Figure taken from [156].

characterize the lateral and longitudinal electromagnetic shower development in the EMC and the shower leakage fraction in the HCAL. Two reference sets of cuts, *loose* and *tight*, are specifically defined for the pp data collected at $\sqrt{s} = 13$ TeV in 2015 and 2016. The set of cuts for discriminating variables employed by the photon identification are defined in [149]. The loose selection is based on shower shapes in the second layer of the electromagnetic calorimeter and on the energy deposited in the hadronic calorimeter. The tight selections add information from the finely segmented strip layer of the calorimeter, and are separately optimised for unconverted and converted photons, to account for the generally broader lateral shower profile of the latter.

5.3.3 Photon isolation

The definition of photon isolation in ATLAS is based on the transverse energy in a cone with angular size ΔR around the direction of the photon candidate. This transverse energy is characterized by two quantities: the calorimeter isolation and the track isolation. The calorimeter isolation E_T^{iso} is obtained from the sum of transverse energies of topological clusters [151] in the calorimeters, after subtracting on an event-by-event basis the energy deposited by the photon candidate and the contribution from the underlying event and pile-up. The method is described in detail in [157–159]. The track isolation p_T^{iso} is obtained by summing the transverse momenta of all the tracks with transverse momentum above 1 GeV and having a distance of closest approach to the primary vertex [144] along the beam axis $|z_0 \sin\theta| < 3$ mm, and excluding the tracks associated with photon conversions. The most commonly adopted isolation criteria are:

- **loose isolation**: based on both the calorimeter isolation and the track isolation, in both cases computed in a cone with $\Delta R = 0.2$:

$$E_T^{iso}|_{\Delta R<0.2} < 0.065 \cdot E_T \quad \text{and} \quad p_T^{iso}|_{\Delta R<0.2} < 0.05 \cdot E_T; \tag{5.3}$$

- **tight isolation**: based on the calorimeter isolation computed in a cone with $\Delta R = 0.4$ and the track isolation computed in a cone with $\Delta R = 0.2$:

$$E_T^{iso}|_{\Delta R<0.4} < 0.022 \cdot E_T + 2.45 \text{ GeV} \quad \text{and} \quad p_T^{iso}|_{\Delta R<0.2} < 0.05 \cdot E_T; \tag{5.4}$$

- **calorimeter-only tight isolation**: based only on the calorimeter isolation computed in a cone with $\Delta R = 0.4$:

$$E_T^{iso}|_{\Delta R<0.4} < 0.022 \cdot E_T + 2.45 \text{ GeV}; \tag{5.5}$$

- **legacy isolation**: requiring a fixed selection on the calorimeter isolation computed in a cone with $\Delta R = 0.4$:

$$E_T^{iso}|_{\Delta R<0.4} < 4 \text{ GeV}. \tag{5.6}$$

The data-MC corrections to the electromagnetic shower shape variables are computed using photon candidates satisfying the calorimeter-only tight isolation criterion. The measurements of photon identification efficiency are performed for isolated photon candidates meeting the loose criterion, apart from the measurement using radiative Z decays, which is performed for the tight criterion and repeated using the loose isolation and the calorimeter-only tight isolation criteria in order to evaluate the potential dependency of the identification efficiency on the photon isolation.

5.3.4 Photon identification efficiency

The efficiency ϵ_{ID} of the tight photon identification criterion is measured in data using three complementary methods:

- **radiative Z decays**: this method uses a clean sample of low-energy photons obtained from $Z \to ll\gamma$ decays ($l = e, \mu$). This allows measurements of ϵ_{ID} from $E_T = 10$ GeV to $E_T \approx 100$ GeV;
- **electron extrapolation**: this method uses a sample of electromagnetic showers from electrons originating from $Z \to ee$ decays, identified using a tag-and-probe method. These showers are modified so that their shape information matches the properties of photon showers, and used to measure ϵ_{ID} in the region $25 < E_T < 150$ GeV;
- **inclusive photons**: this method uses an inclusive photon sample collected using single-photon triggers. The efficiency of a tight track-based isolation criterion is used to obtain the fraction of prompt-photons in the full sample and in the subsample satisfying the tight identification criterion, from which a measurement of ϵ_{ID} can be derived. The measurement is performed over a wide kinematic range spanning $25 < E_T < 1500$ GeV.

The efficiencies are reported in each case for converted and unconverted photons separately. Efficiency are measured as a function of E_T in different intervals of η. In this section, only results in the most central bin, $|\eta| < 0.6$ are reported. The full studies and a more detailed description of the methods are in [149].

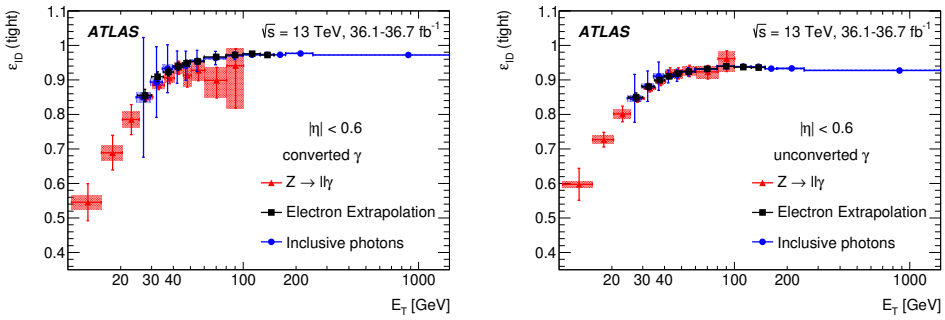

(A) (B)

FIGURE 5.10: Comparison of the data-driven measurements of the identification efficiency for converted (a) and unconverted (b) photons as a function of E_T, for the $|\eta| < 0.6$ pseudorapidity interval. The error bars represent the sum in quadrature of the statistical and systematic uncertainties estimated in each method. The shaded areas correspond to the statistical uncertainties. The Figures have been taken from [149].

The efficiencies ϵ_{ID}, measured in data for each of the three methods, are presented in Figure 5.10 for both converted and unconverted photons. The three methods show excellent agreement over the energy ranges where their measurements overlap, with photon ϵ_{ID} values ranging from 50–60% at $E_T = 10$ GeV, to 95–99% (unconverted) and 88–96% (converted) for photons with E_T above 250 GeV.

Efficiency scale factors (SF) are computed as the ratios of the data-driven values of ϵ_{ID} to the values obtained in simulation. Results from the radiative Z method are shown in Figure 5.11, while those from the other two methods are shown in Figure 5.12. Results are shown for both converted and unconverted photons. The SF values are all compatible with unity, and do not show significant trends as a function of E_T.

To increase the measurement precision in the ranges where measurements from different methods are available, a combination of the three measurements is performed. The SF values are combined rather than the ϵ_{ID} directly, in order to account for the small differences in the composition of the photon samples. The combination is performed using the BLUE algorithm [160]. The combined results are shown in Figure 5.13 for converted and unconverted photons. In the central η region presented here, the SFs are at the level of 1% or less.

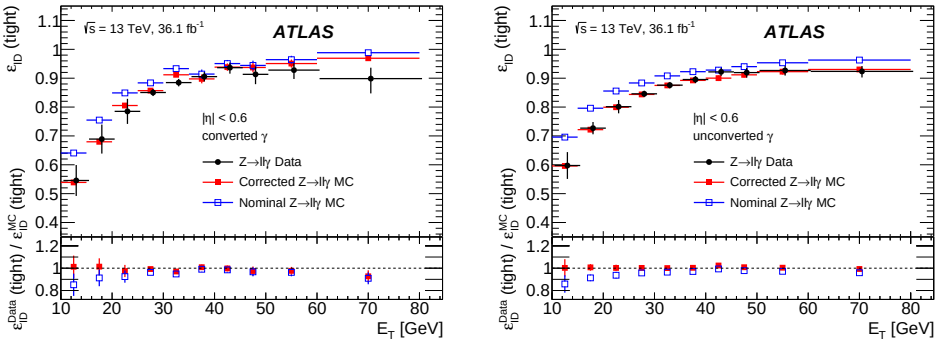

(A) (B)

FIGURE 5.11: Comparison of the measurements of the data-driven identification efficiency for converted (a) and unconverted (b) photons measurements obtained using the radiative Z method with the predictions from $Z \rightarrow ll\gamma$ simulation as a function of photon E_T, for the $|\eta| < 0.6$ pseudorapidity interval. Predictions are shown for both the nominal simulation and with the corrections applied. The bottom panels show the ratio of the data-driven values to the MC predictions. The Figures have been taken from [149].

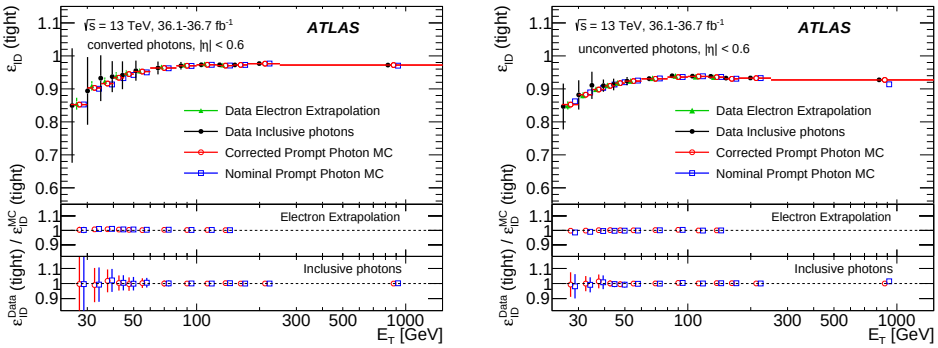

(A) (B)

FIGURE 5.12: Comparison of the measurements of the data-driven identification efficiency for converted (a) and unconverted (b) photons obtained using the electron extrapolation and inclusive photon methods with the predictions from prompt-photon+jet simulation as a function of photon E_T, for the $|\eta| < 0.6$ pseudorapidity interval. Predictions are shown for both the nominal simulation and with the corrections applied. The bottom panels show the ratio of the data-driven values to the MC predictions. The Figures have been taken from [149].

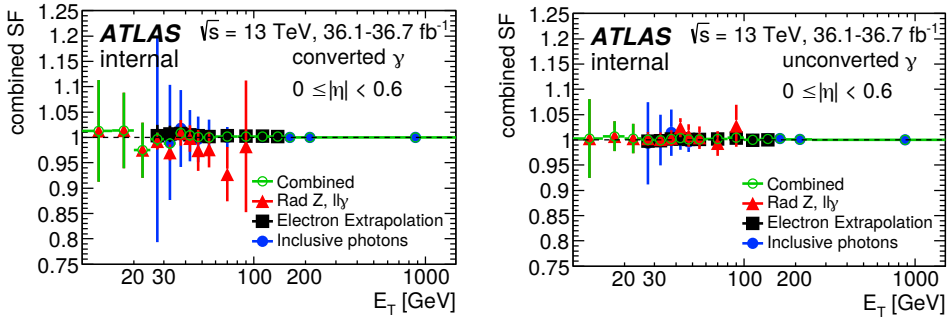

(A) (B)

FIGURE 5.13: Efficiency scale factors (SF) for each method and their combination for converted (a) and unconverted (b) photons, for the $|\eta| < 0.6$ pseudorapidity interval. The Figures have been taken from [149].

5.4 Electron performance

This section will give an overview of the electron performance in ATLAS. The electron reconstruction is very similar to the photon one, as outlined in Section 5.3, therefore, only the main difference will be discussed. The studies presented here are performed with the full 2015 dataset collected by the ATLAS detector at $\sqrt{s} = 13$ TeV, corresponding to $\mathscr{L} = 3.2$ fb^{-1}. More details can be found in [161].

5.4.1 Electron reconstruction

The reconstruction of electrons and photons proceeds with the ATLAS detector in parallel. After the seed-cluster and track reconstruction steps, an electron-specific track fit is performed through a loose matching of track positions extrapolated to the EM calorimeter middle layer and the cluster barycenter using η and ϕ information. The procedure takes into account the energy loss due to bremsstrahlung and the number of precision hits in the silicon detector. Tracks with at least four precision hits and loosely matched to electron cluster serve as input to an optimized GSF fit. The electron reconstruction procedure is completed by the matching of the track candidate to the cluster seed. If more than one track is matched to the same seed, only one is chosen as *primary track*. The choice is based on an algorithm using the cluster-track distance R calculated using different momentum hypotheses, the number of pixel hits and the presence of a hit in the first silicon layer [162]. Electron without associated tracks are considered to be photons. The electron cluster is then reformed using a larger window of 3×7 (5×5) longitudinal towers of cells in the barrel (endcap) of the EM calorimeter and calibrated using multivariate techniques [163] based on MC samples. The four-momentum of the electrons is computed using information from both the final calibrated energy cluster and the best track matched to the original seed cluster. The energy is given by the final calibrated cluster, while the

ϕ and η directions are taken from the corresponding track parameters with respect to the beam-line.

5.4.2 Electron identification

To determine whether the reconstructed electron candidates are signal-like objects or background-like objects such as hadronic jets or converted photons, algorithms for electron identification (ID) are applied. The ID algorithms use quantities related to the electron cluster and track measurements including calorimeter shower shapes and track properties. The full list of those quantities can be found in [161]. The baseline ID algorithm is the lilelihood-based (LH) method. It is a multivariate analysis (MVA) technique that simultaneously evaluates several properties of the electron candidates when making a selection decision. The LH method uses the signal and background probability density functions (PDFs) of the discriminating variables. Based on these PDFs, an overall probability is calculated for the object to be signal or background. Three levels of identification operating points are typically provided for electron ID. These are referred to, in order of increasing background rejection, as *Loose*, *Medium* and *Tight*. Furthermore, their definition are such that the samples selected by them are subsets of one another. Each operating point uses the same variables to define the LH discriminant, but the selection on this discriminant is different for each operating point.

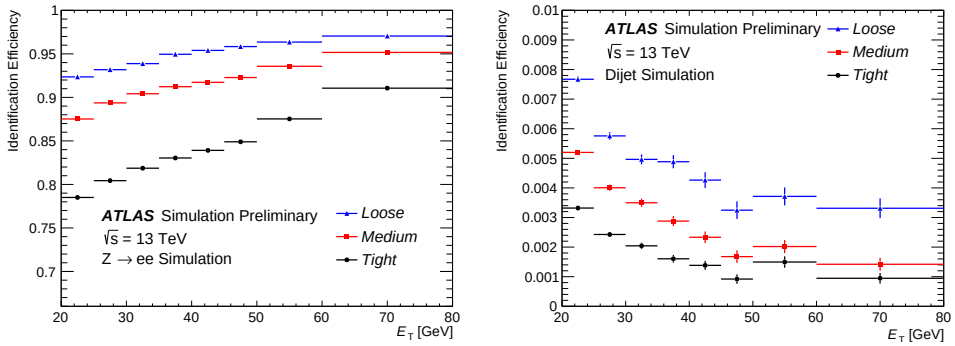

(A) (B)

FIGURE 5.14: The efficiency to identify electrons from $Z \to ee$ decays (a) and the efficiency to identify hadrons as electrons (background rejection) (b) estimated using simulated di-jet samples. The efficiencies are obtained using Monte Carlo simulations, and are measured with respect to reconstructed electrons. The Figures have been taken from [161].

The performance of the LH identification algorithm is illustrated in Figure 5.14. Depending on the operating point, the signal (background) efficiencies for electron candidates with $E_T = 25$ GeV are in the range from 78 to 90% (0.3 to 0.8%) and increase (decrease) with E_T.

5.4.3 Electron isolation

Electron isolation is determined by means of two discriminant criteria:

- **calorimeter isolation discriminator**: it is defined as the sum of the transverse energies of topological clusters, within a cone of $\Delta R = 0.2$ around the cluster of the candidate electron, excluding the energy of the electron itself;
- **tracking based discriminator**: it is defined as the sum of scalar p_T of hard-scatter tracks within a cone of $\Delta R = 0.2$ around the track of the candidate electron, excluding the track associated to the electron itself.

A variety of selection requirements have been defined to select isolated electron candidates. Those are divided in two classes: *efficiency targeted* and *fixed requirement* operating points. The former guarantee the same isolation efficiency as a function of E_T, the latter are constant thresholds on the discriminating variables. The various operating points are defined in [161].

5.4.4 Electron efficiency

The electron efficiency is evaluated using a tag-and-probe method. It employs events containing well-known resonance decays to electrons, namely $Z \to ee$ and $J/\psi \to ee$. A strict selection on one of the electron candidates, *tag*, together with the requirements on the di-electron invariant mass allows for a loose pre-identification of the other electron candidate, *probe*. Each valid combination of electron tag-probe pairs in the event is considered, such that an electron can be the tag in one pair and the probe in another. The probe is used for the measurement of the reconstruction, identification, isolation and trigger efficiencies, after accounting for the residual background contamination, that composes the total efficiency to find and select an electron in the ATLAS detector:

$$\epsilon_{total} = \epsilon_{reconstruction} \times \epsilon_{identification} \times \epsilon_{isolation} \times \epsilon_{trigger}. \tag{5.7}$$

The efficiency are evaluated as a function of η and E_T. MC simulation used in the efficiency calculation need to be corrected to reliably reproduce data efficiencies. Therefore, efficiencies are measured both in data and MC and their ratio is used as a multiplicative correction factor for MC. The scale factors (SFs) are usually close to unity; deviations stem from the mismodelling of tracking properties or shower shapes in the calorimeters. To reduce the impact of different physics processes on the efficiencies, the combination of the different measurements is carried out on the SFs directly.

Figure 5.15 shows the combined electron reconstruction and identification efficiencies in $Z \to ee$ events as a function of η and E_T. The efficiencies are presented for the three different identification point for both data and MC. The SFs, shown in the ratio pads, are in general closer to unity the looser the ID criterion is. Furthermore, they manifest a slo dependence on E_T and η. Their full determination, as well as that of the other ϵ_{total} components is discussed in deep details in [161].

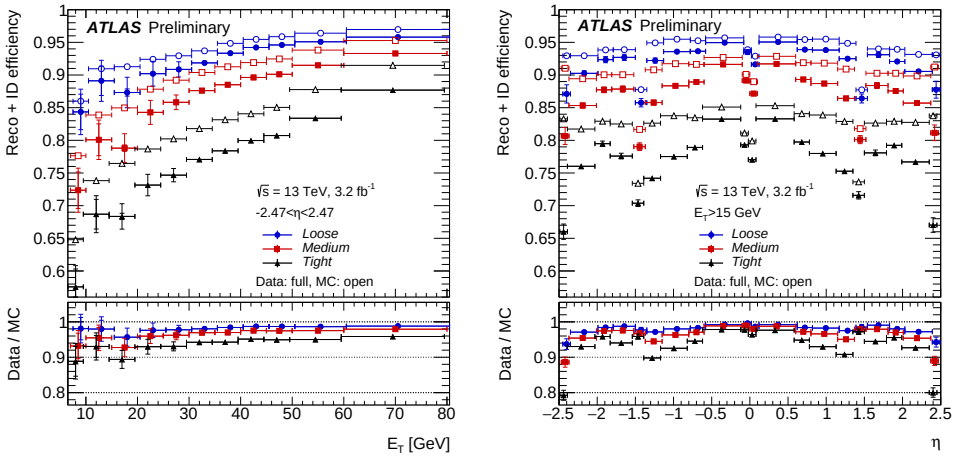

(A) (B)

FIGURE 5.15: Combined electron reconstruction and identification efficiencies in $Z \to ee$ events as a function of E_T, integrated over the full pseudorapidity range (a), and as a function of η, integrated over the full E_T range (b). Two sets of uncertainties are shown: the inner error bars show the statistical uncertainty, the outer error bars show the combined statistical and systematic uncertainty. The Figures have been taken from [161].

5.5 Muon performance

In this Section, an overview of the performance of the muon reconstruction in the 2015 dataset collected at $\sqrt{s} = 13$ TeV, corresponding to an integrated luminosity of 3.2 fb^{-1}, will be given. The results presented here are based on the analysis of a large sample of $J/\psi \to \mu\mu$ and $Z \to \mu\mu$ decays. The complete set of studies can be consulted in [164].

5.5.1 Muon reconstruction

Muon reconstruction is first performed independently in the ID and MS. The information from individual subdetectors is then combined to form the muon tracks that are used in physics analyses. In the ID, muons are reconstructed like any other charged particles as described in Section 5.1. Muon reconstruction in the MS starts with a search for hit patterns inside each muon chamber to form segments. In each MDT chamber and nearby trigger chamber, a Hough transform [165] is used to search for hits aligned on a trajectory in the bending plane of the detector. Segments in the CSC detectors are built using a separate combinatorial search in the η and ϕ directions. Muon track candidates are then built by fitting together hits from segments in different layers using a segment-seeded combinatorial search algorithm. The segments are selected using criteria based on hit multiplicity and fit quality and are matched using their relative positions and angles. At least two matching segments are required to build a track, except in the barrel–endcap transition region where a single high-quality segment can be used to build

a track. The same segment can initially be used to build several track candidates. Later, an overlap removal algorithm selects the best assignment to a single track, or allows for the segment to be shared between two tracks. The hits associated with each track candidate are fitted using a global χ^2 fit. Hits providing large contributions to the χ^2 are removed and the track fit is repeated. The combined muon reconstruction is performed according to various algorithms based on the information provided by the ID, MS, and calorimeters. Four different muon types are defined:

- **combined (CB) muon**: track reconstruction is performed independently in the ID and MS, and a combined track is formed with a global refit that uses the hits from both the ID and MS subdetectors. Most muons are reconstructed following an outside-in pattern recognition, in which the muons are first reconstructed in the MS and then extrapolated inward and matched to an ID track;
- **segment-tagged (ST) muon**: a track in the ID is classified as a muon if, once extrapolated to the MS, it is associated with at least one local track segment in the MDT or CSC chambers. ST muons are used when muons cross only one layer of MS chambers;
- **calorimeter-tagged (CT) muon**: a track in the ID is identified as a muon if it can be matched to an energy deposit in the calorimeter compatible with a minimum-ionizing particle. This type has the lowest purity of all the muon types, so it is used to recover acceptance where the MS is only partially instrumented due to ID and calorimetry cabling and services;
- **extrapolated (ME) muon**: the muon trajectory is reconstructed based only on the MS track and a loose requirement on compatibility with originating from the IP. ME muons are mainly used to extend the acceptance for muon reconstruction into the region $2.5 < |\eta| < 2.7$, which is not covered by the ID.

When two muon types share the same ID track, preference is given to CB muons, then to ST, and finally to CT muons. The overlap with ME muons in the muon system is resolved by analyzing the track hit content and selecting the track with better fit quality and larger number of hits.

5.5.2 Muon identification

Muon identification is performed by applying quality requirements that suppress background, mainly from pion and kaon decays, while selecting prompt muons with high efficiency and guaranteeing a robust momentum measurement. Muon candidates originating from in-flight decays of charged hadrons in the ID are characterized by the presence of a *kink*; therefore, it is expected a poor fit quality of the resulting combined track and that the ID and MS momenta are not compatible. The discriminating variables for CB tracks are:

- q/p significance: defined as the absolute value of the difference between the ratio of the charge and momentum of the muons measured in the ID and MS divided by the sum in quadrature of the corresponding uncertainties;
- ρ': defined as the absolute value of the difference between the transverse momentum measurements in the ID and MS divided by the p_T of the combined track;
- normalized χ^2 of the combined track fit.

Four muon identification selections, *Loose*, *Medium*, *Tight* and *High-p_T*, are provided. *Loose*, *Medium* and *Tight* are inclusive categories. Muons identified with tighter requirements are also included in the looser categories.

- **Medium muons**: this is the ATLAS default identification criteria. Only CB and ME tracks are used. The former are required to have at least three hits in at least two MDT layers, except for tracks in the $|\eta| < 0.1$ region, where tracks with at least one MDT layer but no more than one MDT hole layer are allowed. The latter are required to have at least three MDT/CSC layers, and are employed only in the $2.5 < |\eta| < 2.7$ region to extend the acceptance outside the ID geometrical coverage;
- **Loose muons**: all muon types are used. All CB and ME muons satisfying the *Medium* requirements are included in the *Loose* selection. CT and ST muons are restricted to the $|\eta| < 0.1$ region;
- **Tight muons**: only CB muons with hits in at least two stations of the MS and satisfying the *Medium* selection criteria are considered;
- **high-p_T muons**: the *high-p_T* selection aims to maximise the momentum resolution for tracks with transverse momentum above 100 GeV. CB muons passing the *Medium* selection and having at least three hits in three MS stations are selected.

5.5.3 Muon isolation

Muons originating from the decay of heavy particles are often produced isolated from other particles. Therefore, the measurement of the detector activity around a muon candidate, the *muon isolation*, is a powerful tool for background rejection in many physics analyses. Two variables are defined to assess muon isolation:

- **track-based isolation**: it is defined as the scalar sum of the transverse momenta of the tracks with $p_T > 1$ GeV in a cone of size $\Delta R = \min(10 \text{ GeV}/p_T^{\mu}, 0.3)$ around the muon of transverse momentum p_T^{μ}, excluding the muon track itself;
- **calorimeter-based isolation** it is defined as the sum of the transverse energy of topological clusters in a cone of size $\Delta R = 0.2$ around the muon, after subtracting the contribution from the energy deposit of the muon itself.

5.5.4 Muon efficiency

The muon reconstruction efficiency is determined independently in the ID and MS. Therefore, two different methods are employed. In the $|\eta| < 2.5$ region, a tag-and-probe method is adopted, while a different technique is employed in the $2.5 < |\eta| < 2.7$ region, where muons are reconstructed using only the MS detector.

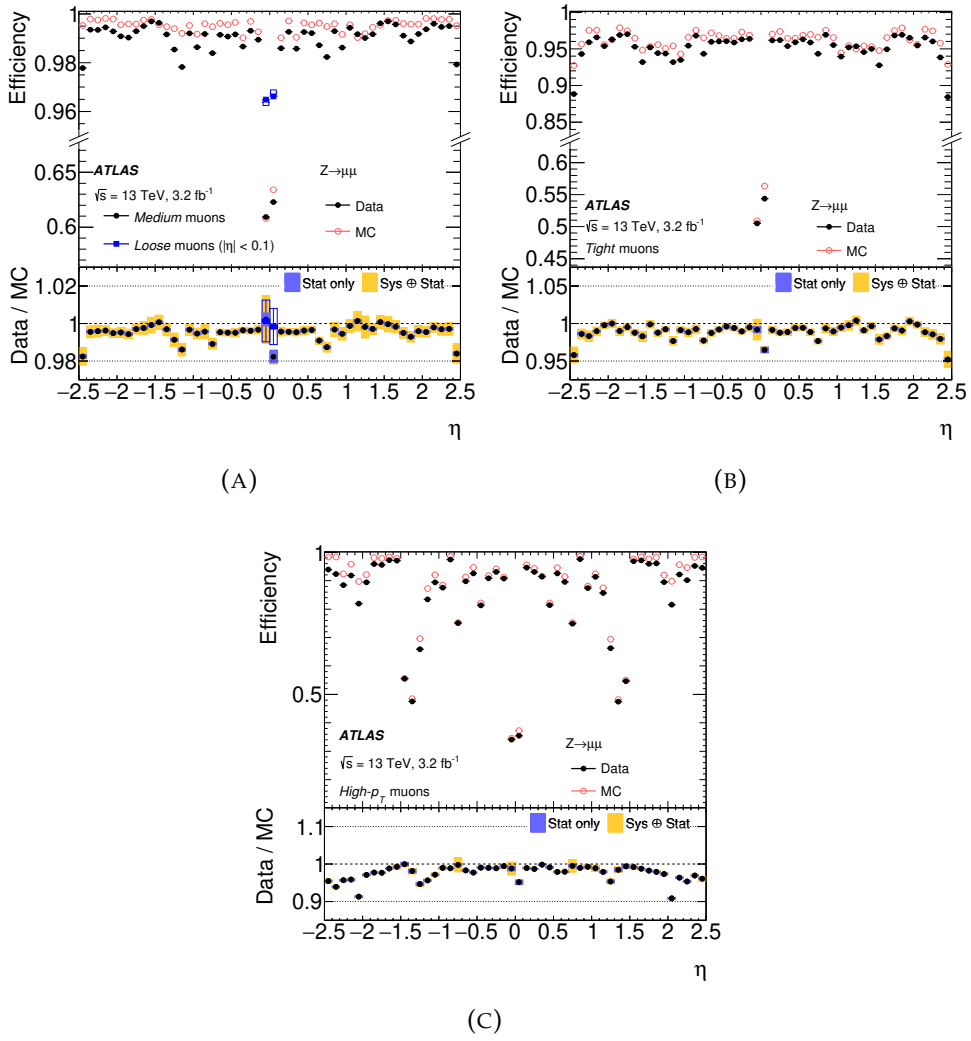

FIGURE 5.16: Muon reconstruction efficiency as a function of η measured in $Z \to \mu\mu$ events for muons with $p_T > 10$ GeV shown for the *Medium* muon selection for the *Loose* selection (squares) in the region $|\eta| < 0.1$, where the *Loose* and *Medium* selections differ significantly (a), for the *Tight* muon selection (b) and for the *High-*p_T uon selection (c). The error bars on the efficiencies indicate the statistical uncertainty. Panels at the bottom show the ratio of the measured to predicted efficiencies, with statistical and systematic uncertainties. The Figures have been taken from [164].

The muon reconstruction efficiency within the ID acceptance for the four different identification selections are shown in Figure 5.16. The efficiencies of the *Loose* and *Medium* selections are very similar throughout the detector with the exception of the region $|\eta| < 0.1$, where the *Loose* selection fills the

MS acceptance gap using the ST and CT muons contributions. The efficiency of these selections is observed to be in excess of 98%, and between 90% and 98% for the *Tight* selection, with all efficiencies in very good agreement with those predicted by the simulation. The efficiency of the *High-p_T* selection is significantly lower, as a consequence of the strict requirements on momentum resolution. On the other hand, for $2.5 < |\eta| < 2.7$, the efficiency is recovered by using the ME muons included in the *Loose* and *Medium* muon selections. The method to evaluate the efficiencies for the muon reconstruction in this very high-η region is described in [166]. The values of the SFs measured using the 2015 dataset are close to 0.9 and are determined with a 3–5% uncertainty.

5.6 Tau performance

In this Section, the performance of tau identification with the ATLAS detector will be presented. The studies presented here only consider hadronic tau lepton decays. The hadronic decay products can contain one or three pions (1- and 3-prong decay mode). The neutral and charged hadrons stemming from the tau lepton decay make up the visible part of the tau lepton, $\tau_{had-vis}$.

The data used in this Section were recorded by the ATLAS experiment during the 2015 LHC run with proton-proton collisions at a center of mass energy of $\sqrt{s} = 13$ TeV, corresponding to an integrated luminosity of 3.2 fb^{-1}. Further details can be found in [167].

5.6.1 Tau reconstruction

Tau candidates are seeded by jets formed with the *anti-k_t* algorithm [168] with a distance parameter of $\Delta R = 0.4$. Three- dimensional clusters of calorimeter cells called TopoClusters [169], calibrated using a local hadronic calibration (LC) [170], serve as inputs to the jet algorithm. Jets seeding are required to be within $|\eta| < 2.5$ and have $p_T > 10$ GeV. Tau candidates in the transition region between the barrel and forward calorimeters, $1.37 < |\eta| < 1.52$, are vetoed. A tau vertex is chosen as the candidate track vertex with the largest fraction of momentum from tracks associated ($\Delta R < 0.2$) with the jet. The tracks must pass requirements on the number of hits in the tracker and have $p_T > 1$ GeV. Additional requirements are placed on the shortest distance from the track to the tau vertex in the transverse plane: $|d_0| < 1$ mm, and the shortest distance in the longitudinal plane, $|\Delta z_0 \sin(\theta)| < 1.5$ mm. Tracks passing those requirements are then associated to core ($0 < \Delta R < 0.2$) and isolation ($0.2 < \Delta R < 0.4$) regions around the tau candidate. The direction of the tau candidate is calculated using the vectorial sum of the TopoClusters within $\Delta R < 0.2$ of the seed jet barycenter, using the tau vertex as the origin. The mass of the tau candidate is set to zero and its energy obtained through dedicated calibration schemes, the baseline calibration and the Boosted Regression Tree (BRT) based calibration, described in detail in [167].

5.6.2 Tau identification

The tau identification algorithm is designed to reject backgrounds from quark- and gluon-initiated jets. The identification uses Boosted Decision Tree (BDT) based methods [171, 172]. The BDT for tau candidates associated with one and three tracks are trained separately with simulated $Z/\gamma^* \rightarrow \tau\tau$ for signal and di-jet events for background. Three working points: *loose*, *medium* and *tight*, are provided, corresponding to different tau identification efficiency values, independent of p_T. The target efficiencies are 0.6, 0.55 and 0.45 for the generated 1-track three working points, and 0.5, 0.4 and 0.3 for the corresponding generated 3-track target efficiencies. The input variables to the BDT are corrected such that the mean of their distribution for signal samples is constant as a function of pile up. This ensures that the efficiency does not depend strongly on the pile up conditions. The complete list of variables used to train the BDT is in [167].

5.6.3 Tau identification efficiency

The performance of tau identification is measured using a tag-and-probe method applied to events enriched in the $Z \rightarrow \tau\tau$ process, with one tau lepton decaying to muon and neutrinos, τ_μ (tag), and the other decaying to hadrons and neutrino, τ_{had} (probe). $Z \rightarrow \tau_\mu\tau_{had}$ events are selected requiring a single-muon trigger with $p_T > 20$ GeV threshold, while the offline reconstructed muon must have $p_T > 22$ GeV. Events are required not to have any other reconstructed electron or muon and to have at least one $\tau_{had-vis}$ candidate with 1- or 3-prongs passing a very loose requirement on the tau identification BDT. The muon and the tau are required to have opposite-sign electric charges. Furthermore, events presenting b-tagged jets are vetoed. Additional cuts are applied to suppress W+jets events:

- $m_T = \sqrt{2p_T^\mu \cdot E_T^{miss}(1 - \cos(\Delta\phi(\mu, E_T^{miss})))} < 50$ GeV;
- $\Sigma \cos\Delta\phi = \cos(\Delta\phi(\mu, E_T^{miss}) + \cos(\Delta\phi(\tau_{had-vis}, E_T^{miss}) > -0.1$;
- 45 GeV$< m_{vis}(\mu, \tau_{had-vis}) < 80$ GeV.

Here p_T^μ is the transverse momentum of the muon, $\Delta\phi(\mu, E_T^{miss})$ is the $\Delta\phi$ separation between the muon and the E_T^{miss} and $m_{vis}(\mu, \tau_{had-vis})$ is the invariant mass of the system made by the muon and the tau candidate. After the selection, the contamination from jet backgrounds before the application of the tau identification poses the greatest challenge. To estimate the background contamination in data, a template fit is performed using a variable with high separation between signal and background, to estimate the normalisation factors for both signal and background. The signal contribution to data before the application of the tau identification requirement is estimated directly from the fit, whilst the signal contribution to data after the application of the various tau identification working points is extracted by subtracting the estimated backgrounds from the data, after applying the same background normalisation factors as those before the identification is applied. The variable used is the track multiplicity, defined as the sum of

the number of core and outer tracks associated to the $\tau_{had-vis}$ candidate. A detailed description of the method can be found in [173].

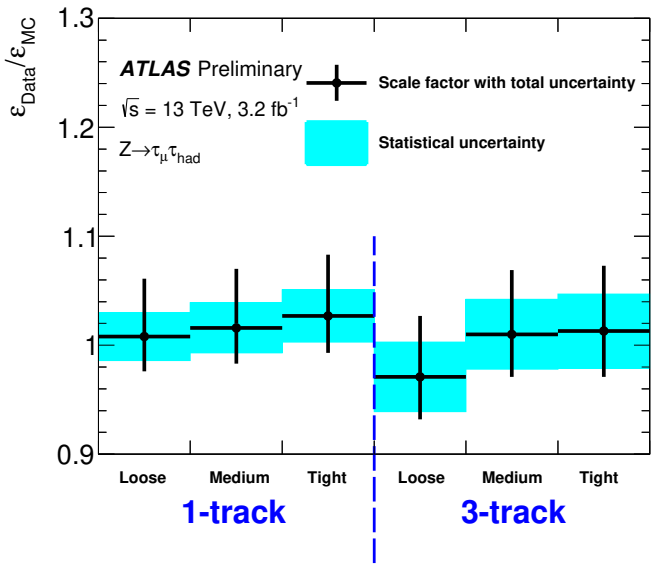

FIGURE 5.17: Tau identification efficiency scale factors for one track and three track τ had-vis candidates with $p_T > 20$ GeV. The combined systematic and statistical uncertainties are shown. Figure taken from [167].

Figure 5.17 shows the SFs derived to take into account the small differences between data and simulation for $\tau_{had-vis}$ signal to pass a certain level of identification. The results are compatible, within uncertainties, with unity.

5.7 Jet performance

Jets are a prevalent feature of the final state for the measurement presented in this thesis. Indeed, as will be shown in Chapter 6, the signature of the $t\bar{t}$ decay in the fully hadronic channel is characterized by six jets, two of which being b-tagged. Jets are reconstructed using a clustering algorithm run on a set of input four-vectors, typically obtained from topologically associated energy deposits, charged-particle tracks, or simulated particles. This Section details the methods used to calibrate the four-momenta of jets in MC simulation and in data collected by the ATLAS detector at $\sqrt{s} = 13$ TeV during the 2015 data-taking period, corresponding to an integrated luminosity of 3.2 fb^{-1}. The jet energy scale (JES) calibration consists of several consecutive stages derived from a combination of MC-based methods and in situ techniques. MC-based calibrations correct the reconstructed jet four-momentum to that found from the simulated stable particles within the jet. The calibrations account for features of the detector, the jet reconstruction algorithm, jet fragmentation and the busy data-taking environment resulting from multiple pp interactions. In situ techniques are used to measure the difference in jet response between data and MC simulation, with residual corrections applied to jets in data only. More details on the studies presented here can be found in [174].

5.7.1 Jet reconstruction

The calorimeter jets are reconstructed at the electromagnetic energy scale (EM scale) with the anti-k_t algorithm [168] and radius parameter $R = 0.4$ using the FastJet package [91]. A collection of three-dimensional, massless, positive-energy TopoClusters [169, 175] made of calorimeter cell energies are used as input to the anti-k_t algorithm. TopoClusters are built from neighboring calorimeter cells containing a significant energy above a noise threshold that is estimated from measurements of calorimeter electronic noise and simulated pile-up noise. The calorimeter cell energies are measured at the EM scale, corresponding to the energy deposited by electromagnetically interacting particles. Jets are reconstructed with the anti-k_t algorithm if they pass a p_T threshold of 7 GeV. Jets referred to as truth jets are reconstructed using the anti-k_t algorithm with $R = 0.4$ using stable, final-state particles from MC generators as input. Candidate particles are required to have a lifetime of $c\tau > 10$ mm and muons, neutrinos, and particles from pile-up activity are excluded. Truth jets are therefore defined as being measured at the particle-level energy scale. Truth jets with $p_T > 7$ GeV and $|\eta| < 4.5$ are used in studies of jet calibration using MC simulation. Reconstructed calorimeter jets are geometrically matched to truth jets using the distance measurement ΔR. Tracks from charged particles used in the jet calibration are reconstructed within the full acceptance of the ID and are required to have a $p_T > 500$ MeV and to be associated with the hard-scatter vertex. Tracks must satisfy quality criteria based on the number of hits in the ID subdetectors outlined in Section 5.2. Tracks are assigned to jets using ghost association [159]. Muon track segments are used in the jet calibration as a proxy for the uncaptured jet energy carried by energetic particles passing through the calorimeters without being fully absorbed. The segments are partial tracks constructed from hits in the MS which serve as inputs to fully reconstructed tracks. Segments are individually assigned to jets using the method of ghost association.

5.7.2 Jet energy scale calibration

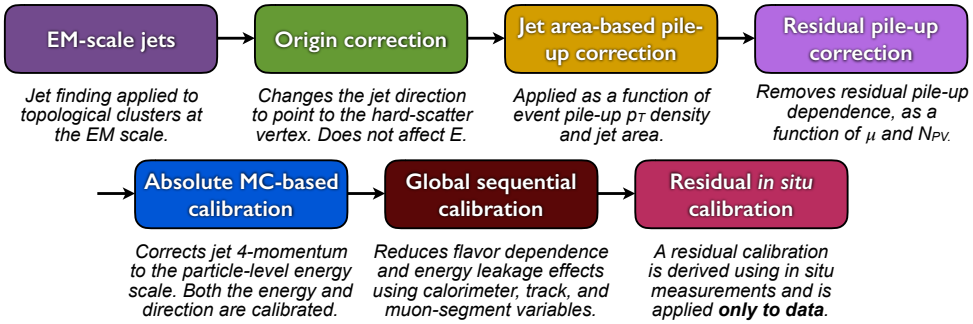

FIGURE 5.18: Calibration stages for EM-scale jets. Other than the origin correction, each stage of the calibration is applied to the four-momentum of the jet. Figure taken from [174].

The calibration scheme for EM-scale calorimeter jets is presented in Figure 5.18. This calibration restores the jet energy scale to that of truth jets reconstructed at the particle-level energy scale. Each stage of the calibration corrects the full four-momentum unless otherwise stated, scaling the jet p_T, energy, and mass. The calibration starts with the origin correction. It recalculates the four-momentum of jets to point to the hard-scatter primary vertex rather than the center of the detector, while keeping the jet energy constant. This correction significantly improves the η resolution of jets. Next, the pile-up correction removes the excess energy due to in-time and out-of-time pile-up. It consists of two components; an area-based p_T density subtraction [159], applied event-by-event, and a residual correction derived from the MC simulation. The absolute JES calibration corrects the jet four-momentum to the particle-level energy scale, as derived using truth jets in di-jet MC events. Further improvements to the reconstructed energy are achieved through the use of calorimeter, MS, and track-based variables in the global sequential calibration. Finally, a residual in situ calibration is applied to correct jets in data using well-measured reference objects, including photons, Z bosons, and calibrated jets. The next Subsections will treat the different calibration steps in more detail.

5.7.3 Pile up corrections

This Subsection will provide an overview of the pile up corrections applied to EM-scale jets. The complete description of the following techniques can be found in [89]. First, an area-based method subtracts the per-event pile up contribution to the p_T of each jet according to its area. The pile up contribution is calculated from the median p_T density ρ of jets in the $\eta - \phi$ plane. The calculation of ρ uses only positive-energy topo-clusters with $|\eta| < 2$ that are clustered using the k_t algorithm [176] with radius parameter $R = 0.4$. The k_t algorithm is chosen for its sensitivity to soft radiation, and is only used in the area-based method. The p_T density of each jet is taken to be p_T/A, where the area A of a jet is calculated using ghost association. In this procedure, simulated ghost particles of infinitesimal momentum are added uniformly in solid angle to the event before jet reconstruction. The area of a jet is then measured from the relative number of ghost particles associated with a jet after clustering. The ρ calculation is derived from the central, lower-occupancy regions of the calorimeter, and does not fully describe the pile up sensitivity in the forward calorimeter region or in the higher-occupancy core of high-p_T jets. Some residual dependence of the anti-k_t jet p_T on the amount of pile up is observed on N_{PV}, sensitive to in-time pile up, and μ, sensitive to out-of-time pile up. The pile-up-corrected p_T , after the area-based and residual corrections, is given by

$$p_T^{corr} = p_T^{reco} - \rho \times A - \alpha \times (N_{PV} - 1) - \beta \times \mu, \tag{5.8}$$

where p_T^{reco} is the EM-scale p_T of the jet before any pile up correction is applied and the coefficients α and β are extracted from fitted distributions of

N_{PV} and μ, respectively, in bins of η for fixed $p_T^{truth} = 25$ GeV, the region where the pile up contributions are most relevant.

5.7.4 Jet energy scale and η calibration

The absolute jet energy scale and η calibration corrects the reconstructed jet four-momentum to the particle-level energy scale and accounts for biases in the jet η reconstruction. Such biases are primarily caused by the transition between different calorimeter technologies and sudden changes in calorimeter granularity. The JES calibration is derived first as a correction of the reconstructed jet energy to the truth jet energy. Isolated reconstructed jets are geometrically matched to truth jets within $\Delta R = 0.3$. An isolated calorimeter jet is required to have no other calorimeter jet of $p_T > 7$ GeV within $\Delta R = 0.6$, and only one truth jet of $p_T^{truth} > 7$ GeV within $\Delta R = 1.0$. The average energy response is defined as the mean of a Gaussian fit to the core of the E^{reco}/E^{truth} distribution for jets, binned in E^{truth} and η_{det}, the jet η pointing to the center of the detector. A numerical inversion procedure [175] is used to derive corrections in E^{reco} from E^{truth}. The average response is parameterized as a function of E^{reco} and the jet calibration factor is taken as the inverse of the average energy response. A second correction to account for a residual η bias, mostly due to jet trepassing calorimeter regions of different geometry or technology, is derived as the difference between the reconstructed η^{reco} and truth η^{truth}, parameterized as a function of E^{truth} and η_{det}. A numerical inversion procedure is again used to derive corrections in E^{reco} from E^{truth}. The η calibration alters only the jet p_T and η.

5.7.5 Global sequential calibration

Residual dependencies of the JES on longitudinal and transverse features of the jet are observed after the previous calibration steps. Five observables [175] are identified that improve the resolution of the JES through the global sequential calibration (GSC). For each observable, an independent jet four-momentum correction is derived as a function of p_T^{truth} and $|\eta_{det}|$ by inverting the reconstructed jet response in MC events. Each stage conserve the average energy at the EM+JES scale by applying an overall constant factor. The five stages are, in order:

- f_{Tile0}: the fraction of jet energy measured in the first layer of the hadronic Tile calorimeter;
- f_{LAr3}: the fraction of jet energy measured in the third layer of the electromagnetic LAr calorimeter;
- n_{trk}: the number of tracks with $p_T > 1$ GeV ghost-associated to the jet;
- $\mathscr{W}_{trk}$: the average p_T-weighted transverse distance in the $\eta - \phi$ plane between the jet axis and all tracks of $p_T > 1$ GeV ghost-associated to the jet;

- $n_{segments}$: the number of muon track segments ghost-associated to the jet.

5.7.6 In situ calibration

The last stages of the jet calibration account for differences in the jet response between data and MC simulation. Those differences are quantified by balancing the p_T of a jet against other well-measured reference objects. The first step is the η-intercalibration. It corrects the average response of forward jets to that of well-measured central jets using di-jet events. Three other in situ calibrations correct for differences in the average response of central jets with respect to those of well-measured reference objects, each focusing on a different p_T region using Z boson, photon, and multijet systems. For each in situ calibration the response $\mathscr{R}_{in\,situ}$ is defined in data and MC simulation as the average ratio of jet p_T to reference object p_T, binned in regions of the reference object p_T. It is proportional to the response of the calorimeter to jets at the EM+JES, but is also sensitive to secondary effects such as gluon radiation and the loss of energy outside of the jet cone.

The ratio

$$c = \frac{\mathscr{R}^{data}_{in\,situ}}{\mathscr{R}^{MC}_{in\,situ}} \tag{5.9}$$

is a useful estimate of the ratio of the JES in data and MC simulation. Through numerical inversion a correction is derived to the jet four-momentum. It is derived as a function of jet p_T and η in the η-intercalibration. The η-intercalibration corrects the jet energy scale of forward jets ($0.8 < |\eta_{det}| < 4.5$) to that of central jets ($|\eta_{det}| < 0.8$) in a di-jet system. The Z/γ+jet balance analyses use a well-calibrated photon or Z boson, the latter decaying into an electron or muon pair, to measure the p_T response of the recoiling jet in the central region up to a p_T of about 950 GeV. Finally, the multijet balance (MJB) analysis calibrates central ($|\eta| < 1.2$), high-p_T jets ($300 < p_T < 2000$ GeV) recoiling against a collection of well-calibrated, lower-p_T jets. Although derived from central jets, the corrections are applicable to forward jets whose energy scales have been equalized by the η-intercalibration procedure. The calibration constants derived in each of these analyses following Equation 5.9 are statistically combined into a final in situ calibration covering the full kinematic region. More details on the individual steps can be found in [174].

5.7.7 Systematic uncertainties

The final calibration includes a set of 80 JES systematic uncertainty terms propagated from the individual calibrations and studies, listed in [174]. The majority (67) of uncertainties comes from $Z \rightarrow \gamma$+jets and MJB in situ calibrations and account for assumptions made in the event topology, MC simulation, sample statistics, and propagated uncertainties of the electron, muon, and photon energy scales. The remaining 13 uncertainties are derived from

other sources. Four pile-up uncertainties are included to account for potential MC mismodeling of N_{PV}, μ, ρ and the residual p_T dependence. Three η-intercalibration uncertainties account for potential physics mismodeling, statistical uncertainties, and the method non-closure in the $2.0 < |\eta_{det}| < 2.6$ region. Three additional flavour response uncertainties account for differences in the jet response and simulated jet composition of light-quark, b-quark, and gluon-initiated jets. An uncertainty in the GSC punch-through correction is also considered, derived as the maximum difference between the jet responses in data and MC simulation as a function of the number of muon segments. One AFII modeling uncertainty accounts for non-closure in the absolute JES calibration of fast-simulation jets. A high-p_T jet uncertainty is derived from single-particle response studies [177] and is applied to jets with $p_T > 2$ TeV, beyond the reach of the in situ methods.

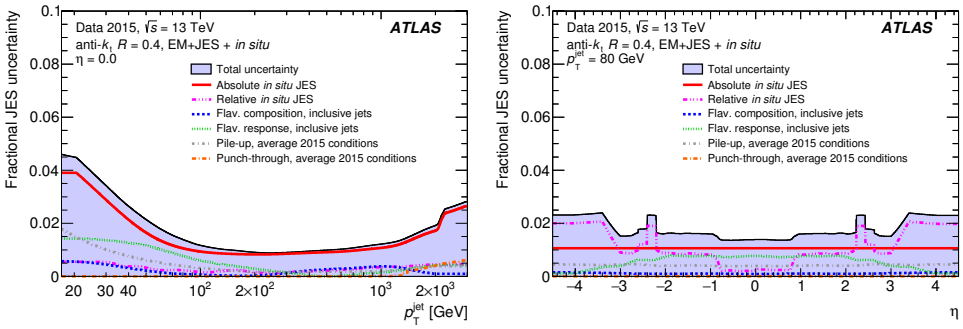

(A) (B)

FIGURE 5.19: Combined uncertainty in the JES of fully calibrated jets as a function of jet p_T at $\eta = 0$ (a) and η at $p_T = 80$ GeV (b). The Figures have been taken from [177].

The full combination of all uncertainties is shown in Figure 5.19 as a function of p_T at $\eta = 0$ and as a function of η at $p_T = 80$ GeV. Each uncertainty is generally treated independently of the others but fully correlated across p_T and η. Exceptions are the electron and photon energy scale measurements, which are treated as fully correlated. The uncertainty is largest at low p_T, starting at 4.5% and decreasing to 1% at 200 GeV. It rises after 200 GeV due to the statistical uncertainties related to the in situ calibrations, and increases sharply after 2 TeV where MJB measurements end and larger uncertainties are taken from the single-particle response. The uncertainty is fairly constant as a function of η and reaches a maximum of 2.5% for the most forward jets. A sharp feature can be seen in the region $2.0 < |\eta| < 2.6$ due to the non-closure uncertainty of the η-intercalibration.

While the 80 uncertainties provide the most accurate understanding of the JES uncertainty, several physics analyses would receive no strong benefit from the rigorous conservation of all correlations. For these cases a reduced set of nuisance parameters (NPs) is made available that seeks to preserve as precisely as possible the correlations across jet p_T and η. As a first step, the global reduction [90] is performed through an eigen-decomposition of the 67

p_T-dependent in situ uncertainties. The five principal components of greatest magnitude are kept separate and the remaining components are quadratically combined into a single NP. This number of independent in situ uncertainty sources is reduced from 67 to 6 NPs, with only percent-level losses to the correlations between jets.

In addition, a strong reduction procedure is able to further reduce the remaining 19 NPs. The combination groups NPs into p_T and η regions where they are most relevant. The η-intercalibration non-closure and the AFII uncertainties are not included in this procedure; the remaining 17 NPs are grouped in 3 NPs, for a total of 5 NPs for the strongly reduced representation. The mean loss on correlation with this procedure is at 13% level, with a maximum of 39%.

5.8 B-tagged jet performance

A precise and efficient identification of jets containing b-hadrons, or *b-jets*, is essential, among others, for precise measurements of SM processes presenting b-jets in the final state. In particular, the measurement which will be presented in Chapter 6 is characterized by the presence of two b-jets coming from the top-antitop quark pair. The studies presented here are performed using data collected by the ATLAS detector during the full 2015 and 2016 data-taking periods, corresponding to $\mathscr{L} = 36.1$ fb^{-1}, using dileptonically decaying selected $t\bar{t}$ events. Among the several algorithm to measure the b-jet tagging efficiency that have been developed during Run 1 [178], a combinatorial likelihood approach, the *Likelihood method* (LH), specifically refined for Run 2, has been used in the measurement which will be presented in Chapter 6. Furthermore, this Section will present, as a cross-check, results from a *Tag-and-Probe* method (T&P) developed during Run 2 [179].

The b-jet tagging efficiency, ϵ_b, is measured for jets in the pseudorapidity range $|\eta| < 2.5$ and with $p_T > 20$ GeV for several operating points (OP), designed to provide a certain b-jet tagging efficiency. Four operating points are defined, corresponding to 60%, 70%, 77% and 85% b-jet tagging efficiencies in simulated $t\bar{t}$ events. Two sets of four operating points are implemented to provide a *single-cut* or a *flat-efficiency* operating point. The former is a fix cut providing the required b-jet tagging efficiency when averaged over the b-jets p_T distribution, the latter has a p_T-varying cut value, ensuring a constant b-jet tagging efficiency in the whole jet p_T spectrum. In physics measurements, data-to-simulation efficiency scale factors can be applied on a jet-by-jet basis to correct the rate of events after applying a b-tagging requirement in MC samples.

5.8.1 MV2c10 b-tagging algorithm

The MV2c10 b-tagging multivariate algorithm, developed for Run 2, utilizes a Boosted Decision Tree (BDT) which uses several input variables exploiting

the long b-hadron lifetime as input, listed in [179]. The BDT was trained on a subset of simulated $t\bar{t}$ events: b-jet are assigned as signal, while c-jets and light-flavoured jets as background. In order to enhance the c-jet rejection, the c-jet fraction in the training is set to 7%, and the light-flavour jet background is set to 93%, as described in [180].

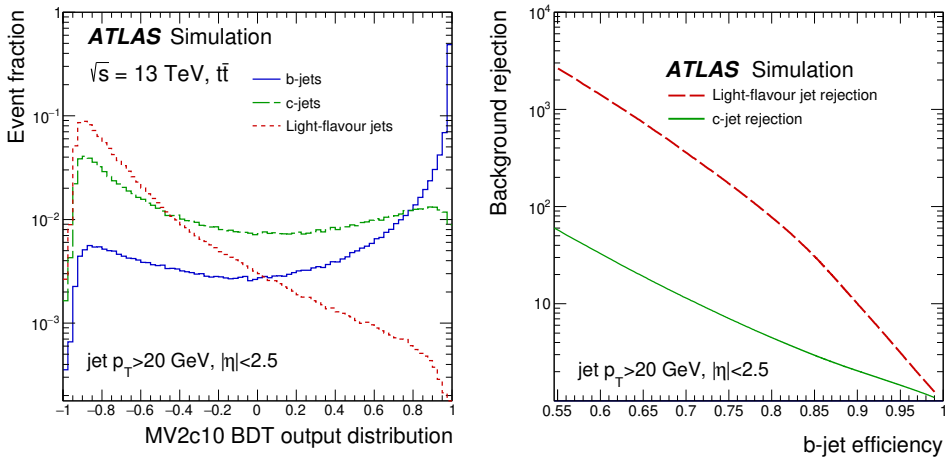

(A) (B)

FIGURE 5.20: (a): The MV2c10 output for b-jets (solid line), c-jets (dashed line) and light-flavour jets (dotted line) in simulated $t\bar{t}$ events. (b): The light-flavour jet (dashed line) and c-jet rejection factors (solid line) as a function of the b-jet tagging efficiency of the MV2c10 b-tagging algorithm. The Figures have been taken from [179].

The MV2c10 output for b-jets, c-jets and light-flavour jets in a statistically independent $t\bar{t}$ sample and the corresponding rejection rates are presented in Figure 5.20. The rejection rates as a function of jet p_T are given in Figure 5.21 for the single-cut OP and the flat-efficiency OP, both for the 70% OP.

5.8.2 Calibration methods

Events are selected by requiring two oppositely charged leptons (ee, $e\mu$ or $\mu\mu$). At least one lepton must be trigger matched. Furthermore, events are vetoed if additional *loose* leptons are present. The T&P method uses only the $t\bar{t} \to e\nu\mu\nu$+ 2-jet category, requiring at least one jet to be tagged by the MV2c10 algorithm at the 85% single-cut efficiency OP. The LH method also exploits events with exactly three jets, as well as events with same-flavour leptons in the final state. For events with same-flavour leptons in the final state, additional requirements of $E_T^{miss} > 60$ GeV and dilepton invariant mass $50 < m_{ll} < 80$ GeV or $m_{ll} > 100$ GeV are applied to suppress the contamination from on-shell Z boson decays, multijet production and decays of γ^*, Υ and J/Ψ particles. To further enhance the b-jet purity of the selected samples in both methods, BDTs were trained using simulated events to separate final states with at least two b-jets (signal) from all other events (background). Each of the input variables is designed to select events with at least two b-jets

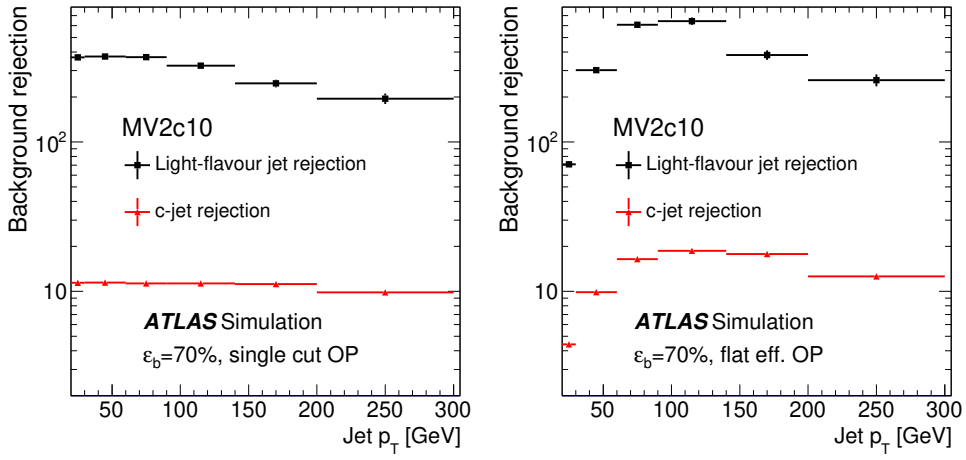

(A) (B)

FIGURE 5.21: The light-flavour jet (squares) and c-jet rejection factors (triangles) at a b-tagging efficiency of 70% single-cut OP (a) and flat-efficiency OP (b) as a function of the jet p_T for the MV2c10 b-tagging algorithms in $t\bar{t}$ events. The Figures have been taken from [179].

based upon the topology and kinematics of the event, rather than exploiting any flavour-tagging-related properties of the jets, to ensure minimal bias in the MV2c10 discriminant. The choice for input variables in the two calibration methods is listed in [179].

T&P method

The b-jet efficiency measurement is performed on a set of *probe* jets. A jet is considered *probe* if the other (*tag*) jet is b-tagged at the 85% fixed cut OP. The efficiency, ϵ_b is measured as

$$\epsilon_b = \frac{f_{tagged} - (1 - f_b)\epsilon_j}{f_b}, \tag{5.10}$$

where

$$f_{tagged} = \frac{N^{pass}_{data} - N^{pass}_{non\,t\bar{s},\,MC}}{N^{pass}_{data} - N^{pass}_{non\,t\bar{s},\,MC}} \tag{5.11}$$

is measured from data. N is the number of probe jets, while N^{pass} refers to the number of probe jets passing a certain b-tagging criterion. The subscripts $data$ and $non\,t\bar{s},\ MC$ indicates the quantity being evaluated from data or MC simulation of background processes. f_b is the fraction of b-jets in simulated $t\bar{t}$ events and ϵ_j is the non-b-jet tagging efficiencies, measured from MC simulations.

LH method

The LH method is performed independently in the $e\mu$ and combined $ee/\mu\mu$ channels in the two and three jets topologies. The b-jet tagging efficiency determination in each of the resulting four channels uses an unbinned maximum likelihood fit. In the two-jet case the following per-event likelihood function is adopted:

$$\begin{aligned}\mathcal{L}(p_{T,1}, p_{T,2}, w_1, w_2) = \frac{1}{2}\sum_{i,\,k} [&f_{bb}\mathscr{P}_{bb}(p_{T,i}, p_{T_k})\mathscr{P}_b(w_i|p_{T,i})\mathscr{P}_b(w_i|p_{T,k}) \\ &+ f_{bj}\mathscr{P}_{bj}(p_{T,i}, p_{T_k})\mathscr{P}_b(w_i|p_{T,i})\mathscr{P}_b(w_i|p_{T,k}) \\ &+ f_{jj}\mathscr{P}_{jj}(p_{T,i}, p_{T_k})\mathscr{P}_b(w_i|p_{T,i})\mathscr{P}_b(w_i|p_{T,k})] \,,\end{aligned} \tag{5.12}$$

where:

- the indices (i, k) run over $(1, 2)$ and $(2, 1)$;
- f_{bb}, f_{bj} are the two independent jet flavour fractions, and $f_{jj} = 1 - f_{bb} - f_{bj}$;
- $\mathscr{P}_f(w|p_T)$ is the PDF for the b-tagging discriminant or weight for a jet of flavour f, for a given transverse momentum;
- $\mathscr{P}_{f_1 f_2}(p_{T,1}, p_{T,2})$ is the two-dimensional PDF for $[p_{T,1}, p_{T,2}]$ for the flavour combination $[f_1, f_2]$.

A histogram with only two bins is used to describe the b-weight PDF for each p_T bin, with the bin above the cut value corresponding to ϵ_b, then corresponding to

$$\epsilon_b = \int_{w_{cut}}^{\infty} dw' \mathscr{P}_b(w', p_T). \tag{5.13}$$

The likelihood function distinguishes between the different flavour fractions, but not between signal and background processes. To extract $\mathscr{P}_b(w|p_T)$ in bins of p_T, the flavour fractions f_{f_1}, f_{f_2} and the other PDFs are are determined from simulation. A slightly more complex likelihood function is defined for the three-jet case, which is conceptually analogous but needs to consider that the jet flavour combinations are increased to four.

5.8.3 b-jet tagging efficiencies

Figure 5.22 shows the measured efficiency in data and simulation as a function of the jet p_T for both the T&P and LH methods, corresponding to the 70% b-jet tagging efficiency single-cut OP. The efficiencies determined in simulation and data agree within their uncertainties, resulting in scale factors close to unity. Figure 5.23 shows the SFs as a function of the jet η, for selected jet p_T bins for both the T&P and LH methods. The data-to-simulation SFs do

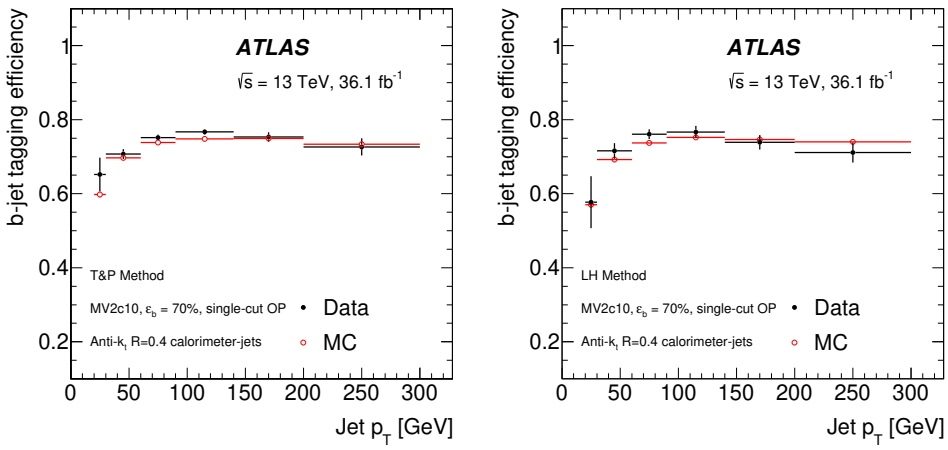

(A) (B)

FIGURE 5.22: The b-jet tagging efficiency measured in data (full circles) and simulation (open circles), corresponding to the 70% b-jet tagging efficiency single-cut OP, as a function of the jet p_T using the T&P (a) and the LH method (b), for R=0.4 calorimeter-jets. The error bars correspond to the total statistical and systematic uncertainties. The Figures have been taken from [179].

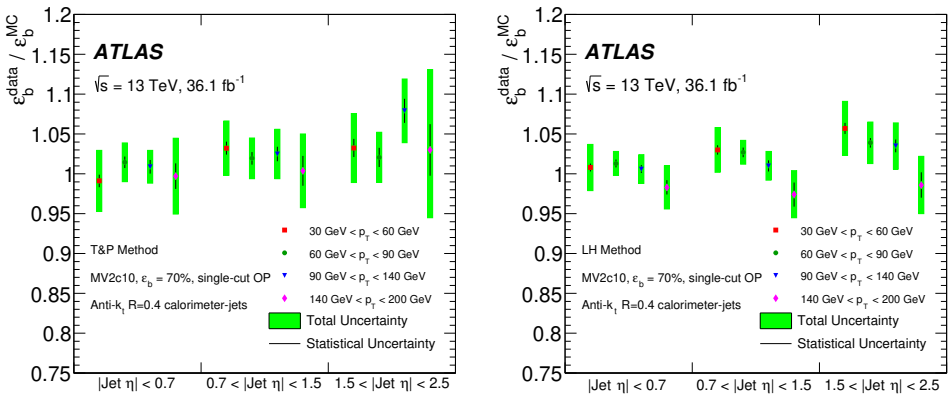

(A) (B)

FIGURE 5.23: Data-to-simulation scale factors, corresponding to the 70% b-jet tagging efficiency single-cut OP, as a function of the jet $|\eta|$ using the T&P (a) and the LH method (b) for R=0.4 calorimeter-jets. Both the statistical uncertainties (error bars) and total uncertainties (shaded region) are shown. The Figures have been taken from [179].

not show a strong dependency on the variables, being the variation at the 5% level. The associated systematic uncertainties can be separated into three categories. These are the efficiency of the tagging algorithm (b-quark tagging efficiency), the efficiency with which jets originating from c-quarks pass the b-tag requirement (c-quark tagging efficiency) and the rate at which light-flavour jets are tagged (misidentified tagging efficiency). The large number of individual uncertainties can be reduced while preserving the bin-to-bin correlations using a method based on an eigenvalue decomposition of the covariance matrix of systematic and statistical variations. It starts from the construction of the covariance matrix corresponding to each source of uncertainty in the six bins of jet p_T used for the calibration. The total covariance matrix is constructed by summing these covariance matrices corresponding to different sources of uncertainty. As the total covariance matrix is a symmetric, positive-definite matrix, an eigenvector decomposition can be performed. The square root of the corresponding eigenvalues gives the six orthogonal variations. Most of the eigenvalue variations are very small and can be neglected without impacting the correlations or total uncertainty. The remaining eigenvalue variations can be further reduced by removing eigenvalue variations below a chosen threshold. Three different schemes of eigenvariation reduction are implemented:

- **loose**: it provides a complete description of the total uncertainty and correlations;
- **medium**: it has a 3% level amount of loss in the total uncertainty and the correlation;
- **tight**: it provides a more aggressive reduction, corresponding to a loss in the total uncertainty and correlation between 10% and 50%.

5.9 E_T^{miss} performance

Although no genuine E_T^{miss} is expected in the final state of the $t\bar{t}$ fully hadronic channel, this Section will present a complete overview of the E_T^{miss} performance at the ATLAS detector, since I was directly involved in those performance studies during my QT. The E_T^{miss} is reconstructed from the signals of all detected particles in the final state, and as such strongly depends on the energy scale and resolution of the reconstructed and calibrated *hard objects* (leptons and jets). Reconstructed momentum flow not attributed to any hard objects are reconstructed as the E_T^{miss} *soft term*. Ideally, reconstructed E_T^{miss} should correspond to the transverse component of the sum of the momenta of invisible particles in the event. However,E_T^{miss} is a complicated event-level quality constructed using many different signals in all detector subsystems, so its reconstruction strogly depends on several detector effects, such as object momentum mismeasurement, miscalibration, particles going

through un-instrumented regions of the detector all impact and contamination from pile up interactions. The dataset used in the following studies correspond to the full data-taking collected by the ATLAS detector in 2015 and 2016, corresponding to an integrated luminosity of 36.1 fb^{-1}.

5.9.1 E_T^{miss} reconstruction

The E_T^{miss} reconstruction estimates the amount of missing transverse momentum in the detector using calibrated detector signals corresponding to muons, electrons, photons, hadronically decaying τ-leptons and jets. The missing transverse momentum vector $\vec{E}_T^{miss}$ x- and y-components are:

$$E_{x(y)}^{miss} = E_{x(y)}^{miss,\mu} + E_{x(y)}^{miss,e} + E_{x(y)}^{miss,\gamma} + E_{x(y)}^{miss,\tau} + E_{x(y)}^{miss,jets} + E_{x(y)}^{miss,soft}, \quad (5.14)$$

where each term is calculated as the negative vectorial sum of transverse momenta of energy deposits or trajectories of charged particles. Energy deposits in the calorimeters and tracks are matched to reconstructed objects in an order chosen to minimise double-counting of detector signals. The E_T^{miss} reconstruction sequence for the *hard-object* contribution starts with μ, e, followed by γ, then hadronically decaying τ-leptons and finally jets. The signals not associated with reconstructed objects form the *soft term*. The total transverse energy in the detector $\sum E_T$ quantifies the total event activity. It is an important observable for understanding the resolution of the E_T^{miss}, especially with increasing pileup contributions, and is defined as the scalar sum of the transverse momenta of reconstructed objects and soft-term signals that contribute to the E_T^{miss} reconstruction:

$$\sum E_T = \sum p_T^{\mu} + \sum p_T^{e} + \sum p_T^{\gamma} + \sum p_T^{\tau} + \sum p_T^{jets} + \sum p_T^{soft}, \quad (5.15)$$

Since the E_x^{miss} and E_y^{miss} are expected to be approximately Gaussian distributed for $Z \to ll$ events [181], with deviations arising from noise and events with large $\sum E_T$, the root-mean-square (RMS) of the combined distributions of E_x^{miss} and E_y^{miss} is used to estimate the resolution. For processes with real E_T^{miss}, the generator-level E_x^{miss} and E_y^{miss} are subtracted from their reconstructed quantities in simulation.

E_T^{miss} hard term

The E_T^{miss} hard term is reconstructed from fully calibrated reconstructed hard objects, as outlined in previous Sections. For the studies presented here, hadronic τ-leptons and photons are not considered, since the topologies taken into account, $Z \to ll$ and VBF $H \to WW \to l\nu l\nu$, do not have a large production of either objects.

Muons CB muons with $p_T > 10$ GeV are included in the E_T^{miss} reconstruction. To avoid double counting, muon track p_T is corrected for energy losses in the detector and any muon energy deposited in the calorimetry system is taken into account using either parametrised estimated or direct measurement [166, 182].

Electrons Electrons satisfying the *medium* likelihood and *loose* isolation criteria with $p_T > 10$ GeV are included in the reconstruction of the missing transverse momentum.

EMTopo jets Jets are reconstructed from three-dimensional TopoClusters using the anti-k_t algorithm with a distance parameter $R = 0.4$. The jets are fully calibrated using the EM+JES scheme and are required to have $p_T > 20$ GeV after the full calibration. The matching of tracks with jets is performed via ghost association. Jets are further filtered using a tagging algorithm to select hard-scatter jets [183]. The jet vertex tagging (JVT) algorithm provides a likelihood discriminant using the following observables:

$$\begin{aligned} corrJVF &= \frac{\sum_m p_{T,m}^{track}(PV_0)}{\sum_l p_{T,l}^{track}(PV_0) + \frac{\sum_{n\geq 1}\sum_l p_{T,l}^{track}(PV_n)}{k \cdot n_{track}^{PU}}} \text{ and} \\ R_{p_T} &= \frac{\sum_k p_{T,k}^{track}(PV_0)}{p_T^{jet}}, \end{aligned} \tag{5.16}$$

where $\sum_m p_{T,m}^{track}(PV_0)$ is the scalar sum of the p_T of the tracks that are associated with the jet and originate from the hard-scatter vertex, the term $\sum_{n\geq 1}\sum_l p_{T,l}^{track}(PV_n) = p_T^{PU}$ denotes the scalar sum of the p_T of the tracks originating from any of the pile up interactions. n_{track}^{PU} is the total number of pile up tracks in the event and $k = 0.01$ is a correction factor to correct for the linear increase of $< p_T^{PU} >$ with n_{track}^{PU}. The two-dimensional likelihood is derived using simulated di-jet events and based on a k-nearest neighbour (kNN) algorithm [184]. For each point in the two-dimensional corrJVF-R_{p_T} plane, the relative probability for a jet at that point to be of signal type is computed as the ratio of the number of hard-scatter jets to the number of hard-scatter plus pile up jets found in a local neighbourhood around the point defined dynamically as the 100 nearest neighbours around the test point using a Euclidean metric.

Figure 5.24 shows the fake rate versus efficiency curves comparing the performance of the four variables JVF, corrJVF, R_{p_T} and JVT in simulated di-jet events. The JVT performance is driven by corrJVF (R_{p_T}) in the region of high signal-jet efficiency (high pile up rejection).

In the studies presented in this Section, JVT is used to reject pileup for jets by requiring $JVT > 0.59$ for jets with $p_T < 60$ GeV and $|\eta| < 2.4$.

Furthermore, for VBF topology, characterized by elevated forward-jet activity, an additional requirement, the forward-jet-vertex tagger (fJVT) [185] is an approach to remove jets with $|\eta| > 2.5$ and $20 < p_T < 50$ GeV coming from

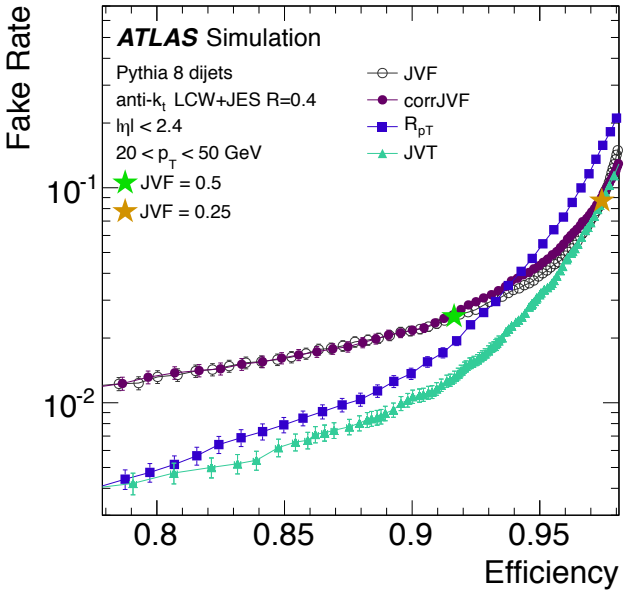

FIGURE 5.24: Fake rate from pile up jets versus hard-scatter jet efficiency curves for JVF, corrJVF, R_{pT}, and JVT. The widely used JVF working points with cut values 0.25 and 0.5 are indicated with gold and green stars. Figure taken from [183].

pileup interactions. The fJVT uses the angular kinematics of other jets in the event to associate forward jets, which do not have tracking information, to pileup vertices by minimizing the other vertex's reconstructed E_T^{miss}.

PFlow jets Particle Flow (PFlow) reconstruction of objects is particularly useful for the E_T^{miss} measurement as it combines the measurements from the inner detector and calorimeter to reconstruct the energy flow of the event. The PFlow algorithm suppresses calorimeter energy deposits arising from charged pileup particles and takes the momentum estimation from tracks whenever the tracker resolution is better than the calorimeter resolution. PFlow jets are constructed with the anti-k_t algorithm with a $R = 0.4$ radius using charged constituents associated with the primary vertex and neutral PFlow constituents as inputs. The PFlow algorithm is described in detail in [186]. After proper jet calibration and reconstruction, the PFlow jets are associated to the hard-scatter interaction with the JVT required to be larger than 0.2 for jets with $p_T < 60$ GeV and $|\eta| < 2.4$. This selection criteria has the same pileup jet rejection as the tighter JVT selection for EMTopo jets with a higher hard-scatter jet efficiency. The E_T^{miss} may be built with either EMTopo jets or PFlow jets. As tracks associated to electrons or muons are not considered in the PFlow shower subtraction, the difference between the two jet reconstruction approaches in the E_T^{miss} reconstruction arises in the *jet* and *soft* terms.

E_T^{miss} soft term

The soft term is comprised of all detector signals not matched to the reconstructed objects defined previously and may contain contributions from the hard scatter as well as the underlying event and pileup interactions. The reconstruction of the soft term is performend using a track-based soft term (TST). The TST includes contributions from tracks not associated to hard objects.

The TST for EMTopo E_T^{miss} Tracks are associated to the hard scatter vertex by considering the longitudinal and the transverse impact parameters d_0 and z_0 defined with respect to the hard scatter vertex position. In order to guarantee excellent track-to-vertex matching for the soft term, tracks are required to satisfy the following requirements:

- $p_T < 0.4$ GeV;
- $\left|\frac{d_0}{\sigma(d_0)}\right| < 2$;
- $|z_0 \sin\theta < 3$ mm.

To avoid double counting particles, the tracks matched to the high-p_T reconstructed objects need to be removed from the soft term. This is achieved by removing the following classes of tracks:

- tracks within $\Delta\eta < 0.2$ and $\Delta\phi < 0.05$ around electrons and photons;
- tracks within a cone of size $\Delta R = 0.2$ around hadronically decaying τ-leptons;
- ID tracks associated with muons;
- tracks ghost-associated to jets;
- isolated tracks with $p_T > 120$ GeV (> 200 GeV for $|\eta| < 1.5$) with relative resolution on their p_T larger than 40% or having no associated calorimeter energy deposit with p_T larger than 65% of the track p_T.

The TST for PFlow E_T^{miss} The E_T^{miss} built using PFlow jets instead of EMTopo jets uses a slightly different definition of the TST. The PFlow-based soft term (PFlow TST) uses tracks associated to charged PFlow constituents which are not associated to any well-identified reconstructed object and surviving the track-to-vertex association. Tracks entering in PFlow TST have similar requirements to the ones used in the EMTopo-based approach including the same track-to-hard-object association. Any differences are due to the different tracks quality requirements considered by the PFlow algorithm and also to the different track-to-vertex association. The different track quality requirements are summarised as follows:

- $p_T > 0.5$ GeV;
- $|\eta| < 2.5$;

- $|z_0 \sin\theta| < 2.0$ mm.

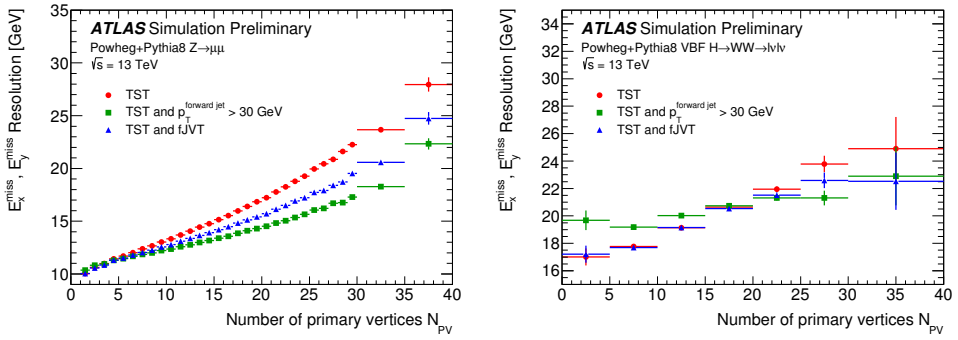

(A) (B)

FIGURE 5.25: Distributions of the E_T^{miss} resolution versus N_{PV} for E_T^{miss} built with three different forward jet selections in a $Z \to \mu\mu$ (a) and VBF $H \to WW$ (b) simulation. The Figures have been taken from [187].

E_T^{miss} working points The selection of jets used to calculate the E_T^{miss} has a large impact on its performance. Therefore, different working points are defined:

- **Loose**: all jets with $20 < p_T < 60$ GeV and $|\eta| < 2.5$ that also pass the JVT criteria and forward jets with $p_T > 20$ GeV are included;
- **Tight**: respect to the *Loose* WP, forward jets ($|\eta| > 2.5$) with $p_T < 30$ GeV are excluded;
- **Forward-JVT (fJVT)**: it is an even tigher criterion. In addition to the *Tight* requirement, forward jets with $20 < p_T < 50$ GeV and failing the *Loose* fJVT criteria are removed.

Figure 5.25 shows the E_T^{miss} resolution in events with zero true E_T^{miss} in $Z \to \mu\mu$ simulation and in events with forward hard scatter jets with VBF $H \to WW$ simulation. In both event topologies, raising the forward jet p_T cut to 30 GeV reduces the slope of the E_T^{miss} resolution versus N_{PV}. The loose operating point of the fJVT also improves the E_T^{miss} resolution. The degradation in resolution observed in the VBF topology after increasing the forward jet p_T cut to 30 GeV is due to removing hard-scatter jets from the VBF.

5.9.2 Systematic uncertainties

The E_T^{miss} is a topological event quantity, so its uncertainty, for the hard-term, is computed using the systematics associated to each object entering their reconstruction. For the hard component, systematic uncertainties on each reconstructed object are propagated to the E_T^{miss} as part of its reconstruction. However, a specific systematic uncertainty for the soft term estimation must be evaluated, since it is specific for the E_T^{miss} reconstruction.

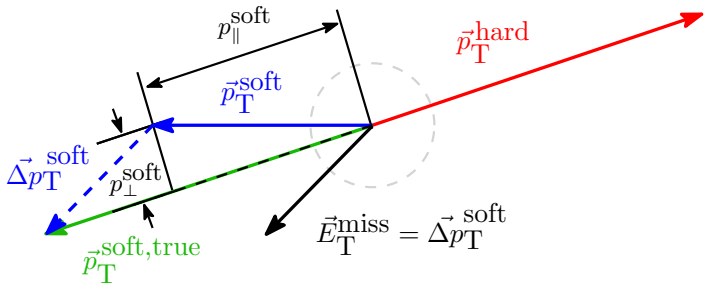

FIGURE 5.26: Sketch of the track-based soft term projections with respect to p_T^{hard} for the calculation of the TST systematic uncertainties. Figure taken from [187].

In an event topology with zero true E_T^{miss}, the soft term momentum p_T^{soft} is expected to be perfectly balanced against p_T^{hard}. Detector resolution effects spoil the equality between the two momenta. Different projections of p_T^{soft} along p_T^{hard} in data and MC are used to study the modelling of the soft term, as shown in Figure 5.26:

- **The parallel scale** Δ_L: it is the mean value of the parallel projection of p_T^{soft} along p_T^{hard}, labelled $p_{\parallel}^{soft}$;
- **The parallel resolution** $\sigma_{\parallel}$: it is the RMS of $p_{\parallel}^{soft}$;
- **The transverse resolution** $\sigma_{\perp}$: it is the RMS of the perpendicular projection of p_T^{soft} along p_T^{hard}, labelled $p_{\perp}^{soft}$.

The systematic uncertainty is computed from the maximal disagreement between data and MC generator for a certain set of p_T^{hard} bins. To account for any differences between event topologies with large numbers of jets and those without any jets, the total systematic is additionally split into jet-inclusive and jet-veto selections and merged later as the maximal variation of these two case.

Figure 5.27 shows $\sigma_{\parallel}$ for the jet-inclusive and jet-veto selections with the EMTopo and PFlow E_T^{miss} reconstruction methods. A good agreements can be observed between the two reconstruction methodologies; furthermore, it can be observed that resolutions in simulation are typically smaller than the ones in data.

5.9.3 E_T^{miss} resolution

The resolutions for the E_T^{miss}, for both the *Loose* and *Tight* WPs, are presented for the $Z \rightarrow ee$ event topology in Figure 5.28 as function of the average number of interactions $< \mu >$ and the number of reconstructed primary vertices in the event N_{PV}. The vertical error bands indicate the hard object uncertainties and the soft term systematic uncertainties added in quadrature. For data, the error bars indicate the statistical uncertainty on the RMS. The data and simulation agree across the full range of spectra. The E_T^{miss} resolution increases roughly linearly at approximately 0.24 (0.13) GeV/$< \mu >$ for the Loose (Tight) WP. The increasing amount of pileup activity degrades

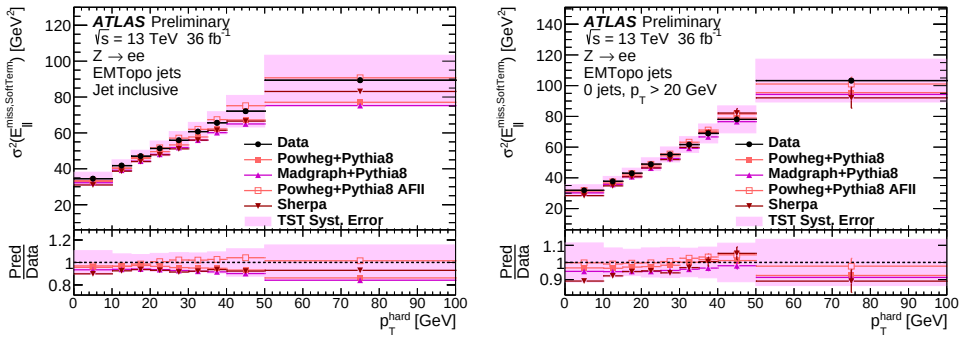

FIGURE 5.27: Parallel resolution plots for the EMTopo TST for the jet-inclusive (a) and jet-veto (b) selections. Analougously, the resoluton plots for the PFlow TST are shown in (c) and (d), respectively. The pink band, centered on data, represents the resulting systematic uncertainty applied to the $Z \rightarrow ee$ MC simulation. The Figures have been taken from [187].

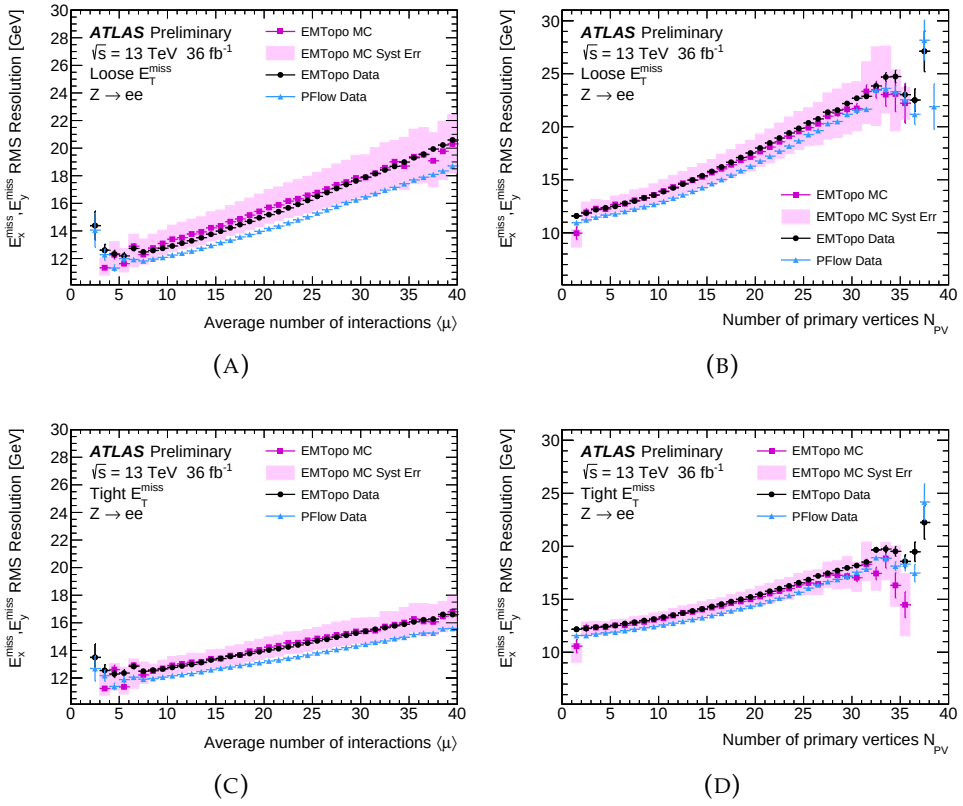

FIGURE 5.28: The RMS obtained from the combined distributions of EMTopo E_x^{miss} and E_y^{miss} for data with EMTopo jets (circular marker) and PFlow jets (triangular marker) and MC simulation with EMTopo jets (square marker) in a $Z \rightarrow ee$ event selection. The resolutions are shown using the Loose E_T^{miss} WP are shown versus $< \mu >$ (a) and N_{PV} (b). The same distributions for the Tight E_T^{miss} WP are shown in (c) and (d), respectively. The pink band indicates the size of the detector level systematic uncertainties. The Figures have been taken from [187].

the E_T^{miss} resolution from around 12 GeV at $N_{PV} = 1$ to around 22 GeV at $N_{PV} = 30$ for the Loose WP. The Tight WP has a smaller degradation from around 12 GeV at $N_{PV} = 1$ to around 18 GeV at $N_{PV} = 30$. The PFlow E_T^{miss} improves the E_T^{miss} resolution consistently across the full range of N_{PV}.

Chapter 6

Analysis strategy and techniques

From this Chapter onward, the analysis object of my research during my Ph.D. will be presented. The differential cross section measurement of the $t\bar{t}$ system decaying in the fully hadronic channel was performed using the 2015 and 2016 data samples collected at $\sqrt{s} = 13$ TeV from pp collisions with the ATLAS detector, corresponding to an integrated luminosity of 3.2 fb^{-1} and 32.9 fb^{-1}, respectively, for a total of $\mathscr{L} = 36.1$ fb^{-1}. A complete overview of the physics process considered in this thesis is given in Section 6.1, while the list of measured spectra will be given in Section 6.2. The reconstructed objects used in the analysis will be described in Section 6.3. A first event selection, based on general properties of the signal event topology will be presented in Section 6.4, followed by the description, in Section 6.5, of the $t\bar{t}$ system reconstruction. The event selection, based on the kinematic properties of the reconstructed top-antitop quark pair, will be presented in Section 6.6. The methods employed to estimate the background contribution to the selected *signal region* will be discussed in Section 6.7. Finally, the measured observables at *reconstructed level* will be presented in Section 6.8.

6.1 The fully hadronic $t\bar{t}$ decay channel in the resolved topology

As seen in Chapter 2, the $t\bar{t}$ production process has a very large cross section at the LHC; allowing detailed studies of the characteristics of $t\bar{t}$ production as a function of different kinematic variables. In this thesis, the cross sections of top quark pair production in the fully hadronic channel, in the resolved regime, are measured for the first time within the ATLAS Collaboration. The fully hadronic decay mode of $t\bar{t}$ is graphically depicted in Figure 6.1 and is characterised by the two intermediate W bosons, coming from the top quarks, decaying hadronically. The final-state configuration at LO therefore contains six jets, two of which originate from b-quarks. More jets may be produced by gluon emission in the initial- or final-state. This analysis focuses on events in which all decay jets from the top quarks are *resolved* as separate $R = 0.4$ jets, in contrast with so-called *boosted* topologies in which one or both of the two top quarks are produced with high momentum resulting in

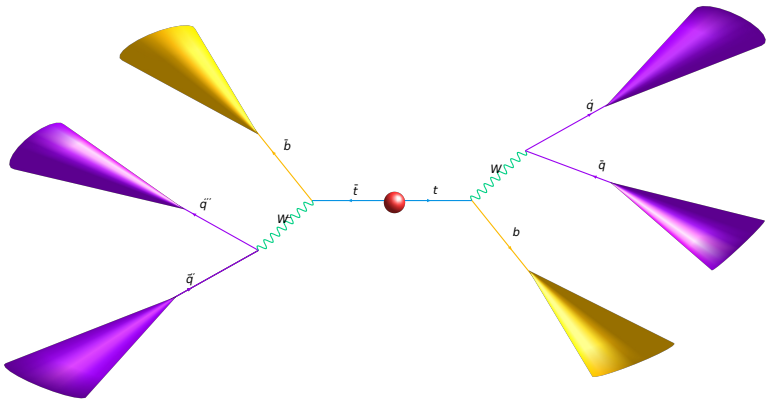

FIGURE 6.1: Pictorical representation of a top-antitop quark pair decaying into the *fully hadronic* channel. The red blob in the center represents the hard-scatter collision. Light-quark (b-quark) initiated jets are represented by purple (yellow) cones.

a overlap between the jets; these are studied using larger radius ($\Delta R = 1.0$) jets which are not considered in this analysis.

The use of the fully hadronic final state effectively complements measurements in other top quark decay channels [188–190]. Unlike in the leptonic decay modes, the four-momenta of the top quarks can be determined directly from the quark decay products, as the kinematic ambiguities arising from the presence of one or two neutrinos in the final state are avoided. Thus, precise measurements can be made of the kinematic correlations between the top quarks and any accompanying jet radiation, in addition to the determination of the top-quark pair kinematics. Furthermore, the resolved jet topology permits probing lower transverse momentum top quarks compared to those observed in the boosted jet topology, as well as jet radiation emitted nearly collinear to the top quark.

The ATLAS Collaboration has already published differential cross section measurements in the fully hadronic channel, using the di-boosted topology, at $\sqrt{s} = 13$ TeV [191] while the CMS Collaboration has published measurements in the di-boosted and resolved topologies at $\sqrt{s} = 8$ TeV [192], as well as the resolved topology at $\sqrt{s} = 13$ TeV [193], using data collected by the CMS detector during 2015. However, the observables that have been measured in the resolved topology remain limited, and in particular at $\sqrt{s} = 13$ TeV only the top p_t has been measured.

6.2 Measured observables

The analysis presented here measures a variety of observables sensitive to the kinematics of the top quark pair production and accompanying IFSR. These variables rely on the reconstruction of the $t\bar{t}$ system, described in Section 6.5. Spectra are measured in data and simulation events, processed as discussed in details in Chapter 4 at different *levels*:

- reconstructed level;
- particle level;
- parton level.

Section 6.3 will give a brief, but complete, overview of the aforementioned *levels*. Since the reconstructed top quarks are indistinguishable, except for *parton level*, where truth generator information is available, they are cathegorized, according to their p_T, as *leading* and *subleading* and denoted as *top1* and *top2*, respectively. Several spectra sensible to additional radiation require the definition of the *extra-jets*, i.e. any reconstructed jet which is not associated to any of the six decay products of the $t\bar{t}$ system. The additional, or extra, hard scatter jets are produced from ISFR.

6.2.1 $t\bar{t}$ system kinematics

The following observables, measured at *reconstructed* (data and MC), *particle* and *parton* (MC only) levels, characterize the four-momentum, hence the kinematics, of the $t\bar{t}$ system:

- transverse momentum of the *leading* (p_T^{top1}) and the *subleading* top (p_T^{top2}), and of the $t\bar{t}$ system ($p_T^{t\bar{t}}$);
- absolute rapidity of the *leading* ($|y_{top1}|$) and the *subleading* top ($|y_{top2}|$), and of the $t\bar{t}$ system ($|y^{t\bar{t}}|$);
- invariant mass of the $t\bar{t}$ systems ($m_{t\bar{t}}$);

6.2.2 ISFR-sensitive $t\bar{t}$ system spectra

Spectra sensitive to ISFR are measured at *reconstructed* and *particle* levels only, since non-perturbative physics and approximate higher-order correction from PS algorithm play an important role in modelling the additional QCD radiation. A precise measurement of the following observables constitutes an essential test for MC modelling:

- N_{jet}: the number of reconstructed jets;
- $\Delta\phi_{t\bar{t}}$: the angular distance in ϕ between reconstructed top quarks;
- $|p_{out}^{t\bar{t}}| = \left|\vec{p}^{top1} \cdot \frac{\vec{p}^{top2}\times\hat{z}}{|\vec{p}^{top2}\times\hat{z}|}\right|$: absolute value of the out-of-plane-momentum;
- $H_T^{t\bar{t}} = p_T^{top1} + p_T^{top2}$: the scalar sum of the p_T of the two top quarks;

- $R_{Wt}^{top1} = \frac{p_T^{W,\,top1}}{p_T^{top1}}$ and $R_{Wt}^{top2} = \frac{p_T^{W,\,top2}}{p_T^{top2}}$: p_T ratio of W-boson to its associated top quark;
- p_T ratio of W-boson to its associated b-quark: $R_{Wb}^{top1} = \frac{p_T^{W,\,top1}}{p_T^{b1}}$ and $R_{Wb}^{top2} = \frac{p_T^{W,\,top2}}{p_T^{b2}}$;
- ΔR_{top}^{extra1}: ΔR between the p_T-leading extra jet and its closest top (using the ΔR distance);
- p_T ratio of leading extra jet and leading top: $R_{extra1}^{top1} = \frac{p_T^{extra1}}{p_T^{top1}}$;
- p_T ratio of leading extra jet and leading jet: $R_{extra1}^{jet1} = \frac{p_T^{extra1}}{p_T^{jet1}}$;
- ΔR_{jet1}^{extra1}: ΔR between leading extra jet and leading jet.

$\Delta\phi$ and $p_{out}^{t\bar{t}}$ are found to be particularly sensitive to additional radiation associated to the production of the top quark pair [194]. Furthermore, $\Delta\phi$ has been found to be sensitive to non-resonant contributions due to hypothetical new particles exchanged in the t-channel [195]. In addition, since the channel used in this analysis does not have neutrinos in the final state, the reconstruction of the top-antitop quark system does not depend on the E_T^{miss}, whose resolution folds in the resolution on all measured jets in the event. Hence, a better resolution is expected for angular variables than in the *leptonic* channels. For the $H_T^{t\bar{t}}$ and the observables depending on the transverse momentum of the decay products of the top quark (R_{Wt}^{top1}, R_{Wt}^{top2}, R_{Wb}^{top1} and R_{Wb}^{top2}) have been found to be sensitive to higher-order corrections [196, 197]. The reconstruction of the top-antitop pair implies that the properties of additional jet emissions can be studied, in particular their correlation with the top system. These observables can only be measured in the hadronic channel. In particular, the p_T-leading hard-object in the event can be unambiguously defined in the fully hadronic channel only, since it can be a neutrino in the semileptonic or dileptonic channels. ΔR_{top}^{extra1}, R_{extra1}^{top1} and R_{extra1}^{jet1} are sensitive to the angular and energy correlations between the additional jets and the top quarks. For ΔR_{top}^{extra1}, the ΔR is taken with respect to the closest top, as collinear emissions are favoured. The first p_T ratio uses the leading top as a reference for the hard scale in the event, while the second is sensitive to emissions beyond the first, in particular soft gluons that may not be resolved as jets, allowing a test of resummation effects. Finally, ΔR_{jet1}^{extra1} can put further constraints on correlations amongst the additional jets themselves, which is particularly interesting for multileg matrix element calculations. Due to the fact that ISR scales as the partonic center of mass energy, it is possible that the leading extra jet is also the hardest object, and therefore sets the scale of the event, making it a good candidate as a reference object.

6.3 Objects definitions

The objects used in this analysis are reconstructed with the ATLAS detector and fully calibrated with the techniques described in Chapter 5 to account for the detector response and inefficiency. They are described below. Since no requirement is applied to photons and the E_T^{miss}, their description is not provided.

6.3.1 Jets

Jets are reconstructed using the anti-k_t jet algorithm with radius parameter $R = 0.4$ from three-dimensional noise-suppressed topological clusters. A JES calibration is applied, as described in 5.7, to suppress pile up and to correct the jet four-momenta on average to match the scale of jets formed from simulated stable interacting particles. Jets must satisfy $p_T > 25$ GeV and $|\eta| < 2.5$ and pass overlap removal with leptons, as described in Subsection 6.3.6 below. To suppress jets originating from pile up interaction, the JVT selection, as described in Subsubsection 5.9.1, is applied, requiring that every jet satisfy $JVT > 0.59$ or $|\eta| > 2.4$ or $p_T > 60$ GeV. In addition, jets are also required to pass *jet cleaning* quality criteria, referred as *LooseBad* [198]. They consist of a set of cuts aiming to reduce non-collision backgrounds and cosmic rays, calorimeter spikes and EM calorimeter noise is defined, based on the following observables:

- Q_{cell}^{LAr}: the pulse quality of the calorimeter cells, defined as the quadratic difference between the actual and expected pulse shapes in a given LAr calorimeter cell, computed online using the four measured samples of the pulse shape, defined as:

$$Q_{cell}^{LAr} = \sum_{j=1}^{4} \left(s_j - A \cdot \left(g_j - \tau g'_j \right), \right) \tag{6.1}$$

  where A is the measured amplitude of the signal, τ the measured time of the signal, $s_j$the amplitude of each sample, j, g_j the normalized predicted ionization shape and g'_j its derivative. More details of these quantities can be found in [199];

- $\langle Q \rangle$: the average jet quality, defined as the energy–squared weighted average of Q_{cell}^{LAr} in the jet. This quantity is normalized such that $0 < \langle Q \rangle < 1$;

- f_Q^{LAr}: fraction of the energy in the LAr calorimeter cells of a jet with poor signal shape quality defined as $Q_{cell}^{LAr} > 4000$;

- f_Q^{HEC}: fraction of the energy in the HEC calorimeter cells of a jet with poor signal shape quality defined as $Q_{cell}^{LAr} > 4000$;

- E_{neg}: the sum of all cells with negative energy of a jet. Negative energy can originate from noisy cells or electronic and pile up noise;

- f_{EM}: the electromagnetic fraction, defined as the ratio of the energy deposited in the electromagnetic calorimeter to the total energy of the jet;
- f_{HEC}: the electromagnetic fraction, defined as the ratio of the energy deposited in the HEC calorimeter to the total energy of the jet;
- f_{max}: the maximum energy fraction in any single calorimeter layer;
- f_{ch}: the jet charged fraction, defined analougously as the R_{p_T} in Equation 5.16.

A jet is identified as *LooseBad* if it satisfies at least one of the following criteria:

1. $f_{HEC} > 0.5$ and $|f_Q^{HEC}| > 0.5$ and $\langle Q \rangle > 0.8$;
2. $E_{neg} > 60$ GeV;
3. $f_{EM} > 0.95$ and $f_Q^{LAr} > 0.8$ and $\langle Q \rangle > 0.8$ and $|\eta| < 2.8$;
4. $f_{max} > 0.99$ and $|\eta| < 2.0$;
5. $f_{EM} < 0.05$ and $f_{ch} < 0.05$ and $|\eta| < 2.0$;
6. $f_{EM} < 0.05$ and $|\eta| > 2.0$.

The first two criteria are introduced to identify jets mainly due to sporadic noise bursts in the HEC. The third selection has the purpose to identify jets due to large coherent noise or isolated pathological cells in the electromagnetic calorimeter. The last three requirements are more general and are used to identify hardware issues, beam-induced background and cosmic muon showers. Any event that contains at least one *LooseBad* jet is vetoed.

6.3.2 Electrons

Electrons are reconstructed from clusters of energy in the calorimeter combined with an ID track that is refitted using GSF and calibrated using a multivariate regression, as described in 5.4. They must satisfy $p_T > 15$ GeV, be in the pseudorapidity range $|\eta| < 1.37$ or $1.52 < |\eta| < 2.47$ and pass the *TightLH* quality criteria and the *Gradient* isolation working point.

6.3.3 Muons

Muons are reconstructed from ID tracks and track segments found in the MS, as described in Section 5.5. They must satisfy $p_T > 15$ GeV, $|\eta| < 2.5$ and fulfil the *Medium* quality and *Gradient* isolation criteria.

6.3.4 τ jets

Hadronic τ jet candidates are identified using clusters from the cores of selected anti-k_t jets with $R = 0.4$ built from TopoClusters calibrated at the LH scale, as discussed in Section 5.6. The *Medium* BDT τ jet working point is

used, and τ candidates must satisfy $p_T > 25$ GeV and $|\eta| < 2.5$. An additional *Loose* BDT working point is used to eliminate electrons faking a τ.

6.3.5 B-Tagging

To identify anti-k_t $R = 0.4$ jets containing b-hadrons, the multivariate discriminant (MV2c10), presented in Section 5.8, is used, which combines information about secondary vertices and impact parameters. In this analysis, the 70% OP is chosen (equivalent to the cut on the output of MV2c10 > 0.8244273). The corresponding rejection factors for charm quarks and light jets are 12.17 and 381.32, respectively.

Scale factors are applied to the simulated event samples to compensate for differences between data and simulation in the b-tagging efficiency for b, c and light-jets. The corrections are consistent with unity with uncertainties at the level of a few percent over most of the jet p_T range, as shown in Figure 5.23.

6.3.6 Overlap removal

In some cases, the same track or energy cluster can be used in the reconstruction of more than one physics object. This would lead to an energy double-counting or a mis-reconstruction of the objects. To avoid this problem, a procedure of *overlap removal* (OR) between objects is performed. Overlapping objects are removed from the event, therefore the object selection outlined in previous Subsections is performed on surviving objects only. The OR procedure, for the objects used in this analysis, is performed in sequential order. The metric used to measure inter-object distances is $\Delta R_y = \sqrt{(\Delta y)^2 + (\Delta\phi)^2}$, where y indicates the rapidity:

- any electron found with an ID track overlapping with any other electron is removed;
- any tau-leptons found within a $\Delta R_y = 0.2$ of a *LooseLH* electron is removed;
- any tau-leptons with $p_T < 50$ GeV found within a $\Delta R_y = 0.2$ of any type of muon with $p_T > 2$ GeV is removed. If a tau-lepton with $p_T > 50$ GeV overlaps with a CB muon, the tau-lepton is removed;
- any CT muons sharing an ID track with electrons is removed;
- any electron found to share a track with a muon is removed;
- any jet found within a $\Delta R_y = 0.2$ of an electron is removed;
- any electron found within $\Delta R_y = 0.4$ of a jet is removed;
- any jet with less than three associated-tracks associated found within $\Delta R_y = 0.2$ of a muon is removed. In addition, the jet is removed if has a muon ID track ghost-associated to it;

- any muon found within $\Delta R_y = 0.4$ of a jet is removed;
- any jet found within a $\Delta R_y = 0.2$ of a tau-lepton is removed.

6.3.7 Event cleaning

Reconstructed events are required to satisfy some quality criteria to remove problematic events which would not be suitable to be used in physics analyses. This *event cleaning* procedure, which mainly interest data, comprises three additional requirements, described below.

Good Run List

During data-taking, the data from specific components may not be usable for physics studies for certain periods of time. For example, a component may be at a non-nominal voltage, readout electronics may need to be reset, or the data may be noisier than usual. Because not all physics studies rely on all components and these issues are often transient, data acquisition continues even in a degraded state. Time-dependent configuration, status, and calibration information for ATLAS is stored in Oracle and SQLite databases using the COOL technology developed by the LCG project [200]. The COOL database contains all the information to assess if each LumiBlock (LB), the fundamental time granularity unity of ATLAS configuration and status, presents any *defect*. After processing, LBs are flagged as *defected* or *ready for physics*. All ready for physics LBs, grouped by *RunNumbers*, i.e. a continuative sequence of LBs with similar detector conditions, are collected in a centrally provided *xml* file, referred as *GoodRunList* (GRL) [201]. Data events are vetoed if not included in the GRL.

Corrupted data

Even after removing LBs with poor detector quality, some events can still not be suitable for physics application. Problematic events presenting corrupted data in the TileCal, LAr or SCT, as well as LAr noise burst or incomplete events due to problems during the write-out procedure, are vetoed. In the following, this set of requirements will be referred as *GoodCalo* cut.

Vertex Requirement

All events (data and MC) are required to have at least one reconstructed primary vertex with at least two associated tracks. The *PriVtx* requirements veto events failing this condition.

6.3.8 Particle level objects definition

As discussed in Chapter 5, particle level objects are defined using only stable particles with mean lifetime $\tau > 30$ ps. Only prompt electrons, muons and neutrinos not originating, either directly or through a τ-lepton decay, from a

Requirement	Description
Multi-jet trigger	HLT_6j45_0eta240
Exactly 0 isolated lepton	μ: $p_T > 15$ GeV, $\|\eta\|$<2.5 e: $p_T > 15$ GeV, $\|\eta\|$<2.47, excluding 1.37<$\|\eta\|$<1.52 τ: $p_T > 25$ GeV, $\|\eta\|$<2.5
At least 6 jets	6^{th} leading jets: $p_T > 55$ GeV Additional jets: $p_T > 25$ GeV
Less than or exactly 2 b-tagged jets	Fixed Cut 70% b-tagging efficiency

TABLE 6.1: Summary of selection requirements for events entering the $t\bar{t}$ reconstruction.

hadron are used. Since the detector has not sufficient resolution to separate the lepton energy from the collinear photons emissions, particle level leptons (electrons and muons) are *dressed*, by adding to them the four-momenta of all photons within $\Delta R = 0.1$. Electrons in the calorimeter transition region ($1.37 < |\eta| < 1.52$) are rejected at detector level but accepted at particle level. Following the reconstructed level object selection, events containing dressed leptons with $p_T > 15$ GeV are vetoed. Particle level jets are obtained by clustering stable particles within $|\eta| < 4.5$ using the anti-k_t algorithm, with radius parameter $R = 0.4$. Dressed leptons and prompt neutrinos are exluded from the jet clustering procedure. The requirements on particle level jets are the same of the reconstructed level ones. A particle level jet is flagged as b-tagged if it contins ghost-associated b-hadrons with $p_T > 5$ GeV. No overlap removal is applied to particle level objects.

6.3.9 Parton level objects definition

The $t\bar{t}$ system at parton, or generator, level is defined from truth information, using top quarks after FSR and before decay. No selection on the $t\bar{t}$, nor top quarks, is applied.

6.4 Topology-based event preselection

Events that are collected under stable condition, which are well reconstructed and passing the *event cleaning* preselection, enter a sequence of cuts based on the topology of the physics process of interest in order to enhance the selection of the top quark pair decaying in the hadronic channel. The first cut is a trigger cut, whose efficiency and features have been discussed in Subsection 2.2.8. The selection requires the `HLT_6j45_0eta240` multi-jet trigger to be fired. This is a multijet trigger requiring 6 jets with a p_T greater than 45 GeV in the high level trigger; all 6 jets must be in the central region of the detector ($|\eta| < 2.4$).

Since the aim of the analysis is to measure quantities in events in which the top-quark pair can be fully reconstructed, each event is required to have at

least six reconstructed jets. The p_T threshold for the six leading jets is 55 GeV; this ensures the largest possible signal efficiency while assuring that the trigger has reached a very high efficiency as demonstrated in Figure 2.17. In addition, the events are required to contain exactly zero reconstructed leptons with the following p_T-thresholds:

- electrons: $p_T > 15$ GeV;
- muons: $p_T > 15$ GeV;
- tau-leptons: $p_T > 25$ GeV;

Since $t\bar{t}$ events contain two b-jets while the main background process ordinarily produces zero, events are also required to have exactly two b-tagged jets in their final state. This requirement strongly suppresses the dominant multi-jet background while selecting a large fraction of top events. While additional (real or spurious) b-tagged jets can arise at a low rate in the signal, the handling of additional b-tagged jets further complicates the top reconstruction due to the additional combinatorics which has to be taken into account, as it will be discussed in Section 6.5. Furthermore, it was found that when permitting a third b-tagged jet, the signal yield is increased by 17%, whereas multi-jet background yield is increased by 61% respectively, reducing the signal purity of the selected data sample. Therefore, events with more than two b-tagged jets are vetoed. Furthermore, additional jets with $p_T < 25$ GeV are rejected. The requirements for events entering the $t\bar{t}$ system reconstruction are summarized in Table 6.1. It is worth noting that the requirement on the number of b-tagged jets is loosen from *exactly* to *less than* two b-tagged jets in the event; this is needed by the data-driven multi-jet background estimation method, as discussed below. After the $t\bar{t}$ system reconstruction has been performed, events are required to have exactly two b-tagged jets in the final state.

6.5 $t\bar{t}$ system reconstruction

In each event, the χ^2 discriminant defined below is evaluated from the invariant masses of the di-jet and three-jet systems for all possible permutations of jets sixtuplets, associated to the decay products of the $t\bar{t}$ system. In each permutation, each candidate b-tagged jet is associated with a pair of non-b-tagged (light) jets, which are considered candidates for the decay products of the W boson that shares a top parent with the b-jet. The permutation are defined according to the following criteria:

1. all possible combinations of *light-jets* pairs are built;
2. *light-jets* pairs are grouped, in quadruplets, using every allowed combination. Combinations containing repeated jets are discarded;
3. *b-jets candidate* pairs are built according to the number of b-tagged jets in the event:
    - **0 b-tagged jets**: pairs are built from any permutation of *light-jets*;

- **1 b-tagged jet**: pairs are formed by permutating 1 *light-jet* and the *b-tagged jet*;
- **2 b-tagged jets**: only 2 pairs are formed: $< b_1; b_2 >$ and $< b_2; b_1 >$, where b_1 and b_2 indicate the two *b-tagged* jets;

4. *b-jets pairs* and *light-jets quadruplets* are matched, in any possible combination, to form the final *sextuplets*. *Sextuplets* containing repeated jets are discarded.

The χ^2 estimator is defined as

$$\chi^2 = \frac{(m_{b_1 j_1 j_2} - m_{b_2 j_3 j_4})^2}{2\sigma_t^2} + \frac{(m_{j_1 j_2} - m_W)^2}{\sigma_W^2} + \frac{(m_{j_3 j_4} - m_W)^2}{\sigma_W^2}, \tag{6.2}$$

where $m_{b_1 j_1 j_2}$ and $m_{b_2 j_3 j_4}$ are the invariant masses of the jets associated with the decay products of the leading and subleading top, respectively. Similarly, $m_{j_1 j_2}$ and $m_{j_3 j_4}$ are the invariant masses of the jets associated with the decay products of the W bosons from the tops. The mass of the W boson, $m_W = 80.385$ GeV, is taken from the PDG [9], while the top mass m_t does not appear explicitly, which avoids sculpting backgrounds to resemble the signal.[1] Finally, σ_t (σ_W), represents the width of the three-jet (dijet) mass distributions for correctly reconstructed top quarks (W bosons).

The resolutions σ_t and σ_W have been extracted from the $W \to qq'$ and $t \to bqq'$ mass distributions at detector level in simulated $t\bar{t}$ MC events, after requiring a truth-ΔR matching requirement; each of the parton-level decay products from the top-quark pair (the 6 quarks) is matched to a reconstructed jet, imposing a $\Delta R < 0.3$ requirement. The core of mass distributions of the three-jet or dijet systems corresponding to each top or W are then fitted with a gaussian, whose width is taken to be σ_t or σ_W, respectively. For comparison, the same procedure is repeated for jets formed from stable particles, however only the detector-level resolutions are used in the analysis.

Figure 6.2 shows the results of gaussian fits to the W boson and top quark mass spectra from parton-matched jets, at detector and particle level, reported in Table 6.2.

Level	σ_W [GeV]	σ_t [GeV]
Reconstructed	8.09	15.95
Particle	4.64	6.47

TABLE 6.2: Parameters of Equation 6.2 extracted from nominal $t\bar{t}$ MC sample at reconstructed and particle level.

As expected due to the resolution of the detector, the detector level distributions are broader with respect to the particle level ones. Both W boson mass peaks contain the nominal value in the PDG well within the determined resolution, hence the χ^2 formula is insensitive to shifts in the central value due

[1] Formally, the χ^2 expression is minimized with respect to m_{top} (by requiring $\partial\chi^2/\partial m_{top} = 0$), which is treated as a free parameter.

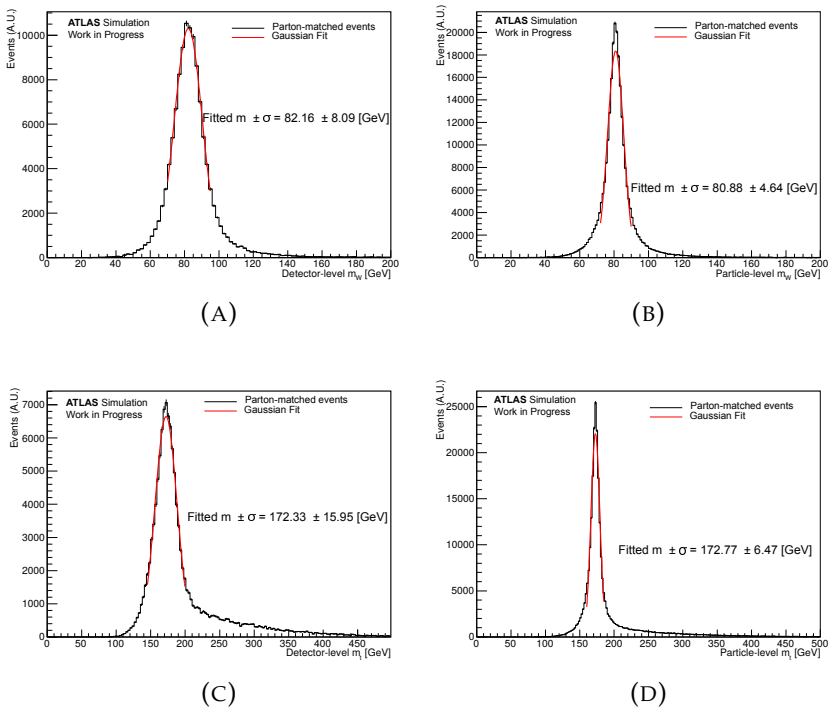

FIGURE 6.2: Mass spectra at detector level of the W boson (a) and top quark (c), determined from parton-matched jets. The particle level results are shown in (b) and (d), respectively. The fitted gaussian is shown in red, with the peak and width parameters shown.

to detector effects, since a displacement by 1.6 GeV causes only a change of 0.04 in the χ^2 value. Furthermore, the $t\bar{t}$ system reconstruction has been found to be very stable with respect to the values of the parameters assumed in the Equation 6.2, as shown in Appendix A. The six-jets combination that minimises the χ^2_{min}, henceforth abbreviated χ^2, is selected as the representation of the event. The top quarks and the W bosons are reconstructed from the four-momenta of this permutation of jets. The implementation of the χ^2 minimization algorithm is reported in Appendix B.

6.6 Event selection

After the $t\bar{t}$ system reconstruction, several cuts are applied to further reject background events in data. The χ^2 is used as a first discriminant to reject background events; multijet events produce larger χ^2 values, hence events are rejected if they have $\chi^2 > 10$. In top pair events, the two b-tagged jets tend to be produced at large angles, while in multijet background the distance between b-tagged jets is smaller since the dominant mechanism for producing b-jets is $g \to b\bar{b}$ which typically results in collinear b-jets. Therefore the angle between the two b-tagged jets, ΔR_{bb}, is required to be larger than 2. Similarly, the larger of the two angles between a b-tagged jet and its associated W boson, ΔR^{max}_{bW}, has good discriminating power, as the moderate boost of

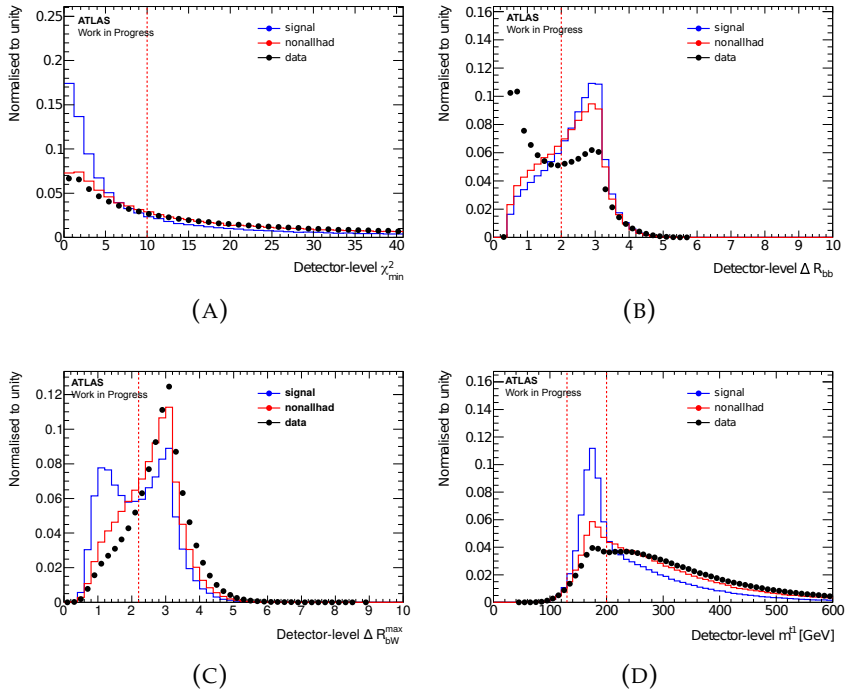

FIGURE 6.3: Distributions of observables used for background rejection, shown in data, non all hadronic $t\bar{t}$ and signal for events preselected as in Section 6.4. The variables shown are the χ^2 discriminant 6.3a, ΔR_{bb} (b), ΔR_{bW}^{max} (c) and m_{top} (d), filled for both top quark candidates in each event. Cut values are indicated by red dashed lines.

tops produced at the LHC implies that the top decay products are rarely in opposite hemispheres. Restricting $\Delta R_{bW}^{max} < 2.2$ reduces the combinatorial background from multijets, while maintaining a good signal efficiency. This also has some rejection power for poorly-reconstructed signal events. Finally, the mass of the two reconstructed tops is required to be close to the nominal PDG value [9] of $m_t = m\bar{t} = 172.5$ GeV, specifically in the window $130 < m_{t\bar{t}} < 200$ GeV. This window contains well-reconstructed hadronic ttbar events, while background events are predominantly in the tails beyond these cuts.

Figure 6.3 shows the distributions of each of the background rejection variables described above after the topology-based selection described in Section 6.4, while Figure 6.4 shows the same distributions with all selection cuts applied with the exception of the cut on the variable shown. The cuts, indicated in the Figures by red, dashed lines, are placed at positions that ensure a good signal purity, but away from regions with a large variation in signal and background distributions, such that the signal efficiency and purity is not sensitive to the precise cut values. The same selection described in this Section is applied both at reconstruction level and at particle level.

The complete event selection cuts are summarized in Table 6.3.

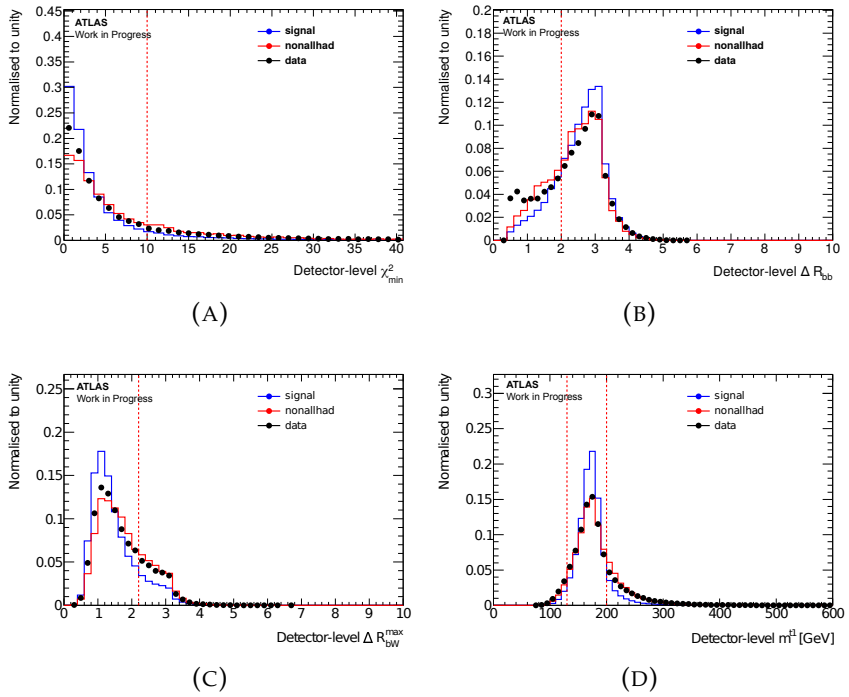

FIGURE 6.4: Distributions of observables used for background rejection, shown in data, non all hadronic $t\bar{t}$ and signal with all selection cuts applied with the exception of the cut on the variable being shown. The variables shown are the χ^2 discriminant (a), ΔR_{bb} (b), ΔR^{max}_{bW} (c) and m_{top} (d), filled for both top quark candidates in each event. Cut values are indicated by red dashed lines.

6.7 Background determination

Despite the good discriminating power of cuts presented in the previous Sections, several physics processes can *mimic* and contaminate the signal region, contributing to the background. There are three main sources of background that can be reconstructed as fully hadronic $t\bar{t}$ events:

1. **$t\bar{t}$-like background**: it is constituted by top-antitop quark pair production decaying into the non all hadronic channels. The dominant process is the semileptonic $t\bar{t}$ decay mode. The two additional jets can either come from pile up interactions or additional gluon emission;

2. **single-top quark background**: as seen in Subsection 1.8.5, single-top quarks can be produced via the t-channel, s-channel or in association with a W-boson. These processes are strongly suppressed by the 2 b-tagged jets requirement, since only one genuine b-tagged jet is expected in the final state. A second, reconstructed b-jet must either come from an misindentified light-jet or from $g \to bb$ splitting, in which one of the splitted b-jet is not reconstructed. Being the process with the highest total cross section, and the presence of a second W-boson in the final state, the dominant process is expected to be the W-boson associated single-top quark production;

Requirement	Description
Multi-jet trigger	HLT_6j45_0eta240
Exactly 0 isolated lepton	μ: $p_T > 15$ GeV, $\|\eta\|$<2.5 e: $p_T > 15$ GeV, $\|\eta\|$<2.47, excluding 1.37<$\|\eta\|$<1.52 τ: $p_T > 25$ GeV, $\|\eta\|$<2.5
At least 6 jets	6^{th} leading jets: $p_T > 55$ GeV Additional jets: $p_T > 25$ GeV
Exactly 2 b-tagged jets	Fixed Cut 70% b-tagging efficiency
Top mass window	$130 < m_{top1} < 200$ GeV $130 < m_{top2} < 200$ GeV
Reconstructed χ^2	$\chi^2 < 10$
ΔR between b-tagged jets	$\Delta R_{bb} > 2.0$
Maximum ΔR between b-tagged jet and its associated W-boson	$\Delta R_{bW}^{max} < 2.2$

TABLE 6.3: Summary of selection requirements for the analysis.

3. **multi-jet QCD background**: it is the expected biggest contribution in the signal region after the event selection. The six jets used in the kinematic reconstruction of the $t\bar{t}$ system arise from the scattering of gluons or u, d, s, c, or b quarks, also referred as (QCD) multi-jet events.

The first two sources of background, as shown in Section 4.4, are well modelled (up to NNLO+NNLL order) by MC event generators, while MC predictions of multi-jet events have large uncertainties coming from the relatively poorly-understood higher-order contributions that produce a pair of massive jets [202, 203]. To avoid these large uncertainties the multijet background is determined using a data-driven technique.

6.7.1 Monte Carlo-based background estimation

Process	Event Yields	Ratio to signal MC-prediction	Ratio to data
$t\bar{t}$ (all-hadronic)	31807.60 ± 142.77	1.00	0.719
$t\bar{t}$ (non all-hadronic)	1650.37 ± 20.42	0.052	0.037
Wt associated production	235.42 ± 7.59	0.0074	0.0053
single-top t-channel	227.41 ± 25.43	0.0071	0.0051
Data	44238	1.39	1.00

TABLE 6.4: Event yields for data, signal and background processes estimated with MC-techniques after the signal region selection. The ratio of each background yields to the signal $t\bar{t}$ and to data yields are shown for convenience. Only statistical uncertainties are given.

The background sources estimated with MC-based tecniques are the non all hadronic $t\bar{t}$ production, the t-channel single-top production and the associated Wt production. Due to its low cross section, the s-channel single-top production has not been considered for this analysis. The event yields for data, signal and MC-estimated background processes are given in Table 6.4. Physical processes other than the signal process involving top quarks in the final state, such as the semi-leptonic decay of a top-antitop pair and single top production in association with a W boson, are strongly suppressed by the lepton veto and top kinematic reconstruction. In particular the t-channel single top quark and Wt contributions are each 1% of the selected signal events (0.05% of data), while the semi- and di-leptonic $t\bar{t}$ yield is 5% of the signal (4% of data). The total single top contribution is shown to be below 2% of the selected data and well within both MC and data statistical error. For this reason it will not be considered further in the analysis.

6.7.2 Data-driven multi-jet QCD background estimation

Table 6.4 clearly shows that top-like backgrounds can not account for the difference between data and signal process. Multi-jet QCD background is expected to contribute $\approx$ 20% of the total yields. This is estimated using a data-driven background estimate, the *ABCD method*. It has been widely used in experimental particle physics for the data-driven determination of QCD multi-jet background in fully hadronic topologies [191, 204, 205], being generally applicable whenever two uncorrelated variables with good discrimination between signal and background can be identified.

	$i=0$	$i=1$
$j=0$	A	B
$j=1$	C	D

TABLE 6.5: Basic division of data into four regions according to the values assumed by parameters i and j.

In its most basic implementation, data is divided into four orthogonal regions, according to the values assumed by two parameters, i and j, as shown in Table 6.5. The signal region is denoted as D (pass both i and j requirements), while background-enriched control regions are defined as A (fail i, fail j), B (pass i, fail j) and C (fail i, pass j). The method is based on two assumptions:

1. the parameters i and j independently good signal-background discrimination power;
2. the parameters i and j are uncorrelated for the background process.

The first criterion ensures that the control regions (A,B,C) may be isolated from the signal process, while the second ensures that the ratios of background events passing selections on parameters i and j are independent. This implies that the pass/fail ratios for parameters i are identical regardless

of whether the background events pass or fail condition j. Hence, $D/B = C/A$, which is easily solved for D. In the analysis, the ABCD method is used to estimate the multi-jet background for each bin in the measured distributions. The differential background estimate D_k for the kth bin of a generic distribution is expressed as:

$$D_k = \frac{C_k}{A_k} \cdot B_k, \tag{6.3}$$

where the control region background yields $\{A, B, C\}_k$ are determined by subtracting the MC predictions, both signal process and the MC-estimated backgrounds, from data.

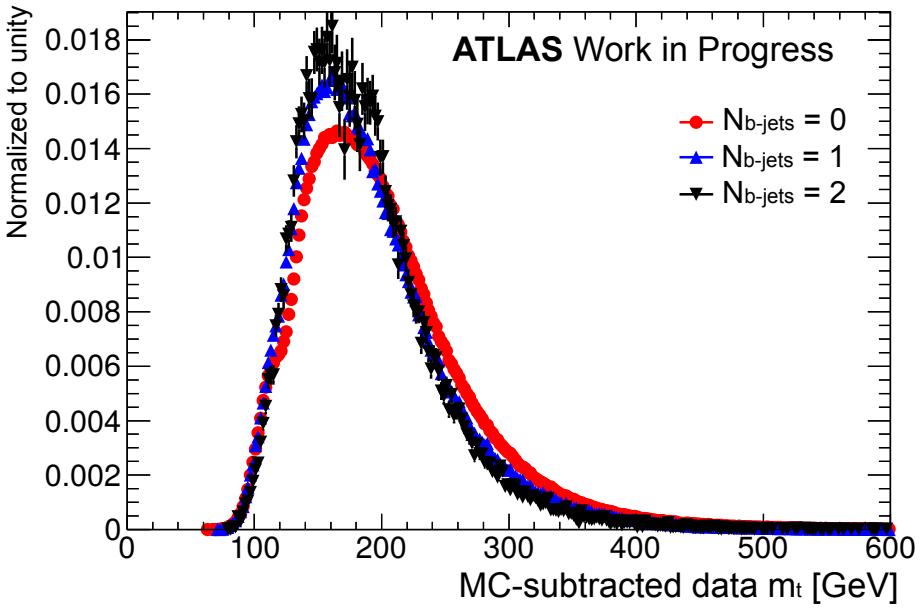

FIGURE 6.5: MC-subtracted data distribution of m_t in exclusive n_{b-jets} regions. All other selection criteria are applied.

Figure 6.5 shows the MC-subtracted m_{top} data distibutions, obtained filling the spectra twice per event (one time for each top) in different n_{b-jet} regions. No significant shape variation of m_{top} is observed between the $n_{b-jet} = 2$ and $n_{b-jet} = 1$ regions, while larger the 0 n_{b-jet} distribution shows larger tails, thus indicanding the presence of some residual correlations. Furthermore, their good discrimination power has already been shown in Figure 6.4. In conclusion, the best performing pair of discriminating variables were found to be the b-tagged jets multiplicity n_{b-jets} (with the $n_{b-jet} = 1$ selection as validation region) and the top mass window m_{top}.

The phase-space consisting of events passing the full event selection, except for m_{top} and n_{b-jet}, is divided into several orthogonal regions, according to the values assumed by those uncorrelated, discriminating variables, as shown in Table 6.6:

- A_0: $n_{b-jets} = 0$ and ($m_{top} < 110$ GeV or $m_{top} > 250$ GeV);

	$m_{top} \in (-\infty, 110) \cup (250, +\infty)$ GeV	$m_{top} \in [110, 130] \cup [200, 250]$ GeV	$m_{top} \in (130, 200)$ GeV
$n_{b-jets} = 0$	A_0	G_0	C_0
$n_{b-jets} = 1$	A_1	G_1	C_1
$n_{b-jets} = 2$	B	G_2	D

TABLE 6.6: Phase-space division into orthogonal regions according to the values assumed by parameters n_{b-jets} and m_{top}.

- A_1: $n_{b-jets} = 1$ and ($m_{top} < 110$ GeV or $m_{top} > 250$ GeV);
- B: $n_{b-jets} = 2$ and ($m_{top} < 110$ GeV or $m_{top} > 250$ GeV);
- G_0: $n_{b-jets} = 0$ and ($110 < m_{top} < 130$ GeV or $200 < m_{top} < 250$ GeV);
- G_1: $n_{b-jets} = 1$ and ($110 < m_{top} < 130$ GeV or $200 < m_{top} < 250$ GeV);
- G_2: $n_{b-jets} = 2$ and ($110 < m_{top} < 130$ GeV or $200 < m_{top} < 250$ GeV);
- C_0: $n_{b-jets} = 0$ and $130 < m_{top} < 200$ GeV;
- C_1: $n_{b-jets} = 1$ and $130 < m_{top} < 200$ GeV;
- D: $n_{b-jets} = 2$ and $130 < m_{top} < 200$ GeV.

Here, A_0, B and C_0 are the *nominal* control regions, A_1 and C_1 are *variated* control regions, used to asses the systematic uncertainty of the method, as described in Chapter 8, $G = G_0 \cup G_1 \cup G_2$ is the gap region, introduced to reduce the signal contamination in the control regions with a negligible increase in the total statistical uncertainty (at 1% level), improving the overall robustness of the estimate. Finally, D is the signal region in which the multi-jet background is estimated.

Region	all hadronic $t\bar{t}$ to data ratio	non all hadronic $t\bar{t}$ to data ratio
A_0	0.32 %	0.06%
C_0	1.14 %	0.10%
A_1	3.75 %	0.75%
C_1	18.67 %	1.37%
B	17.90 %	3.31%
D	72.10 %	3.73%

TABLE 6.7: Signal and $t\bar{t}$-like background contamination in the different regions, defined by the values assumed by n_{b-jets} and m_{top}.

Table 6.7 shows the fractions of signal and background $t\bar{t}$ events estimated from MC in the control regions and the signal region. As expected, the highest signal contamination is observed in regions with non-zero b-tagged jets. Although regions A_0 and C_0 have a very low signal contamination, regions A_1 and C_1 are used to define the primary background estimate, due to the

more stable shape of m_t between the 1 and 2 b-tagged jet regions lower correlation. The multi-jet background estimate is given, according to Equation 6.3, by:

$$D_k = \frac{C_{1,k}}{A_{1,k}} \cdot B_k. \tag{6.4}$$

Process	Event Yields	Ratio to data
$t\bar{t}$ (all-hadronic)	31807.60 ± 142.77	0.719
$t\bar{t}$ (non all-hadronic)	1650.37 ± 20.42	0.037
Multi-jet QCD	10070.61 ± 140.10	0.228
Total prediction	43528.58 ± 201.07	0.984
Data	44238	1.00

TABLE 6.8: Event yields for data, signal and background processes after the signal region selection. The ratio of each yield to data yields is shown for convenience. Only statistical uncertainties are given.

Table 6.8 shows the event yields for all the processes considered in the analysis. The yields for the multi-jet background is extracted from the measured total cross section, $\sigma_{t\bar{t}}$, at reconstructed level, shown in Figure 6.6. A very good agreement between data and the total prediction yields is observed. This is a first indicator of the robustness of the ABCD data-driven method. The complete cutflows for data and simulated background processes, including the single-top quark production, are listed in Appendix C.

6.8 Reconstructed level results

In this Section, the comparison between data and various background contributions at detector level, for the spectra listed in Section 6.2, are presented. Spectra sensitive to the $t\bar{t}$ system kinematics are shown in Figures 6.7, 6.8, 6.9 and 6.10, while ISFR-related spectra are presented in Figure 6.11, 6.12 and 6.13. The signal $t\bar{t}$ model and background processes are represented with different colours and stacked to provide a fair comparison with data. The hashed area indicates the combined statistical and systematic uncertainties, excluding those related to the *modelling* of the $t\bar{t}$ system, as discussed in Chapter 8. In general, the total background estimate summed over all histogram bins is stable, although some variation in the total multijet yield is observed. This is an intrinsic feature of the ABCD method, since the shape of the spectra in the control regions depends on the considered spectrum. However, no particular trends are observed that would indicate a shortcoming of the background estimate. The reconstructed jets multiplicity, shown in Figure 6.11, shows the dependence of the signal purity on the jet multiplicity; the 6-jet

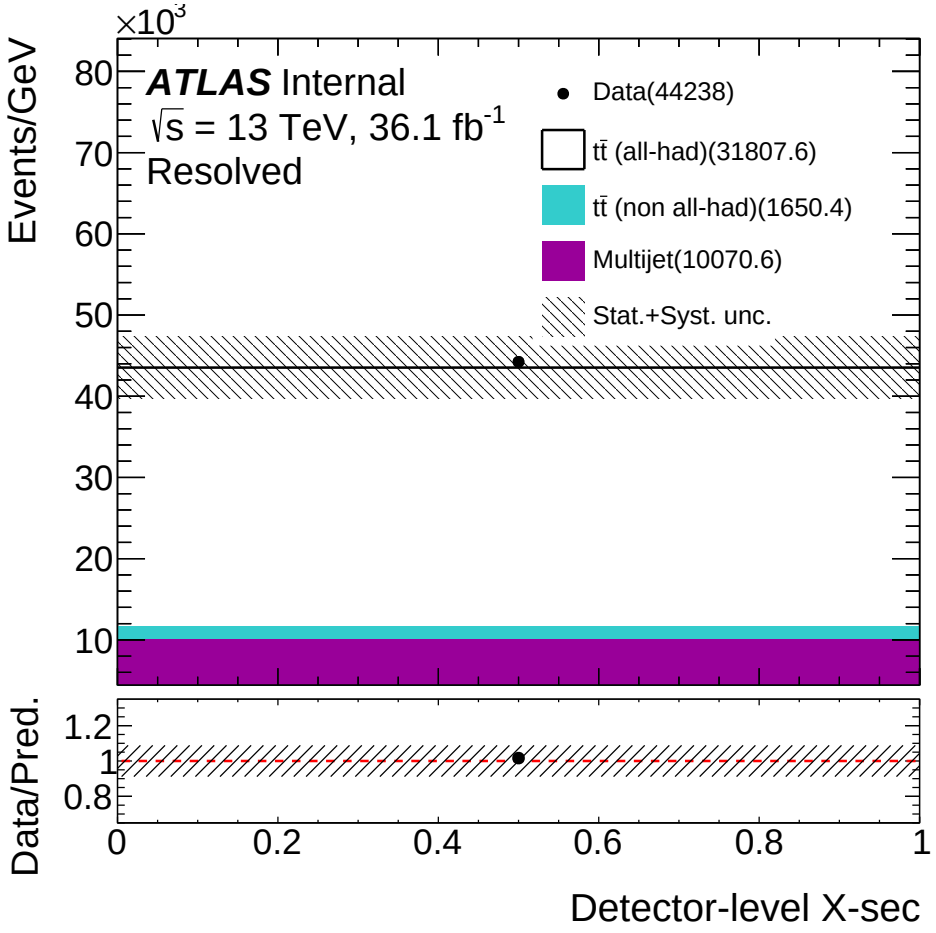

FIGURE 6.6: Reconstructed level distribution in the signal regions as a function of $\sigma_{t\bar{t}}$. The signal prediction (open histogram) is based on the Powheg+Pythia8 generator. The background is the sum of the data-driven multijet estimate (purple histogram) and the MC-based expectation for the contributions of non all-hadronic $t\bar{t}$ production process (light blue histogram). The shaded area represents the total statistical and systematic uncertainties.

bin is entirely pure (with data slightly overestimated by the MC), whereas the combinatorial ambiguities in bins with at least one additional jet contribute to enhanced background contamination. Due to trigger selection biases, the bulk of events contain 1-3 additional jets; for these bins, the background contamination may be as large as 40%, although the relative uncertainty on the total predicted yield is consistent across all jet multiplicity bins. While the total predictions are typically consistent with the data within uncertainties, some mismodelling is observed in a few distributions, notably the p_T^{top2} and $H_T^{t\bar{t}}$. These differences are further discussed in Chapter 9, when comparing the predictions with the *unfolded* data. The unfolding procedure is described in Chapter 7.

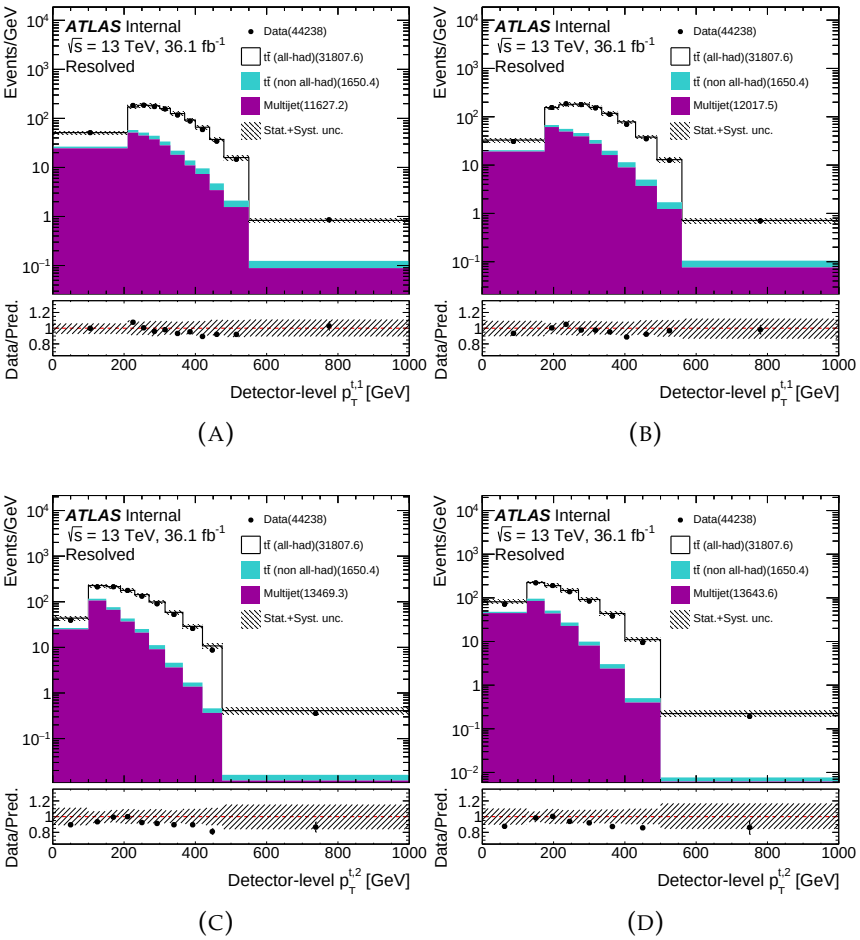

FIGURE 6.7: Reconstructed level distributions in the signal regions as a function of p_T^{top1} for particle (a) and parton level (b) optimized binning and as a function of p_T^{top2} for particle (c) and parton level (d) optimized binning. The signal prediction (open histogram) is based on the Powheg+Pythia8 generator. The background is the sum of the data-driven multijet estimate (purple histogram) and the MC-based expectation for the contributions of non all-hadronic $t\bar{t}$ production process (light blue histogram). The shaded area represents the total statistical and systematic uncertainties.

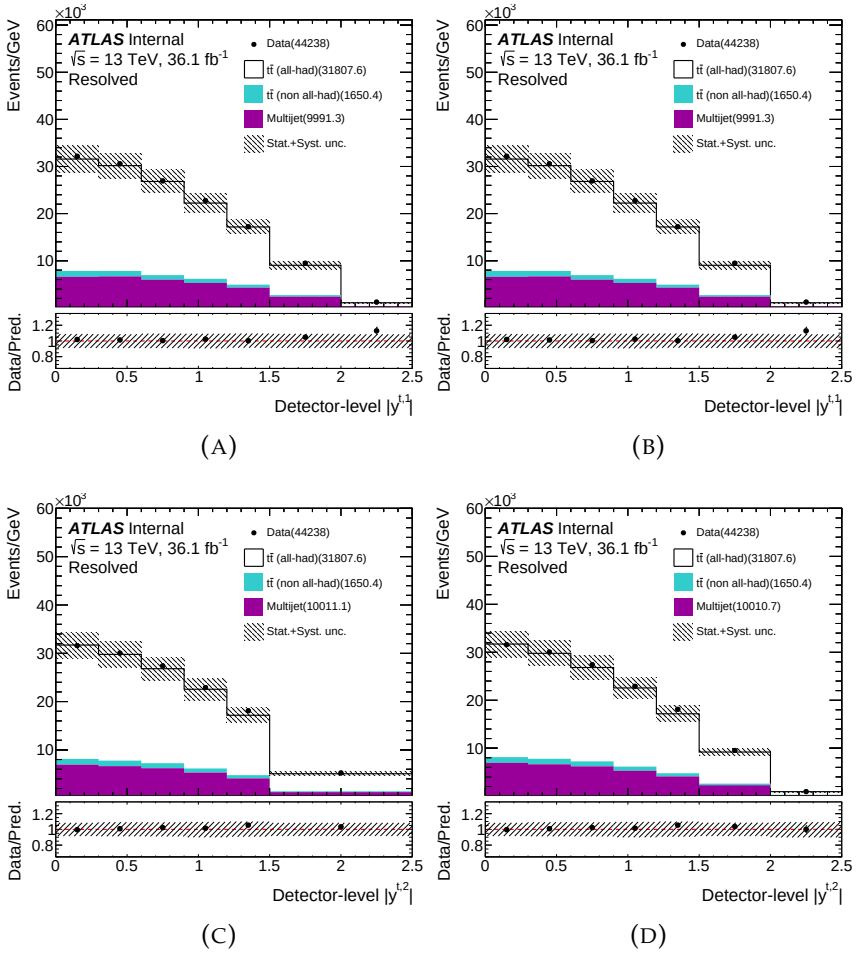

FIGURE 6.8: Reconstructed level distributions in the signal regions as a function of y_{top1} for particle (a) and parton level (b) optimized binning and as a function of y_{top2} for particle (c) and parton level (d) optimized binning. The signal prediction (open histogram) is based on the Powheg+Pythia8 generator. The background is the sum of the data-driven multijet estimate (purple histogram) and the MC-based expectation for the contributions of non all-hadronic $t\bar{t}$ production process (light blue histogram). The shaded area represents the total statistical and systematic uncertainties.

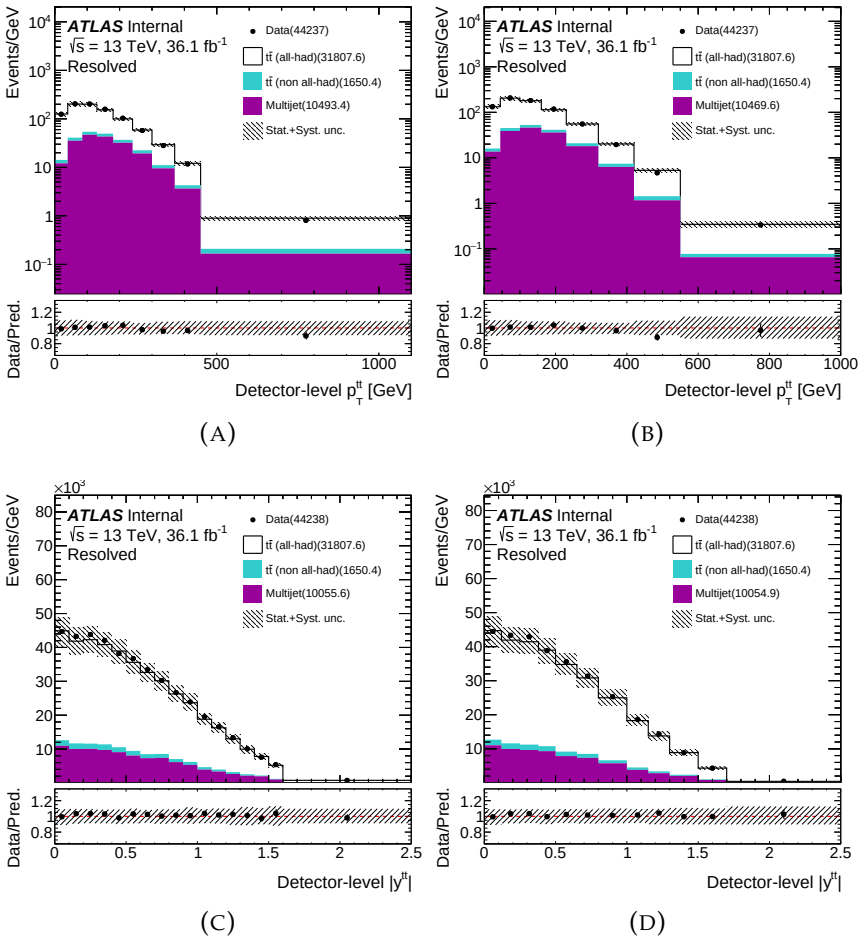

FIGURE 6.9: Reconstructed level distributions in the signal regions as a function of $p_T^{t\bar{t}}$ for particle (a) and parton level (b) optimized binning and as a function of $y_{t\bar{t}}$ for particle (c) and parton level (d) optimized binning. The signal prediction (open histogram) is based on the Powheg+Pythia8 generator. The background is the sum of the data-driven multijet estimate (purple histogram) and the MC-based expectation for the contributions of non all-hadronic $t\bar{t}$ production process (light blue histogram). The shaded area represents the total statistical and systematic uncertainties.

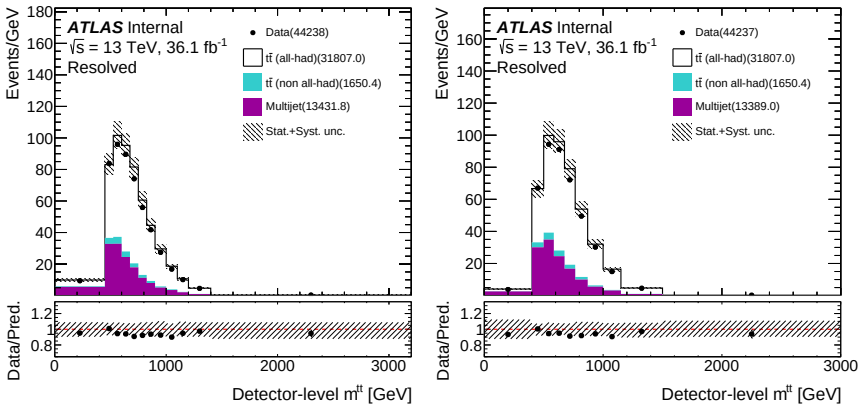

(A) (B)

FIGURE 6.10: Reconstructed level distributions in the signal regions as a function of $m_{t\bar{t}}$ for particle (a) and parton level (b) optimized binning. The signal prediction (open histogram) is based on the Powheg+Pythia8 generator. The background is the sum of the data-driven multijet estimate (purple histogram) and the MC-based expectation for the contributions of non all-hadronic $t\bar{t}$ production process (light blue histogram). The shaded area represents the total statistical and systematic uncertainties.

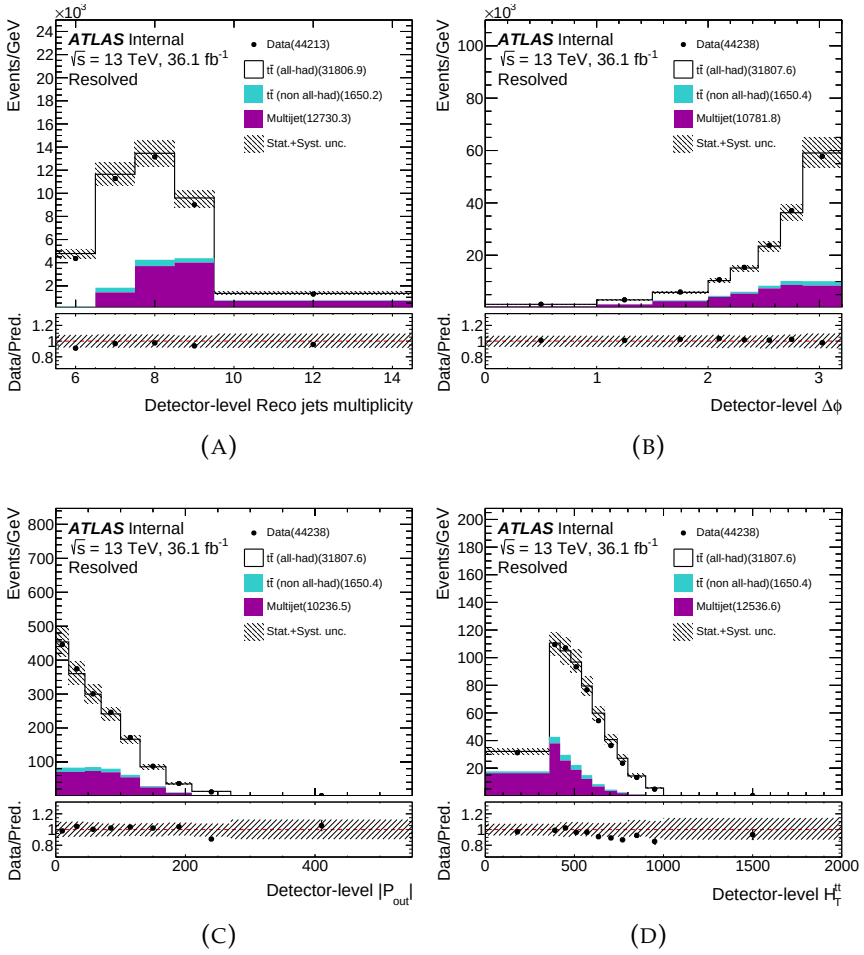

FIGURE 6.11: Reconstructed level distributions in the signal regions as a function of N_{jets} (a), $\Delta\phi_{t\bar{t}}$ (b), $|P_{\text{out}}^{t\bar{t}}|$ (c) and $H_{\text{T}}^{t\bar{t}}$ (d). The signal prediction (open histogram) is based on the Powheg+Pythia8 generator. The background is the sum of the data-driven multijet estimate (purple histogram) and the MC-based expectation for the contributions of non all-hadronic $t\bar{t}$ production process (light blue histogram). The shaded area represents the total statistical and systematic uncertainties.

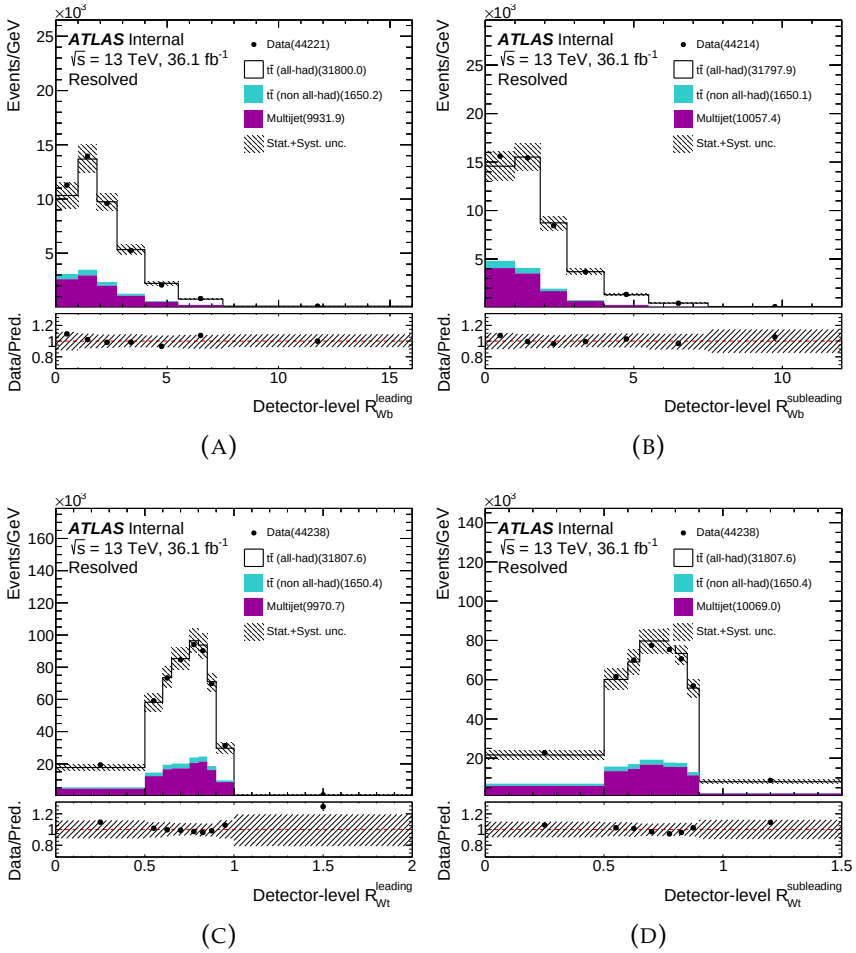

FIGURE 6.12: Reconstructed level distributions in the signal regions as a function of R_{b1}^{W} (a), R_{b2}^{W} (b), R_{t1}^{W} (c) and R_{t2}^{W} (d). The signal prediction (open histogram) is based on the Powheg+Pythia8 generator. The background is the sum of the data-driven multijet estimate (purple histogram) and the MC-based expectation for the contributions of non all-hadronic $t\bar{t}$ production process (light blue histogram). The shaded area represents the total statistical and systematic uncertainties.

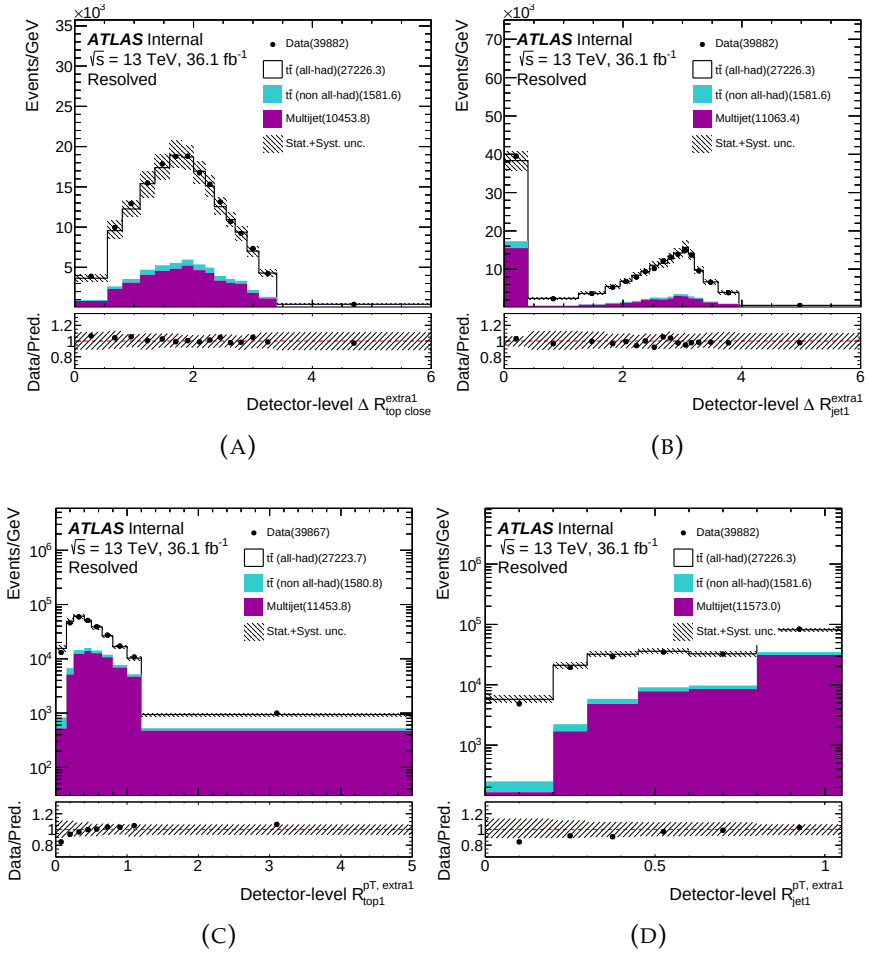

FIGURE 6.13: Reconstructed level distributions in the signal regions as a function of $\Delta R_{\text{top}}^{\text{extra1}}$ (a), $\Delta R_{\text{jet1}}^{\text{extra1}}$ (b), $R_{\text{top1}}^{\text{extra1}}$ (c) and $R_{\text{jet1}}^{\text{extra1}}$ (d). The signal prediction (open histogram) is based on the Powheg+Pythia8 generator. The background is the sum of the data-driven multijet estimate (purple histogram) and the MC-based expectation for the contributions of non all-hadronic $t\bar{t}$ production process (light blue histogram). The shaded area represents the total statistical and systematic uncertainties.

Chapter 7

Unfolding strategy

The distribution of measured spectra at reconstructed level may differ significantly from that of the corresponding *true* physical observable, due to physics and detector effects. In HEP, the most common approach to correct for these effects is through the *unfolding* procedure. Throughout this Chapter, the unfolding strategy adopted in this analysis will be discussed. After an overview of the unfolding problem, in Section 7.1, the iterative D'Agostini unfolding technique will be presented in Section 7.2. Finally, the unfolding procedure adopted in the analysis and the validation tests used to assess the stability and robustness of the unfolding in the analysis are discussed in Sections 7.3 and 7.4, respectively.

7.1 The unfolding problem

When measuring the distribution $f(x)$ of a *true* kinematical variable x, three different detector effects usually take place:

- limited acceptance: not every physic object is reconstructed by the detector. The acceptance depends on the *detector geometry* and the variable x;
- transformation: instead of x, a related quantity y is measured. This is primarly due to the non-linear detector response;
- finite resolution: the measured quantity y is smeared due to the detector finite resolution. The relation between x and y is, therefore, *statistical*.

In addition, there may be further effects of *physical nature* occurring between x and y even with an ideal detector. These effects, such as the *gluon emissions*, *radiative effects* or *hadron fragmentation*, typically takes place in the transition from *parton* to *particle* level.

The mathematical relation between the distribution $f(x)$ of the true variable x and the smeared distribution $g(y)$ of the measured quantity y is given by the Fredholm integral equation [206]:

$$g(y) = \int A(y,\, x) f(x) dx, \tag{7.1}$$

where the resolution function $A(y,\, x)$ represents the response of the detector. The problem to determine $f(x)$ from the measured function $g(y)$ is called *unfolding*, which is an inverse problem. Unfolding can be performed only if the response function $A(y,\, x)$ is known. In HEP, $f(x)$ is *discretely* distributed in histogram bins, therefore, Equation 7.1 is rewritten in the following matricial form:

$$g_j = \sum_i A_{j,i} f_i, \tag{7.2}$$

where j and i represent the bins of the reconstructed and particle (parton) level, respectively. The A matrix is generally not diagonal; this means that an event generated in the $j-th$ bin can be reconstructed in the $i-th$ one. This fenomenom is called *migration*, and its effect can be isolated by factoring out the acceptance inefficiencies of the detector from the response matrix:

$$A_{j,i} = \frac{1}{\epsilon_j} \mathscr{M}_{i,j}, \tag{7.3}$$

where ϵ_j is the detector efficiency of the reconstruction in the $j-th$ bin. The migration matrix, $\mathscr{M}_{i,j}$, expresses the probability than a selected event generated in bin j is reconstructed in bin i. It is built such that the elements in a column are normalized to unity; therefore, once the efficiency is taken into account, the probability of reconstructing a selected event in any bin is exactly one.

The unfolding problem can be summirized as the evaluation of the inverse of the migration matrix; however, this inversion problem, in real HEP measurements, can not be resolved exactly by the use of analytical methods. Several numerical techiniques to evaluate $\mathscr{M}_{i,j}$ exist, such as the *bin-by-bin inversion*, *Singular Value Decomposition*, *simple matrix inversion*, *template fit* and *iterative approaches*. More details on these techniques can be found in [207–209]. Many of these techniques leads to large fluctuations of the inverse matrix. Therefore, *regularization* conditions are introduced [210–212]. They are based on the introduction of *a priori* knowledge about the solution. The addition of a regularization term may actually introduce a bias to the final results; it is therefore important to perform tests on the stability and robustness of the method, as further discussed in Section 7.4.

7.2 The iterative D'Agostini unfolding technique

The unfolding tecnique employed in the analysis is the iterative D'Agostini one [209], as implemented in the RooUnfold framework [213]. It is based on the Bayes' Theorem, which can be expressed in terms of n_C independent causes C_i that can produce the effect E:

$$P(C_i|E) = \frac{P(E|C_i) \cdot P(C_i)}{\sum_{l=1}^{n_C} P(E|C_l) \cdot P(C_l)}. \tag{7.4}$$

The theorem states that, if we observe a single event (effect), the probability that E is caused by C_i, $P(C_i|E)$, is proportional to the probability of the cause, $P(C_i)$, times the probability of the cause to produce the effect, $P(E|C_i)$. The Bayes' theorem allows to increase the knowledge of $P(C_i)$ with the number of observations and, in principle, the *a priori* probability can be assumed uniformely distributed. On the other hand, $P(E|C_i)$ has to be evaluated with MC methods and it is not dependant on the number of observations. As it will be discussed in Chapter 8, the effect of *modelling systematic uncertainties* on the unfolded distributions is assessed by changing the definition of $P(E|C_i)$. If $n(E_j)$ events are observed for the $j-th$ effect E_j, the expected number of events assignable to each of the causes is

$$\hat{n}(C_i) = \frac{1}{\epsilon_i} \sum_{j}^{n_E} n(E_j) \cdot P(C_i|E_j), \tag{7.5}$$

where n_E is the number of possible effects and ϵ_i is the efficiency defined in 7.3. Furthermore, E_j can be identified to the measured quantity and C_i to the generated one. The same Equation can be written in terms of the migration matrix $\mathscr{M}$, making use of the Bayes' theorem:

$$\hat{n}(C_i) = \frac{1}{\epsilon_i} \sum_{j}^{n_E} n(E_j) \cdot \mathscr{M}_{i,j}, \tag{7.6}$$

$$\mathscr{M}_{i,j} = \frac{P(E_j|C_i) \cdot P(C_i)}{[\sum_{l}^{n_E} P(E_l|C_i)] \, [\sum_{l=1}^{n_C} P(E_j|C_l) \cdot P(C_l)]}, \tag{7.7}$$

where the term $\sum_{l}^{n_E} P(E_l|C_i)$ is a normalization condition to the possible effects and $P_0(C_i)$ are the initial predictions of the expected number of events in the $i-th$ bin of the particle (parton) level distribution.

The procedure is iterative in the sense that, after the first iteration, the *priors* are updated taking into account the total number of events, $\hat{N}_{true}$:

$$\begin{aligned} \hat{N}_{true} &= \textstyle\sum_{i}^{n_C} \hat{n}(C_i), \\ \hat{P}(C_i) &= \tfrac{\hat{n}(C_i)}{\hat{N}_{true}}. \end{aligned} \tag{7.8}$$

$\hat{P}(C_i)$ is the updated prior after the first iteration. The procedure can be repeated an arbitrary number of times after updating, at each step, the *priors*.

7.3 Unfolding procedure

For each spectrum, the unfolding procedure starts from the number of events at reconstruction level in bin j, N^j_{reco}. It is defined as:

$$N^j_{reco} = N^j_{reco,\,data} - N^j_{reco,\,background}, \tag{7.9}$$

where $N^j_{reco,\,data}$ denotes the number of data events at reconstructed level, in the $j-th$ bin of the distribution, passing the selection requirements of Section 6.6, while $N^j_{reco,\,background}$ indicates the background events estimated as in Section 6.7. Events are then corrected to account for the effect of the finite acceptance of the detector. The acceptance is defined as the ratio of the number of events passing both the particle (parton) level and reconstruction level selections to the number of events passing the reconstruction level selection:

$$f^j_{\text{acc}} \equiv \left(\frac{N_{\text{reco}\wedge\text{part}}}{N_{\text{reco}}} \right)^j. \tag{7.10}$$

The subscript $part$ can either refer to particle or parton level, according to the considered spectrum. This correction is applied bin-by-bin and corrects for events generated outside the fiducial (full[1]) phase-space which pass the reconstruction level selection. The resulting distribution is then unfolded to the particle (parton) level. The unfolding step uses as input a migration matrix $\mathcal{M}$, which is derived from simulated fully hadronic $t\bar{t}$ events which maps the binned particle (parton) level events to the binned reconstruction level events. The number of bins is optimised for maximum information extraction under stable unfolding conditions; an initial binnings is obtained according to the resolution and the population in each bin. For each spectra x, the RMS of $x^{particle\,(parton)} - x^{reco}$ is determined across 200 fine bins; then the fine bins are merged, starting from the leftmost, until two criteria are simultaneously reached:

- the merged bin width is greater than $\delta\cdot$ RMS, where $\delta = 2$ is a regularisation parameter;
- the merged bin population is at least $0.05 \cdot N$, where N is the number of entries for the considered spectrum.

When both of these criteria are met, the merged bin is accepted and a new bin is defined by merging starting from the next fine bin. If an accepted bin is smaller than the previous one, those bins are merged[2]. The resulting optimized binning is then validated by requiring the unfolding closure and stress tests, described in Section 7.4, are satisfied without intoducing any bias in the

[1] In the case of full phase space, the acceptance correction accounts for the events reconstruced within the kinematic range of the given variable that were generated outside of this range.

[2] For spectra characterised by high-populated tails, such as $\Delta\phi$, two bins are merged if an an accepted bin is larger than the previous one.

unfolded distributions. Finally, the efficiency correction is applied to the unfolded spectrum, correcting the result to the fiducial (full) phase-space. It is defined as the ratio of the number of events passing both the reconstructed and particle (parton) selection criteria, to the number of events passing the particle (parton) level selection:

$$\epsilon \equiv \left(\frac{N_{\text{reco}\wedge\text{part}}}{N_{\text{part}}} \right)^{j} . \tag{7.11}$$

This bin-by-bin correction accounts for the inefficiency of the reconstruction in the event.

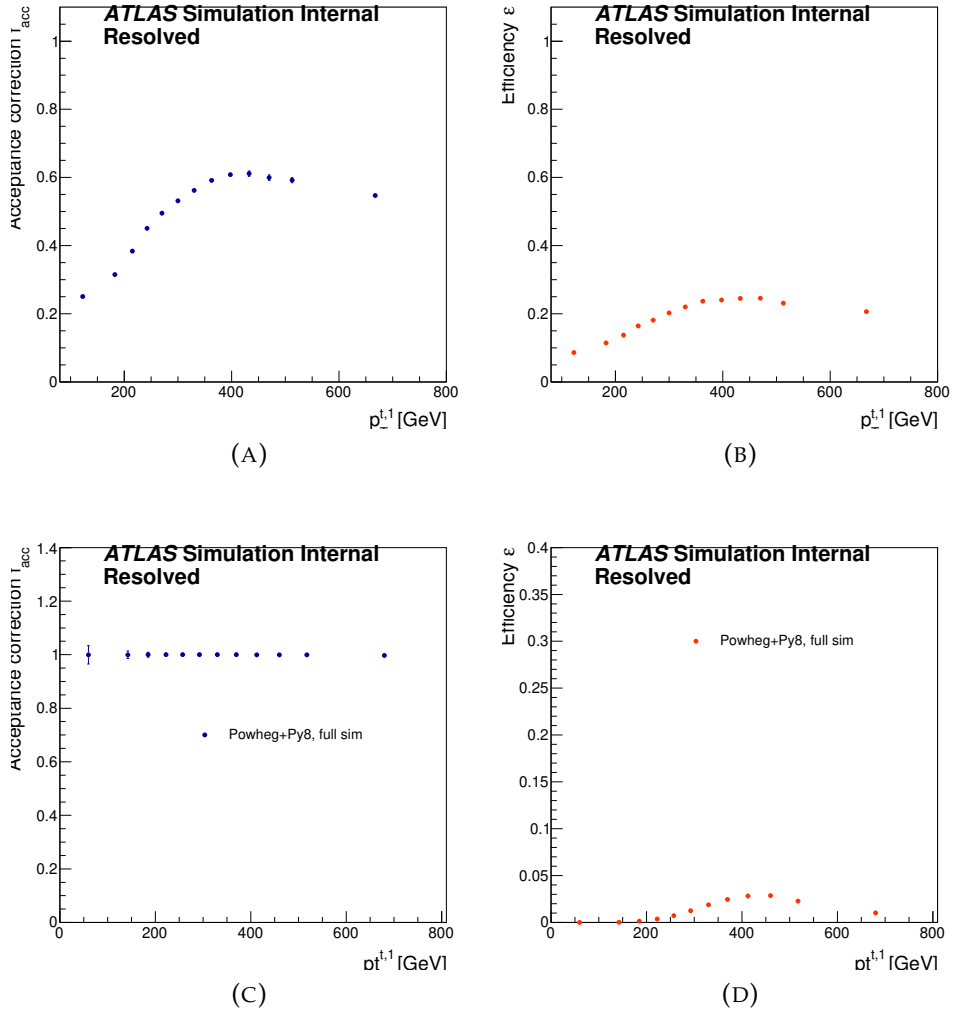

FIGURE 7.1: The acceptance and efficiency corrections for the p_T^{top1} spectrum at particle ((a) and (b), respectively) and parton level ((c) and (d), respectively). The corrections are obtained from the nominal fully hadronic $t\bar{t}$ MC sample.

The corrections and the migration matrices, collectively referred as *corrections*, for the p_T^{top1} distributions at particle and parton level are shown in Figures 7.1 and 7.2, respectively. All corrections are evaluated using the MC

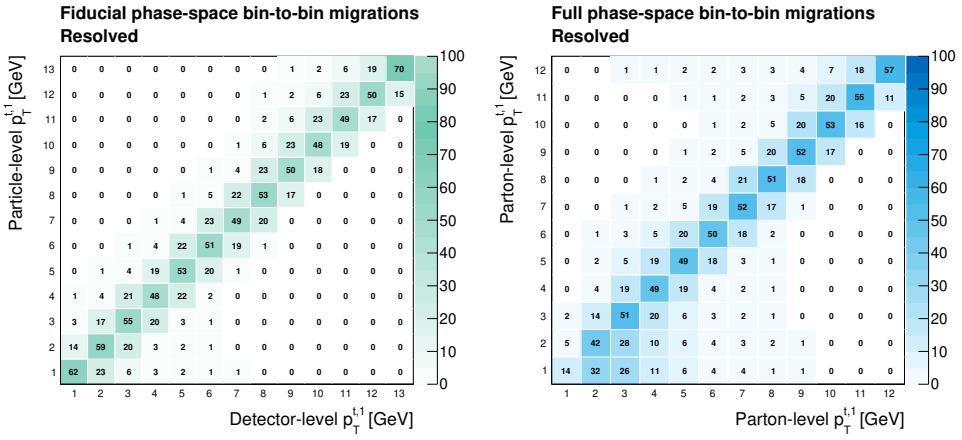

(A) (B)

FIGURE 7.2: The migration matrices from reconstruction to particle (a) and reconstruction to parton levels (b) for the p_T^{top1} spectrum. The corrections are obtained from the nominal fully hadronic $t\bar{t}$ MC sample.

simulation of the signal and are presented in Appendix E. At particle level, the acceptance increases with p_T^{top1}. The small acceptance at low-p_T is imputable to the minimum requirement on the six p_T-leading jets, while the acceptance drop at very high-p_T, observed as well in the efficiency plots, is due to the Lorentz boost of the top quarks decay products, which are no more *resolved* in ΔR. On the other hand, the parton level acceptance correction is flat at 1. This is expected, since no selection requirement is applied at parton level. The unfolding procedure for an observable X at particle (parton) level is summarised by the following expression for the absolute differential cross sections:

$$\frac{\mathrm{d}\sigma^{\text{fid (full)}}}{\mathrm{d}X^i} \equiv \frac{1}{\mathcal{L}\cdot\Delta X^i}\cdot\frac{1}{\epsilon^i}\cdot\sum_j \mathcal{M}_{ij}^{-1}\cdot f_{\text{acc}}^j\cdot\left(N_{\text{reco}}^j - N_{\text{bg}}^j\right), \tag{7.12}$$

where the index j iterates over bins of X at reconstruction level while the i index labels bins at particle (parton) level; ΔX^i is the bin width while $\mathcal{L}$ is the integrated luminosity, and the iterative unfolding procedure is symbolised by $\mathcal{M}_{ij}^{-1}$. The unfolding is performed using four iterations to balance the unfolding stability with respect to the previous iteration (below 0.1%) and the growth of the statistical uncertainty, as it will be shown in Section 7.4. The integrated fiducial (full) cross section is obtained by integrating the unfolded cross section over the bins, and its value is used to compute the normalised differential cross section:

$$\frac{1}{\sigma^{\text{fid (full)}}}\cdot\frac{\mathrm{d}\sigma^{\text{fid (full)}}}{\mathrm{d}X^i}. \tag{7.13}$$

7.4 Unfolding validation

The robustness and reliability of the iterative D'Agostini unfolding technique used in this analysis are assessed though three different tests, which will be presented in the following for a selection of observables. The complete studies are reported in Appendix F.

7.4.1 Closure tests

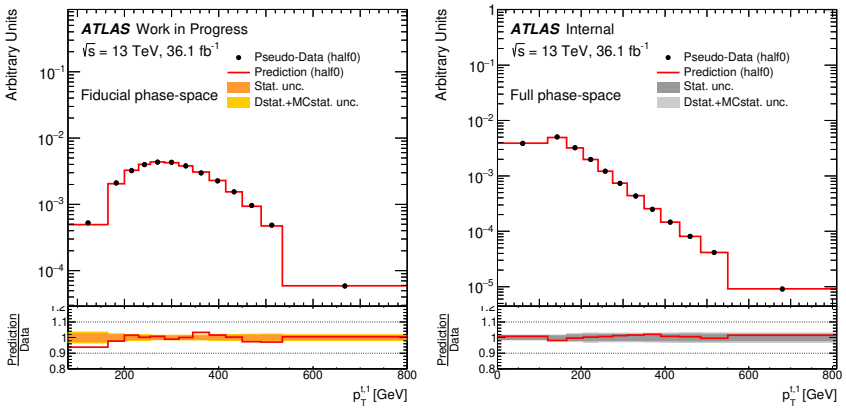

(A) (B)

FIGURE 7.3: Unfolding to particle (a) and parton (b) level closure test of the differential cross section as a function of p_T^{top1}; the observable is normalised in the fiducial phase-space. The shaded area represents the statistical uncertainty.

Closure tests are used to check if the unfolding procedure is able to correctly recover the particle (parton) level spectrum given the reconstructed spectrum. The procedure starts considering the nominal signal MC sample and splitting it into two statistically independant and orthogonal subsamples. The splitting is based on the value assumed by the *eventNumber* variable. It is an unique identification number for the event, which emulates the analougous *eventNumber* used to identify data events. Specifically, the *half-0* subsample is constituted of events with even *eventNumber*, while the *half-1* subsample by events with odd *eventNumber*. One of the subsamples is treated as pseudo-data (*half-0*) and the other one as MC signal (*half-1*). The latter is used in the evaluation of the unfolding corrections, as described in Section 7.3. Those are applied when unfolding the pseudo-data sample. The obtained unfolded pseudo-data are then compared with the corresponding particle (parton) level sub-sample, and the two distributions are found to agree within the statistical uncertainty, as shown in Figure 7.3 for p_T^{top1}.

7.4.2 Stress tests

Stress tests are performed to check whether the specific choice of the MC sample for the training of the unfolding could introduce a bias. This test is

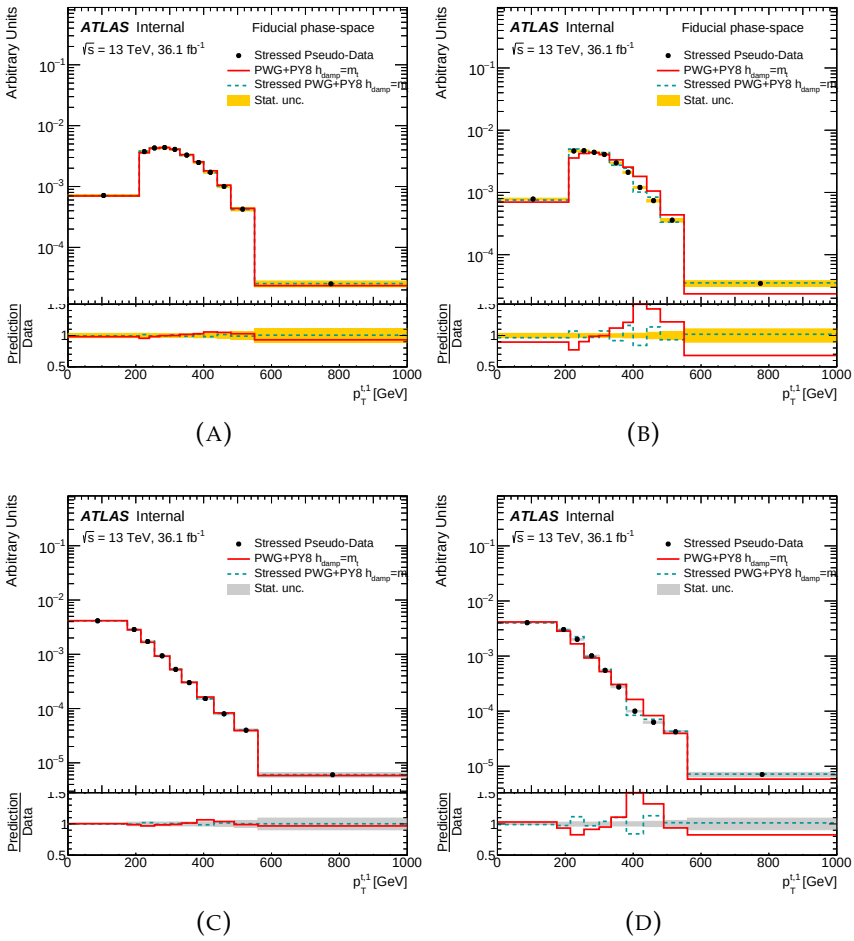

FIGURE 7.4: Linearity stress test using for the normalised cross section as a function of p_T^{top1}. The stress is achieve by re-weigthing the input distribution (red line) by a factor proportional to the data/MC difference. The particle level results have used a factor of 1 (a) or 5 (b). The corresponding parton level results are shown in (c) and (d), respectively.

done by reweighting the MC sample in order to change the shape of the distribution. This varied distribution is used as pseudo-data. The reweighted MC is then unfolded with the nominal MC response and the unfolding result is compared to the reweighted MC at particle level. Non-closure would indicate that the unfolding procedure introduces a bias towards the training particle (parton) level spectrum. The performance of the unfolding procedure is evaluated by applying a *linearity* stress, defined by reweighting the spectra according to the observed discrepancy between data and MC:

$$f(X) = k \cdot \frac{N_{\text{Observed}}(X)}{N_{\text{Expected}}(X)}, \tag{7.14}$$

where X is a generic observable, $f(X)$ is the stressing function, $N_{\text{Observed}}(X)$

is the number of events observed in data and $N_{\text{Expected}}(X)$ is the corresponding number of expected events, evaluated using MC and data-driven methods, as discussed in Chapter 6. k is an additional positive integer factor used to tune the applied stress. k has been varied from 1 to 5 with steps of 1. $f(X)$ is discrete in the sense the reweighting is applied on a bin-by-bin basis. The linearity was tested both with and without efficiency and acceptance corrections applied. Stress tests have been performed for each observable to unfold with all the reweighted shapes.

The results for the stress tests at particle and parton level for $p_T^{\text{top1}}$with $k = 1,\ 5$ are shown in Figure 7.4, where the stressed function is in red. It can be observed that, even with a strong stress applied, the unfolding procedure is able to recover the the re-weighted particle (parton) level spectrum when the re-weighted reconstructed level spectrum is unfolded using un-weighted nominal corrections.

7.4.3 Test on the number of iterations

The number of iterations chosed for the unfolding procedure is four. This choice represents the optimal compromise between the χ^2 between the unfolded result of the $i-th$ iteration and the prior of the same iteration, the residuals between the $i-th$ and the $(i-1)-th$ iterations and the corresponding statistical error. The first two are expected to decrease with increasing iterations. On the other hand, the statistical error is expected to increase, since more iterations implies a reduced regularization. This is confirmed in Figure 7.5, for the p_T^{top1}spectrum. Furthermore, the effect of varying the number of iterations by one (from 4 to 5) was found to be negligible.

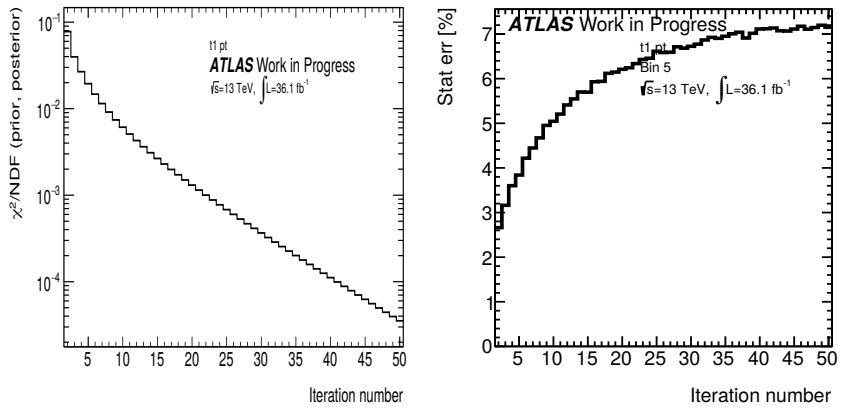

(A)

(B)

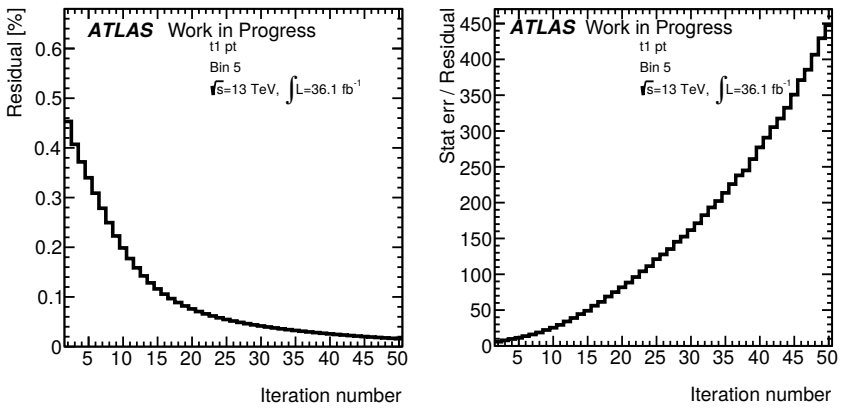

(C)

(D)

FIGURE 7.5: χ^2 (a) between the unfolded result and the prior of the $i-th$ iteration of unfolding to particle level as a function of the N_{iter} for p_T^{top1}. Figures (b), (c) and (d) show the statistical error, the residuals (w.r.t. previous iteration) and their ratio for the fifth bin of p_T^{top1}, respectively.

Chapter 8

Systematic uncertainties

The measurements of the differential cross sections are affected by different sources of systematic uncertainties:

- **detector uncertainties**: they account for the object calibration and reconstruction procedures. An overview has already been given in Chapter 5. The detector uncertainties affecting the analysis will be discussed in Section 8.1;
- **modelling uncertainties**: different MC signal models are considered to evaluate how the $t\bar{t}$ production in the fully hadronic channel simulation impacts on the measurement. These systematic sources are discussed in Section 8.2;
- **background uncertainties**: they take into account the impact of the predicted background normalization and the methods used to perform the data-driven background estimation. They are presented in Section 8.3;
- **luminosity uncertaities**: as discussed in Chapter 2, the luminosity measurement in data is affected by systematic uncertainties. They are briefly discussed in Section 8.4

The impact of each *detector* uncertainty is evaluated by varying the detector level predictions of the signal and backgrounds by one standard deviation for each source of systematic uncertainty, while *modelling* uncertainties are estimated using alternative simulations of the signal sample. At reconstructed level, *detector* and *background* uncertainties are independently propagated in the data-driven multi-jet background estimation, by subtracting the variated MC predictions or changing the definition of the validation regions. Similarly, each uncertainty is independently propagated through the unfolding procedure. The systematic uncertainties affecting the measurement are graphically presented in Section 8.5

8.1 Detector uncertainties

The uncertainties affecting object reconstruction and calibration has been widely discussed in Chapter 5. In this Section, the detector uncertainties

affecting the final measurement are briefly described. Each systematic uncertainty was evaluated before the unfolding procedure. Deviations from the nominal predictions were evaluated separately for the upward and downward variations, whenever available, for each bin of each observable. In the case of a single variation, the uncertainty is estimated by symmetrising the single deviation. The final systematics are evaluated by unfolding the varied MC reconstructed level spectra with nominal corrections and comparing the unfolded result to the particle (parton) level distribution of the nominal MC sample. These uncertainties affects the signal, MC-based background and the data-driven multi-jet background estimation, since, for each systematic source, the nominal MC predictions are replaced by the variated ones, leading to a different multi-jet background estimation.

8.1.1 Jet reconstruction

As discussed in Section 5.7, the uncertainties due to jet JES calibration were estimated by varying the jet energies according to the uncertainties derived from simulation and in-situ calibration measurements using the category reduction model. The uncertainty due to the difference in jet-energy resolution (JER) between the data and MC events was evaluated by smearing the MC jet transverse momentum according to the jet resolution as a function of the jet p_T and η [214]. Given the fully hadronic final state, the JES modelling systematics are the largest experimental systematic uncertainties, contributing at the 5–10% level, while the JER systematics are usually at the level of 1%, except where inflated by the statistical uncertainties.

8.1.2 b-tagging

The systematic uncertainties associated with tagging jets originating from b-quarks, as discussed in Section 5.8, are estimated from data and parametrised as a function of p_T and η. The systematic uncertainties arise from factors used to correct the differences between the simulation and data in dileptonic $t\bar{t}$ events. In the measurement, while the light-jet tagging efficiency systematics are generally sub-percent, the b-tagging efficiency systematics can grow as large as 5%.

8.1.3 Lepton reconstruction

The uncertainties related to the MC modelling of the lepton energy or momentum scale and resolution were estimated from $Z \to ee/\mu\mu$, $J/\psi \to ee/\mu\mu$, and $W \to e\nu$, as briefly discussed in Sections 5.4 and 5.5. These uncertainties are found to be negligible in the analysis presented in this thesis, given the high efficiency of the lepton veto.

8.1.4 τ reconstruction

The uncertainties related to the τ reconstruction are derived from MC simulations, as overviewed in Section 5.6. As for the electrons and muons, these uncertainties have been found to be completely negligible in this measurement.

8.1.5 E_T^{miss} reconstruction

As widely discussed in Section 5.9, the E_T^{miss} uncertainties arise from the propagation of the hard-objects uncertainties in the E_T^{miss} hard-term, while the E_T^{miss} soft-term uncertainties are evaluated from $Z \to ll$ topologies. Since no E_T^{miss} selection is applied in the analysis, the corresponding uncertainties are found to be negligible.

8.2 Modelling uncertainties

For signal modelling systematic uncertainties, alternative samples are compared to the nominal MC sample, where both samples are simulated with AFII due to the high CPU cost of full simulation. The complete list of the alternative samples has been already reported in Section 4.4. Since those source of uncertainties account for the differences arising from a different simulation of the nominal $t\bar{t}$ samples, their impact is evaluated treating the alternative simulation as pseudo-data and unfolding the resulting spectra using the corrections from the nominal AFII sample. The unfolded result is then compared to the particle (parton) level spectrum of the corresponding alternative MC sample. The uncertainty is quoted as the symmetrised relative difference between the two.

8.2.1 Matrix element and parton shower models

The impact of different NLO matrix element calculations and parton shower models in $t\bar{t}$ simulated events is assessed through different settings of Powheg and MadGraph5_aMC@NLO with various parton shower algorithms. The uncertainty due to the choice of matrix element generator is determined by unfolding a MadGraph5_aMC@NLO+Pythia8 sample using corrections and response matrices from the nominal Powheg+Pythia8 sample. The unfolded result is then compared to the particle (parton) level spectrum of the MadGraph5_aMC@NLO+Pythia8 sample. The resulting relative uncertainty is used as the systematic uncertainty from the matrix element generator.

Analougously, the uncertainty due to the choice of fragmentation model is determined by unfolding a Powheg+Herwig7 sample using corrections and response matrices from the nominal sample and comparing the unfolded result to the particle (parton) level spectrum of the Powheg+Herwig7 sample. The resulting systematic uncertainties strongly depend on the variable and the bin. The most significant components are the matrix element and parton

shower variations, which may be as large as 30%, although for most distributions they are a few percent.

8.2.2 Initial and Final State Radiation

The amount of ISR/FSR changes the number of jets in the event as well as the transverse momentum of the $t\bar{t}$ system. In order to evaluate the uncertainty linked to the modelling of the IFSR, $t\bar{t}$ MC samples with modified IS-FSR modelling were used. The alternative samples are generated similarly to the nominal one, except for the choice of tune, scales μ ($\mu_R = \mu_F \doteq \mu$) and h_{damp}, which are particularly sensitive to the amount of QCD radiation:

- **RadHigh**: μ is scaled by 0.5 ($\mu^{Hi} = 0.5 \cdot \mu$), h_{damp} is set to $3 \cdot m_{top}$ and the *radHi* A14 tune is used;
- **RadLow**: μ is scaled by 2 ($\mu^{Low} = 2 \cdot \mu$), h_{damp} is set to the nominal $1.5 \cdot m_{top}$ value and the *radLo* A14 tune is used.

In each case, the spectrum unfolded using the nominal corrections was compared to the particle (parton) level spectrum of the corresponding IFSR sample. Being at the level of a few percent for most bins, the IFSR variations are at most comparable to the parton shower and matrix element uncertainties.

8.2.3 PDF

The impact of the choice of different PDF sets has been assessed using the 30 PDF set of the PDF4LHC15 prescription, as described in Section 1.7.2 . The effect of a different PDF choice modifies the correction use in the unfolding procedure and, potentially, also the migration matrix. The PDF choice effect has been evaluated by unfolding the nominal Powheg+Pythia8 sample reweighted to account for the effect of different PDFs. The PDF uncertainties arising from the 30 variations were combined to define a relative uncertainty as:

$$\delta_{\text{pdf}} \equiv \frac{\sqrt{\sum_{i=1}^{30} \left(U_i \cdot R_0 - T_0\right)^2}}{T_0}, \tag{8.1}$$

where the 0 (i) subscripts denotes the PDF4LHC15 central (varied) PDF set, R represents the distribution at the detector level while T symbolizes the distribution at the particle or parton level, and the unfolding procedure is shortened into the U factor, with subscript on each characterizing the PDF set used to evaluate the spectrum or the corrections. The resulting uncertainties are found to be at the sub-percent level, with few excesses to 1% or 2% in low-statistics bins.

8.2.4 MC sample finite statistics

To account for the limited statistics of the signal sample, pseudo experiments are used to evaluate the impact of finite statistics. The number of events in each bin is smeared by a Gaussian shift with mean equal to the yield of the bin, and standard deviation equal to the statistical uncertainty of the bin, defined as the square root of the sum of the squared weights of the events in the bin. The smeared spectrum is unfolded. The procedure is replicated 10000 times, then the final statistical uncertainty is evaluated from the average over the 10000 toys. The resulting systematic uncertainty was found to be typically below 0.5%, increasing up to 2% in the tails of some distributions.

8.3 Background uncertainties

The background estimation is affected by various systematic uncertainties, that can be due to the MC modelling or, in case of the data-driven estimate, to the specifc method employed. The background uncertainties are propagated through the unfolding procedure as for the detector-related uncertainties. The unfolded distributions are then compared with the nominal particle (parton) level predictions and the size of the uncertainty is considered as the relative shift between the two.

8.3.1 $t\bar{t}$ normalization

The predicted $t\bar{t}$ production cross section has been calculated with the Top++2.0 program [215] to NNLO+NNLL order and assuming a top-quark mass of 172.5 GeV. The calculation is affected by three different sources of systematic uncertainties:

$$\sigma_{t\bar{t}} = 831.76^{+19.77}_{-29.20}\,(\text{scale}) \pm 35.06\ (\text{PDF} + \alpha_S)\,^{+23.18}_{-22.45}\,(\text{mass})\ \text{pb}. \tag{8.2}$$

The first uncertainty comes from the independent variation of the factorisation and renormalisation scales, μ_F and μ_R. The second one is associated to variations in the PDF and α_S, following the PDF4LHC prescriptions, similarly to what has been described in Subsection 8.2.3, and the third is associated to a variation of ± 1 GeV to m_t.

8.3.2 Data-driven multi-jet estimation

Two different sources of uncertainty affecting the multi-jet background estimation have been considered. The first is related to the finite number of events used in the evaluation of the background. This uncertainty is treated in the same way as the MC sample finite statistics, presented in 8.2.4. The second component represents the intrinsic error of the ABCD method employed for the background estimation. The same procedure described in Section 6.7 is repeated using the 0 b-tagged jet regions instead the 1 b-tagged jets regions

as validation regions. The two background predictions are used in the background subtraction step of the unfolding. The background systematic error is given by the difference between the unfolded distributions in the two scenarios. Those two sources of uncertainties are generally comparable, and normally below 5%.

8.4 Luminosity uncertainties

The uncertainty in the combined 2015+2016 integrated luminosity is 2.1%. It is derived, as discussed in Subsection 1.7.3, from a calibration of the luminosity scale using x-y beam-separation scans performed in August 2015 and May 2016.

8.5 Uncertainties affecting the measurement

In this Section, the breakdown of the different sources of systematic uncertainties is displayed for all the measured spectra. In particular, the particle level fractional uncertainties plots are shown in Subsection 8.5.1, while the parton level ones are shown in Subsection 8.5.2. In both cases, they are shown for the absolute and normalised differential cross sections. The corresponding tables can be found in the Appendix D. In almost all cases, the dominant systematics are observed to be one of the following:

- Jet energy scale/resolution: usually dominant in the bulk of distributions;
- Hard scatter, hadronisation or IFSR and PDF variations: usually affects tails of distributions;
- Background estimation systematics: mostly relevant in a small number of bins with larger than usual background contamination.

8.5.1 Systematics breakdown, particle level

In this Subsection, the particle level fractional uncertainties plots are shown (Figures 8.1 – 8.19). In general, the JES/JER and the modelling uncertainties are the dominant ones. The total uncertainties for most spectra is at 20% level for absolute distrubutions, which is reduced to about 15% for the relative ones. The uncertainty sources which exibit the largest reduction are the background and the $t\bar{t}$ normalization ones. It can be noted that low-statistic bins are characterized by large modelling uncertainties (up to 40%).

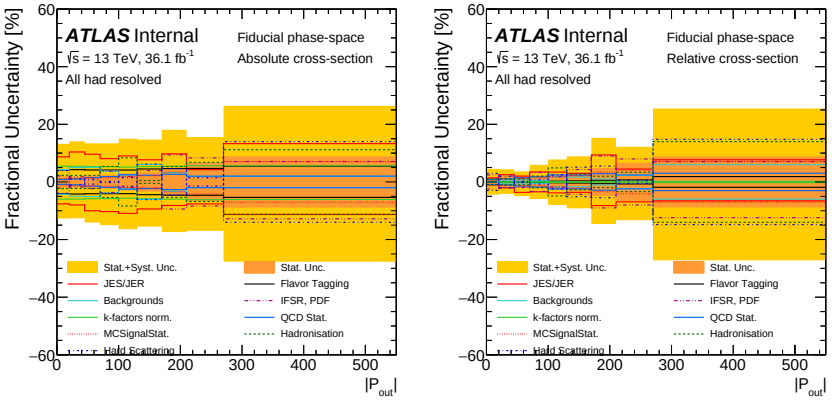

(A) (B)

FIGURE 8.1: Fractional uncertainties in the fiducial phase space as a function of $|P_{\text{out}}^{t\bar{t}}|$: absolute (a) and normalised (b). The shaded area represents the total statistical and systematic uncertainties.

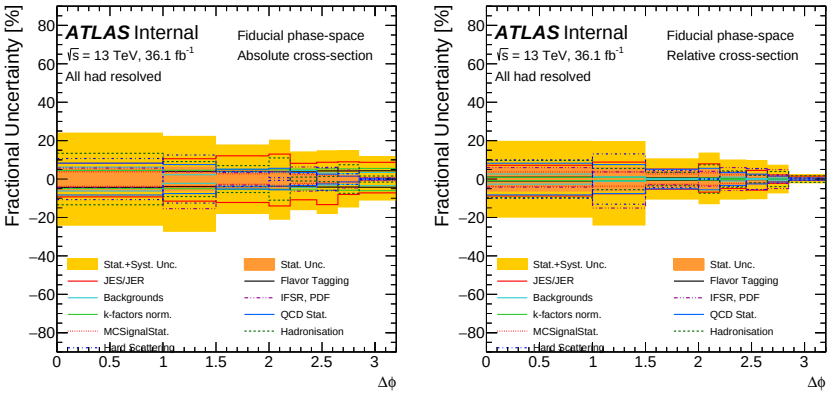

(A) (B)

FIGURE 8.2: Fractional uncertainties in the fiducial phase space as a function of $\Delta\phi_{t\bar{t}}$: absolute (a) and normalised (b). The shaded area represents the total statistical and systematic uncertainties.

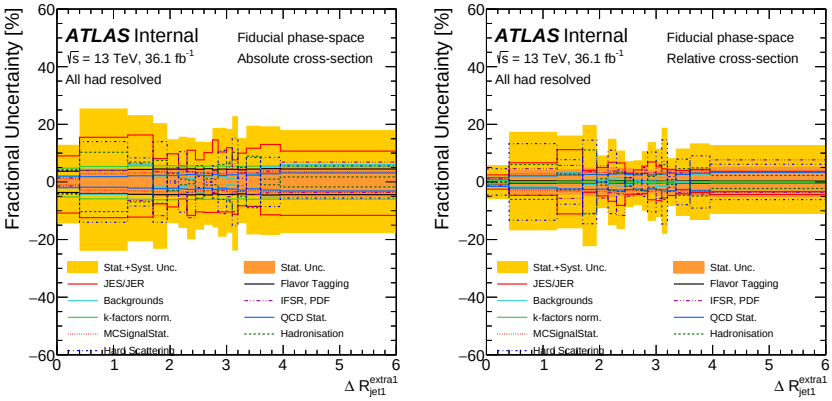

(A) (B)

FIGURE 8.3: Fractional uncertainties in the fiducial phase space as a function of $\Delta R_{\mathrm{jet1}}^{\mathrm{extra1}}$: absolute (a) and normalised (b). The shaded area represents the total statistical and systematic uncertainties.

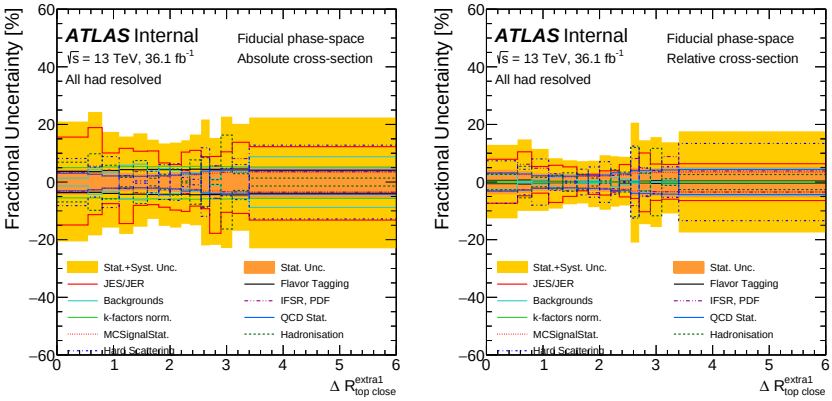

(A) (B)

FIGURE 8.4: Fractional uncertainties in the fiducial phase space as a function of $\Delta R_{\mathrm{topclose}}^{\mathrm{extra1}}$: absolute (a) and normalised (b). The shaded area represents the total statistical and systematic uncertainties.

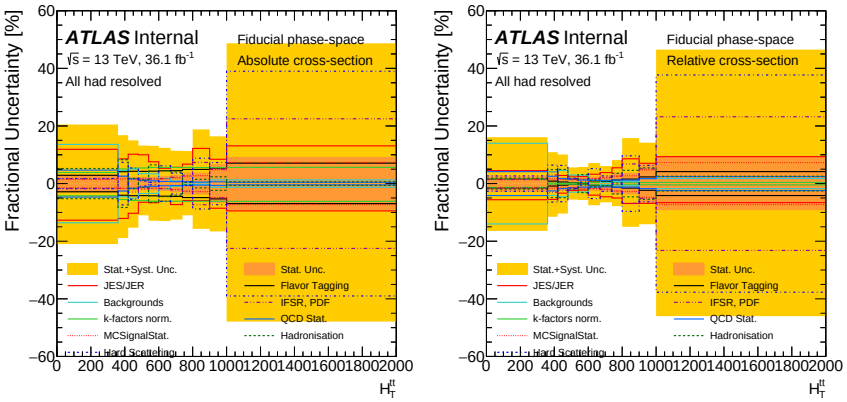

(A) (B)

FIGURE 8.5: Fractional uncertainties in the fiducial phase space as a function of $H_{\mathrm{T}}^{t\bar{t}}$: absolute (a) and normalised (b). The shaded area represents the total statistical and systematic uncertainties.

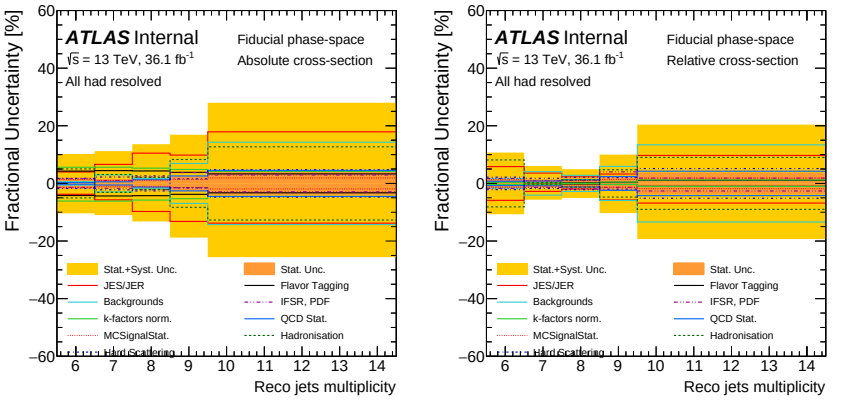

(A) (B)

FIGURE 8.6: Fractional uncertainties in the fiducial phase space as a function of number of jets: absolute (a) and normalised (b). The shaded area represents the total statistical and systematic uncertainties.

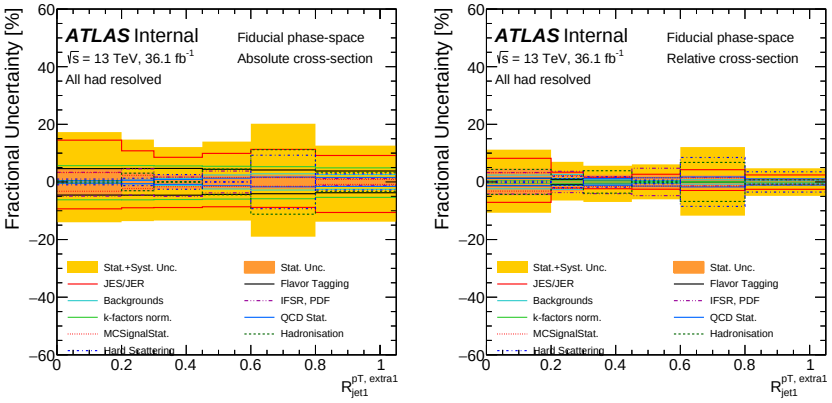

(A) (B)

FIGURE 8.7: Fractional uncertainties in the fiducial phase space as a function of $R_{\mathrm{jet1}}^{\mathrm{extra1}}$: absolute (a) and normalised (b). The shaded area represents the total statistical and systematic uncertainties.

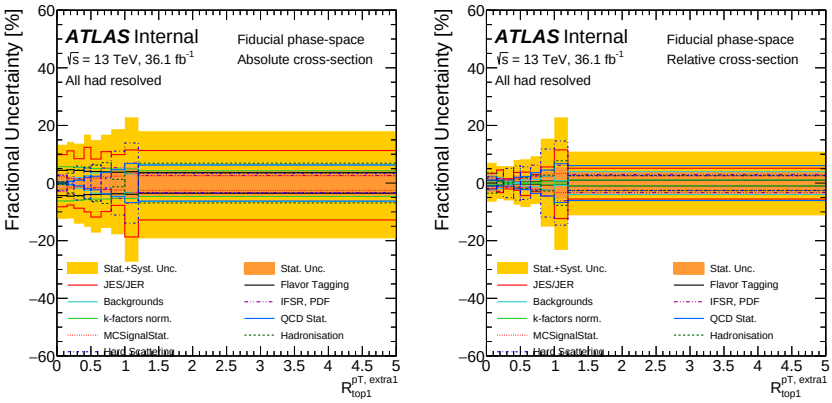

(A) (B)

FIGURE 8.8: Fractional uncertainties in the fiducial phase space as a function of $R_{\mathrm{top1}}^{\mathrm{extra1}}$: absolute (a) and normalised (b). The shaded area represents the total statistical and systematic uncertainties.

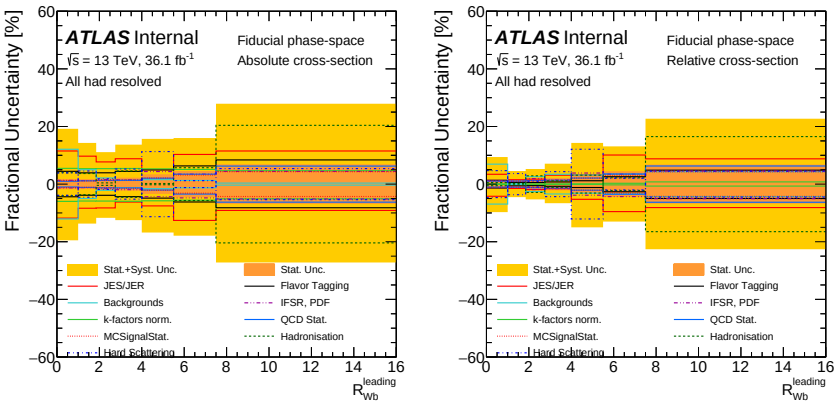

(A) (B)

FIGURE 8.9: Fractional uncertainties in the fiducial phase space as a function of $R_{Wb}^{leading}$: absolute (a) and normalised (b). The shaded area represents the total statistical and systematic uncertainties.

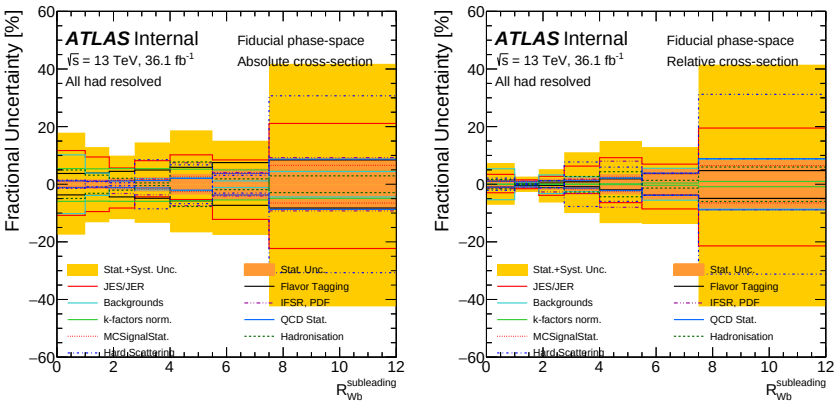

(A) (B)

FIGURE 8.10: Fractional uncertainties in the fiducial phase space as a function of $R_{Wb}^{subleading}$: absolute (a) and normalised (b). The shaded area represents the total statistical and systematic uncertainties.

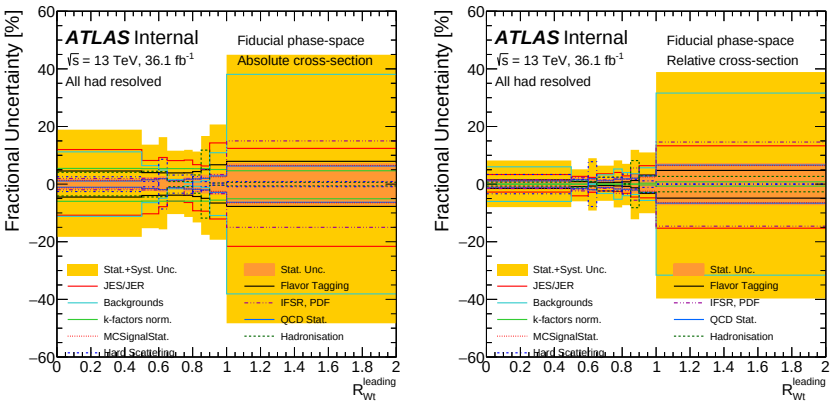

(A) (B)

FIGURE 8.11: Fractional uncertainties in the fiducial phase space as a function of $R_{Wt}^{leading}$: absolute (a) and normalised (b). The shaded area represents the total statistical and systematic uncertainties.

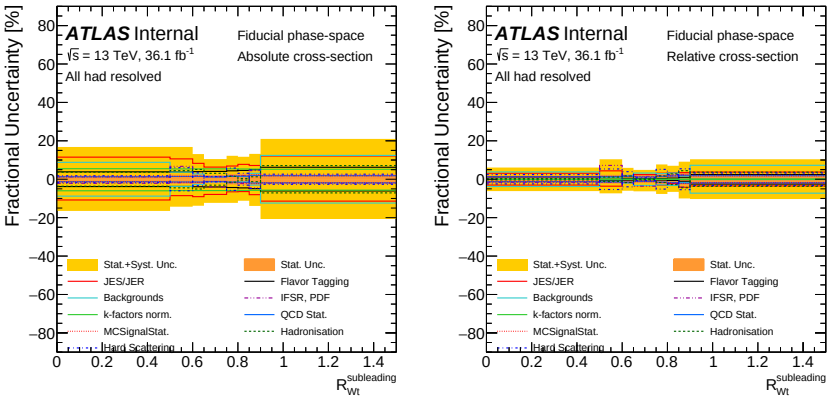

(A) (B)

FIGURE 8.12: Fractional uncertainties in the fiducial phase space as a function of $R_{Wt}^{subleading}$: absolute (a) and normalised (b). The shaded area represents the total statistical and systematic uncertainties.

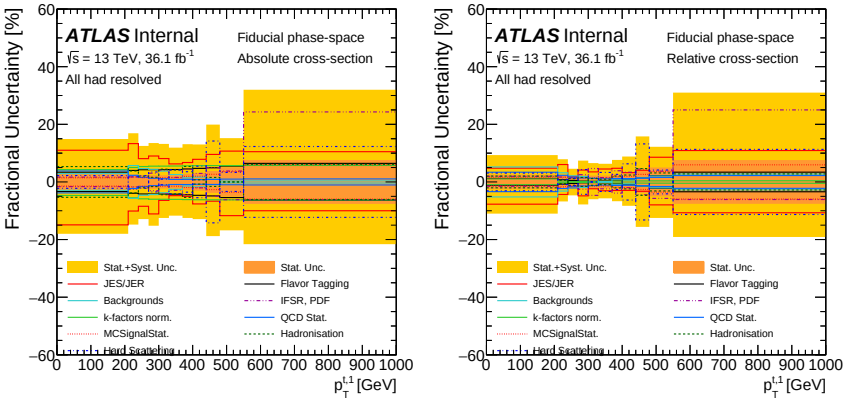

(A) (B)

FIGURE 8.13: Fractional uncertainties in the fiducial phase space as a function of p_T^{top1}: absolute (a) and normalised (b). The shaded area represents the total statistical and systematic uncertainties.

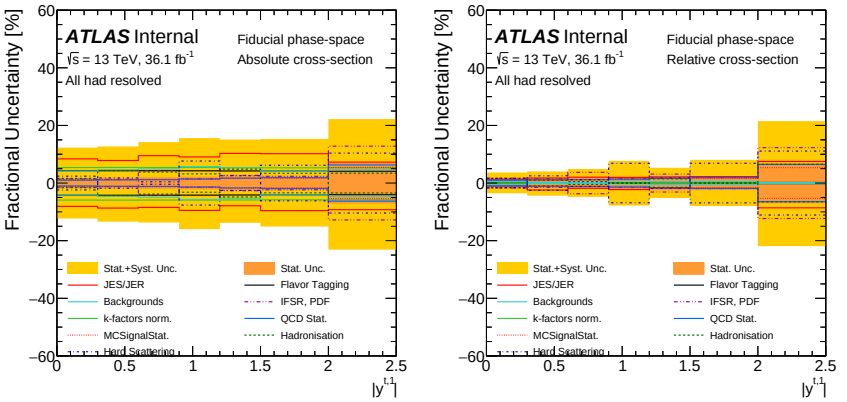

(A) (B)

FIGURE 8.14: Fractional uncertainties in the fiducial phase space as a function of y_{top1}: absolute (a) and normalised (b). The shaded area represents the total statistical and systematic uncertainties.

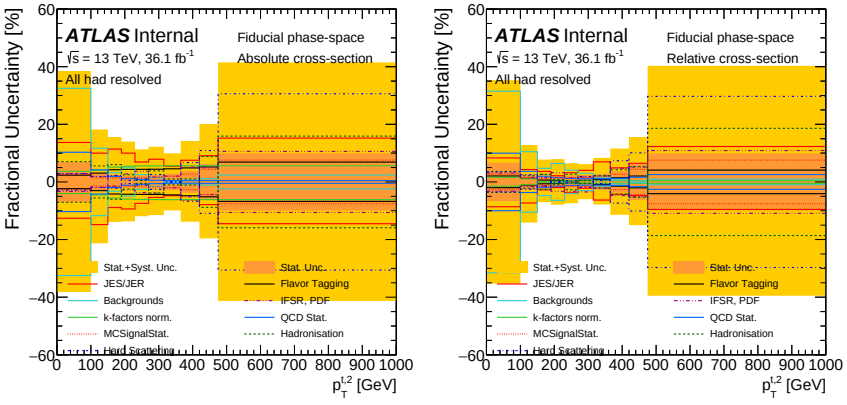

(A) (B)

FIGURE 8.15: Fractional uncertainties in the fiducial phase space as a function of p_T^{top2}: absolute (a) and normalised (b). The shaded area represents the total statistical and systematic uncertainties.

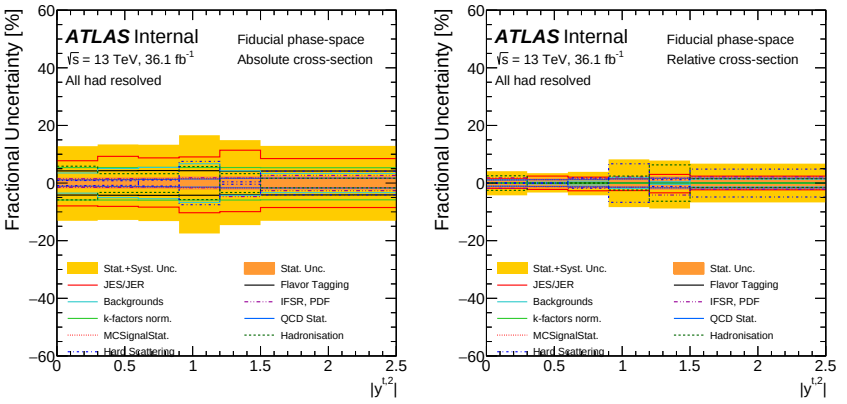

(A) (B)

FIGURE 8.16: Fractional uncertainties in the fiducial phase space as a function of y_{top2}: absolute (a) and normalised (b). The shaded area represents the total statistical and systematic uncertainties.

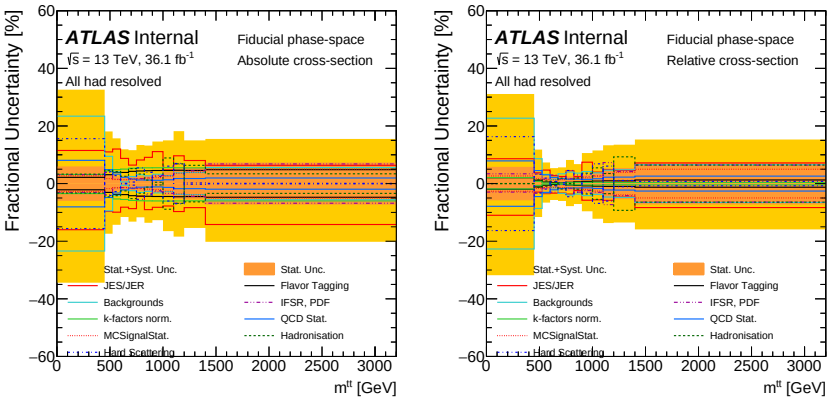

(A) (B)

FIGURE 8.17: Fractional uncertainties in the fiducial phase space as a function of $m_{t\bar{t}}$: absolute (a) and normalised (b). The shaded area represents the total statistical and systematic uncertainties.

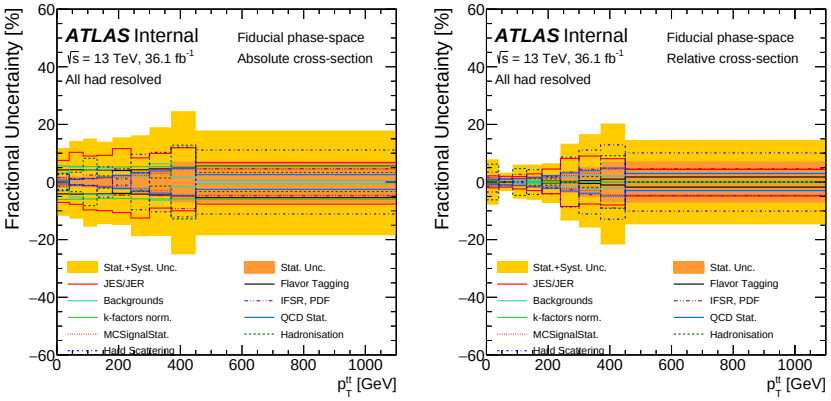

(A) (B)

FIGURE 8.18: Fractional uncertainties in the fiducial phase space as a function of $p_T^{t\bar{t}}$: absolute (a) and normalised (b). The shaded area represents the total statistical and systematic uncertainties.

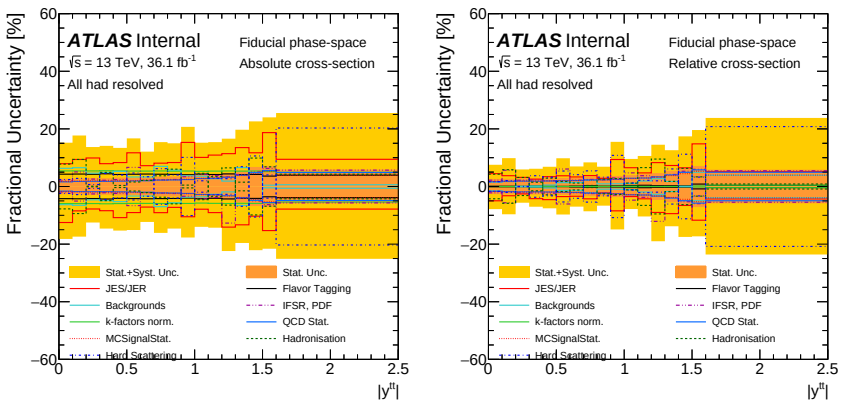

(A) (B)

FIGURE 8.19: Fractional uncertainties in the fiducial phase space as a function of $y_{t\bar{t}}$: absolute (a) and normalised (b). The shaded area represents the total statistical and systematic uncertainties.

8.5.2 Systematics breakdown, parton level

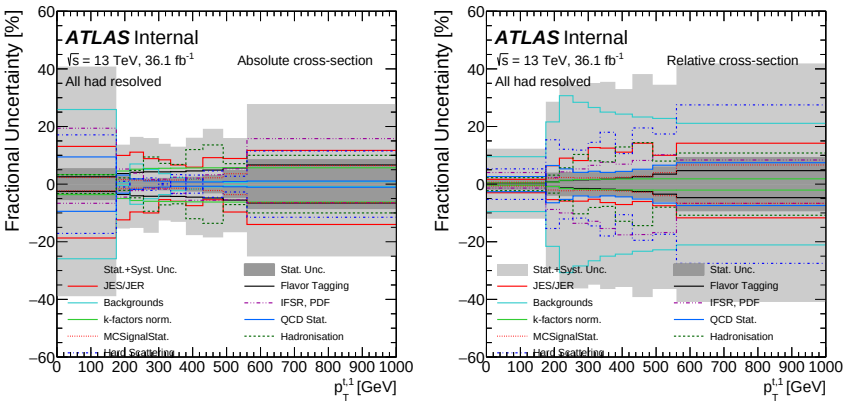

(A) (B)

FIGURE 8.20: Fractional uncertainties in the full phase space as a function of p_T^{top1}: absolute (a) and normalised (b). The shaded area represents the total statistical and systematic uncertainties.

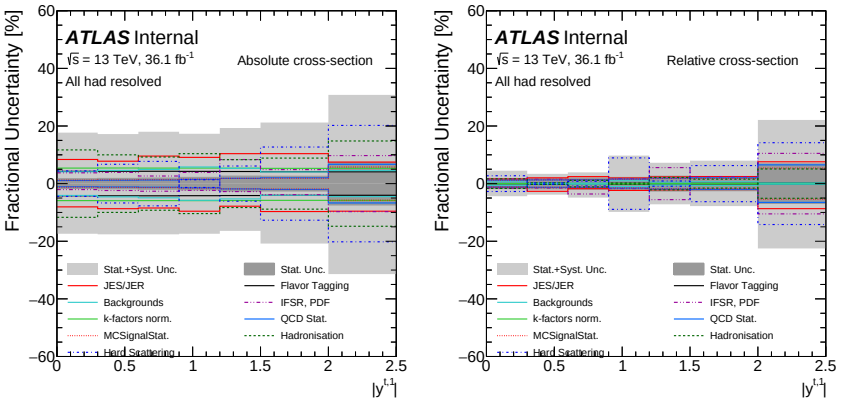

(A) (B)

FIGURE 8.21: Fractional uncertainties in the full phase space as a function of y_{top1}: absolute (a) and normalised (b). The shaded area represents the total statistical and systematic uncertainties.

This Subsection shows the parton level fractional uncertainties plots (Figures 8.20 – 8.26). The same considerations for the particle level results hold also at parton level, being the leading source of systematics the JES/JER and the modelling. The total uncertanties for most spectra is at the 20% level for both absolute and relative spectra. This is due to the amplification of the background uncertainties after the normalization procedure. At the time of writing, this is still being investigated.

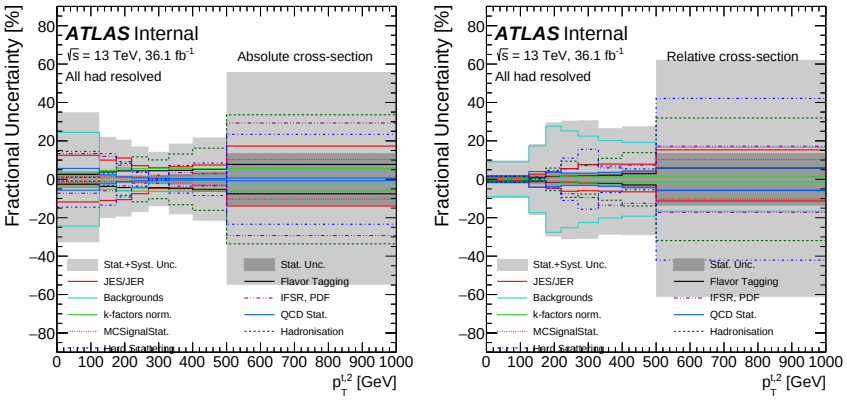

(A) (B)

FIGURE 8.22: Fractional uncertainties in the full phase space as a function of p_T^{top2}: absolute (a) and normalised (b). The shaded area represents the total statistical and systematic uncertainties.

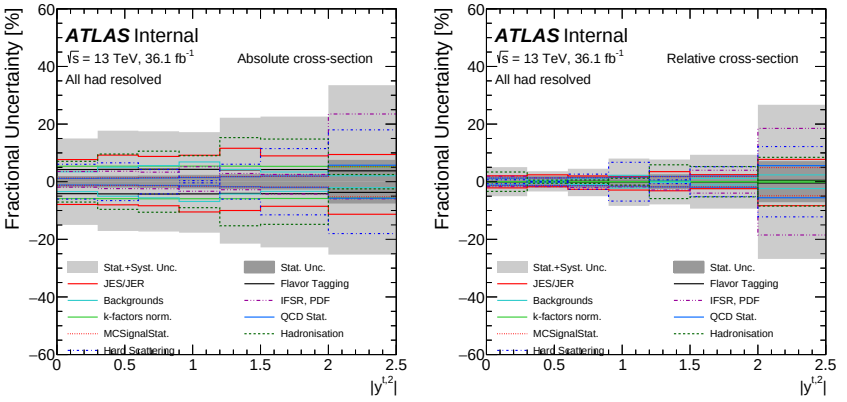

(A) (B)

FIGURE 8.23: Fractional uncertainties in the full phase space as a function of y_{top2}: absolute (a) and normalised (b). The shaded area represents the total statistical and systematic uncertainties.

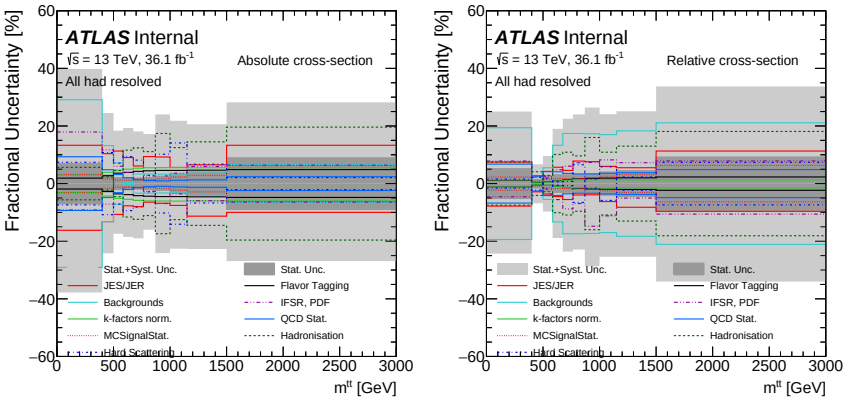

(A) (B)

FIGURE 8.24: Fractional uncertainties in the full phase space as a function of $m_{t\bar{t}}$: absolute (a) and normalised (b). The shaded area represents the total statistical and systematic uncertainties.

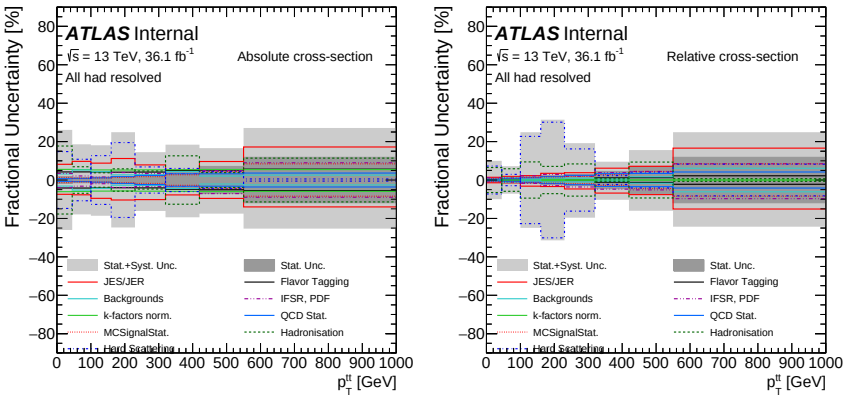

(A) (B)

FIGURE 8.25: Fractional uncertainties in the full phase space as a function of $p_T^{t\bar{t}}$: absolute (a) and normalised (b). The shaded area represents the total statistical and systematic uncertainties.

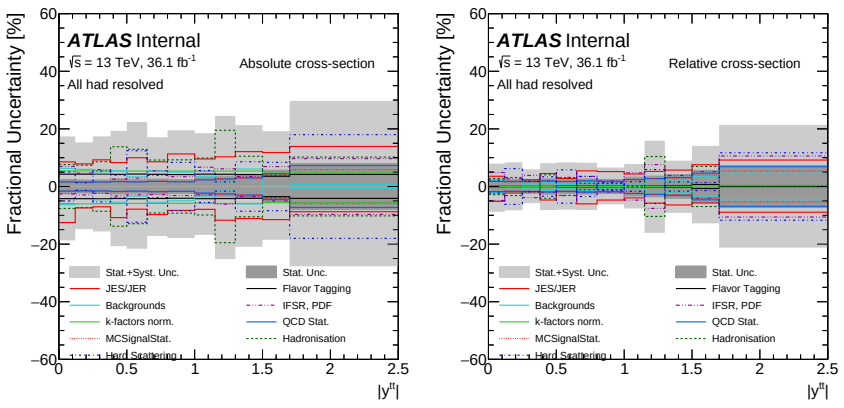

(A) (B)

FIGURE 8.26: Fractional uncertainties in the full phase space as a function of $y_{t\bar{t}}$: absolute (a) and normalised (b). The shaded area represents the total statistical and systematic uncertainties.

Chapter 9

Results

In this Chapter, the measured cross sections unfolded at particle and parton level are compared with several theoretical predictions. Those differ for the ME calculation, PS algorithms and fragmentation models. The comparisons are presented, both for absolute and relative cross sections, in Section 9.1. While the former carry the additional information on the predicted total cross section, either measured in data or theoretically predicted, the latter feature a significant reduction of those systematic uncertainties that are highly correlated across the kinematic bins. Furthermore, the χ^2 values are presented in order to quantify the level of agreement between the measured distributions and the different theoretical predictions.

9.1 Unfolded distributions

In this Section, the unfolded results for all the spectra defined in Section 6.2 are reported. In particular, the particle level results are shown, for the absolute and normalized differential cross section, in Subsection 9.1.1, while the parton level results are reported in Subsection 9.1.2. Each of the presented Figures contains two pads reporting prediction over data ratios; in the first the nominal Powheg+Pythia8 prediction is compared with the alternative ME and Sherpa2.2 samples, while the second pad the nominal sample is compared with the alternative fragmentation model and ISFR samples. In general, a good agreement between the different prediction and the unfolded data is observed. However, a few distributions show some tension, like $H_T^{t\bar{t}}$ and p_T^{top2}, both at particle and parton level. Furthermore, Sherpa2.2 manifests a clear slope in the n_{jets} spectra. The level of agreement between data and predictions will be quantified in the next Section, where the χ^2 values will be presented.

9.1.1 Particle level unfolded distributions

In this Subsection, the measured spectra, unfolded at particle level, are presented (Figures 9.1 – 9.19). In general, the predictions agree with data, within the total uncertainties. However, some tension is observed for one bin for the $|P_{\text{out}}^{t\bar{t}}|$spectrum, the bulk of the $H_{\text{T}}^{t\bar{t}}$distribution and p_T^{top2}; furthermore, the

RadLo sample shows a trend in the ratio plot for $\Delta\phi_{t\bar{t}}$and $p_T^{t\bar{t}}$, while the nominal sample gives a poor description of $R_{\mathrm{jet1}}^{\mathrm{extra1}}$and $R_{\mathrm{top1}}^{\mathrm{extra1}}$.

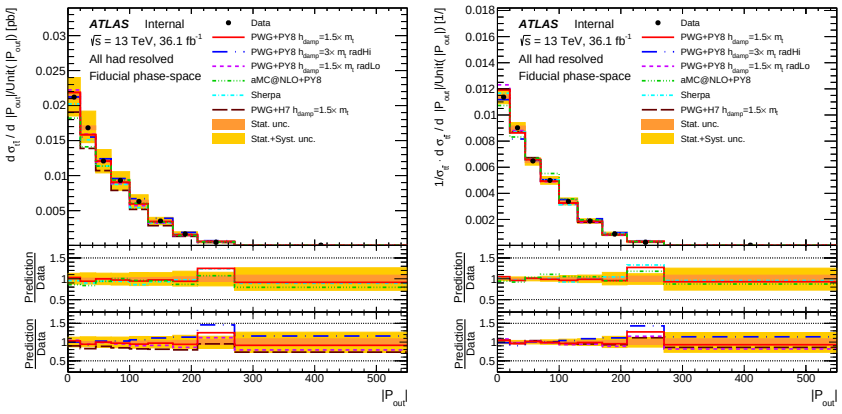

(A) (B)

FIGURE 9.1: Differential cross sections in the fiducial phase space as a function of $|P_{\mathrm{out}}^{t\bar{t}}|$: absolute (a) and normalised (b). The shaded area represents the total statistical and systematic uncertainties.

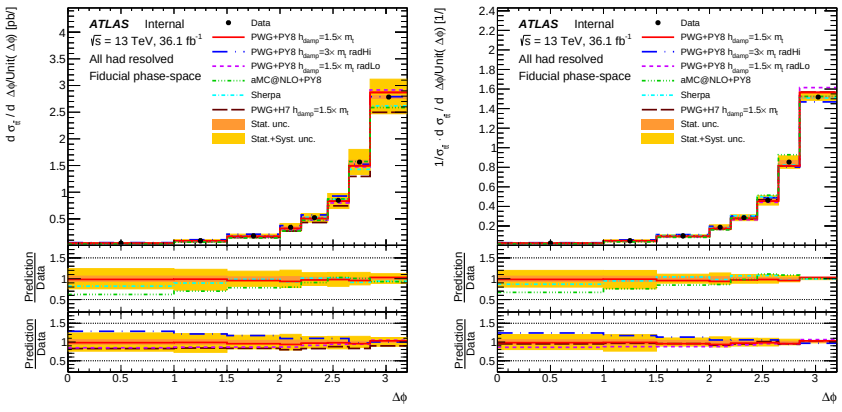

(A) (B)

FIGURE 9.2: Differential cross sections in the fiducial phase space as a function of $\Delta\phi_{t\bar{t}}$: absolute (a) and normalised (b). The shaded area represents the total statistical and systematic uncertainties.

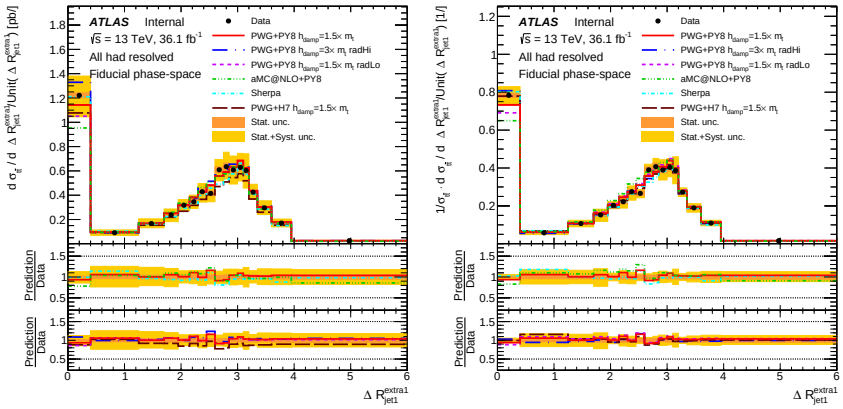

(A) (B)

FIGURE 9.3: Differential cross sections in the fiducial phase space as a function of $\Delta R_{\mathrm{jet1}}^{\mathrm{extra1}}$: absolute (a) and normalised (b). The shaded area represents the total statistical and systematic uncertainties.

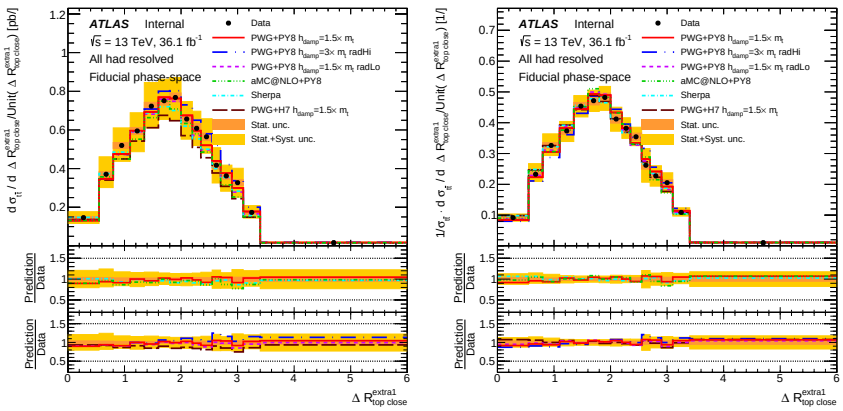

(A) (B)

FIGURE 9.4: Differential cross sections in the fiducial phase space as a function of $\Delta R_{\mathrm{topclose}}^{\mathrm{extra1}}$: absolute (a) and normalised (b). The shaded area represents the total statistical and systematic uncertainties.

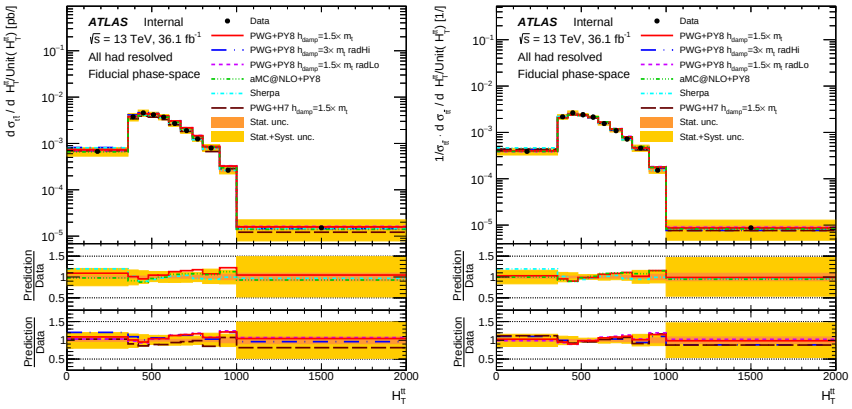

(A) (B)

FIGURE 9.5: Differential cross sections in the fiducial phase space as a function of $H_{\mathrm{T}}^{t\bar{t}}$: absolute (a) and normalised (b). The shaded area represents the total statistical and systematic uncertainties.

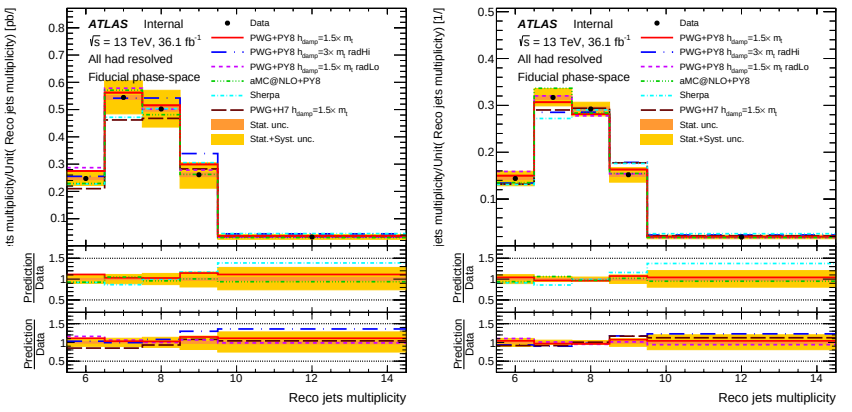

(A) (B)

FIGURE 9.6: Differential cross sections in the fiducial phase space as a function of number of jets: absolute (a) and normalised (b). The shaded area represents the total statistical and systematic uncertainties.

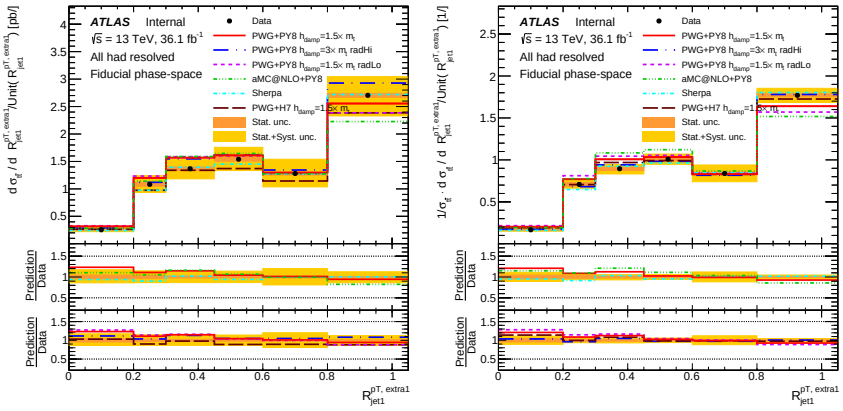

(A) (B)

FIGURE 9.7: Differential cross sections in the fiducial phase space as a function of $R_{\mathrm{jet1}}^{\mathrm{extra1}}$: absolute (a) and normalised (b). The shaded area represents the total statistical and systematic uncertainties.

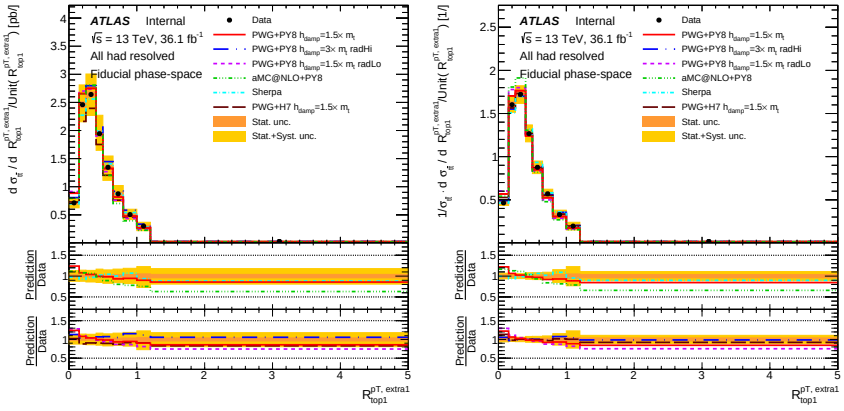

(A) (B)

FIGURE 9.8: Differential cross sections in the fiducial phase space as a function of $R_{\mathrm{top1}}^{\mathrm{extra1}}$: absolute (a) and normalised (b). The shaded area represents the total statistical and systematic uncertainties.

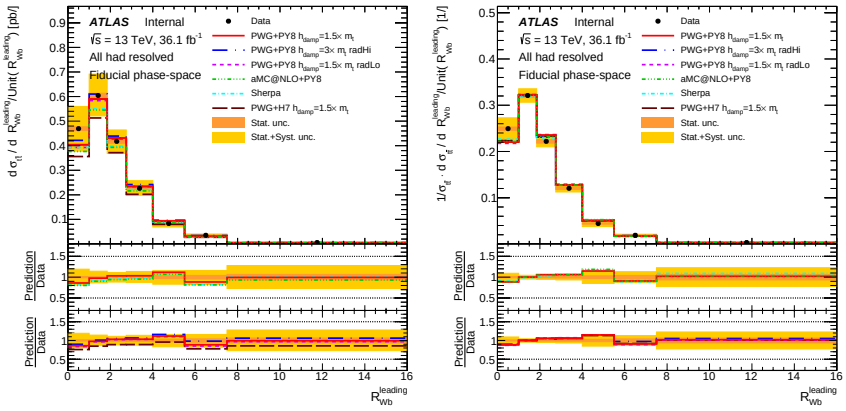

(A) (B)

FIGURE 9.9: Differential cross sections in the fiducial phase space as a function of $R_{Wb}^{leading}$: absolute (a) and normalised (b). The shaded area represents the total statistical and systematic uncertainties.

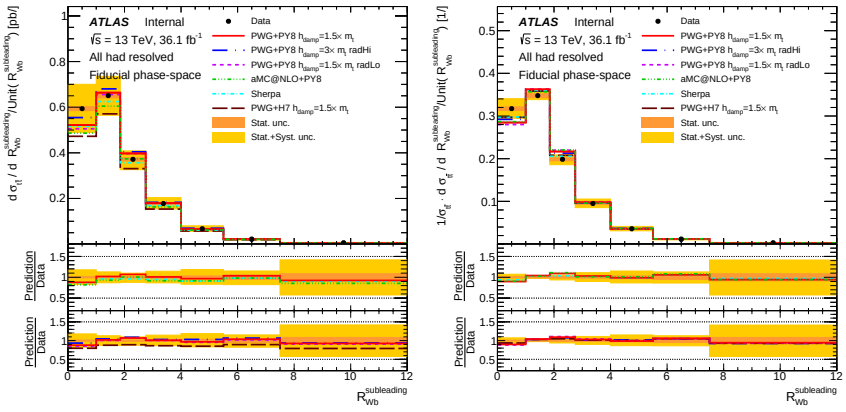

(A) (B)

FIGURE 9.10: Differential cross sections in the fiducial phase space as a function of $R_{Wb}^{subleading}$: absolute (a) and normalised (b). The shaded area represents the total statistical and systematic uncertainties.

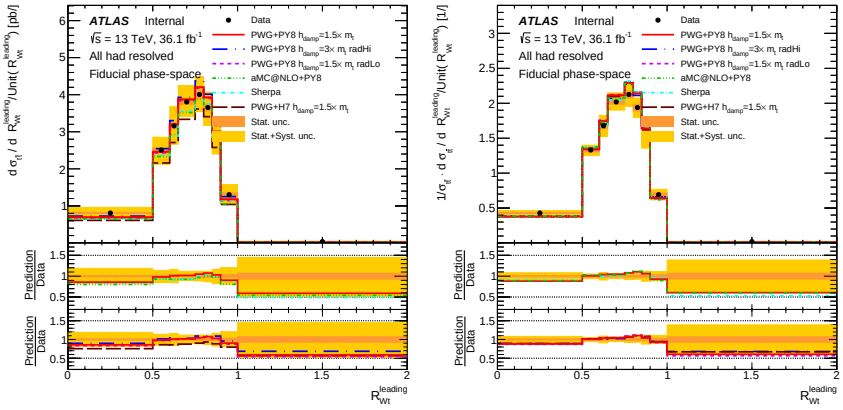

(A) (B)

FIGURE 9.11: Differential cross sections in the fiducial phase space as a function of $R_{Wt}^{leading}$: absolute (a) and normalised (b). The shaded area represents the total statistical and systematic uncertainties.

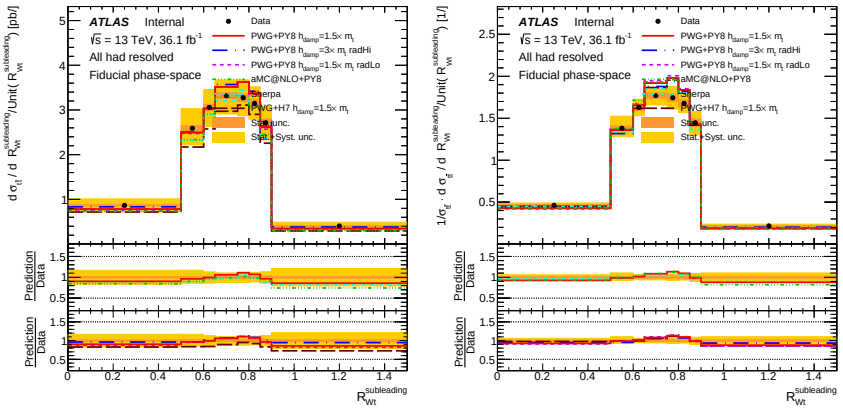

(A) (B)

FIGURE 9.12: Differential cross sections in the fiducial phase space as a function of $R_{Wt}^{subleading}$: absolute (a) and normalised (b). The shaded area represents the total statistical and systematic uncertainties.

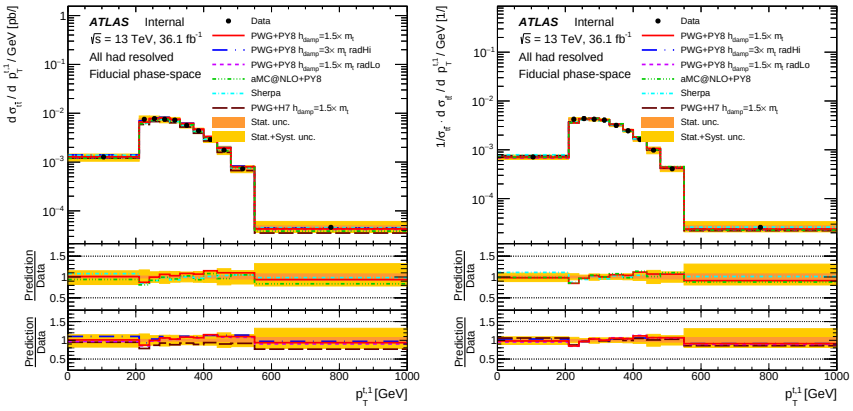

(A) (B)

FIGURE 9.13: Differential cross sections in the fiducial phase space as a function of p_T^{top1}: absolute (a) and normalised (b). The shaded area represents the total statistical and systematic uncertainties.

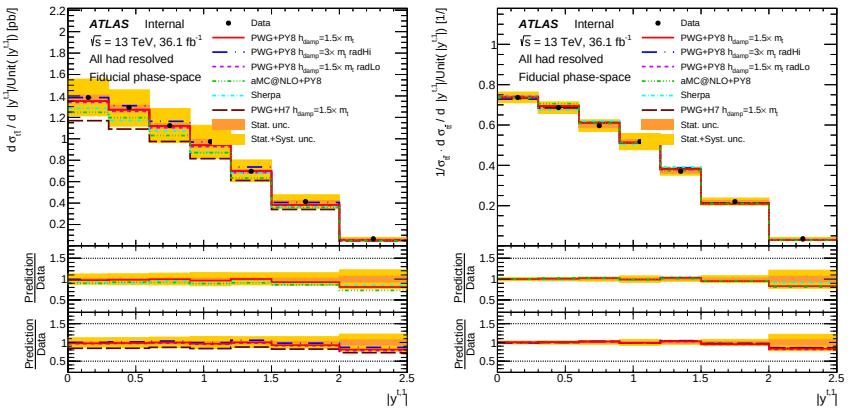

(A) (B)

FIGURE 9.14: Differential cross sections in the fiducial phase space as a function of y_{top1}: absolute (a) and normalised (b). The shaded area represents the total statistical and systematic uncertainties.

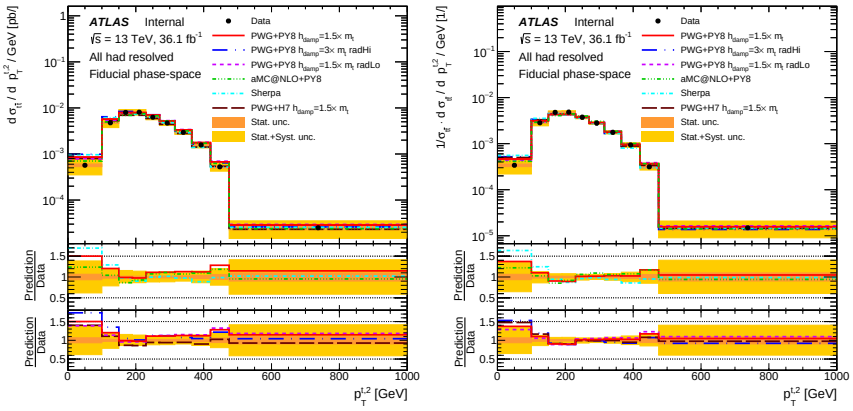

(A) (B)

FIGURE 9.15: Differential cross sections in the fiducial phase space as a function of p_T^{top2}: absolute (a) and normalised (b). The shaded area represents the total statistical and systematic uncertainties.

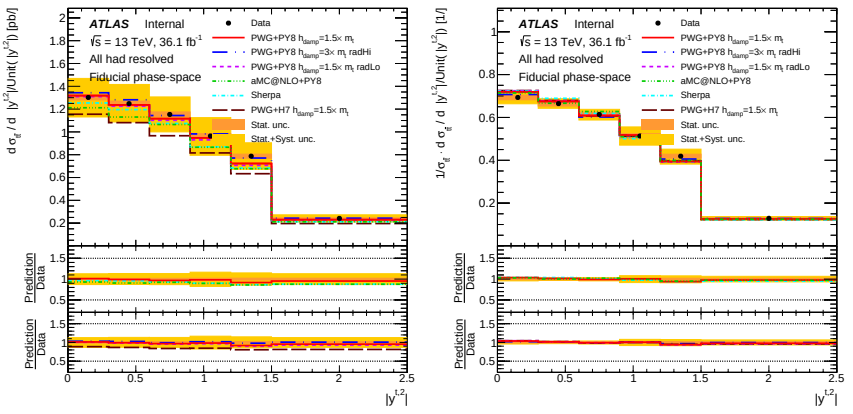

(A) (B)

FIGURE 9.16: Differential cross sections in the fiducial phase space as a function of y_{top2}: absolute (a) and normalised (b). The shaded area represents the total statistical and systematic uncertainties.

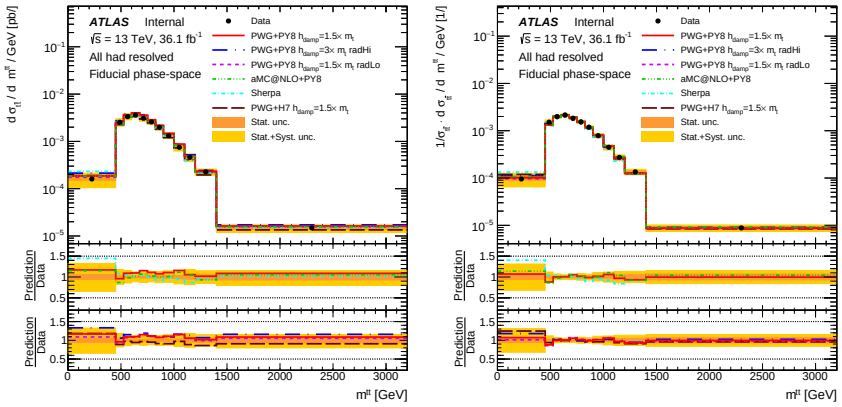

(A) (B)

FIGURE 9.17: Differential cross sections in the fiducial phase space as a function of $m_{t\bar{t}}$: absolute (a) and normalised (b). The shaded area represents the total statistical and systematic uncertainties.

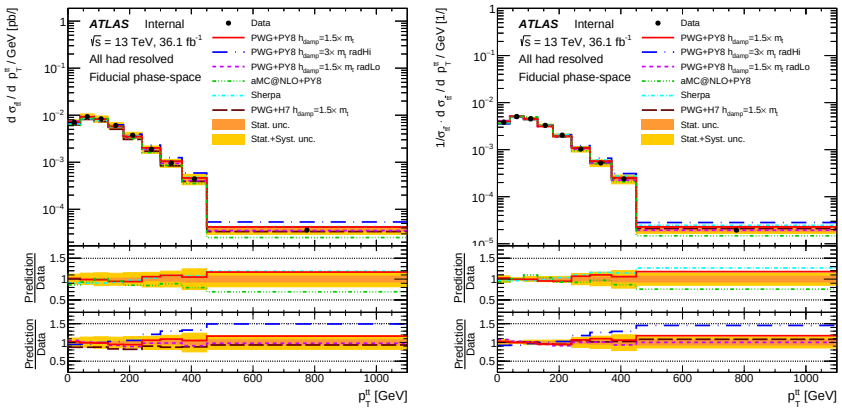

(A) (B)

FIGURE 9.18: Differential cross sections in the fiducial phase space as a function of $p_T^{t\bar{t}}$: absolute (a) and normalised (b). The shaded area represents the total statistical and systematic uncertainties.

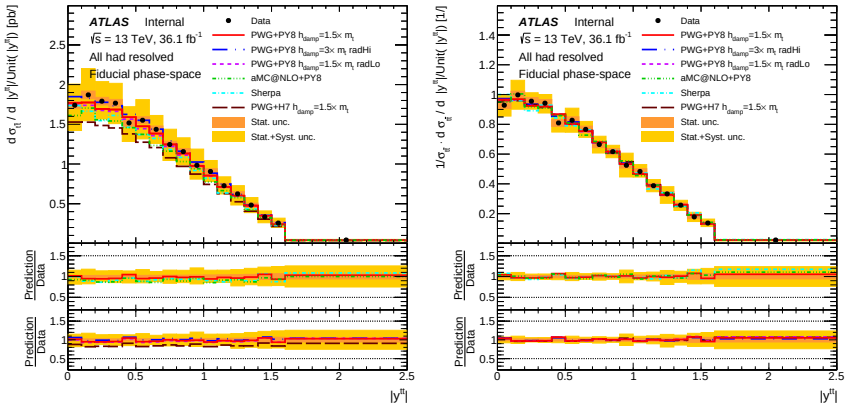

(A) (B)

FIGURE 9.19: Differential cross sections in the fiducial phase space as a function of $y_{t\bar{t}}$: absolute (a) and normalised (b). The shaded area represents the total statistical and systematic uncertainties.

9.1.2 Parton level unfolded distributions

This Subsection shows the measured spectra, unfolded at parton level (Figures 9.20 – 9.26). In general, a good agreement is observed between data and the several MC predictions, although some tension is observed for the first bin of the p_T^{top2}spectrum.

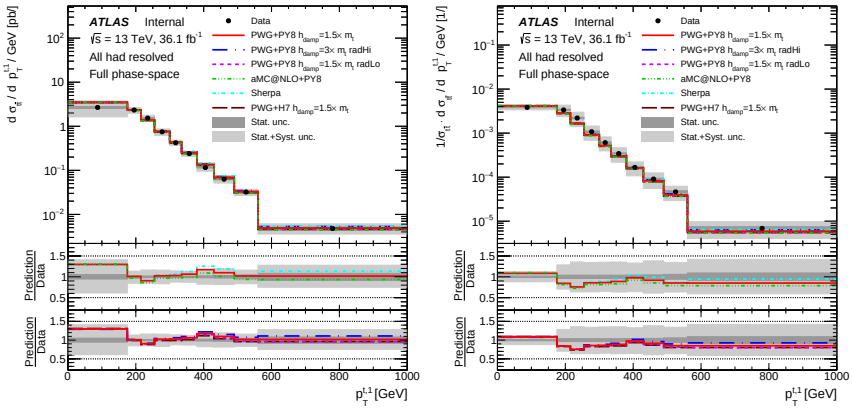

(A) (B)

FIGURE 9.20: Differential cross sections in the full phase space as a function of p_T^{top1}: absolute (a) and normalised (b). The shaded area represents the total statistical and systematic uncertainties.

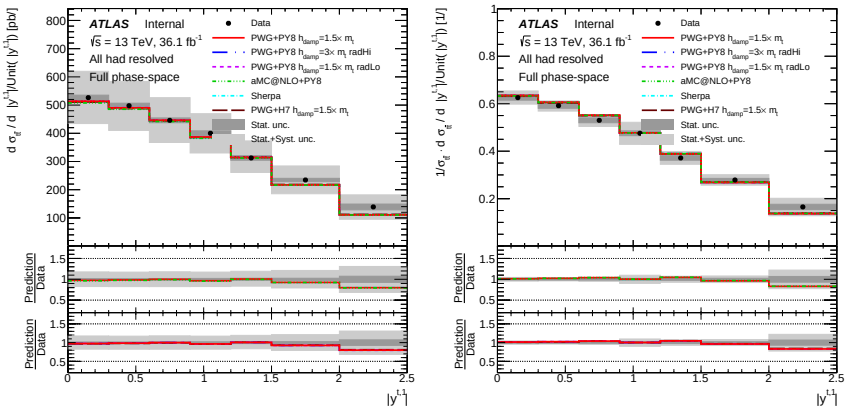

(A) (B)

FIGURE 9.21: Differential cross sections in the full phase space as a function of y_{top1}: absolute (a) and normalised (b). The shaded area represents the total statistical and systematic uncertainties.

9.2 χ^2 evaluation

The χ^2 is evaluated, for each measured spectrum, using the full covariance matrix, COV_{NDF}, which includes all systematics unertainties, by means of the following Equation:

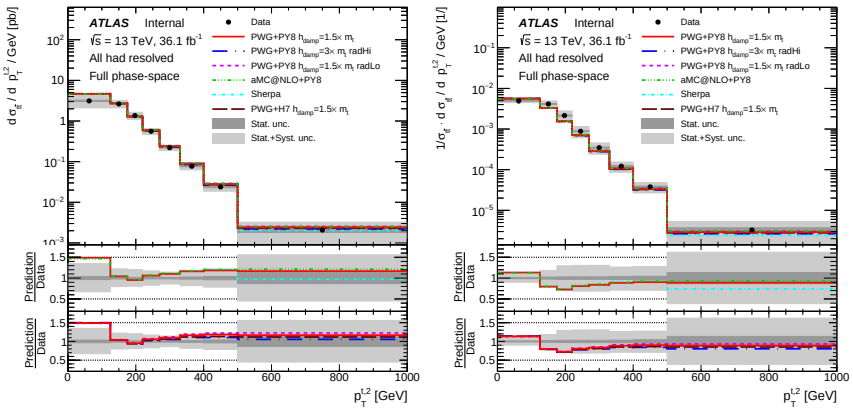

(A) (B)

FIGURE 9.22: Differential cross sections in the full phase space as a function of p_T^{top2}: absolute (a) and normalised (b). The shaded area represents the total statistical and systematic uncertainties.

$$\chi^2 = V_{NDF}^T \cdot COV_{NDF}^{-1} \cdot V_{NDF}, \tag{9.1}$$

where V_{NDF} is the vector of differences between particle (parton) level measured spectra and predictions. NDF indicates the number of degree of freedoms. It corresponds to the number of bins for absolute distributions. For relative ones, the normalization constraint reduce NDF by one. It is thus necessary to remove one row and the corresponding column from the covariance matrix. The removed line correspond to a bin of the distribution, which is also removed from V_{NDF}. The particular choice of the row/column to remove does not affect the calculated χ^2. The χ^2 is used to extract the probability of observing a χ^2 value equal or larger than the observed one when repeating the same measurement (*p-value*).

The covariance matrix is evaluated as the sum of two matrices, obtained with different procedures. The first, COV^{det}, contains all the uncertainties related to the detector calibrations, background modelling and statistical uncertainties, while the second, COV^{th}, contains the uncertainties related to the $t\bar{t}$ modelling.

COV^{det} is obtained using 1000 pseudo-experiments derived from the reconstruction level spectra. For each pseudo-experiment, each bin of the data spectrum, is varied with a Poisson fluctuation. A Gaussia shift is added for each systematic uncertainty by by scaling each bin, varied by the Poisson distribution, with the relative variation from the associated systematic uncertainty effect. Quantitatively, the relative systematic variation, $\Delta_j^{syst_i}$, due to a certain source of systematic variation $syst_i$, is evaluated in each bin j starting from the signal, S, and background, B, predictions as:

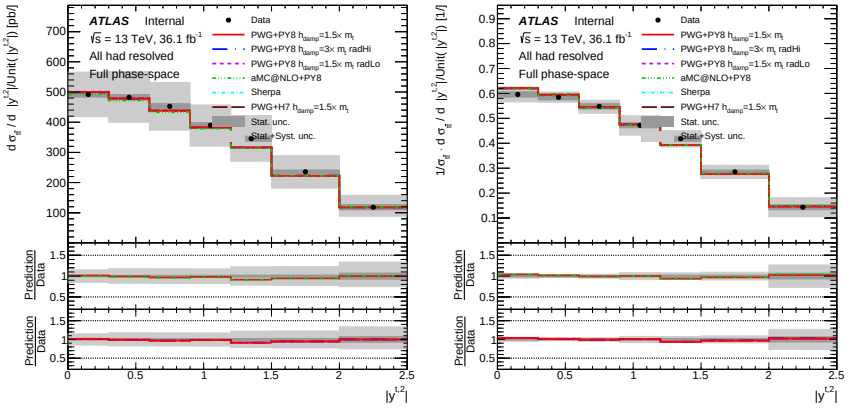

(A) (B)

FIGURE 9.23: Differential cross sections in the full phase space as a function of y_{top2}: absolute (a) and normalised (b). The shaded area represents the total statistical and systematic uncertainties.

$$\Delta_i^{syst_i} = \frac{S_j^{syst_i} + B_j^{syst_i} - S_j^{nominal} - B_j^{nominal}}{S_j^{nominal} + B_j^{nominal}}. \tag{9.2}$$

The number of events N in the bin j for the $k-th$ pseudo-experiment is derived as:

$$N_j^k = P(D_j)\left[1 + \sum_i \lambda_{syst_i} \Delta_j^{syst_i}\right], \tag{9.3}$$

where $P(D_j)$ is a random number extracted from a Poissonian distribution with average equal to the number of events in the $j-th$ bin of the data spectrum, D_j, and λ_{syst_i} is a random number drawn from a Gaussian distribution with $\mu = 0$ and $\sigma = 1$. It does not depend on the particular bin, but it is different for each systematic source. From each pseudo-experiment, the expected bckground is subtracted and the distribution is then unfolded, using the nominal corrections. The COV^{det} matrix is evaluated, in each bin i, j, as:

$$COV^{det}(i,\, j) = < (d\sigma_i - < d\sigma_i >_N) \cdot (d\sigma_j - < d\sigma_j >_N) >_N, \tag{9.4}$$

where $d\sigma$ is the differential cross section and N is the number of pseudo-experiments.

The second matrix, COV^{th}, is obtained from the sum of four separate covariance matrices, corresponding to each of the $t\bar{t}$ uncertainties: generator, parton shower and hadronization, ISFR and PDF. The elements of each matrix are calculated as:

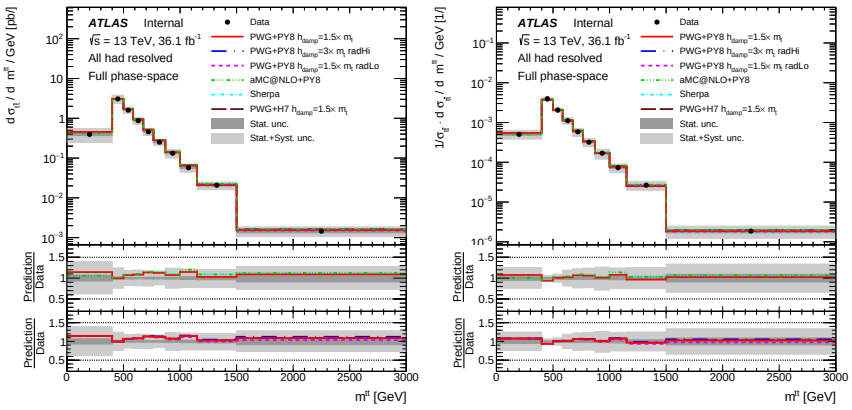

(A) (B)

FIGURE 9.24: Differential cross sections in the full phase space as a function of $m_{t\bar{t}}$: absolute (a) and normalised (b). The shaded area represents the total statistical and systematic uncertainties.

$$COV^{th}_{mod_k}(i,\,j) = CORR^{th}_{mod_k}(i,\,j) \cdot \sqrt{\Delta\sigma_i^{mok_k} \cdot \Delta\sigma_j^{mok_k}}, \tag{9.5}$$

where $\Delta\sigma_i^{mok_k}$ is the relative uncertainty on the cross section in the $i-th$ bin due to the $k-th$ modelling component, mod_k, multiplied by the corresponding measured cross section in the $i-th$ bin. $CORR^{th}(i,\,j)$ is the correlation among bins i and j. Since the modelling uncertainties are evaluated from two independend MC samples, the correlation is assumed to be exactly one in each bin. The separate treatment of the modelling uncertainties is due to the fact that their effect can not be reproduced at reconstructed level and, therefore, pseudo-experiments can not be built.

The correlation matrices for all the unfolded spectra, both absolute and normalized respect to the total cross section, are shown in Appendix G.

The χ^2 values for the absolute and relative differential cross section spectra are shown in Table 9.1 and 9.2, respectively. In general, the p-values for the normalized distributions are closer to unity than the absolute ones, thus indicating a difference also in the normalization and not only on the shape of the distributions. Furthermore, no generator is able to well describe all the presented spectra, and the p-values are strongly dependent on the particular prediction.

In particular, no generator is able to well describe the $|P^{t\bar{t}}_{\text{out}}|$, $R^{leading}_{Wb}$and p_T^{top1}spectra; Powheg+Herwig7 gives the best prediction for $R^{subleading}_{Wt}$, $m_{t\bar{t}}$, $H_{\text{T}}^{t\bar{t}}$, $R^{subleading}_{Wb}$, p_T^{top2}, $p_T^{t\bar{t}}$and $R^{leading}_{Wt}$. On the other hand, the nominal Powheg+Pythia8 sample outperforms for the N_{jets} distribution, while the *RadHi* variation gives a good description of the $R_{\text{jet1}}^{\text{extra1}}$spectra. A general good agreement is observed among different generators for $y_{t\bar{t}}$and y_{top1}, although some tension is observed, for the latter, with the Powheg+Herwig7 prediction. The same tension is observed for y_{top2}, where also the *RadLo* variation gives a poor

Observable	PWG+PY8		PWG+PY8 radHi		PWG+PY8 radLo		aMC@NLO+PY8		PWG+H7	
	χ^2/NDF	p-value	χ^2/NDF	p-value	χ^2/NDF	p-value	χ^2/NDF	p-value	χ^2/NDF	p-value
y^{top1}	5.8/7	0.56	5.1/7	0.65	6.4/7	0.49	6.6/7	0.47	8.5/7	0.29
$P_{out}^{t\bar{t}}$	14.3/9	0.11	32.2/9	<0.01	19.9/9	0.02	20.9/9	0.01	11.8/9	0.22
$R_{Wt}^{subleading}$	10.1/8	0.26	8.2/8	0.41	12.3/8	0.14	7.6/8	0.48	5.7/8	0.69
$m^{t\bar{t}}$	9.3/12	0.68	8.4/12	0.75	10.5/12	0.57	10.8/12	0.54	5.8/12	0.93
$H_T^{t\bar{t}}$	16.0/11	0.14	9.7/11	0.56	21.2/11	0.03	13.9/11	0.24	5.8/11	0.88
$R_{Wb}^{subleading}$	9.2/7	0.24	7.3/7	0.40	11.2/7	0.13	8.7/7	0.28	4.9/7	0.67
p_T^{top2}	16.1/10	0.10	14.5/10	0.15	24.1/10	<0.01	23.5/10	<0.01	6.1/10	0.80
$R_{p_T}^{extrajet1topleading}$	14.5/9	0.10	3.9/9	0.92	28.3/9	<0.01	37.8/9	<0.01	5.4/9	0.80
y^{top2}	3.6/6	0.73	1.9/6	0.93	5.0/6	0.54	2.9/6	0.83	5.8/6	0.44
$R_{Wb}^{leading}$	12.5/7	0.09	9.8/7	0.20	14.4/7	0.04	12.9/7	0.07	7.8/7	0.35
$\Delta R^{extrajet1jetleading}$	15.4/17	0.57	16.3/17	0.50	28.5/17	0.04	55.2/17	<0.01	16.6/17	0.48
$N.jets$	3.9/5	0.56	5.2/5	0.39	7.2/5	0.20	12.5/5	0.03	10.2/5	0.07
$p_T^{t\bar{t}}$	9.0/9	0.44	57.2/9	<0.01	11.1/9	0.27	22.0/9	<0.01	4.4/9	0.88
p_T^{top1}	25.2/11	<0.01	17.2/11	0.10	30.0/11	<0.01	26.6/11	<0.01	11.9/11	0.37
$R_{Wt}^{leading}$	8.2/9	0.52	7.8/9	0.56	9.5/9	0.39	8.0/9	0.54	6.8/9	0.66
$y^{t\bar{t}}$	6.0/17	0.99	4.8/17	1.00	6.7/17	0.99	11.7/17	0.82	10.6/17	0.88
$\Delta\phi$	1.9/8	0.98	17.8/8	0.02	7.4/8	0.49	25.6/8	<0.01	2.5/8	0.96
$R_{p_T}^{extrajet1jetleading}$	19.8/6	<0.01	3.7/6	0.71	40.3/6	<0.01	56.7/6	<0.01	7.6/6	0.27
$\Delta R^{extrajet1topclose}$	6.5/15	0.97	30.1/15	0.01	5.2/15	0.99	11.6/15	0.71	11.3/15	0.73

TABLE 9.1: Comparison of the measured fiducial phase space absolute differential cross sections respect the predictions from several MC generators. For each prediction the χ^2 and the resulting *p-value* are presented. The NDF is equal to the number of bins in the distribution.

Observable	PWG+PY8		PWG+PY8 radHi		PWG+PY8 radLo		aMC@NLO+PY8		PWG+H7	
	χ^2/NDF	p-value	χ^2/NDF	p-value	χ^2/NDF	p-value	χ^2/NDF	p-value	χ^2/NDF	p-value
y^{top1}	2.6/6	0.86	2.9/6	0.82	2.7/6	0.85	2.3/6	0.89	2.1/6	0.91
$P_{out}^{t\bar{t}}$	13.4/8	0.10	35.6/8	<0.01	21.7/8	<0.01	24.5/8	<0.01	12.6/8	0.12
$R_{Wt}^{subleading}$	7.2/7	0.41	6.1/7	0.53	8.8/7	0.27	7.0/7	0.43	7.8/7	0.35
$m^{t\bar{t}}$	9.4/11	0.59	8.1/11	0.70	11.3/11	0.42	13.6/11	0.26	8.7/11	0.65
$H_T^{t\bar{t}}$	9.2/10	0.51	7.0/10	0.73	12.4/10	0.26	9.8/10	0.45	8.2/10	0.61
$R_{Wb}^{subleading}$	7.1/6	0.31	4.0/6	0.68	9.0/6	0.18	7.2/6	0.30	2.7/6	0.84
p_T^{top2}	9.9/9	0.36	11.1/9	0.27	15.0/9	0.09	22.3/9	<0.01	7.1/9	0.63
$R_{p_T}^{extrajet1topleading}$	15.3/8	0.05	3.5/8	0.90	30.9/8	<0.01	40.6/8	<0.01	6.3/8	0.61
y^{top2}	4.2/5	0.52	1.8/5	0.87	5.7/5	0.34	2.9/5	0.72	4.9/5	0.43
$R_{Wb}^{leading}$	10.4/6	0.11	6.4/6	0.38	12.4/6	0.05	13.4/6	0.04	8.2/6	0.22
$\Delta R^{extrajet1jetleading}$	16.5/16	0.42	13.7/16	0.62	31.1/16	0.01	59.9/16	<0.01	15.9/16	0.46
$N.jets$	1.6/4	0.81	4.1/4	0.39	2.7/4	0.60	10.7/4	0.03	4.0/4	0.41
$p_T^{t\bar{t}}$	4.9/8	0.77	35.1/8	<0.01	10.4/8	0.24	16.2/8	0.04	3.5/8	0.90
p_T^{top1}	17.5/10	0.06	11.0/10	0.36	21.4/10	0.02	31.5/10	<0.01	12.4/10	0.26
$R_{Wt}^{leading}$	6.3/8	0.61	5.9/8	0.66	7.7/8	0.46	8.1/8	0.42	5.7/8	0.68
$y^{t\bar{t}}$	4.8/16	1.00	4.6/16	1.00	4.9/16	1.00	6.5/16	0.98	5.6/16	0.99
$\Delta\phi$	0.8/7	1.00	14.4/7	0.04	3.0/7	0.89	28.2/7	<0.01	1.4/7	0.99
$R_{p_T}^{extrajet1jetleading}$	11.0/5	0.05	3.7/5	0.59	18.8/5	<0.01	17.8/5	<0.01	6.8/5	0.24
$\Delta R^{extrajet1topclose}$	9.0/14	0.83	28.9/14	0.01	8.6/14	0.86	15.8/14	0.32	7.6/14	0.91

TABLE 9.2: Comparison of the measured fiducial phase space relative differential cross sections respect the predictions from several MC generators. For each prediction the χ^2 and the resulting *p-value* are presented. The NDF is equal to the number of bins in the distribution minus one.

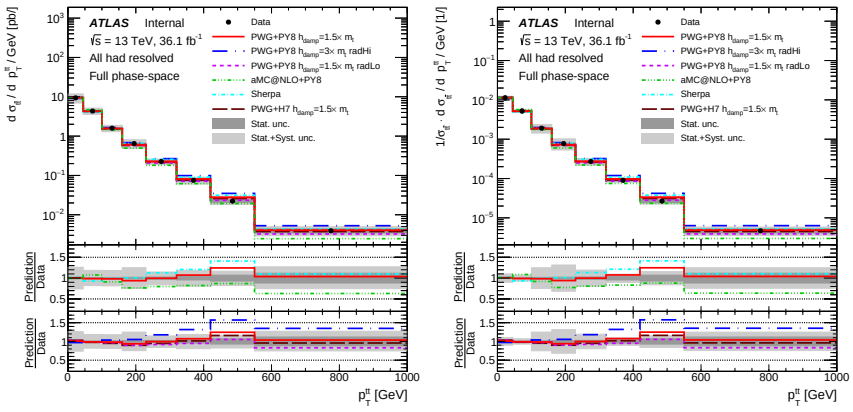

(A) (B)

FIGURE 9.25: Differential cross sections in the full phase space as a function of $p_T^{t\bar{t}}$: absolute (a) and normalised (b). The shaded area represents the total statistical and systematic uncertainties.

description of the observable. Furthermore, the nominal sample and the Powheg+Herwig7 one well describe the $\Delta\phi_{t\bar{t}}$spectrum, while the nominal and *RadLo* variation are the only generators exibiting a large p-value for $\Delta R_{\text{topclose}}^{\text{extra1}}$. On the other hand, $R_{\text{top1}}^{\text{extra1}}$is well described by the *RadHi* variation and Powheg+Herwig7. Finally, both the *RadLo* variation and MadGraph5_aMC@NLO give a poor description of the $\Delta R_{\text{jet1}}^{\text{extra1}}$spectrum.

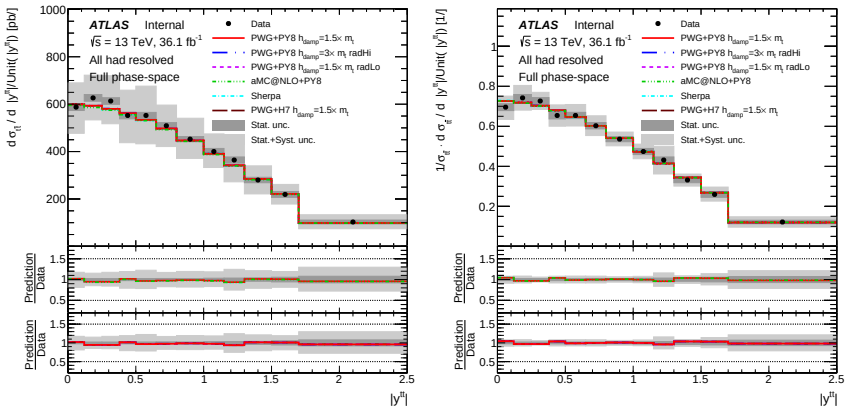

(A) (B)

FIGURE 9.26: Differential cross sections in the full phase space as a function of $y_{t\bar{t}}$: absolute (a) and normalised (b). The shaded area represents the total statistical and systematic uncertainties.

Conclusions

In this thesis, mesurements of the differential cross sections of $t\bar{t}$ production in the fully hadronic channel, resolved regime, have been presented. This is the first time this channel has been explored in ATLAS in the low-p_T top quarks regime.

Data used in the analysis have been collected by the ATLAS detector at the LHC, at $\sqrt{s} = 13$ TeV during the 2015 and 2016 data-taking periods, corresponding to $\mathscr{L} = 36.1$ fb^{-1}.

Despite being the channel with the largest branching ratio, precision measurements are very challenging due to the large background contamination, primarly due to multi-jet QCD events. Therefore, particular attention has been paid to the $t\bar{t}$ system reconstruction and the background rejection.

The former is a mass-based χ^2 minimization, used to identify the jets corresponding to the top quark pair decay products, whose four-momenta are vectorially summed to reconstruct the $t\bar{t}$ system.

The latter is achieved by a cut-based selection using final-state observables with good discriminating power between signal and background processes. The residual multi-jet contamination is then evaluated, bin-by-bin, through a data-driven ABCD method.

The differential distributions at reconstructed level are affected by the resolution of the measurement, the acceptance of the detector and the selection efficiency. Those effects have been accounted for, using the iterative D'Agostini unfolding technique, allowing a direct comparison among results from different experiments and theoretical predictions.

Several spectra, both related to the $t\bar{t}$ kinematics and sensitive to ISFR, have been presented at particle and parton levels. In particular, this is the only channel in which the ISFR-sensitive observables, strictly linked to the definition of the p_T-leading jet and additional jets, can be unambiguously characterized, given the absence of neutrinos in the final state.

Overall a good agreement within the uncertainties is shown for most of the MC predictions used as comparison to data, although some tension has been observed in the low-p_T region of the p_T^{top2}spectrum and the modelization of the six jets exclusive region.

In summary, this first measurement of $t\bar{t}$ production differential cross sections in the resolved kinematic regime with the data collected by the ATLAS detector has provided a precise test of the SM and has given a better understanding of the top quark production.

Furthermore, the major limitation on this analysis is the limited efficiency of the hadronic trigger selection, which is expected to be greatly improved after the HL-LHC upgrade of the ATLAS detector, especially after the installation of the ITk and HGTD, fully described in this thesis, which will provide additional tracking and timing information, which can be used at trigger level, for jet calibration, pile up suppression and flavour tagging.

Appendix A

Stability of the $t\bar{t}$ reconstruction method

As described in Section 6.5, the $t\bar{t}$ system reconstruction relies on the minimisation of a χ^2 mass discriminant. Here, we establish that the analysis is robust against different choices regarding the χ^2 parametrisation and cuts in the top reconstruction.

This χ^2 discriminant depends on two fixed parameters, namely the resolution of the W boson and top quark masses when computed from the correct decay products. These resolutions are extracted from events matched to parton level decay products of the top pair with the criterion $\Delta R < 0.3$. The nominal $t\bar{t}$ Monte Carlo sample is used.

It must be noted that the reconstruction, and therefore the evaluation of χ^2_{min}, has to be performed at both detector and particle level. Since the reconstructed W and tops are different at detector and particle level as shown in Table 6.2, the effect of changing the σ values or the cut on χ^2_{min} at particle level while keeping the reconstruction level unchanged, is studies. This guarantee that the purity of the selected signal is unchanged.

The stability of the kinematic reconstruction against the σ values and the choice of the χ^2_{min} is tested by running the analysis chain and producing the detector-to-particle-level migration matrices in four different configurations, given by the different combinations of resolutions and cuts:

- Resolution comparisons:
  - The resolutions at detector level are the ones evaluated from detector level mass spectra. Similarly, the resolutions at particle level are evaluated from particle level spectra.
  - The resolutions evaluated at detector level are both used for detector and particle level reconstruction.
- χ^2_{min} cut:
  - A fixed cut of χ^2<10 is chosen after Data/MC comparisons at detector level. As shown in Table A.2, this choice leads to a ~57% efficiency at detector level.

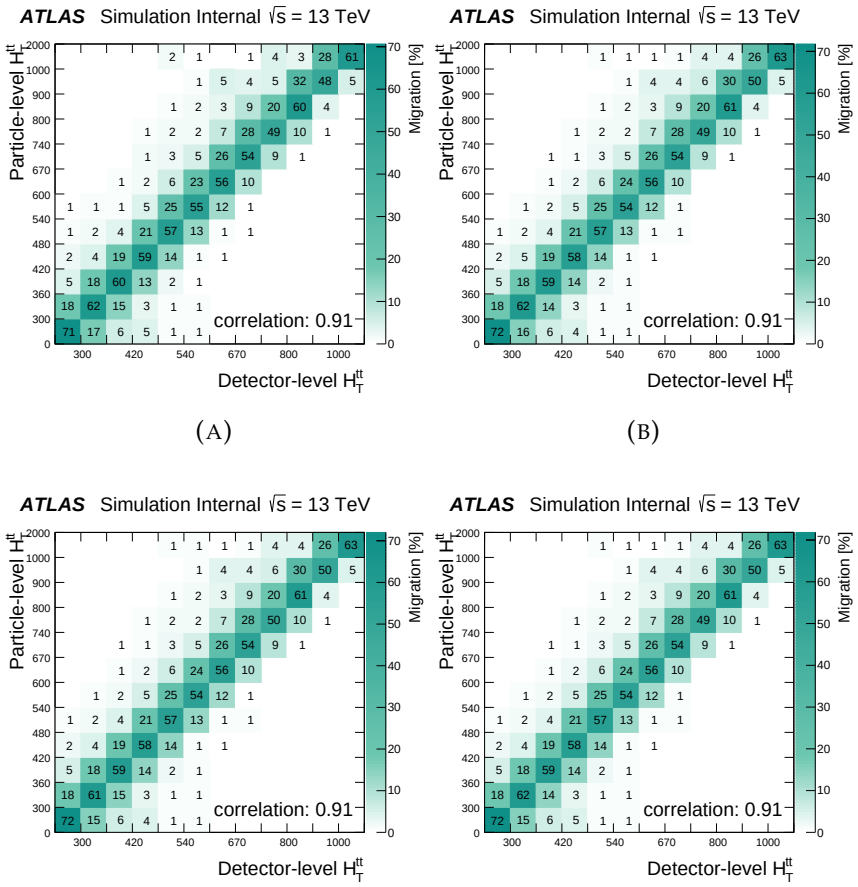

FIGURE A.1: Detector- to particle-level migration matrices for the $H_{t\bar{t}}^T$ spectrum in 4 different configuration: using the fitted resolutions at detector and particle level and a fixed χ^2 cut (a), imposing the detector level resolution at particle level with a fixed χ^2 cut (b), using the fitted resolutions at detector and particle level and a flat efficiency χ^2 cut (c), and imposing the detector level resolution at particle level with a flat efficiency χ^2 cut (d). The relative differences are at 1% level.

– A ~57% efficiency cut is applied. The cut then depends on both the choice of σ and whether detector- or particle-level input four-vectors are used, as shown in Table A.1.

The migration matrices for different spectra with the 4 different configurations are shown in Figures A.1, A.2 and A.3, A.4. The relative difference between the 4 configurations is at most 1%, therefore the analysis is very stable with respect to these parameters. All choices produce very similar results. To simplify the analysis chain, the same cut ($\chi^2 < 10$) and the $sigma$ obtained at detector-level for both particle and detector-level have been used.

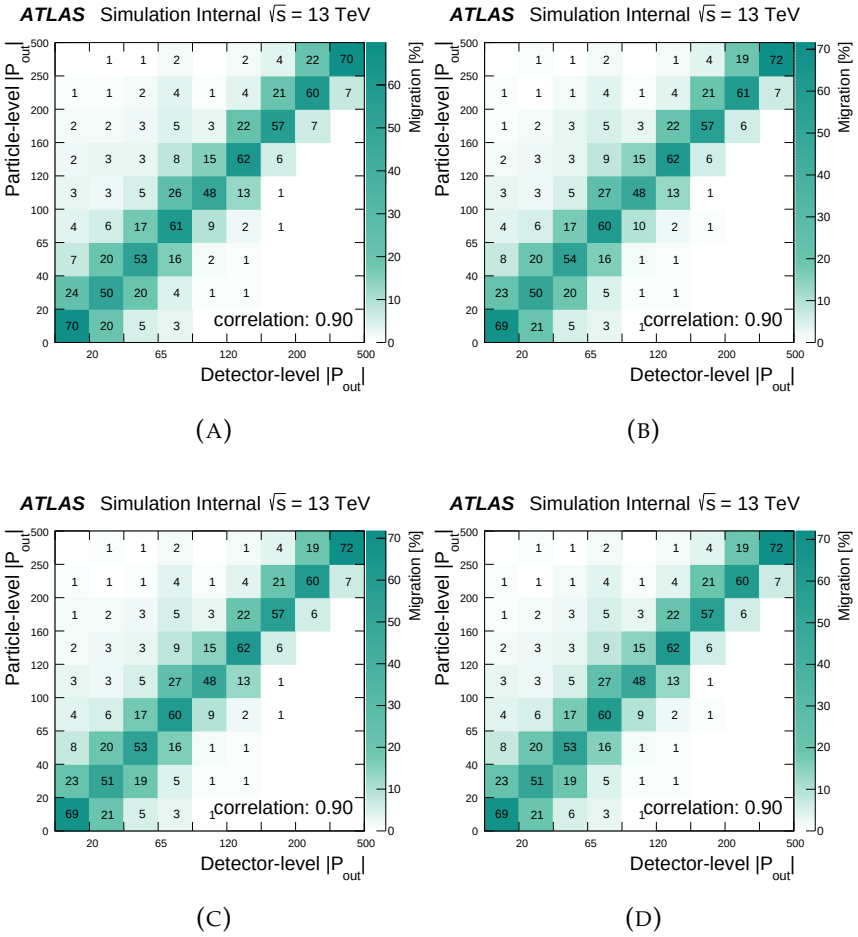

FIGURE A.2: Detector- to particle-level migration matrices for the $|P_{out}|$ spectrum in 4 different configuration: using the fitted resolutions at detector and particle level and a fixed χ^2 cut (a), imposing the detector level resolution at particle level with a fixed χ^2 cut (b), using the fitted resolutions at detector and particle level and a flat efficiency χ^2 cut (c), and imposing the detector level resolution at particle level with a flat efficiency χ^2 cut (d). The relative differences are at 1% level.

	Detector-level, σ_{reco}	particle-level, σ_{reco}	particle-level, $\sigma_{particle}$
χ^2_{min} cut	10.0	9.0	22.5

TABLE A.1: χ^2_{min} cuts leading to ~57% efficiency. The first column shows the cut applied at detector-level while the last two columns show the cut that needs to be applied at particle level to obtain the same efficiency on the signal for two scenarios; when the σ values used in the χ^2 are those obtained at detector-level and when their are evaluated from the particle level distributions. See Table 6.2 for the values.

	Detector-level, σ_{reco}	particle-level, σ_{reco}	particle-level, $\sigma_{particle}$
Efficiency for custom χ^2_{min} cut	0.571	0.576	0.573
Efficiency for χ^2_{min}<10 cut	0.571	0.595	0.426

TABLE A.2: Efficiencies in the different χ^2_{min} cut scenarios. The first column shows the efficiency obtained by applying the nominal cut (10) at detector-level and particle-level for two scenarios; when the σ values used in the χ^2 are those obtained at detector-level and when their are evaluated from the particle level distributions. See Table 6.2 for the values.

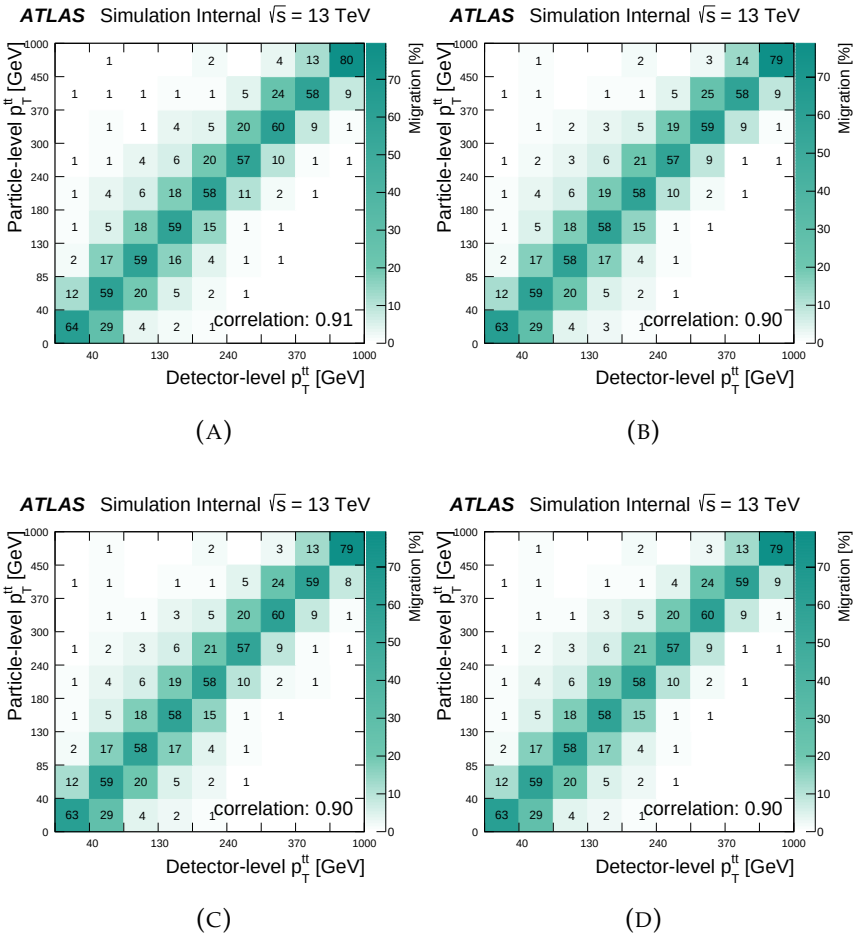

FIGURE A.3: Detector- to particle-level migration matrices for the $p_T^{t\bar{t}}$ spectrum in 4 different configuration: using the fitted resolutions at detector and particle level and a fixed χ^2 cut (a), imposing the detector level resolution at particle level with a fixed χ^2 cut (b), using the fitted resolutions at detector and particle level and a flat efficiency χ^2 cut (c), and imposing the detector level resolution at particle level with a flat efficiency χ^2 cut (d). The relative differences are at 1% level.

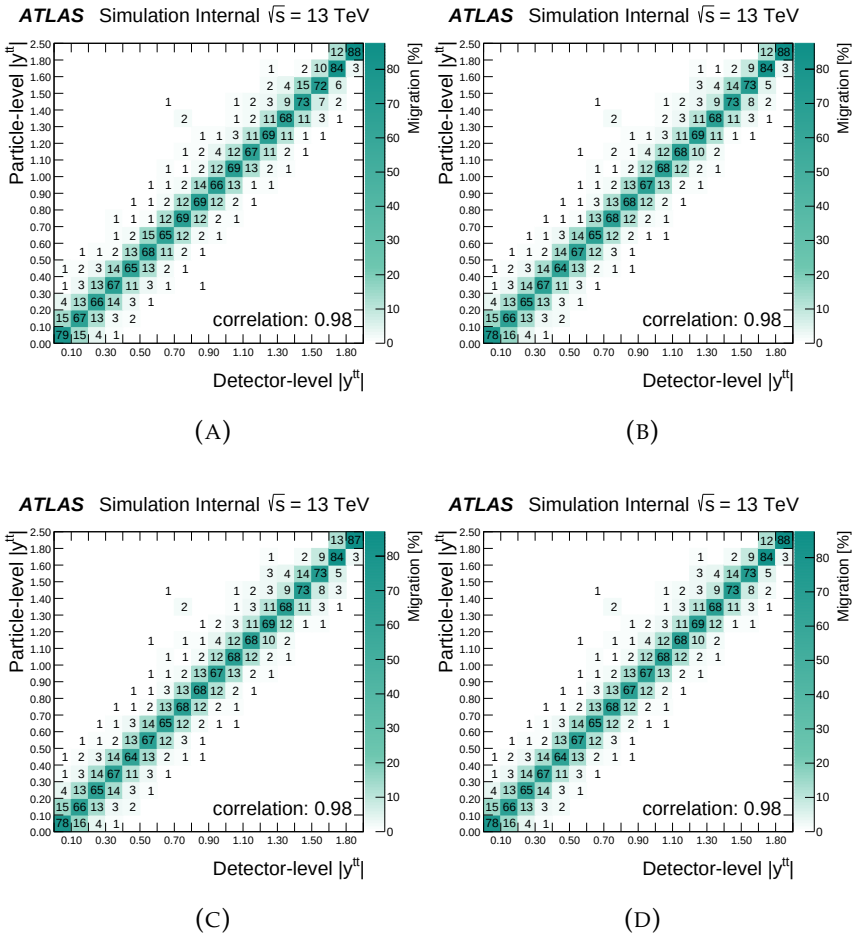

FIGURE A.4: Detector- to particle-level migration matrices for the $|y_T^{t\bar{t}}|$ spectrum in 4 different configuration: using the fitted resolutions at detector and particle level and a fixed χ^2 cut (a), imposing the detector level resolution at particle level with a fixed χ^2 cut (b), using the fitted resolutions at detector and particle level and a flat efficiency χ^2 cut (c), and imposing the detector level resolution at particle level with a flat efficiency χ^2 cut (d). The relative differences are at 1% level.

Appendix B

Implementation of the χ^2 minimization algorithm

Since I was personally responsible of the implementation of the χ^2 minimization algorithm, which represents the core of the $t\bar{t}$ system reconstruction, as described in Section 6.5, I decided to report in this Appendix the implementation of the $C++$ class used in the analysis to build the *jet sextuplets* and minimizing the χ^2.

`TTbarDiffXsTools/Chi2Minimizer.h`

```
#ifndef TTBARDIFFXSTOOLS_CHI2MINIMIZER_H
#define TTBARDIFFXSTOOLS_CHI2MINIMIZER_H
#include <iostream>
#include <vector>
#include <TLorentzVector.h>

namespace top{
  struct jet_combination{
    jet_combination() : w1ja(-1), w1jb(-1), w2ja(-1),
       w2jb(-1), b1(-1), b2(-1), chi2_m1(1e12),
       chi2_m2(1e12), chi2_w1(1e12), chi2_w2(1e12),
       chi2(1e12) {}
    jet_combination(int a, int b, int c, int d, int e, int
       f): w1ja(a), w1jb(b), w2ja(c), w2jb(d), b1(e), b2(f)
       {}
    int w1ja, w1jb, w2ja,
    int w2jb, b1, b2;
    float chi2_m, chi2_m1, chi2_m2;
    float chi2_w1, chi2_w2, chi2;
  };

  class Chi2Minimizer {
   ClassDef(Chi2Minimizer,1);

   public:
    Chi2Minimizer();
```

```
  virtual ~Chi2Minimizer(){}

  int BtagJets(std::string btag_WP, const
     xAOD::JetContainer & m_jets);
  int BtagParticleJets(const xAOD::JetContainer & m_jets);
  int Fit(const xAOD::JetContainer & m_jets);

  double Get_Chi2(){return MinChiSquare;}
  double Get_Chi2_m(){return m_index_jets.chi2_m;}
  double Get_Chi2_m1(){return m_index_jets.chi2_m1;}
  double Get_Chi2_m2(){return m_index_jets.chi2_m2;}
  double Get_Chi2_w1(){return m_index_jets.chi2_w1;}
  double Get_Chi2_w2(){return m_index_jets.chi2_w2;}
  std::vector<int> GetIndexes_BtaggedJets(){return
     m_index_btagged_jets;}
  int GetIndex_w1ja(){return m_index_jets.w1ja;}
  int GetIndex_w1jb(){return m_index_jets.w1jb;}
  int GetIndex_w2ja(){return m_index_jets.w2ja;}
  int GetIndex_w2jb(){return m_index_jets.w2jb;}
  int GetIndex_b1(){return m_index_jets.b1;}
  int GetIndex_b2(){return m_index_jets.b2;}
  std::vector<int> GetIndex_extrajets(){return
     m_index_extrajet;}
  TLorentzVector GetJet_w1ja(){return m_tlv_w1ja;}
  TLorentzVector GetJet_w1jb(){return m_tlv_w1jb;}
  TLorentzVector GetJet_w2ja(){return m_tlv_w2ja;}
  TLorentzVector GetJet_w2jb(){return m_tlv_w2jb;}
  TLorentzVector GetJet_w1(){return m_tlv_w1;}
  TLorentzVector GetJet_w2(){return m_tlv_w2;}
  TLorentzVector GetJet_b1(){return m_tlv_b1;}
  TLorentzVector GetJet_b2(){return m_tlv_b2;}
  TLorentzVector GetJet_top1(){return m_tlv_top1;}
  TLorentzVector GetJet_top2(){return m_tlv_top2;}
  TLorentzVector GetJet_ttbar(){return m_tlv_ttbar;}
  std::vector<TLorentzVector> GetJet_extrajets(){return
     m_tlv_extrajets;}
  void Setptmin_extrajets(double a){m_extrajets_ptmin=a;}
  void SetSigmaW(double a){sigma_w=a;}
  void SetSigmat(double a){sigma_t=a;}

private:
  double MinChiSquare;
  double m_extrajets_ptmin; //MeV
  TLorentzVector m_tlv_w1ja;
  TLorentzVector m_tlv_w1jb;
  TLorentzVector m_tlv_w1;
  TLorentzVector m_tlv_w2ja;
  TLorentzVector m_tlv_w2jb;
  TLorentzVector m_tlv_w2;
  TLorentzVector m_tlv_b1;
```

```
      TLorentzVector m_tlv_b2;
      TLorentzVector m_tlv_top1;
      TLorentzVector m_tlv_top2;
      TLorentzVector m_tlv_ttbar;
      std::vector<int> m_index_extrajet;
      std::vector<TLorentzVector> m_tlv_jets;
      std::vector<TLorentzVector> m_tlv_extrajets;
      jet_combination m_index_jets;
      std::vector<int> m_index_btagged_jets;
      double sigma_t;
      double sigma_w;
      double m_sumET;

      void ReconstructTTbarSystem();
      void GetCombinationList(std::vector<int> elements,
         std::vector< jet_combination > &list);
      void GetCombinationPairs(std::vector<int> elements,
         std::vector< std::pair<int,int> > &pairs);
      bool NotRepeatingPairs(std::pair<int,int> a,
         std::pair<int,int> b);
      double EvaluateChi2(jet_combination &sestuplet);
      void ClearAll();
      void ClearFit();
      void ClearBjets();

   };
}//namespace top
#endif
```

TTbarDiffXsTools/Chi2Minimizer.cxx

```
#include "TTbarDiffXsTools/Chi2Minimizer.h"


namespace top{
  Chi2Minimizer::Chi2Minimizer():
               MinChiSquare(1e12),m_extrajets_ptmin(0.),
               sigma_t(0.),sigma_w(0.)
  {
    ClearAll();
  }

  void Chi2Minimizer::ClearAll(){
    ClearFit();
    ClearBjets();
  }

  void Chi2Minimizer::ClearFit(){
```

```
  m_tlv_jets.clear();
  m_tlv_extrajets.clear();
  m_index_extrajet.clear();
  m_index_jets.w1ja=-1;
  m_index_jets.w1jb=-1;
  m_index_jets.w2ja=-1;
  m_index_jets.w2jb=-1;
  m_index_jets.b1=-1;
  m_index_jets.b2=-1;
  MinChiSquare=1e12;
  m_sumET=0.;
}

void Chi2Minimizer::ClearBjets(){
  m_index_btagged_jets.clear();
}

void Chi2Minimizer::ReconstructTTbarSystem(){
  //TTbar system reconstruction from jets sextuplet
  m_tlv_w1ja=m_tlv_jets.at(m_index_jets.w1ja);
  m_tlv_w1jb=m_tlv_jets.at(m_index_jets.w1jb);
  m_tlv_w2ja=m_tlv_jets.at(m_index_jets.w2ja);
  m_tlv_w2jb=m_tlv_jets.at(m_index_jets.w2jb);
  m_tlv_b1=m_tlv_jets.at(m_index_jets.b1);
  m_tlv_b2=m_tlv_jets.at(m_index_jets.b2);

  m_tlv_w1=m_tlv_w1ja+m_tlv_w1jb;
  m_tlv_w2=m_tlv_w2ja+m_tlv_w2jb;
  m_tlv_top1=m_tlv_w1+m_tlv_b1;
  m_tlv_top2=m_tlv_w2+m_tlv_b2;
  m_tlv_ttbar=m_tlv_top1+m_tlv_top2;
  //Checking that "top1" is also leading
  if(m_tlv_top1.Pt()<m_tlv_top2.Pt()){
    int tmp_index;
    tmp_index=m_index_jets.w1ja;
    m_index_jets.w1ja=m_index_jets.w2ja;
    m_index_jets.w2ja=tmp_index;
    tmp_index=m_index_jets.w1jb;
    m_index_jets.w1jb=m_index_jets.w2jb;
    m_index_jets.w2jb=tmp_index;
    tmp_index=m_index_jets.b1;
    m_index_jets.b1=m_index_jets.b2;
    m_index_jets.b2=tmp_index;
    float tmp_chi;
    tmp_chi=m_index_jets.chi2_m1;
    m_index_jets.chi2_m1=m_index_jets.chi2_m2;
    m_index_jets.chi2_m2=tmp_chi;
    tmp_chi=m_index_jets.chi2_w1;
    m_index_jets.chi2_w1=m_index_jets.chi2_w2;
    m_index_jets.chi2_w2=tmp_chi;
```

```
      m_tlv_w1ja=m_tlv_jets.at(m_index_jets.w1ja);
      m_tlv_w1jb=m_tlv_jets.at(m_index_jets.w1jb);
      m_tlv_w2ja=m_tlv_jets.at(m_index_jets.w2ja);
      m_tlv_w2jb=m_tlv_jets.at(m_index_jets.w2jb);
      m_tlv_b1=m_tlv_jets.at(m_index_jets.b1);
      m_tlv_b2=m_tlv_jets.at(m_index_jets.b2);
      m_tlv_w1=m_tlv_w1ja+m_tlv_w1jb;
      m_tlv_w2=m_tlv_w2ja+m_tlv_w2jb;
      m_tlv_top1=m_tlv_w1+m_tlv_b1;
      m_tlv_top2=m_tlv_w2+m_tlv_b2;
    }
    //Finding extra jets
    int n_jet=m_tlv_jets.size();
    for(int i=0; i<n_jet; ++i){
      //removing jets under threshold
      if(m_tlv_jets.at(i).Pt()<m_extrajets_ptmin) continue;
      if((i!=m_index_jets.w1ja)&&
         (i!=m_index_jets.w1jb)&&
         (i!=m_index_jets.w2ja)&&
         (i!=m_index_jets.w2jb)&&
         (i!=m_index_jets.b1)&&
         (i!=m_index_jets.b2)){
           m_index_extrajet.push_back(i);
           TLorentzVector tmp_tlv=m_tlv_jets.at(i);
           m_tlv_extrajets.push_back(tmp_tlv);
      }
    }
}

double Chi2Minimizer::EvaluateChi2(jet_combination&
    sestuplet){
  //Calculation of Chi2 from jet sextuplet
  double sigma_mbjj = sigma_t;
  double sigma_mjj = sigma_w;
  double mW = 80.4;
  double mt = 173.5;
  double GeV=0.001;
  double mjj1 = (m_tlv_jets.at(sestuplet.w1ja)+
              m_tlv_jets.at(sestuplet.w1jb)).M()*GeV;
  double mjj2 = (m_tlv_jets.at(sestuplet.w2ja)+
              m_tlv_jets.at(sestuplet.w2jb)).M()*GeV;

  double mbjj1 = (m_tlv_jets.at(sestuplet.b1)+
               m_tlv_jets.at(sestuplet.w1ja)+
               m_tlv_jets.at(sestuplet.w1jb)).M()*GeV;
  double mbjj2 = (m_tlv_jets.at(sestuplet.b2)+
               m_tlv_jets.at(sestuplet.w2ja)+
               m_tlv_jets.at(sestuplet.w2jb)).M()*GeV;
```

```
  double dmbjj1 = mbjj1-mt;
  double dmbjj2 = mbjj2-mt;
  double dmbjj = mbjj1-mbjj2;
  double dmjj1 = mjj1-mW;
  double dmjj2 = mjj2-mW;

  double chi_m1 = dmbjj1*dmbjj1/(sigma_mbjj*sigma_mbjj);
  double chi_m2 = dmbjj2*dmbjj2/(sigma_mbjj*sigma_mbjj);
  double chi_m = dmbjj*dmbjj/(2*(sigma_mbjj*sigma_mbjj));
  double chi_w1 = dmjj1*dmjj1/(sigma_mjj*sigma_mjj);
  double chi_w2 = dmjj2*dmjj2/(sigma_mjj*sigma_mjj);

  double chi2 = chi_m + chi_w1 + chi_w2;

  sestuplet.chi2_m = chi_m;
  sestuplet.chi2_m1 = chi_m1;
  sestuplet.chi2_m2 = chi_m2;
  sestuplet.chi2_w1 = chi_w1;
  sestuplet.chi2_w2 = chi_w2;
  sestuplet.chi2 = chi2;
  return chi2;
}

bool Chi2Minimizer::NotRepeatingPairs(std::pair<int,int>
   a, std::pair<int,int> b){
  if(a.first==b.first) return 0;
  if(a.first==b.second) return 0;
  if(a.second==b.first) return 0;
  if(a.second==b.second) return 0;
  return 1;
}

void Chi2Minimizer::GetCombinationPairs(std::vector<int>
   elements, std::vector< std::pair<int,int> > &pairs){
  for(unsigned int i=0; i<elements.size()-1; ++i){
    for(unsigned int j=i+1; j<elements.size(); ++j){
      std::pair <int,int>
         tmp_pair(elements.at(i),elements.at(j));
      pairs.push_back(tmp_pair);
    }
  }
}

void Chi2Minimizer::GetCombinationList(std::vector<int>
   elements, std::vector< jet_combination > &list){
  //This method generates all the possible jet sextuplets
  std::vector < std::pair <int,int> > bjets_pairs;
  std::vector < std::pair<int,int> > wjets_pairs;
  //b-jets pairs
  if(m_index_btagged_jets.size()!=0){
```

```
    //If only one b-tagged jet, build manually by fixing
       the position of the b-tagged jet
    if(m_index_btagged_jets.size()==1){
      for(unsigned int i=0; i<elements.size(); ++i){
        if(elements.at(i)==m_index_btagged_jets.at(0))
           continue;
        std::pair <int,int> tmp_pair
           (elements.at(i),m_index_btagged_jets.at(0));
        bjets_pairs.push_back(tmp_pair);
      }
    }
    //else build pairs from b-tagged jets
    else{
      GetCombinationPairs(m_index_btagged_jets,bjets_pairs);
    }
  }
  //if no b-tagged jets in the event, build pairs from
     light-jets
  else
      GetCombinationPairs(elements,bjets_pairs);
  //Build light-jet pairs
  GetCombinationPairs(elements,wjets_pairs);
  //Building sextuplets
  for(unsigned int b=0; b<bjets_pairs.size(); ++b){
    for(unsigned int w1=0; w1<wjets_pairs.size()-1; ++w1){
      if(!NotRepeatingPairs(bjets_pairs.at(b),wjets_pairs.at(w1)))
         continue;
      for(unsigned int w2=w1+1; w2<wjets_pairs.size();
         ++w2){
        if(!NotRepeatingPairs(bjets_pairs.at(b),wjets_pairs.at(w2)))
           continue;
        if(!NotRepeatingPairs(wjets_pairs.at(w1),wjets_pairs.at(w2)))
           continue;
        //Defining sextuplet with nominal and inverted
           order for b-jet candidates
        jet_combination tmp_combo(
              wjets_pairs.at(w1).first,wjets_pairs.at(w1).second,
              wjets_pairs.at(w2).first,wjets_pairs.at(w2).second,
              bjets_pairs.at(b).first,bjets_pairs.at(b).second);

        jet_combination inv_combo(
              wjets_pairs.at(w1).first,wjets_pairs.at(w1).second,
              wjets_pairs.at(w2).first,wjets_pairs.at(w2).second,
              bjets_pairs.at(b).second,bjets_pairs.at(b).first);
        list.push_back(tmp_combo);
        list.push_back(inv_combo);
      }
    }
  }
}
```

```
int Chi2Minimizer::Fit(const xAOD::JetContainer & m_jets){
  if(m_tlv_jets.size()!=0)
   ClearFit();
  //Filling the vector of jets
  for(const auto& jet: m_jets){
    TLorentzVector temp_tlv;
    temp_tlv.SetPtEtaPhiE(jet->pt(),jet->eta(),jet->phi(),jet->e());
    m_tlv_jets.push_back(temp_tlv);
    m_sumET+=jet->e();
  }
  //Defining jet indeces
  std::vector<int> pos_list;
  for(unsigned int i=0; i<m_tlv_jets.size(); ++i)
    pos_list.push_back(i);
  //Vetoing events with less than 6 jets
  if( (pos_list.size()+m_index_btagged_jets.size()) < 6)
     return 0;
  //Getting combinations
  std::vector< jet_combination > full_combinations;
  GetCombinationList(pos_list,full_combinations);
  double chi2min= 1e12;
  jet_combination mincombo;
  //Looking for X2 minimizing combination
  if(full_combinations.size()==0) return 0;
  for(unsigned int k=0; k<full_combinations.size(); ++k){
    double tmp_chi2=EvaluateChi2(full_combinations.at(k));
    if(tmp_chi2<chi2min){
      chi2min=tmp_chi2;
      mincombo=full_combinations.at(k);
    }
  }
  //Set the indeces of the jets
  m_index_jets=mincombo;
  //Save the Chi2
  MinChiSquare=chi2min;
  //Reconstruct the system
  ReconstructTTbarSystem();
  return 1;
}

int Chi2Minimizer::BtagJets(std::string btag_WP, const
   xAOD::JetContainer& m_jets){
  if(m_index_btagged_jets.size()!=0)
    ClearBjets();
  int counter=0;
  for (const auto& jet: m_jets){
    //This decoration, set in the ATLAS reconstruction
       chain, indicates if a reconstructed jet is b-tagged
    if(jet->isAvailable<char>("isbtagged_"+btag_WP))
```

```
        if(jet->auxdataConst<char>("isbtagged_"+btag_WP))
          m_index_btagged_jets.push_back(counter);
      ++counter;
    }
    return m_index_btagged_jets.size();
  }

  int Chi2Minimizer::BtagParticleJets(const
     xAOD::JetContainer& m_jets){
    if(m_index_btagged_jets.size()!=0)
      ClearBjets();
    int counter=0;
    for (const auto& jet: m_jets){
      //This decoration, set in the ATLAS reconstruction
         chain, indicates if a reconstructed jet is b-tagged
      if(jet->isAvailable<int>("GhostBHadronsFinalCount")){
        //Number of ghost-associated b-hadrons
        int nGhosts = jet->auxdata<int>(
           "GhostBHadronsFinalCount" );
        if(nGhosts >= 1)
          m_index_btagged_jets.push_back(counter);
      }
      ++counter;
    }
    return m_index_btagged_jets.size();
  }
}//namespace top
```

Appendix C

Cutflows for data and MC-estimated processes

In this Appendix, the complete cutflows for data and MC-estimated processes, leading to the yelds in Chapter 6, are reported. In particular:

- **Data**: Table C.1;
- $t\bar{t}$ **fully hadronic**: Table C.2;
- $t\bar{t}$ **non-all hadronic**: Table C.3;
- **W-t associated production**: Table C.4;
- **t-channel single top quark production**: Table C.5.

Cut	Data
Initial	4.53388e+08
GoodRunList	4.43166e+08
Good Calorimeter	4.42544e+08
Primary Vertex	4.42544e+08
Trigger decision	5.15515e+07
Jet Clean	5.15083e+07
Lepton veto	5.03712e+07
Jets requirement	1.68330e+07
Reconstructed χ^2_{min}	8.62475e+06
ΔR_{bb}	5.53870e+06
ΔR_{bW}^{max}	918726
Top Mass	779021
B-jets requirement	44238

TABLE C.1: Complete cutflow for data. Only statistical uncertainties are given. Selection criteria are those stated in Table 6.3.

Cut	$t\bar{t}$ fully hadronic
Initial	1.36992e+07 $\pm$ 3133.23
GoodRunList	1.36992e+07 $\pm$ 3133.23
Good Calorimeter	1.36992e+07 $\pm$ 3133.23
Primary Vertex	1.36992e+07 $\pm$ 3133.23
Trigger decision	946239 $\pm$ 823.215
Jet Clean	945597 $\pm$ 822.925
Lepton veto	911017 $\pm$ 807.826
Jets requirement	400043 $\pm$ 536.110
Reconstructed χ^2_{min}	261402 $\pm$ 421.303
ΔR_{bb}	171931 $\pm$ 341.187
ΔR_{bW}^{max}	96628.3 $\pm$ 293.981
Top Mass	72389.2 $\pm$ 220.236
B-jets requirement	31807.6 $\pm$ 142.767

TABLE C.2: Complete cutflow for $t\bar{t}$ fully hadronic process. Only statistical uncertainties are given. Selection criteria are those stated in Table 6.3.

Cut	$t\bar{t}$ non-all hadronic
Initial	1.63149e+07 $\pm$ 2155.11
GoodRunList	1.63149e+07 $\pm$ 2155.11
Good Calorimeter	1.63149e+07 $\pm$ 2155.11
Primary Vertex	1.63149e+07 $\pm$ 2155.11
Trigger decision	390882 $\pm$ 333.154
Jet Clean	390549 $\pm$ 333.007
Lepton veto	172680 $\pm$ 221.239
Jets requirement	72728.9 $\pm$ 143.824
Reconstructed χ^2_{min}	33392.6 $\pm$ 95.0343
ΔR_{bb}	20707.9 $\pm$ 74.7802
ΔR^{max}_{bW}	8472.76 $\pm$ 63.8985
Top Mass	4692.6 $\pm$ 35.3899
B-jets requirement	1650.37 $\pm$ 20.4185

TABLE C.3: Complete cutflow for $t\bar{t}$ non-all hadronic process. Only statistical uncertainties are given. Selection criteria are those stated in Table 6.3.

Cut	Wt
Initial	2.58851e+06 $\pm$ 834.654
GoodRunList	2.58851e+06 $\pm$ 834.654
Good Calorimeter	2.58851e+06 $\pm$ 834.654
Primary Vertex	2.58851e+06 $\pm$ 834.654
Trigger decision	46947.7 $\pm$ 112.404
Jet Clean	46935.3 $\pm$ 112.388
Lepton veto	38593.7 $\pm$ 101.934
Jets requirement	15430.4 $\pm$ 64.619
B-jets requirement	5182.18 $\pm$ 35.9467
Reconstructed χ^2_{min}	1799.32 $\pm$ 21.0063
ΔR_{bb}	1220.21 $\pm$ 17.3101
ΔR_{bW}^{max}	545.842 $\pm$ 11.611
Top Mass	235.418 $\pm$ 7.58623

TABLE C.4: Complete cutflow for Wt process. Only statistical uncertainties are given. Selection criteria are those stated in Table 6.3.

Cut	single top
Initial	7.83213e+06 $\pm$ 6206.87
GoodRunList	7.83213e+06 $\pm$ 6206.87
Good Calorimeter	7.83213e+06 $\pm$ 6206.87
Primary Vertex	7.83213e+06 $\pm$ 6206.87
Trigger decision	33789.4 $\pm$ 433.228
Jet Clean	33768.8 $\pm$ 433.119
Lepton veto	32787.3 $\pm$ 426.551
Jets requirement	12956.4 $\pm$ 270.641
B-jets requirement	5006.85 $\pm$ 128.592
Reconstructed χ^2_{min}	1418.16 $\pm$ 67.4549
ΔR_{bb}	930.439 $\pm$ 54.3568
ΔR_{bW}^{max}	402.892 $\pm$ 34.4214
Top Mass	227.409 $\pm$ 25.4251

TABLE C.5: Complete cutflow for $t-channel$ single top process. Only statistical uncertainties are given. Selection criteria are those stated in Table 6.3.

Appendix D

Systematic uncertainties breakdown tables

In this Appendix, the the systematic uncertainties tables, broken down by their sources, are shown for all the measured spectra presented in this thesis. The tables for the absolute cross sections unfolded at particle level are shown in Section D.1, while the corresponding relative cross sections are presented in Section D.2. The parton level results are presented in Sections D.3 and D.4 for the absolute and relative cross sections, respectively.

D.1 Absolute cross sections, unfolded to particle level

Bins [GeV]	0–20	20–45	45–70	70–100	100–130	130–170	170–210	210–270	270–550
$d\sigma$ / $d\,P^{tt}_{out}$ [pb/GeV]	$2.12 \cdot 10^{-2}$	$1.68 \cdot 10^{-2}$	$1.21 \cdot 10^{-2}$	$9.31 \cdot 10^{-3}$	$6.32 \cdot 10^{-3}$	$3.52 \cdot 10^{-3}$	$1.67 \cdot 10^{-3}$	$4.79 \cdot 10^{-4}$	$4.82 \cdot 10^{-5}$
Total Uncertainty [%]	$^{+13.2}_{-12.7}$	$^{+14.1}_{-12.6}$	$^{+13.4}_{-14.1}$	$^{+13.4}_{-15.0}$	$^{+15.0}_{-16.4}$	$^{+14.7}_{-15.5}$	$^{+18.1}_{-17.4}$	$^{+15.6}_{-17.0}$	$^{+26.4}_{-27.7}$
Statistics [%]	±1.5	±1.6	±2.0	±2.1	±2.7	±3.1	±4.7	±6.5	±8.6
Systematics [%]	$^{+13.0}_{-12.5}$	$^{+13.9}_{-12.4}$	$^{+13.1}_{-13.8}$	$^{+13.0}_{-14.7}$	$^{+14.4}_{-15.8}$	$^{+14.0}_{-14.8}$	$^{+16.9}_{-16.2}$	$^{+13.4}_{-15.1}$	$^{+23.8}_{-25.3}$
Jet vertex fraction [%]	$^{+0.33}_{-0.35}$	$^{+0.41}_{-0.44}$	$^{+0.51}_{-0.54}$	$^{+0.57}_{-0.60}$	$^{+0.55}_{-0.57}$	$^{+0.49}_{-0.52}$	$^{+0.41}_{-0.44}$	$^{+0.41}_{-0.45}$	$^{+0.30}_{-0.33}$
b-Tagged jet energy scale (JES) [%]	$^{+0.83}_{-0.69}$	$^{+0.94}_{-0.66}$	$^{+1.15}_{-1.00}$	$^{+0.20}_{-1.05}$	$^{+0.43}_{-1.12}$	$^{+0.73}_{-1.14}$	±0.74	$^{+1.04}_{-0.99}$	$^{+1.85}_{-0.46}$
Effective detector NP set 1 (JES) [%]	$^{+2.24}_{-1.74}$	$^{+2.17}_{-1.68}$	$^{+1.84}_{-1.48}$	$^{+1.27}_{-2.02}$	$^{+1.29}_{-2.52}$	$^{+1.19}_{-2.52}$	±2.96	$^{+0.74}_{-0.95}$	$^{+3.46}_{-2.08}$
Effective mixed NP set 1 (JES) [%]	$^{+0.38}_{-0.17}$	$^{+0.52}_{-0.19}$	$^{+0.17}_{-}$	∓0.27	$^{+0.60}_{-0.47}$	∓0.70	±1.26	$^{+0.47}_{-0.37}$	$^{+2.23}_{-2.54}$
Effective mixed NP set 2 (JES) [%]	$^{-0.22}_{+0.14}$	$^{-0.21}_{+0.58}$	$^{-0.33}_{-}$	∓0.27	$^{-0.15}_{+0.75}$	∓0.59	$^{-}_{+1.42}$	$^{-0.31}_{+0.13}$	$^{-0.15}_{+1.13}$
Effective mixed NP set 3 (JES) [%]	-	-	-	∓0.11	$^{+0.28}_{-}$	$^{+0.17}_{-}$	±0.19	$^{-0.26}_{+2.10}$	-
Effective modelling NP set 1 (JES) [%]	$^{+6.20}_{-5.41}$	$^{+7.64}_{-5.62}$	$^{+6.66}_{-7.39}$	$^{+5.74}_{-7.99}$	$^{+6.63}_{-7.45}$	$^{+5.53}_{-5.96}$	$^{+5.05}_{-1.69}$	$^{-5.44}_{+1.27}$	$^{+7.56}_{-6.51}$
Effective modelling NP set 2 (JES) [%]	$^{+1.48}_{-1.28}$	$^{+1.64}_{-1.35}$	$^{+1.23}_{-0.93}$	$^{+0.37}_{-0.90}$	$^{+0.79}_{-1.20}$	∓1.12	±1.75	$^{-1.01}_{+0.74}$	$^{+2.02}_{-2.07}$
Effective modelling NP set 3 (JES) [%]	$^{+0.48}_{-0.64}$	±0.39	$^{+0.45}_{-0.74}$	$^{+0.36}_{-0.50}$	$^{+0.63}_{-0.46}$	∓0.56	±0.99	∓1.22	$^{-1.28}_{+2.10}$
Effective modelling NP set 4 (JES) [%]	$^{+0.39}_{-0.52}$	$^{+0.75}_{-0.42}$	$^{+0.40}_{-0.29}$	$^{+0.24}_{-0.34}$	$^{+0.92}_{-0.87}$	$^{-}_{-0.37}$	±1.10	$^{+0.31}_{-0.38}$	$^{+0.54}_{-0.45}$
Effective statistical NP set 1 (JES) [%]	-	-	-	-	-	-	-	-	-
Effective statistical NP set 2 (JES) [%]	$^{-0.41}_{+0.19}$	$^{-0.19}_{+0.53}$	$^{-0.21}_{+0.44}$	$^{-0.30}_{-}$	$^{-0.89}_{+0.70}$	$^{-0.34}_{+0.59}$	±0.41	$^{-0.18}_{+0.15}$	$^{+0.53}_{-0.34}$
Effective statistical NP set 3 (JES) [%]	∓0.11	±0.23	$^{+0.21}_{-0.12}$	∓0.22	±0.11	-	±0.58	$^{+0.21}_{-}$	$^{-0.34}_{+1.15}$
Effective statistical NP set 4 (JES) [%]	-	$^{+0.26}_{-}$	-	∓0.19	$^{+0.24}_{-}$	$^{+0.27}_{-0.17}$	±0.31	$^{+0.42}_{-}$	$^{-0.51}_{+0.41}$
Effective statistical NP set 5 (JES) [%]	$^{-0.29}_{+0.22}$	$^{-0.31}_{+0.45}$	-	$^{-0.30}_{-}$	$^{-0.37}_{+0.27}$	$^{-0.11}_{+0.20}$	$^{-0.33}_{-}$	±0.40	-
Effective statistical NP set 6 (JES) [%]	$^{+0.11}_{-0.18}$	±0.15	-	∓0.16	$^{+0.44}_{-0.25}$	±0.29	∓0.21	$^{+0.83}_{-0.38}$	$^{-0.79}_{+0.84}$
η intercalibration model (JES) [%]	$^{+1.75}_{-1.30}$	$^{+1.67}_{-1.38}$	$^{+1.75}_{-0.88}$	$^{+0.61}_{-1.74}$	$^{+1.33}_{-2.05}$	$^{+1.29}_{-1.88}$	$^{+1.69}_{-0.91}$	±0.95	$^{+1.30}_{-1.90}$
high E η intercalibration non closure (JES) [%]	-	-	-	-	-	-	-	-	-
neg η intercalibration non closure (JES) [%]	-	-	-	-	-	-	±0.11	∓0.12	-
pos η intercalibration non closure (JES) [%]	-	-	-	-	-	-	-	-	-
η intercalibration total stat (JES) [%]	$^{+0.46}_{-0.50}$	$^{+0.73}_{-0.34}$	$^{+0.54}_{-0.37}$	$^{+0.12}_{-0.45}$	$^{+0.82}_{-0.95}$	$^{+0.61}_{-0.51}$	±0.76	±0.41	$^{-0.40}_{-}$
Flavour composition (JES) [%]	$^{+0.86}_{-0.83}$	$^{+1.15}_{-0.48}$	$^{+1.07}_{-0.13}$	$^{+0.83}_{-1.15}$	$^{+1.48}_{-1.69}$	$^{+1.25}_{-0.96}$	$^{+2.41}_{-}$	-	$^{+1.14}_{-2.24}$
Flavour response (JES) [%]	$^{-3.03}_{+3.17}$	$^{-3.38}_{+3.80}$	$^{-3.41}_{+3.93}$	$^{-3.07}_{+3.17}$	$^{-3.75}_{+2.69}$	$^{-3.92}_{+2.67}$	±3.39	$^{-2.44}_{+0.39}$	$^{-5.61}_{+4.86}$
Pile-up offset μ (JES) [%]	$^{-0.18}_{+0.16}$	$^{-0.17}_{+0.28}$	±0.26	$^{-0.40}_{-}$	$^{-0.39}_{+0.38}$	$^{+0.27}_{-0.55}$	±0.96	$^{+0.54}_{-0.28}$	±0.95
Pile-up offset N_{PV} (JES) [%]	$^{+0.31}_{-0.20}$	±0.93	±0.57	∓0.16	$^{-1.20}_{+0.44}$	$^{+0.64}_{-1.15}$	±1.47	$^{+0.47}_{-1.32}$	$^{-}_{+0.47}$
Pile-up offset p_T (JES) [%]	$^{+0.12}_{-0.29}$	-	±0.59	∓0.41	∓0.29	$^{+0.47}_{-0.54}$	±1.41	$^{+0.27}_{-0.45}$	∓1.40
Pile-up offset ρ topology (JES) [%]	$^{+3.70}_{-3.04}$	$^{+4.33}_{-3.29}$	$^{+4.40}_{-4.02}$	$^{+3.35}_{-4.03}$	$^{+3.20}_{-4.78}$	$^{+2.98}_{-3.84}$	±4.51	$^{+0.66}_{-2.82}$	$^{+5.00}_{-3.14}$
Punch-through (JES) [%]	-	-	-	-	-	-	-	∓0.26	∓0.29
Single particle high-p_T (JES) [%]	-	-	-	-	-	-	-	-	-
b-Quark tagging efficiency (eigenvector 0) [%]	$^{-3.67}_{+3.73}$	$^{-3.75}_{+3.81}$	$^{-3.69}_{+3.75}$	$^{-3.71}_{+3.77}$	$^{-3.76}_{+3.82}$	$^{-4.07}_{+4.15}$	$^{-4.14}_{+4.21}$	$^{-4.07}_{+4.13}$	$^{-4.34}_{+4.43}$
b-Quark tagging efficiency (eigenvector 1) [%]	$^{-0.80}_{+0.81}$	$^{-0.77}_{+0.78}$	∓0.67	∓0.61	∓0.48	$^{-0.55}_{+0.56}$	∓0.73	$^{-1.03}_{+1.04}$	$^{-1.76}_{+1.78}$
b-Quark tagging efficiency (eigenvector 2) [%]	$^{+1.43}_{-1.42}$	$^{+1.43}_{-1.42}$	$^{+1.36}_{-1.35}$	$^{+1.35}_{-1.34}$	$^{+1.28}_{-1.27}$	$^{+1.31}_{-1.30}$	$^{+1.33}_{-1.32}$	$^{+1.36}_{-1.35}$	$^{+1.34}_{-1.33}$
b-Quark tagging efficiency (eigenvector 3) [%]	-	-	-	-	-	-	±0.19	$^{+0.33}_{-0.32}$	±0.44
b-Quark tagging efficiency (eigenvector 4) [%]	∓0.21	∓0.20	∓0.19	∓0.18	∓0.17	∓0.17	∓0.16	∓0.14	-
b-Quark tagging efficiency (eigenvector 5) [%]	-	-	-	-	-	-	-	-	-
c-Quark tagging efficiency (eigenvector 0) [%]	±0.66	$^{+0.64}_{-0.63}$	±0.58	±0.61	$^{+0.54}_{-0.53}$	±0.58	±0.59	±0.75	±0.92
c-Quark tagging efficiency (eigenvector 1) [%]	±0.30	±0.27	±0.21	±0.22	±0.19	±0.26	±0.23	±0.34	±0.46
c-Quark tagging efficiency (eigenvector 2) [%]	-	-	-	-	-	-	-	±0.12	±0.16
Light-jet tagging efficiency (eigenvector 0) [%]	$^{+0.47}_{-0.48}$	±0.65	±0.66	±0.50	±0.54	±0.72	$^{+1.05}_{-1.04}$	$^{+0.98}_{-0.97}$	$^{+1.83}_{-1.81}$
Light-jet tagging efficiency (eigenvector 1) [%]	-	-	-	-	-	-	-	±0.11	±0.31
Light-jet tagging efficiency (eigenvector 2) [%]	-	-	-	-	-	-	-	-	-
Light-jet tagging efficiency (eigenvector 3) [%]	-	-	-	-	-	-	-	-	-
Light-jet tagging efficiency (eigenvector 4) [%]	-	-	-	-	-	-	-	-	-
Light-jet tagging efficiency (eigenvector 5) [%]	-	-	-	-	-	-	-	-	-
Light-jet tagging efficiency (eigenvector 6) [%]	-	-	-	-	-	-	-	-	-
Light-jet tagging efficiency (eigenvector 7) [%]	-	-	-	-	-	-	-	-	-
Light-jet tagging efficiency (eigenvector 8) [%]	-	-	-	-	-	-	-	-	-
Light-jet tagging efficiency (eigenvector 9) [%]	-	-	-	-	-	-	-	-	-
Light-jet tagging efficiency (eigenvector 10) [%]	-	-	-	-	-	-	-	-	-
b-Quark tagging extrapolation [%]	-	-	-	-	-	∓0.13	∓0.14	∓0.24	∓0.42
b-Quark tagging extrapolation from c-Quark [%]	-	-	-	-	-	-	-	-	-
JET JER cross calibration forward [%]	-	-	-	-	-	-	-	-	-
JET JER noise forward [%]	-	-	-	-	-	-	-	-	-
JET JER NP0 [%]	-	-	-	-	-	-	-	-	-
JET JER NP1 [%]	∓0.13	-	$^{-0.68}_{-}$	-	∓0.15	±0.33	∓0.24	$^{+0.34}_{-0.13}$	∓1.61
JET JER NP2 [%]	∓0.28	±0.64	$^{+0.18}_{-2.85}$	$^{-0.37}_{+1.63}$	±0.74	∓0.89	∓0.52	$^{+1.72}_{-1.71}$	∓1.77
JET JER NP3 [%]	$^{-0.50}_{+0.22}$	$^{+0.51}_{-}$	∓0.59	$^{-1.58}_{+1.28}$	$^{+0.35}_{-0.26}$	$^{+0.14}_{-0.97}$	∓1.36	$^{-0.64}_{+0.34}$	$^{+2.86}_{-0.29}$
JET JER NP4 [%]	-	$^{+0.57}_{-0.28}$	$^{+0.13}_{-1.31}$	$^{-0.21}_{+0.60}$	±1.26	$^{-0.94}_{+0.61}$	$^{+0.72}_{-1.59}$	∓0.59	$^{-1.62}_{+2.96}$
JET JER NP5 [%]	±0.34	±0.25	-	$^{-}_{-0.70}$	±1.36	∓1.17	$^{+1.06}_{-0.95}$	$^{-}_{+0.29}$	$^{-0.58}_{+0.28}$
JET JER NP6 [%]	∓0.41	$^{-}_{+0.71}$	$^{-0.97}_{+0.26}$	∓1.47	±1.49	$^{+0.18}_{-0.55}$	$^{-0.85}_{-}$	±1.42	∓1.69
JET JER NP7 [%]	$^{+0.23}_{-0.42}$	$^{-0.24}_{+0.85}$	∓0.48	$^{+0.42}_{-0.62}$	±0.79	∓0.55	$^{+0.73}_{-1.40}$	$^{+0.59}_{-0.36}$	$^{-1.96}_{+2.45}$
JET JER NP8 [%]	-	-	-	-	-	-	-	-	-
QCD estimation [%]	±4.29	±4.99	±5.07	±3.75	±2.42	±6.07	±3.23	±1.95	∓1.92
K-factor normalization mass [%]	$^{+2.72}_{-2.63}$	$^{+2.72}_{-2.63}$	$^{+2.65}_{-2.56}$	$^{+2.63}_{-2.55}$	$^{+2.57}_{-2.49}$	$^{+2.65}_{-2.57}$	$^{+2.72}_{-2.63}$	$^{+2.81}_{-2.72}$	$^{+2.78}_{-2.69}$
K-factor normalization PDFAS [%]	±4.11	±4.11	±4.00	±3.98	±3.88	±4.01	±4.12	±4.25	±4.40
K-factor normalization scale [%]	$^{+2.32}_{-3.42}$	$^{+2.32}_{-3.43}$	$^{+2.26}_{-3.33}$	$^{+2.24}_{-3.32}$	$^{+2.19}_{-3.23}$	$^{+2.26}_{-3.34}$	$^{+2.32}_{-3.43}$	$^{+2.39}_{-3.54}$	$^{+2.37}_{-3.50}$
Luminosity [%]	∓2.05	∓2.05	∓2.05	∓2.05	∓2.05	∓2.05	∓2.05	∓2.05	∓2.05
MCSignal stat. [%]	±1.14	±1.21	±1.40	±1.51	±1.86	±2.17	±3.41	±4.13	±7.06
QCD stat. [%]	±0.82	±1.02	±1.48	±1.86	±2.50	±2.32	±2.66	±2.00	±2.03
ISR/FSR + scale [%]	±1.74	±1.27	$^{-1.85}_{+0.15}$	∓3.38	∓0.52	$^{+3.28}_{-}$	∓8.76	∓7.24	$^{-10.6}_{+0.11}$
Alternate hard-scattering model [%]	±3.95	∓1.03	±0.75	±0.21	∓1.50	±6.15	∓4.58	±1.46	∓14.0
Alternate parton-shower model [%]	±2.34	±2.26	±2.26	±5.39	±8.35	±0.51	±5.35	±6.79	∓11.2
Inter PDF [%]	-	-	-	-	-	-	-	±0.24	±0.17
Intra PDF [%]	±0.15	±0.15	±0.12	±0.13	±0.14	±0.19	±0.22	±0.26	±0.53

TABLE D.1: Table of systematics for the absolute differential cross-section at the particle level for the $|P^{t\bar{t}}_{\text{out}}|$ observable.

Bins [Unit $\Delta\phi$]	0–1	1–1.50	1.50–2	2–2.20	2.20–2.45	2.45–2.65	2.65–2.85	2.85–3.20
$d\sigma$ / $d\Delta\phi$ [pb/ Unit $\Delta\phi$]	$4.24 \cdot 10^{-2}$	$8.93 \cdot 10^{-2}$	$1.81 \cdot 10^{-1}$	$3.42 \cdot 10^{-1}$	$5.23 \cdot 10^{-1}$	$8.48 \cdot 10^{-1}$	$1.56 \cdot 10^{0}$	$2.78 \cdot 10^{0}$
Total Uncertainty [%]	$^{+24.2}_{-24.3}$	$^{+22.5}_{-27.5}$	$^{+18.0}_{-18.2}$	$^{+20.5}_{-21.2}$	$^{+14.4}_{-16.2}$	$^{+15.0}_{-18.2}$	$^{+15.1}_{-14.8}$	$^{+12.0}_{-11.2}$
Statistics [%]	±6.3	±6.1	±4.3	±5.0	±3.5	±3.0	±2.0	±0.9
Systematics [%]	$^{+21.5}_{-21.7}$	$^{+20.0}_{-25.4}$	$^{+16.5}_{-16.7}$	$^{+18.7}_{-19.6}$	$^{+13.4}_{-15.3}$	$^{+14.3}_{-17.7}$	$^{+14.8}_{-14.5}$	$^{+11.9}_{-11.1}$
Jet vertex fraction [%]	$^{+0.83}_{-0.84}$	$^{+0.63}_{-0.66}$	$^{+0.66}_{-0.69}$	$^{+0.58}_{-0.61}$	$^{+0.52}_{-0.56}$	$^{+0.59}_{-0.61}$	$^{+0.52}_{-0.55}$	$^{+0.35}_{-0.37}$
b-Tagged jet energy scale (JES) [%]	$^{-0.75}_{+0.52}$	±0.85	$^{+0.88}_{-0.22}$	$^{+1.48}_{-1.08}$	$^{+0.46}_{-2.01}$	$^{+0.19}_{-1.11}$	$^{+0.72}_{-0.95}$	$^{+0.91}_{-0.77}$
Effective detector NP set 1 (JES) [%]	±1.51	$^{+0.64}_{-0.61}$	$^{+1.88}_{-2.15}$	$^{+3.99}_{-4.17}$	$^{+0.73}_{-2.15}$	$^{+1.90}_{-3.26}$	$^{+1.10}_{-1.07}$	$^{+2.11}_{-1.57}$
Effective mixed NP set 1 (JES) [%]	±0.83	±1.71	∓1.05	$^{+1.72}_{-1.38}$	$^{-0.28}_{+0.34}$	$^{+0.57}_{-0.87}$	-	$^{+0.38}_{-0.20}$
Effective mixed NP set 2 (JES) [%]	$^{+0.31}_{-}$	±1.32	$^{-0.51}_{+0.25}$	$^{-0.92}_{+1.58}$	-	$^{-0.70}_{+0.15}$	∓0.16	$^{-0.27}_{+0.35}$
Effective mixed NP set 3 (JES) [%]	±0.47	±0.25	$^{+0.23}_{-0.19}$	±0.17	∓0.27	$^{+0.17}_{-}$	-	-
Effective modelling NP set 1 (JES) [%]	$^{+1.79}_{-4.94}$	$^{+5.33}_{-6.90}$	$^{+7.91}_{-8.11}$	$^{+6.24}_{-9.61}$	$^{+6.23}_{-7.62}$	$^{+6.12}_{-9.03}$	$^{+7.13}_{-6.43}$	$^{+6.19}_{-5.25}$
Effective modelling NP set 2 (JES) [%]	$^{+1.73}_{-0.14}$	±1.49	∓1.12	$^{+1.29}_{-1.54}$	∓0.72	$^{+0.81}_{-2.23}$	$^{+0.81}_{-0.54}$	$^{+1.56}_{-1.28}$
Effective modelling NP set 3 (JES) [%]	$^{-0.37}_{-}$	∓0.22	$^{+0.36}_{-1.49}$	$^{+0.84}_{-0.47}$	$^{+1.06}_{-0.46}$	$^{+0.14}_{-0.47}$	$^{+0.45}_{-0.67}$	$^{+0.31}_{-0.17}$
Effective modelling NP set 4 (JES) [%]	±0.98	±0.92	$^{+0.31}_{-0.84}$	$^{+1.81}_{-0.95}$	$^{+0.12}_{-0.15}$	$^{+0.39}_{-0.84}$	$^{+0.12}_{-0.22}$	$^{+0.57}_{-0.47}$
Effective statistical NP set 1 (JES) [%]	-	-	-	-	-	-	-	-
Effective statistical NP set 2 (JES) [%]	∓0.24	±0.84	$^{-0.94}_{+0.65}$	$^{-0.37}_{+1.10}$	$^{-0.70}_{+0.48}$	$^{-0.77}_{+0.21}$	∓0.30	$^{-0.22}_{+0.34}$
Effective statistical NP set 3 (JES) [%]	±0.28	±0.44	∓0.15	±0.60	$^{-}_{-0.17}$	∓0.18	$^{+0.25}_{-0.28}$	-
Effective statistical NP set 4 (JES) [%]	$^{-0.18}_{+0.37}$	$^{-0.55}_{+0.30}$	-	±0.30	∓0.20	$^{+0.44}_{-0.34}$	$^{-0.14}_{+0.12}$	$^{+0.18}_{-0.13}$
Effective statistical NP set 5 (JES) [%]	$^{-0.18}_{+0.43}$	$^{+0.25}_{-0.16}$	-	$^{-0.28}_{+0.61}$	∓0.38	$^{-0.29}_{+0.30}$	$^{-0.22}_{-}$	$^{-0.25}_{+0.31}$
Effective statistical NP set 6 (JES) [%]	$^{-0.16}_{+0.35}$	±0.26	±0.23	$^{+0.32}_{-0.23}$	$^{+0.10}_{-0.21}$	$^{+0.31}_{-0.27}$	-	$^{+0.13}_{-}$
η intercalibration model (JES) [%]	$^{+1.58}_{-0.65}$	±0.36	$^{+1.69}_{-2.39}$	$^{+4.06}_{-3.94}$	$^{+1.07}_{-1.21}$	$^{+1.28}_{-2.78}$	$^{+1.09}_{-1.06}$	$^{+1.54}_{-1.11}$
high E η intercalibration non closure (JES) [%]	-	-	-	-	-	-	-	-
neg η intercalibration non closure (JES) [%]	$^{+0.19}_{-0.15}$	±0.11	-	-	-	-	-	-
pos η intercalibration non closure (JES) [%]	∓0.37	-	-	-	-	-	-	-
η intercalibration total stat (JES) [%]	∓0.19	$^{-}_{+0.88}$	$^{+0.60}_{-0.90}$	$^{+2.16}_{-1.75}$	$^{+0.59}_{-0.48}$	$^{+0.60}_{-1.04}$	$^{-}_{-0.48}$	$^{+0.57}_{-0.30}$
Flavour composition (JES) [%]	±0.52	±1.86	±1.54	$^{+3.89}_{-2.97}$	$^{+1.82}_{-1.20}$	$^{+1.21}_{-1.68}$	$^{+0.25}_{-0.32}$	$^{+1.01}_{-0.58}$
Flavour response (JES) [%]	$^{-1.94}_{+0.71}$	$^{-4.27}_{+4.37}$	$^{-5.39}_{+5.05}$	$^{-4.33}_{+3.59}$	$^{-3.42}_{+2.50}$	$^{-4.78}_{+3.06}$	$^{-2.65}_{+3.32}$	$^{-2.79}_{+3.24}$
Pile-up offset μ (JES) [%]	$^{-0.29}_{+0.18}$	$^{+0.40}_{-0.89}$	$^{-0.29}_{+0.20}$	±0.49	∓0.15	∓0.22	$^{-0.14}_{+0.17}$	$^{-}_{+0.21}$
Pile-up offset N_{PV} (JES) [%]	±0.57	$^{-}_{-0.21}$	$^{-0.70}_{+1.80}$	$^{+0.67}_{-0.61}$	∓0.84	∓0.15	$^{+0.42}_{-0.15}$	$^{+0.53}_{-}$
Pile-up offset p_T (JES) [%]	$^{+0.88}_{-0.62}$	±0.35	$^{-0.77}_{+1.31}$	±0.29	∓0.22	$^{-}_{-0.34}$	-	$^{+0.26}_{-0.27}$
Pile-up offset ρ topology (JES) [%]	$^{+1.80}_{-2.07}$	$^{+3.04}_{-3.31}$	$^{+5.73}_{-4.94}$	$^{+5.80}_{-5.04}$	$^{+3.07}_{-4.72}$	$^{+3.84}_{-5.60}$	$^{+3.46}_{-3.12}$	$^{+3.69}_{-2.99}$
Punch-through (JES) [%]	$^{-}_{-0.24}$	-	-	-	-	-	-	-
Single particle high-p_T (JES) [%]	-	-	-	-	-	-	-	-
b-Quark tagging efficiency (eigenvector 0) [%]	$^{-4.02}_{+4.11}$	$^{-3.66}_{+3.71}$	$^{-3.61}_{+3.67}$	$^{-3.47}_{+3.53}$	$^{-3.75}_{+3.81}$	$^{-3.81}_{+3.87}$	$^{-3.77}_{+3.83}$	$^{-3.75}_{+3.82}$
b-Quark tagging efficiency (eigenvector 1) [%]	-	-	∓0.28	∓0.30	∓0.44	∓0.53	∓0.63	∓0.92
b-Quark tagging efficiency (eigenvector 2) [%]	$^{+1.17}_{-1.16}$	$^{+1.13}_{-1.12}$	$^{+1.21}_{-1.20}$	$^{+1.25}_{-1.24}$	$^{+1.29}_{-1.28}$	$^{+1.34}_{-1.33}$	$^{+1.37}_{-1.36}$	$^{+1.44}_{-1.43}$
b-Quark tagging efficiency (eigenvector 3) [%]	∓0.47	∓0.35	∓0.22	∓0.23	∓0.13	-	-	±0.16
b-Quark tagging efficiency (eigenvector 4) [%]	-	∓0.12	∓0.14	∓0.16	∓0.17	∓0.17	∓0.19	∓0.21
b-Quark tagging efficiency (eigenvector 5) [%]	-	-	-	-	-	-	-	-
c-Quark tagging efficiency (eigenvector 0) [%]	±0.75	±0.35	±0.45	±0.54	±0.52	±0.52	±0.61	±0.67
c-Quark tagging efficiency (eigenvector 1) [%]	±0.29	±0.13	±0.13	±0.21	±0.19	±0.17	±0.21	±0.30
c-Quark tagging efficiency (eigenvector 2) [%]	-	-	-	-	-	-	-	-
Light-jet tagging efficiency (eigenvector 0) [%]	±0.74	±0.62	$^{+0.67}_{-0.66}$	$^{+0.41}_{-0.42}$	±0.59	$^{+0.77}_{-0.76}$	±0.60	±0.59
Light-jet tagging efficiency (eigenvector 1) [%]	±0.15	-	±0.13	-	-	-	-	-
Light-jet tagging efficiency (eigenvector 2) [%]	-	-	-	-	-	-	-	-
Light-jet tagging efficiency (eigenvector 3) [%]	-	-	-	-	-	-	-	-
Light-jet tagging efficiency (eigenvector 4) [%]	-	-	-	-	-	-	-	-
Light-jet tagging efficiency (eigenvector 5) [%]	-	-	-	-	-	-	-	-
Light-jet tagging efficiency (eigenvector 6) [%]	-	-	-	-	-	-	-	-
Light-jet tagging efficiency (eigenvector 7) [%]	-	-	-	-	-	-	-	-
Light-jet tagging efficiency (eigenvector 8) [%]	-	-	-	-	-	-	-	-
Light-jet tagging efficiency (eigenvector 9) [%]	-	-	-	-	-	-	-	-
Light-jet tagging efficiency (eigenvector 10) [%]	-	-	-	-	-	-	-	-
b-Quark tagging extrapolation [%]	∓0.21	∓0.15	∓0.14	∓0.10	-	-	-	-
b-Quark tagging extrapolation from c-Quark [%]	-	-	-	-	-	-	-	-
JET JER cross calibration forward [%]	-	-	-	-	-	-	-	-
JET JER noise forward [%]	-	-	-	-	-	-	-	-
JET JER NP0 [%]	-	-	-	-	-	-	-	-
JET JER NP1 [%]	∓4.21	∓0.37	$^{+0.50}_{-}$	$^{+0.56}_{-0.16}$	∓0.45	∓0.58	$^{-0.19}_{-}$	-
JET JER NP2 [%]	∓3.19	∓1.95	-	$^{-0.19}_{+2.87}$	$^{+0.45}_{-1.12}$	∓1.27	±0.54	-
JET JER NP3 [%]	∓0.89	∓1.34	±0.40	$^{+0.81}_{-}$	$^{+0.17}_{-0.71}$	∓1.63	±0.36	$^{-0.32}_{+0.13}$
JET JER NP4 [%]	$^{+1.46}_{-2.96}$	∓2.80	$^{-0.97}_{+0.96}$	±2.02	$^{-1.82}_{+0.35}$	$^{+0.78}_{-2.26}$	±0.70	$^{+0.22}_{-}$
JET JER NP5 [%]	$^{-1.33}_{+2.99}$	∓2.41	±1.20	$^{+1.05}_{-1.00}$	$^{+0.12}_{-1.76}$	$^{+0.14}_{-0.16}$	-	±0.32
JET JER NP6 [%]	$^{-0.95}_{+1.24}$	∓3.62	±1.14	$^{+0.62}_{-0.29}$	∓1.36	∓0.51	$^{-}_{+0.87}$	∓0.18
JET JER NP7 [%]	±2.39	∓2.95	±1.59	±1.29	∓0.97	$^{+0.19}_{-0.86}$	∓0.54	±0.16
JET JER NP8 [%]	-	-	-	-	-	-	-	-
QCD estimation [%]	±6.19	±2.25	±3.69	±3.58	±4.51	±3.15	±2.83	±3.46
K-factor normalization mass [%]	$^{+2.24}_{-2.17}$	$^{+2.29}_{-2.22}$	$^{+2.48}_{-2.40}$	$^{+2.40}_{-2.32}$	$^{+2.57}_{-2.49}$	$^{+2.66}_{-2.57}$	$^{+2.65}_{-2.57}$	$^{+2.75}_{-2.66}$
K-factor normalization PDFAS [%]	±3.39	±3.47	±3.75	±3.63	±3.90	±4.02	±4.01	±4.16
K-factor normalization scale [%]	$^{+1.91}_{-2.82}$	$^{+1.95}_{-2.89}$	$^{+2.11}_{-3.12}$	$^{+2.05}_{-3.02}$	$^{+2.19}_{-3.24}$	$^{+2.27}_{-3.35}$	$^{+2.26}_{-3.34}$	$^{+2.34}_{-3.46}$
Luminosity [%]	∓2.05	∓2.05	∓2.05	∓2.05	∓2.05	∓2.05	∓2.05	∓2.05
MCSignal stat. [%]	±3.78	±3.73	±2.70	±3.27	±2.28	±2.01	±1.49	±0.68
QCD stat. [%]	±8.29	±7.55	±5.15	±5.59	±3.38	±2.51	±1.47	±0.40
ISR/FSR + scale [%]	$^{+4.30}_{-2.07}$	$^{-14.9}_{+0.31}$	$^{+2.07}_{-1.53}$	$^{+2.01}_{-1.97}$	∓5.86	∓5.47	±4.38	$^{-0.12}_{+0.14}$
Alternate hard-scattering model [%]	±10.7	∓12.5	∓3.85	±0.72	∓3.11	±6.09	±2.78	±0.17
Alternate parton-shower model [%]	±13.4	±9.10	±7.00	±11.0	∓1.01	±1.34	±7.45	±1.59
Inter PDF [%]	-	-	-	-	-	-	-	-
Intra PDF [%]	±0.15	±0.15	-	±0.21	±0.22	±0.13	±0.18	±0.12

TABLE D.2: Table of systematics for the absolute differential cross-section at the particle level for the $\Delta\phi_{t\bar{t}}$ observable.

Bins [GeV]	0–0.40	0.40–1.25	1.25–1.70	1.70–1.95	1.95–2.15	2.15–2.30	2.30–2.45	2.45–2.60	2.60–2.75	2.75–2.85	2.85–3	3–3.10	3.10–3.20	3.20–3.35	3.35–3.60	3.60–3.95	3.95–6
$d\sigma$ / $d\Delta R^{extra1,jet1leading}$ [pb/GeV]	$1.22 \cdot 10^{0}$	$9.13 \cdot 10^{-2}$	$1.67 \cdot 10^{-1}$	$2.38 \cdot 10^{-1}$	$3.18 \cdot 10^{-1}$	$3.46 \cdot 10^{-1}$	$4.29 \cdot 10^{-1}$	$4.15 \cdot 10^{-1}$	$6.09 \cdot 10^{-1}$	$6.35 \cdot 10^{-1}$	$6.08 \cdot 10^{-1}$	$6.28 \cdot 10^{-1}$	$6.03 \cdot 10^{-1}$	$4.25 \cdot 10^{-1}$	$2.96 \cdot 10^{-1}$	$1.71 \cdot 10^{-1}$	$2.44 \cdot 10^{-2}$
Total Uncertainty [%]	+12.9 −14.4	+25.5 −23.0	+23.2 −20.6	+20.4 −21.2	+14.8 −14.3	+15.7 −16.0	+15.4 −19.0	+14.0 −16.6	+13.9 −14.9	+18.7 −15.8	+18.8 −19.6	+18.4 −17.6	+22.8 −23.8	+15.2 −14.3	+19.5 −18.2	+19.3 −18.4	+18.0 −17.7
Statistics [%]	±1.6	±4.0	±4.2	±4.8	±4.4	±5.0	±4.7	±4.6	±3.8	±4.5	±3.9	±4.5	±4.6	±4.7	±4.2	±4.8	±5.1
Systematics [%]	+12.6 −14.1	+24.9 −23.1	+22.5 −19.8	+19.4 −22.1	+13.5 −12.9	+14.2 −14.6	+14.0 −18.8	+12.6 −15.4	+12.8 −13.9	+17.6 −14.5	+18.1 −18.2	+17.3 −16.6	+22.0 −22.9	+13.8 −14.2	+18.7 −17.3	+18.2 −17.2	+16.8 −16.3
Jet vertex fraction [%]	+0.55 −0.58	+0.53 −0.56	+0.42 −0.45	+0.37 −0.41	+0.42 −0.45	+0.45 −0.49	+0.54 −0.56	+0.44 −0.47	+0.56 −0.58	+0.51 −0.54	+0.52 −0.54	+0.59 −0.60	+0.59 −0.52	+0.58 −0.60	+0.69 −0.62	+0.50 −0.54	+0.55 −0.57
b-Tagged jet energy scale (JES) [%]	+0.77 −0.77	+2.07 −2.07	+1.59 −1.59	+0.62 −0.62	+0.78 −0.78	+0.54 −0.54	+0.86 −0.86	+0.60 −0.60	+0.60 −0.60	+0.67 −0.67	+0.72 −0.72	±1.03	±0.58	±0.58	+0.66 −0.66	+1.80 −1.80	+1.66 −1.66
Effective detector NP set 1 (JES) [%]	+1.54 −1.90	+3.89 −2.39	+2.83 −1.86	+1.68 −0.83	+1.88 −0.80	+1.85 −0.68	+1.78 −1.66	+1.79 −1.69	+1.59 −4.14	+3.50 −2.14	+1.38 −2.21	+1.76 −1.59	−0.39 +0.31	+2.45 −1.05	+3.07 −1.51	+2.49 −2.46	+2.70 −2.70
Effective mixed NP set 1 (JES) [%]	+0.53 −0.38	+0.34 −0.86	+0.32 −0.20	±0.35	−0.12 +0.73	±1.28	±0.32	+0.33 −0.93	−1.98 −0.59	+0.93 −0.50	+0.34	±0.71	±1.07	±0.16	±0.18	+0.30 −0.24	+0.88 −0.24
Effective mixed NP set 2 (JES) [%]	+0.48	+0.13 −0.13	+0.22	+0.42 −0.39	±0.63	−0.19 +0.17	+0.43 −0.36	+1.01 −0.16	−0.54 +0.59	+0.22	−0.54 +0.08	+0.89	−0.44 +0.51	−0.41 +0.31	±0.43	+0.24 −0.34	
Effective mixed NP set 3 (JES) [%]		+0.13 −0.13		±0.14				+0.16				±0.17	±0.35	±0.15	±0.25	+0.18 −0.18	
Effective modelling NP set 1 (JES) [%]	+6.34 −7.64	+11.9 −5.85	+10.1 −5.51	+5.84 −3.42	+6.32 −4.25	+2.61 −3.29	+7.05 −4.28	+6.02 −8.02	+7.80 −6.14	+9.36 −6.92	+6.80 −5.80	+8.06 −5.74	+5.48 −8.69	+5.59 −6.02	+7.54 −8.23	+9.11 −8.35	+7.12 −8.91
Effective modelling NP set 2 (JES) [%]	+0.92 −0.82	+1.85 −1.85	+1.37 −1.37	+0.60 −0.60	+0.90 −0.90	±0.26	+0.29 −1.20	+0.29 −1.79	+0.21 −2.41	+0.25 −1.65	+0.25 −1.96	+0.22 −0.22	±0.30	−1.07	−1.07	−1.18	−1.11
Effective modelling NP set 3 (JES) [%]	+0.44 −0.24	+0.88 −0.58	+0.79 −1.07	±0.20 −1.07	±0.47	+1.06 −0.43	−0.59 +0.46	+0.48 −0.43	+0.75 −1.19	+1.50 −0.47	−0.15	−0.45	+0.30 −1.73	−0.23 +0.32	±0.23 −0.46	+1.59 −0.11	+0.30 −0.54
Effective modelling NP set 4 (JES) [%]	+0.58 −0.38	+0.39 −0.34	+0.54 −0.59	+0.56	−0.27	±0.65	+0.46 +0.50 −0.10	−0.64	+0.46 −0.82	+1.34 −0.87	+0.29	+0.76 −0.45	+0.13 −1.10	+0.46 −0.65	+0.76 −0.69	+0.59 −0.14	+0.80 −0.67
Effective statistical NP set 1 (JES) [%]	-	±0.15	-	-	-	±0.11	-	-	-	-	-	-	-	-	-	-	-
Effective statistical NP set 2 (JES) [%]	−0.51 +0.53	+0.51	−0.46 +0.52	±0.62	−0.39 −0.02	±0.53	-	±0.45	−0.71 +0.50	+0.75 −0.29	-	−0.52 +0.45	−1.39 −0.28	−0.41 +0.21	−0.35 +0.73	−0.39 −0.06	−0.14 −0.18
Effective statistical NP set 3 (JES) [%]	-	±0.45	−0.19	±0.10	±0.32	+0.79 −0.43	±0.12	−0.33	+0.50 −0.50	±0.23	±0.17	-	±0.16	+0.13 −0.13	−0.20	±0.27	±0.23
Effective statistical NP set 4 (JES) [%]	-	−0.54	±0.16	+0.62 −0.13	+0.66	±0.29	±0.12	-	±0.22	±0.39	±0.18	+0.41	±0.34	±0.55	±0.48	±0.19	±0.11
Effective statistical NP set 5 (JES) [%]	−0.18	±0.26	−0.23	-	−0.51	±0.23	±0.17	−0.36	-	−0.28	−0.66	−0.32	−0.38	−0.18	−0.26	-	−0.60
Effective statistical NP set 6 (JES) [%]	-	±0.12	±0.22	±0.33	−0.25 +0.25	±0.29	+0.20 −0.72	−0.19 +0.19 −0.44	+0.21 −0.28	+0.28 −0.23	±0.23	−0.14 −0.28	±0.19	−0.57	±0.47	+0.15 −0.26	+0.18 −0.18
η intercalibration model (JES) [%]	+1.39 −1.83	+2.21 −2.81	+1.62 −0.90	±0.64	+2.40 −0.60	±0.67	−0.82	+0.72 −1.41	+1.41 −1.88	+2.52 −1.80	+1.31 −1.94	+1.72 −1.64	+1.80 −1.20	+1.12 −1.18	+2.92 −0.79	+2.85 −1.42	+1.89 −3.87
high E η intercalibration non closure (JES) [%]	-	-	-	-	-	-	-	-	-	-	-	-	-	-	-	-	-
neg η intercalibration non closure (JES) [%]	-	±0.11	-	-	-	-	-	-	±0.14	±0.18	-	-	-	-	±0.11	±0.10	±0.18
pos η intercalibration non closure (JES) [%]	-	-	-	-	-	-	-	-	-	-	-	-	-	±0.12	-	-	±0.10
η intercalibration total stat (JES) [%]	±0.63 −0.59	±0.80 −0.49	+0.30 −0.27	±0.63	−0.98 +0.85	±0.80	-	−0.46 +0.63	+0.99 −1.24	+1.24 −2.18	+1.39 −0.24	+0.74 −1.20	±0.49 −1.15	−0.14 −0.26	+1.01 −0.49	+1.16 −0.28	+0.52 −0.50
Flavour composition (JES) [%]	−0.96 −1.56	−1.12 −1.82	−0.63 −1.73	−0.55 −2.07	−0.70 −2.35	−0.14 −1.40	+0.97 −1.72	−1.35 −1.33	−1.97 −3.27	−1.70 −3.06	−0.40 −1.30	−1.61 −2.52	−1.99 −2.02	−0.34 −2.31	−0.66 −2.13	−0.49 −1.63	−1.20 −3.08
Flavour response (JES) [%]	+3.46 −3.91	+4.07 −4.07	−0.28 −2.43	−2.43 +2.43	+5.41	+1.42	+3.49 −2.37	−2.37	+2.89 −0.96	+6.68	−0.29	−0.52	−3.98	+0.73 −0.73	+4.52 −0.62	−4.57	+4.22 −3.77
Pile-up offset μ (JES) [%]	−0.15	±0.49	±0.41	+0.50 −0.50	−0.29 −0.80	±0.95	−0.12 −0.44	±0.45	−0.96	+0.13 −1.46	±0.36	±0.28	±0.49	−0.58 −0.88	−0.62 −0.89	±0.47	−0.77 −0.77
Pile-up offset N_{PV} (JES) [%]	+0.24	±1.75	±0.36	±0.40	−1.09	±0.38	+0.44 −0.15	−0.38	+0.80 −0.36	+0.40 −0.12	+0.40	±0.40	+1.32 −1.58	+1.01 −1.04	+0.89 −0.41	±0.26	±0.84
Pile-up offset p_T (JES) [%]	+0.15 −1.06	+1.04 −2.96	+0.70 −1.28	±0.67	−0.29 +1.07	±0.28	±0.12 −1.30	+0.26 −0.73	−0.36 +0.31	+0.79	−0.60	+0.18 −0.31	+1.14 −2.65	+0.39 −1.42	±0.52 −1.04	±0.12 −1.52	±0.75 −1.21
Pile-up offset ρ topology (JES) [%]	−4.64	−5.35	−3.48	−2.27	−3.09 −2.65	−2.53	+1.24 −3.57	−0.84 −3.58	−0.61 −4.28	−1.02 −4.81	−1.40 −4.13	−4.24 −3.34	−3.54	−1.75	−2.64	−4.78	−4.66
Punch-through (JES) [%]	-	-	-	-	-	-	-	-	-	-	-	-	-	-	-	−0.16	-
Single particle high-p_T (JES) [%]	-	-	-	-	-	-	-	-	-	-	-	-	-	-	-	-	-
b-Quark tagging efficiency (eigenvector 0) [%]	−3.39 ±3.35	−3.64 ±3.79	−3.84 ±3.89	−3.97 ±4.04	−3.96 ±4.03	−3.87 ±3.91	−3.98 ±4.05	−3.92 ±3.99	−4.06 ±4.14	−3.75 ±3.81	−3.94 ±4.01	−3.89 ±3.97	−3.87 ±3.95	−3.75 ±3.82	−3.95 ±4.02	−4.08 ±4.17	−3.99 ±4.07
b-Quark tagging efficiency (eigenvector 1) [%]	±0.30	±0.86	±0.91	±0.92	±0.87	−0.94	±0.90	±0.76	±0.84	±0.85	−0.91	−0.84	±0.77	±0.82	±0.88	±0.82	±0.81
b-Quark tagging efficiency (eigenvector 2) [%]	+1.22 −1.37	+1.38 −1.42	+1.42 −1.42	+1.43 −1.43	+1.41 −1.41	+1.43 −1.43	+1.42 −1.42	±1.37	+1.42 −1.42	+1.35 −1.35	+1.40 −1.40	+0.85 ±1.36	+1.38 −1.37	+1.36 −1.35	+1.41 −1.40	+1.42 −1.41	+1.43 −1.42
b-Quark tagging efficiency (eigenvector 3) [%]	±0.22	±0.31	±0.23	±0.19	±0.20	±0.18	±0.17	±0.15	±0.11	±0.10	±0.14	±0.10	-	-	-	-	-
b-Quark tagging efficiency (eigenvector 4) [%]	±0.17	±0.21	±0.20	±0.19	±0.17	±0.19	±0.19	±0.19	±0.18	±0.17	±0.18	±0.18	±0.16	±0.16	±0.17	±0.18	±0.19
b-Quark tagging efficiency (eigenvector 5) [%]	-	-	-	-	-	-	-	-	-	-	-	-	-	-	-	-	-
c-Quark tagging efficiency (eigenvector 0) [%]	±0.48	±0.59	±0.71	±0.68	±0.73	±0.65	+0.71 −0.70	±0.63	+0.65 −0.64	+0.53 −0.52	+0.79 −0.78	±0.55	±0.52	±0.55	±0.70	±0.72	±0.63
c-Quark tagging efficiency (eigenvector 1) [%]	±0.16	±0.27	±0.28	±0.25	±0.29	±0.30	±0.25	±0.25	±0.27	±0.21	±0.33	±0.21	±0.19	±0.20	+0.26 −0.27	±0.24	±0.28
c-Quark tagging efficiency (eigenvector 2) [%]	-	-	-	-	-	-	-	-	-	-	-	-	-	-	-	-	-
Light-jet tagging efficiency (eigenvector 0) [%]	+0.76 −0.75	+0.79 −0.82	+1.48 −1.47	±0.28	±0.48	±0.67	±0.83	±0.38	±0.70	±0.45	±0.35	±0.81	+0.77 −0.76	±0.43	±0.53	±0.73	±0.64
Light-jet tagging efficiency (eigenvector 1) [%]	-	-	-	-	-	-	-	-	-	-	-	-	-	-	-	-	-
Light-jet tagging efficiency (eigenvector 2) [%]	-	-	-	-	-	-	-	-	-	-	-	-	-	-	-	-	-
Light-jet tagging efficiency (eigenvector 3) [%]	-	-	-	-	-	-	-	-	-	-	-	-	-	-	-	-	-
Light-jet tagging efficiency (eigenvector 4) [%]	-	-	-	-	-	-	-	-	-	-	-	-	-	-	-	-	-
Light-jet tagging efficiency (eigenvector 5) [%]	-	-	-	-	-	-	-	-	-	-	-	-	-	-	-	-	-
Light-jet tagging efficiency (eigenvector 6) [%]	-	-	-	-	-	-	-	-	-	-	-	-	-	-	-	-	-
Light-jet tagging efficiency (eigenvector 7) [%]	-	-	-	-	-	-	-	-	-	-	-	-	-	-	-	-	-
Light-jet tagging efficiency (eigenvector 8) [%]	-	-	-	-	-	-	-	-	-	-	-	-	-	-	-	-	-
Light-jet tagging efficiency (eigenvector 9) [%]	-	-	-	-	-	-	-	-	-	-	-	-	-	-	-	-	-
Light-jet tagging efficiency (eigenvector 10) [%]	-	-	-	-	-	-	-	-	-	-	-	-	-	-	-	-	-
b-Quark tagging extrapolation [%]	∓0.11	-	-	-	-	-	-	∓0.11	-	-	∓0.14	-	-	∓0.11	∓0.11	-	-
b-Quark tagging extrapolation from c-Quark [%]	-	-	-	-	-	-	-	-	-	-	-	-	-	-	-	-	-
JET JER cross calibration forward [%]	-	-	-	-	-	-	-	-	-	-	-	-	-	-	-	-	-
JET JER noise forward [%]	-	-	-	-	-	-	-	-	-	-	-	-	-	-	-	-	-
JET JER NP0 [%]	-	-	-	-	-	-	-	-	-	-	-	-	-	-	-	-	-
JET JER NP1 [%]	−0.42	∓1.40	±3.24	−0.32	±0.86	±1.05	−3.69 +0.13	+0.43	±0.44	∓1.68	+3.11 −0.26	−3.39 +0.24	−0.33	±0.15	±0.37	−1.11	+0.10 −0.12
JET JER NP2 [%]	±1.02	−1.80 +2.01	±6.77	−2.34	±2.66	±0.33	±4.94	+0.59 −0.56	±2.00	+0.63 −1.68	±3.48	−1.66	+0.90 −1.20	±1.64	+0.69 −2.00	−0.10 −0.30	−0.23 +2.68
JET JER NP3 [%]	±0.86	−2.01	±2.62	±0.92	±1.25	±1.79	±3.00	+0.15 −0.97	−0.97	-	±2.51	±1.23	+0.81	±1.00	±1.06	±0.75	−2.68 +1.49
JET JER NP4 [%]	±1.39	±0.92	±3.97	+0.67 −0.81	±1.90	+0.78 −0.92	+1.28 −2.01	−1.00	−1.08	−0.90	±1.92	±1.26	±1.31	−1.45 −0.31	−0.76 +0.55	−0.46 +0.16	±0.94
JET JER NP5 [%]	+0.24	−0.32	±2.37	+0.23	−0.65	+0.65	−0.52	±0.98	+1.00 −0.57	+0.63	±1.64	±0.74	±1.65	−1.92	+0.31	±0.23	±0.25
JET JER NP6 [%]	±0.16	±1.05	±2.66	+0.17 −0.84	±1.28	+0.45 −0.54	−1.51 +0.32	±1.48	±0.37	±0.54	±1.34	±2.08	±0.33	±0.64	−0.18 −0.81	±1.21	−1.54 +1.22
JET JER NP7 [%]	−0.32	+0.71 −0.93	±3.39	−1.12	±1.12	+0.72 −1.47	−1.37	±1.21	±0.46	±0.76	±1.77	±3.91	−0.65 +0.72	±0.15 −1.07	−0.22 +2.01	±0.97	−2.31 −0.93
JET JER NP8 [%]	-	-	-	-	-	-	-	-	-	-	-	-	-	-	-	-	-
QCD estimation [%]	±1.88	±4.39	±6.01	±1.73	±3.14	±1.50	±1.16	±3.49	±2.07	±2.36	±1.94	±1.01	±1.08	±3.36	±2.50	±5.33	±6.03
K-factor normalization mass [%]	±2.38 −2.38	±2.67 −2.56	±2.78 −2.78	±2.81 −2.72	±2.81 −2.72	±2.74 −2.66	±2.77 −2.68	±2.74 −2.65	±2.74 −2.66	±2.72 −2.66	±2.72 −2.63	±2.70 −2.61	±2.73 −2.64	±2.68 −2.59	±2.73 −2.65	±2.73 −2.65	±2.73 −2.66
K-factor normalization PDFAS [%]	±3.60	±4.04	±4.21	±4.25	±4.25	±4.15	±4.19	±4.14	±4.15	±4.12	±4.11	±4.08	±4.12	±4.05	±4.13	±4.14	±4.16
K-factor normalization scale [%]	+3.01 −3.00	+2.27 −3.36	+2.37 −3.51	+2.49 −3.54	+2.39 −3.54	+2.34 −3.48	+2.36 −3.49	+2.33 −3.45	+2.34 −3.46	+2.32 −3.43	+2.32 −3.42	+2.30 −3.40	+2.32 −3.43	+2.28 −3.39	+2.33 −3.44	+2.32 −3.45	+2.31 −3.46
Luminosity [%]	±2.05	±2.05	±2.05	±2.05	±2.05	±2.05	±2.05	±2.05	±2.05	±2.05	±2.05	±2.05	±2.05	±2.05	±2.05	±2.05	±2.05
MCSignal stat. [%]	±1.05	±2.86	±3.08	±3.44	±3.27	±3.48	±3.44	±3.10	±2.97	±3.41	±2.74	±3.16	±3.35	±3.28	±3.05	±3.36	±3.53
QCD stat. [%]	±2.03	±1.83	±2.13	±2.33	±2.20	±2.42	±2.58	±2.37	±2.21	±2.63	±2.20	±2.46	±2.50	±2.83	±2.38	±2.82	±3.13
ISR/FSR + scale [%]	±0.95	±2.72	±5.68	−1.12 +0.62	±3.65	±2.28	±1.8 −4.7	±2.72 −4.26	−3.43 +0.40	±1.42	±0.94	±4.04	−0.91 +0.44	±0.13	−0.96 +0.44	±1.69	−2.52 +0.62
Alternate hard-scattering model [%]	±4.03	±14.0	±8.36	±14.0	±0.35	±10.5	±3.61	±1.97	±5.60	±11.0	±6.32	±15.2	±1.29	±8.52	±8.54	±5.59	
Alternate parton-shower model [%]	±4.19	±10.3	±6.91	±7.45	±2.92	±0.96	±0.62	±5.68	±1.09	±0.92	±6.06	±6.91	±10.3	±4.98	±8.93	±0.98	±1.73
Inter PDF [%]	-	-	-	-	-	±0.14	-	±0.15	±0.13	-	-	-	-	-	-	-	±0.12
Intra PDF [%]	±0.10	±0.16	±0.30	±0.21	±0.22	±0.16	±0.10	±0.21	±0.17	±0.15	±0.17	±0.14	±0.18	±0.12	±0.10	±0.16	±0.20

TABLE D.3: Table of systematics for the absolute differential cross-section at the particle level for the $\Delta R_{\text{jet1}}^{\text{extra1}}$ observable.

Bins [GeV]	0–0.55	0.55–0.80	0.80–1.10	1.10–1.35	1.35–1.60	1.60–1.80	1.80–2	2–2.20	2.20–2.35	2.35–2.55	2.55–2.70	2.70–2.90	2.90–3.10	3.10–3.40	3.40–6
$d\sigma$ / $d\Delta R^{extraJ1topclose}$ [pb/GeV]	$1.46 \cdot 10^{-1}$	$3.71 \cdot 10^{-1}$	$5.20 \cdot 10^{-1}$	$5.95 \cdot 10^{-1}$	$7.23 \cdot 10^{-1}$	$7.51 \cdot 10^{-1}$	$7.68 \cdot 10^{-1}$	$6.57 \cdot 10^{-1}$	$6.09 \cdot 10^{-1}$	$5.65 \cdot 10^{-1}$	$4.17 \cdot 10^{-1}$	$3.62 \cdot 10^{-1}$	$3.27 \cdot 10^{-1}$	$1.73 \cdot 10^{-1}$	$1.64 \cdot 10^{-2}$
Total Uncertainty [%]	+21.0 −20.6	+24.3 −18.5	+17.4 −15.8	+15.8 −18.0	+16.9 −15.5	+14.7 −12.8	+13.4 −15.2	+13.7 −15.8	±14.5	+16.5 −15.0	+21.7 −22.0	+15.3 −21.8	+22.7 −22.9	+20.2 −16.9	+22.4 −23.0
Statistics [%]	±4.1	±3.6	±2.8	±2.9	±2.7	±3.0	±3.0	±3.3	±3.9	±3.4	±4.7	±4.7	±4.6	±5.0	±5.2
Systematics [%]	+20.1 −19.7	+23.7 −17.8	+16.9 −15.2	+15.2 −17.5	+16.4 −15.0	+14.1 −12.1	+12.7 −14.6	+12.9 −15.1	±13.3	+15.7 −14.1	+20.5 −20.9	+13.7 −20.7	+21.6 −21.8	+18.9 −15.3	+21.1 −21.7
Jet vertex fraction [%]	±0.64	−0.60	−0.54	−0.52	−0.54	−0.46	−0.52	−0.58	−0.57	−0.60	−0.54	−0.57	−0.71	−0.64	−0.65
b-Tagged jet energy scale (JES) [%]	+0.99 −0.74	+1.42 −0.80	+0.36 −1.28	+1.17 −0.48	+1.00 −0.94	+0.82 −1.39	+0.64 −1.32	+0.59 −0.57	+0.22 −0.83	+0.73 −0.71	+1.96 −0.87	+1.06	+0.85 −0.76	±0.95	
Effective detector NP set 1 (JES) [%]	+2.47 −2.28	+4.28 −3.45	+1.60 −1.11	+2.07 −3.24	+1.99 −1.22	+2.48 −1.56	+1.39 −1.49	+0.54 −1.65	+2.30 −1.05	+2.01 −1.01	+0.84 −2.88	+3.54	+2.73 −1.91	+2.30 −0.42	+3.11 −2.19
Effective mixed NP set 1 (JES) [%]	±0.28	+1.43 −0.98	+0.32 −0.60	±0.90	±0.12	+0.47 −0.15	+0.22 −0.18	±0.15	+0.77	±0.39	±0.74	±1.38	+0.21 −0.64	±1.63	
Effective mixed NP set 2 (JES) [%]	±0.22	+1.56 +1.05	−0.41 +0.20	−0.56 −0.16	-	−0.24	+0.38 +0.31	±0.20	−0.33 +0.44	−0.27 +0.34	+0.53 −0.19	±0.84	−0.23 +0.19	+0.67 −0.11	−0.46 +0.70
Effective mixed NP set 3 (JES) [%]	−0.17	-	−0.12	±0.23	-	±0.13	-	-	−0.20	+0.17 −0.14	±0.28	±0.12	-	±0.37	-
Effective modelling NP set 1 (JES) [%]	+12.1 −9.98	+12.4 −7.29	+7.53 −5.65	+7.24 −8.84	+7.09 −5.53	+7.47 −5.46	+4.60 −6.15	+4.77 −7.38	+6.13 −7.62	+7.26 −5.73	+6.68 −4.95	+3.68 −11.7	+5.14 −5.29	+9.83 −7.40	+6.59 −8.63
Effective modelling NP set 2 (JES) [%]	+0.87 −0.38	+2.25 −2.01	+0.90 −0.80	+0.44 −2.46	+1.08 −0.34	+1.03 −1.41	+0.97 −1.18	+0.29 −0.15	+0.83 −2	+1.13 −0.30	+0.53 −1.29	±2.26	+0.71 −0.91	+2.73 −0.63	+2.23 −1.43
Effective modelling NP set 3 (JES) [%]	+1.17 −0.92	±0.55	±0.33	+0.19 −1.20	+0.53 −0.42	+0.75 −0.47	±0.24	+0.52 −0.54	+0.69 −0.37	+0.66 −0.27	±0.26	±1.12	+0.39 −0.87	±0.50	+0.21 −0.62
Effective modelling NP set 4 (JES) [%]	±0.25	+0.83 −0.91	+0.75 −0.54	±1.09	+0.78 −0.28	+0.42 −0.37	+0.60 −0.39	±0.22	+0.84 −0.38	+0.58 −0.21	+0.64 -	±1.05	+0.13 -	±0.93	+1.05 −0.93
Effective statistical NP set 1 (JES) [%]	-	-	-	-	-	-	-	-	-	-	-	-	-	±0.14	-
Effective statistical NP set 2 (JES) [%]	−1.30	−0.31	−0.46	−0.79	−0.13	−0.22	−0.28	-	±0.68	−0.23	-	±0.33	−0.63	±0.50	−0.74
Effective statistical NP set 3 (JES) [%]	-	+0.25	+0.91	-	+0.87	+0.17	+0.69	+0.14	+0.86	+0.36	-	-	+0.48	-	+0.59
Effective statistical NP set 4 (JES) [%]	−0.14	+0.24	−0.18	±0.32	+0.30	+0.17	-	+0.16 −0.10	±0.10	+0.22 −0.19	+0.48 −0.22	±0.47	±0.13	+0.45 −0.15	-
Effective statistical NP set 5 (JES) [%]	−0.33	+0.50 −0.32	+0.31 −0.42	-	±0.14	+0.22 −0.17	+0.19	-	±0.35	-	+0.53 +0.22	±0.29	±0.25	+0.23 −0.32	+0.29 −0.15
Effective statistical NP set 6 (JES) [%]	±0.36	±0.13	+0.73 −0.15	±0.25	-	+0.25 −0.19	-	±0.11	−0.23 +0.17	±0.13	±0.31	±0.19	+0.30 −0.15	-	+0.22 −0.25
η intercalibration model (JES) [%]	+1.35 −3.34	+3.38 −2.36	+2.04 −0.58	+1.13 −2.74	+1.74 −0.56	+1.69 −1.48	+1.24 −1.22	+1.39 −1.14	+2.31 −1.70	+1.80 −0.78	+0.12 −1.30	−2.69	+3.04 −1.71	+2.82 −0.10	+1.58 −2.96
high E η intercalibration non closure (JES) [%]	-	-	-	-	-	-	-	-	-	-	-	-	-	-	-
neg η intercalibration non closure (JES) [%]	-	±0.11	-	-	-	-	-	-	-	-	-	±0.11	+0.10 −0.11	-	+0.27
pos η intercalibration non closure (JES) [%]	-	-	-	-	-	-	-	-	-	-	-	-	-	±0.14	+0.11 −0.12
η intercalibration total stat (JES) [%]	−0.95	+0.58 −0.82	+0.94 −0.70	+0.49 −0.80	+0.84 −0.26	+0.33 −0.43	+0.91 −0.26	+0.46 −0.19	+0.95 −0.96	+0.60 −0.30	-	±0.83	+0.94 −0.56	±0.43	+0.82 −0.90
Flavour composition (JES) [%]	+1.22 −0.78	+1.58 −2.14	+1.05 −0.67	±0.93 −1.41	+1.71 −0.90	+1.15 −0.62	+1.25 −0.45	+0.89 −1.05	+1.22 −1.64	+1.64 −0.52	±0.43 −2.29	+0.39 −2.29	+1.33 −1.85	±1.87	+2.10 −1.50
Flavour response (JES) [%]	−5.96	−3.63	−1.52	−5.49	−2.00	−2.62	−3.10	−5.36	−4.00	−2.09	−2.72	−7.66	−4.10	−4.34	−4.45
Pile-up offset μ (JES) [%]	+5.57 ±0.93	+7.09 −0.12	+2.55 ±0.39	+4.12 ±0.59	+3.65 ±0.39	+4.35 ±0.25	+2.38 ±0.30	+1.54 -	−0.13 ±0.27	+3.97 −0.43	+2.61 ±0.65	−1.72 ±0.87	+0.78 ±0.10	+4.53 ±0.72	+5.67 −0.58
Pile-up offset N_{PV} (JES) [%]	±0.57	±0.80	+1.62 −0.56	+0.40 −0.93	±0.64	±0.60	-	+0.31 −0.60	+0.22 −0.64	+1.32 +0.81	+0.39 −0.34	±1.24	−0.58	−0.46 +0.76	±1.48
Pile-up offset p_T (JES) [%]	±0.27	±0.67	+0.87 −0.63	±0.65	+0.56 −0.51	-	±0.43	-	−0.26	±0.44	±0.51	±1.24	±0.77	+1.39 −0.28	−0.72
Pile-up offset ρ topology (JES) [%]	+5.96 −5.93	+7.95 −4.52	+3.13 −2.24	+5.16 −5.78	+4.16 −2.93	+5.16 −3.18	+2.54 −3.41	+2.05 −4.29	+4.45 −3.64	+4.05 −3.03	+3.50 −3.61	+1.92 −7.12	+3.05 −3.30	+5.84 −4.24	+5.16 −3.55
Punch-through (JES) [%]	-	-	-	-	-	-	-	-	±0.14	-	-	-	-	-	±0.22
Single particle high-p_T (JES) [%]	-	-	-	-	-	-	-	-	-	-	-	-	-	-	-
b-Quark tagging efficiency (eigenvector 0) [%]	−3.29 +3.34	−3.15 +3.19	−3.53 +3.58	−3.80 +3.88	−3.77 +3.84	−3.88 +3.95	−3.91 +3.97	−3.88 +3.95	−3.85 +3.91	−4.00 +4.07	−3.96 +4.02	−3.98 +4.05	−3.92 +4.00	−3.99 +4.07	−3.56 +3.62
b-Quark tagging efficiency (eigenvector 1) [%]	±0.61	±0.73	±0.77	±0.80	±0.79	−0.65 +0.66	±0.63	−0.63 +0.64	−0.62 +0.63	±0.57	±0.54	±0.57	±0.54	−0.64 +0.65	±0.52
b-Quark tagging efficiency (eigenvector 2) [%]	+1.30 −1.29	+1.28 −1.27	+1.39 −1.29	±1.37 −1.37	+1.38 −1.37	+1.37 −1.36	+1.37 −1.36	+1.37 −1.36	+1.35 −1.34	+1.38 −1.37	±1.37	±1.34	+1.40 −1.39	+1.43 −1.42	+1.32 −1.31
b-Quark tagging efficiency (eigenvector 3) [%]	-	±0.10	±0.13	±0.13	±0.10	-	-	-	-	-	-	-	±0.12	-	±0.12
b-Quark tagging efficiency (eigenvector 4) [%]	±0.19	±0.17	±0.18	±0.20	±0.19	±0.18	±0.18	±0.17	±0.17	±0.18	±0.17	±0.17	±0.17	±0.20	±0.17
b-Quark tagging efficiency (eigenvector 5) [%]	-	-	-	-	-	-	-	-	-	-	-	-	-	-	-
c-Quark tagging efficiency (eigenvector 0) [%]	±0.52	±0.43	±0.60	±0.57	±0.62	±0.68	±0.60	±0.55	±0.62	±0.65	±0.64	+0.63 −0.62	±0.68	±0.60	±0.56
c-Quark tagging efficiency (eigenvector 1) [%]	±0.28	±0.17	±0.24	±0.22	±0.24	±0.25	±0.22	±0.19	±0.23	±0.30	±0.29	±0.18	±0.26	±0.19	±0.23
c-Quark tagging efficiency (eigenvector 2) [%]	-	-	-	-	-	-	-	-	-	-	-	-	-	-	-
Light-jet tagging efficiency (eigenvector 0) [%]	+0.40 −0.38	+0.53 −0.58	±0.45	+0.77 −0.76	±0.62	±0.83	±0.39	±0.73	±0.57	±0.77	±0.54	±0.52	+0.99 −0.98	+0.95 −0.94	±0.48
Light-jet tagging efficiency (eigenvector 1) [%]	-	-	-	-	-	-	-	-	-	-	-	-	-	-	-
Light-jet tagging efficiency (eigenvector 2) [%]	-	-	-	-	-	-	-	-	-	-	-	-	-	-	-
Light-jet tagging efficiency (eigenvector 3) [%]	-	-	-	-	-	-	-	-	-	-	-	-	-	-	-
Light-jet tagging efficiency (eigenvector 4) [%]	-	-	-	-	-	-	-	-	-	-	-	-	-	-	-
Light-jet tagging efficiency (eigenvector 5) [%]	-	-	-	-	-	-	-	-	-	-	-	-	-	-	-
Light-jet tagging efficiency (eigenvector 6) [%]	-	-	-	-	-	-	-	-	-	-	-	-	-	-	-
Light-jet tagging efficiency (eigenvector 7) [%]	-	-	-	-	-	-	-	-	-	-	-	-	-	-	-
Light-jet tagging efficiency (eigenvector 8) [%]	-	-	-	-	-	-	-	-	-	-	-	-	-	-	-
Light-jet tagging efficiency (eigenvector 9) [%]	-	-	-	-	-	-	-	-	-	-	-	-	-	-	-
Light-jet tagging efficiency (eigenvector 10) [%]	-	-	-	-	-	-	-	-	-	-	-	-	-	-	-
b-Quark tagging extrapolation [%]	±0.13	-	±0.12	-	-	-	-	-	-	±0.10	±0.14	±0.10	±0.14	-	-
b-Quark tagging extrapolation from c-Quark [%]	-	-	-	-	-	-	-	-	-	-	-	-	-	-	-
JET JER cross calibration forward [%]	-	-	-	-	-	-	-	-	-	-	-	-	-	-	-
JET JER noise forward [%]	-	-	-	-	-	-	-	-	-	-	-	-	-	-	-
JET JER NP0 [%]	-	-	-	-	-	-	-	-	-	-	-	-	-	-	-
JET JER NP1 [%]	−0.82	+3.20 −0.21	−0.19 +0.11	±1.83	±0.58	−1.28	−0.56	+0.65	−0.17	+2.54 −0.11	±1.66	±1.82	−1.28	−0.41	±2.13
JET JER NP2 [%]	±1.11	+4.22 −0.78	±2.05	±3.21	±2.77	+0.37 −0.31	+0.19 −1.78	±0.56	±1.89	±3.24	+0.69 −2.80	±0.82	±3.19	+0.61 −2.22	±3.46
JET JER NP3 [%]	−1.30	±1.52	±2.29	±1.55	−0.45	±0.86	±1.27	±1.78	+0.81 −0.39	−0.25	±2.28	±2.62	−0.10	±1.80	
JET JER NP4 [%]	+1.10 −1.62	+1.75 ±2.10	±0.50	±1.29	±1.81	+0.27 −0.23	−1.95	±0.15	±0.78	±1.07	+0.64 −0.61	±1.68	±3.27	+0.90 −0.70	±0.59
JET JER NP5 [%]	−3.52	±1.89	−0.16 +2.46	+0.52 −1.70	±1.41	+0.35 −1.18	±0.45	−0.62	−0.31	±1.77	−0.11 +0.56	±1.73	±0.83	−1.70 −1.26	±0.98
JET JER NP6 [%]	±2.30	±1.49	−0.77 +0.44	±2.62	±1.12	±0.70	+0.61 −0.95	±0.23	±0.39	±1.28	+1.84 −0.22	±2.20	±1.75	±1.67	±0.39
JET JER NP7 [%]	±2.27	±1.02	±0.68	±1.55	±1.00	±0.38	+0.20 −0.21	−1.19 +0.70	−0.31 −0.44	±1.00	+1.35 −1.31	±3.11	+2.41 −1.76	−1.96 +0.84	−0.60 −0.34
JET JER NP8 [%]	-	-	-	-	-	-	-	-	-	-	-	-	-	-	-
QCD estimation [%]	±1.34	±4.25	±3.36	±5.85	±6.21	±3.74	±4.64	±4.03	±2.49	±3.08	±3.60	±0.96	±4.09	±3.39	±8.80
K-factor normalization mass [%]	+2.50 −2.42	+2.49 −2.41	+2.61 −2.53	+2.68 −2.59	+2.69 −2.61	+2.66 −2.58	+2.73 −2.64	+2.69 −2.61	+2.66 −2.57	+2.72 −2.63	+2.64 −2.56	+2.67 −2.59	+2.67 −2.59	+2.62 −2.54	+2.58 −2.50
K-factor normalization PDFAS [%]	±3.78	±3.77	±3.95	±4.05	±4.07	±4.03	±4.13	±4.08	±4.02	±4.11	±4.00	±4.05	±4.05	±3.97	±3.90
K-factor normalization scale [%]	+2.13 −3.14	+2.13 −3.14	+2.23 −3.29	+2.28 −3.37	+2.29 −3.39	+2.27 −3.35	+2.33 −3.44	+2.30 −3.40	+2.27 −3.35	+2.32 −3.42	+2.25 −3.33	+2.28 −3.37	+2.28 −3.37	+2.24 −3.31	+2.20 −3.25
Luminosity [%]	±2.05	±2.05	±2.05	±2.05	±2.05	±2.05	±2.05	±2.05	±2.05	±2.05	±2.05	±2.05	±2.05	±2.05	±2.05
MCSignal stat. [%]	±3.10	±2.64	±2.12	±2.06	±1.95	±2.05	±2.07	±2.21	±2.73	±2.48	±3.15	±3.08	±3.36	±3.38	±3.45
QCD stat. [%]	±3.04	±2.70	±2.13	±2.11	±2.00	±2.12	±2.20	±2.41	±3.16	±2.78	±3.80	±3.92	±4.07	±4.10	±4.25
ISR/FSR + scale [%]	±1.15	+1.63 −0.17	+1.09 −0.56	±0.98	±3.04	+0.96	−1.80 +0.23	±0.95	±2.94	±0.93	±8.20	±4.74	+0.61 −0.31	+7.42 −0.42	+1.06 −0.75
Alternate hard-scattering model [%]	±8.18	±5.20	±8.84	±2.19	±0.39	±3.74	±6.05	±6.38	±1.58	±0.94	±11.9	±5.61	±4.76	±6.09	±12.8
Alternate parton-shower model [%]	±6.89	±9.82	±5.83	±1.62	±7.47	±1.32	±2.68	±4.53	±0.30	±7.69	±8.47	±0.82	±16.3	±2.91	±1.38
Inter PDF [%]	-	-	-	-	-	-	-	-	-	±0.21	-	-	±0.11	-	±0.20
Intra PDF [%]	±0.17	-	±0.12	±0.13	±0.17	±0.10	±0.26	±0.11	-	±0.24	-	±0.24	±0.13	±0.13	±0.24

TABLE D.4: Table of systematics for the absolute differential cross-section at the particle level for the $\Delta R^{\text{extra1}}_{\text{topclose}}$ observable.

Bins [GeV]	0–360	360–420	420–480	480–540	540–600	600–670	670–740	740–800	800–900	900–1000	1000–2000
$d\sigma$ / dH_T^{tt} [pb/GeV]	$6.74 \cdot 10^{-4}$	$3.76 \cdot 10^{-3}$	$4.57 \cdot 10^{-3}$	$4.16 \cdot 10^{-3}$	$3.70 \cdot 10^{-3}$	$2.69 \cdot 10^{-3}$	$1.89 \cdot 10^{-3}$	$1.25 \cdot 10^{-3}$	$7.95 \cdot 10^{-4}$	$2.64 \cdot 10^{-4}$	$1.51 \cdot 10^{-5}$
Total Uncertainty [%]	+20.5 −21.0	+16.8 −18.9	+15.0 −15.3	+13.2 −11.0	+13.1 −12.9	+12.4 −13.0	+11.4 −13.5	+11.3 −11.6	+18.8 −15.7	+16.4 −16.6	+48.7 −47.9
Statistics [%]	±2.8	±2.5	±2.1	±2.1	±2.1	±2.3	±2.7	±3.6	±3.5	±6.5	±9.0
Systematics [%]	+19.7 −20.2	+16.3 −18.4	+14.6 −15.0	+12.9 −10.7	+12.8 −12.5	+12.0 −12.6	+10.8 −12.0	+10.3 −10.0	+18.3 −15.0	+14.2 −14.4	+47.3 −46.4
Jet vertex fraction [%]	+0.60 −0.62	+0.59 −0.61	+0.48 −0.51	+0.43 −0.45	+0.36 −0.39	+0.31 −0.33	+0.24 −0.27	+0.25 −0.27	+0.17 −0.19	+0.18 −0.20	+0.28 −0.29
b-Tagged jet energy scale (JES) [%]	+0.33 −1.25	+0.83 −0.84	+0.81 −0.66	+1.09 −0.57	+0.88 −0.87	+0.33 −0.90	+1.28 −1.04	∓0.83	+2.01 −0.44	-	+0.52 −0.48
Effective detector NP set 1 (JES) [%]	+1.83 −3.08	+1.29 −2.28	+2.67 −1.95	+2.06 −1.42	+1.75 −0.64	+0.81 −1.52	+1.00 −2.08	+1.01	+3.57 −1.17	−0.87 +0.76	+3.74 −1.15
Effective mixed NP set 1 (JES) [%]	+0.26 −0.35	±0.20	±0.51	-	+0.28	−0.80 +0.15	∓1.35	+0.92 −0.65	+3.11 −0.26	+1.50 −3.21	+0.57 −3.92
Effective mixed NP set 2 (JES) [%]	±0.29	−0.16	−0.29 +0.15	−0.30 +0.48	±0.48	∓0.45	−0.90 +0.25	∓0.65	−0.15 +2.12	−0.56 +0.17	−0.10 +1.27
Effective mixed NP set 3 (JES) [%]	+0.23	−0.23	-	±0.15	−0.31	+0.12 −0.18	-	∓0.13	+0.27 −0.11	−0.15 +0.36	+0.87 −0.22
Effective modelling NP set 1 (JES) [%]	+9.07 −8.71	+5.85 −8.90	+7.21 −7.41	+6.91 −4.64	+5.40 −5.05	+4.30 −3.84	+3.51 −4.89	+3.28 −3.23	+6.36 −3.28	+1.07 −4.19	+6.31 −4.70
Effective modelling NP set 2 (JES) [%]	+0.65 −1.50	+0.35 −0.81	+1.39 −1.01	+1.50 −1.30	+1.40 −0.81	+0.25 −0.90	+0.54 −1.22	+1.28 −1.28	+3.54 −0.89	+1.24 −2.32	+3.88 −2.11
Effective modelling NP set 3 (JES) [%]	+0.91 −1.28	+0.85 −1.04	+0.40 −0.34	+0.62 −0.19	±0.52	∓0.89	−0.59 +0.31	−0.20 +0.68	−0.56 +1.65	+0.10 −0.14	±2.10
Effective modelling NP set 4 (JES) [%]	+0.91 −0.20	+0.17 −0.55	+0.62 −0.33	+0.71 −0.34	+0.46 −0.13	∓0.41	+0.26 −1.02	∓0.59	+2.00 −0.16	- −0.74	+2.05 −0.11
Effective statistical NP set 1 (JES) [%]	-	-	-	-	-	-	-	∓0.14	±0.21	−0.19	+0.38 −0.16
Effective statistical NP set 2 (JES) [%]	−0.32 +0.58	−0.61 +0.27	−0.34 +0.49	±0.60	∓0.24	−0.58 +0.15	−0.22	∓0.38	±0.71	±0.53	±1.40
Effective statistical NP set 3 (JES) [%]	±0.32	+0.36 −0.23	−0.22	±0.21	±0.30	-	−0.48 +0.11	∓0.65	±1.72	−0.28 +0.17	−0.20 +0.52
Effective statistical NP set 4 (JES) [%]	-	−0.33 +0.41	-	+0.41 −0.17	+0.19 −0.12	−0.46 -	+0.13 −0.25	∓0.74	±0.58	±0.43	−0.67 +0.24
Effective statistical NP set 5 (JES) [%]	-	-	−0.27 +0.55	−0.32 +0.42	−0.40 +0.22	−0.30 −0.38	∓0.23	+0.10 −0.50	±0.41	-	+0.20
Effective statistical NP set 6 (JES) [%]	+0.17 -	+0.17 -	-	±0.20	-	+0.20 −0.35	∓0.14	∓0.37	±0.84	±0.38	+0.24 −0.74
η intercalibration model (JES) [%]	+1.95 −2.67	+1.84 −1.96	+2.08 −1.27	+1.67 −1.04	+1.10 −1.03	+0.44 −0.93	+0.84 −1.01	∓0.63	+2.36 −0.18	+1.36 −0.78	−0.11 +0.38 −0.16 +1.21 −1.01
high E η intercalibration non closure (JES) [%]	-	-	-	-	-	-	-	-	-	-	-
neg η intercalibration non closure (JES) [%]	-	-	-	-	-	-	-	-	-	-	-
pos η intercalibration non closure (JES) [%]	±0.16	-	-	-	-	-	-	-	-	-	-
η intercalibration total stat (JES) [%]	+0.73 −0.55	+0.38 −0.72	+0.69 −0.41	+0.79 −0.26	+0.33 −0.10	+0.30 −0.64	- −0.33	- −0.68	-	±1.12	±0.61	+1.24 −0.30
Flavour composition (JES) [%]	+0.88 −0.64	+0.93 −1.27	+1.48 −0.87	+1.67 −0.39	+0.70 −0.43	+0.47 −0.79	+0.42 −0.55	∓0.52	+1.19	±1.18	+1.03 −0.43
Flavour response (JES) [%]	−5.24	−4.36	−3.97	−2.41	−1.91	−2.11	−2.17	−2.35	−0.81	−2.15	−4.39
Pile-up offset μ (JES) [%]	+4.54 −0.35	+3.39 ∓0.45	+3.27	+3.90 ±0.46	+2.84 +0.26	+1.38 -	+1.39 −0.29	+3.10 ∓1.09	+3.39 ±0.74	+2.45 ±1.11	+3.37 ±0.38
Pile-up offset N_{PV} (JES) [%]	+0.54 −1.18	+0.87 +0.87	+0.37 +0.87	+0.90	±0.69	∓0.42	- −0.85	∓1.21	±1.51	−0.95 +1.15	±1.25
Pile-up offset p_T (JES) [%]	+1.20 −0.74	−0.44 ∓0.21	−0.43 +0.83	-	±0.30	∓0.51	+0.21 −0.38	∓0.17	±1.78	−1.28	±1.69
Pile-up offset ρ topology (JES) [%]	+0.44 +4.40	+3.86	−0.52 +4.35	+4.36	−0.12 +3.16	+1.82	+2.14	+2.78	+3.38	+1.40	+3.43
Punch-through (JES) [%]	−5.13 -	−4.45 -	−4.43 -	−2.56 -	−2.60 -	−2.78 -	−2.25 -	−2.50 ∓0.20	−1.40 -	−1.80 -	−1.68 +0.32
Single particle high-p_T (JES) [%]	-	-	-	-	-	-	-	-	-	-	-
b-Quark tagging efficiency (eigenvector 0) [%]	−2.45 +2.49	−3.76 +3.82	−3.86 +3.93	−3.78 +3.84	−3.78 +3.84	−3.80 +3.87	−3.77 +3.84	−4.03 +4.11	−3.86 +3.93	−4.00 +4.07	−4.87 +4.98
b-Quark tagging efficiency (eigenvector 1) [%]	∓0.27	∓0.16	∓0.36	∓0.53	−0.77 +0.78	∓1.06	∓1.33	−1.76 +1.78	−2.12 +2.13	−2.93 +2.93	−4.51 +4.63
b-Quark tagging efficiency (eigenvector 2) [%]	+1.13 −1.12	±1.30	+1.37 −1.36	+1.39 −1.38	+1.43 −1.42	+1.45 −1.44	+1.44 −1.43	+1.46 −1.45	+1.38 −1.37	+1.23 −1.22	±0.91
b-Quark tagging efficiency (eigenvector 3) [%]	∓0.52	∓0.35	∓0.13	-	±0.23	±0.40	±0.50	±0.62	+0.71 −0.70	±0.84	±0.76
b-Quark tagging efficiency (eigenvector 4) [%]	∓0.11	∓0.20	∓0.23	∓0.24	∓0.23	∓0.21	∓0.16	∓0.12	-	-	-
b-Quark tagging efficiency (eigenvector 5) [%]	±0.14	±0.10	-	-	-	-	-	-	-	-	-
c-Quark tagging efficiency (eigenvector 0) [%]	±0.35	±0.55	±0.56	±0.63	±0.67	±0.78	±0.70	±0.84	±0.87	±0.88	±0.87
c-Quark tagging efficiency (eigenvector 1) [%]	-	±0.17	±0.21	±0.26	±0.30	±0.35	±0.33	±0.42	±0.43	±0.42	±0.44
c-Quark tagging efficiency (eigenvector 2) [%]	-	-	-	-	-	±0.10	±0.11	±0.16	±0.17	±0.17	±0.18
Light-jet tagging efficiency (eigenvector 0) [%]	±0.51	±0.29	±0.53	+0.67 −0.66	±0.67	+0.66 −0.65	+0.77 −0.78	±0.76	±0.87	±0.73	+1.25 −1.24
Light-jet tagging efficiency (eigenvector 1) [%]	-	-	-	-	-	-	-	-	-	-	-
Light-jet tagging efficiency (eigenvector 2) [%]	-	-	-	-	-	-	-	-	-	-	-
Light-jet tagging efficiency (eigenvector 3) [%]	-	-	-	-	-	-	-	-	-	-	-
Light-jet tagging efficiency (eigenvector 4) [%]	-	-	-	-	-	-	-	-	-	-	-
Light-jet tagging efficiency (eigenvector 5) [%]	-	-	-	-	-	-	-	-	-	-	-
Light-jet tagging efficiency (eigenvector 6) [%]	-	-	-	-	-	-	-	-	-	-	-
Light-jet tagging efficiency (eigenvector 7) [%]	-	-	-	-	-	-	-	-	-	-	-
Light-jet tagging efficiency (eigenvector 8) [%]	-	-	-	-	-	-	-	-	-	-	-
Light-jet tagging efficiency (eigenvector 9) [%]	-	-	-	-	-	-	-	-	-	-	-
Light-jet tagging efficiency (eigenvector 10) [%]	-	-	-	-	-	-	-	-	-	-	-
b-Quark tagging extrapolation [%]	-	-	-	-	-	∓0.14	∓0.15	∓0.21	∓0.23	∓0.27	∓0.24
b-Quark tagging extrapolation from c-Quark [%]	-	-	-	-	-	-	-	-	-	-	-
JET JER cross calibration forward [%]	-	-	-	-	-	-	-	-	-	-	-
JET JER noise forward [%]	-	-	-	-	-	-	-	-	-	-	-
JET JER NP0 [%]	-	-	-	-	-	-	-	-	-	-	-
JET JER NP1 [%]	−0.86 -	+0.69 -	∓1.34 -	−0.20 -	∓0.38 -	±0.11	+1.11 −0.13	−0.51 -	+1.88 −0.19	±1.88	+0.81 −0.31
JET JER NP2 [%]	∓0.20	−0.53 +0.13	+0.37 −1.80	+0.33 −0.14	−0.74 +0.49	∓0.53	-	−0.17 +1.74	−0.62 +2.39	±2.94	∓1.46
JET JER NP3 [%]	+0.49 −0.20	∓1.03	−0.40 +0.47	−0.96 +0.10	−0.97	−0.18 +0.11	+0.36	−0.96 +0.99	±0.89	±1.73	∓1.53
JET JER NP4 [%]	+1.11 −1.35	−1.88 +0.86	+1.03 −0.81	- +0.53	∓0.32	+0.59 −0.67	+0.75 −0.73	−0.85 +1.17	±1.25	+2.37 −0.26	±2.21
JET JER NP5 [%]	−0.22 +0.93	- −0.75	+0.30 −0.13	-	+0.14 −0.50	∓0.41	±1.65	∓0.39	±1.69	+1.36	−0.38 +1.63
JET JER NP6 [%]	−2.28 +2.01	+0.91 −2.62	−0.59 +0.64	+0.26 −0.16	+0.19 −0.86	−0.47 +0.35	±0.54	+1.27 −0.70	±0.83	−0.41 +2.61	+0.28
JET JER NP7 [%]	−0.29 +0.91	∓0.60	+0.26 −0.33	+0.20 −0.16	+0.37 −0.70	∓0.55	±1.33	+0.33 −0.67	−0.12 +1.43	±2.36	−1.08 +0.28
JET JER NP8 [%]	-	-	-	-	-	-	-	-	-	-	-
QCD estimation [%]	∓13.6	±4.57	±5.05	±3.45	±3.38	±1.79	±0.91	∓0.30	∓0.30	∓1.30	∓1.28
K-factor normalization mass [%]	+1.92 −1.86	+2.52 −2.44	+2.66 −2.58	+2.71 −2.62	+2.79 −2.70	+2.79 −2.70	+2.79 −2.70	+2.82 −2.73	+2.78 −2.69	+2.79 −2.70	+2.81 −2.72
K-factor normalization PDFAS [%]	±2.90	±3.82	±4.03	±4.09	±4.22	±4.23	±4.22	±4.27	±4.21	±4.22	±4.25
K-factor normalization scale [%]	+1.63 −2.42	+2.15 −3.18	+2.27 −3.35	+2.31 −3.41	+2.38 −3.51	+2.38 −3.52	+2.38 −3.51	+2.40 −3.55	+2.37 −3.50	+2.38 −3.51	+2.39 −3.54
Luminosity [%]	∓2.05	∓2.05	∓2.05	∓2.05	∓2.05	∓2.05	∓2.05	∓2.05	∓2.05	∓2.05	∓2.05
MCSignal stat. [%]	±1.48	±1.64	±1.53	±1.49	±1.59	±1.71	±2.02	±2.62	±2.77	±4.79	±7.33
QCD stat. [%]	±4.68	±2.58	±1.62	±1.20	±0.95	±0.75	±0.67	±0.65	±0.54	±0.63	±0.45
ISR/FSR + scale [%]	∓0.72	+1.91 -	−2.47 +0.77	∓1.11	−0.31 +0.21	-	−0.63 +0.85	∓0.51	∓6.80	±1.25	±21.3
Alternate hard-scattering model [%]	∓1.77	±7.38	∓5.43	∓0.86	±0.42	±6.18	±3.62	±0.71	∓8.81	±7.31	±39.0
Alternate parton-shower model [%]	±5.24	±8.28	∓1.80	±1.30	±6.50	±4.53	±4.04	∓0.41	∓1.47	∓2.36	±0.62
Inter PDF [%]	-	-	-	-	-	-	-	∓0.11	-	-	±0.36
Intra PDF [%]	±0.23	-	±0.10	-	±0.12	±0.14	±0.16	±0.13	±0.21	±0.17	±0.51

TABLE D.5: Table of systematics for the absolute differential cross-section at the particle level for the $H_{\mathrm{T}}^{t\bar{t}}$ observable.

Bins [Unit $N.jets$]	5.50–6.50	6.50–7.50	7.50–8.50	8.50–9.50	9.50–14.50
$d\sigma$ / $dN.jets$ [pb/ Unit $N.jets$]	$2.47 \cdot 10^{-1}$	$5.44 \cdot 10^{-1}$	$5.02 \cdot 10^{-1}$	$2.61 \cdot 10^{-1}$	$3.26 \cdot 10^{-2}$
Total Uncertainty [%]	$^{+10.2}_{-10.4}$	$^{+11.2}_{-11.0}$	$^{+13.6}_{-13.2}$	$^{+16.9}_{-18.8}$	$^{+28.0}_{-25.6}$
Statistics [%]	± 1.7	± 1.3	± 1.6	± 2.5	± 3.7
Systematics [%]	$^{+9.98}_{-10.1}$	$^{+11.0}_{-10.9}$	$^{+13.4}_{-12.9}$	$^{+16.4}_{-18.4}$	$^{+27.3}_{-24.9}$
Jet vertex fraction [%]	-	$^{+0.26}_{-0.28}$	$^{+0.52}_{-0.55}$	$^{+0.80}_{-0.82}$	$^{+1.00}_{-1.01}$
b-Tagged jet energy scale (JES) [%]	$^{+0.92}_{-0.93}$	$^{+0.87}_{-0.95}$	$^{+0.62}_{-0.78}$	$^{+0.65}_{-0.86}$	$^{+0.64}_{-}$
Effective detector NP set 1 (JES) [%]	$^{+1.40}_{-1.02}$	$^{+1.54}_{-1.32}$	$^{+2.26}_{-2.18}$	$^{+1.43}_{-2.43}$	$^{+2.75}_{-1.36}$
Effective mixed NP set 1 (JES) [%]	$^{+0.23}_{-0.20}$	$^{+0.31}_{-0.18}$	$^{+0.33}_{-0.37}$	$^{+0.15}_{-0.32}$	± 0.54
Effective mixed NP set 2 (JES) [%]	$^{-0.26}_{+0.13}$	$^{-0.19}_{+0.28}$	$^{-0.53}_{+0.22}$	± 0.21	$^{-}_{+0.63}$
Effective mixed NP set 3 (JES) [%]	-	-	-	± 0.14	$^{+0.20}_{-}$
Effective modelling NP set 1 (JES) [%]	$^{+1.73}_{-2.16}$	$^{+4.61}_{-4.15}$	$^{+7.70}_{-6.96}$	$^{+7.22}_{-9.66}$	$^{+12.3}_{-10.3}$
Effective modelling NP set 2 (JES) [%]	$^{+2.15}_{-1.67}$	$^{+1.72}_{-1.67}$	$^{+0.78}_{-0.80}$	$^{+0.51}_{-1.06}$	$^{-0.53}_{+0.60}$
Effective modelling NP set 3 (JES) [%]	-	± 0.13	$^{+0.72}_{-0.77}$	$^{+0.68}_{-0.44}$	$^{+0.73}_{-0.76}$
Effective modelling NP set 4 (JES) [%]	$^{+0.39}_{-0.58}$	$^{+0.50}_{-0.47}$	$^{+0.51}_{-0.60}$	$^{+0.37}_{-0.10}$	$^{+0.77}_{-0.12}$
Effective statistical NP set 1 (JES) [%]	-	-	-	-	-
Effective statistical NP set 2 (JES) [%]	-	± 0.27	$^{-0.65}_{+0.38}$	$^{-0.38}_{+0.59}$	$^{-0.80}_{+0.77}$
Effective statistical NP set 3 (JES) [%]	-	-	$^{+0.18}_{-0.13}$	± 0.31	± 0.13
Effective statistical NP set 4 (JES) [%]	$^{+0.21}_{-0.13}$	$^{-}_{-0.21}$	-	-	± 0.17
Effective statistical NP set 5 (JES) [%]	$^{-0.35}_{+0.42}$	$^{-0.27}_{+0.21}$	$^{-0.25}_{+0.15}$	$^{-0.18}_{+0.12}$	± 0.51
Effective statistical NP set 6 (JES) [%]	$^{+0.12}_{-0.14}$	$^{+0.17}_{-0.19}$	-	-	± 0.37
η intercalibration model (JES) [%]	$^{+0.32}_{-0.45}$	$^{+1.35}_{-0.52}$	$^{+1.35}_{-2.08}$	$^{+1.89}_{-2.29}$	$^{+3.49}_{-1.47}$
high E η intercalibration non closure (JES) [%]	-	-	-	-	-
neg η intercalibration non closure (JES) [%]	-	-	-	∓ 0.11	-
pos η intercalibration non closure (JES) [%]	-	-	-	-	-
η intercalibration total stat (JES) [%]	$^{+0.22}_{-0.20}$	$^{+0.34}_{-}$	$^{+0.68}_{-0.76}$	$^{+0.52}_{-0.75}$	$^{+1.12}_{-0.82}$
Flavour composition (JES) [%]	± 0.23	$^{+0.37}_{-}$	$^{+1.30}_{-1.29}$	$^{+1.17}_{-1.15}$	$^{+3.58}_{-1.81}$
Flavour response (JES) [%]	$^{-0.91}_{+0.74}$	$^{-1.79}_{+2.36}$	$^{-3.78}_{+4.27}$	$^{-4.89}_{+3.00}$	$^{-5.71}_{+7.40}$
Pile-up offset μ (JES) [%]	$^{-0.22}_{-}$	-	$^{-0.28}_{+0.23}$	-	± 0.54
Pile-up offset N_{PV} (JES) [%]	∓ 0.32	± 0.49	$^{+0.34}_{-}$	$^{+0.14}_{-0.31}$	$^{+0.70}_{-}$
Pile-up offset p_T (JES) [%]	$^{+0.17}_{-0.21}$	$^{+0.16}_{-0.11}$	$^{+0.18}_{-0.29}$	$^{-}_{-0.17}$	$^{-0.30}_{+0.40}$
Pile-up offset ρ topology (JES) [%]	$^{+1.26}_{-1.20}$	$^{+2.42}_{-2.09}$	$^{+4.71}_{-4.13}$	$^{+4.02}_{-5.64}$	$^{+8.09}_{-5.34}$
Punch-through (JES) [%]	-	-	-	-	-
Single particle high-p_T (JES) [%]	-	-	-	-	-
b-Quark tagging efficiency (eigenvector 0) [%]	$^{-3.67}_{+3.74}$	$^{-3.92}_{+4.00}$	$^{-3.86}_{+3.93}$	$^{-3.45}_{+3.50}$	$^{-2.84}_{+2.87}$
b-Quark tagging efficiency (eigenvector 1) [%]	$^{-0.91}_{+0.92}$	∓ 0.81	∓ 0.66	∓ 0.50	$^{-0.32}_{+0.31}$
b-Quark tagging efficiency (eigenvector 2) [%]	$^{+1.53}_{-1.52}$	$^{+1.47}_{-1.46}$	± 1.34	± 1.21	$^{+1.09}_{-1.08}$
b-Quark tagging efficiency (eigenvector 3) [%]	± 0.13	-	-	-	-
b-Quark tagging efficiency (eigenvector 4) [%]	∓ 0.25	∓ 0.20	∓ 0.18	∓ 0.15	∓ 0.14
b-Quark tagging efficiency (eigenvector 5) [%]	-	-	-	-	-
c-Quark tagging efficiency (eigenvector 0) [%]	± 0.74	± 0.62	± 0.61	± 0.51	$^{+0.63}_{-0.62}$
c-Quark tagging efficiency (eigenvector 1) [%]	± 0.39	± 0.26	± 0.24	± 0.17	± 0.15
c-Quark tagging efficiency (eigenvector 2) [%]	-	-	-	-	-
Light-jet tagging efficiency (eigenvector 0) [%]	± 0.48	± 0.54	$^{+0.69}_{-0.70}$	± 0.62	$^{+0.90}_{-0.88}$
Light-jet tagging efficiency (eigenvector 1) [%]	-	-	-	-	-
Light-jet tagging efficiency (eigenvector 2) [%]	-	-	-	-	-
Light-jet tagging efficiency (eigenvector 3) [%]	-	-	-	-	-
Light-jet tagging efficiency (eigenvector 4) [%]	-	-	-	-	-
Light-jet tagging efficiency (eigenvector 5) [%]	-	-	-	-	-
Light-jet tagging efficiency (eigenvector 6) [%]	-	-	-	-	-
Light-jet tagging efficiency (eigenvector 7) [%]	-	-	-	-	-
Light-jet tagging efficiency (eigenvector 8) [%]	-	-	-	-	-
Light-jet tagging efficiency (eigenvector 9) [%]	-	-	-	-	-
Light-jet tagging efficiency (eigenvector 10) [%]	-	-	-	-	-
b-Quark tagging extrapolation [%]	∓ 0.10	-	-	∓ 0.10	∓ 0.23
b-Quark tagging extrapolation from c-Quark [%]	-	-	-	-	-
JET JER cross calibration forward [%]	-	-	-	-	-
JET JER noise forward [%]	-	-	-	-	-
JET JER NP0 [%]	-	-	-	-	-
JET JER NP1 [%]	-	-	-	∓ 1.26	± 0.43
JET JER NP2 [%]	∓ 0.61	± 0.93	∓ 0.21	∓ 1.85	$^{-0.59}_{+0.65}$
JET JER NP3 [%]	∓ 0.90	$^{-0.22}_{+0.75}$	∓ 0.24	∓ 0.68	$^{-1.91}_{+0.93}$
JET JER NP4 [%]	$^{+0.50}_{-0.32}$	± 0.19	$^{+0.42}_{-}$	∓ 1.25	± 0.98
JET JER NP5 [%]	$^{-}_{+0.30}$	∓ 0.18	$^{-}_{+0.36}$	∓ 0.42	$^{+1.91}_{-0.31}$
JET JER NP6 [%]	$^{-0.10}_{+0.41}$	∓ 0.39	-	∓ 1.08	± 1.94
JET JER NP7 [%]	$^{-0.39}_{+0.82}$	$^{+0.28}_{-0.24}$	-	∓ 0.87	± 0.92
JET JER NP8 [%]	-	-	-	-	-
QCD estimation [%]	± 0.60	± 2.96	± 1.70	∓ 6.92	∓ 14.3
K-factor normalization mass [%]	$^{+2.79}_{-2.71}$	$^{+2.80}_{-2.71}$	$^{+2.64}_{-2.55}$	$^{+2.41}_{-2.34}$	$^{+2.07}_{-2.01}$
K-factor normalization PDFAS [%]	± 4.23	± 4.24	± 3.99	± 3.65	± 3.14
K-factor normalization scale [%]	$^{+2.38}_{-3.52}$	$^{+2.39}_{-3.53}$	$^{+2.25}_{-3.32}$	$^{+2.06}_{-3.04}$	$^{+1.77}_{-2.61}$
Luminosity [%]	∓ 2.05	∓ 2.05	∓ 2.05	∓ 2.05	∓ 2.05
MCSignal stat. [%]	± 1.37	± 0.99	± 1.08	± 1.42	± 1.90
QCD stat. [%]	± 0.29	± 0.56	± 1.26	± 2.59	± 4.51
ISR/FSR + scale [%]	$^{+0.83}_{-0.15}$	$^{-1.37}_{-}$	∓ 1.92	$^{+3.46}_{-0.47}$	∓ 2.21
Alternate hard-scattering model [%]	∓ 1.77	± 2.22	± 2.62	∓ 1.58	∓ 4.75
Alternate parton-shower model [%]	∓ 5.03	± 3.10	± 2.09	± 8.30	± 12.7

Bins [GeV]	0–0.20	0.20–0.30	0.30–0.45	0.45–0.60	0.60–0.80	0.80–1.05
$d\sigma$ / $dR_{p_T}^{extrajet1jetleading}$ [pb/GeV]	$2.57 \cdot 10^{-1}$	$1.08 \cdot 10^{0}$	$1.37 \cdot 10^{0}$	$1.54 \cdot 10^{0}$	$1.28 \cdot 10^{0}$	$2.70 \cdot 10^{0}$
Total Uncertainty [%]	+17.3 −14.0	+14.7 −13.6	+12.1 −13.4	+14.0 −13.4	+20.2 −19.0	+12.6 −13.8
Statistics [%]	±4.4	±3.1	±2.3	±2.2	±2.2	±1.3
Systematics [%]	+16.4 −12.9	+14.2 −13.0	+11.7 −13.1	+13.7 −13.0	+19.9 −18.8	+12.4 −13.7
Jet vertex fraction [%]	+0.38 −0.40	+0.44 −0.46	+0.50 −0.52	+0.52 −0.54	+0.53 −0.55	+0.55 −0.57
b-Tagged jet energy scale (JES) [%]	+0.43 −1.32	+1.20 −0.83	+1.02 −1.19	+0.53 −0.68	±0.70	+0.68 −0.73
Effective detector NP set 1 (JES) [%]	+1.72 −1.61	+2.63 −2.28	+1.68 −2.20	+2.64 −1.74	+1.70 −1.13	+1.66 −2.03
Effective mixed NP set 1 (JES) [%]	+1.38 −1.65	+0.71 −0.75	+0.21 −0.44	- −0.27	−0.20 +0.97	+0.49 −0.36
Effective mixed NP set 2 (JES) [%]	−0.58 +0.52	−0.10 +0.17	−0.30 +0.27	∓0.30	- +0.57	−0.25 +0.37
Effective mixed NP set 3 (JES) [%]	- −0.19	-	-	-	-	-
Effective modelling NP set 1 (JES) [%]	+8.54 −5.24	+8.01 −6.53	+6.63 −6.12	+6.54 −6.33	+8.07 −6.64	+6.48 −7.70
Effective modelling NP set 2 (JES) [%]	+0.29 −0.65	+1.47 −1.14	+1.00 −1.37	+1.61 −1.08	+1.29 −0.69	+0.48 −1.02
Effective modelling NP set 3 (JES) [%]	±0.15	±0.62	+0.29 −0.19	+0.66 −1.03	+0.37 −0.39	+0.49 −0.33
Effective modelling NP set 4 (JES) [%]	+0.46 −0.55	+0.79 −0.69	+0.42 −0.35	+0.29 −0.55	±0.69	+0.49 −0.47
Effective statistical NP set 1 (JES) [%]	-	-	-	-	-	-
Effective statistical NP set 2 (JES) [%]	−0.27 +0.68	−0.30 +0.44	−0.14 +0.42	−0.32 +0.38	−0.31 +0.25	−0.52 +0.45
Effective statistical NP set 3 (JES) [%]	∓0.21	-	+0.14 −0.10	∓0.43	±0.52	-
Effective statistical NP set 4 (JES) [%]	∓0.29	- −0.37	-	∓0.26	±0.54	-
Effective statistical NP set 5 (JES) [%]	∓0.74	- +0.32	-	−0.56 +0.38	−0.17 +0.54	−0.21 -
Effective statistical NP set 6 (JES) [%]	∓0.47	+0.37 −0.19	-	∓0.16	±0.28	- −0.12
η intercalibration model (JES) [%]	+3.46 −0.59	+1.42 −1.41	+0.91 −1.42	+1.60 −1.61	+2.31 −1.02	+1.62 −1.80
high E η intercalibration non closure (JES) [%]	-	-	-	-	-	-
neg η intercalibration non closure (JES) [%]	−0.11 +0.15	-	-	-	-	-
pos η intercalibration non closure (JES) [%]	-	-	-	-	-	-
η intercalibration total stat (JES) [%]	+0.77 −0.42	+0.51 −0.40	+0.78 −0.38	+0.35 −0.47	+0.42 −0.37	+0.65 −0.62
Flavour composition (JES) [%]	+0.76 −0.69	+1.13 −0.85	+1.11 −0.82	+0.83 −0.51	+1.12 −0.91	+1.40 −1.04
Flavour response (JES) [%]	−2.90 +5.92	−2.92 +3.17	−3.43 +2.75	−2.98 +4.09	−2.69 +4.13	−4.25 +3.41
Pile-up offset μ (JES) [%]	±0.15	∓0.19	±0.47	±0.24	±0.14	−0.23 -
Pile-up offset N_{PV} (JES) [%]	±0.51	+0.39 −0.30	+0.51 −0.32	±0.77	+0.66 −0.40	+0.26
Pile-up offset p_T (JES) [%]	±0.56	+0.42 −0.54	+0.14 −0.55	- −0.21	±0.30	-
Pile-up offset ρ topology (JES) [%]	+5.79 −2.97	+4.40 −3.79	+3.11 −3.70	+4.42 −3.32	+4.61 −3.82	+3.85 −4.25
Punch-through (JES) [%]	-	-	-	-	-	-
Single particle high-p_T (JES) [%]	-	-	-	-	-	-
b-Quark tagging efficiency (eigenvector 0) [%]	−3.69 +3.75	−3.94 +4.01	−4.09 +4.17	−3.94 +4.01	−3.72 +3.79	−3.40 +3.46
b-Quark tagging efficiency (eigenvector 1) [%]	−1.82 +1.84	−1.42 +1.44	∓1.06	∓0.70	∓0.60	∓0.37
b-Quark tagging efficiency (eigenvector 2) [%]	+1.46 −1.45	+1.46 −1.45	+1.46 −1.45	±1.39	+1.34 −1.33	±1.24
b-Quark tagging efficiency (eigenvector 3) [%]	±0.48	±0.33	±0.31	±0.12	-	∓0.17
b-Quark tagging efficiency (eigenvector 4) [%]	∓0.16	∓0.16	∓0.17	∓0.20	∓0.19	∓0.17
b-Quark tagging efficiency (eigenvector 5) [%]	-	-	-	-	-	-
c-Quark tagging efficiency (eigenvector 0) [%]	±0.83	±0.77	±0.69	±0.70	±0.57	±0.48
c-Quark tagging efficiency (eigenvector 1) [%]	±0.40	±0.34	±0.28	±0.27	±0.22	±0.16
c-Quark tagging efficiency (eigenvector 2) [%]	±0.12	-	-	-	-	-
Light-jet tagging efficiency (eigenvector 0) [%]	+0.76 −0.75	+0.73 −0.74	+0.71 −0.70	±0.42	±0.51	±0.69
Light-jet tagging efficiency (eigenvector 1) [%]	-	-	-	-	-	-
Light-jet tagging efficiency (eigenvector 2) [%]	-	-	-	-	-	-
Light-jet tagging efficiency (eigenvector 3) [%]	-	-	-	-	-	-
Light-jet tagging efficiency (eigenvector 4) [%]	-	-	-	-	-	-
Light-jet tagging efficiency (eigenvector 5) [%]	-	-	-	-	-	-
Light-jet tagging efficiency (eigenvector 6) [%]	-	-	-	-	-	-
Light-jet tagging efficiency (eigenvector 7) [%]	-	-	-	-	-	-
Light-jet tagging efficiency (eigenvector 8) [%]	-	-	-	-	-	-
Light-jet tagging efficiency (eigenvector 9) [%]	-	-	-	-	-	-
Light-jet tagging efficiency (eigenvector 10) [%]	-	-	-	-	-	-
b-Quark tagging extrapolation [%]	∓0.14	∓0.10	-	-	-	-
b-Quark tagging extrapolation from c-Quark [%]	-	-	-	-	-	-
JET JER cross calibration forward [%]	-	-	-	-	-	-
JET JER noise forward [%]	-	-	-	-	-	-
JET JER NP0 [%]	-	-	-	-	-	-
JET JER NP1 [%]	±2.35	+0.75	∓0.72	∓0.18	+1.17 −0.13	∓1.11
JET JER NP2 [%]	−0.92 +4.41	−0.80 +1.82	∓0.94	±1.15	±0.50	∓1.21
JET JER NP3 [%]	±4.04	−0.68 +1.15	∓1.11	−0.28 +0.48	±1.26	∓0.95
JET JER NP4 [%]	±1.33	±0.57	∓0.11	±0.51	±1.02	∓1.36
JET JER NP5 [%]	±1.30	- +0.63	−0.30 +0.23	+0.79 −0.84	−0.39 +1.10	- −0.50
JET JER NP6 [%]	−0.92 +0.51	- −0.33	∓0.28	+0.67 −0.15	−0.40 +1.21	∓0.54
JET JER NP7 [%]	±2.07	−0.75 +1.17	- −0.74	∓0.86	±1.60	+0.16 −0.75
JET JER NP8 [%]	-	-	-	-	-	-
QCD estimation [%]	∓0.38	∓0.61	±1.24	±2.43	±2.82	±2.56
K-factor normalization mass [%]	+2.82 −2.73	+2.83 −2.74	+2.78 −2.69	+2.71 −2.62	+2.65 −2.56	+2.44 −2.36
K-factor normalization PDFAS [%]	±4.27	±4.28	±4.21	±4.10	±4.01	±3.69
K-factor normalization scale [%]	+2.40 −3.55	+2.41 −3.56	+2.37 −3.50	+2.31 −3.41	+2.26 −3.34	+2.08 −3.07
Luminosity [%]	∓2.05	∓2.05	∓2.05	∓2.05	∓2.05	∓2.05
MCSignal stat. [%]	±3.24	±2.29	±1.64	±1.54	±1.52	±0.87
QCD stat. [%]	±0.43	±0.61	±0.85	±1.30	±1.69	±1.56
ISR/FSR + scale [%]	−3.70 +0.74	∓3.92	−4.73 +0.40	±3.45	∓0.39	∓0.79
Alternate hard-scattering model [%]	±0.99	∓1.27	±2.55	-	±9.27	∓2.82
Alternate parton-shower model [%]	∓0.33	±3.04	±0.13	±4.46	±11.2	±3.39
Inter PDF [%]	-	-	-	-	-	-
Intra PDF [%]	±0.25	±0.12	-	±0.17	±0.18	±0.11

TABLE D.7: Table of systematics for the absolute differential cross-section at the particle level for the *Rutgers* t observable

Bins [GeV]	0–0.15	0.15–0.25	0.25–0.40	0.40–0.50	0.50–0.65	0.65–0.80	0.80–1	1–1.20	1.20–5
$d\sigma$ / $dR_{pt}^{extrajet1topleading}$ [pb/GeV]	$7.13 \cdot 10^{-1}$	$2.46 \cdot 10^{0}$	$2.64 \cdot 10^{0}$	$1.94 \cdot 10^{0}$	$1.35 \cdot 10^{0}$	$8.74 \cdot 10^{-1}$	$5.05 \cdot 10^{-1}$	$2.99 \cdot 10^{-1}$	$2.57 \cdot 10^{-2}$
Total Uncertainty [%]	+13.3 −12.4	+14.3 −12.3	+13.7 −14.1	+16.8 −15.2	+14.9 −17.2	+16.8 −15.6	+18.7 −17.8	+22.8 −27.3	+18.0 −19.2
Statistics [%]	±3.0	±2.1	±1.7	±2.5	±2.5	±3.4	±3.8	±5.3	±4.1
Systematics [%]	+12.7 −11.8	+14.0 −12.0	+13.5 −13.9	+16.4 −14.8	+14.4 −16.8	+15.9 −14.6	+17.6 −16.6	+20.9 −25.6	+16.2 −17.5
Jet vertex fraction [%]	+0.37 −0.39	+0.45 −0.47	+0.51 −0.54	+0.54 −0.57	+0.58 −0.60	+0.57 −0.60	+0.53 −0.57	+0.67 −0.70	+0.69 −0.70
b-Tagged jet energy scale (JES) [%]	+0.89 −0.81	+1.13 −0.99	+0.37 −0.81	+1.38 −0.83	+0.12 −1.26	+0.89 −0.85	+1.65 −0.39	+0.27 −0.75	±0.34
Effective detector NP set 1 (JES) [%]	+1.74 −1.79	+2.47 −2.23	+1.93 −1.45	+2.06 −2.24	+1.42 −2.24	+1.94 −1.63	+1.77 −0.69	∓1.77	+2.62 −2.63
Effective mixed NP set 1 (JES) [%]	±0.88	+0.49 −0.25	−0.14 -	−0.21 +0.19	-	+1.21 −0.91	±0.98	∓1.63	+1.88 −1.05
Effective mixed NP set 2 (JES) [%]	−0.43 +0.23	−0.14 +0.41	−0.21 +0.10	−0.55 +0.17	−0.31 +0.14	−0.67 +0.61	±1.34	- −0.76	±0.39
Effective mixed NP set 3 (JES) [%]	-	-	-	-	-	-	-	±0.20	+0.21 −0.46
Effective modelling NP set 1 (JES) [%]	+6.56 −5.98	+8.15 −4.98	+5.90 −6.70	+9.41 −7.04	+6.05 −8.93	+7.40 −6.94	+0.26 +7.24 −5.46	+5.40 −11.7	+5.99 −8.57
Effective modelling NP set 2 (JES) [%]	+0.60 −0.71	+1.63 −1.36	+1.22 −0.87	+1.02 −1.41	+0.26 −0.76	+0.89 −2.02	+1.12 -	∓2.04	+1.02 −0.27
Effective modelling NP set 3 (JES) [%]	+0.35 −0.19	+0.64 −0.27	+0.46 −0.51	+0.31 −0.60	+0.50 −0.89	±0.39	±0.95	∓0.76	+0.10 −0.90
Effective modelling NP set 4 (JES) [%]	+0.38 −0.49	+0.78 −0.40	+0.41 −0.37	+0.33 −0.71	+0.14 −0.33	+1.17 −0.92	±1.04	∓0.66	+0.86 −0.17
Effective statistical NP set 1 (JES) [%]	-	-	-	-	-	-	-	−0.17 -	-
Effective statistical NP set 2 (JES) [%]	−0.18 +0.50	−0.17 +0.55	−0.29 +0.36	−0.63 +0.16	−0.73 +0.27	−0.35 +0.72	±0.69	∓0.58	−0.76 +0.56
Effective statistical NP set 3 (JES) [%]	-	+0.10 −0.17	+0.25 −0.18	-	∓0.15	+0.33 −0.10	±0.78	−0.55 +0.20	-
Effective statistical NP set 4 (JES) [%]	∓0.17	- −0.14	±0.16	+0.19 −0.34	- −0.32	-	±0.54	∓0.71	−0.33 +0.49
Effective statistical NP set 5 (JES) [%]	∓0.20	−0.16 +0.26	−0.26 +0.45	−0.51 +0.21	∓0.28	−0.19 +0.46	±0.37	∓0.82	-
Effective statistical NP set 6 (JES) [%]	- −0.25	+0.20 -	±0.12 -	- −0.22	+0.10 −0.23	+0.39 −0.26	±0.33	−0.41 +0.12	+0.26 −0.16
η intercalibration model (JES) [%]	+2.21 −1.10	+1.45 −1.54	+1.70 −1.17	+2.13 −1.69	+1.34 −2.14	+1.69 −1.53	+0.78 −0.46	∓3.07	+3.15 −1.85
high E η intercalibration non closure (JES) [%]	-	-	-	-	-	-	-	-	-
neg η intercalibration non closure (JES) [%]	-	-	-	-	-	-	±0.27	-	∓0.18
pos η intercalibration non closure (JES) [%]	-	-	-	-	-	-	-	-	-
η intercalibration total stat (JES) [%]	+0.55 −0.32	+0.86 −0.34	+0.36 −0.48	+0.34 −0.73	+0.56 −0.81	+1.24 −0.75	±1.13	∓0.71	+0.43 −0.58
Flavour composition (JES) [%]	+0.54 −0.86	+1.35 −0.68	+0.91 −0.60	+0.99 −1.44	+1.48 −1.25	+1.87 −1.21	+1.07 −0.26	±0.43	+2.28 −1.51
Flavour response (JES) [%]	−3.05 +3.47	−2.64 +3.70	−3.28 +3.42	−3.39 +4.71	−3.87 +2.99	−3.80 +4.39	−3.00 +1.92	−6.79 +2.19	−5.81 +5.41
Pile-up offset μ (JES) [%]	−0.16 +0.20	±0.30	−0.10 +0.26	+0.21 −0.20	−0.43 -	- +0.55	±0.55	∓1.27	+0.32 −0.64
Pile-up offset N_{PV} (JES) [%]	+0.71 -	±0.58	+0.25 −0.28	+1.22 -	- −0.69 +0.50	+0.24 −1.18	±0.69	−0.62 +1.24	+0.64 −0.28
Pile-up offset p_T (JES) [%]	+0.47 −0.50	+0.39 −0.13	∓0.12	+0.62 −0.61	∓0.18	∓0.52	±0.61	∓0.72	−0.24 +1.15
Pile-up offset ρ topology (JES) [%]	+4.56 −3.39	+4.26 −3.27	+3.66 −3.40	+5.06 −4.74	+2.99 −4.29	+4.91 −3.63	+3.37 −2.65	+3.91 −8.49	+5.09 −5.01
Punch-through (JES) [%]	-	-	-	-	-	-	-	+0.13 −0.38	-
Single particle high-p_T (JES) [%]	-	-	-	-	-	-	-	-	-
b-Quark tagging efficiency (eigenvector 0) [%]	−3.57 +3.63	−4.00 +4.08	−3.93 +4.00	−3.68 +3.75	−3.61 +3.67	−3.52 +3.57	−3.39 +3.45	−3.57 +3.62	−3.16 +3.22
b-Quark tagging efficiency (eigenvector 1) [%]	−1.51 +1.52	−1.12 +1.13	∓0.69	∓0.50	∓0.44	∓0.46	±0.27	±0.20	∓0.11
b-Quark tagging efficiency (eigenvector 2) [%]	+1.50 −1.49	+1.46 −1.45	+1.39 −1.38	±1.30	+1.28 −1.27	±1.27	+1.22 −1.21	±1.24	+1.12 −1.11
b-Quark tagging efficiency (eigenvector 3) [%]	±0.43	±0.34	-	-	∓0.11	∓0.15	∓0.24	−0.25 +0.24	∓0.35
b-Quark tagging efficiency (eigenvector 4) [%]	∓0.21	∓0.19	∓0.20	∓0.16	∓0.17	∓0.17	∓0.15	∓0.15	∓0.14
b-Quark tagging efficiency (eigenvector 5) [%]	-	-	-	-	-	-	-	-	-
c-Quark tagging efficiency (eigenvector 0) [%]	+0.82 −0.81	±0.75	+0.65 −0.64	±0.47	±0.53	±0.51	±0.41	±0.44	±0.50
c-Quark tagging efficiency (eigenvector 1) [%]	±0.40	+0.32 −0.31	±0.24	±0.17	±0.20	±0.18	±0.11	±0.23	-
c-Quark tagging efficiency (eigenvector 2) [%]	±0.12	-	-	-	-	-	-	-	-
Light-jet tagging efficiency (eigenvector 0) [%]	±0.73	±0.66	+0.54 −0.55	±0.49	±0.64	±0.64	±0.70	±0.81	+0.87 −0.85
Light-jet tagging efficiency (eigenvector 1) [%]	-	-	-	-	-	-	-	-	±0.19
Light-jet tagging efficiency (eigenvector 2) [%]	-	-	-	-	-	-	-	-	-
Light-jet tagging efficiency (eigenvector 3) [%]	-	-	-	-	-	-	-	-	-
Light-jet tagging efficiency (eigenvector 4) [%]	-	-	-	-	-	-	-	-	-
Light-jet tagging efficiency (eigenvector 5) [%]	-	-	-	-	-	-	-	-	-
Light-jet tagging efficiency (eigenvector 6) [%]	-	-	-	-	-	-	-	-	-
Light-jet tagging efficiency (eigenvector 7) [%]	-	-	-	-	-	-	-	-	-
Light-jet tagging efficiency (eigenvector 8) [%]	-	-	-	-	-	-	-	-	-
Light-jet tagging efficiency (eigenvector 9) [%]	-	-	-	-	-	-	-	-	-
Light-jet tagging efficiency (eigenvector 10) [%]	-	-	-	-	-	-	-	-	-
b-Quark tagging extrapolation [%]	∓0.11	∓0.11	-	-	-	∓0.11	-	∓0.14	∓0.21
b-Quark tagging extrapolation from c-Quark [%]	-	-	-	-	-	-	-	-	-
JET JER cross calibration forward [%]	-	-	-	-	-	-	-	-	-
JET JER noise forward [%]	-	-	-	-	-	-	-	-	-
JET JER NP0 [%]	-	-	-	-	-	-	-	-	-
JET JER NP1 [%]	-	+1.31 -	−0.81 -	∓0.30	∓0.41	−0.96 +0.11	∓0.34	−2.96 +0.22	±0.49
JET JER NP2 [%]	−1.03 +1.23	- +2.56	+0.40 −0.91	−0.21 +0.49	+0.20 −1.56	∓0.35	−0.42 +1.12	∓3.79	+0.74 −2.68
JET JER NP3 [%]	−0.58 +2.51	±0.69	∓0.75	- +1.32	∓0.75	−0.20 +0.66	−0.02 +0.39	∓1.93	+1.21 −1.93
JET JER NP4 [%]	+0.43 −0.14	±1.35	+0.35 −0.38	−0.44 +0.86	∓1.70	+1.05 −1.65	−0.35 +2.05	∓5.58	∓1.24
JET JER NP5 [%]	- +0.41	±0.43	-	−0.15 +0.47	∓0.89	+0.68 −0.90	+1.53 −0.42	−0.70 +0.15	- +0.19
JET JER NP6 [%]	∓1.04	±0.60	−0.32	+0.39 −0.51	- −1.00 +0.52	−0.33 -	+1.29 −0.70	−1.79 +0.83	∓1.43
JET JER NP7 [%]	+0.25 -	±0.76	∓0.30	±0.59	∓1.60	+0.53 −0.72	±1.35	∓2.71	±0.49
JET JER NP8 [%]	-	-	-	-	-	-	-	-	-
QCD estimation [%]	-	±0.44	±1.82	±2.56	±3.47	±3.66	±4.76	±3.22	±6.39
K-factor normalization mass [%]	+2.83 −2.74	+2.82 −2.73	+2.71 −2.62	+2.60 −2.52	+2.52 −2.44	+2.51 −2.43	+2.40 −2.32	+2.45 −2.37	+2.12 −2.05
K-factor normalization PDFAS [%]	±4.28	±4.27	±4.10	±3.94	±3.82	±3.80	±3.63	±3.71	±3.21
K-factor normalization scale [%]	+2.41 −3.57	+2.40 −3.55	+2.31 −3.41	+2.22 −3.28	+2.15 −3.18	+2.14 −3.17	+2.04 −3.02	+2.09 −3.09	+1.81 −2.67
Luminosity [%]	∓2.05	∓2.05	∓2.05	∓2.05	∓2.05	∓2.05	∓2.05	∓2.05	∓2.05
MCSignal stat. [%]	±2.19	±1.57	±1.21	±1.74	±1.67	±2.19	±2.44	±3.33	±2.56
QCD stat. [%]	±0.39	±0.65	±0.97	±1.97	±2.33	±3.72	±4.59	±6.78	±6.24
ISR/FSR + scale [%]	∓1.71	−3.42 +0.44	−0.51 +0.90	∓1.03	+0.62 -	+4.76 −0.50	∓4.73	∓6.11	+0.57 −2.12
Alternate hard-scattering model [%]	±2.59	∓0.35	±5.90	∓5.22	±6.49	∓1.71	∓11.1	∓13.9	±3.36
Alternate parton-shower model [%]	±0.51	±3.40	±4.55	±5.56	±6.16	±7.10	±1.28	∓3.86	±6.89
Inter PDF [%]	-	-	-	-	-	-	-	-	-
Intra PDF [%]	±0.16	-	±0.16	±0.18	±0.15	±0.15	±0.18	±0.20	-

TABLE D.8: Table of systematics for the absolute differential cross-section at the particle level for the *Rptxonetl* observable.

Bins [GeV]	0–1	1–1.85	1.85–2.75	2.75–4	4–5.50	5.50–7.50	7.50–16
$d\sigma$ / $dR_{Wb}^{leading}$ [pb/GeV]	$4.69 \cdot 10^{-1}$	$6.04 \cdot 10^{-1}$	$4.18 \cdot 10^{-1}$	$2.27 \cdot 10^{-1}$	$8.34 \cdot 10^{-2}$	$3.51 \cdot 10^{-2}$	$5.29 \cdot 10^{-3}$
Total Uncertainty [%]	$^{+19.2}_{-19.5}$	$^{+14.3}_{-13.7}$	$^{+11.1}_{-11.7}$	$^{+13.7}_{-12.5}$	$^{+15.7}_{-16.8}$	$^{+16.0}_{-17.9}$	$^{+27.9}_{-27.2}$
Statistics [%]	±1.5	±1.5	±1.8	±2.0	±3.1	±4.3	±6.6
Systematics [%]	$^{+19.1}_{-19.4}$	$^{+14.2}_{-13.5}$	$^{+10.8}_{-11.4}$	$^{+13.4}_{-12.2}$	$^{+15.1}_{-16.2}$	$^{+14.7}_{-16.7}$	$^{+26.0}_{-25.2}$
Jet vertex fraction [%]	$^{+0.65}_{-0.68}$	$^{+0.40}_{-0.42}$	$^{+0.37}_{-0.40}$	$^{+0.31}_{-0.34}$	$^{+0.47}_{-0.49}$	$^{+0.66}_{-0.68}$	$^{+0.71}_{-0.73}$
b-Tagged jet energy scale (JES) [%]	$^{+1.08}_{-1.01}$	$^{+0.64}_{-0.77}$	$^{+1.13}_{-0.89}$	$^{+0.90}_{-1.03}$	$^{+0.22}_{-0.71}$	∓1.11	$^{-0.80}_{+1.02}$
Effective detector NP set 1 (JES) [%]	$^{+2.39}_{-2.55}$	$^{+1.90}_{-1.91}$	$^{+1.59}_{-1.32}$	$^{+2.13}_{-1.38}$	$^{+0.97}_{-1.59}$	$^{+0.16}_{-1.25}$	±1.60
Effective mixed NP set 1 (JES) [%]	$^{+0.46}_{-0.96}$	-	±0.29	±0.35	$^{+0.78}_{-0.77}$	$^{+1.04}_{-0.73}$	$^{+1.31}_{-0.98}$
Effective mixed NP set 2 (JES) [%]	$^{-0.50}_{+0.51}$	$^{-0.33}_{-}$	$^{-0.29}_{+0.37}$	±0.22	-	$^{-}_{+0.56}$	∓0.46
Effective mixed NP set 3 (JES) [%]	-	-	-	$^{+0.16}_{-}$	-	-	-
Effective modelling NP set 1 (JES) [%]	$^{+8.56}_{-8.43}$	$^{+6.90}_{-6.32}$	$^{+5.70}_{-5.95}$	$^{+6.13}_{-4.58}$	$^{+3.21}_{-4.66}$	$^{+2.18}_{-6.88}$	$^{+5.27}_{-4.09}$
Effective modelling NP set 2 (JES) [%]	$^{+1.04}_{-1.51}$	$^{+1.39}_{-1.18}$	$^{+1.15}_{-1.21}$	$^{+1.51}_{-0.62}$	$^{+0.34}_{-1.10}$	$^{-}_{-}$	$^{-}_{-0.38}$
Effective modelling NP set 3 (JES) [%]	$^{+0.29}_{-0.42}$	$^{+0.21}_{-0.52}$	$^{+0.49}_{-0.43}$	$^{+0.78}_{-0.34}$	±0.39	$^{+0.14}_{-0.24}$	$^{-1.33}_{+0.54}$
Effective modelling NP set 4 (JES) [%]	$^{+0.73}_{-0.72}$	$^{+0.41}_{-0.60}$	$^{+0.58}_{-0.27}$	$^{+0.45}_{-0.24}$	$^{+0.13}_{-0.17}$	±0.28	∓0.30
Effective statistical NP set 1 (JES) [%]	-	-	-	-	-	-	∓0.10
Effective statistical NP set 2 (JES) [%]	$^{-0.57}_{+0.52}$	$^{-0.34}_{+0.29}$	$^{-0.32}_{+0.30}$	$^{-0.15}_{+0.46}$	±0.20	$^{-0.26}_{+0.18}$	$^{-0.89}_{+0.12}$
Effective statistical NP set 3 (JES) [%]	-	$^{+0.25}_{-0.22}$	$^{-}_{-0.28}$	-	±0.30	$^{-0.50}_{+0.59}$	±0.54
Effective statistical NP set 4 (JES) [%]	$^{+0.23}_{-0.10}$	-	-	-	±0.49	±0.21	∓0.49
Effective statistical NP set 5 (JES) [%]	$^{-0.26}_{+0.28}$	$^{-0.32}_{+0.24}$	$^{-0.30}_{+0.21}$	$^{-0.14}_{+0.23}$	±0.22	$^{-}_{-0.26}$	-
Effective statistical NP set 6 (JES) [%]	$^{+0.22}_{-}$	-	∓0.28	$^{+0.31}_{-0.16}$	±0.22	$^{+0.28}_{-0.13}$	$^{+0.18}_{-0.30}$
η intercalibration model (JES) [%]	$^{+1.48}_{-1.97}$	$^{+1.56}_{-1.31}$	$^{+1.42}_{-1.35}$	$^{+2.16}_{-0.91}$	±0.74	$^{+1.97}_{-1.78}$	∓1.20
high E η intercalibration non closure (JES) [%]	-	-	-	-	-	-	-
neg η intercalibration non closure (JES) [%]	-	-	-	-	-	-	$^{+0.12}_{-0.17}$
pos η intercalibration non closure (JES) [%]	-	-	-	-	-	-	-
η intercalibration total stat (JES) [%]	$^{+0.70}_{-0.82}$	$^{+0.32}_{-0.50}$	$^{+0.57}_{-0.35}$	$^{+0.73}_{-0.21}$	±0.54	$^{+0.54}_{-0.35}$	∓1.43
Flavour composition (JES) [%]	$^{+1.46}_{-1.23}$	$^{+1.17}_{-0.99}$	$^{+0.66}_{-0.53}$	$^{+1.37}_{-0.29}$	$^{+0.64}_{-0.29}$	$^{+0.18}_{-1.28}$	$^{+1.27}_{-0.36}$
Flavour response (JES) [%]	$^{-4.04}_{+3.51}$	$^{-2.65}_{+4.05}$	$^{-3.50}_{+2.45}$	$^{-2.45}_{+3.21}$	$^{-3.16}_{+1.93}$	$^{-5.24}_{+3.71}$	$^{-1.24}_{+5.97}$
Pile-up offset μ (JES) [%]	∓0.15	$^{-0.31}_{+0.21}$	-	±0.32	±0.43	$^{-0.29}_{-}$	$^{-}_{-0.82}$
Pile-up offset N_{PV} (JES) [%]	$^{+0.14}_{-}$	±0.43	-	$^{+0.71}_{-0.22}$	$^{+0.51}_{-0.41}$	−0.81	±0.59
Pile-up offset p_T (JES) [%]	$^{+0.18}_{-0.48}$	$^{+0.36}_{-0.10}$	-	$^{-}_{-0.25}$	$^{-0.55}_{+0.27}$	∓0.38	$^{+0.93}_{-0.67}$
Pile-up offset ρ topology (JES) [%]	±5.04	$^{+4.29}_{-3.48}$	$^{+3.30}_{-3.35}$	$^{+3.29}_{-2.40}$	$^{+1.37}_{-3.15}$	$^{+1.16}_{-3.42}$	±5.22
Punch-through (JES) [%]	-	-	-	-	-	-	-
Single particle high-p_T (JES) [%]	-	-	-	-	-	-	-
b-Quark tagging efficiency (eigenvector 0) [%]	$^{-3.60}_{+3.66}$	$^{-3.35}_{+3.40}$	$^{-3.46}_{+3.52}$	$^{-3.93}_{+4.01}$	$^{-4.46}_{+4.55}$	$^{-5.92}_{+6.05}$	$^{-7.95}_{+8.15}$
b-Quark tagging efficiency (eigenvector 1) [%]	∓1.84	$^{-0.82}_{+0.83}$	∓0.41	∓0.24	-	±0.54	±1.62
b-Quark tagging efficiency (eigenvector 2) [%]	$^{+1.34}_{-1.33}$	$^{+1.39}_{-1.38}$	$^{+1.39}_{-1.38}$	$^{+1.47}_{-1.46}$	$^{+1.46}_{-1.45}$	$^{+1.20}_{-1.19}$	±0.57
b-Quark tagging efficiency (eigenvector 3) [%]	±0.65	±0.36	∓0.19	∓0.51	∓0.65	∓0.68	∓0.38
b-Quark tagging efficiency (eigenvector 4) [%]	-	∓0.29	∓0.27	∓0.17	-	-	-
b-Quark tagging efficiency (eigenvector 5) [%]	-	-	±0.11	±0.14	±0.11	-	∓0.10
c-Quark tagging efficiency (eigenvector 0) [%]	±0.50	±0.62	±0.67	±0.68	$^{+0.68}_{-0.67}$	$^{+0.60}_{-0.61}$	±0.52
c-Quark tagging efficiency (eigenvector 1) [%]	±0.10	±0.23	±0.30	±0.33	±0.38	±0.46	±0.35
c-Quark tagging efficiency (eigenvector 2) [%]	-	-	-	±0.16	±0.19	±0.17	±0.18
Light-jet tagging efficiency (eigenvector 0) [%]	±0.63	$^{+0.66}_{-0.65}$	±0.51	±0.55	±0.66	±0.70	±0.65
Light-jet tagging efficiency (eigenvector 1) [%]	-	-	-	-	-	-	-
Light-jet tagging efficiency (eigenvector 2) [%]	-	-	-	-	-	-	∓0.15
Light-jet tagging efficiency (eigenvector 3) [%]	-	-	-	-	-	-	-
Light-jet tagging efficiency (eigenvector 4) [%]	-	-	-	-	-	-	-
Light-jet tagging efficiency (eigenvector 5) [%]	-	-	-	-	-	-	-
Light-jet tagging efficiency (eigenvector 6) [%]	-	-	-	-	-	-	-
Light-jet tagging efficiency (eigenvector 7) [%]	-	-	-	-	-	-	-
Light-jet tagging efficiency (eigenvector 8) [%]	-	-	-	-	-	-	-
Light-jet tagging efficiency (eigenvector 9) [%]	-	-	-	-	-	-	-
Light-jet tagging efficiency (eigenvector 10) [%]	-	-	-	-	-	-	-
b-Quark tagging extrapolation [%]	-	-	∓0.11	∓0.17	∓0.20	∓0.21	∓0.22
b-Quark tagging extrapolation from c-Quark [%]	-	-	-	-	-	-	-
JET JER cross calibration forward [%]	-	-	-	-	-	-	-
JET JER noise forward [%]	-	-	-	-	-	-	-
JET JER NP0 [%]	-	-	-	-	-	-	-
JET JER NP1 [%]	∓0.97	$^{-0.17}_{-}$	$^{+0.53}_{-0.15}$	$^{-0.54}_{-}$	±0.21	$^{+3.52}_{-0.32}$	$^{-2.42}_{-}$
JET JER NP2 [%]	∓1.19	$^{+0.13}_{-}$	±0.59	$^{-0.12}_{+0.31}$	$^{+0.35}_{-0.97}$	$^{-0.16}_{+2.65}$	±1.76
JET JER NP3 [%]	∓1.00	∓0.35	±0.17	$^{-0.45}_{+0.15}$	∓0.55	±1.92	∓0.25
JET JER NP4 [%]	∓0.66	±0.22	$^{+0.31}_{-0.67}$	$^{-0.31}_{+0.88}$	$^{+1.71}_{-2.19}$	±4.32	$^{-2.47}_{+4.17}$
JET JER NP5 [%]	$^{+0.16}_{-1.32}$	±0.21	$^{-0.44}_{+0.35}$	$^{-}_{+0.74}$	±0.82	±4.68	∓2.82
JET JER NP6 [%]	∓0.91	±0.56	−0.94	$^{+0.68}_{-0.29}$	$^{-1.10}_{+0.92}$	±3.19	±0.81
JET JER NP7 [%]	∓1.24	±0.46	$^{-0.21}_{-}$	±0.23	∓0.24	±2.66	±0.66
JET JER NP8 [%]	-	-	-	-	-	-	-
QCD estimation [%]	±12.1	±5.00	±2.14	±1.28	±1.56	±1.28	±0.36
K-factor normalization mass [%]	$^{+2.73}_{-2.64}$	$^{+2.67}_{-2.59}$	$^{+2.68}_{-2.60}$	$^{+2.71}_{-2.62}$	$^{+2.64}_{-2.56}$	$^{+2.54}_{-2.46}$	$^{+2.32}_{-2.25}$
K-factor normalization PDFAS [%]	±4.13	±4.05	±4.06	±4.10	±3.99	±3.85	±3.52
K-factor normalization scale [%]	$^{+2.33}_{-3.44}$	$^{+2.28}_{-3.37}$	$^{+2.28}_{-3.38}$	$^{+2.31}_{-3.41}$	$^{+2.25}_{-3.33}$	$^{+2.17}_{-3.20}$	$^{+1.98}_{-2.93}$
Luminosity [%]	∓2.05	∓2.05	∓2.05	∓2.05	∓2.05	∓2.05	∓2.05
MCSignal stat. [%]	±1.20	±1.11	±1.28	±1.46	±2.14	±3.14	±4.30
QCD stat. [%]	±1.00	±1.14	±1.27	±1.33	±2.05	±3.45	±6.26
ISR/FSR + scale [%]	∓0.48	∓0.45	±0.92	$^{-1.27}_{+0.28}$	∓3.79	$^{-3.60}_{+1.47}$	$^{+0.96}_{-2.83}$
Alternate hard-scattering model [%]	∓3.87	±4.56	±1.85	±5.23	∓11.3	∓1.20	±5.39
Alternate parton-shower model [%]	±3.98	±3.68	±0.43	±4.57	±0.21	±5.70	±20.4
Inter PDF [%]	-	-	-	-	-	-	∓0.21
Intra PDF [%]	±0.13	±0.17	±0.18	-	-	±0.18	±0.17

TABLE D.9: Table of systematics for the absolute differential cross-section at the particle level for the $R_{Wb}^{leading}$ observable.

Bins [GeV]	0–1	1–1.85	1.85–2.75	2.75–4	4–5.50	5.50–7.50	7.50–12
$d\sigma$ / $dR_{Wb}^{subleading}$ [pb/GeV]	$5.94 \cdot 10^{-1}$	$6.51 \cdot 10^{-1}$	$3.72 \cdot 10^{-1}$	$1.78 \cdot 10^{-1}$	$6.75 \cdot 10^{-2}$	$2.15 \cdot 10^{-2}$	$5.23 \cdot 10^{-3}$
Total Uncertainty [%]	$^{+17.9}_{-17.5}$	$^{+12.9}_{-13.2}$	$^{+9.93}_{-12.1}$	$^{+14.5}_{-13.4}$	$^{+18.7}_{-16.7}$	$^{+15.1}_{-17.6}$	$^{+41.8}_{-42.4}$
Statistics [%]	±1.4	±1.4	±1.9	±2.3	±3.3	±5.2	±8.5
Systematics [%]	$^{+17.8}_{-17.4}$	$^{+12.8}_{-13.0}$	$^{+9.58}_{-11.9}$	$^{+14.2}_{-13.0}$	$^{+18.1}_{-16.0}$	$^{+13.2}_{-16.0}$	$^{+39.5}_{-40.1}$
Jet vertex fraction [%]	$^{+0.67}_{-0.70}$	$^{+0.40}_{-0.43}$	$^{+0.30}_{-0.32}$	$^{+0.32}_{-0.34}$	$^{+0.36}_{-0.39}$	$^{+0.56}_{-0.58}$	$^{+0.62}_{-0.63}$
b-Tagged jet energy scale (JES) [%]	$^{+0.96}_{-0.83}$	$^{+0.51}_{-0.62}$	$^{+1.03}_{-1.35}$	$^{+1.28}_{-0.66}$	-	∓2.07	∓3.72
Effective detector NP set 1 (JES) [%]	$^{+2.06}_{-2.20}$	$^{+2.23}_{-1.90}$	$^{+1.02}_{-1.79}$	$^{+1.85}_{-0.49}$	$^{+2.79}_{-0.41}$	$^{+0.28}_{-3.21}$	∓3.14
Effective mixed NP set 1 (JES) [%]	$^{+0.28}_{-0.30}$	$^{+0.33}_{-}$	$^{+0.23}_{-0.35}$	±0.30	$^{+1.04}_{-0.46}$	$^{+0.42}_{-2.58}$	∓2.13
Effective mixed NP set 2 (JES) [%]	$^{-0.28}_{+0.40}$	$^{-0.13}_{+0.22}$	∓0.36	$^{-0.26}_{+0.62}$	$^{-0.35}_{+0.71}$	$^{-0.95}_{+0.37}$	∓0.85
Effective mixed NP set 3 (JES) [%]	±0.13	-	$^{-0.16}_{-}$	-	$^{-}_{-0.21}$	∓0.36	$^{-}_{+0.22}$
Effective modelling NP set 1 (JES) [%]	$^{+8.93}_{-8.09}$	$^{+6.55}_{-7.09}$	$^{+3.86}_{-5.65}$	$^{+5.37}_{-3.15}$	$^{+4.86}_{-0.94}$	$^{+4.25}_{-4.93}$	∓10.2
Effective modelling NP set 2 (JES) [%]	$^{+0.82}_{-0.76}$	$^{+1.51}_{-1.21}$	$^{+0.86}_{-1.79}$	$^{+1.19}_{-0.41}$	$^{+2.40}_{-0.84}$	$^{+0.71}_{-3.46}$	∓1.80
Effective modelling NP set 3 (JES) [%]	$^{+0.55}_{-0.44}$	$^{+0.45}_{-0.44}$	$^{+0.30}_{-0.55}$	$^{+0.45}_{-0.10}$	±0.30	$^{-1.76}_{+0.56}$	$^{-2.31}_{+0.42}$
Effective modelling NP set 4 (JES) [%]	$^{+0.60}_{-0.44}$	$^{+0.51}_{-0.34}$	$^{+0.38}_{-0.60}$	$^{+0.32}_{-}$	$^{+0.92}_{-0.81}$	$^{+0.23}_{-1.89}$	∓1.03
Effective statistical NP set 1 (JES) [%]	-	-	-	-	-	-	-
Effective statistical NP set 2 (JES) [%]	$^{-0.41}_{+0.54}$	$^{-0.39}_{+0.41}$	$^{-0.31}_{+0.19}$	±0.16	$^{-0.17}_{+0.60}$	∓0.90	$^{-}_{-1.65}$
Effective statistical NP set 3 (JES) [%]	±0.21	$^{+0.14}_{-0.11}$	$^{-}_{-0.37}$	$^{-0.10}_{+0.16}$	$^{-0.12}_{+0.24}$	∓0.21	∓0.71
Effective statistical NP set 4 (JES) [%]	±0.17	-	$^{-0.27}_{-}$	±0.30	±0.40	$^{+0.65}_{-0.66}$	$^{+0.63}_{-1.27}$
Effective statistical NP set 5 (JES) [%]	$^{-}_{+0.26}$	$^{-0.42}_{+0.33}$	$^{-0.39}_{+0.18}$	$^{-0.23}_{-}$	$^{-0.15}_{+0.27}$	$^{+0.18}_{-}$	$^{+0.47}_{-1.03}$
Effective statistical NP set 6 (JES) [%]	±0.19	$^{+0.20}_{-0.19}$	∓0.14	-	$^{+0.23}_{-0.18}$	-	∓0.81
η intercalibration model (JES) [%]	$^{+2.28}_{-1.65}$	$^{+1.37}_{-1.66}$	$^{+0.83}_{-1.18}$	$^{+1.50}_{-0.80}$	$^{+1.47}_{-0.27}$	$^{+0.64}_{-1.67}$	∓3.44
high E η intercalibration non closure (JES) [%]	-	-	-	-	-	-	-
neg η intercalibration non closure (JES) [%]	-	-	-	-	-	∓0.28	±0.28
pos η intercalibration non closure (JES) [%]	-	-	-	-	-	-	-
η intercalibration total stat (JES) [%]	$^{+0.75}_{-0.63}$	$^{+0.54}_{-0.39}$	$^{+0.21}_{-0.52}$	$^{+0.57}_{-0.16}$	$^{+0.86}_{-0.11}$	∓0.95	∓1.73
Flavour composition (JES) [%]	$^{+1.85}_{-1.26}$	$^{+0.98}_{-0.83}$	$^{+0.52}_{-0.54}$	±0.64	$^{+0.88}_{-0.23}$	$^{+0.24}_{-0.79}$	∓0.79
Flavour response (JES) [%]	$^{-3.99}_{+3.75}$	$^{-3.73}_{+4.03}$	$^{-2.45}_{+1.93}$	$^{-1.17}_{+2.44}$	$^{-2.10}_{+4.52}$	$^{-4.11}_{+2.35}$	∓5.93
Pile-up offset μ (JES) [%]	$^{-}_{+0.28}$	∓0.29	-	±0.16	±0.29	∓1.34	∓0.88
Pile-up offset N_{PV} (JES) [%]	$^{+0.72}_{-0.36}$	±0.19	∓0.39	±0.65	±1.02	$^{+0.51}_{-2.76}$	∓2.02
Pile-up offset p_T (JES) [%]	$^{+0.21}_{-}$	-	∓0.37	-	±0.98	∓1.04	∓2.49
Pile-up offset ρ topology (JES) [%]	$^{+5.06}_{-4.64}$	$^{+4.13}_{-3.68}$	$^{+2.24}_{-3.72}$	$^{+2.94}_{-1.23}$	$^{+3.36}_{-0.29}$	$^{+2.55}_{-4.17}$	∓6.17
Punch-through (JES) [%]	-	-	-	-	-	±0.12	∓0.13
Single particle high-p_T (JES) [%]	-	-	-	-	-	-	-
b-Quark tagging efficiency (eigenvector 0) [%]	$^{-3.10}_{+3.14}$	$^{-3.43}_{+3.48}$	$^{-3.95}_{+4.02}$	$^{-4.45}_{+4.54}$	$^{-5.45}_{+5.58}$	$^{-7.16}_{+7.36}$	$^{-8.07}_{+8.26}$
b-Quark tagging efficiency (eigenvector 1) [%]	∓1.15	$^{-0.71}_{+0.72}$	∓0.55	∓0.48	-	$^{+0.63}_{-0.64}$	$^{+1.12}_{-1.15}$
b-Quark tagging efficiency (eigenvector 2) [%]	$^{+1.36}_{-1.35}$	$^{+1.39}_{-1.38}$	$^{+1.46}_{-1.45}$	$^{+1.49}_{-1.48}$	$^{+1.32}_{-1.31}$	±0.87	±0.42
b-Quark tagging efficiency (eigenvector 3) [%]	±0.52	-	∓0.26	$^{-0.41}_{+0.40}$	∓0.49	∓0.33	-
b-Quark tagging efficiency (eigenvector 4) [%]	∓0.24	$^{-0.24}_{+0.25}$	∓0.17	-	-	-	-
b-Quark tagging efficiency (eigenvector 5) [%]	-	-	±0.11	±0.10	-	-	∓0.12
c-Quark tagging efficiency (eigenvector 0) [%]	±0.47	±0.64	±0.69	±0.73	$^{+0.77}_{-0.76}$	±0.70	±0.62
c-Quark tagging efficiency (eigenvector 1) [%]	-	±0.24	±0.34	$^{+0.43}_{-0.42}$	±0.47	±0.58	$^{+0.69}_{-0.68}$
c-Quark tagging efficiency (eigenvector 2) [%]	-	-	±0.12	±0.18	±0.22	±0.20	±0.18
Light-jet tagging efficiency (eigenvector 0) [%]	±0.60	±0.49	±0.77	$^{+0.71}_{-0.73}$	±0.68	±0.22	$^{+0.77}_{-0.76}$
Light-jet tagging efficiency (eigenvector 1) [%]	-	-	-	-	-	-	-
Light-jet tagging efficiency (eigenvector 2) [%]	-	-	-	-	-	∓0.13	-
Light-jet tagging efficiency (eigenvector 3) [%]	-	-	-	-	-	-	-
Light-jet tagging efficiency (eigenvector 4) [%]	-	-	-	-	-	-	-
Light-jet tagging efficiency (eigenvector 5) [%]	-	-	-	-	-	-	-
Light-jet tagging efficiency (eigenvector 6) [%]	-	-	-	-	-	-	-
Light-jet tagging efficiency (eigenvector 7) [%]	-	-	-	-	-	-	-
Light-jet tagging efficiency (eigenvector 8) [%]	-	-	-	-	-	-	-
Light-jet tagging efficiency (eigenvector 9) [%]	-	-	-	-	-	-	-
Light-jet tagging efficiency (eigenvector 10) [%]	-	-	-	-	-	-	-
b-Quark tagging extrapolation [%]	-	-	∓0.12	∓0.16	∓0.22	∓0.20	$^{-0.26}_{+0.27}$
b-Quark tagging extrapolation from c-Quark [%]	-	-	-	-	-	-	-
JET JER cross calibration forward [%]	-	-	-	-	-	-	-
JET JER noise forward [%]	-	-	-	-	-	-	-
JET JER NP0 [%]	-	-	-	-	-	-	-
JET JER NP1 [%]	∓0.52	∓0.33	$^{-0.78}_{-}$	$^{+1.03}_{-}$	$^{+2.88}_{-}$	$^{-1.45}_{+0.45}$	$^{-4.54}_{-}$
JET JER NP2 [%]	$^{+0.13}_{-0.64}$	$^{+0.15}_{-0.27}$	∓0.84	$^{-0.21}_{+2.20}$	±2.48	∓2.06	∓4.87
JET JER NP3 [%]	$^{+0.51}_{-1.15}$	$^{-0.90}_{+0.58}$	∓1.10	$^{-0.15}_{+1.20}$	±1.68	∓2.87	∓7.73
JET JER NP4 [%]	-	$^{+0.35}_{-0.44}$	∓1.02	±1.19	±1.36	∓1.85	$^{-4.55}_{+0.59}$
JET JER NP5 [%]	±0.61	$^{+0.15}_{-0.39}$	$^{-}_{-0.40}$	$^{-0.14}_{+0.67}$	±1.12	$^{+0.78}_{-1.90}$	∓8.14
JET JER NP6 [%]	±0.20	∓0.28	∓0.62	$^{-0.56}_{+1.24}$	±1.86	∓3.16	∓4.30
JET JER NP7 [%]	$^{-}_{+0.32}$	∓0.76	∓0.44	±1.22	±1.51	∓1.53	∓6.04
JET JER NP8 [%]	-	-	-	-	-	-	-
QCD estimation [%]	±10.2	±3.88	±1.27	±1.94	±2.26	∓1.16	∓4.40
K-factor normalization mass [%]	$^{+2.71}_{-2.62}$	$^{+2.67}_{-2.59}$	$^{+2.70}_{-2.62}$	$^{+2.70}_{-2.62}$	$^{+2.60}_{-2.52}$	$^{+2.48}_{-2.41}$	$^{+2.24}_{-2.16}$
K-factor normalization PDFAS [%]	±4.10	±4.05	±4.09	±4.09	±3.94	±3.76	±3.38
K-factor normalization scale [%]	$^{+2.31}_{-3.41}$	$^{+2.28}_{-3.37}$	$^{+2.31}_{-3.41}$	$^{+2.30}_{-3.40}$	$^{+2.22}_{-3.28}$	$^{+2.12}_{-3.13}$	$^{+1.91}_{-2.82}$
Luminosity [%]	∓2.05	∓2.05	∓2.05	∓2.05	∓2.05	∓2.05	∓2.05
MCSignal stat. [%]	±1.06	±1.05	±1.34	±1.71	±2.53	±3.74	±6.53
QCD stat. [%]	±1.13	±1.03	±1.12	±1.27	±2.03	±3.73	±8.72
ISR/FSR + scale [%]	±0.60	∓0.59	$^{-2.92}_{+0.21}$	$^{-3.26}_{+0.47}$	±6.99	∓1.57	∓6.54
Alternate hard-scattering model [%]	∓1.41	±0.91	∓0.51	±8.52	±6.73	∓3.08	∓30.7
Alternate parton-shower model [%]	±4.94	±3.14	±2.06	±0.47	±7.74	±1.87	∓2.91
Inter PDF [%]	-	-	-	-	-	±0.25	-
Intra PDF [%]	±0.12	±0.16	±0.13	±0.12	±0.20	±0.26	±0.27

TABLE D.10: Table of systematics for the absolute differential cross-section at the particle level for the $R_{Wb}^{subleading}$ observable.

Bins [GeV]	0–0.50	0.50–0.60	0.60–0.65	0.65–0.75	0.75–0.80	0.80–0.85	0.85–0.90	0.90–1	1–2
$d\sigma$ / $dR_{Wt}^{leading}$ [pb/GeV]	$8.08 \cdot 10^{-1}$	$2.51 \cdot 10^{0}$	$3.16 \cdot 10^{0}$	$3.81 \cdot 10^{0}$	$4.01 \cdot 10^{0}$	$3.65 \cdot 10^{0}$	$2.92 \cdot 10^{0}$	$1.30 \cdot 10^{0}$	$3.20 \cdot 10^{-2}$
Total Uncertainty [%]	$^{+18.9}_{-18.3}$	$^{+13.7}_{-15.3}$	$^{+16.3}_{-15.7}$	$^{+11.6}_{-10.4}$	$^{+11.9}_{-11.4}$	$^{+11.3}_{-13.3}$	$^{+16.7}_{-17.6}$	$^{+20.7}_{-19.3}$	$^{+44.9}_{-48.3}$
Statistics [%]	±1.7	±2.1	±2.6	±1.7	±2.3	±2.5	±3.0	±3.4	±7.1
Systematics [%]	$^{+18.7}_{-18.1}$	$^{+13.4}_{-14.9}$	$^{+15.8}_{-15.2}$	$^{+11.3}_{-10.1}$	$^{+11.4}_{-10.8}$	$^{+10.7}_{-12.8}$	$^{+16.1}_{-17.1}$	$^{+20.1}_{-18.6}$	$^{+43.4}_{-46.9}$
Jet vertex fraction [%]	$^{+0.67}_{-0.69}$	$^{+0.42}_{-0.44}$	$^{+0.36}_{-0.38}$	$^{+0.35}_{-0.37}$	$^{+0.31}_{-0.33}$	$^{+0.32}_{-0.35}$	$^{+0.49}_{-0.51}$	$^{+0.78}_{-0.80}$	$^{+1.08}_{-1.09}$
b-Tagged jet energy scale (JES) [%]	$^{+1.17}_{-0.70}$	$^{+0.50}_{-1.19}$	$^{+0.55}_{-0.98}$	$^{+1.06}_{-0.51}$	$^{+1.02}_{-0.42}$	$^{+0.46}_{-1.36}$	∓0.82	$^{+0.89}_{-1.18}$	$^{+3.24}_{-1.85}$
Effective detector NP set 1 (JES) [%]	$^{+2.64}_{-2.28}$	$^{+0.86}_{-2.41}$	$^{+2.06}_{-1.90}$	$^{+1.84}_{-0.58}$	$^{+2.06}_{-1.30}$	$^{+1.17}_{-2.10}$	$^{+0.87}_{-1.80}$	$^{+3.46}_{-2.71}$	$^{+1.02}_{-1.75}$
Effective mixed NP set 1 (JES) [%]	$^{+0.82}_{-1.00}$	∓0.44	$^{-0.39}_{+0.23}$	±0.72	±0.48	$^{+0.47}_{-0.58}$	$^{+0.31}_{-0.43}$	$^{+1.51}_{-0.95}$	$^{+1.58}_{-2.51}$
Effective mixed NP set 2 (JES) [%]	$^{-0.44}_{+0.63}$	∓0.50	$^{-0.55}_{+0.36}$	$^{-}_{+0.38}$	±0.27	∓0.31	∓0.24	$^{-0.22}_{+0.87}$	∓1.57
Effective mixed NP set 3 (JES) [%]	-	∓0.13	-	-	±0.13	∓0.18	$^{+0.23}_{-}$	±0.12	∓0.60
Effective modelling NP set 1 (JES) [%]	$^{+8.86}_{-8.00}$	$^{+6.64}_{-7.11}$	$^{+6.61}_{-5.62}$	$^{+5.20}_{-4.67}$	$^{+5.72}_{-4.04}$	$^{+5.28}_{-6.14}$	$^{+3.65}_{-6.78}$	$^{+9.32}_{-8.76}$	$^{+6.24}_{-13.4}$
Effective modelling NP set 2 (JES) [%]	$^{+1.21}_{-1.47}$	$^{+0.44}_{-1.06}$	$^{+1.50}_{-1.55}$	$^{+1.59}_{-0.48}$	$^{+1.21}_{-0.82}$	$^{+0.61}_{-1.12}$	$^{+0.26}_{-1.35}$	$^{+2.88}_{-1.77}$	∓3.17
Effective modelling NP set 3 (JES) [%]	$^{+0.37}_{-0.26}$	∓0.56	$^{+0.17}_{-0.42}$	$^{+0.65}_{-0.53}$	±0.68	±0.45	$^{+1.06}_{-0.18}$	$^{+0.21}_{-0.24}$	∓1.64
Effective modelling NP set 4 (JES) [%]	$^{+0.88}_{-0.74}$	$^{-}_{-0.54}$	$^{+0.46}_{-0.89}$	$^{+0.67}_{-0.15}$	±0.55	$^{-}_{-0.57}$	$^{+0.19}_{-0.51}$	$^{+0.88}_{-0.14}$	∓1.84
Effective statistical NP set 1 (JES) [%]	-	-	-	-	-	-	-	-	-
Effective statistical NP set 2 (JES) [%]	$^{-0.62}_{+0.66}$	$^{-0.39}_{-}$	$^{-0.35}_{+0.24}$	$^{-0.22}_{+0.35}$	±0.45	$^{-0.46}_{-}$	$^{-0.20}_{+0.63}$	$^{-0.19}_{+0.60}$	∓1.34
Effective statistical NP set 3 (JES) [%]	$^{-}_{+0.20}$	∓0.23	$^{+0.32}_{-0.45}$	±0.26	±0.11	-	$^{+0.31}_{-0.13}$	±0.65	∓1.61
Effective statistical NP set 4 (JES) [%]	±0.31	∓0.35	$^{+0.21}_{-0.23}$	-	∓0.11	-	$^{-0.18}_{+0.35}$	$^{+0.63}_{-}$	∓1.08
Effective statistical NP set 5 (JES) [%]	$^{-0.15}_{+0.36}$	$^{-0.40}_{-}$	$^{-0.59}_{+0.33}$	$^{-0.29}_{+0.37}$	±0.16	∓0.18	$^{-0.20}_{+0.25}$	±0.49	∓1.40
Effective statistical NP set 6 (JES) [%]	$^{+0.28}_{-}$	∓0.17	-	-	$^{+0.19}_{-}$	$^{+0.10}_{-0.31}$	$^{+0.25}_{-0.12}$	$^{+0.70}_{-}$	∓1.42
η intercalibration model (JES) [%]	$^{+1.65}_{-1.73}$	$^{+0.95}_{-1.74}$	$^{+1.31}_{-1.39}$	$^{+1.75}_{-0.55}$	$^{+1.49}_{-0.86}$	$^{+1.16}_{-2.00}$	$^{+1.53}_{-1.22}$	$^{-2.82}_{-2.13}$	∓4.00
high E η intercalibration non closure (JES) [%]	-	-	-	-	-	-	-	-	-
neg η intercalibration non closure (JES) [%]	-	-	-	-	-	-	-	±0.10	∓0.13
pos η intercalibration non closure (JES) [%]	-	-	-	-	-	-	-	-	±0.24
η intercalibration total stat (JES) [%]	$^{+0.94}_{-0.89}$	∓0.54	$^{+0.29}_{-0.52}$	$^{+0.68}_{-0.16}$	±0.71	$^{+0.30}_{-0.63}$	$^{+0.70}_{-0.31}$	$^{+0.64}_{-0.77}$	∓1.60
Flavour composition (JES) [%]	$^{+1.92}_{-1.14}$	$^{+0.18}_{-1.37}$	$^{+0.85}_{-0.68}$	$^{+1.13}_{-0.16}$	$^{+1.22}_{-0.31}$	$^{+0.72}_{-1.11}$	$^{+0.80}_{-0.89}$	$^{+1.35}_{-0.66}$	$^{+2.11}_{-1.37}$
Flavour response (JES) [%]	$^{-3.84}_{+4.13}$	$^{-3.26}_{+2.57}$	$^{-1.71}_{+3.62}$	$^{-2.22}_{+3.16}$	$^{-2.93}_{+2.91}$	$^{-3.76}_{+1.86}$	$^{-3.86}_{+3.40}$	$^{-4.42}_{+5.93}$	$^{-9.60}_{+2.16}$
Pile-up offset μ (JES) [%]	∓0.11	∓0.47	$^{-0.24}_{+0.43}$	±0.29	±0.55	∓0.37	±0.33	$^{-0.35}_{+0.27}$	$^{+0.49}_{-3.06}$
Pile-up offset N_{PV} (JES) [%]	±0.25	∓0.61	±0.49	±0.67	±0.49	$^{-}_{-0.97}$	∓0.23	$^{+0.76}_{-0.43}$	$^{+0.18}_{-2.08}$
Pile-up offset p_T (JES) [%]	$^{+0.19}_{-0.27}$	$^{+0.28}_{-0.63}$	±0.28	±0.52	$^{-0.18}_{-}$	∓0.38	$^{-0.95}_{-}$	$^{+0.71}_{-0.17}$	∓2.39
Pile-up offset ρ topology (JES) [%]	$^{+5.34}_{-4.67}$	$^{+3.18}_{-4.14}$	$^{+4.17}_{-3.24}$	$^{+3.69}_{-2.19}$	$^{+3.03}_{-2.41}$	$^{+2.61}_{-3.85}$	$^{+1.98}_{-3.53}$	$^{+3.66}_{-4.65}$	$^{+4.36}_{-8.09}$
Punch-through (JES) [%]	-	-	-	-	-	-	-	-	-
Single particle high-p_T (JES) [%]	-	-	-	-	-	-	-	-	-
b-Quark tagging efficiency (eigenvector 0) [%]	$^{-3.65}_{+3.71}$	$^{-3.32}_{+3.37}$	$^{-3.32}_{+3.36}$	$^{-3.39}_{+3.44}$	$^{-3.46}_{+3.51}$	$^{-3.85}_{+3.92}$	$^{-4.51}_{+4.59}$	$^{-6.27}_{+6.43}$	$^{-7.40}_{+7.57}$
b-Quark tagging efficiency (eigenvector 1) [%]	$^{-1.08}_{+1.99}$	∓1.10	∓0.81	∓0.55	∓0.36	∓0.26	-	±0.93	$^{+1.84}_{-1.83}$
b-Quark tagging efficiency (eigenvector 2) [%]	±1.33	$^{+1.41}_{-1.40}$	$^{+1.39}_{-1.38}$	$^{+1.37}_{-1.36}$	±1.39	$^{+1.48}_{-1.47}$	$^{+1.54}_{-1.53}$	±1.15	±0.56
b-Quark tagging efficiency (eigenvector 3) [%]	±0.67	±0.61	±0.43	-	∓0.31	∓0.57	∓0.75	∓0.91	$^{-1.08}_{+1.09}$
b-Quark tagging efficiency (eigenvector 4) [%]	-	∓0.24	∓0.33	∓0.33	∓0.25	∓0.15	-	-	±0.14
b-Quark tagging efficiency (eigenvector 5) [%]	-	-	-	-	±0.14	±0.16	±0.14	-	-
c-Quark tagging efficiency (eigenvector 0) [%]	±0.52	±0.57	±0.67	±0.69	±0.63	±0.71	$^{+0.67}_{-0.66}$	±0.49	-
c-Quark tagging efficiency (eigenvector 1) [%]	±0.10	±0.20	±0.24	±0.30	±0.30	±0.33	±0.33	±0.33	±0.39
c-Quark tagging efficiency (eigenvector 2) [%]	-	-	-	-	±0.13	±0.15	±0.13	±0.16	-
Light-jet tagging efficiency (eigenvector 0) [%]	$^{+0.60}_{-0.61}$	±0.72	$^{+0.73}_{-0.72}$	$^{+0.62}_{-0.61}$	±0.48	±0.56	$^{+0.62}_{-0.61}$	±0.57	$^{-0.32}_{+0.31}$
Light-jet tagging efficiency (eigenvector 1) [%]	-	-	-	-	-	-	-	-	-
Light-jet tagging efficiency (eigenvector 2) [%]	-	-	-	-	-	-	-	-	-
Light-jet tagging efficiency (eigenvector 3) [%]	-	-	-	-	-	-	-	-	-
Light-jet tagging efficiency (eigenvector 4) [%]	-	-	-	-	-	-	-	-	-
Light-jet tagging efficiency (eigenvector 5) [%]	-	-	-	-	-	-	-	-	-
Light-jet tagging efficiency (eigenvector 6) [%]	-	-	-	-	-	-	-	-	-
Light-jet tagging efficiency (eigenvector 7) [%]	-	-	-	-	-	-	-	-	-
Light-jet tagging efficiency (eigenvector 8) [%]	-	-	-	-	-	-	-	-	-
Light-jet tagging efficiency (eigenvector 9) [%]	-	-	-	-	-	-	-	-	-
Light-jet tagging efficiency (eigenvector 10) [%]	-	-	-	-	-	-	-	-	-
b-Quark tagging extrapolation [%]	-	-	-	∓0.11	∓0.14	∓0.17	∓0.16	∓0.14	-
b-Quark tagging extrapolation from c-Quark [%]	-	-	-	-	-	-	-	-	-
JET JER cross calibration forward [%]	-	-	-	-	-	-	-	-	-
JET JER noise forward [%]	-	-	-	-	-	-	-	-	-
JET JER NP0 [%]	-	-	-	-	-	-	-	-	-
JET JER NP1 [%]	∓0.18	$^{-1.62}_{-}$	$^{-0.18}_{-}$	$^{+0.80}_{-}$	∓0.11	-	∓0.16	-	$^{-3.96}_{+}$
JET JER NP2 [%]	∓0.54	∓0.30	$^{-1.71}$	-	$^{-0.19}_{+1.54}$	∓0.36	±0.54	$^{+1.26}_{-0.45}$	$^{+0.47}_{-3.32}$
JET JER NP3 [%]	-	$^{-1.60}_{+0.20}$	$^{+0.16}_{-0.48}$	±0.14	$^{-0.36}_{+0.25}$	∓0.97	$^{-0.72}$	±1.04	∓3.36
JET JER NP4 [%]	$^{+0.12}_{-0.28}$	$^{-}_{+0.37}$	$^{+0.18}_{-0.60}$	±0.24	∓1.14	-	±1.21	$^{+1.82}_{-1.18}$	∓1.54
JET JER NP5 [%]	-	$^{+0.61}_{-2.22}$	$^{+0.33}$	$^{-0.23}_{+0.44}$	±1.39	∓0.71	±0.68	±1.95	∓2.31
JET JER NP6 [%]	∓0.28	∓0.89	$^{+0.31}_{-0.33}$	±0.40	$^{-0.19}_{-}$	∓0.99	±1.00	$^{-0.40}_{+1.05}$	$^{+0.34}_{-0.71}$
JET JER NP7 [%]	$^{-}_{-0.54}$	$^{+0.78}_{-0.53}$	$^{+0.22}_{-0.13}$	∓0.38	±0.75	$^{-0.59}_{+0.16}$	$^{-0.88}_{+0.31}$	±1.14	$^{-}_{-1.65}$
JET JER NP8 [%]	-	-	-	-	-	-	-	-	-
QCD estimation [%]	±11.2	±6.42	±4.89	±1.58	∓0.55	±0.75	±1.18	±10.9	±38.1
K-factor normalization mass [%]	$^{+2.72}_{-2.63}$	$^{+2.68}_{-2.60}$	$^{+2.70}_{-2.61}$	$^{+2.69}_{-2.60}$	$^{+2.69}_{-2.61}$	$^{+2.68}_{-2.59}$	$^{+2.69}_{-2.61}$	$^{+2.53}_{-2.45}$	$^{+2.31}_{-2.24}$
K-factor normalization PDFAS [%]	±4.12	±4.06	±4.08	±4.07	±4.08	±4.05	±4.07	±3.83	±3.50
K-factor normalization scale [%]	$^{+2.32}_{-3.43}$	$^{+2.29}_{-3.38}$	$^{+2.30}_{-3.40}$	$^{+2.29}_{-3.39}$	$^{+2.30}_{-3.40}$	$^{+2.28}_{-3.38}$	$^{+2.29}_{-3.39}$	$^{+2.16}_{-3.19}$	$^{+1.97}_{-2.92}$
Luminosity [%]	∓2.05	∓2.05	∓2.05	∓2.05	∓2.05	∓2.05	∓2.05	∓2.05	∓2.05
MCSignal stat. [%]	±1.29	±1.57	±1.87	±1.23	±1.67	±1.75	±2.15	±2.52	±6.48
QCD stat. [%]	±1.10	±1.52	±1.89	±1.20	±1.68	±1.80	±2.00	±2.82	±6.31
ISR/FSR + scale [%]	∓1.46	±1.26	∓0.83	$^{+0.40}_{-}$	$^{-3.33}_{+0.67}$	$^{-1.99}_{+0.45}$	$^{+4.63}_{-}$	∓2.12	∓13.5
Alternate hard-scattering model [%]	∓2.58	∓0.92	±8.63	±3.14	±3.20	∓2.69	∓0.87	∓0.35	±0.89
Alternate parton-shower model [%]	±4.11	±4.46	±4.35	±0.89	±0.88	±3.17	±11.8	±0.40	±0.62
Inter PDF [%]	-	-	-	-	-	-	-	-	-
Intra PDF [%]	±0.14	±0.12	±0.24	±0.11	±0.14	-	±0.10	±0.20	±0.45

TABLE D.11: Table of systematics for the absolute differential cross-section at the particle level for the $R_{Wt}^{leading}$ observable.

Bins [GeV]	0–0.50	0.50–0.60	0.60–0.65	0.65–0.75	0.75–0.80	0.80–0.85	0.85–0.90	0.90–1.50
$d\sigma$ / $dR_{Wt}^{subleading}$ [pb/GeV]	$8.67 \cdot 10^{-1}$	$2.59 \cdot 10^{0}$	$3.06 \cdot 10^{0}$	$3.32 \cdot 10^{0}$	$3.27 \cdot 10^{0}$	$3.15 \cdot 10^{0}$	$2.71 \cdot 10^{0}$	$4.04 \cdot 10^{-1}$
Total Uncertainty [%]	$^{+16.8}_{-16.5}$	$^{+16.8}_{-14.3}$	$^{+13.1}_{-13.8}$	$^{+10.5}_{-12.3}$	$^{+12.2}_{-12.3}$	$^{+11.7}_{-11.2}$	$^{+13.2}_{-13.9}$	$^{+21.0}_{-20.7}$
Statistics [%]	±1.6	±2.1	±2.2	±1.8	±2.4	±2.6	±3.0	±2.3
Systematics [%]	$^{+16.6}_{-16.4}$	$^{+16.5}_{-14.0}$	$^{+12.7}_{-13.4}$	$^{+10.1}_{-12.0}$	±11.8	$^{+11.2}_{-10.6}$	$^{+12.5}_{-13.2}$	$^{+20.7}_{-20.4}$
Jet vertex fraction [%]	$^{+0.67}_{-0.70}$	$^{+0.44}_{-0.46}$	$^{+0.35}_{-0.37}$	$^{+0.29}_{-0.32}$	$^{+0.30}_{-0.33}$	$^{+0.30}_{-0.33}$	$^{+0.44}_{-0.46}$	$^{+0.70}_{-0.72}$
b-Tagged jet energy scale (JES) [%]	$^{+0.96}_{-0.85}$	$^{+0.80}_{-0.50}$	$^{+0.45}_{-0.88}$	$^{+0.31}_{-0.23}$	$^{+1.72}_{-0.88}$	$^{+0.45}_{-1.35}$	$^{+0.34}_{-2.34}$	$^{+1.22}_{-1.01}$
Effective detector NP set 1 (JES) [%]	$^{+1.89}_{-2.47}$	$^{+2.88}_{-0.75}$	$^{+1.51}_{-1.67}$	$^{+1.15}_{-2.03}$	$^{+1.97}_{-1.29}$	$^{+1.87}_{-1.09}$	$^{+0.70}_{-1.36}$	$^{+2.73}_{-2.45}$
Effective mixed NP set 1 (JES) [%]	$^{+0.22}_{-0.64}$	±0.77	$^{+0.15}_{-0.23}$	$^{+0.18}_{-0.42}$	$^{-0.13}_{+0.22}$	±0.39	$^{-}_{-0.69}$	$^{+0.86}_{-0.81}$
Effective mixed NP set 2 (JES) [%]	$^{-0.51}_{+0.46}$	±0.59	±0.20	∓0.23	$^{-0.57}_{-}$	$^{-0.31}_{+0.29}$	$^{-0.61}_{-}$	$^{-0.36}_{+0.72}$
Effective mixed NP set 3 (JES) [%]	-	±0.10	-	$^{-0.16}_{-}$	-	$^{-0.12}_{-}$	$^{+0.10}_{-0.34}$	-
Effective modelling NP set 1 (JES) [%]	$^{+8.77}_{-7.77}$	$^{+6.70}_{-6.14}$	$^{+5.98}_{-6.93}$	$^{+4.41}_{-5.37}$	$^{+4.39}_{-4.90}$	$^{+5.19}_{-4.73}$	$^{+5.78}_{-5.77}$	$^{+8.49}_{-7.70}$
Effective modelling NP set 2 (JES) [%]	$^{+0.64}_{-0.89}$	±1.66	$^{+1.30}_{-1.39}$	$^{+0.96}_{-1.84}$	$^{+1.55}_{-0.94}$	$^{+1.55}_{-0.84}$	$^{+0.84}_{-1.50}$	$^{+1.17}_{-1.86}$
Effective modelling NP set 3 (JES) [%]	$^{+0.21}_{-0.38}$	$^{+1.29}_{-0.14}$	$^{+0.50}_{-0.35}$	$^{+0.12}_{-0.62}$	$^{+0.14}_{-0.18}$	$^{+0.59}_{-0.25}$	$^{-0.44}_{+0.15}$	$^{+0.40}_{-0.70}$
Effective modelling NP set 4 (JES) [%]	±0.58	±0.73	$^{+0.59}_{-0.29}$	$^{+0.28}_{-0.56}$	$^{+0.28}_{-0.40}$	$^{+0.49}_{-0.56}$	∓0.70	$^{+0.93}_{-0.62}$
Effective statistical NP set 1 (JES) [%]	-	-	-	-	-	-	-	-
Effective statistical NP set 2 (JES) [%]	$^{-0.59}_{+0.42}$	$^{-0.17}_{+0.84}$	$^{-0.15}_{+0.51}$	$^{-0.31}_{+0.13}$	$^{-0.22}_{+0.20}$	$^{-0.22}_{+0.19}$	∓0.25	$^{-0.48}_{+0.62}$
Effective statistical NP set 3 (JES) [%]	-	±0.49	$^{+0.14}_{-0.16}$	±0.18	$^{+0.13}_{-}$	$^{-}_{-0.24}$	∓0.60	±0.12
Effective statistical NP set 4 (JES) [%]	$^{+0.23}_{-0.21}$	±0.24	-	$^{-0.18}_{-}$	$^{+0.26}_{-0.19}$	±0.16	$^{+0.13}_{-0.58}$	±0.16
Effective statistical NP set 5 (JES) [%]	$^{-}_{+0.21}$	$^{-0.14}_{+0.45}$	$^{-0.48}_{+0.35}$	$^{-0.48}_{+0.18}$	$^{-0.33}_{+0.14}$	∓0.33	∓0.27	±0.30
Effective statistical NP set 6 (JES) [%]	$^{+0.24}_{-}$	±0.24	$^{+0.16}_{-0.26}$	∓0.12	$^{+0.12}_{-0.20}$	$^{-}_{-}$	$^{-}_{-0.27}$	$^{+0.23}_{-0.12}$
η intercalibration model (JES) [%]	$^{+2.40}_{-1.88}$	$^{+1.88}_{-1.15}$	$^{+1.01}_{-1.02}$	$^{+0.76}_{-1.31}$	$^{+1.17}_{-1.20}$	$^{+1.17}_{-1.06}$	$^{+1.15}_{-0.67}$	$^{+1.80}_{-2.03}$
high E η intercalibration non closure (JES) [%]	-	-	-	-	-	-	-	-
neg η intercalibration non closure (JES) [%]	-	-	-	-	-	-	$^{-}_{-0.19}$	-
pos η intercalibration non closure (JES) [%]	-	-	-	-	-	-	-	-
η intercalibration total stat (JES) [%]	$^{+0.66}_{-0.80}$	$^{+1.16}_{-}$	$^{+0.58}_{-0.10}$	$^{-}_{-0.48}$	$^{+0.35}_{-0.43}$	$^{+0.34}_{-0.31}$	∓0.25	$^{+1.09}_{-0.86}$
Flavour composition (JES) [%]	$^{+1.65}_{-1.51}$	$^{+1.87}_{-0.43}$	$^{+1.07}_{-0.43}$	$^{+0.61}_{-0.81}$	$^{+0.48}_{-0.53}$	$^{+0.51}_{-0.28}$	$^{-}_{-0.28}$	$^{+1.47}_{-0.77}$
Flavour response (JES) [%]	$^{-4.13}_{+3.71}$	$^{-3.05}_{+3.95}$	$^{-3.31}_{+3.26}$	$^{-2.89}_{+2.62}$	$^{-1.69}_{+2.17}$	$^{-1.99}_{+3.00}$	$^{-2.60}_{+1.83}$	$^{-4.81}_{+5.24}$
Pile-up offset μ (JES) [%]	$^{-0.11}_{+0.32}$	±0.66	∓0.37	∓0.18	$^{+0.13}_{-0.15}$	$^{-}_{+0.11}$	∓0.71	±0.46
Pile-up offset N_{PV} (JES) [%]	$^{+0.60}_{-0.54}$	±1.31	∓0.21	∓0.29	$^{-0.11}_{+0.37}$	±0.38	∓0.25	±0.20
Pile-up offset p_T (JES) [%]	$^{+0.18}_{-0.35}$	±0.63	$^{-}_{-0.38}$	∓0.31	$^{-0.10}_{+0.46}$	∓0.34	$^{+0.32}_{-0.56}$	$^{+0.49}_{-0.62}$
Pile-up offset ρ topology (JES) [%]	$^{+4.92}_{-4.54}$	$^{+4.25}_{-3.40}$	$^{+3.52}_{-3.64}$	$^{+2.71}_{-3.10}$	$^{+3.05}_{-2.37}$	$^{+3.40}_{-2.43}$	$^{+2.40}_{-2.55}$	$^{+4.87}_{-5.12}$
Punch-through (JES) [%]	-	-	-	-	-	-	-	-
Single particle high-p_T (JES) [%]	-	-	-	-	-	-	-	-
b-Quark tagging efficiency (eigenvector 0) [%]	$^{-3.11}_{+3.15}$	$^{-3.21}_{+3.26}$	$^{-3.42}_{+3.47}$	$^{-3.55}_{+3.62}$	$^{-3.86}_{+3.93}$	$^{-4.07}_{+4.15}$	$^{-4.54}_{+4.64}$	$^{-5.83}_{+5.98}$
b-Quark tagging efficiency (eigenvector 1) [%]	$^{-1.36}_{+1.38}$	$^{-0.92}_{+0.93}$	∓0.80	$^{-0.69}_{+0.70}$	∓0.57	∓0.48	∓0.26	±0.46
b-Quark tagging efficiency (eigenvector 2) [%]	$^{+1.37}_{-1.36}$	±1.37	$^{+1.37}_{-1.36}$	$^{+1.40}_{-1.39}$	$^{+1.46}_{-1.45}$	$^{+1.47}_{-1.46}$	$^{+1.42}_{-1.41}$	$^{+1.22}_{-1.21}$
b-Quark tagging efficiency (eigenvector 3) [%]	±0.69	±0.41	$^{+0.20}_{-0.19}$	-	∓0.32	∓0.43	∓0.55	∓0.68
b-Quark tagging efficiency (eigenvector 4) [%]	∓0.22	$^{-0.29}_{+0.30}$	∓0.29	∓0.25	∓0.16	-	-	-
b-Quark tagging efficiency (eigenvector 5) [%]	-	-	-	±0.10	±0.13	±0.13	±0.10	-
c-Quark tagging efficiency (eigenvector 0) [%]	±0.47	±0.62	±0.70	±0.67	$^{+0.74}_{-0.73}$	±0.69	±0.63	±0.58
c-Quark tagging efficiency (eigenvector 1) [%]	-	±0.20	±0.28	±0.29	±0.36	±0.35	±0.34	±0.42
c-Quark tagging efficiency (eigenvector 2) [%]	-	-	-	-	±0.14	±0.16	±0.15	±0.14
Light-jet tagging efficiency (eigenvector 0) [%]	±0.61	±0.52	±0.57	±0.66	±0.65	±0.64	±0.56	$^{+0.63}_{-0.65}$
Light-jet tagging efficiency (eigenvector 1) [%]	-	-	-	-	-	-	-	-
Light-jet tagging efficiency (eigenvector 2) [%]	-	-	-	-	-	-	-	-
Light-jet tagging efficiency (eigenvector 3) [%]	-	-	-	-	-	-	-	-
Light-jet tagging efficiency (eigenvector 4) [%]	-	-	-	-	-	-	-	-
Light-jet tagging efficiency (eigenvector 5) [%]	-	-	-	-	-	-	-	-
Light-jet tagging efficiency (eigenvector 6) [%]	-	-	-	-	-	-	-	-
Light-jet tagging efficiency (eigenvector 7) [%]	-	-	-	-	-	-	-	-
Light-jet tagging efficiency (eigenvector 8) [%]	-	-	-	-	-	-	-	-
Light-jet tagging efficiency (eigenvector 9) [%]	-	-	-	-	-	-	-	-
Light-jet tagging efficiency (eigenvector 10) [%]	-	-	-	-	-	-	-	-
b-Quark tagging extrapolation [%]	-	-	-	∓0.11	∓0.13	∓0.14	∓0.13	∓0.15
b-Quark tagging extrapolation from c-Quark [%]	-	-	-	-	-	-	-	-
JET JER cross calibration forward [%]	-	-	-	-	-	-	-	-
JET JER noise forward [%]	-	-	-	-	-	-	-	-
JET JER NP0 [%]	-	-	-	-	-	-	-	-
JET JER NP1 [%]	∓0.81	$^{+1.39}_{-0.11}$	$^{-0.34}_{-}$	$^{-0.73}_{-}$	∓0.23	∓0.68	±0.23	±0.47
JET JER NP2 [%]	$^{-}_{-0.66}$	±0.84	$^{+0.17}_{-0.44}$	∓0.73	$^{-}_{-0.34}$	±0.33	$^{-0.15}_{+0.45}$	$^{-0.31}_{-}$
JET JER NP3 [%]	∓0.91	±1.02	∓0.89	$^{-1.13}_{+0.68}$	∓1.10	$^{+0.72}_{-0.52}$	∓0.32	$^{-1.01}_{+1.27}$
JET JER NP4 [%]	$^{-0.28}_{+0.35}$	±0.96	$^{+0.35}_{-0.57}$	$^{+0.22}_{-0.45}$	$^{+0.34}_{-1.00}$	$^{+0.16}_{-0.0}$	$^{-0.64}_{+0.54}$	$^{+0.19}_{-0.48}$
JET JER NP5 [%]	±0.67	$^{-0.21}_{+1.11}$	$^{-0.13}_{+0.23}$	∓1.00	$^{-}_{-0.82}$	-	∓0.77	±0.39
JET JER NP6 [%]	$^{+0.55}_{-0.13}$	$^{-0.20}_{+0.75}$	∓0.52	∓0.18	$^{-0.37}_{+0.21}$	$^{-1.00}_{+1.32}$	∓1.61	$^{+0.14}_{-0.78}$
JET JER NP7 [%]	$^{-0.15}_{+0.16}$	±1.25	$^{+0.28}_{-0.59}$	∓0.42	∓0.82	±0.50	∓0.39	$^{+0.90}_{-0.66}$
JET JER NP8 [%]	-	-	-	-	-	-	-	-
QCD estimation [%]	±8.80	±3.71	±2.74	±1.43	±1.74	±1.40	±3.06	±12.4
K-factor normalization mass [%]	$^{+2.74}_{-2.65}$	$^{+2.68}_{-2.59}$	$^{+2.69}_{-2.60}$	$^{+2.69}_{-2.61}$	$^{+2.70}_{-2.62}$	$^{+2.66}_{-2.58}$	$^{+2.63}_{-2.55}$	$^{+2.59}_{-2.51}$
K-factor normalization PDFAS [%]	±4.14	±4.05	±4.06	±4.07	±4.09	±4.03	±3.98	±3.92
K-factor normalization scale [%]	$^{+2.33}_{-3.45}$	$^{+2.28}_{-3.38}$	$^{+2.29}_{-3.38}$	$^{+2.29}_{-3.39}$	$^{+2.31}_{-3.41}$	$^{+2.27}_{-3.35}$	$^{+2.24}_{-3.32}$	$^{+2.21}_{-3.26}$
Luminosity [%]	∓2.05	∓2.05	∓2.05	∓2.05	∓2.05	∓2.05	∓2.05	∓2.05
MCSignal stat. [%]	±1.22	±1.53	±1.62	±1.30	±1.73	±1.83	±2.28	±1.79
QCD stat. [%]	±1.29	±1.44	±1.45	±1.16	±1.46	±1.62	±1.96	±1.86
ISR/FSR + scale [%]	$^{-1.74}_{-}$	$^{+6.53}_{-0.89}$	$^{+0.40}_{-}$	$^{-3.85}_{+0.62}$	$^{+0.28}_{-0.50}$	$^{-1.13}_{+0.21}$	∓3.86	$^{+0.60}_{-1.14}$
Alternate hard-scattering model [%]	∓1.81	±6.02	∓3.33	±1.37	±5.81	±3.10	∓4.84	∓2.63
Alternate parton-shower model [%]	±3.65	±4.47	±5.09	±3.09	±1.53	±0.42	∓1.28	±7.11
Inter PDF [%]	-	-	-	-	-	-	-	-
Intra PDF [%]	±0.11	±0.15	±0.14	±0.11	±0.20	±0.10	±0.14	±0.20

TABLE D.12: Table of systematics for the absolute differential cross-section at the particle level for the $R_{Wt}^{subleading}$ observable.

Bins [GeV]	0–210	210–240	240–270	270–300	300–330	330–370	370–400	400–440	440–480	480–550	550–1000
$d\sigma$ / $d p_T^{top1}$ [pb/GeV]	$1.27 \cdot 10^{-3}$	$7.52 \cdot 10^{-3}$	$7.77 \cdot 10^{-3}$	$7.52 \cdot 10^{-3}$	$7.24 \cdot 10^{-3}$	$5.64 \cdot 10^{-3}$	$4.38 \cdot 10^{-3}$	$2.89 \cdot 10^{-3}$	$1.75 \cdot 10^{-3}$	$7.28 \cdot 10^{-4}$	$4.60 \cdot 10^{-5}$
Total Uncertainty [%]	+14.9 −18.0	+16.9 −14.8	+12.5 −12.9	+13.5 −15.2	+13.2 −12.5	+11.9 −11.7	+13.1 −12.5	+13.0 −12.9	+19.9 −18.8	+15.2 −16.8	+32.0 −21.6
Statistics [%]	±2.5	±2.3	±2.1	±2.1	±2.0	±2.1	±2.6	±2.8	±3.5	±4.8	±7.4
Systematics [%]	+14.1 −17.4	+16.5 −14.3	+12.1 −12.5	+13.2 −14.9	+12.9 −12.1	+11.6 −11.3	+12.6 −12.0	±12.5	+19.3 −18.2	+13.9 −15.6	+30.6 −19.3
Jet vertex fraction [%]	+0.64 −0.66	+0.53 −0.55	+0.46 −0.49	+0.42 −0.44	+0.37 −0.39	+0.35 −0.38	+0.32 −0.35	+0.32 −0.34	+0.29 −0.32	+0.35 −0.37	+0.42 −0.44
b-Tagged jet energy scale (JES) [%]	+0.83 −1.69	+1.02 −0.76	+1.06 −0.28	+0.45 −1.15	+0.35 −0.63	+0.80 −0.96	+0.97 −0.48	+0.93 −0.68	+0.34 −0.43	+0.74 −1.33	+1.07 −0.75
Effective detector NP set 1 (JES) [%]	+1.74 −3.32	+3.21 −1.95	+1.22 −1.57	+2.01 −2.51	+1.57 −0.77	+1.14 −0.93	+1.64 −1.29	+1.76 −1.17	+2.08 −0.86	+1.07 −2.75	±2.42
Effective mixed NP set 1 (JES) [%]	- −0.79	±0.94	−0.53	+0.23 −0.31	±0.46	−0.54	+0.38 −0.22	+1.22 −1.20	+2.33 −1.73	+1.92 −3.05	+2.41 −1.24
Effective mixed NP set 2 (JES) [%]	∓0.18	±0.83	∓0.27	−0.81 +0.15	±0.42	−0.29 +0.31	−0.65 +0.18	−0.61 +0.82	−0.40 +0.33	∓0.73	±2.52
Effective mixed NP set 3 (JES) [%]	∓0.12	±0.23	-	-	−0.10 +0.11	-	∓0.11	+0.45	±0.10	∓0.29	±1.09
Effective modelling NP set 1 (JES) [%]	+8.53 −10.1	+8.58 −7.27	+5.90 −6.06	+5.69 −7.59	+5.71 −4.91	+4.51 −3.20	+4.42 −2.85	+5.41 −5.59	+6.10 −4.87	+5.93 −6.32	+2.56 −2.13
Effective modelling NP set 2 (JES) [%]	+0.70 −1.72	+1.41 −1.36	+1.08 −1.03	+1.70 −1.31	+0.34 −0.65	±0.35	+1.17 −0.97	+1.22 −1.45	+1.60 −1.80	+1.52 −1.36	+2.08 −0.59
Effective modelling NP set 3 (JES) [%]	+0.11 −1.51	+1.63 −0.29	+0.56 −0.70	−0.45	+0.98 −0.57	±0.30	−0.31 +0.62	−0.39 +0.64	−0.38 +0.43	∓1.34	±2.40
Effective modelling NP set 4 (JES) [%]	+0.70 −0.47	+0.96 −0.34	+0.29 −0.30	+0.43 −0.95	+0.48	+0.43 −0.30	+0.54 −0.84	+0.87 −0.88	+0.41 −0.38	∓0.73	+2.97 −0.26
Effective statistical NP set 1 (JES) [%]	-	-	-	-	-	-	∓0.10	±0.12	-	∓0.13	−0.31
Effective statistical NP set 2 (JES) [%]	−0.51 +0.16	−0.50 +0.95	- +0.24	−0.42 +0.51	−0.10 +0.26	−0.31 +0.28	−0.53 -	−0.22 +0.57	−0.33 +0.18	∓0.21	±1.58
Effective statistical NP set 3 (JES) [%]	-	+0.44 −0.17	+0.21 −0.12	∓0.27	+0.67 −0.42	-	- +0.32	−0.47 +0.66	±0.10	∓1.05	- +2.09
Effective statistical NP set 4 (JES) [%]	−0.16	±0.21	-	∓0.41	- +0.27	+0.39 −0.52	+0.25 −0.35	±0.24	+0.31 −0.19	∓0.22	−0.46 +0.94
Effective statistical NP set 5 (JES) [%]	−0.16 +0.23	−0.19 +0.48	−0.30 +0.17	−0.41 +0.25	−0.41 +0.33	−0.12 +0.10	−0.23 -	+0.36	±0.33	∓0.40	−0.16 +0.18
Effective statistical NP set 6 (JES) [%]	- −0.14	+0.31 −0.10	-	∓0.47	+0.33	−0.17	+0.11 −0.32	+0.45 −0.15	±0.27	∓0.26	+1.38 −0.21
η intercalibration model (JES) [%]	+2.16 −2.68	+2.57 −1.30	+1.32 −1.30	+1.28 −1.97	±0.81	+1.38 −1.22	+1.10 −0.31	+1.14 −0.54	+1.63 −0.29	+0.36 −1.53	+0.56 −0.20
high E η intercalibration non closure (JES) [%]	-	-	-	-	-	-	-	-	-	-	-
neg η intercalibration non closure (JES) [%]	-	-	-	-	-	-	-	-	-	-	-
pos η intercalibration non closure (JES) [%]	-	-	-	-	-	-	-	-	-	-	-
η intercalibration total stat (JES) [%]	+0.54 −0.60	+0.75 −0.52	+0.48 −0.17	+0.58 −0.74	+0.42	+0.49 −0.41	- −0.63	+0.81 −0.31	+0.54 −0.45	∓0.57	±2.06
Flavour composition (JES) [%]	+0.79 −1.09	+1.78 −0.87	+1.16 −0.12	+1.28 −1.40	+0.89 −0.48	+0.72 −0.18	+0.23 −0.89	+1.22 −0.86	+1.05 −0.47	∓0.57	±2.56
Flavour response (JES) [%]	−5.75 +3.44	−3.25 +5.51	−3.69 +2.90	−4.03 +2.86	−1.91 +3.07	−1.32 +2.03	−1.65 +2.67	−2.87 +2.29	−1.91 +4.63	−3.61 +2.38	∓1.69
Pile-up offset μ (JES) [%]	−0.47 +0.37	-	+0.32 -	+0.24	−0.47 +0.46	-	+0.20 −0.17	- +0.22	−0.21 +0.22	+0.20 +0.26	±1.66
Pile-up offset N_{PV} (JES) [%]	−0.63 +0.24	±1.61	+0.18 −0.58	−0.20	±0.63	∓0.31	+0.37 −0.24	+1.26 −0.43	−1.07	∓0.93	−0.31 +1.02
Pile-up offset p_T (JES) [%]	∓0.62	±0.85	∓0.23	+0.21 −0.64	+0.76 −0.32	−0.42 +0.11	±0.31	+0.47 −0.66	- −0.48	+0.67 −0.48	+0.22 −0.48
Pile-up offset ρ topology (JES) [%]	+4.17 −6.15	+5.47 −4.10	+3.45 −3.29	+3.79 −3.74	+3.73 −2.70	+2.52 −2.11	+2.60 −2.45	+2.80 −2.46	+3.51 −2.08	+2.23 −4.28	±1.34
Punch-through (JES) [%]	-	-	-	-	-	-	-	-	-	-	-
Single particle high-p_T (JES) [%]	-	-	-	-	-	-	-	-	-	-	-
b-Quark tagging efficiency (eigenvector 0) [%]	−3.00 +3.05	−3.62 +3.68	−3.83 +3.90	−3.80 +3.86	−3.74 +3.80	−3.73 +3.80	−3.84 +3.90	−3.94 +4.01	−3.95 +4.02	−4.22 +4.29	−4.72 +4.81
b-Quark tagging efficiency (eigenvector 1) [%]	∓0.18	∓0.19	∓0.34	∓0.54	−0.68 +0.69	−0.90 +0.91	−1.25 +1.26	−1.49 +1.50	−1.99 +2.00	−2.66 +2.69	−3.83 +3.89
b-Quark tagging efficiency (eigenvector 2) [%]	+1.20 −1.19	+1.29 −1.28	+1.39 −1.38	+1.43 −1.42	+1.40 −1.39	+1.42 −1.41	+1.45 −1.44	+1.43 −1.42	+1.37 −1.36	+1.30 −1.29	±0.85
b-Quark tagging efficiency (eigenvector 3) [%]	∓0.56	∓0.33	∓0.14	-	±0.20	±0.32	±0.45	±0.50	±0.62	±0.77	±0.50
b-Quark tagging efficiency (eigenvector 4) [%]	∓0.13	∓0.21	∓0.24	∓0.24	∓0.22	∓0.20	∓0.16	∓0.14	-	-	-
b-Quark tagging efficiency (eigenvector 5) [%]	±0.13	-	-	-	-	-	-	-	-	-	-
c-Quark tagging efficiency (eigenvector 0) [%]	±0.33	+0.57 −0.56	±0.60	±0.62	±0.65	±0.73	±0.70	±0.76	±0.76	±1.01	+0.79 −0.78
c-Quark tagging efficiency (eigenvector 1) [%]	-	±0.21	±0.22	±0.26	±0.28	±0.33	+0.32 −0.31	+0.36 −0.35	±0.35	±0.47	±0.39
c-Quark tagging efficiency (eigenvector 2) [%]	-	-	-	-	-	±0.10	±0.11	±0.14	±0.13	±0.18	±0.19
Light-jet tagging efficiency (eigenvector 0) [%]	+0.47 −0.46	±0.40	±0.48	±0.50	+0.68 −0.67	+0.68 −0.67	±0.73	+0.83 −0.84	+0.94 −0.93	+0.93 −0.92	+1.02 −1.01
Light-jet tagging efficiency (eigenvector 1) [%]	-	-	-	-	-	-	-	-	-	-	±0.26
Light-jet tagging efficiency (eigenvector 2) [%]	-	-	-	-	-	-	-	-	-	-	-
Light-jet tagging efficiency (eigenvector 3) [%]	-	-	-	-	-	-	-	-	-	-	-
Light-jet tagging efficiency (eigenvector 4) [%]	-	-	-	-	-	-	-	-	-	-	-
Light-jet tagging efficiency (eigenvector 5) [%]	-	-	-	-	-	-	-	-	-	-	-
Light-jet tagging efficiency (eigenvector 6) [%]	-	-	-	-	-	-	-	-	-	-	-
Light-jet tagging efficiency (eigenvector 7) [%]	-	-	-	-	-	-	-	-	-	-	-
Light-jet tagging efficiency (eigenvector 8) [%]	-	-	-	-	-	-	-	-	-	-	-
Light-jet tagging efficiency (eigenvector 9) [%]	-	-	-	-	-	-	-	-	-	-	-
Light-jet tagging efficiency (eigenvector 10) [%]	-	-	-	-	-	-	-	-	-	-	-
b-Quark tagging extrapolation [%]	-	-	-	-	-	∓0.13	∓0.14	∓0.19	∓0.21	∓0.28	∓0.40
b-Quark tagging extrapolation from c-Quark [%]	-	-	-	-	-	-	-	-	-	-	-
JET JER cross calibration forward [%]	-	-	-	-	-	-	-	-	-	-	-
JET JER noise forward [%]	-	-	-	-	-	-	-	-	-	-	-
JET JER NP0 [%]	-	-	-	-	-	-	-	-	-	-	-
JET JER NP1 [%]	−2.20 -	+1.37 −0.11	+0.28 -	∓2.19	±0.19	+1.01 -	±0.68	∓0.19 -	−0.44	+2.96 −0.16	∓0.45
JET JER NP2 [%]	∓2.04	±1.14	∓0.94	∓1.31	±0.52	±0.36	±0.32	±1.00	−0.88 +0.86	±1.55	∓2.15
JET JER NP3 [%]	∓1.25	±1.59	−1.12 +0.10	∓1.71	±0.48	-	−0.16	±1.21	−1.49 +0.50	±3.16	∓4.65
JET JER NP4 [%]	+0.10 −1.96	±1.28	∓0.78	−1.85 +0.10	±0.72	±0.89	+0.34 −0.74	∓0.86	+0.45 −0.69	±3.29	+1.24 −0.83
JET JER NP5 [%]	∓0.93	±1.05	±0.43	+0.11 −1.04	−0.10 +0.20	+0.32	±0.30	−0.34 +0.40	+0.38 −0.17	+2.50	+1.47 −2.04
JET JER NP6 [%]	∓1.69	±0.81	∓0.48	∓1.37	±0.61	±0.34	±0.89	−0.60 -	∓0.35	+1.89 -	−0.31 +1.78
JET JER NP7 [%]	−1.10 -	±0.72	+0.15 -	∓1.49	±0.43	−0.24 +0.66	+0.90 -	∓0.34	+0.30 −0.67	±3.59	+1.08 −2.64
JET JER NP8 [%]	-	-	-	-	-	-	-	-	-	-	-
QCD estimation [%]	∓2.90	±5.68	±4.62	±4.39	±3.76	±2.57	±1.41	±1.70	±0.97	±0.31	∓0.38
K-factor normalization mass [%]	+2.14 −2.07	+2.50 −2.42	+2.67 −2.58	+2.73 −2.65	+2.74 −2.65	+2.76 −2.67	+2.79 −2.70	+2.82 −2.73	+2.83 −2.74	+2.83 −2.74	+2.85 −2.76
K-factor normalization PDFAS [%]	±3.24	±3.78	±4.04	±4.14	±4.14	±4.17	±4.23	±4.26	±4.28	±4.29	±4.32
K-factor normalization scale [%]	+1.82 −2.69	+2.13 −3.15	+2.27 −3.36	+2.33 −3.44	+2.33 −3.45	+2.35 −3.47	+2.38 −3.52	+2.40 −3.55	+2.41 −3.56	+2.42 −3.57	+2.43 −3.59
Luminosity [%]	∓2.05	∓2.05	∓2.05	∓2.05	∓2.05	∓2.05	∓2.05	∓2.05	∓2.05	∓2.05	∓2.05
MCSignal stat. [%]	±1.43	±1.70	±1.52	±1.50	±1.51	±1.51	±1.92	±1.99	±2.65	±3.60	±5.96
QCD stat. [%]	±3.81	±2.30	±1.58	±1.27	±1.10	±0.89	±0.91	±0.81	±0.87	±0.98	±1.05
ISR/FSR + scale [%]	+0.83 −0.71	−1.93 +0.37	−0.37 +0.10	∓2.63	±3.85	−2.46 +0.41	∓3.95	+2.18 −0.41	∓4.16	−5.01 +1.13	+23.6 −1.41
Alternate hard-scattering model [%]	∓2.22	±1.79	±2.18	∓3.47	±0.97	±4.20	±3.54	∓5.47	±14.2	∓3.30	±12.3
Alternate parton-shower model [%]	±5.34	±3.81	±2.03	±1.61	±4.43	±4.19	±5.37	±0.75	∓1.56	-	±6.11
Inter PDF [%]	-	-	-	-	-	±0.11	-	∓0.11	-	±0.20	-
Intra PDF [%]	±0.22	±0.12	±0.12	-	-	±0.16	±0.13	±0.16	±0.19	±0.23	±0.47

TABLE D.13: Table of systematics for the absolute differential cross-section at the particle level for the p_T^{top1} observable.

Bins [Unit y^{top1}]	0–0.30	0.30–0.60	0.60–0.90	0.90–1.20	1.20–1.50	1.50–2	2–2.50
$d\sigma$ / dy^{top1} [pb/ Unit y^{top1}]	$1.39 \cdot 10^{0}$	$1.29 \cdot 10^{0}$	$1.12 \cdot 10^{0}$	$9.74 \cdot 10^{-1}$	$6.97 \cdot 10^{-1}$	$4.14 \cdot 10^{-1}$	$6.56 \cdot 10^{-2}$
Total Uncertainty [%]	±12.3	+12.7 −13.4	+14.2 −13.7	+15.6 −16.0	+15.1 −13.8	+15.3 −15.1	+22.2 −23.1
Statistics [%]	±1.5	±1.6	±1.8	±2.0	±2.4	±2.3	±6.9
Systematics [%]	±12.1	+12.5 −13.2	+14.0 −13.5	+15.3 −15.7	+14.7 −13.4	+14.9 −14.6	+19.4 −20.4
Jet vertex fraction [%]	+0.44 −0.47	+0.45 −0.47	+0.52 −0.53	+0.44 −0.47	+0.42 −0.45	+0.43 −0.46	+0.35 −0.39
b-Tagged jet energy scale (JES) [%]	+0.57 −0.89	+0.45 −0.80	+1.01 −0.78	+1.07 −0.92	+1.11 −0.80	+0.71 −0.90	+0.92 −1.27
Effective detector NP set 1 (JES) [%]	+1.69 −1.46	+1.11 −1.90	+2.34 −1.69	+2.31 −2.24	+2.18 −1.31	+2.11 −1.90	+0.86 −2.49
Effective mixed NP set 1 (JES) [%]	+0.46 −0.17	∓0.23	±0.37	+0.66 −0.58	+0.18 −0.34	+0.60 −0.36	+1.07 −1.94
Effective mixed NP set 2 (JES) [%]	−0.34 +0.36	∓0.18	−0.20 +0.35	−0.40 +0.44	−0.31 +0.28	−0.18 +0.29	−0.32 +0.81
Effective mixed NP set 3 (JES) [%]	-	-	-	-	-	−0.15 -	±0.37
Effective modelling NP set 1 (JES) [%]	+6.30 −6.36	+6.10 −6.56	+6.71 −6.16	+6.00 −6.23	+7.28 −5.79	+6.87 −6.83	+2.31 −3.18
Effective modelling NP set 2 (JES) [%]	+0.99 −0.92	+0.64 −1.29	+1.16 −0.95	+1.38 −1.49	+2.01 −1.19	+1.26 −0.88	+0.81 −2.05
Effective modelling NP set 3 (JES) [%]	+0.38 −0.34	+0.25 −0.40	+0.69 −0.64	+0.37 −0.22	-	+0.46 −0.26	∓1.28
Effective modelling NP set 4 (JES) [%]	+0.50 −0.40	+0.21 −0.38	+0.68 −0.25	+0.62 −0.94	+0.42 −0.30	+0.63 −0.45	+0.67 −0.74
Effective statistical NP set 1 (JES) [%]	-	-	-	-	-	-	-
Effective statistical NP set 2 (JES) [%]	−0.32 +0.33	−0.34 +0.27	−0.35 +0.42	−0.37 +0.57	-	−0.55 +0.49	−0.28 +0.54
Effective statistical NP set 3 (JES) [%]	-	- −0.16	-	±0.20	∓0.19	-	−0.28 +0.60
Effective statistical NP set 4 (JES) [%]	+0.12 −0.14	-	-	±0.14	-	- −0.28	+0.96 −0.12
Effective statistical NP set 5 (JES) [%]	−0.30 +0.12	−0.15 +0.21	−0.21 +0.27	−0.23 +0.41	−0.31 -	−0.25 +0.29	−0.39 +1.01
Effective statistical NP set 6 (JES) [%]	+0.13 −0.15	-	+0.15 -	+0.31 -	-	- −0.12	+0.84 −0.18
η intercalibration model (JES) [%]	+1.01 −0.76	+0.63 −0.93	+1.39 −1.32	+2.11 −2.35	+2.41 −1.25	+2.85 −2.23	+1.48 −4.32
high E η intercalibration non closure (JES) [%]	-	-	-	-	-	-	-
neg η intercalibration non closure (JES) [%]	-	-	-	-	-	-	+0.29 −0.18
pos η intercalibration non closure (JES) [%]	-	-	-	-	-	-	+0.34 −0.12
η intercalibration total stat (JES) [%]	+0.49 −0.44	+0.35 −0.37	+0.61 −0.54	+0.74 −0.59	+0.32 −0.14	+0.76 −0.66	+0.81 −0.74
Flavour composition (JES) [%]	+0.86 −0.69	+1.04 −0.79	+1.12 −0.67	+0.95 −1.08	+1.37 −0.43	+1.59 −1.00	+0.44 −0.27
Flavour response (JES) [%]	−2.65 +3.25	−2.92 +2.40	−3.19 +3.45	−3.73 +3.55	−3.44 +3.73	−4.18 +4.31	−1.19 +3.61
Pile-up offset μ (JES) [%]	±0.19	-	−0.14 +0.38	∓0.17	-	−0.23 +0.26	−2.08 +0.84
Pile-up offset N_{PV} (JES) [%]	+0.55 −0.26	-	±0.23	+0.41 −0.13	+0.51 −0.42	±0.32	±0.91
Pile-up offset p_T (JES) [%]	+0.31 −0.33	-	- +0.26	+0.20 −0.37	-	+0.25 −0.14	∓0.97
Pile-up offset ρ topology (JES) [%]	+3.50 −3.38	+3.43 −3.46	+4.07 −3.64	+3.72 −4.11	+4.43 −3.17	+4.26 −3.62	+1.59 −1.41
Punch-through (JES) [%]	-	-	-	-	-	-	-
Single particle high-p_T (JES) [%]	-	-	-	-	-	-	-
b-Quark tagging efficiency (eigenvector 0) [%]	−3.78 +3.84	−3.80 +3.87	−3.81 +3.88	−3.80 +3.86	−3.73 +3.80	−3.66 +3.72	−3.66 +3.72
b-Quark tagging efficiency (eigenvector 1) [%]	∓0.71	∓0.74	−0.70 +0.71	∓0.69	∓0.68	∓0.68	∓0.61
b-Quark tagging efficiency (eigenvector 2) [%]	+1.38 −1.37	+1.39 −1.38	+1.39 −1.38	+1.37 −1.36	±1.38	+1.38 −1.37	+1.34 −1.33
b-Quark tagging efficiency (eigenvector 3) [%]	-	-	-	-	-	-	-
b-Quark tagging efficiency (eigenvector 4) [%]	∓0.19	∓0.19	∓0.19	∓0.19	∓0.19	∓0.20	∓0.18
b-Quark tagging efficiency (eigenvector 5) [%]	-	-	-	-	-	-	-
c-Quark tagging efficiency (eigenvector 0) [%]	±0.64	+0.62 −0.61	±0.63	±0.59	±0.62	±0.59	±0.53
c-Quark tagging efficiency (eigenvector 1) [%]	±0.27	±0.24	±0.27	±0.25	±0.24	±0.24	±0.21
c-Quark tagging efficiency (eigenvector 2) [%]	-	-	-	-	-	-	±0.10
Light-jet tagging efficiency (eigenvector 0) [%]	+0.66 −0.65	+0.64 −0.65	+0.61 −0.60	±0.52	±0.56	+0.63 −0.62	±0.69
Light-jet tagging efficiency (eigenvector 1) [%]	-	-	-	-	-	-	-
Light-jet tagging efficiency (eigenvector 2) [%]	-	-	-	-	-	-	-
Light-jet tagging efficiency (eigenvector 3) [%]	-	-	-	-	-	-	-
Light-jet tagging efficiency (eigenvector 4) [%]	-	-	-	-	-	-	-
Light-jet tagging efficiency (eigenvector 5) [%]	-	-	-	-	-	-	-
Light-jet tagging efficiency (eigenvector 6) [%]	-	-	-	-	-	-	-
Light-jet tagging efficiency (eigenvector 7) [%]	-	-	-	-	-	-	-
Light-jet tagging efficiency (eigenvector 8) [%]	-	-	-	-	-	-	-
Light-jet tagging efficiency (eigenvector 9) [%]	-	-	-	-	-	-	-
Light-jet tagging efficiency (eigenvector 10) [%]	-	-	-	-	-	-	-
b-Quark tagging extrapolation [%]	∓0.11	-	∓0.10	-	∓0.10	-	∓0.11
b-Quark tagging extrapolation from c-Quark [%]	-	-	-	-	-	-	-
JET JER cross calibration forward [%]	-	-	-	-	-	-	-
JET JER noise forward [%]	-	-	-	-	-	-	-
JET JER NP0 [%]	-	-	-	-	-	-	-
JET JER NP1 [%]	-	∓0.95	±0.20	∓0.46	±0.29	+0.35 −0.18	∓1.06
JET JER NP2 [%]	- −0.50	∓0.79	±0.29	±0.47	±0.15	−0.19 +0.60	+0.86 −1.97
JET JER NP3 [%]	+0.14 −0.10	∓0.39	−0.20 +0.77	∓1.38	∓0.26	∓0.31	±0.65
JET JER NP4 [%]	- −0.13	∓0.74	+0.83 −0.21	±0.28	∓0.21	±0.34	−2.38 +2.14
JET JER NP5 [%]	-	±0.24	±0.41	∓0.44	- +0.53	+0.34 −0.64	−3.30 +1.48
JET JER NP6 [%]	±0.17	∓0.42	±0.84	∓0.58	±0.19	∓0.65	∓1.81
JET JER NP7 [%]	−0.22 +0.32	- −0.88	±0.79	∓0.32	+0.52 −0.10	+0.32 −0.37	+1.97 −1.59
JET JER NP8 [%]	-	-	-	-	-	-	-
QCD estimation [%]	±4.16	±4.60	±4.91	±5.71	±5.25	±4.11	±4.55
K-factor normalization mass [%]	+2.69 −2.60	+2.70 −2.62	+2.69 −2.60	+2.69 −2.61	+2.67 −2.59	+2.64 −2.56	+2.66 −2.57
K-factor normalization PDFAS [%]	±4.07	±4.09	±4.06	±4.08	±4.04	±4.00	±4.02
K-factor normalization scale [%]	+2.29 −3.39	+2.30 −3.40	+2.29 −3.38	+2.30 −3.39	+2.28 −3.37	+2.25 −3.33	+2.27 −3.35
Luminosity [%]	∓2.05	∓2.05	∓2.05	∓2.05	∓2.05	∓2.05	∓2.05
MCSignal stat. [%]	±1.13	±1.21	±1.28	±1.45	±1.69	±1.73	±5.40
QCD stat. [%]	±1.01	±1.09	±1.16	±1.38	±1.70	±1.86	±6.29
ISR/FSR + scale [%]	±0.73	+0.35	∓4.08	±0.15	±2.04	∓1.54	∓11.6
Alternate hard-scattering model [%]	±2.39	∓1.78	∓0.43	±7.65	±2.55	∓6.17	∓10.4
Alternate parton-shower model [%]	±1.62	±4.33	±3.83	±3.18	±4.83	±3.39	∓3.43
Inter PDF [%]	-	-	-	-	±0.17	±0.15	-
Intra PDF [%]	±0.22	±0.16	-	±0.12	±0.16	±0.22	±0.35

TABLE D.14: Table of systematics for the absolute differential cross-section at the particle level for the y_{top1} observable.

Bins [GeV]	0–100	100–150	150–190	190–230	230–270	270–315	315–365	365–420	420–475	475–1000
$d\sigma$ / $d p_T^{top2}$ [pb/GeV]	$5.69 \cdot 10^{-4}$	$4.76 \cdot 10^{-3}$	$8.00 \cdot 10^{-3}$	$8.08 \cdot 10^{-3}$	$6.28 \cdot 10^{-3}$	$4.69 \cdot 10^{-3}$	$2.95 \cdot 10^{-3}$	$1.57 \cdot 10^{-3}$	$5.27 \cdot 10^{-4}$	$2.50 \cdot 10^{-5}$
Total Uncertainty [%]	+38.5 −38.2	+18.2 −21.3	+15.6 −13.9	+14.0 −13.7	+11.3 −11.9	+12.2 −11.5	+9.94 −9.88	+14.2 −13.8	+20.1 −19.6	+41.5 −41.3
Statistics [%]	±6.6	±2.8	±2.1	±1.9	±2.1	±2.2	±2.6	±3.5	±6.0	±9.7
Systematics [%]	+36.4 −36.1	+17.5 −20.7	+15.3 −13.5	+13.7 −13.5	+11.0 −11.6	+11.8 −11.2	+9.37 −9.31	+13.5 −13.0	+18.7 −18.1	+39.6 −39.4
Jet vertex fraction [%]	+0.57 −0.59	+0.60 −0.63	+0.57 −0.60	+0.44 −0.46	+0.34 −0.36	+0.24 −0.27	+0.18 −0.21	+0.19 −0.21	-	+0.16 −0.18
b-Tagged jet energy scale (JES) [%]	∓1.16	+1.16 −0.76	+0.42 −0.68	+1.24 −0.89	+0.65 −1.09	+1.15 −0.78	+0.33 −0.22	+0.11 −1.52	+1.04 −0.59	+1.32 −1.22
Effective detector NP set 1 (JES) [%]	+3.68 −2.37	+0.81 −3.39	+2.23 −1.75	+2.53 −1.91	+1.30 −1.51	+1.98 −1.06	+0.54 −0.52	+1.67 −1.49	+2.45 −2.00	+4.13 −2.28
Effective mixed NP set 1 (JES) [%]	+0.93 −1.19	+0.34 −0.74	±0.57	+0.17 −0.20	∓0.28	±0.36	∓0.44	+1.25 −1.21	+1.95 −1.88	+6.31 −5.80
Effective mixed NP set 2 (JES) [%]	−1.03 +1.01	-	±0.43	−0.29 +0.25	∓0.62	−0.16 +0.60	- +0.15	−1.41 +0.22	−0.64 +1.72	+0.77
Effective mixed NP set 3 (JES) [%]	+0.64	∓0.10	±0.12	-	-	-	-	−0.19	−0.23	±0.41
Effective modelling NP set 1 (JES) [%]	+6.51 −6.82	+7.71 −10.6	+8.30 −6.80	+6.82 −6.57	+4.87 −4.98	+5.11 −3.69	+2.79 −2.59	+4.73 −3.26	+3.69 −3.72	+6.89 −8.35
Effective modelling NP set 2 (JES) [%]	+0.44 −1.50	∓1.82	+1.40 −0.25	+1.72 −1.37	+0.99 −1.32	+1.63 −0.96	+0.37 −0.41	+1.74 −1.87	+2.38 −2.35	+3.18 −3.39
Effective modelling NP set 3 (JES) [%]	+1.64 −0.43	+0.68 −1.23	+0.86 −0.62	+0.20 −0.26	∓0.42	±0.55	±0.37	−1.51 +0.20	±0.73	−1.04 +3.03
Effective modelling NP set 4 (JES) [%]	+1.16 −0.76	+0.38 −0.55	+0.72 -	+0.56 −0.63	+0.17 −0.61	+0.72 −0.22	-	∓1.51	+2.04 −0.65	+0.68 -
Effective statistical NP set 1 (JES) [%]	-	-	-	-	-	-	-	-	-	-
Effective statistical NP set 2 (JES) [%]	−0.98 +1.26	−0.60 +0.44	−0.27 +0.46	−0.27 +0.24	−0.24 +0.28	−0.23 +0.38	- +0.19	−0.10 +0.20	−0.20 +0.51	±0.54
Effective statistical NP set 3 (JES) [%]	±0.45	±0.33	+0.29 -	- −0.20	∓0.19	±0.21	+0.44 −0.13	∓1.22	−0.46 +1.07	−0.47 +0.96
Effective statistical NP set 4 (JES) [%]	+0.23 −0.17	−0.13 +0.29	- +0.35	+0.27 −0.24	∓0.27	+0.44 −0.21	-	∓0.71	+0.37 -	±0.43
Effective statistical NP set 5 (JES) [%]	−0.27 +0.63	-	- +0.28	−0.55 +0.36	−0.41 +0.38	−0.31 +0.23	-	-	+0.43 -	±0.29
Effective statistical NP set 6 (JES) [%]	+0.57 -	-	±0.22	-	- −0.34	±0.31	-	+0.20 −0.47	+0.53 −0.29	+0.27 -
η intercalibration model (JES) [%]	+3.06 −0.21	+2.17 −3.16	+1.93 −1.13	+1.76 −1.88	+0.67 −1.12	+1.30 −0.70	+0.37 −0.18	+0.99 −0.38	+2.30 −2.12	+0.94 −1.57
high E η intercalibration non closure (JES) [%]	-	-	-	-	-	-	-	-	-	-
neg η intercalibration non closure (JES) [%]	±0.21	-	-	-	-	-	-	-	-	-
pos η intercalibration non closure (JES) [%]	-	±0.12	-	-	-	-	-	-	-	-
η intercalibration total stat (JES) [%]	+1.42 −1.54	+0.57 −0.74	+0.67 −0.40	+0.42 −0.43	+0.32 −0.43	+0.68 -	-	+0.52 −0.62	+0.93 −0.96	±0.82
Flavour composition (JES) [%]	+2.18 −0.47	+0.99 −1.21	+1.08 −0.91	+1.35 −0.83	+0.67 −0.53	+0.96 −0.29	-	+0.60 −0.17	+1.64 −0.73	±0.43
Flavour response (JES) [%]	−5.27 +5.50	−5.61 +2.89	−3.30 +4.66	−3.58 +3.54	−2.64 +2.51	−1.85 +2.78	−0.76 +0.59	−1.61 +3.17	−2.62 +1.97	−6.63 +3.95
Pile-up offset μ (JES) [%]	±0.58	−1.15 +0.44	±0.48	−0.23 +0.30	−0.26	±0.60	-	∓0.53	±1.32	±0.24
Pile-up offset N_{PV} (JES) [%]	−0.69 +4.02	−0.83 +0.48	+1.54 −0.65	+0.56 −0.39	+0.20 -	-	∓0.30	-	±0.98	−1.59 -
Pile-up offset p_T (JES) [%]	−1.42 +1.88	−0.51 +0.14	±0.53	+0.21 −0.80	+0.14 −0.21	+0.20 −0.26	±0.37	∓0.64	+0.81 −0.41	±3.11
Pile-up offset ρ topology (JES) [%]	+3.72 −3.23	+3.81 −6.27	+4.73 −3.38	+4.68 −4.28	+2.54 −2.63	+3.39 −2.19	+1.00 −1.25	+2.95 −1.93	+2.51 −2.98	+2.02 −3.74
Punch-through (JES) [%]	-	-	-	-	-	-	-	+0.17 −0.16	-	+0.36
Single particle high-p_T (JES) [%]	-	-	-	-	-	-	-	-	-	-
b-Quark tagging efficiency (eigenvector 0) [%]	−1.75 +1.76	−2.68 +2.72	−3.85 +3.92	−3.92 +3.99	−3.86 +3.93	−3.77 +3.84	−3.77 +3.84	−3.86 +3.93	−3.96 +4.03	−4.64 +4.74
b-Quark tagging efficiency (eigenvector 1) [%]	∓0.54	∓0.28	∓0.29	∓0.47	−0.75 +0.76	−1.06 +1.07	−1.45 +1.46	−1.99 +2.01	−2.58 +2.61	−3.52 +4.62
b-Quark tagging efficiency (eigenvector 2) [%]	+1.19 −1.18	±1.13	+1.31 −1.30	+1.39 −1.38	+1.44 −1.43	+1.45 −1.44	+1.46 −1.45	+1.44 −1.43	+1.31 −1.30	+0.93 −0.92
b-Quark tagging efficiency (eigenvector 3) [%]	∓0.52	∓0.40	∓0.21	-	±0.19	±0.42	±0.55	±0.70	+0.80 −0.79	±0.94
b-Quark tagging efficiency (eigenvector 4) [%]	-	∓0.14	∓0.20	∓0.23	∓0.24	∓0.21	∓0.15	∓0.11	-	-
b-Quark tagging efficiency (eigenvector 5) [%]	±0.16	±0.12	-	-	-	-	-	-	-	-
c-Quark tagging efficiency (eigenvector 0) [%]	±0.30	+0.42 −0.41	+0.52 −0.51	±0.63	±0.71	±0.74	±0.77	±0.89	±0.86	±0.90
c-Quark tagging efficiency (eigenvector 1) [%]	-	-	+0.18 −0.17	±0.25	±0.32	±0.35	+0.38 −0.37	±0.46	±0.42	±0.45
c-Quark tagging efficiency (eigenvector 2) [%]	-	-	-	-	-	±0.10	±0.13	±0.17	±0.17	±0.18
Light-jet tagging efficiency (eigenvector 0) [%]	+0.52 −0.51	+0.50 −0.49	±0.65	±0.50	+0.59 −0.58	±0.71	+0.79 −0.78	+0.67 −0.66	+0.93 −0.92	±0.83
Light-jet tagging efficiency (eigenvector 1) [%]	-	-	-	-	-	-	-	-	-	-
Light-jet tagging efficiency (eigenvector 2) [%]	±0.14	-	-	-	-	-	-	-	-	-
Light-jet tagging efficiency (eigenvector 3) [%]	-	-	-	-	-	-	-	-	-	-
Light-jet tagging efficiency (eigenvector 4) [%]	-	-	-	-	-	-	-	-	-	-
Light-jet tagging efficiency (eigenvector 5) [%]	-	-	-	-	-	-	-	-	-	-
Light-jet tagging efficiency (eigenvector 6) [%]	-	-	-	-	-	-	-	-	-	-
Light-jet tagging efficiency (eigenvector 7) [%]	-	-	-	-	-	-	-	-	-	-
Light-jet tagging efficiency (eigenvector 8) [%]	-	-	-	-	-	-	-	-	-	-
Light-jet tagging efficiency (eigenvector 9) [%]	-	-	-	-	-	-	-	-	-	-
Light-jet tagging efficiency (eigenvector 10) [%]	-	-	-	-	-	-	-	-	-	-
b-Quark tagging extrapolation [%]	-	-	-	-	-	∓0.12	∓0.17	∓0.21	∓0.21	∓0.32
b-Quark tagging extrapolation from c-Quark [%]	-	-	-	-	-	-	-	-	-	-
JET JER cross calibration forward [%]	-	-	-	-	-	-	-	-	-	-
JET JER noise forward [%]	-	-	-	-	-	-	-	-	-	-
JET JER NP0 [%]	-	-	-	-	-	-	-	-	-	-
JET JER NP1 [%]	−3.97 -	±0.52	+0.47 -	∓0.79	∓1.02	±0.51	+1.88 −0.14	−0.85 +0.34	+1.64 −0.52	+3.87 −0.74
JET JER NP2 [%]	∓3.61	−0.40 +1.32	- −0.93	-	- −1.42	−0.31 +0.77	±2.52	∓0.33	−2.29 +3.61	±0.88
JET JER NP3 [%]	∓2.05	±0.99	+0.10 −0.12	−0.88 +0.10	∓1.11	−0.43 +0.53	±1.06	±0.36	−0.53 +0.48	∓2.20
JET JER NP4 [%]	∓4.49	±0.63	- −0.21	+0.76 −0.27	∓1.15	+0.62 -	±1.56	∓0.41	±0.99	−0.13 +3.12
JET JER NP5 [%]	−1.35 +0.17	±0.68	+0.30 −0.80	±0.57	∓1.11	±0.55	- +1.61	∓0.22	−0.44 +1.37	−0.24 +0.48
JET JER NP6 [%]	∓0.52	−0.45 +0.89	∓0.56	−0.18 -	∓0.88	±1.01	±0.94	∓0.53	−0.14 +0.81	±2.36
JET JER NP7 [%]	+2.19	−0.24 +0.15	∓0.23	+0.47 −0.44	∓0.60	±0.70	±1.38	∓0.61	±0.98	−1.55 +4.34
JET JER NP8 [%]	-	-	-	-	-	-	-	-	-	-
QCD estimation [%]	∓32.5	∓11.7	±3.23	±4.90	±2.57	±1.53	±0.25	∓0.71	∓1.12	∓2.40
K-factor normalization mass [%]	+1.84 −1.78	+2.06 −2.00	+2.56 −2.48	+2.71 −2.63	+2.78 −2.69	+2.79 −2.70	+2.80 −2.71	+2.79 −2.70	+2.79 −2.70	+2.80 −2.71
K-factor normalization PDFAS [%]	±2.78	±3.12	±3.87	±4.10	±4.20	±4.22	±4.24	±4.22	±4.22	±4.24
K-factor normalization scale [%]	+1.56 −2.31	+1.76 −2.60	+2.18 −3.22	+2.31 −3.42	+2.37 −3.50	+2.38 −3.52	+2.39 −3.53	+2.38 −3.52	+2.38 −3.52	+2.39 −3.53
Luminosity [%]	∓2.05	∓2.05	∓2.05	∓2.05	∓2.05	∓2.05	∓2.05	∓2.05	∓2.05	∓2.05
MCSignal stat. [%]	±2.70	±1.41	±1.41	±1.40	±1.50	±1.66	±1.97	±2.70	±4.38	±7.59
QCD stat. [%]	±10.3	±4.18	±1.93	±1.14	±0.81	±0.58	±0.47	±0.44	±0.48	±0.47
ISR/FSR + scale [%]	+1.04 −1.89	±1.33	+1.77 −0.51	±2.42	∓3.40	−3.55 +0.41	±0.50	∓4.38	+2.25 -	±7.39
Alternate hard-scattering model [%]	∓2.85	∓1.85	±2.20	±0.54	±1.10	±2.58	±0.12	∓6.72	±10.9	±30.6
Alternate parton-shower model [%]	±7.06	±5.55	±6.02	±2.47	±0.53	±3.83	±1.03	∓1.06	±8.83	∓15.9
Inter PDF [%]	-	-	-	-	-	-	-	-	-	±0.20
Intra PDF [%]	±0.19	±0.21	±0.16	±0.10	±0.13	±0.13	±0.16	±0.12	±0.14	±0.34

TABLE D.15: Table of systematics for the absolute differential cross-section at the particle level for the p_T^{top2} observable.

Bins [Unit y^{top2}]	0–0.30	0.30–0.60	0.60–0.90	0.90–1.20	1.20–1.50	1.50–2.50
$d\sigma$ / dy^{top2} [pb/ Unit y^{top2}]	$1.30 \cdot 10^{0}$	$1.25 \cdot 10^{0}$	$1.15 \cdot 10^{0}$	$9.64 \cdot 10^{-1}$	$7.87 \cdot 10^{-1}$	$2.42 \cdot 10^{-1}$
Total Uncertainty [%]	$^{+12.8}_{-13.1}$	$^{+13.4}_{-12.8}$	$^{+13.3}_{-13.2}$	$^{+16.6}_{-17.5}$	$^{+14.9}_{-14.6}$	$^{+12.9}_{-13.1}$
Statistics [%]	±1.7	±1.8	±1.9	±2.1	±2.2	±2.2
Systematics [%]	$^{+12.6}_{-12.9}$	$^{+13.2}_{-12.6}$	±13.0	$^{+16.4}_{-17.3}$	$^{+14.5}_{-14.2}$	$^{+12.5}_{-12.7}$
Jet vertex fraction [%]	$^{+0.44}_{-0.46}$	$^{+0.45}_{-0.47}$	$^{+0.47}_{-0.50}$	$^{+0.49}_{-0.51}$	$^{+0.44}_{-0.46}$	$^{+0.44}_{-0.46}$
b-Tagged jet energy scale (JES) [%]	$^{+0.82}_{-0.60}$	$^{+0.98}_{-0.94}$	$^{+0.31}_{-0.70}$	$^{+1.25}_{-1.12}$	$^{+0.64}_{-1.01}$	$^{+0.61}_{-0.85}$
Effective detector NP set 1 (JES) [%]	$^{+1.76}_{-1.58}$	$^{+2.28}_{-1.51}$	±1.41	$^{+1.59}_{-2.01}$	$^{+2.47}_{-2.18}$	$^{+1.80}_{-2.34}$
Effective mixed NP set 1 (JES) [%]	±0.24	$^{+0.42}_{-0.38}$	$^{+0.26}_{-0.34}$	±0.17	$^{+0.65}_{-0.61}$	$^{+0.19}_{-0.37}$
Effective mixed NP set 2 (JES) [%]	±0.31	$^{-0.54}_{+0.51}$	$^{-0.15}_{-}$	$^{-0.14}_{+0.15}$	$^{-0.29}_{+0.35}$	$^{-0.66}_{+0.21}$
Effective mixed NP set 3 (JES) [%]	-	±0.15	∓0.12	-	-	∓0.10
Effective modelling NP set 1 (JES) [%]	$^{+5.74}_{-6.07}$	$^{+6.14}_{-5.74}$	$^{+5.94}_{-6.33}$	$^{+6.98}_{-7.85}$	$^{+8.47}_{-6.28}$	$^{+6.06}_{-5.58}$
Effective modelling NP set 2 (JES) [%]	$^{+1.11}_{-0.67}$	$^{+1.62}_{-1.04}$	$^{+0.62}_{-0.96}$	$^{+0.92}_{-1.51}$	$^{+1.63}_{-1.68}$	$^{+0.99}_{-1.29}$
Effective modelling NP set 3 (JES) [%]	$^{+0.52}_{-0.38}$	$^{+0.32}_{-0.11}$	$^{+0.17}_{-0.54}$	$^{+0.53}_{-0.47}$	$^{+0.39}_{-0.23}$	$^{+0.29}_{-0.40}$
Effective modelling NP set 4 (JES) [%]	$^{+0.53}_{-0.24}$	$^{+0.54}_{-0.60}$	$^{+0.34}_{-0.50}$	$^{+0.38}_{-0.25}$	$^{+0.84}_{-0.45}$	$^{+0.39}_{-0.71}$
Effective statistical NP set 1 (JES) [%]	-	-	-	-	-	-
Effective statistical NP set 2 (JES) [%]	$^{-0.30}_{+0.41}$	$^{-0.31}_{+0.59}$	$^{-0.32}_{+0.13}$	$^{-0.24}_{+0.34}$	$^{-0.19}_{+0.33}$	$^{-0.69}_{+0.33}$
Effective statistical NP set 3 (JES) [%]	$^{+0.17}_{-0.12}$	-	$^{-}_{-0.21}$	±0.24	-	-
Effective statistical NP set 4 (JES) [%]	±0.23	$^{+0.16}_{-0.26}$	$^{-0.22}_{-}$	$^{+0.30}_{-}$	-	$^{+0.14}_{-0.24}$
Effective statistical NP set 5 (JES) [%]	$^{-0.19}_{+0.25}$	$^{-0.39}_{+0.35}$	$^{-0.28}_{-}$	$^{-0.14}_{+0.32}$	±0.16	$^{-0.34}_{+0.20}$
Effective statistical NP set 6 (JES) [%]	-	$^{+0.42}_{-0.12}$	∓0.26	±0.10	±0.14	$^{+0.13}_{-0.28}$
η intercalibration model (JES) [%]	$^{+1.13}_{-1.10}$	$^{+1.77}_{-1.45}$	$^{+1.17}_{-1.13}$	$^{+1.40}_{-1.29}$	$^{+1.92}_{-2.45}$	$^{+2.03}_{-1.23}$
high E η intercalibration non closure (JES) [%]	-	-	-	-	-	-
neg η intercalibration non closure (JES) [%]	-	-	-	-	-	-
pos η intercalibration non closure (JES) [%]	-	-	-	-	-	-
η intercalibration total stat (JES) [%]	$^{+0.63}_{-0.26}$	$^{+0.70}_{-0.63}$	$^{+0.18}_{-0.28}$	$^{+0.37}_{-0.44}$	$^{+0.79}_{-0.47}$	$^{+0.56}_{-0.81}$
Flavour composition (JES) [%]	$^{+0.93}_{-0.68}$	$^{+0.91}_{-0.81}$	$^{+1.44}_{-0.57}$	$^{+0.92}_{-0.30}$	$^{+1.26}_{-1.36}$	$^{+1.16}_{-1.14}$
Flavour response (JES) [%]	$^{-2.64}_{+2.60}$	$^{-3.01}_{+3.72}$	$^{-2.80}_{+3.58}$	$^{-3.77}_{+2.56}$	$^{-4.10}_{+4.46}$	$^{-3.56}_{+3.28}$
Pile-up offset μ (JES) [%]	±0.22	$^{-}_{+0.33}$	∓0.27	$^{-}_{+0.31}$	$^{-}_{+0.31}$	$^{-0.42}_{-}$
Pile-up offset N_{PV} (JES) [%]	±0.20	±0.41	-	∓0.21	±0.77	±0.54
Pile-up offset p_T (JES) [%]	±0.19	$^{+0.25}_{-}$	∓0.36	$^{+0.14}_{-}$	$^{+0.34}_{-0.33}$	$^{+0.14}_{-0.22}$
Pile-up offset ρ topology (JES) [%]	$^{+3.17}_{-3.26}$	$^{+3.90}_{-3.32}$	$^{+4.05}_{-3.15}$	$^{+4.09}_{-4.26}$	$^{+4.50}_{-4.35}$	$^{+3.14}_{-3.29}$
Punch-through (JES) [%]	-	-	-	-	-	-
Single particle high-p_T (JES) [%]	-	-	-	-	-	-
b-Quark tagging efficiency (eigenvector 0) [%]	$^{-3.74}_{+3.80}$	$^{-3.81}_{+3.87}$	$^{-3.86}_{+3.93}$	$^{-3.83}_{+3.89}$	$^{-3.65}_{+3.71}$	$^{-3.71}_{+3.77}$
b-Quark tagging efficiency (eigenvector 1) [%]	∓0.73	$^{-0.71}_{+0.72}$	∓0.67	∓0.68	$^{-0.75}_{+0.76}$	∓0.69
b-Quark tagging efficiency (eigenvector 2) [%]	±1.37	$^{+1.38}_{-1.37}$	$^{+1.40}_{-1.39}$	$^{+1.38}_{-1.37}$	±1.38	$^{+1.37}_{-1.36}$
b-Quark tagging efficiency (eigenvector 3) [%]	-	-	-	-	-	-
b-Quark tagging efficiency (eigenvector 4) [%]	∓0.19	∓0.19	∓0.19	∓0.19	∓0.19	∓0.20
b-Quark tagging efficiency (eigenvector 5) [%]	-	-	-	-	-	-
c-Quark tagging efficiency (eigenvector 0) [%]	±0.61	±0.64	±0.63	±0.60	±0.60	±0.59
c-Quark tagging efficiency (eigenvector 1) [%]	±0.24	±0.29	±0.27	±0.25	±0.24	±0.21
c-Quark tagging efficiency (eigenvector 2) [%]	-	-	-	-	-	-
Light-jet tagging efficiency (eigenvector 0) [%]	$^{+0.63}_{-0.62}$	±0.65	$^{+0.65}_{-0.64}$	±0.60	±0.44	$^{+0.64}_{-0.66}$
Light-jet tagging efficiency (eigenvector 1) [%]	-	-	-	-	-	-
Light-jet tagging efficiency (eigenvector 2) [%]	-	-	-	-	-	-
Light-jet tagging efficiency (eigenvector 3) [%]	-	-	-	-	-	-
Light-jet tagging efficiency (eigenvector 4) [%]	-	-	-	-	-	-
Light-jet tagging efficiency (eigenvector 5) [%]	-	-	-	-	-	-
Light-jet tagging efficiency (eigenvector 6) [%]	-	-	-	-	-	-
Light-jet tagging efficiency (eigenvector 7) [%]	-	-	-	-	-	-
Light-jet tagging efficiency (eigenvector 8) [%]	-	-	-	-	-	-
Light-jet tagging efficiency (eigenvector 9) [%]	-	-	-	-	-	-
Light-jet tagging efficiency (eigenvector 10) [%]	-	-	-	-	-	-
b-Quark tagging extrapolation [%]	-	∓0.11	∓0.10	-	-	-
b-Quark tagging extrapolation from c-Quark [%]	-	-	-	-	-	-
JET JER cross calibration forward [%]	-	-	-	-	-	-
JET JER noise forward [%]	-	-	-	-	-	-
JET JER NP0 [%]	-	-	-	-	-	-
JET JER NP1 [%]	∓0.65	∓0.11	±0.73	∓0.22	∓1.19	±0.29
JET JER NP2 [%]	∓0.66	±1.31	∓1.55	∓0.50	$^{-0.73}_{-}$	±1.17
JET JER NP3 [%]	∓0.25	$^{-0.46}_{+0.57}$	$^{+0.20}_{-0.48}$	$^{-1.04}_{+0.36}$	$^{-}_{-1.33}$ $^{+0.42}$	$^{+0.18}_{-0.55}$
JET JER NP4 [%]	$^{+0.27}_{-1.08}$	±1.09	∓1.31	$^{-}_{-0.30}$	±0.58	±1.01
JET JER NP5 [%]	$^{-0.30}_{+0.18}$	±0.30	$^{+0.55}_{-0.11}$	$^{+0.40}_{-0.22}$	$^{+0.19}_{-0.69}$	∓0.51
JET JER NP6 [%]	∓0.39	$^{-0.17}_{+0.53}$	$^{+0.15}_{-0.62}$	$^{+0.16}_{-0.97}$	$^{-0.39}_{+0.30}$	$^{-0.18}_{+0.81}$
JET JER NP7 [%]	-	±0.15	-	$^{+0.56}_{-0.91}$	-	$^{-0.38}_{+0.12}$
JET JER NP8 [%]	-	-	-	-	-	-
QCD estimation [%]	±3.50	±5.06	±5.44	±6.71	±4.25	±3.32
K-factor normalization mass [%]	$^{+2.68}_{-2.60}$	$^{+2.68}_{-2.60}$	$^{+2.70}_{-2.62}$	$^{+2.69}_{-2.61}$	$^{+2.69}_{-2.60}$	$^{+2.65}_{-2.57}$
K-factor normalization PDFAS [%]	±4.06	±4.06	±4.09	±4.07	±4.07	±4.01
K-factor normalization scale [%]	$^{+2.28}_{-3.38}$	$^{+2.29}_{-3.38}$	$^{+2.30}_{-3.40}$	$^{+2.29}_{-3.39}$	$^{+2.29}_{-3.39}$	$^{+2.26}_{-3.34}$
Luminosity [%]	∓2.05	∓2.05	∓2.05	∓2.05	∓2.05	∓2.05
MCSignal stat. [%]	±1.20	±1.28	±1.37	±1.52	±1.70	±1.63
QCD stat. [%]	±1.10	±1.19	±1.27	±1.41	±1.65	±1.70
ISR/FSR + scale [%]	±0.86	∓0.76	-	$^{+1.02}_{-0.62}$	$^{-4.36}_{+0.44}$	∓2.06
Alternate hard-scattering model [%]	±0.89	±0.81	∓1.03	±7.51	∓0.43	∓4.11
Alternate parton-shower model [%]	±5.84	±3.26	±3.25	±5.73	∓3.28	±1.66
Inter PDF [%]	-	-	-	-	-	±0.20
Intra PDF [%]	±0.14	±0.18	±0.16	-	±0.11	±0.20

TABLE D.16: Table of systematics for the absolute differential cross-section at the particle level for the y_{top2} observable.

Bins [GeV]	0–450	450–525	525–600	600–675	675–750	750–825	825–900	900–1000	1000–1100	1100–1200	1200–1400	1400–3200
$d\sigma$ / $dm^{t\bar{t}}$ [pb/GeV]	$1.60 \cdot 10^{-4}$	$2.54 \cdot 10^{-3}$	$3.33 \cdot 10^{-3}$	$3.60 \cdot 10^{-3}$	$3.08 \cdot 10^{-3}$	$2.58 \cdot 10^{-3}$	$1.99 \cdot 10^{-3}$	$1.32 \cdot 10^{-3}$	$7.50 \cdot 10^{-4}$	$4.58 \cdot 10^{-4}$	$2.27 \cdot 10^{-4}$	$1.48 \cdot 10^{-5}$
Total Uncertainty [%]	+32.6 −34.4	+18.1 −17.4	+15.7 −14.3	+11.9 −11.6	+11.6 −13.2	+13.4 −11.7	+13.2 −13.6	+14.6 −12.7	+15.9 −16.5	+18.2 −18.4	+15.0 −15.4	+15.5 −20.2
Statistics [%]	±5.7	±2.7	±2.3	±2.1	±2.2	±2.3	±2.7	±2.9	±3.8	±5.0	±5.2	±7.1
Systematics [%]	+30.9 −32.9	+17.1 −16.4	+15.1 −13.7	+11.5 −11.1	+11.2 −12.8	+13.0 −11.3	+12.7 −13.1	+14.1 −12.2	+14.2 −15.8	+17.0 −17.2	+13.3 −13.8	+12.7 −18.1
Jet vertex fraction [%]	+0.62 −0.63	+0.69 −0.70	+0.47 −0.50	+0.39 −0.42	+0.41 −0.43	+0.35 −0.38	+0.28 −0.31	+0.31 −0.33	+0.25 −0.28	+0.28 −0.31	+0.28 −0.30	+0.23 −0.26
b-Tagged jet energy scale (JES) [%]	∓0.13	±0.50	+0.37 −0.49	+1.13 −0.91	+0.71 −0.96	+0.69 −0.65	+1.21 −1.38	+1.00 −0.98	∓0.68	+1.35 −1.51	∓0.45	+1.97 −1.69
Effective detector NP set 1 (JES) [%]	+0.31 −2.59	+1.75 −1.50	+2.47 −2.19	+2.18 −1.60	±1.41	+1.25 −0.94	+2.49 −2.24	+2.72 −1.20	+0.23 −2.02	+2.59 −2.61	+1.04 −0.76	+0.77 −2.55
Effective mixed NP set 1 (JES) [%]	- −0.42	±0.87	+0.37 −0.27	±0.33	∓0.34	±0.44	+0.98 −0.48	+0.72 −1.59	+0.27 −1.08	+1.37 −0.32	+1.54 −0.95	+0.59 −3.76
Effective mixed NP set 2 (JES) [%]	+0.69 −0.39	−0.15 +0.69	+0.42	+0.13	−0.36	±0.14	−0.50 +0.57	−0.81 +0.96	∓0.59	±0.72	−0.57 +0.12	−1.84 +0.93
Effective mixed NP set 3 (JES) [%]	∓0.40	-	±0.21	-	-	±0.10	−0.15 -	+0.52 −0.16	-	−0.27 -	−0.23 -	+0.26 -
Effective modelling NP set 1 (JES) [%]	+3.98 −8.05	+8.00 −7.20	+8.65 −7.43	+5.90 −5.51	+4.48 −6.68	+6.25 −3.19	+6.01 −5.67	+5.44 −4.73	+3.53 −5.18	+6.01 −5.04	+5.51 −5.85	+2.77 −8.23
Effective modelling NP set 2 (JES) [%]	∓1.16	+0.65 −1.07	+1.64 −1.57	+1.96 −0.88	+0.35 −0.89	+1.23 −0.25	+1.75 −1.66	+1.58 −1.48	+0.76 −1.77	+2.45 −2.64	+1.78 −0.10	+0.47 −3.58
Effective modelling NP set 3 (JES) [%]	∓1.85	+1.46 −0.50	+0.77 −0.77	+0.59	+0.42 −0.45	+0.16 −0.31	±0.45	−0.55 +0.32	-	±0.56	−0.53	−0.53 +0.62
Effective modelling NP set 4 (JES) [%]	±0.45	+0.71 −0.11	+0.82 −0.37	+0.35 −0.41	+0.24 −0.38	+0.38 −0.19	+0.55 −0.87	+1.30 −0.95	∓0.36	+0.34 −0.68	±0.28	+0.35 −1.90
Effective statistical NP set 1 (JES) [%]	-	-	-	-	-	-	-	-	-	−0.20	±0.25	-
Effective statistical NP set 2 (JES) [%]	−1.50 +0.15	−0.61 +0.35	−0.18 +0.95	−0.15 +0.44	+0.16	−0.32 +0.46	−0.30	−0.72 +0.69	+0.19	∓0.32	∓0.28	−0.56 +0.61
Effective statistical NP set 3 (JES) [%]	∓0.22	±0.49	±0.34	+0.33 −0.29	−0.22	-	−0.16 +0.19	−0.53 +0.59	±0.25	−0.43 +0.36	∓0.36	−0.49 +0.71
Effective statistical NP set 4 (JES) [%]	∓0.63	±0.34	+0.25 -	−0.11 +0.15	+0.37 −0.21	+0.18 −0.23	∓0.18 −0.23	+0.55 −0.19	-	+0.19 −0.47	−0.36 +0.11	∓1.22
Effective statistical NP set 5 (JES) [%]	∓0.16	∓0.10	−0.47 +0.87	−0.23 +0.12	−0.19 +0.27	-	−0.23 +0.12	−0.31 +0.53	∓0.20	±0.23	−0.17 +0.34	∓0.23
Effective statistical NP set 6 (JES) [%]	∓0.48	-	±0.44	-	+0.16 −0.13	-	∓0.16	+0.82 −0.59	+0.17	-	−0.40 +0.10	+0.54 −0.79
η intercalibration model (JES) [%]	+1.59 −2.27	+2.09 −1.67	+2.27 −1.71	+1.44 −0.76	+1.11 −1.02	+0.35 −0.65	+1.41 −2.05	+2.69 −1.25	∓1.25	+3.10 −1.13	+0.89 −1.36	+1.08 −3.00
high E η intercalibration non closure (JES) [%]	-	-	-	-	-	-	-	-	-	-	-	-
neg η intercalibration non closure (JES) [%]	+0.14 −0.10	-	-	-	-	-	-	-	∓0.12	-	-	-
pos η intercalibration non closure (JES) [%]	±0.20	∓0.15	-	-	-	-	-	-	-	-	-	±0.15
η intercalibration total stat (JES) [%]	∓1.79	+0.61 −0.23	+1.29 −0.16	+0.49 −0.21	+0.31 −0.58	+0.66 −0.22	+0.22 −0.55	+1.30 −0.80	∓0.14	∓0.43	+0.20 −0.11	+0.35 −1.12
Flavour composition (JES) [%]	∓1.30	+1.77 −0.36	+2.07 −0.95	+0.91 −0.28	+0.48 −0.42	+0.93 −0.29	+0.62 −1.32	+1.75 −0.74	∓0.41	+0.25 −0.71	+0.50 −0.90	+0.36 −0.41
Flavour response (JES) [%]	−6.97	−5.72	−3.51	−2.45	−2.66	−1.45	−3.78	−2.55	−2.18	−3.29	−3.03	−5.60
Pile-up offset μ (JES) [%]	∓0.96	+3.60 -	+3.78 ±0.67	+3.17 +0.29	+2.17 -0.16	+2.95 ±0.54	+4.00 −0.26	+3.22 -	+0.76 −0.64	+2.20 −0.93	+2.90 +0.45	+1.60 −0.51
Pile-up offset N_{PV} (JES) [%]	−2.26	+0.99	±0.97	±0.69	−0.45	∓0.12	+0.88	−0.42 +0.16	∓0.23	+0.87 −0.95	−0.61 ∓0.97	+0.26 ∓1.28
Pile-up offset p_T (JES) [%]	+1.83 −1.39	−0.31 −0.21	+0.51	+0.28	−0.92 +0.17	−0.22	−0.28 +0.50	-	+0.34	+1.87	+0.49	∓2.16
Pile-up offset ρ topology (JES) [%]	+1.05 +3.87	+0.81 +4.78	−0.16 +4.67	−0.15 +3.40	−0.63 +2.51	+3.34	−0.74 +3.69	+0.24 +3.98	−0.64 +1.30	−1.00 +3.14	+0.54 +1.90	+2.35
Punch-through (JES) [%]	−5.87 -	−3.55 -	−3.42 -	−3.65 -	−3.29 -	−1.73 -	−3.93 -	−2.21 -	−3.39 -	−3.03 -	−2.90 ±0.15	−5.18 -
Single particle high-p_T (JES) [%]	-	-	-	-	-	-	-	-	-	-	-	-
b-Quark tagging efficiency (eigenvector 0) [%]	−1.81 ∓1.83	−2.77 +2.80	−3.47 +3.53	−3.44 +3.50	−3.74 +3.80	−3.80 +3.86	−3.84 +3.91	−3.85 +3.92	−3.87 +3.94	−3.89 +3.96	−3.82 +3.88	−3.98 +4.05
b-Quark tagging efficiency (eigenvector 1) [%]	∓0.24	∓0.25	∓0.36	∓0.52	∓0.72	∓0.97	−1.14 +1.15	∓1.31	−1.44 +1.45	−1.53 +1.54	−1.50 +1.51	−1.75 +1.77
b-Quark tagging efficiency (eigenvector 2) [%]	±0.94	+1.14 −1.13	+1.29 −1.28	+1.31 −1.30	+1.39 −1.38	+1.43 −1.42	±1.42	+1.41 −1.40	+1.38 −1.37	+1.37 −1.36	+1.32 −1.31	±1.34
b-Quark tagging efficiency (eigenvector 3) [%]	∓0.47	∓0.37	∓0.20	-	±0.12	±0.27	±0.36	±0.41	±0.44	+0.46 −0.45	±0.41	±0.51
b-Quark tagging efficiency (eigenvector 4) [%]	-	∓0.16	∓0.20	∓0.21	∓0.22	∓0.20	±0.18	∓0.16	∓0.15	±0.13	±0.14	∓0.15
b-Quark tagging efficiency (eigenvector 5) [%]	±0.11	±0.11	-	-	-	-	-	-	-	-	-	-
c-Quark tagging efficiency (eigenvector 0) [%]	±0.23	±0.36	+0.49 −0.59	+0.61 −0.69	±0.68	±0.75	±0.76	±0.72	±0.72	+0.77 −0.76	±0.79	+0.76 −0.75
c-Quark tagging efficiency (eigenvector 1) [%]	-	-	±0.12	±0.25	±0.28	±0.34	±0.35	±0.33	±0.34	±0.34	±0.38	+0.38 −0.37
c-Quark tagging efficiency (eigenvector 2) [%]	-	-	-	-	-	-	±0.11	±0.11	±0.11	±0.12	±0.11	±0.14
Light-jet tagging efficiency (eigenvector 0) [%]	±0.28	+0.11 −0.12	+0.64 −0.63	±0.52	±0.72	±0.65	±0.64	±0.80	±0.47	±0.65	+0.82 −0.86	+0.92 −0.91
Light-jet tagging efficiency (eigenvector 1) [%]	-	-	-	-	-	-	-	-	-	-	-	-
Light-jet tagging efficiency (eigenvector 2) [%]	-	-	-	-	-	-	-	-	-	-	-	-
Light-jet tagging efficiency (eigenvector 3) [%]	-	-	-	-	-	-	-	-	-	-	-	-
Light-jet tagging efficiency (eigenvector 4) [%]	-	-	-	-	-	-	-	-	-	-	-	-
Light-jet tagging efficiency (eigenvector 5) [%]	-	-	-	-	-	-	-	-	-	-	-	-
Light-jet tagging efficiency (eigenvector 6) [%]	-	-	-	-	-	-	-	-	-	-	-	-
Light-jet tagging efficiency (eigenvector 7) [%]	-	-	-	-	-	-	-	-	-	-	-	-
Light-jet tagging efficiency (eigenvector 8) [%]	-	-	-	-	-	-	-	-	-	-	-	-
Light-jet tagging efficiency (eigenvector 9) [%]	-	-	-	-	-	-	-	-	-	-	-	-
Light-jet tagging efficiency (eigenvector 10) [%]	-	-	-	-	-	-	-	-	-	-	-	-
b-Quark tagging extrapolation [%]	-	-	-	-	-	∓0.11	∓0.15	∓0.14	∓0.16	∓0.20	∓0.15	∓0.27
b-Quark tagging extrapolation from c-Quark [%]	-	-	-	-	-	-	-	-	-	-	-	-
JET JER cross calibration forward [%]	-	-	-	-	-	-	-	-	-	-	-	-
JET JER noise forward [%]	-	-	-	-	-	-	-	-	-	-	-	-
JET JER NP0 [%]	-	-	-	-	-	-	-	-	-	-	-	-
JET JER NP1 [%]	−4.26	-	+0.66	∓1.18	−0.82	+0.55 −0.21	−0.22 +0.12	+2.23	−0.64 +0.36	+0.31 −0.52	±1.39	∓1.93
JET JER NP2 [%]	∓3.86	+0.35 −0.99	±1.35	∓1.46	∓0.51	±0.59	−0.12 +0.56	−0.59 +3.81	+0.30 −1.15	+0.89 −2.78	−1.47 +2.13	−1.70 +0.61
JET JER NP3 [%]	∓3.02	+0.53 −0.25	±1.12	∓1.33	∓1.32	−0.31 +0.19	−0.21 +0.18	±1.83	∓0.19	∓2.13	∓0.40	−1.58 +0.12
JET JER NP4 [%]	∓4.35	+0.75 −2.04	±1.23	∓0.62	∓1.52	±0.52	−0.28 +0.32	±2.67	∓0.17	+0.28 −3.16	+1.05	∓0.53
JET JER NP5 [%]	−0.48 +1.08	+0.78 −0.27	−0.16	+0.15 −2.07	-	±0.51	−0.44 +0.40	±1.34	∓1.31	−0.82 +1.12	±1.80	∓1.09
JET JER NP6 [%]	∓2.80	−0.58 +1.50	∓0.31	∓0.56	∓0.62	−0.36 +0.74	±0.38	±2.52	∓0.44	−1.08 +1.64	−1.56	−0.48 +0.60
JET JER NP7 [%]	−0.21 +1.02	∓0.50	−0.21 +0.98	∓0.98	∓0.19	+0.45 −0.64	±0.34	±1.20	−1.17 +1.18	∓1.07	+0.84 −0.43	∓1.35
JET JER NP8 [%]	-	-	-	-	-	-	-	-	-	-	-	-
QCD estimation [%]	∓23.4	∓9.46	∓4.08	±0.58	±2.45	±3.06	±2.69	±3.24	±2.79	±3.72	±3.84	±5.58
K-factor normalization mass [%]	+1.58 −1.53	+2.18 −2.11	+2.43 −2.35	+2.51 −2.43	+2.66 −2.58	+2.71 −2.63	+2.73 −2.65	+2.74 −2.66	+2.77 −2.68	+2.74 −2.65	+2.72 −2.64	+2.73 −2.65
K-factor normalization PDFAS [%]	±2.39	±3.31	±3.67	±3.80	±4.03	±4.10	±4.14	±4.15	±4.19	±4.15	±4.12	±4.14
K-factor normalization scale [%]	+1.34 −1.99	+1.86 −2.75	+2.07 −3.06	+2.14 −3.16	+2.27 −3.35	+2.31 −3.42	+2.33 −3.44	+2.34 −3.46	+2.36 −3.49	+2.34 −3.45	+2.32 −3.43	+2.33 −3.44
Luminosity [%]	∓2.05	∓2.05	∓2.05	∓2.05	∓2.05	∓2.05	∓2.05	∓2.05	∓2.05	∓2.05	∓2.05	∓2.05
MCSignal stat. [%]	±2.69	±1.75	±1.42	±1.37	±1.48	±1.65	±1.92	±2.08	±2.64	±3.58	±3.96	±5.01
QCD stat. [%]	±8.08	±4.83	±3.27	±2.20	±1.56	±1.26	±1.22	±1.14	±1.33	±1.76	±1.76	±1.95
ISR/FSR + scale [%]	+1.53 −1.41	±3.47	−0.51 +0.59	+2.09 -	∓0.87	±0.49	−2.87 +0.52	∓1.90	−2.12 +0.64	±5.76	∓2.00	∓4.61
Alternate hard-scattering model [%]	∓15.6	±4.12	±2.77	-	±0.54	±5.46	±3.89	∓2.51	∓6.05	±6.99	∓0.23	-
Alternate parton-shower model [%]	±3.28	±4.61	±4.20	±2.53	±5.20	±3.33	±1.22	∓0.47	±8.90	±6.86	∓6.34	∓3.40
Inter PDF [%]	-	-	-	-	-	-	-	-	-	-	-	∓0.17
Intra PDF [%]	±0.17	±0.18	±0.11	±0.12	±0.10	±0.10	±0.13	-	±0.18	±0.18	±0.12	±0.24

TABLE D.17: Table of systematics for the absolute differential cross-section at the particle level for the $m_{t\bar{t}}$ observable.

Bins [GeV]	0–40	40–85	85–130	130–180	180–240	240–300	300–370	370–450	450–1100
$d\sigma$ / dp_T^{tt} [pb/GeV]	$7.11 \cdot 10^{-3}$	$9.33 \cdot 10^{-3}$	$8.38 \cdot 10^{-3}$	$6.08 \cdot 10^{-3}$	$3.75 \cdot 10^{-3}$	$1.90 \cdot 10^{-3}$	$9.61 \cdot 10^{-4}$	$4.44 \cdot 10^{-4}$	$3.60 \cdot 10^{-5}$
Total Uncertainty [%]	$^{+11.8}_{-11.7}$	$^{+14.2}_{-12.7}$	$^{+15.1}_{-15.5}$	$^{+14.0}_{-14.6}$	$^{+15.5}_{-14.9}$	$^{+16.2}_{-18.8}$	$^{+19.0}_{-18.7}$	$^{+24.6}_{-25.1}$	$^{+17.9}_{-18.5}$
Statistics [%]	±1.8	±1.5	±1.7	±2.0	±2.4	±3.6	±4.9	±6.8	±6.9
Systematics [%]	±11.5	$^{+14.1}_{-12.5}$	$^{+14.9}_{-15.3}$	$^{+13.6}_{-14.3}$	$^{+15.0}_{-14.4}$	$^{+15.2}_{-18.0}$	$^{+17.7}_{-17.4}$	$^{+22.7}_{-23.3}$	$^{+15.7}_{-16.3}$
Jet vertex fraction [%]	$^{+0.19}_{-0.21}$	$^{+0.40}_{-0.43}$	$^{+0.50}_{-0.53}$	$^{+0.53}_{-0.56}$	$^{+0.56}_{-0.59}$	$^{+0.61}_{-0.65}$	$^{+0.58}_{-0.61}$	$^{+0.57}_{-0.59}$	$^{+0.46}_{-0.50}$
b-Tagged jet energy scale (JES) [%]	$^{+1.11}_{-1.05}$	$^{+1.00}_{-0.59}$	$^{+0.63}_{-1.17}$	$^{+0.62}_{-1.05}$	$^{+0.49}_{-0.51}$	∓1.49	±1.14	±1.80	±0.63
Effective detector NP set 1 (JES) [%]	$^{+2.19}_{-1.65}$	$^{+2.12}_{-1.77}$	$^{+1.44}_{-1.85}$	$^{+1.88}_{-2.48}$	$^{+2.44}_{-1.72}$	$^{+0.47}_{-1.51}$	±1.71	$^{+0.81}_{-0.44}$	$^{+1.77}_{-1.31}$
Effective mixed NP set 1 (JES) [%]	±0.36	$^{+0.16}_{-0.14}$	∓0.38	$^{+0.65}_{-0.74}$	±0.86	$^{+0.35}_{-0.91}$	±1.35	∓0.81	$^{+1.71}_{-2.22}$
Effective mixed NP set 2 (JES) [%]	$^{-0.26}_{+0.15}$	$^{-0.24}_{+0.44}$	∓0.26	$^{-0.38}_{+0.13}$	$^{-0.39}_{+0.45}$	$^{-0.16}_{+0.93}$	±0.45	±0.21	$^{-0.10}_{+0.11}$
Effective mixed NP set 3 (JES) [%]	-	-	-	-	-	-	±0.12	$^{+0.55}_{-0.16}$	∓0.61
Effective modelling NP set 1 (JES) [%]	$^{+4.86}_{-4.93}$	$^{+7.61}_{-5.47}$	$^{+6.92}_{-7.20}$	$^{+6.38}_{-7.10}$	$^{+7.99}_{-7.62}$	$^{+2.93}_{-7.33}$	$^{+4.25}_{-4.35}$	$^{+7.26}_{-5.24}$	$^{+4.26}_{-5.22}$
Effective modelling NP set 2 (JES) [%]	$^{+1.95}_{-1.51}$	$^{+1.43}_{-1.39}$	$^{+0.83}_{-1.06}$	$^{+1.25}_{-1.83}$	$^{+0.64}_{-0.14}$	∓0.77	±2.19	∓1.48	$^{+1.86}_{-1.18}$
Effective modelling NP set 3 (JES) [%]	$^{+0.56}_{-0.34}$	$^{+0.21}_{-0.37}$	$^{+0.62}_{-0.93}$	±0.17	$^{+0.68}_{-0.53}$	±0.39	$^{-0.36}_{+0.38}$	$^{-0.36}_{+0.33}$	±0.38
Effective modelling NP set 4 (JES) [%]	$^{+0.49}_{-0.52}$	$^{+0.78}_{-0.44}$	$^{-}_{-0.39}$	$^{+0.40}_{-0.72}$	$^{+0.81}_{-0.24}$	$^{+0.42}_{-0.29}$	$^{+0.70}_{-0.21}$	±0.39	$^{+0.27}_{-0.98}$
Effective statistical NP set 1 (JES) [%]	-	-	-	-	-	-	∓0.10	±0.10	$^{+0.11}_{-0.18}$
Effective statistical NP set 2 (JES) [%]	$^{-0.20}_{+0.34}$	$^{-0.17}_{+0.43}$	$^{-0.52}_{+0.30}$	$^{-0.41}_{+0.21}$	$^{-0.47}_{+0.60}$	$^{-0.34}_{+0.56}$	∓0.31	±0.73	∓0.74
Effective statistical NP set 3 (JES) [%]	$^{-}_{-0.21}$	$^{+0.13}_{-}$	$^{+0.11}_{-0.22}$	$^{-0.21}_{+0.15}$	$^{+0.46}_{-}$	±0.19	±0.69	$^{-0.38}_{+0.12}$	$^{+0.10}_{-0.24}$
Effective statistical NP set 4 (JES) [%]	$^{+0.19}_{-0.17}$	$^{+0.23}_{-0.17}$	-	$^{-}_{-0.28}$	±0.24	$^{+0.30}_{-0.29}$	-	±0.54	$^{-0.93}_{+0.73}$
Effective statistical NP set 5 (JES) [%]	∓0.47	$^{-0.16}_{+0.23}$	$^{-0.25}$	$^{-0.33}_{+0.16}$	$^{-}_{+0.34}$	$^{-0.36}_{+0.13}$	±0.41	$^{-}_{+0.38}$	∓0.44
Effective statistical NP set 6 (JES) [%]	$^{+0.15}_{-0.13}$	-	∓0.22	$^{+0.15}_{-0.27}$	±0.13	±0.42	$^{+0.25}_{-0.23}$	±0.50	∓0.28
η intercalibration model (JES) [%]	$^{+1.40}_{-0.94}$	$^{+1.73}_{-1.43}$	$^{+1.03}_{-1.78}$	$^{+1.67}_{-1.05}$	$^{+2.32}_{-2.45}$	$^{+0.78}_{-1.84}$	$^{+1.26}_{-}$	±1.74	$^{+0.74}_{-0.68}$
high E η intercalibration non closure (JES) [%]	-	-	-	-	-	-	-	-	-
neg η intercalibration non closure (JES) [%]	-	-	-	-	±0.11	-	-	-	±0.15
pos η intercalibration non closure (JES) [%]	-	-	-	-	-	-	-	-	-
η intercalibration total stat (JES) [%]	$^{+0.53}_{-0.34}$	$^{+0.71}_{-0.37}$	$^{+0.24}_{-0.52}$	$^{+0.46}_{-0.61}$	$^{+0.66}_{-0.54}$	$^{+0.85}_{-0.58}$	$^{+0.35}_{-0.38}$	±1.00	∓0.93
Flavour composition (JES) [%]	$^{+0.47}_{-0.35}$	$^{+1.06}_{-0.36}$	$^{+1.06}_{-1.14}$	$^{+1.25}_{-0.87}$	$^{+2.34}_{-0.97}$	$^{+0.39}_{-1.20}$	$^{+0.13}_{-1.32}$	±2.69	$^{+0.59}_{-1.27}$
Flavour response (JES) [%]	$^{+2.48}_{-2.76}$	$^{+3.97}_{-3.13}$	$^{+3.11}_{-3.28}$	$^{+3.53}_{-3.20}$	$^{+4.74}_{-3.90}$	$^{+1.28}_{-4.14}$	$^{+3.10}_{-1.69}$	$^{+2.31}_{-2.63}$	$^{+1.67}_{-2.83}$
Pile-up offset μ (JES) [%]	$^{-0.19}_{-}$	±0.27	$^{-0.36}_{-}$	$^{-0.50}_{+0.13}$	±0.47	$^{+0.11}_{-0.29}$	±0.54	±0.70	∓1.15
Pile-up offset N_{PV} (JES) [%]	$^{+0.22}_{-0.16}$	$^{+0.81}_{-0.25}$	$^{+0.28}_{-0.30}$	$^{-0.41}_{+0.91}$	$^{+0.36}_{-0.27}$	∓0.71	±0.38	±1.25	$^{+0.11}_{-0.49}$
Pile-up offset p_T (JES) [%]	∓0.26	$^{+0.66}_{-0.55}$	∓0.14	$^{+0.28}_{-0.24}$	±0.28	$^{-0.41}_{-}$	$^{-0.23}_{+0.64}$	$^{+0.54}_{-1.23}$	$^{+0.47}_{-0.24}$
Pile-up offset ρ topology (JES) [%]	$^{+3.49}_{-3.09}$	$^{+4.19}_{-3.22}$	$^{+3.78}_{-3.72}$	$^{+3.95}_{-4.31}$	$^{+4.19}_{-3.95}$	$^{+1.96}_{-5.01}$	$^{+3.44}_{-0.89}$	$^{+4.65}_{-2.43}$	$^{+1.81}_{-1.68}$
Punch-through (JES) [%]	-	-	-	-	±0.12	∓0.17	$^{-}_{-0.26}$	$^{+0.14}_{-0.15}$	∓0.20
Single particle high-p_T (JES) [%]	-	-	-	-	-	-	-	-	-
b-Quark tagging efficiency (eigenvector 0) [%]	$^{-3.65}_{+3.71}$	$^{-3.75}_{+3.82}$	$^{-3.77}_{+3.83}$	$^{-3.73}_{+3.80}$	$^{-3.60}_{+3.65}$	$^{-3.82}_{+3.87}$	$^{-4.10}_{+4.18}$	$^{-4.26}_{+4.32}$	$^{-4.66}_{+4.76}$
b-Quark tagging efficiency (eigenvector 1) [%]	∓0.83	$^{-0.75}_{+0.76}$	$^{-0.67}_{+0.68}$	∓0.60	$^{-0.57}_{+0.58}$	∓0.70	∓0.67	$^{-0.60}_{+0.59}$	∓1.15
b-Quark tagging efficiency (eigenvector 2) [%]	$^{+1.48}_{-1.47}$	$^{+1.42}_{-1.41}$	$^{+1.39}_{-1.38}$	$^{+1.33}_{-1.32}$	$^{+1.27}_{-1.26}$	$^{+1.33}_{-1.32}$	$^{+1.29}_{-1.28}$	$^{+1.28}_{-1.27}$	±1.31
b-Quark tagging efficiency (eigenvector 3) [%]	±0.10	-	-	-	-	-	-	-	±0.15
b-Quark tagging efficiency (eigenvector 4) [%]	∓0.24	∓0.21	∓0.19	∓0.18	∓0.15	∓0.16	∓0.13	∓0.12	∓0.12
b-Quark tagging efficiency (eigenvector 5) [%]	-	-	-	-	-	-	-	-	-
c-Quark tagging efficiency (eigenvector 0) [%]	±0.68	$^{+0.65}_{-0.64}$	$^{+0.62}_{-0.61}$	±0.57	±0.45	±0.64	±0.56	$^{+0.85}_{-0.84}$	±0.84
c-Quark tagging efficiency (eigenvector 1) [%]	±0.34	±0.26	±0.23	±0.22	±0.17	±0.25	±0.19	±0.34	±0.40
c-Quark tagging efficiency (eigenvector 2) [%]	-	-	-	-	-	-	-	±0.17	±0.20
Light-jet tagging efficiency (eigenvector 0) [%]	±0.39	±0.62	$^{+0.54}_{-0.55}$	$^{+0.74}_{-0.73}$	±0.58	±0.44	±0.88	$^{+1.37}_{-1.35}$	$^{+1.80}_{-1.77}$
Light-jet tagging efficiency (eigenvector 1) [%]	-	-	-	-	-	-	-	±0.26	±0.50
Light-jet tagging efficiency (eigenvector 2) [%]	-	-	-	-	-	-	-	-	-
Light-jet tagging efficiency (eigenvector 3) [%]	-	-	-	-	-	-	-	-	-
Light-jet tagging efficiency (eigenvector 4) [%]	-	-	-	-	-	-	-	-	-
Light-jet tagging efficiency (eigenvector 5) [%]	-	-	-	-	-	-	-	-	-
Light-jet tagging efficiency (eigenvector 6) [%]	-	-	-	-	-	-	-	-	-
Light-jet tagging efficiency (eigenvector 7) [%]	-	-	-	-	-	-	-	-	-
Light-jet tagging efficiency (eigenvector 8) [%]	-	-	-	-	-	-	-	-	-
Light-jet tagging efficiency (eigenvector 9) [%]	-	-	-	-	-	-	-	-	-
Light-jet tagging efficiency (eigenvector 10) [%]	-	-	-	-	-	-	-	-	-
b-Quark tagging extrapolation [%]	-	-	-	-	∓0.10	∓0.14	∓0.11	∓0.34	∓0.64
b-Quark tagging extrapolation from c-Quark [%]	-	-	-	-	-	-	-	-	-
JET JER cross calibration forward [%]	-	-	-	-	-	-	-	-	-
JET JER noise forward [%]	-	-	-	-	-	-	-	-	-
JET JER NP0 [%]	-	-	-	-	-	-	-	-	-
JET JER NP1 [%]	∓0.30	$^{-0.32}_{-}$	$^{-0.80}_{-}$	±1.27	$^{+0.63}_{-0.13}$	∓2.93	±3.05	∓3.51	$^{-0.22}_{-}$
JET JER NP2 [%]	-	∓0.51	$^{-0.52}_{+0.36}$	-	±1.77	∓4.10	±2.63	∓3.71	$^{+1.15}_{-0.29}$
JET JER NP3 [%]	∓0.27	∓0.57	∓0.80	$^{-0.31}_{+0.88}$	±0.61	∓2.25	±2.02	$^{+0.35}_{-0.91}$	$^{+0.48}_{-1.33}$
JET JER NP4 [%]	∓0.29	±0.47	∓0.61	±0.49	±1.72	∓2.26	±2.32	∓2.60	$^{+1.60}_{-0.45}$
JET JER NP5 [%]	$^{-}_{+0.39}$	$^{+0.22}_{-0.40}$	∓0.43	±1.35	±0.71	∓2.92	±1.69	±0.29	-
JET JER NP6 [%]	∓0.29	$^{-0.36}_{+0.43}$	∓0.86	-	±1.85	∓1.94	±3.58	∓1.88	±0.99
JET JER NP7 [%]	$^{-}_{+0.31}$	$^{-}_{+0.23}$	∓0.83	±0.63	$^{+0.22}_{-0.20}$	∓0.86	±1.64	$^{+2.07}_{-0.10}$	$^{-0.84}_{+0.30}$
JET JER NP8 [%]	-	-	-	-	-	-	-	-	-
QCD estimation [%]	±3.04	±5.16	±4.20	±4.44	±1.98	±2.09	±6.30	±1.68	±0.58
K-factor normalization mass [%]	$^{+2.75}_{-2.67}$	$^{+2.71}_{-2.63}$	$^{+2.67}_{-2.59}$	$^{+2.59}_{-2.51}$	$^{+2.60}_{-2.51}$	$^{+2.66}_{-2.58}$	$^{+2.68}_{-2.59}$	$^{+2.66}_{-2.57}$	$^{+2.75}_{-2.66}$
K-factor normalization PDFAS [%]	±4.17	±4.10	±4.05	±3.92	±3.93	±4.03	±4.05	±4.02	±4.16
K-factor normalization scale [%]	$^{+2.35}_{-3.47}$	$^{+2.31}_{-3.42}$	$^{+2.28}_{-3.37}$	$^{+2.21}_{-3.26}$	$^{+2.21}_{-3.27}$	$^{+2.27}_{-3.36}$	$^{+2.28}_{-3.38}$	$^{+2.27}_{-3.35}$	$^{+2.34}_{-3.47}$
Luminosity [%]	∓2.05	∓2.05	∓2.05	∓2.05	∓2.05	∓2.05	∓2.05	∓2.05	∓2.05
MCSignal stat. [%]	±1.41	±1.18	±1.25	±1.45	±1.70	±2.31	±3.03	±4.44	±4.55
QCD stat. [%]	±0.68	±0.87	±1.20	±1.71	±2.28	±3.17	±3.84	±4.67	±2.55
ISR/FSR + scale [%]	$^{-}_{+0.60}$	$^{+0.40}_{-}$	$^{+2.04}_{-0.42}$	$^{-1.11}_{-}$	∓4.14	$^{+2.26}_{-1.65}$	∓3.50	$^{-8.08}_{+1.62}$	$^{+0.51}_{-1.40}$
Alternate hard-scattering model [%]	∓2.58	±1.09	±1.17	±5.26	∓1.10	±9.61	∓10.3	∓12.1	±11.1
Alternate parton-shower model [%]	∓3.00	±3.36	±8.21	±2.14	±4.53	±3.21	±1.41	±12.8	±3.31
Inter PDF [%]	-	-	-	-	∓0.10	-	-	-	∓0.26
Intra PDF [%]	±0.19	±0.15	±0.16	±0.17	±0.11	-	±0.13	±0.26	±0.24

TABLE D.18: Table of systematics for the absolute differential cross-section at the particle level for the p_T^{tt} observable.

Bins [Unit $y^{t\bar{t}}$]	0–0.10	0.10–0.20	0.20–0.30	0.30–0.40	0.40–0.50	0.50–0.60	0.60–0.70	0.70–0.80	0.80–0.90	0.90–1	1–1.10	1.10–1.20	1.20–1.30	1.30–1.40	1.40–1.50	1.50–1.60	1.60–2.50
$d\sigma$ / $d\,y^{t\bar{t}}$ [pb/ Unit $y^{t\bar{t}}$]	$1.74 \cdot 10^{0}$	$1.87 \cdot 10^{0}$	$1.79 \cdot 10^{0}$	$1.77 \cdot 10^{0}$	$1.52 \cdot 10^{0}$	$1.55 \cdot 10^{0}$	$1.44 \cdot 10^{0}$	$1.25 \cdot 10^{0}$	$1.16 \cdot 10^{0}$	$9.84 \cdot 10^{-1}$	$9.06 \cdot 10^{-1}$	$7.27 \cdot 10^{-1}$	$6.23 \cdot 10^{-1}$	$4.82 \cdot 10^{-1}$	$3.34 \cdot 10^{-1}$	$2.56 \cdot 10^{-1}$	$4.01 \cdot 10^{-2}$
Total Uncertainty [%]	+15.2 −18.2	+17.7 −17.4	+13.7 −12.5	+14.1 −14.6	+13.4 −15.3	+16.7 −15.1	+12.1 −12.3	+15.4 −16.1	+15.0 −14.6	+20.7 −17.7	+15.2 −14.0	+15.4 −14.3	+16.6 −22.4	+19.7 −19.6	+22.6 −22.1	+24.0 −21.6	+25.5 −25.1
Statistics [%]	±2.5	±2.5	±2.6	±2.6	±2.9	±2.8	±2.9	±3.2	±3.2	±3.5	±3.8	±4.1	±4.5	±5.2	±6.5	±6.9	±5.7
Systematics [%]	+14.8 −17.9	+17.3 −17.1	+13.2 −12.1	+13.6 −14.2	+12.8 −14.8	+16.2 −14.6	+11.4 −11.9	+14.7 −15.4	+14.3 −13.9	+20.1 −17.2	+14.2 −13.5	+14.2 −13.8	+15.3 −21.3	+18.2 −18.2	+20.6 −20.1	+21.7 −20.9	+24.1 −23.6
Jet vertex fraction [%]	−0.47	−0.50	−0.47	−0.46	−0.48	−0.45	−0.49	−0.43	−0.48	−0.50	−0.53	−0.44	−0.46	−0.37	−0.47	−0.49	−0.41
b-Tagged jet energy scale (JES) [%]	+0.58 −1.58	+1.34 −0.84	+0.66 −0.72	+0.62 −0.90	+0.47 −0.62	+0.62 −1.23	+0.52 −0.82	+1.84 −0.10	+0.48 −0.69	+1.50 −0.25	+1.20 −0.50	+0.47 −1.08	+0.63 −2.04	+2.93 −1.16	+0.60 −1.34	±1.09	−0.34
Effective detector NP set 1 (JES) [%]	+1.56 −2.38	+2.11 −1.01	+2.20 −1.78	+0.89 −1.09	+1.63 −1.89	+3.12 −2.51	+1.42 −1.11	+1.12 −1.76	+1.59 −1.45	+2.51 −1.18	+1.59 −0.71	+2.96 −2.44	+1.64 −1.14	+1.95 −2.97	+2.77 −3.12	+2.15 −0.91	+1.39 −1.22
Effective mixed NP set 1 (JES) [%]	±0.73	±0.91	±0.15	±0.21	±0.65	−0.46	-	−0.12	−0.20	±0.42	±0.18	+0.24 −0.50	±0.24	−0.50	−0.54	±1.11	±1.57
Effective mixed NP set 2 (JES) [%]	−0.50	-	−0.44 −0.29	-	−0.68 −0.44	−0.54 −0.34	+0.30	-	−0.45	−0.13 −0.08	+0.63 −0.23	−0.47 −1.05	−0.59	−0.99 +1.43	−0.54	±0.56	−0.29
Effective mixed NP set 3 (JES) [%]	-	-	-	∓0.14	-	±0.33	-	−0.17	±0.20	−0.15	±0.10	-	+0.16	−0.24	-	−0.15	∓0.30
Effective modelling NP set 1 (JES) [%]	+6.15 −6.03	+6.24 −5.68	+6.65 −6.02	+6.15 −5.84	+5.28 −5.28	+8.13 −7.57	+5.10 −5.03	+5.47 −5.72	+6.22 −5.34	+9.17 −7.47	+6.04 −5.78	+6.36 −5.83	+4.90 −5.28	+10.1 −4.29	+6.40 −2.23	+7.37 −2.54	+6.15 −6.21
Effective modelling NP set 2 (JES) [%]	+0.02 −1.77	−1.08 −0.47	+1.20 −1.37	−0.26 −0.39	+1.25 −1.04	+1.57 −2.03	+1.03 −0.76	+0.72 −1.68	−1.34 −0.91	±1.56 −0.60	+0.78 −1.30	−1.65 −0.80	−1.28 −0.43	+1.29 −2.15	+2.17 −1.06	−1.04	−2.41
Effective modelling NP set 3 (JES) [%]	−0.81	−0.57	−0.50	−0.62	-	−0.43	±0.22	−0.34	−0.15	−0.82	−0.31	+0.08 −0.56	+0.52	±0.36	−0.32	±1.02	+0.28
Effective modelling NP set 4 (JES) [%]	-	+0.90 −0.17	+0.61 −0.71	+0.26 −0.33	−0.48 −0.47	+0.59 −0.99	+0.52 −0.22	-	+0.22 −0.28	+0.82 −0.39	−0.10 +0.18	−1.43 −1.63	±0.42	+1.32 −1.90	+0.91 −0.61	±0.94	+0.21 −0.60
Effective statistical NP set 1 (JES) [%]	-	-	-	-	-	-	-	-	-	-	-	-	-	-	-	-	-
Effective statistical NP set 2 (JES) [%]	−0.58	−0.20	−0.25	−0.31 +0.14	−0.58	−0.72 +0.58	±0.43	±0.17	−0.40 +0.44	−0.45 +0.61	−0.21	+0.72	−0.25 +0.22	−0.57 +1.74	−1.10 +0.17	±0.92	+0.60
Effective statistical NP set 3 (JES) [%]	∓0.19	+0.57 −0.18	±0.10	-	∓0.27	∓0.13	±0.20	+0.28 −0.25	±0.14	+0.14 −0.28	+0.29 −0.26	±0.50	±0.38	±0.39	+0.58 −0.28	±0.26	−0.80 +0.29
Effective statistical NP set 4 (JES) [%]	−0.27	±0.10	-	+0.14 −0.16	−0.54	−0.29	±0.45	−0.16	+0.18 −0.26	-	−0.22 +0.36	±0.51	±0.21	+0.74 −0.11	-	+0.41 −0.26	−0.48
Effective statistical NP set 5 (JES) [%]	∓0.23	−0.23	−0.20	−0.19	−0.48	−0.43	−0.14	−0.20	−0.50	−0.16	-	−0.25	±0.29	−0.32	−0.54	±0.48	∓0.43
Effective statistical NP set 6 (JES) [%]	-	+0.43	+0.11	+0.11	+0.15	+0.34	−0.51	-	+0.46	+0.44	-	+0.35	-	+1.03	+0.24	-	+0.70
η intercalibration model (JES) [%]	±0.12	-	-	-	+0.14	+0.26	±0.33	−0.13	-	+0.14	-	±0.65	-	+0.78	+0.88	−0.11	-
η intercalibration non closure (JES) [%]	+1.38 −1.88	+1.41 −1.50	+1.88 −0.97	∓1.14	+0.74 −1.23	−0.61 −1.41	+0.46 −0.39	+1.17 −1.60	+1.53 −1.14	−0.19 −1.53	±2.17	+2.31 −2.11	±1.70 −2.65	+3.27 −2.47	+1.92 −3.14	±3.19	+3.29 −1.80
high E η intercalibration non closure (JES) [%]	-	-	-	-	-	-	-	-	-	-	-	-	-	-	-	-	-
neg η intercalibration non closure (JES) [%]	-	-	-	-	-	-	-	-	-	-	±0.17	-	±0.11	+0.16 −0.21	±0.17	+0.30 −0.10	+0.12 −0.21
pos η intercalibration non closure (JES) [%]	-	-	-	-	-	-	-	-	-	-	-	-	-	-	+0.10 −0.10	+0.26 −0.26	-
η intercalibration total stat (JES) [%]	+0.25 −0.87	+0.90 −0.30	+0.60 −0.53	+0.53 −0.31	+0.71 −0.25	±0.57	−0.32	+0.23 −0.35	+0.89 −0.07	+0.40 −0.17	+1.20 −0.45	+0.15 −0.49	+1.77 −1.22	±0.65	+0.46 −0.47
Flavour composition (JES) [%]	+0.85 −1.20	+1.33 −0.90	+1.01 −0.60	+0.33 −0.61	+0.62 −0.74	+1.94 −0.71	+0.41 −0.53	+0.40 −0.75	+1.17 −0.95	+2.02 −1.23	±1.49 −3.18	+1.56 −1.39	+0.88 −1.54	+1.93 −4.38	+2.17 −1.40	±0.74 −1.71	+0.22 −0.64
Flavour response (JES) [%]	+2.51 −2.51	+3.24 −3.08	+3.03 −3.83	+2.50	+3.11	+4.32 −0.57	+2.90	+1.98	+3.21	+4.19	+3.28	+4.49 −0.20	+3.40 −0.88	+4.39 −0.76	+4.81	+7.60	+3.74
Pile-up offset μ (JES) [%]	−0.66	±0.35	+0.20	-	−0.17	±0.61	±0.71	±0.61	±0.41	−0.35 +0.60	−0.47	−0.47	±0.18	−0.38	−0.81	±0.69	+1.01
Pile-up offset N_{PV} (JES) [%]	±0.79	+0.19 −0.56	±0.46	±0.65	+0.49 −0.65	±0.21	±0.19	−0.97	+0.94 −0.17	±1.00	±0.75	−0.14 −0.45	+1.40 −0.45	+0.69 −0.58	±0.49	±1.93	−0.87 −0.58
Pile-up offset p_T (JES) [%]	±0.55	-	+0.52	+0.40 −0.32	±0.14	±0.36	±0.21	±0.68	±0.44	±0.44	±0.39	−0.40	±0.25	+0.23 −0.33	±0.33	±0.27	+0.30 −0.26
Pile-up offset ρ topology (JES) [%]	+2.60 −5.26	+3.66 −3.91	+4.50 −2.62	−3.52 −3.96	+4.03 −4.17	+4.90 −3.17	+2.65 −3.43	+3.90 −3.02	+2.71 −3.14	+6.18 −2.91	+3.34 −2.44	+4.29 −3.27	+4.33 −4.89	+2.72 −4.99	+4.24 −2.31	+5.30 −4.46	+3.01 −1.95
Punch-through (JES) [%]	-	-	−0.13	±0.10	-	-	±0.11	-	-	-	-	-	-	+0.11 −0.19	-	-	-
Single particle high-p_T (JES) [%]	-	-	-	-	-	-	-	-	-	-	-	-	-	-	-	-	-
b-Quark tagging efficiency (eigenvector 0) [%]	−3.82 +3.88	−3.85 +3.92	−3.78 +3.84	−3.94 +4.01	−3.68 +3.74	−3.77 +3.83	−3.80 +3.87	−3.75 +3.82	−3.75 +3.82	−3.63 +3.69	−3.76 +3.82	−3.71 +3.78	−3.84 +3.91	−3.69 +3.75	−3.73 +3.79	−3.22 +3.27	−3.43 +3.50
b-Quark tagging efficiency (eigenvector 1) [%]	∓0.72	∓0.67	∓0.69	∓0.70	∓0.73	∓0.70	−0.75	∓0.64	−0.66	∓0.73	−0.72	−0.69	∓0.81	∓0.68	−0.73	−0.68	∓0.69
b-Quark tagging efficiency (eigenvector 2) [%]	±1.38	+1.39 −1.38	+1.38 −1.35	+1.39 −1.38	+1.38 −1.37	+1.39 −1.38	+1.41 −1.40	+1.39 −1.38	+1.37 −1.36	+1.34 −1.33	+1.40 −1.37	+1.39 −1.39	+1.40 −1.39	+1.38 −1.37	+1.39 −1.38	+1.29	+1.31 −1.30
b-Quark tagging efficiency (eigenvector 3) [%]	-	-	-	-	-	-	-	-	-	-	-	-	±0.13	-	-	-	-
b-Quark tagging efficiency (eigenvector 4) [%]	∓0.19	∓0.19	∓0.18	∓0.18	∓0.19	∓0.19	∓0.20	∓0.20	∓0.18	∓0.18	∓0.19	∓0.18	∓0.21	∓0.19	−0.20 +0.21	∓0.17	∓0.20
b-Quark tagging efficiency (eigenvector 5) [%]	-	-	-	-	-	-	-	-	-	-	-	-	-	-	-	-	-
c-Quark tagging efficiency (eigenvector 0) [%]	±0.61	±0.65	±0.60	±0.65	+0.65 −0.64	±0.62	±0.67	+0.62 −0.61	±0.64	±0.53	±0.55	±0.64	±0.60	±0.60	±0.61	±0.38	±0.52
c-Quark tagging efficiency (eigenvector 1) [%]	±0.24	±0.28	±0.22	±0.28	±0.26	±0.27	±0.27	±0.23	±0.26	±0.24	±0.20	±0.29	±0.22	±0.22	±0.26	±0.17	±0.23
c-Quark tagging efficiency (eigenvector 2) [%]	-	-	-	-	-	-	-	-	-	-	-	-	-	-	-	-	-
Light-jet tagging efficiency (eigenvector 0) [%]	±0.53	±0.60	±0.63	±0.57	±0.63	±0.65	+0.72 −0.76	+0.85 −0.84	±0.50	±0.52	+0.96 −0.95	+0.20 −0.19	±0.84	+0.34 −0.35	±0.40	-	±0.76
Light-jet tagging efficiency (eigenvector 1) [%]	-	-	-	-	-	-	-	-	-	-	-	-	-	-	-	-	-
Light-jet tagging efficiency (eigenvector 2) [%]	-	-	-	-	-	-	-	-	-	-	-	-	-	-	-	-	-
Light-jet tagging efficiency (eigenvector 3) [%]	-	-	-	-	-	-	-	-	-	-	-	-	-	-	-	-	-
Light-jet tagging efficiency (eigenvector 4) [%]	-	-	-	-	-	-	-	-	-	-	-	-	-	-	-	-	-
Light-jet tagging efficiency (eigenvector 5) [%]	-	-	-	-	-	-	-	-	-	-	-	-	-	-	-	-	-
Light-jet tagging efficiency (eigenvector 6) [%]	-	-	-	-	-	-	-	-	-	-	-	-	-	-	-	-	-
Light-jet tagging efficiency (eigenvector 7) [%]	-	-	-	-	-	-	-	-	-	-	-	-	-	-	-	-	-
Light-jet tagging efficiency (eigenvector 8) [%]	-	-	-	-	-	-	-	-	-	-	-	-	-	-	-	-	-
Light-jet tagging efficiency (eigenvector 9) [%]	-	-	-	-	-	-	-	-	-	-	-	-	-	-	-	-	-
Light-jet tagging efficiency (eigenvector 10) [%]	-	-	-	-	-	-	-	-	-	-	-	-	-	-	-	-	-
b-Quark tagging extrapolation [%]	-	±0.11	-	±0.11	±0.12	-	±0.14	-	±0.10	-	-	-	-	-	-	-	-
b-Quark tagging extrapolation from c-Quark [%]	-	-	-	-	-	-	-	-	-	-	-	-	-	-	-	-	-
JET JER cross calibration forward [%]	-	-	-	-	-	-	-	-	-	-	-	-	-	-	-	-	-
JET JER noise forward [%]	-	-	-	-	-	-	-	-	-	-	-	-	-	-	-	-	-
JET JER NP0 [%]	-	-	-	-	-	-	-	-	-	-	-	-	-	-	-	-	-
JET JER NP1 [%]	−1.12	+0.52	+1.23	−2.53	−0.86	±0.80	∓1.21	∓1.73	+1.19 −0.14	±4.14	∓0.33	±2.46	∓4.40	−2.29 +0.34	+0.30 −0.19	±4.55	∓1.10
JET JER NP2 [%]	∓0.23	±0.20	±0.82	∓1.26	∓2.31	±0.77	∓1.10	∓1.76	±0.94	±1.84	−0.25 +1.12	±0.79	∓3.52	+0.58 −3.01	∓1.05	−0.32 +0.92	±1.56
JET JER NP3 [%]	−1.50 +0.30	±1.38	±0.12	+0.39 −0.48	∓1.52	±0.75	−0.92 −0.58	∓1.60	−0.26 −0.46	−0.35 +1.03	±1.03 −0.39	+0.92 −0.29	∓3.76	∓2.60	±2.40	±2.91	−0.28
JET JER NP4 [%]	−0.91	±1.12	±0.23	±0.98	+0.48 −2.70	±1.08	−0.21 −0.11	∓0.17 −0.65	±2.84	+2.93 −0.89	−0.89	±2.35	−3.39	+1.83 −1.85	±5.83	−0.16
JET JER NP5 [%]	±0.92	−0.23	±1.04	−0.68	+0.23 −0.85	−0.11	−0.11	±1.00	±0.51	±3.39	±1.03	±1.34	∓3.66	+0.43 −2.49	−0.92	±4.51	±0.51
JET JER NP6 [%]	±1.19	±1.26	−0.80 −0.20	±0.49	∓0.47	±1.15	±0.33	+0.19 −0.25	−0.56	±2.59	+0.56 −0.80	+0.42 −1.35	∓1.69	∓3.84	±4.00	±4.77	±1.45
JET JER NP7 [%]	+0.41 −1.52	−0.80 +1.52	±0.54	±1.18	−0.39	−0.15 ±0.79	∓0.73	+0.35 −1.50	−0.56 −0.43	±2.33	−0.49 +1.51	−1.81	−2.64	∓2.08	∓0.72 −0.88	±3.11	+0.36 −1.55
JET JER NP8 [%]	-	-	-	-	-	-	-	-	-	-	-	-	-	-	-	-	-
QCD estimation [%]	±6.32	±6.52	±4.63	±4.90	±5.26	±3.31	±3.30	±7.00	±5.68	±3.72	±3.59	±2.70	±1.87	±6.55	±4.80	∓0.46	±0.61
K-factor normalization mass [%]	+2.70 −2.61	+2.69 −2.61	+2.73 −2.61	+2.73 −2.64	+2.78 −2.61	+2.67 −2.59	+2.67 −2.58	+2.69 −2.60	+2.65 −2.57	+2.68 −2.59	+2.62 −2.54	+2.60 −2.58	+2.69 −2.60	+2.66 −2.58	+2.68 −2.59	+2.58 −2.50	+2.46 −2.39
K-factor normalization PDFAS [%]	±4.08	±4.08	±4.08	±4.13	±4.08	±4.05	±4.04	±4.06	±4.02	±4.05	±3.97	±4.03	±4.07	±4.03	±4.05	±3.90	±3.73
K-factor normalization scale [%]	+2.30 −3.40	+2.30 −3.39	+2.30 −3.40	+2.33 −3.44	+2.30 −3.40	+2.28 −3.37	+2.27 −3.36	+2.29 −3.38	+2.26 −3.35	+2.28 −3.37	+2.24 −3.31	+2.27 −3.35	+2.29 −3.38	+2.27 −3.35	+2.28 −3.38	+2.20 −3.25	+2.10 −3.11
Luminosity [%]	±2.05	±2.05	±2.05	±2.05	±2.05	±2.05	±2.05	±2.05	±2.05	±2.05	±2.05	±2.05	±2.05	±2.05	±2.05	±2.05	±2.05
MCSignal stat. [%]	±1.74	±1.88	±1.97	±1.93	±1.99	±2.08	±2.14	±2.28	±2.36	±2.51	±2.84	±3.00	±3.32	±3.82	±4.49	±5.29	±4.00
QCD stat. [%]	±1.62	±1.76	±1.81	±1.79	±1.86	±1.94	±1.99	±2.23	±2.28	±2.41	±2.77	±2.83	±3.21	±3.85	±4.76	±5.56	±4.86
ISR/FSR + scale [%]	±0.76	±4.68	±1.67	±0.96	±1.32	±6.30	+0.65	±0.38	±0.60	∓2.28	±3.17	±2.37	−12.2 +0.24	−1.85 +1.89	±2.14	±3.39	±3.95
Alternate hard-scattering model [%]	±2.41	±2.81	±0.68	±4.51	±4.00	∓4.67	±3.39	±6.19	±3.99	±10.1	±1.98	±2.89	±2.73	±6.88	±10.6	±4.03	∓20.3
Alternate parton-shower model [%]	±7.77	±9.39	±0.11	±4.91	±0.36	±1.57	±2.11	±3.73	±6.01	±0.48	±4.57	±3.42	±6.47	±1.50	±9.87	±6.83	±4.26
Inter PDF [%]	-	-	-	-	-	-	-	-	-	-	-	-	-	-	±0.22	-	±0.54
Intra PDF [%]	±0.11	-	±0.11	±0.10	-	±0.10	-	±0.11	-	±0.14	±0.17	-	±0.12	±0.17	±0.64	±0.31	±0.55

TABLE D.19: Table of systematics for the absolute differential cross-section at the particle level for the $y_{t\bar{t}}$ observable.

D.2 Relative cross sections, unfolded to particle level

D.3 Absolute cross sections, unfolded to parton level

Bins [Unit $p_T^{\text{topleading}}$]	0–175	175–215	215–255	255–300	300–335	335–380	380–430	430–490	490–560	560–1000
$d\sigma$ / $d p_T^{\text{topleading}}$ [pb/ Unit $p_T^{\text{topleading}}$]	$2.67 \cdot 10^{0}$	$2.34 \cdot 10^{0}$	$1.53 \cdot 10^{0}$	$7.50 \cdot 10^{-1}$	$4.22 \cdot 10^{-1}$	$2.39 \cdot 10^{-1}$	$1.16 \cdot 10^{-1}$	$6.30 \cdot 10^{-2}$	$3.22 \cdot 10^{-2}$	$4.78 \cdot 10^{-3}$
Total Uncertainty [%]	+40.8 −38.9	+13.7 −15.4	+16.4 −15.2	+16.0 −16.9	+14.0 −12.6	+13.0 −13.1	+16.1 −17.7	+19.2 −18.5	+16.0 −16.7	+27.8 −25.1
Statistics [%]	±5.3	±2.6	±1.9	±1.7	±1.9	±1.9	±2.3	±3.0	±4.6	±8.4
Systematics [%]	+39.3 −37.3	+12.9 −14.8	+16.1 −14.9	+15.8 −16.7	+13.7 −12.3	±12.8	+15.8 −17.4	+18.9 −18.1	+14.8 −15.5	+25.7 −22.7
Jet vertex fraction [%]	+0.64 −0.65	+0.59 −0.62	+0.52 −0.54	+0.43 −0.46	+0.37 −0.40	+0.34 −0.36	+0.32 −0.35	+0.31 −0.33	+0.29 −0.32	+0.48 −0.50
b-Tagged jet energy scale (JES) [%]	+0.87 −1.49	+0.82 −1.85	+1.01 −0.85	+0.67 −0.60	+0.62 −0.40	+0.79 −1.11	+0.42 −0.71	+0.70 −0.16	+1.30 −1.87	+1.14 −0.43
Effective detector NP set 1 (JES) [%]	+3.35 −4.41	+1.28 −2.51	+2.49 −2.00	+1.74 −2.12	+1.55 −0.34	+1.02 −1.38	+1.59 −1.54	+2.26 −0.58	+1.04 −1.92	+3.21 −1.69
Effective mixed NP set 1 (JES) [%]	+1.60 −0.55	∓0.41	±0.24	-	±0.88	∓0.31	+0.50 −1.49	+1.86 −0.43	+2.40 −2.33	+3.52 −5.62
Effective mixed NP set 2 (JES) [%]	±0.91	∓0.30	−0.11 +0.21	−0.63 +0.25	±0.50	−0.41 +0.25	−0.90 +0.34	±0.65	∓1.60	±2.99
Effective mixed NP set 3 (JES) [%]	+0.44 −0.19	-	−0.12 +0.14	-	-	∓0.20	-	−0.12 +0.19	−0.62	±1.76
Effective modelling NP set 1 (JES) [%]	+8.09 −12.0	+7.55 −8.28	+7.67 −7.22	+6.08 −7.27	+5.89 −4.03	+4.85 −3.87	+4.04 −4.86	+5.76 −3.65	+6.09 −6.18	+2.39 −4.38
Effective modelling NP set 2 (JES) [%]	+1.15 −1.73	+0.57 −1.65	+1.49 −1.46	+1.25 −1.06	+0.78 -	+0.34 −1.03	+1.15 −1.62	+1.76 −0.50	+1.74 −0.85	+3.50 −4.58
Effective modelling NP set 3 (JES) [%]	+1.11 −2.00	∓1.17	+1.18 −0.59	+0.36 −0.48	+1.17 −0.49	-	−0.76 +0.29	+1.27	∓0.97	+2.31
Effective modelling NP set 4 (JES) [%]	+1.96 −0.50	+0.21 −0.44	+0.53 −0.54	+0.48 −0.61	±0.50	+0.29 −0.44	+0.39 −1.02	+0.75 −0.26	- −1.22	±3.17
Effective statistical NP set 1 (JES) [%]	-	-	-	-	-	-	-	−0.15 -	-	+1.12 −0.22
Effective statistical NP set 2 (JES) [%]	−0.36 +0.96	−0.56 +0.16	−0.32 +0.44	−0.30 +0.49	+0.26	−0.39 +0.16	−0.54 +0.34	±0.16	−0.63 +0.11	±2.74
Effective statistical NP set 3 (JES) [%]	-	∓0.12	+0.38 −0.17	∓0.22	+0.76 −0.28	-	−0.64	±0.76	−1.16	±1.85
Effective statistical NP set 4 (JES) [%]	-	∓0.15	-	- −0.18	±0.11	+0.25 −0.17	+0.20 −0.51	+0.38 -	−0.57 +0.17	- +1.95
Effective statistical NP set 5 (JES) [%]	±0.53	−0.47 +0.42	−0.23 +0.20	−0.38 +0.25	−0.29 +0.43	∓0.18	−0.28 -	±0.23	+0.52 −0.49	+0.43
Effective statistical NP set 6 (JES) [%]	±0.65	+0.21 −0.28	∓0.10	- −0.17	±0.33	- −0.28	+0.26 −0.24	−0.12 +0.16	+0.39 −0.80	±2.23
η intercalibration model (JES) [%]	+3.33 −3.03	+1.73 −2.46	+1.78 −1.24	+1.52 −1.74	+1.01 −0.76	±1.18	+0.89 −0.77	±1.27	+1.05 −1.79	+1.87 −0.56
high E η intercalibration non closure (JES) [%]	-	-	-	-	-	-	-	-	-	-
neg η intercalibration non closure (JES) [%]	-	-	-	-	-	-	-	-	-	-
pos η intercalibration non closure (JES) [%]	±0.14	-	-	-	-	-	-	-	-	-
η intercalibration total stat (JES) [%]	+1.14 −0.95	+0.28 −0.49	+0.42 −0.36	+0.69 −0.52	+0.48 −0.10	+0.40 −0.39	+0.37 −0.59	-	+0.74 −1.32	±2.80
Flavour composition (JES) [%]	+0.68 −1.12	+1.03 −0.62	+1.37 −0.78	+1.37 −0.87	+0.93 −0.38	+0.48 −0.42	+0.74 −0.90	+0.68 −0.25	+0.80 −1.13	±3.18
Flavour response (JES) [%]	−7.81 +5.00	−4.96 +3.04	−3.36 +4.48	−3.83 +2.86	−1.56 +3.26	−1.71 +2.06	−2.46 +1.84	−1.60 +3.87	−2.79 +2.77	−5.79 +1.31
Pile-up offset μ (JES) [%]	−0.59 +1.21	∓0.72	+0.16 −0.11	±0.21	−0.30 +0.52	∓0.19	+0.12	+0.21 −0.11	−0.94 +0.70	±1.51
Pile-up offset N_{PV} (JES) [%]	−3.42 +1.32	+0.20 −0.24	±1.08	+0.29 −0.45	±0.55	+0.20 −0.50	+0.42 −0.68	±0.81	−2.01 +0.84	±1.47
Pile-up offset p_T (JES) [%]	−1.74 +0.87	∓0.64	±0.38	+0.19 −0.44	- +0.21	+0.45 −0.35	+0.27 −0.59	±0.17	+0.72 −0.32	+1.63 −0.38
Pile-up offset ρ topology (JES) [%]	+5.20 −8.49	+3.55 −5.09	+4.97 −4.00	+3.49 −3.40	+3.79 −2.34	+2.55 −2.61	+2.22 −2.62	+3.28 −1.71	+2.79 −3.12	+1.64 −2.22
Punch-through (JES) [%]	-	-	-	-	-	±0.11	-	-	±0.10	-
Single particle high-p_T (JES) [%]	-	-	-	-	-	-	-	-	-	-
b-Quark tagging efficiency (eigenvector 0) [%]	−2.10 +2.14	−3.28 +3.33	−3.72 +3.79	−3.84 +3.91	−3.75 +3.81	−3.75 +3.81	−3.86 +3.93	−3.94 +4.01	−4.29 +4.37	−4.85 +4.95
b-Quark tagging efficiency (eigenvector 1) [%]	∓0.24	∓0.14	∓0.21	∓0.44	−0.66 +0.67	−0.92 +0.93	−1.35 +1.36	−1.91 +1.93	−2.80 +2.83	−4.01 +4.09
b-Quark tagging efficiency (eigenvector 2) [%]	+1.07 −1.06	+1.23 −1.22	+1.34 −1.33	+1.42 −1.41	+1.41 −1.40	+1.43 −1.42	+1.45 −1.44	+1.39 −1.38	+1.26 −1.25	+0.82 −0.81
b-Quark tagging efficiency (eigenvector 3) [%]	∓0.61	∓0.52	∓0.31	-	±0.21	±0.34	±0.48	±0.62	±0.75	±0.50
b-Quark tagging efficiency (eigenvector 4) [%]	-	∓0.15	∓0.22	∓0.25	∓0.23	∓0.20	∓0.15	∓0.10	-	-
b-Quark tagging efficiency (eigenvector 5) [%]	±0.15	±0.12	-	-	-	-	-	-	-	-
c-Quark tagging efficiency (eigenvector 0) [%]	±0.37	±0.38	±0.52	±0.64	±0.65	±0.72	±0.72	±0.82	±0.96	+0.84 −0.83
c-Quark tagging efficiency (eigenvector 1) [%]	-	-	±0.19	±0.26	+0.29 −0.28	±0.32	±0.33	±0.37	±0.44	±0.44
c-Quark tagging efficiency (eigenvector 2) [%]	-	-	-	-	-	±0.10	±0.12	±0.14	±0.16	±0.23
Light-jet tagging efficiency (eigenvector 0) [%]	+0.40 −0.39	±0.50	+0.48 −0.47	±0.48	±0.67	±0.65	+0.81 −0.82	±0.87	+1.02 −1.01	+0.91 −0.90
Light-jet tagging efficiency (eigenvector 1) [%]	-	-	-	-	-	-	-	-	-	±0.28
Light-jet tagging efficiency (eigenvector 2) [%]	-	-	-	-	-	-	-	-	-	-
Light-jet tagging efficiency (eigenvector 3) [%]	-	-	-	-	-	-	-	-	-	-
Light-jet tagging efficiency (eigenvector 4) [%]	-	-	-	-	-	-	-	-	-	-
Light-jet tagging efficiency (eigenvector 5) [%]	-	-	-	-	-	-	-	-	-	-
Light-jet tagging efficiency (eigenvector 6) [%]	-	-	-	-	-	-	-	-	-	-
Light-jet tagging efficiency (eigenvector 7) [%]	-	-	-	-	-	-	-	-	-	-
Light-jet tagging efficiency (eigenvector 8) [%]	-	-	-	-	-	-	-	-	-	-
Light-jet tagging efficiency (eigenvector 9) [%]	-	-	-	-	-	-	-	-	-	-
Light-jet tagging efficiency (eigenvector 10) [%]	-	-	-	-	-	-	-	-	-	-
b-Quark tagging extrapolation [%]	-	-	-	-	-	∓0.13	∓0.16	∓0.21	∓0.27	∓0.47
b-Quark tagging extrapolation from c-Quark [%]	-	-	-	-	-	-	-	-	-	-
JET JER cross calibration forward [%]	-	-	-	-	-	-	-	-	-	-
JET JER noise forward [%]	-	-	-	-	-	-	-	-	-	-
JET JER NP0 [%]	-	-	-	-	-	-	-	-	-	-
JET JER NP1 [%]	∓0.63	−0.76	∓0.40	∓1.21	±0.16	+1.00	∓0.17	+0.91 −0.10	±0.95	+1.85 −0.96
JET JER NP2 [%]	−0.19 +0.41	∓1.20	∓0.28	∓1.11	±0.57	±0.83	−1.08 +0.15	±1.33	−0.81 +0.42	−0.91 +0.26
JET JER NP3 [%]	∓2.14	−1.03	±0.64	∓1.74	±0.29	±0.48	−0.93 +0.34	±0.91	−0.25 +0.29	∓1.29
JET JER NP4 [%]	+1.79 −0.59	∓2.17	+0.51 −0.28	∓1.19	±0.92	±1.06	∓1.43	±1.01	±0.92	+1.06 −3.30
JET JER NP5 [%]	−2.36	∓0.80	±0.96	+0.20 −0.63	∓0.18	+1.10	∓0.58	±1.15	±0.39	+0.63 −0.24
JET JER NP6 [%]	−0.65 +1.79	∓1.76	−0.60 +0.51	∓1.35	+0.28 -	±0.67	−0.27 +0.11	±0.58	+0.28 −1.35	±2.49
JET JER NP7 [%]	∓1.20	−0.82 +0.62	+0.41 −0.13	∓0.97	±0.21	±0.85	∓0.69	∓0.78	−0.34 +2.14	+0.35 −1.63
JET JER NP8 [%]	-	-	-	-	-	-	-	-	-	-
QCD estimation [%]	∓25.9	∓0.47	±7.00	±5.07	±3.63	±2.30	±1.73	±0.93	±0.55	∓0.84
K-factor normalization mass [%]	+1.66 −1.60	+2.27 −2.20	+2.59 −2.50	+2.72 −2.63	+2.74 −2.66	+2.77 −2.68	+2.80 −2.71	+2.83 −2.74	+2.84 −2.75	+2.83 −2.74
K-factor normalization PDFAS [%]	±2.51	±3.44	±3.91	±4.11	±4.15	±4.19	±4.24	±4.28	±4.30	±4.29
K-factor normalization scale [%]	+1.41 −2.09	+1.94 −2.86	+2.20 −3.26	+2.32 −3.42	+2.34 −3.46	+2.36 −3.49	+2.39 −3.53	+2.41 −3.56	+2.42 −3.58	+2.42 −3.57
Luminosity [%]	∓2.05	∓2.05	∓2.05	∓2.05	∓2.05	∓2.05	∓2.05	∓2.05	∓2.05	∓2.05
MCSignal stat. [%]	±2.31	±1.60	±1.39	±1.24	±1.41	±1.42	±1.68	±2.21	±3.62	±6.44
QCD stat. [%]	±9.44	±3.13	±1.80	±1.14	±1.03	±0.80	±0.74	±0.74	±0.92	±1.07
ISR/FSR + scale [%]	+19.3 −6.17	+4.92 −4.13	+3.48 −1.63	∓0.78	±0.79	−2.78 +1.84	−3.34 +1.14	−5.10 +2.31	−4.05 +3.90	+14.4 −0.22
Alternate hard-scattering model [%]	∓17.1	±0.99	±1.84	∓2.17	±0.24	±3.31	∓3.14	±4.58	±2.73	±11.5
Alternate parton-shower model [%]	±3.25	∓2.17	∓4.75	∓9.42	∓7.20	∓6.83	∓12.0	∓13.6	∓7.10	∓10.0
Inter PDF [%]	∓0.56	∓0.24	∓0.14	∓0.11	-	-	-	-	-	-
Intra PDF [%]	±0.73	±0.77	±0.68	±0.60	±0.56	±0.57	±0.46	±0.40	±0.31	±0.28

TABLE D.20: Table of systematics for the absolute differential cross-section at the parton level for the p_T^{top1} observable.

Bins [Unit $y^{topleading}$]	0–0.30	0.30–0.60	0.60–0.90	0.90–1.20	1.20–1.50	1.50–2	2–2.50
$d\sigma$ / $dy^{topleading}$ [pb/ Unit $y^{topleading}$]	$5.26 \cdot 10^2$	$4.98 \cdot 10^2$	$4.46 \cdot 10^2$	$4.00 \cdot 10^2$	$3.13 \cdot 10^2$	$2.34 \cdot 10^2$	$1.39 \cdot 10^2$
Total Uncertainty [%]	$^{+17.7}_{-17.4}$	$^{+17.2}_{-17.6}$	$^{+18.0}_{-17.6}$	$^{+17.3}_{-17.4}$	$^{+19.3}_{-16.4}$	$^{+21.2}_{-20.8}$	$^{+30.8}_{-31.4}$
Statistics [%]	± 1.6	± 1.8	± 1.9	± 2.1	± 2.6	± 2.5	± 7.4
Systematics [%]	$^{+17.5}_{-17.3}$	$^{+17.1}_{-17.4}$	$^{+17.8}_{-17.4}$	$^{+17.0}_{-17.2}$	$^{+18.9}_{-16.0}$	$^{+20.9}_{-20.4}$	$^{+28.5}_{-29.3}$
Jet vertex fraction [%]	$^{+0.44}_{-0.47}$	$^{+0.44}_{-0.47}$	$^{+0.52}_{-0.54}$	$^{+0.44}_{-0.47}$	$^{+0.42}_{-0.45}$	$^{+0.43}_{-0.46}$	$^{+0.34}_{-0.39}$
b-Tagged jet energy scale (JES) [%]	$^{+0.55}_{-0.89}$	$^{+0.42}_{-0.79}$	$^{+1.02}_{-0.77}$	$^{+1.09}_{-0.92}$	$^{+1.14}_{-0.80}$	$^{+0.70}_{-0.90}$	$^{+0.94}_{-1.30}$
Effective detector NP set 1 (JES) [%]	$^{+1.68}_{-1.44}$	$^{+1.05}_{-1.91}$	$^{+2.38}_{-1.68}$	$^{+2.35}_{-2.27}$	$^{+2.19}_{-1.28}$	$^{+2.13}_{-1.91}$	$^{+0.82}_{-2.55}$
Effective mixed NP set 1 (JES) [%]	$^{+0.48}_{-0.17}$	∓ 0.27	± 0.37	$^{+0.69}_{-0.60}$	$^{+0.16}_{-0.35}$	$^{+0.62}_{-0.35}$	$^{+1.15}_{-2.06}$
Effective mixed NP set 2 (JES) [%]	$^{-0.35}_{+0.37}$	∓ 0.18	$^{-0.19}_{+0.36}$	$^{-0.40}_{+0.46}$	$^{-0.31}_{+0.27}$	$^{-0.17}_{+0.28}$	$^{-0.32}_{+0.85}$
Effective mixed NP set 3 (JES) [%]	-	-	-	-	-	$^{-0.17}$	± 0.39
Effective modelling NP set 1 (JES) [%]	$^{+6.29}_{-6.37}$	$^{+6.07}_{-6.57}$	$^{+6.73}_{-6.16}$	$^{+5.97}_{-6.22}$	$^{+7.34}_{-5.75}$	$^{+6.94}_{-6.90}$	$^{+2.06}_{-2.98}$
Effective modelling NP set 2 (JES) [%]	$^{+0.99}_{-0.90}$	$^{+0.60}_{-1.30}$	$^{+1.16}_{-0.93}$	$^{+1.40}_{-1.52}$	$^{+2.08}_{-1.20}$	$^{+1.26}_{-0.85}$	$^{+0.79}_{-2.09}$
Effective modelling NP set 3 (JES) [%]	$^{+0.38}_{-0.33}$	$^{+0.24}_{-0.41}$	$^{+0.71}_{-0.66}$	$^{+0.37}_{-0.21}$	-	$^{+0.48}_{-0.26}$	∓ 1.38
Effective modelling NP set 4 (JES) [%]	$^{+0.50}_{-0.40}$	$^{+0.19}_{-0.37}$	$^{+0.69}_{-0.23}$	$^{+0.63}_{-0.98}$	$^{+0.41}_{-0.29}$	$^{+0.64}_{-0.45}$	$^{+0.69}_{-0.76}$
Effective statistical NP set 1 (JES) [%]	-	-	-	-	-	-	-
Effective statistical NP set 2 (JES) [%]	$^{-0.32}_{+0.33}$	$^{-0.34}_{+0.26}$	$^{-0.36}_{+0.43}$	$^{-0.38}_{+0.58}$	-	$^{-0.57}_{+0.50}$	$^{-0.28}_{+0.56}$
Effective statistical NP set 3 (JES) [%]	-	$^{-}_{-0.16}$	-	± 0.21	∓ 0.21	-	$^{-0.31}_{+0.65}$
Effective statistical NP set 4 (JES) [%]	$^{+0.12}_{-0.14}$	-	-	± 0.15	-	∓ 0.30	$^{+1.02}_{-0.12}$
Effective statistical NP set 5 (JES) [%]	$^{-0.31}_{+0.11}$	$^{-0.14}_{+0.21}$	$^{-0.21}_{+0.27}$	$^{-0.23}_{+0.42}$	$^{-0.32}_{-}$	$^{-0.25}_{+0.29}$	$^{-0.40}_{+1.07}$
Effective statistical NP set 6 (JES) [%]	$^{+0.14}_{-0.15}$	-	-	$^{+0.32}_{-}$	-	-	$^{+0.89}_{-0.18}$
η intercalibration model (JES) [%]	$^{+0.98}_{-0.72}$	$^{+0.57}_{-0.90}$	$^{+1.38}_{-1.32}$	$^{+2.15}_{-2.41}$	$^{+2.46}_{-1.23}$	$^{+2.96}_{-2.27}$	$^{+1.53}_{-4.55}$
high E η intercalibration non closure (JES) [%]	-	-	-	-	-	-	-
neg η intercalibration non closure (JES) [%]	-	-	-	-	-	-	$^{+0.31}_{-0.20}$
pos η intercalibration non closure (JES) [%]	-	-	-	-	-	-	$^{+0.37}_{-0.13}$
η intercalibration total stat (JES) [%]	$^{+0.48}_{-0.44}$	$^{+0.34}_{-0.36}$	$^{+0.62}_{-0.55}$	$^{+0.75}_{-0.60}$	$^{+0.30}_{-0.11}$	$^{+0.78}_{-0.68}$	$^{+0.84}_{-0.78}$
Flavour composition (JES) [%]	$^{+0.84}_{-0.69}$	$^{+1.04}_{-0.79}$	$^{+1.12}_{-0.66}$	$^{+0.94}_{-1.10}$	$^{+1.39}_{-0.40}$	$^{+1.64}_{-1.02}$	$^{+0.42}_{-0.25}$
Flavour response (JES) [%]	$^{-2.60}_{+3.25}$	$^{-2.90}_{+2.34}$	$^{-3.20}_{+3.46}$	$^{-3.77}_{+3.56}$	$^{-3.45}_{+3.74}$	$^{-4.27}_{+4.39}$	$^{-1.09}_{+3.68}$
Pile-up offset μ (JES) [%]	± 0.19	-	$^{-0.14}_{+0.40}$	∓ 0.20	± 0.14	$^{-0.23}_{+0.27}$	$^{-2.22}_{+0.90}$
Pile-up offset N_{PV} (JES) [%]	$^{+0.58}_{-0.29}$	-	± 0.22	$^{+0.42}_{-0.14}$	$^{+0.52}_{-0.45}$	± 0.32	± 0.99
Pile-up offset p_T (JES) [%]	$^{+0.32}_{-0.35}$	-	$^{-}_{+0.29}$	$^{+0.20}_{-0.38}$	-	$^{+0.26}_{-0.13}$	∓ 1.04
Pile-up offset ρ topology (JES) [%]	$^{+3.48}_{-3.36}$	$^{+3.40}_{-3.45}$	$^{+4.09}_{-3.66}$	$^{+3.71}_{-4.16}$	$^{+4.47}_{-3.14}$	$^{+4.31}_{-3.64}$	$^{+1.46}_{-1.27}$
Punch-through (JES) [%]	-	-	-	-	-	-	-
Single particle high-p_T (JES) [%]	-	-	-	-	-	-	-
b-Quark tagging efficiency (eigenvector 0) [%]	$^{-3.78}_{+3.84}$	$^{-3.81}_{+3.87}$	$^{-3.81}_{+3.88}$	$^{-3.80}_{+3.87}$	$^{-3.73}_{+3.80}$	$^{-3.65}_{+3.71}$	$^{-3.65}_{+3.71}$
b-Quark tagging efficiency (eigenvector 1) [%]	∓ 0.71	$^{-0.74}_{+0.75}$	$^{-0.70}_{+0.71}$	∓ 0.69	∓ 0.68	∓ 0.68	∓ 0.60
b-Quark tagging efficiency (eigenvector 2) [%]	$^{+1.38}_{-1.37}$	$^{+1.39}_{-1.38}$	$^{+1.39}_{-1.38}$	$^{+1.37}_{-1.36}$	± 1.38	$^{+1.38}_{-1.37}$	$^{+1.34}_{-1.33}$
b-Quark tagging efficiency (eigenvector 3) [%]	-	-	-	-	-	-	-
b-Quark tagging efficiency (eigenvector 4) [%]	∓ 0.19	∓ 0.19	∓ 0.19	∓ 0.19	∓ 0.19	∓ 0.20	∓ 0.18
b-Quark tagging efficiency (eigenvector 5) [%]	-	-	-	-	-	-	-
c-Quark tagging efficiency (eigenvector 0) [%]	± 0.64	± 0.61	± 0.63	± 0.59	$^{+0.63}_{-0.62}$	$^{+0.59}_{-0.58}$	± 0.52
c-Quark tagging efficiency (eigenvector 1) [%]	± 0.27	± 0.24	± 0.27	± 0.25	± 0.24	± 0.24	± 0.21
c-Quark tagging efficiency (eigenvector 2) [%]	-	-	-	-	-	-	± 0.10
Light-jet tagging efficiency (eigenvector 0) [%]	$^{+0.66}_{-0.65}$	$^{+0.64}_{-0.65}$	$^{+0.61}_{-0.60}$	$^{+0.52}_{-0.51}$	± 0.56	$^{+0.63}_{-0.62}$	$^{+0.70}_{-0.69}$
Light-jet tagging efficiency (eigenvector 1) [%]	-	-	-	-	-	-	-
Light-jet tagging efficiency (eigenvector 2) [%]	-	-	-	-	-	-	-
Light-jet tagging efficiency (eigenvector 3) [%]	-	-	-	-	-	-	-
Light-jet tagging efficiency (eigenvector 4) [%]	-	-	-	-	-	-	-
Light-jet tagging efficiency (eigenvector 5) [%]	-	-	-	-	-	-	-
Light-jet tagging efficiency (eigenvector 6) [%]	-	-	-	-	-	-	-
Light-jet tagging efficiency (eigenvector 7) [%]	-	-	-	-	-	-	-
Light-jet tagging efficiency (eigenvector 8) [%]	-	-	-	-	-	-	-
Light-jet tagging efficiency (eigenvector 9) [%]	-	-	-	-	-	-	-
Light-jet tagging efficiency (eigenvector 10) [%]	-	-	-	-	-	-	-
b-Quark tagging extrapolation [%]	∓ 0.11	-	∓ 0.10	-	∓ 0.10	-	∓ 0.11
b-Quark tagging extrapolation from c-Quark [%]	-	-	-	-	-	-	-
JET JER cross calibration forward [%]	-	-	-	-	-	-	-
JET JER noise forward [%]	-	-	-	-	-	-	-
JET JER NP0 [%]	-	-	-	-	-	-	-
JET JER NP1 [%]	-	∓ 1.01	± 0.23	∓ 0.48	± 0.32	$^{+0.40}_{-0.19}$	∓ 1.14
JET JER NP2 [%]	$^{-}_{-0.53}$	∓ 0.84	± 0.32	± 0.51	± 0.16	$^{-0.21}_{+0.67}$	$^{+0.92}_{-2.05}$
JET JER NP3 [%]	$^{+0.18}_{-0.11}$	∓ 0.40	$^{-0.19}_{+0.83}$	∓ 1.46	∓ 0.26	∓ 0.30	± 0.71
JET JER NP4 [%]	-	∓ 0.78	$^{+0.89}_{-0.21}$	± 0.31	∓ 0.22	± 0.37	$^{-2.52}_{+2.32}$
JET JER NP5 [%]	-	± 0.24	± 0.44	∓ 0.47	$^{-}_{+0.58}$	$^{+0.39}_{-0.70}$	$^{-3.51}_{+1.56}$
JET JER NP6 [%]	± 0.20	∓ 0.45	± 0.90	∓ 0.60	± 0.21	∓ 0.69	∓ 1.93
JET JER NP7 [%]	$^{-0.24}_{+0.36}$	$^{-}_{-0.94}$	± 0.86	∓ 0.33	$^{+0.55}_{-}$	$^{+0.33}_{-0.38}$	$^{+2.11}_{-1.67}$
JET JER NP8 [%]	-	-	-	-	-	-	-
QCD estimation [%]	± 4.11	± 4.60	± 4.92	± 5.78	± 5.30	± 4.05	± 4.51
K-factor normalization mass [%]	$^{+2.69}_{-2.60}$	$^{+2.70}_{-2.62}$	$^{+2.69}_{-2.60}$	$^{+2.69}_{-2.61}$	$^{+2.67}_{-2.59}$	$^{+2.64}_{-2.56}$	$^{+2.65}_{-2.57}$
K-factor normalization PDFAS [%]	± 4.07	± 4.09	± 4.06	± 4.08	± 4.04	± 4.00	± 4.02
K-factor normalization scale [%]	$^{+2.29}_{-3.39}$	$^{+2.30}_{-3.40}$	$^{+2.29}_{-3.38}$	$^{+2.30}_{-3.39}$	$^{+2.28}_{-3.37}$	$^{+2.25}_{-3.33}$	$^{+2.26}_{-3.34}$
Luminosity [%]	∓ 2.05	∓ 2.05	∓ 2.05	∓ 2.05	∓ 2.05	∓ 2.05	∓ 2.05
MCSignal stat. [%]	± 1.22	± 1.29	± 1.36	± 1.55	± 1.82	± 1.88	± 5.76
QCD stat. [%]	± 1.09	± 1.16	± 1.24	± 1.47	± 1.83	± 2.02	± 6.71
ISR/FSR + scale [%]	$^{+3.29}_{-1.02}$	$^{+3.43}_{-1.50}$	∓ 1.88	$^{+3.37}_{-1.34}$	$^{+8.05}_{-1.58}$	$^{+4.11}_{-2.81}$	∓ 6.90
Alternate hard-scattering model [%]	∓ 4.41	∓ 6.71	∓ 7.71	± 1.34	∓ 6.11	∓ 12.7	∓ 20.2
Alternate parton-shower model [%]	∓ 11.7	∓ 9.99	∓ 9.24	∓ 10.4	∓ 8.31	∓ 8.86	∓ 14.8
Inter PDF [%]	∓ 0.63	∓ 0.59	∓ 0.42	∓ 0.23	-	∓ 0.23	∓ 1.70
Intra PDF [%]	± 1.16	± 1.19	± 1.17	± 1.10	± 1.34	± 1.81	± 3.32

TABLE D.21: Table of systematics for the absolute differential cross-section at the parton level for the y_{top1} observable.

Bins [Unit $p_T^{topsubleading}$]	0–125	125–175	175–220	220–270	270–330	330–400	400–500	500–1000
$d\sigma$ / $dp_T^{topsubleading}$ [pb/ Unit $p_T^{topsubleading}$]	$3.13 \cdot 10^{0}$	$2.63 \cdot 10^{0}$	$1.36 \cdot 10^{0}$	$5.59 \cdot 10^{-1}$	$2.21 \cdot 10^{-1}$	$7.71 \cdot 10^{-2}$	$2.39 \cdot 10^{-2}$	$2.08 \cdot 10^{-3}$
Total Uncertainty [%]	$^{+34.9}_{-32.8}$	$^{+22.1}_{-20.2}$	$^{+20.6}_{-19.4}$	$^{+17.1}_{-17.0}$	$^{+14.3}_{-14.0}$	$^{+18.6}_{-18.2}$	$^{+21.8}_{-21.6}$	$^{+55.9}_{-54.9}$
Statistics [%]	±3.6	±2.0	±1.7	±1.7	±1.9	±2.4	±3.9	±13.
Systematics [%]	$^{+34.2}_{-32.1}$	$^{+21.9}_{-19.9}$	$^{+20.4}_{-19.2}$	±16.9	$^{+14.1}_{-13.8}$	$^{+18.3}_{-18.0}$	$^{+21.3}_{-21.1}$	$^{+53.3}_{-52.2}$
Jet vertex fraction [%]	$^{+0.55}_{-0.57}$	$^{+0.62}_{-0.64}$	$^{+0.51}_{-0.54}$	$^{+0.37}_{-0.40}$	$^{+0.24}_{-0.26}$	$^{+0.16}_{-0.19}$	$^{+0.12}_{-0.14}$	$^{+0.32}_{-0.33}$
b-Tagged jet energy scale (JES) [%]	$^{+0.36}_{-0.66}$	$^{+0.40}_{-0.83}$	$^{+1.36}_{-0.90}$	$^{+0.72}_{-0.85}$	$^{+0.64}_{-0.65}$	$^{+0.79}_{-0.83}$	$^{+0.68}_{-0.84}$	$^{+0.44}_{-1.50}$
Effective detector NP set 1 (JES) [%]	$^{+2.06}_{-2.73}$	$^{+1.58}_{-2.39}$	$^{+2.68}_{-2.03}$	$^{+1.50}_{-1.55}$	$^{+1.48}_{-0.93}$	$^{+1.19}_{-1.03}$	$^{+2.22}_{-1.32}$	$^{+3.77}_{-2.91}$
Effective mixed NP set 1 (JES) [%]	$^{+0.60}_{-1.24}$	±0.39	$^{+0.60}_{-}$	∓0.28	$^{-0.11}_{+0.23}$	$^{+0.53}_{-1.13}$	$^{+1.94}_{-1.31}$	$^{+5.89}_{-0.71}$
Effective mixed NP set 2 (JES) [%]	$^{-0.40}_{+0.85}$	±0.23	$^{-0.22}_{+0.45}$	∓0.43	$^{-0.19}_{+0.18}$	$^{-0.36}_{+0.38}$	$^{-1.02}_{+1.04}$	±1.34
Effective mixed NP set 3 (JES) [%]	$^{+0.28}_{-}$	-	-	-	-	$^{+0.21}_{-0.12}$	$^{+0.11}_{-0.22}$	±0.58
Effective modelling NP set 1 (JES) [%]	$^{+8.24}_{-8.01}$	$^{+7.81}_{-8.34}$	$^{+7.59}_{-7.52}$	$^{+4.94}_{-5.36}$	$^{+4.12}_{-2.28}$	$^{+4.28}_{-3.09}$	$^{+3.82}_{-3.73}$	$^{+6.13}_{-4.40}$
Effective modelling NP set 2 (JES) [%]	∓0.96	$^{+0.27}_{-0.73}$	$^{+2.15}_{-1.37}$	±1.22	$^{+1.02}_{-0.86}$	$^{+1.34}_{-1.14}$	$^{+2.12}_{-1.73}$	$^{+4.35}_{-3.33}$
Effective modelling NP set 3 (JES) [%]	$^{+1.07}_{-0.78}$	±1.13	$^{+0.21}_{-}$	$^{+0.12}_{-0.61}$	$^{+0.62}_{-0.17}$	$^{-0.80}_{+0.74}$	$^{-0.15}_{+1.12}$	$^{-0.27}_{+0.34}$
Effective modelling NP set 4 (JES) [%]	$^{+0.99}_{-0.69}$	$^{+0.42}_{-}$	$^{+0.83}_{-0.47}$	$^{+0.18}_{-0.56}$	$^{+0.20}_{-0.27}$	$^{+0.40}_{-0.35}$	$^{+1.02}_{-1.07}$	±2.14
Effective statistical NP set 1 (JES) [%]	-	-	-	-	-	-	-	-
Effective statistical NP set 2 (JES) [%]	$^{-0.63}_{+0.96}$	$^{-0.52}_{+0.44}$	$^{-0.36}_{+0.47}$	$^{-0.17}_{-}$	$^{-0.16}_{+0.28}$	$^{-}_{+0.11}$	$^{-0.26}_{+0.61}$	±1.45
Effective statistical NP set 3 (JES) [%]	±0.46	±0.28	-	-	$^{+0.27}_{-0.23}$	$^{-0.31}_{+0.36}$	$^{-0.79}_{+0.77}$	±1.06
Effective statistical NP set 4 (JES) [%]	±0.26	$^{-0.23}_{+0.30}$	$^{+0.33}_{-}$	$^{-}_{-0.33}$	$^{+0.13}_{-0.19}$	$^{+0.37}_{-0.52}$	±0.37	$^{-}_{+0.64}$
Effective statistical NP set 5 (JES) [%]	±0.31	$^{-0.16}_{+0.18}$	$^{-}_{-0.41}$	$^{-0.23}_{-0.45}$	$^{-0.40}_{+0.22}$	-	±0.24	-
Effective statistical NP set 6 (JES) [%]	$^{+0.37}_{-}$	-	$^{+0.19}_{-0.11}$	∓0.17	-	$^{+0.18}_{-0.15}$	$^{+0.66}_{-0.37}$	±0.97
η intercalibration model (JES) [%]	$^{+2.92}_{-2.20}$	$^{+1.84}_{-1.80}$	$^{+2.07}_{-2.06}$	$^{+0.78}_{-1.00}$	$^{+0.99}_{-0.50}$	$^{+0.58}_{-0.39}$	$^{+1.53}_{-1.19}$	$^{+2.34}_{-0.81}$
high E η intercalibration non closure (JES) [%]	-	-	-	-	-	-	-	-
neg η intercalibration non closure (JES) [%]	±0.11	-	-	-	-	-	-	-
pos η intercalibration non closure (JES) [%]	±0.15	-	-	-	-	-	-	-
η intercalibration total stat (JES) [%]	$^{+1.30}_{-1.16}$	$^{+0.49}_{-0.53}$	$^{+0.66}_{-0.46}$	$^{+0.24}_{-0.35}$	$^{+0.40}_{-}$	$^{+0.16}_{-0.28}$	$^{+1.18}_{-0.44}$	±1.36
Flavour composition (JES) [%]	$^{+1.47}_{-0.63}$	$^{+1.41}_{-1.22}$	$^{+1.28}_{-0.96}$	$^{+0.64}_{-0.60}$	+0.68	$^{+0.22}_{-0.17}$	$^{+1.07}_{-0.43}$	±2.28
Flavour response (JES) [%]	$^{-5.32}_{+5.19}$	$^{-4.15}_{+3.34}$	$^{-3.98}_{+4.16}$	$^{-2.51}_{+2.65}$	$^{-1.52}_{+2.02}$	$^{-1.68}_{+2.24}$	$^{-1.14}_{+1.69}$	$^{-5.39}_{+3.69}$
Pile-up offset μ (JES) [%]	$^{-0.40}_{+0.59}$	$^{-0.17}_{+0.32}$	$^{-}_{+0.28}$	∓0.25	±0.43	$^{-}_{-0.19}$	±0.36	±0.85
Pile-up offset N_{PV} (JES) [%]	$^{-0.53}_{+2.35}$	$^{+0.57}_{-0.14}$	$^{+1.02}_{-0.80}$	$^{+0.22}_{-0.10}$	∓0.30	$^{+0.44}_{-0.38}$	±0.45	±1.36
Pile-up offset p_T (JES) [%]	$^{-0.78}_{+0.61}$	±0.24	$^{+0.62}_{-0.57}$	$^{+0.10}_{-0.38}$	∓0.13	$^{+0.55}_{-0.22}$	$^{+0.91}_{-0.38}$	±1.29
Pile-up offset ρ topology (JES) [%]	$^{+4.81}_{-4.84}$	$^{+3.93}_{-4.26}$	$^{+4.78}_{-4.66}$	$^{+3.03}_{-2.86}$	$^{+2.41}_{-2.00}$	$^{+2.65}_{-1.62}$	$^{+1.92}_{-1.98}$	$^{+1.40}_{-2.27}$
Punch-through (JES) [%]	-	-	-	-	-	-	-	$^{-}_{+0.66}$
Single particle high-p_T (JES) [%]	-	-	-	-	-	-	-	-
b-Quark tagging efficiency (eigenvector 0) [%]	$^{-2.11}_{+2.14}$	$^{-3.43}_{+3.48}$	$^{-3.96}_{+4.03}$	$^{-3.93}_{+3.99}$	$^{-3.81}_{+3.88}$	$^{-3.78}_{+3.85}$	$^{-3.97}_{+4.05}$	$^{-4.97}_{+5.08}$
b-Quark tagging efficiency (eigenvector 1) [%]	∓0.42	∓0.20	∓0.35	∓0.66	$^{-1.08}_{+1.09}$	$^{-1.61}_{+1.65}$	$^{-2.60}_{+2.63}$	$^{-5.35}_{+5.51}$
b-Quark tagging efficiency (eigenvector 2) [%]	±1.13	±1.22	$^{+1.36}_{-1.35}$	±1.43	$^{+1.47}_{-1.46}$	$^{+1.47}_{-1.46}$	$^{+1.33}_{-1.32}$	±0.68
b-Quark tagging efficiency (eigenvector 3) [%]	∓0.43	∓0.36	∓0.12	±0.13	±0.44	±0.63	±0.81	$^{+0.82}_{-0.81}$
b-Quark tagging efficiency (eigenvector 4) [%]	∓0.12	∓0.17	∓0.22	∓0.25	∓0.21	∓0.14	-	±0.10
b-Quark tagging efficiency (eigenvector 5) [%]	±0.13	±0.10	-	-	-	-	-	-
c-Quark tagging efficiency (eigenvector 0) [%]	±0.34	±0.45	$^{+0.60}_{-0.59}$	$^{+0.70}_{-0.69}$	$^{+0.76}_{-0.75}$	$^{+0.82}_{-0.81}$	$^{+0.88}_{-0.87}$	±0.93
c-Quark tagging efficiency (eigenvector 1) [%]	-	±0.13	±0.23	±0.31	±0.36	±0.41	±0.43	±0.48
c-Quark tagging efficiency (eigenvector 2) [%]	-	-	-	-	±0.10	±0.16	±0.17	±0.20
Light-jet tagging efficiency (eigenvector 0) [%]	$^{+0.44}_{-0.43}$	±0.60	$^{+0.56}_{-0.55}$	±0.56	$^{+0.71}_{-0.72}$	±0.73	±0.84	$^{+1.09}_{-1.08}$
Light-jet tagging efficiency (eigenvector 1) [%]	-	-	-	-	-	-	-	-
Light-jet tagging efficiency (eigenvector 2) [%]	-	-	-	-	-	-	-	-
Light-jet tagging efficiency (eigenvector 3) [%]	-	-	-	-	-	-	-	-
Light-jet tagging efficiency (eigenvector 4) [%]	-	-	-	-	-	-	-	-
Light-jet tagging efficiency (eigenvector 5) [%]	-	-	-	-	-	-	-	-
Light-jet tagging efficiency (eigenvector 6) [%]	-	-	-	-	-	-	-	-
Light-jet tagging efficiency (eigenvector 7) [%]	-	-	-	-	-	-	-	-
Light-jet tagging efficiency (eigenvector 8) [%]	-	-	-	-	-	-	-	-
Light-jet tagging efficiency (eigenvector 9) [%]	-	-	-	-	-	-	-	-
Light-jet tagging efficiency (eigenvector 10) [%]	-	-	-	-	-	-	-	-
b-Quark tagging extrapolation [%]	-	-	-	-	∓0.13	∓0.18	∓0.23	∓0.34
b-Quark tagging extrapolation from c-Quark [%]	-	-	-	-	-	-	-	-
JET JER cross calibration forward [%]	-	-	-	-	-	-	-	-
JET JER noise forward [%]	-	-	-	-	-	-	-	-
JET JER NP0 [%]	-	-	-	-	-	-	-	-
JET JER NP1 [%]	-	-	∓0.55	∓1.07	±0.74	$^{+0.83}_{-}$	±0.39	±5.50
JET JER NP2 [%]	$^{-0.15}_{+0.96}$	∓0.36	$^{+0.25}_{-1.61}$	$^{-}_{-0.83}$	$^{-}_{+1.01}$	$^{-0.62}_{+1.33}$	±2.14	$^{-1.92}_{+2.13}$
JET JER NP3 [%]	±1.25	±0.43	∓0.88	∓1.19	$^{-0.20}_{+0.52}$	$^{-0.26}_{+1.04}$	$^{+1.22}_{-}$	$^{+1.06}_{-3.22}$
JET JER NP4 [%]	$^{+0.64}_{-1.18}$	$^{-0.10}_{+0.68}$	$^{+0.30}_{-0.66}$	∓0.54	±0.58	±0.87	±0.87	±6.80
JET JER NP5 [%]	$^{-0.25}_{+1.81}$	$^{+0.25}_{-0.70}$	$^{+0.20}_{-0.17}$	∓0.69	±0.40	±1.03	$^{-0.13}_{+1.02}$	$^{-1.71}_{+1.63}$
JET JER NP6 [%]	$^{-0.64}_{+1.76}$	∓0.80	∓0.52	∓0.49	±0.48	±0.58	±0.58	$^{-0.38}_{+2.84}$
JET JER NP7 [%]	$^{-}_{+1.40}$	$^{-}_{-0.26}$	∓0.65	∓0.47	±0.52	±0.43	$^{-0.14}_{+0.92}$	$^{-0.95}_{+7.50}$
JET JER NP8 [%]	-	-	-	-	-	-	-	-
QCD estimation [%]	∓24.4	∓2.42	±6.04	±4.06	±1.77	-	∓0.92	∓3.08
K-factor normalization mass [%]	$^{+1.90}_{-1.84}$	$^{+2.34}_{-2.26}$	$^{+2.68}_{-2.59}$	$^{+2.79}_{-2.70}$	$^{+2.81}_{-2.72}$	$^{+2.81}_{-2.72}$	$^{+2.79}_{-2.70}$	$^{+2.77}_{-2.68}$
K-factor normalization PDFAS [%]	±2.88	±3.54	±4.05	±4.22	±4.26	±4.25	±4.22	±4.19
K-factor normalization scale [%]	$^{+1.62}_{-2.39}$	$^{+1.99}_{-2.95}$	$^{+2.28}_{-3.37}$	$^{+2.38}_{-3.52}$	$^{+2.40}_{-3.54}$	$^{+2.39}_{-3.54}$	$^{+2.38}_{-3.51}$	$^{+2.36}_{-3.49}$
Luminosity [%]	∓2.05	∓2.05	∓2.05	∓2.05	∓2.05	∓2.05	∓2.05	∓2.05
MCSignal stat. [%]	±1.46	±1.21	±1.24	±1.26	±1.41	±1.85	±2.94	±10.3
QCD stat. [%]	±5.67	±2.32	±1.24	±0.78	±0.50	±0.39	±0.35	±0.67
ISR/FSR + scale [%]	$^{+13.3}_{-7.08}$	$^{+11.8}_{-5.84}$	$^{+7.19}_{-3.15}$	$^{+3.73}_{-1.39}$	±1.55	∓2.98	$^{-1.60}_{-}$	±27.4
Alternate hard-scattering model [%]	∓14.5	∓13.4	∓9.19	∓3.56	±0.35	∓7.20	∓8.47	±23.4
Alternate parton-shower model [%]	∓0.97	∓3.24	∓8.31	∓11.7	∓10.1	∓13.2	∓16.2	∓33.6
Inter PDF [%]	∓0.57	∓0.39	∓0.19	∓0.15	-	-	-	∓0.10
Intra PDF [%]	±0.70	±0.55	±0.56	±0.57	±0.51	±0.48	±0.31	±0.40

TABLE D.22: Table of systematics for the absolute differential cross-section at the parton level for the p_T^{top2} observable.

Bins [Unit $y^{topsubleading}$]	0–0.30	0.30–0.60	0.60–0.90	0.90–1.20	1.20–1.50	1.50–2	2–2.50
$d\sigma$ / $dy^{topsubleading}$ [pb/ Unit $y^{topsubleading}$]	$4.92 \cdot 10^2$	$4.83 \cdot 10^2$	$4.53 \cdot 10^2$	$3.90 \cdot 10^2$	$3.45 \cdot 10^2$	$2.36 \cdot 10^2$	$1.18 \cdot 10^2$
Total Uncertainty [%]	±15.0	+17.7 −17.1	+17.5 −17.3	+17.2 −17.7	+22.2 −21.5	+22.6 −22.8	+33.5 −25.3
Statistics [%]	±1.8	±1.8	±1.9	±2.1	±2.4	±2.5	±7.3
Systematics [%]	±14.8	+17.5 −16.9	+17.3 −17.1	+17.0 −17.4	+21.9 −21.2	+22.3 −22.5	+31.7 −22.9
Jet vertex fraction [%]	+0.44 −0.46	+0.45 −0.47	+0.48 −0.50	+0.49 −0.51	+0.43 −0.46	+0.41 −0.44	±0.63
b-Tagged jet energy scale (JES) [%]	+0.83 −0.59	+0.97 −0.94	+0.31 −0.71	+1.24 −1.13	+0.64 −1.02	+0.56 −0.73	+0.89 −1.77
Effective detector NP set 1 (JES) [%]	+1.75 −1.56	+2.28 −1.49	+1.40 −1.38	+1.57 −2.01	+2.51 −2.21	+1.97 −2.22	+0.62 −3.66
Effective mixed NP set 1 (JES) [%]	±0.25	+0.42 −0.38	+0.26 −0.35	+0.17 −0.19	+0.66 −0.61	+0.13 −0.22	+0.66 −1.61
Effective mixed NP set 2 (JES) [%]	±0.32	−0.54 +0.51	−0.15 -	−0.12 +0.13	−0.29 +0.35	−0.64 +0.22	−1.03 +0.12
Effective mixed NP set 3 (JES) [%]	-	±0.15	∓0.12	-	-	-	∓0.37
Effective modelling NP set 1 (JES) [%]	+5.69 −6.06	+6.09 −5.71	+5.93 −6.36	+7.07 −7.95	+8.61 −6.32	+6.38 −5.61	+3.67 −4.77
Effective modelling NP set 2 (JES) [%]	+1.11 −0.64	+1.62 −1.02	+0.61 −0.97	+0.89 −1.55	+1.67 −1.71	+1.25 −1.18	∓2.22
Effective modelling NP set 3 (JES) [%]	+0.52 −0.38	+0.31 −0.11	+0.16 −0.54	+0.53 −0.48	+0.40 −0.22	+0.33 −0.32	- −1.02
Effective modelling NP set 4 (JES) [%]	+0.54 −0.23	+0.54 −0.60	+0.33 −0.51	+0.38 −0.24	+0.86 −0.44	+0.42 −0.65	+0.18 −1.30
Effective statistical NP set 1 (JES) [%]	-	-	-	-	-	-	-
Effective statistical NP set 2 (JES) [%]	−0.30 +0.41	−0.31 +0.59	−0.31 +0.13	−0.23 +0.32	−0.18 +0.34	−0.66 +0.38	∓1.08
Effective statistical NP set 3 (JES) [%]	+0.18 −0.12	-	- −0.21	±0.25	-	∓0.13	±0.23
Effective statistical NP set 4 (JES) [%]	±0.25	+0.16 −0.26	−0.23 -	+0.28 -	-	+0.14 −0.23	+0.15 −0.32
Effective statistical NP set 5 (JES) [%]	−0.19 +0.25	−0.40 +0.34	−0.29 -	−0.13 +0.31	±0.16	−0.45 +0.19	±0.45
Effective statistical NP set 6 (JES) [%]	-	+0.42 −0.12	∓0.26	-	±0.15	+0.17 −0.37	−0.22 +0.25
η intercalibration model (JES) [%]	+1.11 −1.08	+1.76 −1.44	+1.16 −1.12	+1.38 −1.31	+1.94 −2.50	+1.99 −1.35	+2.65 −0.43
high E η intercalibration non closure (JES) [%]	-	-	-	-	-	-	-
neg η intercalibration non closure (JES) [%]	-	-	-	-	-	-	∓0.56
pos η intercalibration non closure (JES) [%]	-	-	-	-	-	-	±0.43
η intercalibration total stat (JES) [%]	+0.64 −0.25	+0.70 −0.62	+0.16 −0.28	+0.35 −0.43	+0.80 −0.47	+0.58 −0.73	+0.48 −1.64
Flavour composition (JES) [%]	+0.92 −0.67	+0.91 −0.81	+1.45 −0.55	+0.93 −0.29	+1.26 −1.38	+1.27 −1.14	+0.39 −1.54
Flavour response (JES) [%]	−2.60 +2.56	−2.98 +3.72	−2.80 +3.60	−3.81 +2.58	−4.18 +4.50	−3.74 +3.44	−2.46 +2.13
Pile-up offset μ (JES) [%]	±0.23	- +0.32	∓0.28	- +0.30	- +0.32	∓0.39	−0.79 +0.64
Pile-up offset N_{PV} (JES) [%]	±0.19	+0.41 −0.42	-	∓0.22	±0.80	±0.86	−1.65 +0.36
Pile-up offset p_T (JES) [%]	±0.20	+0.25 -	∓0.37	+0.13 −0.10	+0.35 −0.34	+0.11 −0.24	+0.39 −0.11
Pile-up offset ρ topology (JES) [%]	+3.14 −3.24	+3.89 −3.29	+4.09 −3.14	+4.15 −4.32	+4.54 −4.40	+3.12 −3.18	+2.91 −4.06
Punch-through (JES) [%]	-	-	-	-	-	-	∓0.15
Single particle high-p_T (JES) [%]	-	-	-	-	-	-	-
b-Quark tagging efficiency (eigenvector 0) [%]	−3.74 +3.80	−3.81 +3.87	−3.86 +3.94	−3.83 +3.90	−3.65 +3.71	−3.75 +3.82	−3.31 +3.37
b-Quark tagging efficiency (eigenvector 1) [%]	∓0.73	∓0.71	∓0.67	∓0.68	∓0.76	∓0.70	∓0.60
b-Quark tagging efficiency (eigenvector 2) [%]	±1.37	+1.38 −1.37	+1.40 −1.39	+1.38 −1.37	±1.38	+1.38 −1.37	+1.31 −1.30
b-Quark tagging efficiency (eigenvector 3) [%]	-	-	-	-	-	-	-
b-Quark tagging efficiency (eigenvector 4) [%]	∓0.19	∓0.19	∓0.19	∓0.19	∓0.19	∓0.20	∓0.18
b-Quark tagging efficiency (eigenvector 5) [%]	-	-	-	-	-	-	-
c-Quark tagging efficiency (eigenvector 0) [%]	±0.61	+0.65 −0.64	±0.63	±0.60	±0.60	±0.59	±0.58
c-Quark tagging efficiency (eigenvector 1) [%]	±0.24	±0.29	±0.27	±0.26	±0.24	±0.21	±0.18
c-Quark tagging efficiency (eigenvector 2) [%]	-	-	-	-	-	-	-
Light-jet tagging efficiency (eigenvector 0) [%]	±0.63	+0.66 −0.65	±0.65	±0.59	±0.43	+0.64 −0.67	±0.59
Light-jet tagging efficiency (eigenvector 1) [%]	-	-	-	-	-	-	-
Light-jet tagging efficiency (eigenvector 2) [%]	-	-	-	-	-	-	-
Light-jet tagging efficiency (eigenvector 3) [%]	-	-	-	-	-	-	-
Light-jet tagging efficiency (eigenvector 4) [%]	-	-	-	-	-	-	-
Light-jet tagging efficiency (eigenvector 5) [%]	-	-	-	-	-	-	-
Light-jet tagging efficiency (eigenvector 6) [%]	-	-	-	-	-	-	-
Light-jet tagging efficiency (eigenvector 7) [%]	-	-	-	-	-	-	-
Light-jet tagging efficiency (eigenvector 8) [%]	-	-	-	-	-	-	-
Light-jet tagging efficiency (eigenvector 9) [%]	-	-	-	-	-	-	-
Light-jet tagging efficiency (eigenvector 10) [%]	-	-	-	-	-	-	-
b-Quark tagging extrapolation [%]	-	∓0.11	∓0.11	-	-	-	-
b-Quark tagging extrapolation from c-Quark [%]	-	-	-	-	-	-	-
JET JER cross calibration forward [%]	-	-	-	-	-	-	-
JET JER noise forward [%]	-	-	-	-	-	-	-
JET JER NP0 [%]	-	-	-	-	-	-	-
JET JER NP1 [%]	∓0.68	-	+0.79 -	∓0.21	∓1.27	∓0.16	±3.83
JET JER NP2 [%]	∓0.68	±1.30	∓1.57	∓0.62	−0.76	±1.04	±2.92
JET JER NP3 [%]	- −0.25	−0.43 +0.57	+0.19 −0.46	−1.09 +0.37	−1.42 +0.45	∓0.69	±3.24
JET JER NP4 [%]	+0.27 −1.12	±1.08	∓1.30	- −0.35	±0.65	±1.02	+1.51 −1.80
JET JER NP5 [%]	−0.32 +0.19	±0.31	+0.60 −0.13	+0.46 −0.28	+0.17 −0.71	−0.88 +0.75	+1.91 −1.04
JET JER NP6 [%]	∓0.41	−0.17 +0.54	+0.18 −0.67	+0.18 −1.06	−0.40 +0.31	−0.25 +1.00	±0.19
JET JER NP7 [%]	-	±0.16	-	+0.59 −0.94	-	−0.46 +0.48	∓2.36
JET JER NP8 [%]	-	-	-	-	-	-	-
QCD estimation [%]	±3.45	±5.04	±5.60	±6.86	±4.27	±3.36	±2.07
K-factor normalization mass [%]	+2.68 −2.60	+2.68 −2.60	+2.70 −2.62	+2.69 −2.61	+2.69 −2.60	+2.66 −2.57	+2.58 −2.50
K-factor normalization PDFAS [%]	±4.06	±4.06	±4.09	±4.08	±4.07	±4.02	±3.91
K-factor normalization scale [%]	+2.28 −3.38	+2.29 −3.38	+2.30 −3.41	+2.30 −3.39	+2.29 −3.39	+2.26 −3.35	+2.20 −3.26
Luminosity [%]	∓2.05	∓2.05	∓2.05	∓2.05	∓2.05	∓2.05	∓2.05
MCSignal stat. [%]	±1.27	±1.31	±1.41	±1.56	±1.79	±1.87	±5.23
QCD stat. [%]	±1.16	±1.21	±1.31	±1.45	±1.74	±1.94	±5.72
ISR/FSR + scale [%]	+3.02 −0.41	+3.12 −1.51	+2.73 −1.56	+4.81 −2.67	+1.87 −1.79	+0.54 −3.49	+22.8 −1.72
Alternate hard-scattering model [%]	∓6.04	∓6.55	∓4.23	∓0.39	∓6.06	∓11.5	∓18.0
Alternate parton-shower model [%]	∓7.07	∓9.60	∓10.6	∓9.02	∓15.3	∓14.8	∓2.49
Inter PDF [%]	∓0.54	∓0.54	∓0.45	∓0.35	∓0.18	∓0.28	∓0.60
Intra PDF [%]	±1.23	±1.18	±1.14	±1.16	±1.16	±1.56	±2.12

TABLE D.23: Table of systematics for the absolute differential cross-section at the parton level for the y_{top2} observable.

Bins [Unit m^{tt}]	0–400	400–500	500–585	585–675	675–765	765–870	870–1000	1000–1150	1150–1500	1500–3000
$d\sigma$ / dm^{tt} [pb/ Unit m^{tt}]	$3.94 \cdot 10^{-1}$	$3.07 \cdot 10^{0}$	$1.60 \cdot 10^{0}$	$8.70 \cdot 10^{-1}$	$4.56 \cdot 10^{-1}$	$2.50 \cdot 10^{-1}$	$1.32 \cdot 10^{-1}$	$5.71 \cdot 10^{-2}$	$2.07 \cdot 10^{-2}$	$1.45 \cdot 10^{-3}$
Total Uncertainty [%]	+39.8 −37.8	+24.5 −24.2	+18.4 −17.4	+19.3 −18.5	+18.1 −19.0	+17.2 −16.0	+24.0 −24.1	+21.8 −22.6	+20.6 −22.7	+28.2 −26.9
Statistics [%]	±7.0	±2.9	±2.0	±1.8	±1.9	±2.0	±2.3	±3.3	±3.8	±8.9
Systematics [%]	+37.9 −35.9	+23.8 −23.5	+18.0 −17.0	+19.1 −18.2	+17.9 −18.8	+17.0 −15.8	+23.8 −23.9	+21.4 −22.2	+19.9 −22.1	+25.9 −24.4
Jet vertex fraction [%]	+0.62 −0.63	+0.69 −0.70	+0.56 −0.59	+0.41 −0.44	+0.39 −0.42	+0.32 −0.35	+0.29 −0.31	+0.26 −0.29	+0.25 −0.28	+0.26 −0.29
b-Tagged jet energy scale (JES) [%]	±2.02	+0.40 −0.31	+0.64 −1.19	+0.73 −0.64	+0.59 −0.81	+1.30 −1.05	+0.86 −0.89	+0.43 −1.03	+0.43 −1.01	+1.00 −0.37
Effective detector NP set 1 (JES) [%]	+0.91 −1.08	+1.43 −1.96	+2.49 −2.39	+1.95 −1.76	+1.44 −1.45	+2.21 −1.41	+2.09 −1.16	+0.84 −1.98	+1.30 −2.15	+1.06 −0.76
Effective mixed NP set 1 (JES) [%]	±1.44	+0.82 −0.51	+0.37 −0.41	±0.39	+0.23 −0.20	+0.59 −	+0.64 −0.86	+1.14 −0.98	+0.27 −1.88	+1.47 −1.15
Effective mixed NP set 2 (JES) [%]	±1.20	±0.22	−0.30 +0.17	+0.25	−0.20 +0.26	−0.37 +0.53	−0.56 +0.35	∓0.63	−0.61 +0.10	−0.57 −
Effective mixed NP set 3 (JES) [%]	+0.55 −0.18	-	-	-	-	-	-	+0.13 −0.12	−0.35 +0.19	+0.43 -
Effective modelling NP set 1 (JES) [%]	+6.42 −7.44	+6.54 −9.58	+8.08 −7.62	+6.67 −5.56	+4.44 −5.93	+6.24 −4.39	+6.04 −4.68	+4.33 −4.82	+3.64 −7.37	+7.14 −3.75
Effective modelling NP set 2 (JES) [%]	−0.34 +2.90	+0.27 −1.53	+1.51 −2.03	+1.18 −0.74	+0.56 −0.62	+1.27 −0.94	+1.69 −1.23	+1.59 −1.97	+0.94 −2.01	+1.39 −0.68
Effective modelling NP set 3 (JES) [%]	+1.75 −0.66	+0.77 −0.84	+0.49 −0.92	+0.77 −0.51	+0.51 −0.43	±0.39	∓0.19 +0.59	+0.41 -	−0.78 -	±1.21
Effective modelling NP set 4 (JES) [%]	±1.52	+0.60 -	+0.45 −0.46	+0.48 −0.35	+0.46 −0.35	+0.66 −0.27	−1.03	−0.54	−0.23	−1.13
Effective statistical NP set 1 (JES) [%]	-	-	-	-	-	-	-	-	-	-
Effective statistical NP set 2 (JES) [%]	−1.16 +0.77	−0.88 +0.48	−0.54 +0.62	−0.11 +0.54	−0.14 +0.35	−0.24 +0.31	−0.47 +0.34	-	-	−0.97 +0.80
Effective statistical NP set 3 (JES) [%]	±0.31	±0.21	+0.23 −0.17	+0.39 −0.22	-	±0.27	−0.25	−0.36 +0.13	−0.25 ∓0.14	+0.44 -
Effective statistical NP set 4 (JES) [%]	+0.38 -	±0.37	∓0.13	−0.14 +0.17	+0.37 −0.36	+0.23 -	+0.22 -	- −0.39	∓0.21	- −0.49
Effective statistical NP set 5 (JES) [%]	±0.28	−0.10	−0.54	−0.24	−0.21	−0.11	−0.23	∓0.33	-	∓0.34
Effective statistical NP set 6 (JES) [%]	+0.65 −0.11	+0.11 +0.28 −0.19	+0.39 +0.15 −0.12	+0.30 -	+0.25 +0.16 −0.26	+0.15 +0.22 -	+0.28 +0.13 −0.24	+0.13 −0.16	−0.33 +0.35	+0.43 −0.65
η intercalibration model (JES) [%]	+2.70 −1.10	+2.88 −1.91	+1.77 −2.14	+1.54 −0.87	+0.91 −0.89	+0.95 −1.20	+2.16 −1.18	+0.96 −1.38	+0.86 −2.03	+2.05 −0.14
high E η intercalibration non closure (JES) [%]	-	-	-	-	-	-	-	-	-	-
neg η intercalibration non closure (JES) [%]	-	-	-	-	-	-	-	∓0.14	-	-
pos η intercalibration non closure (JES) [%]	-	-	-	-	-	-	-	-	-	-
η intercalibration total stat (JES) [%]	+1.15 −0.61	+0.31 −0.88	+0.60 −0.41	+0.75 −0.12	+0.45 −0.58	+0.76 −0.30	+0.61 −0.57	∓0.26	±0.26	+0.74 −0.92
Flavour composition (JES) [%]	+0.69 -	+0.99 −1.28	+1.84 −1.04	+1.38 −0.24	+0.52 −0.65	+1.05 −0.49	+1.19 −0.66	- −0.51	- −0.97	±1.66 −2.26
Flavour response (JES) [%]	−7.07 +5.26	−5.84 +4.83	−4.08 +4.34	−2.33 +2.85	−2.67 +1.90	−1.94 +3.78	−2.65 +3.39	−2.52 +1.25	−4.09 +1.47	+4.30 −0.26
Pile-up offset μ (JES) [%]	±1.45	∓0.86	∓0.16	±0.63	-	±0.50	∓0.27	−0.66 +0.32	∓0.39	+0.22 +1.68
Pile-up offset N_{PV} (JES) [%]	−2.20 +3.40	- +0.35	±0.31	±0.81	+0.63 −0.97	±0.58	+0.22 −0.60	- −0.38	∓1.27	+2.15
Pile-up offset p_T (JES) [%]	−1.28 +2.27	−0.27 +0.36	+0.23	+0.26	- −0.73	±0.32	- −0.28	+0.62 −0.47	±1.01	−0.41
Pile-up offset ρ topology (JES) [%]	+4.28 −5.81	±4.73	+5.02 −4.28	+3.56 −3.26	+2.28 −3.27	+3.94 −2.53	+3.81 −2.26	+1.63 −3.21	+2.13 −4.01	+3.16 −2.21
Punch-through (JES) [%]	-	-	-	-	-	-	-	-	-	+0.29 -
Single particle high-p_T (JES) [%]	-	-	-	-	-	-	-	-	-	-
b-Quark tagging efficiency (eigenvector 0) [%]	−1.56 +1.58	−2.41 +3.44	−3.24 +3.30	−3.46 +3.52	−3.74 +3.80	−3.84 +3.90	−3.88 +3.95	−3.87 +3.94	−3.89 +3.96	−4.01 +4.09
b-Quark tagging efficiency (eigenvector 1) [%]	∓0.16	−0.21 +0.20	∓0.30	∓0.46	∓0.69	−1.01 +1.02	−1.30 +1.31	−1.49 +1.50	−1.54 +1.56	−1.79 +1.81
b-Quark tagging efficiency (eigenvector 2) [%]	±0.84	+1.06 −1.05	+1.25 −1.24	+1.31 −1.30	+1.39 −1.38	+1.44 −1.43	+1.43 −1.42	+1.38 −1.37	+1.34 −1.33	±1.32
b-Quark tagging efficiency (eigenvector 3) [%]	∓0.50	∓0.45	∓0.29	-	±0.12	±0.31	±0.42	+0.47 −0.46	±0.43	±0.57
b-Quark tagging efficiency (eigenvector 4) [%]	-	∓0.12	∓0.18	∓0.21	∓0.22	∓0.20	∓0.16	∓0.14	±0.14	∓0.14
b-Quark tagging efficiency (eigenvector 5) [%]	±0.11	±0.11	±0.10	-	-	-	-	-	-	-
c-Quark tagging efficiency (eigenvector 0) [%]	±0.17	±0.29	±0.43	±0.58	±0.68	+0.78 −0.77	±0.74	+0.72 −0.71	±0.78	±0.85
c-Quark tagging efficiency (eigenvector 1) [%]	-	-	±0.11	±0.22	±0.29	±0.35	±0.34	±0.34	±0.37	±0.41
c-Quark tagging efficiency (eigenvector 2) [%]	-	-	-	-	-	±0.10	±0.11	±0.11	±0.12	±0.16
Light-jet tagging efficiency (eigenvector 0) [%]	±0.23	±0.20	+0.49 −0.48	±0.53	+0.72 −0.71	+0.67 −0.66	±0.73	±0.49	+0.88 −0.89	±0.78
Light-jet tagging efficiency (eigenvector 1) [%]	-	-	-	-	-	-	-	-	-	-
Light-jet tagging efficiency (eigenvector 2) [%]	-	-	-	-	-	-	-	-	-	-
Light-jet tagging efficiency (eigenvector 3) [%]	-	-	-	-	-	-	-	-	-	-
Light-jet tagging efficiency (eigenvector 4) [%]	-	-	-	-	-	-	-	-	-	-
Light-jet tagging efficiency (eigenvector 5) [%]	-	-	-	-	-	-	-	-	-	-
Light-jet tagging efficiency (eigenvector 6) [%]	-	-	-	-	-	-	-	-	-	-
Light-jet tagging efficiency (eigenvector 7) [%]	-	-	-	-	-	-	-	-	-	-
Light-jet tagging efficiency (eigenvector 8) [%]	-	-	-	-	-	-	-	-	-	-
Light-jet tagging efficiency (eigenvector 9) [%]	-	-	-	-	-	-	-	-	-	-
Light-jet tagging efficiency (eigenvector 10) [%]	-	-	-	-	-	-	-	-	-	-
b-Quark tagging extrapolation [%]	-	-	-	-	-	∓0.13	∓0.15	∓0.15	∓0.19	∓0.32
b-Quark tagging extrapolation from c-Quark [%]	-	-	-	-	-	-	-	-	-	-
JET JER cross calibration forward [%]	-	-	-	-	-	-	-	-	-	-
JET JER noise forward [%]	-	-	-	-	-	-	-	-	-	-
JET JER NP0 [%]	-	-	-	-	-	-	-	-	-	-
JET JER NP1 [%]	−1.15	−0.74	∓0.32	∓1.04	∓0.94	±0.96	+1.06 −0.12	−0.19 +0.10	−0.63	+2.74 −0.45
JET JER NP2 [%]	∓3.42	∓0.97	−0.24 -	∓1.11	∓0.66	±1.46	−0.49 +1.55	+0.43 −0.98	∓1.45	±3.37
JET JER NP3 [%]	+0.82 −3.60	∓1.30	−0.28 +0.35	−0.82 +0.36	∓0.97	−0.40 +0.28	±0.80	+0.34 −0.26	∓2.79	±1.89
JET JER NP4 [%]	+2.08 −7.12	+0.68 −2.02	+0.36 −0.35	∓0.36	∓0.68	±0.90	±0.64	+0.31 −0.44	∓0.51	+1.73 -
JET JER NP5 [%]	±2.62	±0.45	−0.55 +0.14	+0.29 −1.26	+0.13 −0.36	+1.19	±0.70	∓0.54	∓1.61	±4.11
JET JER NP6 [%]	−3.27 +2.95	−2.04 +1.00	∓0.96	−0.52	∓0.77	±0.70	±0.88	−0.30 -	∓1.69	±4.74
JET JER NP7 [%]	±2.34	−0.19 +0.95	−0.92 -	∓0.66	- −0.51	±0.53	±0.92	−1.30 +0.70	- −1.37	±3.11
JET JER NP8 [%]	-	-	-	-	-	-	-	-	-	-
QCD estimation [%]	∓29.1	∓13.2	∓7.17	∓0.31	±3.34	±3.33	±3.26	±2.95	±4.09	±6.60
K-factor normalization mass [%]	+1.43 −1.38	+1.96 −1.89	+2.34 −2.26	+2.49 −2.41	+2.66 −2.58	+2.74 −2.65	+2.76 −2.67	+2.77 −2.68	+2.74 −2.65	+2.75 −2.66
K-factor normalization PDFAS [%]	±2.17	±2.96	±3.53	±3.77	±4.03	±4.15	±4.17	±4.19	±4.14	±4.16
K-factor normalization scale [%]	+1.22 −1.80	+1.67 −2.46	+1.99 −2.94	+2.12 −3.14	+2.27 −3.35	+2.34 −3.45	+2.35 −3.47	+2.36 −3.49	+2.33 −3.45	+2.34 −3.46
Luminosity [%]	∓2.05	∓2.05	∓2.05	∓2.05	∓2.05	∓2.05	∓2.05	∓2.05	∓2.05	∓2.05
MCSignal stat. [%]	±3.16	±1.64	±1.26	±1.19	±1.28	±1.42	±1.67	±2.29	±2.88	±6.22
QCD stat. [%]	±9.32	±4.82	±3.15	±2.05	±1.36	±1.04	±0.95	±1.16	±1.29	±2.39
ISR/FSR + scale [%]	+17.6 −8.53	+11.5 −6.91	+5.86 −2.97	+3.66 −0.50	±0.72	±2.13	−6.66 +1.91	−2.59 +2.66	±5.11	+0.11 −0.48
Alternate hard-scattering model [%]	∓7.39	∓10.8	∓7.11	∓9.37	∓8.14	∓2.86	∓10.2	∓14.1	∓6.73	∓2.09
Alternate parton-shower model [%]	±5.63	±2.30	±4.53	∓11.6	∓12.4	∓11.1	∓17.4	∓12.5	∓14.5	∓19.6
Inter PDF [%]	±0.63	±0.37	±0.13	-	-	±0.10	±0.20	±0.16	±0.16	±0.45
Intra PDF [%]	±0.71	±0.47	±0.45	±0.48	±0.57	±0.64	±0.71	±0.85	±0.93	±1.46

TABLE D.24: Table of systematics for the absolute differential cross-section at the parton level for the $m_{t\bar{t}}$ observable.

Bins [Unit $p_T^{t\bar{t}}$]	0–45	45–100	100–160	160–230	230–320	320–420	420–550	550–1000
$d\sigma$ / $dp_T^{t\bar{t}}$ [pb/ Unit $p_T^{t\bar{t}}$]	$9.39 \cdot 10^{0}$	$4.34 \cdot 10^{0}$	$1.59 \cdot 10^{0}$	$6.47 \cdot 10^{-1}$	$2.27 \cdot 10^{-1}$	$7.52 \cdot 10^{-2}$	$2.22 \cdot 10^{-2}$	$3.91 \cdot 10^{-3}$
Total Uncertainty [%]	+26.1 −26.0	+18.6 −17.9	+18.1 −18.6	+24.9 −24.7	+14.5 −16.1	+18.4 −19.4	+16.6 −17.5	+27.1 −25.3
Statistics [%]	±1.7	±1.3	±1.5	±1.9	±2.6	±4.3	±7.0	±11.
Systematics [%]	+26.0 −25.9	+18.5 −17.8	+18.0 −18.5	+24.7 −24.5	+14.0 −15.6	+17.4 −18.4	+14.0 −15.1	+22.6 −20.4
Jet vertex fraction [%]	+0.19 −0.21	+0.42 −0.44	+0.52 −0.55	+0.56 −0.59	+0.61 −0.64	+0.59 −0.62	+0.49 −0.52	+0.47 −0.48
b-Tagged jet energy scale (JES) [%]	+1.08 −0.98	+0.94 −0.83	+0.86 −0.91	+0.37 −0.85	- −1.10	+0.72 −0.32	±0.82	±2.37
Effective detector NP set 1 (JES) [%]	+2.26 −1.76	+2.09 −1.59	+1.30 −1.89	+2.46 −2.52	+1.53 −1.54	+0.10 −0.22	+1.54 −1.85	±2.53
Effective mixed NP set 1 (JES) [%]	±0.34	±0.10	∓0.24	+0.74 −0.65	+1.35 −0.46	∓0.81	+0.93 −0.40	+3.56 −2.62
Effective mixed NP set 2 (JES) [%]	−0.38 +0.29	- +0.17	−0.21 +0.14	−0.70 +0.26	−0.52 +0.93	+0.49 −0.25	±0.67	−1.30 +1.81
Effective mixed NP set 3 (JES) [%]	-	-	-	-	+0.26 −0.17	- +0.26	∓0.55	±1.15
Effective modelling NP set 1 (JES) [%]	+5.27 −4.97	+7.37 −5.73	+6.56 −7.10	+7.60 −7.48	+5.16 −7.19	+2.60 −5.83	+5.87 −5.19	+6.47 −1.40
Effective modelling NP set 2 (JES) [%]	+1.94 −1.40	+1.55 −1.44	+0.70 −1.20	+0.77 −0.99	+0.37 −0.20	+0.27 −0.24	+1.26 −0.31	+2.96 −1.22
Effective modelling NP set 3 (JES) [%]	+0.58 −0.31	+0.43 −0.51	+0.54 −0.67	- −0.28	±0.65	−0.79 +0.25	∓0.32	±2.29
Effective modelling NP set 4 (JES) [%]	+0.65 −0.59	+0.56 −0.21	+0.14 −0.52	+0.56 −0.66	+0.86 −0.65	±0.27	−0.19 +0.50	+1.32 −1.55
Effective statistical NP set 1 (JES) [%]	-	-	-	-	-	-	-	+0.20 -
Effective statistical NP set 2 (JES) [%]	−0.28 +0.48	- +0.34	−0.52 +0.21	−0.48 +0.42	−0.65 +0.61	-	∓0.24	±1.36
Effective statistical NP set 3 (JES) [%]	+0.15 −0.14	-	- −0.23	-	±0.36	- +0.37	+0.60 −0.62	−1.19 +1.32
Effective statistical NP set 4 (JES) [%]	+0.27 −0.33	±0.11	∓0.10	+0.16 −0.19	+0.21 -	−0.33 +0.25	−0.14 +0.52	−0.81 +0.72
Effective statistical NP set 5 (JES) [%]	−0.48 +0.54	−0.18 +0.21	−0.28 +0.10	−0.12 +0.20	−0.19 -	- +0.29	+0.56 −0.24	−0.77 +0.16
Effective statistical NP set 6 (JES) [%]	+0.15 −0.17	-	∓0.20	+0.11 −0.12	+0.42 −0.13	-	- +0.87	∓0.86
η intercalibration model (JES) [%]	+1.56 −1.18	+1.52 −1.25	+1.35 −1.53	+2.04 −1.82	+1.35 −2.00	+0.75 -	∓0.47	±3.30
high E η intercalibration non closure (JES) [%]	-	-	-	-	-	-	-	-
neg η intercalibration non closure (JES) [%]	-	-	-	-	-	-	±0.14	-
pos η intercalibration non closure (JES) [%]	-	-	-	-	-	-	+0.15 −0.11	-
η intercalibration total stat (JES) [%]	+0.70 −0.45	+0.56 −0.20	+0.35 −0.58	+0.47 −0.71	+0.65 −0.81	+0.47 -	±0.32	+1.39 -
Flavour composition (JES) [%]	+0.71 −0.42	+0.84 −0.45	+1.05 −0.90	+2.33 −0.92	+0.86 −1.46	+0.51 −1.30	+0.22 −0.79	±2.41
Flavour response (JES) [%]	−2.99 +2.81	−2.82 +3.35	−3.19 +3.36	−3.78 +5.01	−3.85 +2.81	∓3.24	−3.21 +2.59	±3.97
Pile-up offset μ (JES) [%]	-	−0.14 +0.25	−0.22 +0.12	- +0.41	∓0.31	±0.62	∓0.81	±2.07
Pile-up offset N_{PV} (JES) [%]	+0.27 −0.14	+0.64 −0.18	-	±0.24	+0.26 −0.36	∓0.58	−0.11 +0.34	±2.78
Pile-up offset p_T (JES) [%]	-	+0.38 −0.47	-	+0.15 −0.12	±0.21	∓0.63	+0.68 −0.53	±2.02
Pile-up offset ρ topology (JES) [%]	+3.60 −3.08	+3.94 −3.11	+3.82 −3.90	+4.57 −4.65	+3.43 −4.16	+1.01 −2.24	+2.89 −1.85	±5.09
Punch-through (JES) [%]	-	-	-	-	-	-	- −0.21	- −0.51
Single particle high-p_T (JES) [%]	-	-	-	-	-	-	-	-
b-Quark tagging efficiency (eigenvector 0) [%]	−3.66 +3.73	−3.73 +3.80	−3.74 +3.81	−3.68 +3.74	−3.74 +3.79	−4.30 +4.38	−4.51 +4.59	−4.60 +4.71
b-Quark tagging efficiency (eigenvector 1) [%]	∓0.84	∓0.74	∓0.65	−0.56 +0.57	∓0.64	−0.65 +0.64	∓0.90	−1.39 +1.38
b-Quark tagging efficiency (eigenvector 2) [%]	+1.49 −1.48	+1.42 −1.41	±1.36	+1.29 −1.28	+1.29 −1.28	+1.30 −1.29	±1.31	+1.22 −1.21
b-Quark tagging efficiency (eigenvector 3) [%]	-	-	-	-	-	-	-	±0.33
b-Quark tagging efficiency (eigenvector 4) [%]	∓0.24	∓0.21	∓0.19	∓0.16	∓0.14	∓0.13	∓0.10	∓0.14
b-Quark tagging efficiency (eigenvector 5) [%]	-	-	-	-	-	-	-	-
c-Quark tagging efficiency (eigenvector 0) [%]	±0.70	±0.64	±0.58	+0.52 −0.51	+0.58 −0.57	±0.66	±0.85	±0.81
c-Quark tagging efficiency (eigenvector 1) [%]	±0.35	±0.26	±0.21	±0.20	±0.22	±0.23	+0.37 −0.36	±0.43
c-Quark tagging efficiency (eigenvector 2) [%]	-	-	-	-	-	±0.10	±0.18	±0.18
Light-jet tagging efficiency (eigenvector 0) [%]	+0.43 −0.42	±0.57	+0.63 −0.64	±0.60	±0.46	+1.44 −1.42	+1.26 −1.25	+2.01 −1.99
Light-jet tagging efficiency (eigenvector 1) [%]	-	-	-	-	-	±0.11	±0.37	±0.76
Light-jet tagging efficiency (eigenvector 2) [%]	-	-	-	-	-	-	-	±0.17
Light-jet tagging efficiency (eigenvector 3) [%]	-	-	-	-	-	-	-	-
Light-jet tagging efficiency (eigenvector 4) [%]	-	-	-	-	-	-	-	-
Light-jet tagging efficiency (eigenvector 5) [%]	-	-	-	-	-	-	-	-
Light-jet tagging efficiency (eigenvector 6) [%]	-	-	-	-	-	-	-	-
Light-jet tagging efficiency (eigenvector 7) [%]	-	-	-	-	-	-	-	-
Light-jet tagging efficiency (eigenvector 8) [%]	-	-	-	-	-	-	-	-
Light-jet tagging efficiency (eigenvector 9) [%]	-	-	-	-	-	-	-	-
Light-jet tagging efficiency (eigenvector 10) [%]	-	-	-	-	-	-	-	-
b-Quark tagging extrapolation [%]	-	-	-	-	∓0.13	∓0.21	∓0.44	∓0.88
b-Quark tagging extrapolation from c-Quark [%]	-	-	-	-	-	-	-	-
JET JER cross calibration forward [%]	-	-	-	-	-	-	-	-
JET JER noise forward [%]	-	-	-	-	-	-	-	-
JET JER NP0 [%]	-	-	-	-	-	-	-	-
JET JER NP1 [%]	±0.32	-	−0.72 -	±0.53	∓0.62	∓0.66	∓3.93	+6.72 −0.28
JET JER NP2 [%]	±1.19	∓0.55	∓0.33	−0.25 +1.25	+0.72 −2.07	∓1.10	+0.20 −3.10	±5.15
JET JER NP3 [%]	∓0.52	±0.23	−1.19 +0.26	±0.74	∓1.42	∓0.33	∓1.83	±2.66
JET JER NP4 [%]	±0.78	+0.39 −0.24	∓0.71	±0.85	∓0.97	∓0.79	∓2.05	±2.80
JET JER NP5 [%]	±0.46	−0.10 +0.26	- −0.64	±0.96	∓0.74	+0.19 −0.34	∓1.88	±2.08
JET JER NP6 [%]	±0.11	−0.59 +0.41	∓0.58	±0.65	+0.22 −0.50	+0.57 −0.81	∓1.74	±5.30
JET JER NP7 [%]	±0.56	-	∓0.69	+0.70 −0.22	−0.20 +0.55	+1.33 −1.50	∓1.85	±3.22
JET JER NP8 [%]	-	-	-	-	-	-	-	-
QCD estimation [%]	±3.14	±5.21	±4.35	±2.73	±2.79	±4.38	±2.08	∓2.54
K-factor normalization mass [%]	+2.76 −2.68	+2.70 −2.62	+2.63 −2.55	+2.59 −2.51	+2.65 −2.56	+2.69 −2.60	+2.73 −2.64	+2.71 −2.63
K-factor normalization PDFAS [%]	±4.18	±4.09	±3.98	±3.92	±4.01	±4.06	±4.13	±4.10
K-factor normalization scale [%]	+2.36 −3.48	+2.31 −3.41	+2.24 −3.31	+2.21 −3.26	+2.26 −3.34	+2.29 −3.38	+2.33 −3.44	+2.31 −3.42
Luminosity [%]	∓2.05	∓2.05	∓2.05	∓2.05	∓2.05	∓2.05	∓2.05	∓2.05
MCSignal stat. [%]	±1.34	±1.00	±1.06	±1.35	±1.76	±2.74	±4.40	±8.41
QCD stat. [%]	±0.69	±0.80	±1.13	±1.76	±2.36	±3.23	±3.24	±3.63
ISR/FSR + scale [%]	−3.49 +2.99	−2.89 +1.61	−1.36 +0.81	∓3.56	∓2.81	∓1.86	−5.49 +2.06	∓2.89
Alternate hard-scattering model [%]	∓14.8	±10.8	±12.7	±19.5	±6.82	∓6.02	∓4.35	∓0.56
Alternate parton-shower model [%]	∓17.7	∓6.91	∓3.77	∓5.82	∓4.70	∓12.6	∓3.86	∓11.4
Inter PDF [%]	∓0.50	∓0.48	∓0.44	∓0.39	∓0.27	-	∓0.25	∓0.59
Intra PDF [%]	±0.93	±0.81	±0.71	±0.66	±0.60	±0.50	±0.49	±1.10

TABLE D.25: Table of systematics for the absolute differential cross-section at the parton level for the $p_T^{t\bar{t}}$ observable.

Bins [Unit y^{tt}]	0–0.12	0.12–0.25	0.25–0.38	0.38–0.50	0.50–0.65	0.65–0.80	0.80–1	1–1.15	1.15–1.30	1.30–1.50	1.50–1.70	1.70–2.50
$d\sigma$ / dy^{tt} [pb/ Unit y^{tt}]	$5.87 \cdot 10^2$	$6.27 \cdot 10^2$	$6.13 \cdot 10^2$	$5.52 \cdot 10^2$	$5.52 \cdot 10^2$	$5.09 \cdot 10^2$	$4.52 \cdot 10^2$	$4.00 \cdot 10^2$	$3.64 \cdot 10^2$	$2.80 \cdot 10^2$	$2.19 \cdot 10^2$	$1.03 \cdot 10^2$
Total Uncertainty [%]	+17.4 −18.7	+15.3 −14.8	+17.4 −15.6	+19.3 −20.7	+22.4 −21.6	+17.1 −17.2	+19.5 −17.9	+18.5 −16.8	+24.5 −25.2	+21.3 −20.9	+19.2 −18.5	+29.7 −27.7
Statistics [%]	±2.4	±2.2	±2.2	±2.5	±2.3	±2.5	±2.3	±3.2	±3.5	±4.1	±5.6	±7.9
Systematics [%]	+17.1 −18.5	+14.9 −14.4	+17.1 −15.3	+19.0 −20.4	+22.1 −21.4	+16.7 −16.8	+19.2 −17.6	+17.9 −16.2	+24.0 −24.7	+20.5 −20.1	+17.3 −16.6	+27.0 −24.8
Jet vertex fraction [%]	+0.41 −0.44	+0.50 −0.52	+0.39 −0.51	+0.46 −0.48	+0.43 −0.46	+0.42 −0.45	+0.47 −0.49	+0.47 −0.49	+0.45 −0.47	+0.38 −0.41	+0.44 −0.46	+0.39 −0.41
b-Tagged jet energy scale (JES) [%]	+1.08 −1.22	+0.71 −0.92	+0.55 −0.97	+0.29 −0.58	+0.85 −0.77	+0.84 −0.73	+0.89 −0.51	+0.72 −0.52	+0.95 −1.93	+1.48 −1.29	+1.35 −0.20	−1.47 +0.25
Effective detector NP set 1 (JES) [%]	+1.75 −2.48	+1.83 −1.80	+1.76 −1.00	+1.36 −1.92	+2.26 −2.00	+1.53 −1.69	+1.97 −1.26	+2.10 −0.74	+2.40 −2.20	+2.30 −3.07	+1.75 −1.80	+1.68 −1.39
Effective mixed NP set 1 (JES) [%]	+0.36 −0.63	±0.28	±0.16	+0.45 −0.18	+0.19 −0.69	-	±0.28	+0.51 −0.50	+0.56 -	+1.25 −1.01	+0.63 −0.30	∓0.81
Effective mixed NP set 2 (JES) [%]	−0.50	-	−0.21	−0.66	−0.29	−0.35	−0.27	-	−0.35	−0.65	−0.33	+0.52
Effective mixed NP set 3 (JES) [%]	+0.17 -	+0.29 -	+0.14 -	+0.40 -	+0.36 ±0.23	−0.14 -	+0.30 -	±0.33 -	+0.27 -	+0.90 -	+0.67 -	−0.65 −0.47
Effective modelling NP set 1 (JES) [%]	+6.57 −9.19	+5.55 −5.38	+6.91 −5.75	+5.34 −7.72	+7.07 −5.70	+5.23 −5.34	+7.65 −5.40	+6.16 −5.00	+5.30 −7.78	+8.69 −5.56	+6.26 −7.34	+7.35 −2.35
Effective modelling NP set 2 (JES) [%]	+0.77 −1.42	+1.30 −0.96	+0.92 −1.02	+1.05 −0.96	+1.27 −1.46	+0.96 −1.63	+1.31 −0.53	+1.14 −0.95	+1.45 −0.68	±1.71	+1.68 −1.88	+0.81 −1.81
Effective modelling NP set 3 (JES) [%]	+0.19 −0.77	+0.93 −0.47	±0.42	∓0.11	+0.20 −0.12	+0.22 −0.25	+0.53 −0.47	±0.78	+0.70 −0.93	∓0.36	±0.43	−0.44 +0.33
Effective modelling NP set 4 (JES) [%]	+0.45 −0.58	+0.48 −0.19	+0.51 −0.53	+0.36 −0.54	+0.66 −0.61	- −0.36	+0.49 −0.29	+0.47 −0.25	±0.42	+1.55 −0.88	+0.78 −0.11	∓0.31
Effective statistical NP set 1 (JES) [%]	-	-	-	-	-	-	-	-	-	-	-	-
Effective statistical NP set 2 (JES) [%]	−0.58 +0.36	−0.12 +0.39	−0.21 +0.23	−0.56 -	−0.33 +0.54	-	−0.42 +0.60	- +0.22	−0.27 +0.46	−0.80 +1.14	−0.42 +0.62	∓0.54
Effective statistical NP set 3 (JES) [%]	- −0.24	+0.31 −0.12	±0.11	∓0.26	-	+0.22 -	+0.16 −0.15	±0.35	-	±0.36	−0.18 +0.57	∓0.98
Effective statistical NP set 4 (JES) [%]	+0.14 −0.11	−0.14 +0.10	+0.16 −0.20	+0.14 −0.52	-	-	+0.13 -	+0.41	-	+0.42 −0.10	+0.30 −0.77	∓0.51
Effective statistical NP set 5 (JES) [%]	−0.16 +0.14	−0.31 -	−0.22 +0.29	−0.37 -	−0.21 +0.36	−0.25 +0.26	−0.34 +0.45	±0.10	-	−0.40 +0.73	−0.16 +0.29	∓0.44
Effective statistical NP set 6 (JES) [%]	- −0.14	-	-	+0.12 −0.35	+0.27 −0.11	-	-	±0.29	-	+0.64 −0.22	∓0.21	∓0.54
η intercalibration model (JES) [%]	+1.46 −1.80	+0.99 −1.54	+1.26 −0.65	+0.39 −1.54	+1.94 −0.86	+0.49 −1.52	+2.42 −1.27	+2.03 -	+2.30 −2.68	+2.38 −3.72	+3.22 −1.30	±3.28
high E η intercalibration non closure (JES) [%]	-	-	-	-	-	-	-	-	-	-	-	-
neg η intercalibration non closure (JES) [%]	-	-	-	-	-	-	-	±0.10	-	-	+0.33 −0.26	-
pos η intercalibration non closure (JES) [%]	-	-	-	-	-	-	-	-	-	-	∓0.17	- +0.74
η intercalibration total stat (JES) [%]	+0.63 −0.88	+0.52 −0.37	+0.31 −0.38	+0.43 −0.22	+0.65 −0.52	+0.21 −0.30	+0.52 −0.49	+0.69 −0.31	+0.54 −0.29	+1.38 −1.00	+0.36 −0.26	−0.80 −0.15
Flavour composition (JES) [%]	+1.25 −1.18	+1.02 −0.72	+0.86 −0.50	+0.48 −1.22	+1.44 −0.60	+0.31 −0.55	+1.57 −0.69	±1.55	+1.20 −0.97	+2.07 −1.88	±0.53	+0.18 −0.36
Flavour response (JES) [%]	−2.57	−2.64	−1.59	−4.20	−2.72	−3.54	−2.40	−3.48	−3.82	−4.44	−4.48	−1.03
Pile-up offset μ (JES) [%]	+2.81 −0.39	+2.83 ±0.12	+3.43 -	+3.04 -	+3.63 −0.13	+2.48 ∓0.38	+3.61 +0.22	+3.65 -	+3.87 −0.30	+4.03 −0.84	+4.46 ±0.24	+7.63 ±1.86
Pile-up offset N_{PV} (JES) [%]	+0.13 ∓0.77	+0.41 −0.42	+0.18 ±0.63	+0.23 −0.15	+0.44 −0.29	+0.23 −0.35	−0.13 ±0.99	+0.59 ±0.80	+0.15 ±0.44	+0.55 +0.26 −0.61	±0.97	−0.54 +3.53
Pile-up offset p_T (JES) [%]	∓0.20	+0.24 −0.40	+0.46 −0.26	±0.21	−0.15	∓0.64	±0.41	±0.31	+0.10 −0.13	+0.10 −0.75	∓0.47	±1.80
Pile-up offset ρ topology (JES) [%]	+3.05 −5.48	+3.44 −3.09	+4.16 −2.68	+3.86 −4.19	+3.91 −2.98	+3.67 −3.50	+4.34 −2.95	+3.37 −2.63	+4.83 −4.36	+3.02 −4.03	+3.44 −4.84	±5.34
Punch-through (JES) [%]	-	-	-	-	-	-	-	-	-	∓0.10	-	- −0.24
Single particle high-p_T (JES) [%]	-	-	-	-	-	-	-	-	-	-	-	-
b-Quark tagging efficiency (eigenvector 0) [%]	−3.82 +3.88	−3.83 +3.89	−3.86 +3.93	−3.76 +3.82	−3.81 +3.87	−3.73 +3.80	−3.69 +3.75	−3.77 +3.84	−3.78 +3.85	−3.72 +3.77	−3.16 +3.20	−3.69 +3.77
b-Quark tagging efficiency (eigenvector 1) [%]	∓0.71	∓0.71	+0.69 −0.68	∓0.71	∓0.71	∓0.70	∓0.69	−0.71	∓0.78	+0.71 −0.70	−0.61 +0.65	−0.77 +0.78
b-Quark tagging efficiency (eigenvector 2) [%]	+1.39 −1.38	+1.38 −1.37	+1.37 −1.36	+1.38 −1.37	+1.41 −1.40	+1.39 −1.38	+1.36 −1.35	+1.40 −1.39	+1.39 −1.38	+1.39 −1.38	+1.28 −1.27	+1.35 −1.34
b-Quark tagging efficiency (eigenvector 3) [%]	-	-	-	-	-	-	-	-	-	-	-	-
b-Quark tagging efficiency (eigenvector 4) [%]	∓0.19	∓0.19	∓0.18	∓0.19	∓0.20	∓0.19	∓0.18	∓0.19	±0.20	∓0.19	∓0.18	±0.20
b-Quark tagging efficiency (eigenvector 5) [%]	-	-	-	-	-	-	-	-	-	-	-	-
c-Quark tagging efficiency (eigenvector 0) [%]	±0.61	±0.63	±0.65	±0.63	±0.65	±0.62	±0.59	+0.59 −0.60	±0.60	±0.61	±0.35	±0.68
c-Quark tagging efficiency (eigenvector 1) [%]	±0.25	±0.25	±0.27	±0.27	±0.27	±0.25	±0.25	±0.23	±0.25	±0.23	+0.17 −0.16	±0.28
c-Quark tagging efficiency (eigenvector 2) [%]	-	-	-	-	-	-	-	-	-	-	-	-
Light-jet tagging efficiency (eigenvector 0) [%]	+0.53 −0.52	±0.61	±0.64	±0.56	+0.74 −0.76	±0.75	±0.51	+0.84 −0.82	±0.47	+0.35 −0.36	±0.37	+0.64 −0.63
Light-jet tagging efficiency (eigenvector 1) [%]	-	-	-	-	-	-	-	-	-	-	-	-
Light-jet tagging efficiency (eigenvector 2) [%]	-	-	-	-	-	-	-	-	-	-	-	-
Light-jet tagging efficiency (eigenvector 3) [%]	-	-	-	-	-	-	-	-	-	-	-	-
Light-jet tagging efficiency (eigenvector 4) [%]	-	-	-	-	-	-	-	-	-	-	-	-
Light-jet tagging efficiency (eigenvector 5) [%]	-	-	-	-	-	-	-	-	-	-	-	-
Light-jet tagging efficiency (eigenvector 6) [%]	-	-	-	-	-	-	-	-	-	-	-	-
Light-jet tagging efficiency (eigenvector 7) [%]	-	-	-	-	-	-	-	-	-	-	-	-
Light-jet tagging efficiency (eigenvector 8) [%]	-	-	-	-	-	-	-	-	-	-	-	-
Light-jet tagging efficiency (eigenvector 9) [%]	-	-	-	-	-	-	-	-	-	-	-	-
Light-jet tagging efficiency (eigenvector 10) [%]	-	-	-	-	-	-	-	-	-	-	-	-
b-Quark tagging extrapolation [%]	-	-	∓0.11	∓0.12	∓0.11	∓0.10	-	-	-	-	-	-
b-Quark tagging extrapolation from c-Quark [%]	-	-	-	-	-	-	-	-	-	-	-	-
JET JER cross calibration forward [%]	-	-	-	-	-	-	-	-	-	-	-	-
JET JER noise forward [%]	-	-	-	-	-	-	-	-	-	-	-	-
JET JER NP0 [%]	-	-	-	-	-	-	-	-	-	-	-	-
JET JER NP1 [%]	−0.19 -	∓0.31	−0.74 -	∓0.99	+0.61 -	−2.38 -	±2.78	±0.64	∓1.81	−1.44 +0.15	±2.63	∓0.94
JET JER NP2 [%]	±1.02	∓0.22	+0.37 −0.79	∓2.14	−0.11 ±1.13	∓2.98	±1.54	±3.11	∓1.54	∓2.20	−0.62 ±4.07	-
JET JER NP3 [%]	−0.36 +0.65	−0.40 +0.25	+0.24 −0.42	∓1.14	±0.82	∓2.51	+1.65 −0.39	−0.89 +0.75	∓3.22	∓0.65	±1.05	±1.91
JET JER NP4 [%]	+0.45	+0.22 −0.14	∓0.25	∓2.11	±1.42	∓1.31	±1.18	±1.11	∓1.25	∓1.42	±2.97	±2.30
JET JER NP5 [%]	+0.33 −0.51	−0.29 +0.53	±0.24	+0.18 −0.71	±0.33	∓1.19	±2.01	−0.33 -	∓2.08	∓0.95	- +2.79	∓0.30
JET JER NP6 [%]	∓0.43	−0.54 +0.34	-	+0.61 −0.26	±0.71	∓1.65	±1.17	−0.24 +0.57	∓0.99	∓2.57	±1.98	±1.51
JET JER NP7 [%]	+0.43 −0.78	−0.56 +0.53	∓0.15	∓0.19	−0.11 +0.85	−2.07	±1.25	- +0.45	∓0.92	−1.63	±1.59	+1.69 -
JET JER NP8 [%]	-	-	-	-	-	-	-	-	-	-	-	-
QCD estimation [%]	±6.28	±5.95	±4.62	±5.47	±3.34	±5.49	±4.95	±3.58	±1.58	±6.07	±0.35	∓0.72
K-factor normalization mass [%]	+2.70 −2.61	+2.71 −2.63	+2.71 −2.62	+2.70 −2.61	+2.67 −2.59	+2.68 −2.59	+2.67 −2.58	+2.64 −2.56	+2.67 −2.59	+2.67 −2.59	+2.52 −2.44	+2.48 −2.40
K-factor normalization PDFAS [%]	±4.08	±4.10	±4.10	±4.08	±4.05	±4.05	±4.03	±4.00	±4.05	±4.05	±3.82	±3.75
K-factor normalization scale [%]	+2.30 −3.40	+2.31 −3.42	+2.31 −3.41	+2.30 −3.40	+2.28 −3.37	+2.28 −3.37	+2.27 −3.36	+2.25 −3.33	+2.28 −3.37	+2.28 −3.37	+2.15 −3.18	+2.11 −3.12
Luminosity [%]	∓2.05	∓2.05	∓2.05	∓2.05	∓2.05	∓2.05	∓2.05	∓2.05	∓2.05	∓2.05	∓2.05	∓2.05
MCSignal stat. [%]	±1.67	±1.63	±1.66	±1.80	±1.69	±1.86	±1.70	±2.36	±2.67	±2.90	±4.06	±5.84
QCD stat. [%]	±1.57	±1.50	±1.52	±1.69	±1.58	±1.79	±1.64	±2.28	±2.57	±2.99	±4.48	±7.28
ISR/FSR + scale [%]	+6.55 −1.13	+1.94 −1.75	+5.43 −0.85	+1.14 −2.36	∓1.90	+4.92 −1.63	+2.60 −2.25	+6.08 −0.84	∓5.33	±0.95	+5.16 −1.92	∓7.37
Alternate hard-scattering model [%]	∓5.01	∓1.31	∓5.36	∓3.95	∓12.4	∓3.87	∓8.38	∓5.54	∓1.61	∓8.59	∓8.39	∓18.0
Alternate parton-shower model [%]	∓7.63	∓7.36	∓8.60	∓13.8	∓12.9	∓9.18	∓9.26	∓9.89	∓19.5	∓10.5	∓3.93	∓10.2
Inter PDF [%]	∓0.52	∓0.52	∓0.44	∓0.33	∓0.11	±0.10	±0.18	-	-	∓0.48	∓0.73	∓1.29
Intra PDF [%]	±1.57	±1.58	±1.43	±1.41	±1.37	±1.36	±1.35	±1.44	±1.52	±1.54	±2.02	±1.83

TABLE D.26: Table of systematics for the absolute differential cross-section at the parton level for the $y_{t\bar{t}}$ observable.

D.4 Relative cross sections, unfolded to parton level

Bins [Unit $p_T^{topleading}$]	0–175	175–215	215–255	255–300	300–335	335–380	380–430	430–490	490–560	560–1000
$1/\sigma \cdot d\sigma$ / $dp_T^{topleading}$	$3.84 \cdot 10^{-3}$	$3.36 \cdot 10^{-3}$	$2.20 \cdot 10^{-3}$	$1.08 \cdot 10^{-3}$	$6.07 \cdot 10^{-4}$	$3.43 \cdot 10^{-4}$	$1.67 \cdot 10^{-4}$	$9.06 \cdot 10^{-5}$	$4.63 \cdot 10^{-5}$	$6.87 \cdot 10^{-6}$
Total Uncertainty [%]	$^{+12.3}_{-12.0}$	$^{+28.6}_{-29.6}$	$^{+35.7}_{-36.2}$	$^{+34.4}_{-36.2}$	$^{+35.1}_{-34.9}$	$^{+35.5}_{-36.4}$	$^{+33.0}_{-35.7}$	$^{+38.2}_{-39.2}$	$^{+34.5}_{-36.4}$	$^{+41.9}_{-40.9}$
Statistics [%]	±1.7	±3.8	±4.0	±3.7	±3.9	±3.9	±4.2	±4.6	±5.9	±9.2
Systematics [%]	$^{+11.9}_{-11.6}$	$^{+27.5}_{-28.6}$	$^{+35.0}_{-35.5}$	$^{+33.8}_{-35.7}$	$^{+34.5}_{-34.4}$	$^{+35.0}_{-35.9}$	$^{+32.3}_{-35.1}$	$^{+37.5}_{-38.5}$	$^{+33.1}_{-35.1}$	$^{+39.7}_{-38.5}$
Jet vertex fraction [%]	-	-	-	∓0.16	$^{-0.23}_{+0.22}$	$^{-0.26}_{+0.25}$	∓0.27	$^{-0.29}_{+0.28}$	$^{-0.30}_{+0.29}$	∓0.11
b-Tagged jet energy scale (JES) [%]	-	∓0.44	±0.56	$^{-0.18}_{+0.82}$	$^{-0.23}_{+1.02}$	$^{-}_{+0.30}$	$^{-0.43}_{+0.71}$	$^{-0.15}_{+1.27}$	$^{+0.44}_{-0.46}$	±0.99
Effective detector NP set 1 (JES) [%]	$^{+0.43}_{-0.66}$	$^{-1.58}_{+1.30}$	$^{-0.39}_{+1.83}$	$^{-1.12}_{+1.70}$	$^{-1.31}_{+3.56}$	$^{-1.82}_{+2.47}$	$^{-1.27}_{+2.31}$	$^{-0.63}_{+3.31}$	$^{-1.80}_{+1.91}$	±2.15
Effective mixed NP set 1 (JES) [%]	$^{+0.42}_{-0.10}$	$^{-1.42}_{-}$	$^{-1.02}_{+0.71}$	$^{-1.15}_{+0.46}$	$^{-1.10}_{+1.35}$	$^{-1.47}_{+0.34}$	∓1.04	±0.68	$^{+1.21}_{-1.88}$	$^{+2.31}_{-5.19}$
Effective mixed NP set 2 (JES) [%]	±0.23	∓0.97	∓0.45	∓0.93	$^{+0.19}_{-0.52}$	∓0.71	∓1.20	∓0.26	∓1.89	±2.30
Effective mixed NP set 3 (JES) [%]	-	$^{-0.30}_{-}$	$^{-0.44}_{+0.28}$	$^{-0.27}_{+0.16}$	$^{-0.33}_{+0.30}$	∓0.36	$^{-0.21}_{+0.11}$	$^{-0.44}_{+0.33}$	∓0.47	±1.43
Effective modelling NP set 1 (JES) [%]	$^{+0.29}_{-1.50}$	$^{-0.20}_{+2.72}$	$^{-}_{+3.91}$	$^{-1.56}_{+3.85}$	$^{-1.73}_{+7.49}$	$^{-2.70}_{+7.67}$	$^{-3.46}_{+6.56}$	$^{-1.86}_{+7.91}$	$^{-1.55}_{+5.08}$	$^{-4.99}_{+7.10}$
Effective modelling NP set 2 (JES) [%]	-	∓0.53	±0.38	±0.58	$^{-0.31}_{+1.56}$	$^{-0.75}_{+0.61}$	-	±1.15	±0.79	$^{+2.37}_{-3.00}$
Effective modelling NP set 3 (JES) [%]	$^{+0.22}_{-0.96}$	$^{-1.15}_{+0.47}$	±1.07	$^{-0.51}_{+1.18}$	±1.16	$^{-0.88}_{+1.62}$	$^{-1.63}_{+1.97}$	$^{-0.88}_{+2.97}$	$^{-1.85}_{+1.49}$	$^{-0.89}_{+4.02}$
Effective modelling NP set 4 (JES) [%]	$^{+0.42}_{-}$	$^{-1.29}_{-}$	∓0.99	∓1.03	$^{-1.39}_{+0.99}$	$^{-1.22}_{-}$	∓1.12	$^{-0.76}_{+0.22}$	±1.43	±1.61
Effective statistical NP set 1 (JES) [%]	-	-	-	-	-	∓0.10	-	$^{-}_{-0.16}$	-	$^{+1.12}_{-0.26}$
Effective statistical NP set 2 (JES) [%]	±0.17	∓0.62	$^{-}_{-0.34}$	$^{-}_{-0.29}$	$^{+0.31}_{-0.52}$	∓0.61	∓0.43	$^{+0.54}_{-0.73}$	∓0.67	±1.94
Effective statistical NP set 3 (JES) [%]	-	$^{-0.26}_{-}$	$^{+0.24}_{-0.15}$	∓0.20	$^{+0.62}_{-0.26}$	$^{-}_{-}$	$^{-0.78}_{-}$	$^{-}_{+0.78}$	$^{-1.30}_{-}$	±1.87
Effective statistical NP set 4 (JES) [%]	-	∓0.19	-	∓0.22	-	$^{+0.20}_{-0.21}$	$^{+0.14}_{-0.55}$	$^{+0.32}_{-}$	$^{-0.62}_{+0.13}$	$^{-0.10}_{+1.92}$
Effective statistical NP set 5 (JES) [%]	±0.24	$^{-0.77}_{-}$	∓0.52	∓0.67	$^{-0.59}_{-}$	∓0.48	∓0.58	∓0.27	$^{+0.22}_{-0.89}$	$^{-0.36}_{-}$
Effective statistical NP set 6 (JES) [%]	±0.14	∓0.40	∓0.54	∓0.44	$^{-0.42}_{+0.20}$	∓0.48	∓0.36	$^{-0.63}_{-}$	∓0.92	±1.72
η intercalibration model (JES) [%]	$^{+0.45}_{-0.35}$	$^{-1.09}_{+0.22}$	$^{-1.05}_{+1.47}$	$^{-1.30}_{+0.97}$	$^{-1.80}_{+1.97}$	$^{-1.63}_{+1.54}$	$^{-1.91}_{+1.96}$	$^{-1.54}_{+3.09}$	$^{-1.76}_{+0.91}$	$^{-0.96}_{+2.18}$
high E η intercalibration non closure (JES) [%]	-	-	-	-	-	-	-	-	-	-
neg η intercalibration non closure (JES) [%]	-	-	-	-	-	-	-	-	-	-
pos η intercalibration non closure (JES) [%]	-	-	∓0.11	-	∓0.11	∓0.11	∓0.10	∓0.10	∓0.11	∓0.10
η intercalibration total stat (JES) [%]	$^{+0.19}_{-0.14}$	$^{-0.66}_{+0.31}$	$^{-0.52}_{+0.44}$	$^{-0.24}_{+0.29}$	$^{-0.45}_{+0.71}$	$^{-0.54}_{+0.41}$	$^{-0.57}_{+0.21}$	$^{-0.82}_{+0.79}$	∓0.52	±2.45
Flavour composition (JES) [%]	∓0.12	±0.37	±0.56	±0.56	±0.62	$^{-0.31}_{+0.58}$	-	$^{-0.12}_{+0.74}$	-	±2.35
Flavour response (JES) [%]	$^{-1.15}_{+0.44}$	$^{+1.90}_{-1.43}$	$^{+3.61}_{-}$	$^{+3.11}_{-1.60}$	$^{+5.55}_{-1.22}$	$^{+5.38}_{-2.37}$	$^{+4.57}_{-2.57}$	$^{+5.50}_{-0.63}$	$^{+4.22}_{-1.68}$	$^{+1.01}_{-3.08}$
Pile-up offset μ (JES) [%]	$^{-}_{+0.32}$	∓0.98	$^{+0.66}_{-0.98}$	$^{+0.69}_{-0.66}$	$^{+0.19}_{-0.35}$	$^{+0.47}_{-1.06}$	$^{+0.40}_{-0.75}$	$^{+0.71}_{-0.99}$	±0.44	±1.69
Pile-up offset N_{PV} (JES) [%]	$^{-1.08}_{+0.38}$	$^{+2.64}_{-1.17}$	$^{+3.53}_{-0.66}$	$^{+2.72}_{-1.38}$	$^{+2.98}_{-0.38}$	$^{+2.64}_{-1.43}$	$^{+2.86}_{-1.61}$	$^{+3.26}_{-0.76}$	$^{+0.36}_{-}$	$^{+3.93}_{-0.80}$
Pile-up offset p_T (JES) [%]	$^{-0.47}_{+0.31}$	$^{+0.80}_{-1.18}$	$^{+1.68}_{-0.29}$	$^{+1.48}_{-0.99}$	$^{+1.27}_{-0.33}$	$^{+1.75}_{-0.90}$	$^{+1.57}_{-1.14}$	$^{+1.34}_{-0.38}$	$^{+2.02}_{-0.87}$	$^{+2.94}_{-0.93}$
Pile-up offset ρ topology (JES) [%]	$^{+0.36}_{-1.29}$	$^{-1.20}_{+2.37}$	±3.54	$^{-1.26}_{+4.19}$	$^{-0.97}_{+5.33}$	$^{-2.16}_{+5.04}$	$^{-2.47}_{+5.03}$	$^{-1.46}_{+6.02}$	$^{-1.92}_{+4.49}$	$^{-3.02}_{+5.46}$
Punch-through (JES) [%]	-	-	-	-	-	±0.10	-	-	±0.10	-
Single particle high-p_T (JES) [%]	-	-	-	-	-	-	-	-	-	-
b-Quark tagging efficiency (eigenvector 0) [%]	$^{+0.41}_{-0.39}$	$^{-0.79}_{+0.76}$	$^{-1.25}_{+1.20}$	$^{-1.36}_{+1.32}$	$^{-1.27}_{+1.23}$	$^{-1.27}_{+1.22}$	$^{-1.38}_{+1.34}$	$^{-1.47}_{+1.42}$	$^{-1.83}_{+1.77}$	$^{-2.40}_{+2.34}$
b-Quark tagging efficiency (eigenvector 1) [%]	-	±0.15	-	∓0.15	∓0.37	∓0.63	∓1.06	$^{-1.62}_{+1.63}$	$^{-2.51}_{+2.53}$	$^{-3.75}_{+3.78}$
b-Quark tagging efficiency (eigenvector 2) [%]	-	-	±0.19	$^{+0.27}_{-0.28}$	±0.26	$^{+0.28}_{-0.29}$	$^{+0.30}_{-0.31}$	±0.25	$^{+0.11}_{-0.12}$	$^{-0.31}_{+0.32}$
b-Quark tagging efficiency (eigenvector 3) [%]	∓0.10	-	±0.19	$^{+0.48}_{-0.47}$	$^{+0.72}_{-0.71}$	$^{+0.85}_{-0.84}$	$^{+0.99}_{-0.98}$	$^{+1.13}_{-1.12}$	$^{+1.26}_{-1.25}$	$^{+1.01}_{-1.00}$
b-Quark tagging efficiency (eigenvector 4) [%]	-	-	∓0.10	∓0.13	∓0.11	-	-	-	-	±0.12
b-Quark tagging efficiency (eigenvector 5) [%]	-	-	-	-	∓0.10	∓0.10	∓0.11	∓0.11	∓0.13	∓0.12
c-Quark tagging efficiency (eigenvector 0) [%]	-	-	±0.11	±0.23	±0.24	±0.30	±0.31	±0.41	±0.55	$^{+0.43}_{-0.42}$
c-Quark tagging efficiency (eigenvector 1) [%]	-	-	±0.15	±0.21	±0.24	±0.28	±0.29	±0.33	±0.40	±0.40
c-Quark tagging efficiency (eigenvector 2) [%]	-	-	-	-	-	±0.12	±0.14	±0.16	±0.18	±0.24
Light-jet tagging efficiency (eigenvector 0) [%]	-	-	-	-	$^{+0.23}_{-0.24}$	$^{+0.21}_{-0.22}$	$^{+0.37}_{-0.39}$	$^{+0.43}_{-0.44}$	±0.58	$^{+0.46}_{-0.47}$
Light-jet tagging efficiency (eigenvector 1) [%]	-	-	-	-	-	-	-	-	-	±0.34
Light-jet tagging efficiency (eigenvector 2) [%]	-	-	-	-	-	-	-	-	-	-
Light-jet tagging efficiency (eigenvector 3) [%]	-	-	-	-	-	-	-	-	-	-
Light-jet tagging efficiency (eigenvector 4) [%]	-	-	-	-	-	-	-	-	-	-
Light-jet tagging efficiency (eigenvector 5) [%]	-	-	-	-	-	-	-	-	-	-
Light-jet tagging efficiency (eigenvector 6) [%]	-	-	-	-	-	-	-	-	-	-
Light-jet tagging efficiency (eigenvector 7) [%]	-	-	-	-	-	-	-	-	-	-
Light-jet tagging efficiency (eigenvector 8) [%]	-	-	-	-	-	-	-	-	-	-
Light-jet tagging efficiency (eigenvector 9) [%]	-	-	-	-	-	-	-	-	-	-
Light-jet tagging efficiency (eigenvector 10) [%]	-	-	-	-	-	-	-	-	-	-
b-Quark tagging extrapolation [%]	-	-	-	-	-	∓0.10	∓0.13	∓0.18	∓0.24	∓0.44
b-Quark tagging extrapolation from c-Quark [%]	-	-	-	-	-	-	-	-	-	-
JET JER cross calibration forward [%]	-	-	-	-	-	-	-	-	-	-
JET JER noise forward [%]	-	-	-	-	-	-	-	-	-	-
JET JER NP0 [%]	-	-	-	-	-	-	-	-	-	-
JET JER NP1 [%]	-	$^{-0.16}_{-}$	$^{+0.19}_{-}$	∓0.62	±0.76	$^{+1.60}_{-}$	$^{+0.46}_{-0.16}$	$^{+1.52}_{-}$	±1.55	$^{+2.46}_{-0.95}$
JET JER NP2 [%]	$^{-}_{+0.29}$	∓1.31	$^{+0.14}_{-0.40}$	∓1.23	$^{+0.76}_{-}$	±0.86	$^{-0.90}_{-}$	±1.21	$^{-0.62}_{+0.30}$	$^{-0.72}_{+0.14}$
JET JER NP3 [%]	∓0.56	±1.65	±2.27	$^{-0.16}_{+0.87}$	±1.80	±1.95	±1.53	±2.54	±1.49	±0.66
JET JER NP4 [%]	±0.47	∓1.48	$^{-0.79}_{+0.41}$	$^{-2.47}_{+0.55}$	$^{-0.80}_{+1.63}$	$^{-0.24}_{+0.95}$	∓1.42	$^{-0.72}_{+1.72}$	$^{-0.39}_{+1.25}$	∓2.62
JET JER NP5 [%]	$^{-}_{-0.68}$	$^{-0.77}_{+1.54}$	±2.69	±1.07	±1.53	$^{-}_{+2.84}$	$^{-0.12}_{+1.12}$	±2.89	±2.12	±1.46
JET JER NP6 [%]	±0.49	±1.30	$^{+0.10}_{-0.77}$	$^{+0.48}_{-2.61}$	$^{+0.59}_{-1.33}$	$^{+1.31}_{-0.60}$	$^{+0.43}_{-1.16}$	$^{+1.29}_{-0.83}$	$^{+0.09}_{-2.61}$	±1.28
JET JER NP7 [%]	∓0.26	±0.73	$^{+1.37}_{-}$	$^{+0.81}_{-0.86}$	±1.16	±1.15	$^{+0.81}_{-0.58}$	±1.74	±2.25	$^{+1.31}_{-1.52}$
JET JER NP8 [%]	-	-	-	-	-	-	-	-	-	-
QCD estimation [%]	∓9.52	±21.6	±30.7	±28.4	±26.6	±25.0	±24.3	±23.3	±22.8	±21.1
K-factor normalization mass [%]	∓0.22	±0.37	±0.68	±0.81	$^{+0.83}_{-0.84}$	$^{+0.86}_{-0.87}$	$^{+0.89}_{-0.90}$	±0.92	$^{+0.93}_{-0.94}$	$^{+0.92}_{-0.93}$
K-factor normalization PDFAS [%]	∓0.34	±0.56	±1.02	±1.21	±1.25	±1.29	±1.34	±1.37	±1.39	±1.38
K-factor normalization scale [%]	$^{-0.19}_{+0.30}$	$^{+0.32}_{-0.49}$	$^{+0.58}_{-0.90}$	$^{+0.69}_{-1.06}$	$^{+0.71}_{-1.10}$	$^{+0.73}_{-1.13}$	$^{+0.76}_{-1.17}$	$^{+0.78}_{-1.21}$	$^{+0.79}_{-1.22}$	$^{+0.79}_{-1.22}$
Luminosity [%]	-	-	-	-	-	-	-	-	-	-
MCSignal stat. [%]	±0.66	±2.05	±2.30	±2.14	±2.20	±2.20	±2.39	±2.78	±4.01	±6.65
QCD stat. [%]	±2.62	±6.47	±5.30	±4.09	±4.47	±4.08	±4.42	±5.17	±6.57	±7.43
ISR/FSR + scale [%]	$^{+3.98}_{-1.21}$	$^{-8.54}_{+0.93}$	$^{-8.80}_{+3.56}$	$^{-13.5}_{+4.81}$	$^{-12.7}_{+6.12}$	$^{-15.2}_{+7.22}$	$^{-17.5}_{+6.49}$	$^{-17.2}_{+7.71}$	$^{-16.3}_{+9.39}$	$^{-9.23}_{+5.04}$
Alternate hard-scattering model [%]	∓5.30	±15.4	±12.1	±11.8	±14.5	±18.0	±10.6	±19.5	±17.4	±27.5
Alternate parton-shower model [%]	±2.25	∓3.12	∓5.68	∓10.3	∓8.10	∓7.73	∓12.9	∓14.4	∓8.00	∓10.8
Inter PDF [%]	∓0.11	±0.21	±0.30	±0.33	±0.44	±0.52	±0.38	±0.37	±0.54	±0.44
Intra PDF [%]	-	-	-	∓0.11	∓0.15	∓0.14	∓0.25	∓0.30	∓0.40	∓0.43

TABLE D.27: Table of systematics for the normalised differential cross-section at the parton level for the p_T^{top1} observable.

Bins [Unit $y^{topleading}$]	0–0.30	0.30–0.60	0.60–0.90	0.90–1.20	1.20–1.50	1.50–2	2–2.50
$1/\sigma \cdot d\sigma$ / $dy^{topleading}$	$6.26 \cdot 10^{-1}$	$5.92 \cdot 10^{-1}$	$5.30 \cdot 10^{-1}$	$4.75 \cdot 10^{-1}$	$3.71 \cdot 10^{-1}$	$2.79 \cdot 10^{-1}$	$1.65 \cdot 10^{-1}$
Total Uncertainty [%]	$^{+4.49}_{-4.37}$	$^{+3.39}_{-3.83}$	$^{+3.91}_{-4.85}$	$^{+9.73}_{-9.81}$	$^{+7.24}_{-7.18}$	$^{+7.98}_{-7.80}$	$^{+22.1}_{-22.5}$
Statistics [%]	±1.7	±1.8	±1.9	±2.1	±2.5	±2.4	±6.8
Systematics [%]	$^{+3.79}_{-3.64}$	$^{+2.21}_{-2.84}$	$^{+2.82}_{-4.02}$	$^{+9.24}_{-9.33}$	$^{+6.25}_{-6.19}$	$^{+7.10}_{-6.90}$	$^{+19.2}_{-19.6}$
Jet vertex fraction [%]	-	-	-	-	-	-	-
b-Tagged jet energy scale (JES) [%]	∓0.24	$^{-0.37}_{-}$	±0.22	$^{+0.29}_{-}$	±0.33	-	$^{+0.13}_{-0.42}$
Effective detector NP set 1 (JES) [%]	$^{-0.15}_{+0.37}$	∓0.77	±0.52	$^{+0.50}_{-0.47}$	±0.53	$^{+0.28}_{-0.10}$	∓0.99
Effective mixed NP set 1 (JES) [%]	±0.18	$^{-0.65}_{+0.19}$	$^{-}_{+0.48}$	$^{+0.30}_{-0.24}$	$^{-0.22}_{-}$	±0.23	$^{+0.76}_{-1.70}$
Effective mixed NP set 2 (JES) [%]	-	$^{-}_{-0.38}$	-	$^{-0.13}_{+0.14}$	-	-	$^{-}_{+0.54}$
Effective mixed NP set 3 (JES) [%]	-	-	-	-	-	$^{-0.19}_{-}$	±0.36
Effective modelling NP set 1 (JES) [%]	$^{-}_{-0.26}$	∓0.48	$^{+0.50}_{-}$	∓0.21	±1.07	$^{+0.69}_{-0.83}$	$^{-3.89}_{+3.34}$
Effective modelling NP set 2 (JES) [%]	$^{-0.16}_{+0.27}$	∓0.54	$^{-}_{+0.24}$	$^{+0.24}_{-0.34}$	$^{+0.91}_{-}$	±0.33	∓0.92
Effective modelling NP set 3 (JES) [%]	±0.11	-	$^{+0.44}_{-0.32}$	±0.13	$^{-0.18}_{+0.33}$	±0.21	∓1.64
Effective modelling NP set 4 (JES) [%]	-	$^{-0.32}_{-}$	±0.23	$^{+0.11}_{-0.51}$	$^{-0.10}_{+0.18}$	±0.12	$^{+0.17}_{-0.29}$
Effective statistical NP set 1 (JES) [%]	-	-	-	-	-	-	-
Effective statistical NP set 2 (JES) [%]	-	∓0.11	-	$^{-}_{+0.20}$	$^{+0.33}_{-0.29}$	$^{-0.23}_{+0.11}$	±0.18
Effective statistical NP set 3 (JES) [%]	-	-	-	±0.18	∓0.20	-	$^{-0.36}_{+0.66}$
Effective statistical NP set 4 (JES) [%]	-	∓0.12	-	±0.19	$^{-0.17}_{-}$	∓0.21	$^{+0.88}_{-}$
Effective statistical NP set 5 (JES) [%]	∓0.16	-	-	±0.13	∓0.24	-	$^{-0.15}_{+0.78}$
Effective statistical NP set 6 (JES) [%]	-	∓0.17	-	±0.15	-	∓0.10	$^{+0.72}_{-}$
η intercalibration model (JES) [%]	$^{-0.62}_{+0.92}$	$^{-1.02}_{+0.73}$	$^{-0.23}_{+0.31}$	$^{+0.52}_{-0.79}$	±0.82	$^{+1.32}_{-0.66}$	∓2.97
high E η intercalibration non closure (JES) [%]	-	-	-	-	-	-	-
neg η intercalibration non closure (JES) [%]	-	-	-	-	-	-	$^{+0.28}_{-0.18}$
pos η intercalibration non closure (JES) [%]	-	-	-	-	-	-	$^{+0.34}_{-0.12}$
η intercalibration total stat (JES) [%]	-	$^{-0.22}_{+0.12}$	-	$^{+0.19}_{-0.11}$	$^{-0.25}_{+0.37}$	$^{+0.21}_{-0.19}$	$^{+0.28}_{-0.29}$
Flavour composition (JES) [%]	$^{-0.23}_{-}$	-	-	∓0.36	±0.34	$^{+0.55}_{-0.28}$	$^{-0.65}_{+0.50}$
Flavour response (JES) [%]	$^{-}_{+0.55}$	$^{+0.24}_{-1.03}$	-	$^{-0.65}_{+0.15}$	$^{-0.31}_{+0.32}$	$^{-1.16}_{+0.95}$	±2.12
Pile-up offset μ (JES) [%]	$^{-0.14}_{+0.24}$	$^{+0.19}_{-0.15}$	±0.20	$^{-}_{-0.40}$	$^{+0.23}_{-}$	-	$^{-2.00}_{+0.70}$
Pile-up offset N_{PV} (JES) [%]	$^{-}_{+0.27}$	$^{-0.44}_{-}$	$^{-}_{+0.19}$	$^{+0.11}_{-0.13}$	$^{+0.22}_{-0.45}$	±0.10	$^{-}_{+0.99}$
Pile-up offset p_T (JES) [%]	$^{-0.28}_{+0.26}$	-	$^{-}_{+0.48}$	$^{+0.14}_{-0.19}$	±0.19	±0.20	∓1.10
Pile-up offset ρ topology (JES) [%]	$^{-0.16}_{-0.20}$	∓0.27	$^{+0.38}_{-0.25}$	$^{-}_{-0.77}$	±0.75	$^{+0.60}_{-0.24}$	$^{-2.14}_{+2.21}$
Punch-through (JES) [%]	-	-	-	-	-	-	-
Single particle high-p_T (JES) [%]	-	-	-	-	-	-	-
b-Quark tagging efficiency (eigenvector 0) [%]	-	-	-	-	-	$^{+0.11}_{-0.10}$	±0.11
b-Quark tagging efficiency (eigenvector 1) [%]	-	-	-	-	-	-	-
b-Quark tagging efficiency (eigenvector 2) [%]	-	-	-	-	-	-	-
b-Quark tagging efficiency (eigenvector 3) [%]	-	-	-	-	-	-	-
b-Quark tagging efficiency (eigenvector 4) [%]	-	-	-	-	-	-	-
b-Quark tagging efficiency (eigenvector 5) [%]	-	-	-	-	-	-	-
c-Quark tagging efficiency (eigenvector 0) [%]	-	-	-	-	-	-	-
c-Quark tagging efficiency (eigenvector 1) [%]	-	-	-	-	-	-	-
c-Quark tagging efficiency (eigenvector 2) [%]	-	-	-	-	-	-	-
Light-jet tagging efficiency (eigenvector 0) [%]	-	-	-	-	-	-	-
Light-jet tagging efficiency (eigenvector 1) [%]	-	-	-	-	-	-	-
Light-jet tagging efficiency (eigenvector 2) [%]	-	-	-	-	-	-	-
Light-jet tagging efficiency (eigenvector 3) [%]	-	-	-	-	-	-	-
Light-jet tagging efficiency (eigenvector 4) [%]	-	-	-	-	-	-	-
Light-jet tagging efficiency (eigenvector 5) [%]	-	-	-	-	-	-	-
Light-jet tagging efficiency (eigenvector 6) [%]	-	-	-	-	-	-	-
Light-jet tagging efficiency (eigenvector 7) [%]	-	-	-	-	-	-	-
Light-jet tagging efficiency (eigenvector 8) [%]	-	-	-	-	-	-	-
Light-jet tagging efficiency (eigenvector 9) [%]	-	-	-	-	-	-	-
Light-jet tagging efficiency (eigenvector 10) [%]	-	-	-	-	-	-	-
b-Quark tagging extrapolation [%]	-	-	-	-	-	-	-
b-Quark tagging extrapolation from c-Quark [%]	-	-	-	-	-	-	-
JET JER cross calibration forward [%]	-	-	-	-	-	-	-
JET JER noise forward [%]	-	-	-	-	-	-	-
JET JER NP0 [%]	-	-	-	-	-	-	-
JET JER NP1 [%]	±0.18	$^{-0.85}_{-}$	±0.38	$^{-0.33}_{-}$	±0.48	$^{+0.56}_{-0.10}$	∓1.05
JET JER NP2 [%]	$^{-}_{-0.37}$	∓0.68	±0.48	±0.67	±0.32	$^{-0.20}_{+0.83}$	$^{+0.92}_{-1.89}$
JET JER NP3 [%]	$^{+0.51}_{-0.16}$	∓0.44	±0.78	∓1.14	$^{-}_{-0.32}$	-	±0.66
JET JER NP4 [%]	-	∓0.76	$^{+0.86}_{-0.20}$	±0.33	∓0.21	±0.35	$^{-2.55}_{+2.34}$
JET JER NP5 [%]	$^{+0.24}_{-}$	$^{+0.38}_{-}$	±0.35	∓0.56	±0.49	$^{+0.52}_{-0.79}$	$^{-3.39}_{+1.47}$
JET JER NP6 [%]	±0.43	∓0.27	±1.08	∓0.38	±0.44	∓0.51	∓1.76
JET JER NP7 [%]	$^{-0.43}_{+0.55}$	∓0.76	$^{-}_{+1.05}$	∓0.48	±0.36	$^{+0.14}_{-0.20}$	$^{+1.91}_{-1.49}$
JET JER NP8 [%]	-	-	-	-	-	-	-
QCD estimation [%]	∓0.59	∓0.12	±0.17	±1.00	±0.54	∓0.64	∓0.21
K-factor normalization mass [%]	-	-	-	-	-	-	-
K-factor normalization PDFAS [%]	-	-	-	-	-	-	-
K-factor normalization scale [%]	-	-	-	-	-	-	-
Luminosity [%]	-	-	-	-	-	-	-
MCSignal stat. [%]	±1.22	±1.29	±1.35	±1.52	±1.78	±1.79	±5.41
QCD stat. [%]	±1.20	±1.28	±1.34	±1.55	±1.88	±2.00	±6.51
ISR/FSR + scale [%]	±1.00	±0.74	$^{-3.32}_{+0.12}$	±0.69	±5.24	$^{+1.40}_{-0.81}$	∓8.74
Alternate hard-scattering model [%]	±2.73	±0.26	∓0.81	±8.93	±0.91	∓6.27	∓14.2
Alternate parton-shower model [%]	∓1.67	±0.28	±1.12	∓0.20	±2.15	±1.55	∓5.09
Inter PDF [%]	∓0.16	∓0.11	-	±0.24	±0.51	±0.23	∓1.23
Intra PDF [%]	∓0.25	∓0.21	∓0.24	∓0.31	-	±0.38	±1.88

TABLE D.28: Table of systematics for the normalised differential cross-section at the parton level for the y_{top1} observable.

Bins [Unit $p_T^{topsubleading}$]	0–125	125–175	175–220	220–270	270–330	330–400	400–500	500–1000
$1/\sigma \cdot d\sigma$ / $dp_T^{topsubleading}$	$4.94 \cdot 10^{-3}$	$4.14 \cdot 10^{-3}$	$2.15 \cdot 10^{-3}$	$8.82 \cdot 10^{-4}$	$3.48 \cdot 10^{-4}$	$1.22 \cdot 10^{-4}$	$3.77 \cdot 10^{-5}$	$3.28 \cdot 10^{-6}$
Total Uncertainty [%]	+9.88 −9.78	+18.4 −18.6	+29.6 −29.8	+30.5 −31.1	+30.7 −31.0	+26.6 −28.8	+27.6 −29.1	+62.2 −61.2
Statistics [%]	±1.3	±2.4	±2.9	±3.0	±3.0	±3.4	±4.5	±13.
Systematics [%]	+9.61 −9.51	+17.7 −18.0	+29.1 −29.4	+30.2 −30.8	+30.3 −30.6	+26.0 −28.3	+26.7 −28.2	+59.5 −58.5
Jet vertex fraction [%]	-	-	-	−0.16 +0.17	∓0.30	−0.37 +0.38	−0.41 +0.42	−0.22 +0.23
b-Tagged jet energy scale (JES) [%]	-	∓0.11	+0.89 −0.18	+0.26 −0.13	±0.17	+0.32 −0.11	+0.22 −0.12	∓0.79
Effective detector NP set 1 (JES) [%]	- −0.20	−0.40 +0.14	±0.67	−0.48 +1.00	−0.50 +1.64	−0.78 +1.54	±1.24	+1.74 −0.39
Effective mixed NP set 1 (JES) [%]	- −0.42	−0.19 +1.22	±0.77	−0.81 +0.77	−0.63 +1.06	- −0.31	+1.40 −0.50	±5.33
Effective mixed NP set 2 (JES) [%]	−0.12 +0.20	+0.52 −0.59	- −0.18	∓0.71	- −0.46	∓0.25	−0.74 +0.39	±1.36
Effective mixed NP set 3 (JES) [%]	-	∓0.16	−0.25 +0.10	−0.32	−0.20	-	∓0.21	±0.38
Effective modelling NP set 1 (JES) [%]	+0.32 −0.23	∓0.58	−0.27 +0.30	−2.73 +2.64	−3.49 +4.90	−3.34 +5.10	−3.77 +4.41	−1.63 +3.68
Effective modelling NP set 2 (JES) [%]	−0.29 -	±0.23	+1.89 −0.40	+0.96 −0.25	±0.76 −0.33	+1.09 −0.18	+1.86 −0.77	+4.09 −2.39
Effective modelling NP set 3 (JES) [%]	-	+0.17 −0.37	−0.73 +0.72	−0.82 +0.13	+0.58	−1.75 +1.50	−1.10 +1.89	−1.22 +1.10
Effective modelling NP set 4 (JES) [%]	+0.15 −0.13	−0.41 +0.49	-	∓0.66	−0.64 +0.29	−0.43 +0.20	+0.17 −0.52	±1.64
Effective statistical NP set 1 (JES) [%]	-	-	-	-	-	-	-	-
Effective statistical NP set 2 (JES) [%]	- +0.16	- −0.34	+0.19 −0.31	+0.39 −0.70	+0.40 −0.51	+0.46 −0.67	+0.30 −0.17	±1.50
Effective statistical NP set 3 (JES) [%]	-	-	∓0.27	∓0.43	∓0.33	−0.69 +0.26	−1.16 +0.68	±0.68
Effective statistical NP set 4 (JES) [%]	-	−0.25	+0.31 −0.29	∓0.44	+0.11 −0.40	+0.35 −0.73	+0.35	−0.10 +0.43
Effective statistical NP set 5 (JES) [%]	±0.16	∓0.27	−0.52	−0.56	∓0.51	∓0.35	+0.13 −0.25	∓0.28
Effective statistical NP set 6 (JES) [%]	-	−0.23 -	-	∓0.35	−0.26 -	∓0.10	+0.37 −0.32	±1.02
η intercalibration model (JES) [%]	+0.36 −0.17	−0.69 +0.24	∓0.46	−1.73 +1.05	−1.51 +1.56	−1.92 +1.67	−0.99 +0.85	−0.20 +1.24
high E η intercalibration non closure (JES) [%]	-	-	-	-	-	-	-	-
neg η intercalibration non closure (JES) [%]	-	-	-	-	-	∓0.11	-	-
pos η intercalibration non closure (JES) [%]	-	∓0.10	∓0.13	∓0.12	∓0.10	∓0.10	∓0.10	∓0.10
η intercalibration total stat (JES) [%]	+0.23 −0.21	−0.56 +0.41	−0.40 +0.49	−0.81 +0.59	−0.65 +0.91	−0.89 +0.67	±0.51	±1.94
Flavour composition (JES) [%]	±0.10	- −0.49	∓0.22	−0.74 +0.13	−0.70 +0.57	−1.15 +0.56	−0.32 +0.30	±1.94
Flavour response (JES) [%]	−0.52 +0.53	+0.71 −1.24	+0.88 −0.44	+2.43 −1.89	+3.47 −2.49	+3.30 −2.29	+3.87 −2.81	∓0.89
Pile-up offset μ (JES) [%]	-	+0.13 −0.16	+0.27 −0.20	+0.25 −0.73	+0.41 -	+0.33 −0.68	+0.37 −0.12	±1.16
Pile-up offset N_{PV} (JES) [%]	−0.33 +0.78	+0.77 −1.67	+1.22 −2.33	+0.42 −1.64	∓1.68	+0.64 −1.92	+0.31 −1.09	+1.56 −0.48
Pile-up offset p_T (JES) [%]	−0.29 +0.20	+0.53 −0.16	+1.11 −0.98	+0.59 −0.79	+0.36 −0.54	+1.04 −0.63	+1.40 −0.79	±1.78
Pile-up offset ρ topology (JES) [%]	±0.27	−0.56 +0.32	+0.24 -	−1.43 +1.79	−2.02 +2.69	−1.79 +3.09	−2.49 +2.71	−2.99 +2.41
Punch-through (JES) [%]	-	-	-	-	-	-	-	- +0.65
Single particle high-p_T (JES) [%]	-	-	-	-	-	-	-	-
b-Quark tagging efficiency (eigenvector 0) [%]	+0.47 −0.46	−0.87 +0.84	−1.42 +1.38	−1.38 +1.34	−1.27 +1.23	−1.23 +1.20	−1.43 +1.39	−2.45 +2.40
b-Quark tagging efficiency (eigenvector 1) [%]	-	±0.22	-	∓0.23	∓0.66	∓1.22	−2.18 +2.19	−4.95 +5.06
b-Quark tagging efficiency (eigenvector 2) [%]	-	-	+0.17 −0.18	+0.24 −0.25	±0.28	±0.28	±0.14	∓0.49
b-Quark tagging efficiency (eigenvector 3) [%]	-	-	±0.22	±0.48	±0.79	±0.98	+1.16 −1.15	+1.17 −1.16
b-Quark tagging efficiency (eigenvector 4) [%]	-	-	-	∓0.10	-	-	-	±0.25
b-Quark tagging efficiency (eigenvector 5) [%]	-	-	-	-	-	-	∓0.10	∓0.11
c-Quark tagging efficiency (eigenvector 0) [%]	-	-	±0.19	±0.29	±0.35	±0.41	±0.47	±0.52
c-Quark tagging efficiency (eigenvector 1) [%]	-	-	±0.19	±0.27	±0.32	±0.37	±0.39	±0.44
c-Quark tagging efficiency (eigenvector 2) [%]	-	-	-	-	±0.10	±0.15	±0.17	±0.19
Light-jet tagging efficiency (eigenvector 0) [%]	-	±0.11	-	-	+0.22 −0.23	±0.24	±0.35	±0.59
Light-jet tagging efficiency (eigenvector 1) [%]	-	-	-	-	-	-	-	-
Light-jet tagging efficiency (eigenvector 2) [%]	-	-	-	-	-	-	-	-
Light-jet tagging efficiency (eigenvector 3) [%]	-	-	-	-	-	-	-	-
Light-jet tagging efficiency (eigenvector 4) [%]	-	-	-	-	-	-	-	-
Light-jet tagging efficiency (eigenvector 5) [%]	-	-	-	-	-	-	-	-
Light-jet tagging efficiency (eigenvector 6) [%]	-	-	-	-	-	-	-	-
Light-jet tagging efficiency (eigenvector 7) [%]	-	-	-	-	-	-	-	-
Light-jet tagging efficiency (eigenvector 8) [%]	-	-	-	-	-	-	-	-
Light-jet tagging efficiency (eigenvector 9) [%]	-	-	-	-	-	-	-	-
Light-jet tagging efficiency (eigenvector 10) [%]	-	-	-	-	-	-	-	-
b-Quark tagging extrapolation [%]	-	-	-	-	-	∓0.13	∓0.18	∓0.29
b-Quark tagging extrapolation from c-Quark [%]	-	-	-	-	-	-	-	-
JET JER cross calibration forward [%]	-	-	-	-	-	-	-	-
JET JER noise forward [%]	-	-	-	-	-	-	-	-
JET JER NP0 [%]	-	-	-	-	-	-	-	-
JET JER NP1 [%]	-	+0.24 -	∓0.42	∓0.94	±0.88	+0.97 -	±0.53	±5.64
JET JER NP2 [%]	±0.41	∓0.70	+0.40 −2.14	+0.19 −1.36	±0.46	−0.46 +0.78	±1.59	−1.77 +1.58
JET JER NP3 [%]	±0.39	+0.30 −0.71	∓1.27	∓1.60	∓0.33	−0.39 +0.19	+1.08 −0.89	+0.93 −4.03
JET JER NP4 [%]	+0.18 −0.42	−0.55 +1.45	−0.14 +0.10	−0.99 +0.32	±0.79	±1.20	±0.91	−0.42 +7.62
JET JER NP5 [%]	−0.12 +0.66	+0.38 −1.82	+0.33 −1.29	∓1.80	+0.46 −0.72	+0.16	∓0.11	−1.58 +0.49
JET JER NP6 [%]	−0.11 +0.67	+0.30 −1.87	- −1.30	- −1.37	+1.02 −1.03	+1.10 −0.50	+0.60 −0.50	±1.73
JET JER NP7 [%]	- +0.49	- −1.15	∓1.53	∓1.36	+0.54 −0.45	+0.13 −0.46	-	−0.93 +6.54
JET JER NP8 [%]	-	-	-	-	-	-	-	-
QCD estimation [%]	∓9.08	±17.4	±27.6	±25.2	±22.5	±20.2	±19.2	±16.6
K-factor normalization mass [%]	∓0.18	+0.24 −0.25	+0.57 −0.58	±0.69	±0.71	+0.70 −0.71	+0.68 −0.69	+0.66 −0.67
K-factor normalization PDFAS [%]	∓0.27	±0.37	±0.86	±1.03	±1.06	±1.05	±1.03	±1.00
K-factor normalization scale [%]	−0.15 +0.24	+0.21 −0.32	+0.49 −0.76	+0.59 −0.91	+0.60 −0.94	+0.60 −0.93	+0.58 −0.91	+0.57 −0.88
Luminosity [%]	-	-	-	-	-	-	-	-
MCSignal stat. [%]	±0.48	±1.30	±1.69	±1.74	±1.80	±2.13	±3.14	±10.3
QCD stat. [%]	±1.74	±4.03	±3.71	±3.23	±3.20	±3.67	±4.22	±5.89
ISR/FSR + scale [%]	+1.22 −0.95	+0.36	−4.25 +3.22	−7.34 +5.09	−9.29 +6.90	−13.3 +5.54	−12.1 +6.62	±13.7
Alternate hard-scattering model [%]	∓1.52	∓0.32	±4.60	±11.0	±15.6	±6.90	±5.44	±42.1
Alternate parton-shower model [%]	±1.66	∓0.66	∓5.86	∓9.42	∓7.72	∓10.9	∓13.9	∓31.9
Inter PDF [%]	-	-	±0.29	±0.33	±0.47	±0.54	±0.47	±0.38
Intra PDF [%]	-	-	-	-	∓0.13	∓0.17	∓0.33	∓0.25

TABLE D.29: Table of systematics for the normalised differential cross-section at the parton level for the p_T^{top2} observable.

Bins [Unit $y^{topsubleading}$]	0–0.30	0.30–0.60	0.60–0.90	0.90–1.20	1.20–1.50	1.50–2	2–2.50
$1/\sigma \cdot d\sigma$ / $dy^{topsubleading}$	$5.96 \cdot 10^{-1}$	$5.84 \cdot 10^{-1}$	$5.48 \cdot 10^{-1}$	$4.72 \cdot 10^{-1}$	$4.18 \cdot 10^{-1}$	$2.85 \cdot 10^{-1}$	$1.43 \cdot 10^{-1}$
Total Uncertainty [%]	$^{+5.06}_{-5.04}$	$^{+3.63}_{-3.39}$	$^{+4.49}_{-5.03}$	$^{+8.03}_{-8.39}$	$^{+7.70}_{-7.88}$	±9.34	$^{+26.7}_{-26.8}$
Statistics [%]	±1.7	±1.8	±1.9	±2.1	±2.3	±2.4	±6.9
Systematics [%]	$^{+4.38}_{-4.35}$	$^{+2.52}_{-2.17}$	$^{+3.54}_{-4.20}$	$^{+7.43}_{-7.81}$	$^{+6.87}_{-7.07}$	±8.63	$^{+24.7}_{-24.8}$
Jet vertex fraction [%]	-	-	-	-	-	-	$^{+0.16}_{-0.14}$
b-Tagged jet energy scale (JES) [%]	±0.31	$^{+0.19}_{-}$	$^{-0.46}_{+0.19}$	$^{+0.46}_{-0.23}$	∓0.12	$^{-0.21}_{+0.17}$	$^{+0.11}_{-0.87}$
Effective detector NP set 1 (JES) [%]	$^{-}_{+0.35}$	±0.47	$^{-0.39}_{+0.53}$	∓0.22	$^{+0.69}_{-0.31}$	$^{+0.16}_{-0.32}$	∓1.79
Effective mixed NP set 1 (JES) [%]	$^{-}_{+0.58}$	-	-	$^{-0.15}_{+0.13}$	$^{+0.33}_{-0.28}$	$^{-0.20}_{+0.10}$	$^{+0.32}_{-1.28}$
Effective mixed NP set 2 (JES) [%]	±0.36	$^{-0.20}_{+0.25}$	$^{+0.17}_{-0.21}$	$^{+0.21}_{-0.12}$	-	∓0.31	∓0.70
Effective mixed NP set 3 (JES) [%]	-	±0.17	∓0.11	±0.10	-	-	∓0.35
Effective modelling NP set 1 (JES) [%]	$^{-0.56}_{+0.13}$	$^{-0.18}_{+0.51}$	∓0.33	$^{+0.73}_{-1.87}$	$^{+2.18}_{-0.14}$	±0.61	$^{-2.46}_{+1.51}$
Effective modelling NP set 2 (JES) [%]	±0.57	±0.59	$^{+0.41}_{+0.24}$	∓0.34	$^{+0.64}_{-0.51}$	±0.22	∓1.95
Effective modelling NP set 3 (JES) [%]	±0.17	$^{-}_{+0.28}$	∓0.18	$^{+0.18}_{-}$	±0.17	-	∓0.63
Effective modelling NP set 4 (JES) [%]	±0.27	-	∓0.14	$^{-}_{+0.26}$	±0.38	∓0.14	∓0.79
Effective statistical NP set 1 (JES) [%]	-	-	-	-	-	-	-
Effective statistical NP set 2 (JES) [%]	-	±0.24	$^{-}_{-0.20}$	-	$^{+0.20}_{-}$	$^{-0.27}_{-}$	∓0.69
Effective statistical NP set 3 (JES) [%]	-	-	-	±0.16	$^{-0.13}_{-}$	∓0.15	±0.24
Effective statistical NP set 4 (JES) [%]	±0.15	$^{-}_{-0.16}$	$^{-0.33}_{+0.13}$	±0.18	$^{-0.18}_{-}$	-	$^{-}_{-0.22}$
Effective statistical NP set 5 (JES) [%]	-	$^{-0.20}_{+0.11}$	∓0.15	-	$^{+0.21}_{-}$	∓0.25	±0.65
Effective statistical NP set 6 (JES) [%]	-	$^{+0.31}_{-}$	∓0.20	-	±0.10	$^{-}_{-0.28}$	$^{-0.33}_{+0.34}$
η intercalibration model (JES) [%]	$^{-0.48}_{+0.26}$	$^{+0.15}_{-0.10}$	$^{-0.44}_{+0.22}$	$^{-0.22}_{-}$	$^{+0.33}_{-1.17}$	$^{+0.38}_{-}$	±1.02
high E η intercalibration non closure (JES) [%]	-	-	-	-	-	-	-
neg η intercalibration non closure (JES) [%]	-	-	-	-	-	±0.10	∓0.54
pos η intercalibration non closure (JES) [%]	-	-	-	-	-	-	±0.41
η intercalibration total stat (JES) [%]	±0.29	$^{+0.17}_{-}$	$^{-0.37}_{+0.26}$	$^{-0.17}_{+0.11}$	±0.27	$^{-}_{-0.19}$	∓1.10
Flavour composition (JES) [%]	$^{-0.13}_{+0.16}$	-	±0.38	$^{-0.12}_{+0.55}$	$^{+0.20}_{-0.55}$	$^{+0.21}_{-0.31}$	∓0.71
Flavour response (JES) [%]	$^{+0.62}_{-0.67}$	±0.44	±0.42	∓0.65	$^{-1.00}_{+1.20}$	$^{-0.55}_{+0.18}$	$^{+0.76}_{-1.09}$
Pile-up offset μ (JES) [%]	±0.25	±0.15	∓0.43	±0.14	±0.14	∓0.25	$^{-0.63}_{+0.46}$
Pile-up offset N_{PV} (JES) [%]	$^{-}_{+0.19}$	$^{+0.20}_{-0.39}$	∓0.11	∓0.27	±0.59	±0.65	$^{-1.85}_{+0.38}$
Pile-up offset p_T (JES) [%]	±0.23	±0.11	∓0.43	-	$^{+0.21}_{-0.18}$	-	±0.25
Pile-up offset ρ topology (JES) [%]	$^{-0.55}_{+0.34}$	±0.29	±0.44	$^{+0.41}_{-0.76}$	$^{+0.79}_{-0.85}$	$^{-0.57}_{+0.41}$	∓0.77
Punch-through (JES) [%]	-	-	-	-	-	-	∓0.14
Single particle high-p_T (JES) [%]	-	-	-	-	-	-	-
b-Quark tagging efficiency (eigenvector 0) [%]	-	-	∓0.12	-	-	-	$^{+0.45}_{-0.42}$
b-Quark tagging efficiency (eigenvector 1) [%]	-	-	-	-	-	-	±0.10
b-Quark tagging efficiency (eigenvector 2) [%]	-	-	-	-	-	-	-
b-Quark tagging efficiency (eigenvector 3) [%]	-	-	-	-	-	-	-
b-Quark tagging efficiency (eigenvector 4) [%]	-	-	-	-	-	-	-
b-Quark tagging efficiency (eigenvector 5) [%]	-	-	-	-	-	-	-
c-Quark tagging efficiency (eigenvector 0) [%]	-	-	-	-	-	-	-
c-Quark tagging efficiency (eigenvector 1) [%]	-	-	-	-	-	-	-
c-Quark tagging efficiency (eigenvector 2) [%]	-	-	-	-	-	-	-
Light-jet tagging efficiency (eigenvector 0) [%]	-	-	-	-	$^{-0.17}_{+0.18}$	-	-
Light-jet tagging efficiency (eigenvector 1) [%]	-	-	-	-	-	-	-
Light-jet tagging efficiency (eigenvector 2) [%]	-	-	-	-	-	-	-
Light-jet tagging efficiency (eigenvector 3) [%]	-	-	-	-	-	-	-
Light-jet tagging efficiency (eigenvector 4) [%]	-	-	-	-	-	-	-
Light-jet tagging efficiency (eigenvector 5) [%]	-	-	-	-	-	-	-
Light-jet tagging efficiency (eigenvector 6) [%]	-	-	-	-	-	-	-
Light-jet tagging efficiency (eigenvector 7) [%]	-	-	-	-	-	-	-
Light-jet tagging efficiency (eigenvector 8) [%]	-	-	-	-	-	-	-
Light-jet tagging efficiency (eigenvector 9) [%]	-	-	-	-	-	-	-
Light-jet tagging efficiency (eigenvector 10) [%]	-	-	-	-	-	-	-
b-Quark tagging extrapolation [%]	-	-	-	-	-	-	-
b-Quark tagging extrapolation from c-Quark [%]	-	-	-	-	-	-	-
JET JER cross calibration forward [%]	-	-	-	-	-	-	-
JET JER noise forward [%]	-	-	-	-	-	-	-
JET JER NP0 [%]	-	-	-	-	-	-	-
JET JER NP1 [%]	∓0.74	∓0.15	$^{+0.72}_{-}$	∓0.27	∓1.33	∓0.22	±3.76
JET JER NP2 [%]	∓0.80	±1.18	$^{-}_{-1.69}$	$^{-}_{-0.74}$	∓0.71	±0.92	±2.80
JET JER NP3 [%]	$^{+0.16}_{-0.25}$	$^{-0.27}_{+0.56}$	$^{+0.35}_{-0.46}$	$^{-0.94}_{+0.37}$	$^{-1.27}_{+0.45}$	∓0.70	±3.40
JET JER NP4 [%]	∓0.88	$^{-0.10}_{+1.32}$	∓1.06	∓0.27	±0.89	±0.91	$^{+1.22}_{-1.57}$
JET JER NP5 [%]	$^{-0.47}_{+0.22}$	$^{-0.13}_{+0.34}$	$^{+0.45}_{-}$	$^{+0.32}_{-0.25}$	$^{-}_{-0.69}$	$^{-1.03}_{+0.77}$	$^{+1.77}_{-1.02}$
JET JER NP6 [%]	∓0.29	$^{-}_{+0.52}$	$^{-0.30}_{-0.68}$	$^{+0.30}_{-1.07}$	$^{-0.28}_{+0.30}$	$^{-0.13}_{+0.99}$	±0.31
JET JER NP7 [%]	$^{-}_{+0.16}$	±0.37	$^{-}_{+0.38}$	$^{+0.58}_{-0.74}$	±0.10	$^{-0.47}_{+0.68}$	∓2.16
JET JER NP8 [%]	-	-	-	-	-	-	-
QCD estimation [%]	∓1.05	±0.46	±0.99	±2.20	∓0.27	∓1.13	∓2.37
K-factor normalization mass [%]	-	-	-	-	-	-	-
K-factor normalization PDFAS [%]	-	-	-	-	-	-	∓0.13
K-factor normalization scale [%]	-	-	-	-	-	-	-
Luminosity [%]	-	-	-	-	-	-	-
MCSignal stat. [%]	±1.27	±1.31	±1.39	±1.54	±1.77	±1.78	±4.90
QCD stat. [%]	±1.25	±1.30	±1.39	±1.53	±1.81	±1.92	±5.57
ISR/FSR + scale [%]	$^{-1.15}_{+1.41}$	$^{-1.06}_{+0.29}$	$^{-1.43}_{+0.24}$	$^{+0.55}_{-0.88}$	$^{-2.25}_{-}$	∓3.54	±17.9
Alternate hard-scattering model [%]	±0.68	±0.13	±2.62	±6.73	±0.65	∓5.18	∓12.2
Alternate parton-shower model [%]	±3.36	±0.54	∓0.60	±1.19	∓5.86	∓5.26	±8.46
Inter PDF [%]	∓0.11	∓0.11	-	-	±0.24	±0.14	∓0.17
Intra PDF [%]	-	∓0.11	∓0.16	∓0.13	∓0.14	±0.25	±0.80

TABLE D.30: Table of systematics for the normalised differential cross-section at the parton level for the y_{top2} observable.

Bins [Unit m^{tt}]	0–400	400–500	500–585	585–675	675–765	765–870	870–1000	1000–1150	1150–1500	1500–3000
$1/\sigma \cdot \mathrm{d}\sigma$ / $\mathrm{d}m^{tt}$	$5.04 \cdot 10^{-4}$	$3.93 \cdot 10^{-3}$	$2.05 \cdot 10^{-3}$	$1.11 \cdot 10^{-3}$	$5.83 \cdot 10^{-4}$	$3.20 \cdot 10^{-4}$	$1.69 \cdot 10^{-4}$	$7.30 \cdot 10^{-5}$	$2.65 \cdot 10^{-5}$	$1.86 \cdot 10^{-6}$
Total Uncertainty [%]	$^{+25.0}_{-24.3}$	$^{+6.70}_{-6.86}$	$^{+9.57}_{-9.69}$	$^{+19.0}_{-18.9}$	$^{+22.5}_{-23.6}$	$^{+24.0}_{-22.9}$	$^{+26.4}_{-28.7}$	$^{+24.1}_{-25.4}$	$^{+25.1}_{-25.4}$	$^{+33.7}_{-34.0}$
Statistics [%]	±5.1	±1.5	±2.8	±3.0	±3.0	±3.0	±3.2	±4.0	±4.4	±9.2
Systematics [%]	$^{+23.4}_{-22.7}$	$^{+5.93}_{-6.11}$	$^{+8.00}_{-8.15}$	$^{+18.2}_{-18.1}$	$^{+21.9}_{-23.0}$	$^{+23.5}_{-22.4}$	$^{+25.9}_{-28.2}$	$^{+23.3}_{-24.7}$	$^{+24.2}_{-24.5}$	$^{+31.4}_{-31.7}$
Jet vertex fraction [%]	-	∓0.11	-	$^{-0.16}_{+0.15}$	∓0.17	$^{-0.25}_{+0.24}$	$^{-0.28}_{+0.27}$	$^{-0.31}_{+0.30}$	$^{-0.32}_{+0.31}$	$^{-0.31}_{+0.30}$
b-Tagged jet energy scale (JES) [%]	$^{-0.27}_{+2.10}$	∓0.23	$^{+0.15}_{-1.12}$	$^{+0.23}_{-0.57}$	$^{-}_{-0.73}$	$^{+0.80}_{-0.98}$	$^{+0.36}_{-0.81}$	∓0.96	∓0.94	$^{+0.50}_{-0.29}$
Effective detector NP set 1 (JES) [%]	$^{-0.66}_{+0.69}$	∓0.20	$^{+0.88}_{-0.64}$	$^{+0.35}_{-}$	$^{-0.15}_{+0.31}$	±0.61	±0.60	∓0.74	∓0.40	$^{-0.52}_{+1.02}$
Effective mixed NP set 1 (JES) [%]	±1.39	$^{+0.11}_{-0.56}$	∓0.46	$^{-0.55}_{+0.33}$	$^{-1.09}_{+0.18}$	∓0.15	∓0.91	$^{+0.43}_{-1.03}$	∓1.93	$^{+0.76}_{-1.20}$
Effective mixed NP set 2 (JES) [%]	±1.03	∓0.18	∓0.46	∓0.20	∓0.36	$^{-0.52}_{+0.11}$	∓0.72	∓0.79	∓0.77	∓0.73
Effective mixed NP set 3 (JES) [%]	$^{+0.42}_{-}$	∓0.12	-	$^{-0.11}_{+0.13}$	-	$^{-0.13}_{+0.17}$	-	-	$^{-0.48}_{+0.28}$	±0.30
Effective modelling NP set 1 (JES) [%]	$^{-0.17}_{+0.35}$	∓1.95	±1.37	±2.39	$^{-2.03}_{+1.99}$	$^{-0.34}_{+3.66}$	$^{-0.53}_{+3.35}$	$^{-2.13}_{+3.19}$	$^{-2.78}_{+0.43}$	±4.35
Effective modelling NP set 2 (JES) [%]	$^{-0.89}_{+3.43}$	∓1.03	$^{+0.94}_{-1.53}$	$^{+0.61}_{-0.24}$	-	$^{+0.71}_{-0.44}$	$^{+1.15}_{-0.73}$	$^{+1.02}_{-1.47}$	$^{+0.38}_{-1.32}$	$^{+0.83}_{-0.18}$
Effective modelling NP set 3 (JES) [%]	±0.89	∓0.17	∓0.35	-	$^{-0.34}_{+0.24}$	$^{-0.82}_{+1.08}$	$^{-1.03}_{+0.57}$	$^{-0.93}_{+1.10}$	$^{-1.62}_{+0.69}$	±0.92
Effective modelling NP set 4 (JES) [%]	±1.08	∓0.14	∓0.51	$^{+0.16}_{∓0.40}$	∓0.40	∓0.33	∓1.08	∓0.69	∓0.65	∓1.18
Effective statistical NP set 1 (JES) [%]	-	-	-	-	-	-	-	-	-	-
Effective statistical NP set 2 (JES) [%]	$^{-0.44}_{+0.22}$	∓0.17	±0.17	$^{+0.60}_{-}$	$^{+0.57}_{-0.19}$	$^{+0.47}_{-0.22}$	$^{+0.24}_{-0.20}$	$^{+0.68}_{-0.62}$	$^{+0.75}_{-0.79}$	$^{-0.26}_{+0.25}$
Effective statistical NP set 3 (JES) [%]	±0.10	-	$^{-0.23}_{-}$	$^{+0.17}_{-0.28}$	∓0.19	$^{-0.15}_{+0.21}$	$^{-0.47}_{-}$	$^{-0.58}_{-}$	∓0.29	$^{+0.22}_{-0.13}$
Effective statistical NP set 4 (JES) [%]	$^{+0.24}_{-0.11}$	±0.28	∓0.23	$^{-0.27}_{-}$	$^{+0.23}_{-0.45}$	$^{-}_{-0.16}$	$^{-}_{-0.16}$	∓0.49	∓0.34	∓0.58
Effective statistical NP set 5 (JES) [%]	$^{+0.41}_{-}$	-	$^{-0.41}_{+0.20}$	$^{-0.12}_{+0.10}$	-	-	-	∓0.29	-	∓0.21
Effective statistical NP set 6 (JES) [%]	±0.36	-	∓0.13	$^{-0.30}_{+0.29}$	∓0.14	-	∓0.15	∓0.15	$^{-0.62}_{+0.47}$	$^{+0.14}_{-0.53}$
η intercalibration model (JES) [%]	±0.47	$^{+0.59}_{-0.35}$	∓0.58	$^{-0.71}_{+0.69}$	$^{-1.33}_{+0.68}$	$^{-1.29}_{+0.36}$	$^{-0.11}_{+0.39}$	$^{-1.28}_{+0.18}$	∓1.38	$^{-0.21}_{+1.44}$
high E η intercalibration non closure (JES) [%]	-	-	-	-	-	-	-	-	-	-
neg η intercalibration non closure (JES) [%]	-	-	-	-	-	-	-	∓0.10	-	-
pos η intercalibration non closure (JES) [%]	-	-	-	-	-	-	-	-	-	-
η intercalibration total stat (JES) [%]	±0.53	∓0.29	-	±0.48	-	±0.30	-	$^{-0.71}_{+0.34}$	$^{-0.69}_{+0.35}$	$^{+0.12}_{-0.31}$
Flavour composition (JES) [%]	$^{-0.37}_{+0.74}$	∓0.51	$^{+0.75}_{-0.27}$	±0.53	$^{-0.54}_{+0.12}$	$^{-}_{+0.27}$	±0.11	$^{-1.04}_{+0.25}$	∓0.99	±0.98
Flavour response (JES) [%]	$^{-2.18}_{+0.89}$	$^{-0.89}_{+0.48}$	±0.95	$^{+2.79}_{-1.41}$	$^{+2.43}_{-2.32}$	$^{+1.20}_{-0.52}$	$^{+2.45}_{-0.89}$	$^{+2.59}_{-2.94}$	$^{+0.94}_{-2.73}$	$^{+2.87}_{-}$
Pile-up offset μ (JES) [%]	±1.22	∓0.68	$^{-0.28}_{-}$	±0.40	$^{+0.31}_{-0.24}$	±0.27	$^{-}_{-0.51}$	$^{-0.48}_{-}$	∓0.62	∓0.10
Pile-up offset N_{PV} (JES) [%]	$^{-1.89}_{+2.51}$	$^{+0.24}_{-0.50}$	$^{+0.63}_{-0.80}$	$^{+1.13}_{-0.38}$	$^{+0.95}_{-1.83}$	$^{+0.71}_{-0.28}$	$^{+0.54}_{-1.46}$	$^{+0.41}_{-1.23}$	∓1.78	$^{+2.00}_{-0.92}$
Pile-up offset p_T (JES) [%]	$^{-1.00}_{+1.70}$	$^{-}_{-0.19}$	$^{+0.51}_{-0.59}$	$^{+0.54}_{-0.57}$	$^{+0.34}_{-1.29}$	$^{+0.61}_{-0.37}$	$^{+0.37}_{-0.84}$	$^{+0.90}_{-1.02}$	$^{-}_{-1.57}$	$^{+2.44}_{-0.96}$
Pile-up offset ρ topology (JES) [%]	∓1.38	$^{+0.40}_{-0.25}$	±0.67	$^{-0.71}_{+1.28}$	$^{-1.95}_{+1.28}$	$^{-0.36}_{+2.05}$	$^{-0.48}_{+2.33}$	$^{-2.57}_{+1.34}$	$^{-2.09}_{+0.50}$	$^{-1.11}_{+2.38}$
Punch-through (JES) [%]	-	-	-	-	-	-	-	-	-	$^{+0.27}_{-}$
Single particle high-p_T (JES) [%]	-	-	-	-	-	-	-	-	-	-
b-Quark tagging efficiency (eigenvector 0) [%]	$^{+1.14}_{-1.10}$	±0.26	$^{-0.58}_{+0.57}$	$^{-0.81}_{+0.78}$	$^{-1.09}_{+1.06}$	$^{-1.19}_{+1.16}$	$^{-1.24}_{+1.20}$	$^{-1.23}_{+1.19}$	$^{-1.25}_{+1.21}$	$^{-1.37}_{+1.33}$
b-Quark tagging efficiency (eigenvector 1) [%]	±0.19	±0.14	-	∓0.11	∓0.34	∓0.66	∓0.95	$^{-1.13}_{+1.14}$	$^{-1.19}_{+1.20}$	$^{-1.44}_{+1.45}$
b-Quark tagging efficiency (eigenvector 2) [%]	∓0.27	-	$^{+0.12}_{-0.13}$	±0.18	$^{+0.26}_{-0.27}$	$^{+0.31}_{-0.32}$	$^{+0.30}_{-0.31}$	±0.26	±0.22	$^{+0.20}_{-0.21}$
b-Quark tagging efficiency (eigenvector 3) [%]	∓0.20	∓0.15	-	±0.21	±0.42	±0.61	±0.72	$^{+0.77}_{-0.76}$	±0.73	$^{+0.87}_{-0.86}$
b-Quark tagging efficiency (eigenvector 4) [%]	-	-	-	-	-	-	-	-	-	-
b-Quark tagging efficiency (eigenvector 5) [%]	-	-	-	-	-	-	-	-	-	-
c-Quark tagging efficiency (eigenvector 0) [%]	∓0.21	-	-	±0.20	±0.30	±0.39	±0.36	±0.33	±0.40	$^{+0.46}_{-0.47}$
c-Quark tagging efficiency (eigenvector 1) [%]	∓0.16	-	-	±0.14	±0.21	±0.27	±0.26	±0.26	±0.29	$^{+0.32}_{-0.33}$
c-Quark tagging efficiency (eigenvector 2) [%]	-	-	-	-	-	-	±0.10	±0.11	±0.11	±0.15
Light-jet tagging efficiency (eigenvector 0) [%]	∓0.12	∓0.15	±0.12	±0.17	±0.35	±0.30	±0.36	±0.12	$^{+0.51}_{-0.53}$	$^{+0.41}_{-0.42}$
Light-jet tagging efficiency (eigenvector 1) [%]	-	-	-	-	-	-	-	-	-	-
Light-jet tagging efficiency (eigenvector 2) [%]	-	-	-	-	-	-	-	-	-	-
Light-jet tagging efficiency (eigenvector 3) [%]	-	-	-	-	-	-	-	-	-	-
Light-jet tagging efficiency (eigenvector 4) [%]	-	-	-	-	-	-	-	-	-	-
Light-jet tagging efficiency (eigenvector 5) [%]	-	-	-	-	-	-	-	-	-	-
Light-jet tagging efficiency (eigenvector 6) [%]	-	-	-	-	-	-	-	-	-	-
Light-jet tagging efficiency (eigenvector 7) [%]	-	-	-	-	-	-	-	-	-	-
Light-jet tagging efficiency (eigenvector 8) [%]	-	-	-	-	-	-	-	-	-	-
Light-jet tagging efficiency (eigenvector 9) [%]	-	-	-	-	-	-	-	-	-	-
Light-jet tagging efficiency (eigenvector 10) [%]	-	-	-	-	-	-	-	-	-	-
b-Quark tagging extrapolation [%]	-	-	-	-	-	-	∓0.11	∓0.11	∓0.15	∓0.28
b-Quark tagging extrapolation from c-Quark [%]	-	-	-	-	-	-	-	-	-	-
JET JER cross calibration forward [%]	-	-	-	-	-	-	-	-	-	-
JET JER noise forward [%]	-	-	-	-	-	-	-	-	-	-
JET JER NP0 [%]	-	-	-	-	-	-	-	-	-	-
JET JER NP1 [%]	$^{-0.47}_{-}$	-	$^{+0.35}_{-}$	∓0.36	∓0.26	±1.65	$^{+1.76}_{-0.13}$	±0.48	-	$^{+3.45}_{-0.46}$
JET JER NP2 [%]	∓2.28	-	-	-	-	±2.65	$^{-0.27}_{+2.74}$	±0.65	$^{-1.23}_{+0.71}$	±4.59
JET JER NP3 [%]	$^{+0.91}_{-2.46}$	∓0.13	$^{+1.23}_{-0.20}$	$^{-0.74}_{+1.55}$	$^{+0.50}_{-0.80}$	$^{-0.32}_{+1.47}$	±2.00	±0.91	$^{-2.11}_{+0.36}$	±2.11
JET JER NP4 [%]	$^{+1.33}_{-4.87}$	$^{-}_{+0.35}$	$^{-0.37}_{+2.07}$	$^{-1.09}_{+2.29}$	$^{+0.67}_{-1.21}$	$^{-0.12}_{+3.35}$	$^{-}_{+2.86}$	$^{-0.42}_{+1.97}$	$^{-1.25}_{+2.00}$	±2.35
JET JER NP5 [%]	$^{-}_{+2.08}$	$^{+0.31}_{-0.44}$	∓0.68	$^{+0.15}_{-1.78}$	$^{-}_{-0.89}$	$^{-0.17}_{+0.66}$	±0.49	∓0.67	∓2.13	±3.56
JET JER NP6 [%]	$^{-1.68}_{+2.04}$	$^{+0.43}_{+0.11}$	$^{+0.66}_{-1.17}$	$^{+1.71}_{-1.39}$	$^{+1.13}_{-1.64}$	$^{+2.27}_{-0.18}$	$^{+2.54}_{-0.68}$	$^{+1.33}_{-0.81}$	$^{+0.96}_{-2.55}$	±3.82
JET JER NP7 [%]	±1.60	$^{-0.32}_{+0.15}$	∓1.05	∓1.45	∓1.30	$^{+0.40}_{-0.50}$	$^{+0.79}_{-0.59}$	∓1.43	∓2.15	±2.30
JET JER NP8 [%]	-	-	-	-	-	-	-	-	-	-
QCD estimation [%]	∓19.4	∓1.40	±5.50	±13.3	±17.4	±17.4	±17.3	±17.0	±18.3	±21.1
K-factor normalization mass [%]	∓0.62	∓0.11	±0.26	±0.41	±0.58	$^{+0.65}_{-0.66}$	$^{+0.67}_{-0.68}$	$^{+0.68}_{-0.69}$	$^{+0.65}_{-0.66}$	$^{+0.66}_{-0.67}$
K-factor normalization PDFAS [%]	∓0.92	∓0.16	±0.39	±0.62	±0.86	±0.98	±1.00	±1.02	±0.98	±0.99
K-factor normalization scale [%]	$^{-0.53}_{+0.82}$	$^{-}_{+0.14}$	$^{+0.22}_{-0.34}$	$^{+0.35}_{-0.54}$	$^{+0.49}_{-0.76}$	$^{+0.56}_{-0.87}$	$^{+0.57}_{-0.89}$	$^{+0.58}_{-0.90}$	$^{+0.56}_{-0.86}$	$^{+0.57}_{-0.88}$
Luminosity [%]	-	-	-	-	-	-	-	-	-	-
MCSignal stat. [%]	±2.28	±0.89	±1.51	±1.71	±1.73	±1.81	±2.01	±2.54	±3.08	±6.33
QCD stat. [%]	±6.76	±2.58	±4.15	±4.11	±3.53	±3.35	±3.37	±3.58	±3.76	±4.87
ISR/FSR + scale [%]	$^{+7.49}_{-3.94}$	$^{+1.96}_{-2.24}$	$^{-3.26}_{+1.89}$	$^{-5.27}_{+4.49}$	$^{-8.60}_{+5.77}$	$^{-6.67}_{+6.98}$	$^{-14.7}_{+7.02}$	$^{-10.9}_{+7.81}$	$^{-3.94}_{+6.54}$	$^{-8.51}_{+4.50}$
Alternate hard-scattering model [%]	±1.56	∓2.22	±1.87	∓0.60	±0.74	±6.53	∓1.60	∓5.83	±2.29	±7.38
Alternate parton-shower model [%]	±7.49	±4.11	∓2.84	∓10.1	∓10.9	∓9.60	∓16.0	∓10.9	∓13.0	∓18.1
Inter PDF [%]	∓0.34	-	±0.15	±0.25	±0.33	±0.38	±0.49	±0.45	±0.45	±0.74
Intra PDF [%]	±0.15	-	-	-	-	-	±0.16	±0.30	±0.38	±0.91

TABLE D.31: Table of systematics for the normalised differential cross-section at the parton level for the $m_{t\bar{t}}$ observable.

Bins [Unit p_T^{tt}]	0–45	45–100	100–160	160–230	230–320	320–420	420–550	550–1000
$1/\sigma \cdot \mathrm{d}\sigma$ / $\mathrm{d}p_T^{tt}$	$1.12 \cdot 10^{-2}$	$5.21 \cdot 10^{-3}$	$1.91 \cdot 10^{-3}$	$7.75 \cdot 10^{-4}$	$2.72 \cdot 10^{-4}$	$9.01 \cdot 10^{-5}$	$2.66 \cdot 10^{-5}$	$4.69 \cdot 10^{-6}$
Total Uncertainty [%]	$^{+10.0}_{-9.98}$	$^{+7.20}_{-7.12}$	±24.9	±31.4	$^{+19.2}_{-19.6}$	$^{+9.54}_{-10.3}$	$^{+15.6}_{-16.0}$	$^{+24.9}_{-24.3}$
Statistics [%]	±1.0	±1.3	±1.7	±2.2	±2.8	±4.4	±7.0	±11.
Systematics [%]	$^{+9.92}_{-9.89}$	$^{+6.97}_{-6.89}$	$^{+24.7}_{-24.8}$	±31.3	$^{+18.7}_{-19.1}$	$^{+7.23}_{-8.26}$	$^{+12.7}_{-13.2}$	$^{+19.8}_{-19.1}$
Jet vertex fraction [%]	$^{-0.13}_{+0.14}$	-	$^{+0.19}_{-0.20}$	$^{+0.23}_{-0.24}$	$^{+0.28}_{-0.29}$	$^{+0.25}_{-0.27}$	$^{+0.15}_{-0.17}$	$^{+0.14}_{-0.13}$
b-Tagged jet energy scale (JES) [%]	-	-	-	$^{-0.57}_{-}$	∓0.94	$^{-0.22}_{+0.59}$	$^{-0.13}_{+1.66}$	±1.79
Effective detector NP set 1 (JES) [%]	-	±0.14	∓0.75	$^{+0.37}_{-0.80}$	$^{-0.53}_{+0.19}$	$^{-1.93}_{+1.53}$	∓0.52	±4.34
Effective mixed NP set 1 (JES) [%]	±0.11	-	∓0.50	$^{+0.48}_{-0.61}$	$^{+1.09}_{-0.43}$	∓0.78	$^{+0.67}_{-0.37}$	$^{+3.30}_{-2.59}$
Effective mixed NP set 2 (JES) [%]	-	$^{+0.22}_{-}$	-	$^{-0.42}_{-}$	$^{-0.24}_{+0.67}$	$^{+0.77}_{-0.50}$	$^{+0.95}_{-}$	$^{-1.02}_{+1.55}$
Effective mixed NP set 3 (JES) [%]	-	-	-	-	$^{+0.30}_{-0.21}$	±0.22	∓0.59	±1.10
Effective modelling NP set 1 (JES) [%]	$^{-0.78}_{+0.67}$	$^{+1.18}_{-0.12}$	$^{+0.42}_{-1.57}$	$^{+1.40}_{-1.97}$	∓1.66	∓3.31	$^{-0.22}_{+0.45}$	±4.46
Effective modelling NP set 2 (JES) [%]	$^{+0.36}_{-}$	∓0.11	$^{-0.85}_{+0.12}$	$^{-0.79}_{+0.33}$	$^{-1.19}_{+1.13}$	$^{-1.28}_{+1.09}$	$^{-0.30}_{+1.02}$	±1.35
Effective modelling NP set 3 (JES) [%]	-	∓0.12	$^{-}_{-0.29}$	$^{-0.45}_{-}$	±0.54	$^{-1.28}_{+0.64}$	$^{-0.81}_{+0.21}$	±2.68
Effective modelling NP set 4 (JES) [%]	$^{-}_{-0.12}$	±0.25	∓0.41	∓0.19	$^{+0.30}_{-0.18}$	$^{-0.28}_{+0.67}$	$^{-0.75}_{+0.97}$	$^{+0.75}_{-1.08}$
Effective statistical NP set 1 (JES) [%]	-	-	-	-	-	-	-	$^{+0.23}_{-}$
Effective statistical NP set 2 (JES) [%]	-	$^{+0.18}_{-}$	∓0.26	$^{-0.21}_{-}$	$^{-0.39}_{+0.20}$	$^{+0.31}_{-0.33}$	$^{-0.15}_{-0.42}$	±1.63
Effective statistical NP set 3 (JES) [%]	-	-	∓0.12	$^{-0.15}_{+0.11}$	±0.47	$^{-0.19}_{+0.48}$	$^{+0.48}_{-0.51}$	$^{-1.31}_{+1.43}$
Effective statistical NP set 4 (JES) [%]	$^{-}_{-0.16}$	$^{-}_{+0.22}$	$^{-0.21}_{-}$	-	±0.14	$^{-0.51}_{+0.43}$	$^{-0.32}_{+0.70}$	$^{-0.99}_{+0.89}$
Effective statistical NP set 5 (JES) [%]	$^{-0.14}_{+0.17}$	$^{+0.16}_{-0.14}$	$^{-}_{-0.25}$	$^{+0.22}_{-0.16}$	$^{+0.15}_{-0.32}$	$^{+0.26}_{-}$	$^{+0.91}_{-0.60}$	∓0.43
Effective statistical NP set 6 (JES) [%]	-	-	∓0.14	-	$^{+0.29}_{-}$	±0.10	$^{-0.18}_{+0.99}$	∓0.74
η intercalibration model (JES) [%]	-	-	∓0.26	$^{+0.50}_{-0.55}$	∓0.74	$^{-0.76}_{+1.25}$	$^{-1.97}_{+0.99}$	±2.74
high E η intercalibration non closure (JES) [%]	-	-	-	-	-	-	-	-
neg η intercalibration non closure (JES) [%]	-	-	-	-	-	-	±0.14	-
pos η intercalibration non closure (JES) [%]	-	-	-	-	-	-	$^{+0.13}_{-0.12}$	-
η intercalibration total stat (JES) [%]	-	$^{-}_{+0.20}$	∓0.25	∓0.30	$^{-}_{-0.39}$	$^{-0.13}_{+0.36}$	$^{-0.49}_{+0.74}$	±0.77
Flavour composition (JES) [%]	$^{-0.15}_{+0.11}$	-	$^{+0.17}_{-0.36}$	$^{+1.44}_{-0.37}$	∓0.92	∓0.76	∓0.65	±2.55
Flavour response (JES) [%]	$^{-}_{-0.28}$	±0.23	$^{-0.17}_{+0.23}$	$^{-0.78}_{+1.84}$	∓0.85	∓3.14	∓0.50	±4.67
Pile-up offset μ (JES) [%]	-	-	∓0.12	±0.26	$^{-}_{-0.46}$	$^{+0.72}_{-0.14}$	∓0.71	±1.92
Pile-up offset N_{PV} (JES) [%]	-	$^{+0.29}_{-}$	$^{-0.26}_{+0.19}$	$^{-0.19}_{+0.35}$	∓0.25	∓0.47	$^{-0.46}_{+0.45}$	±2.89
Pile-up offset p_T (JES) [%]	$^{-0.12}_{+0.10}$	$^{+0.26}_{-0.30}$	$^{-}_{+0.17}$	-	$^{-0.10}_{+0.38}$	∓0.74	$^{+0.56}_{-0.37}$	±2.19
Pile-up offset ρ topology (JES) [%]	$^{-0.13}_{+0.18}$	±0.19	$^{-}_{-0.66}$	$^{+0.79}_{-1.44}$	∓0.92	$^{-2.62}_{+1.05}$	$^{-0.82}_{+1.45}$	±5.31
Punch-through (JES) [%]	-	-	-	-	-	-	∓0.20	∓0.51
Single particle high-p_T (JES) [%]	-	-	-	-	-	-	-	-
b-Quark tagging efficiency (eigenvector 0) [%]	-	-	-	-	-	$^{-0.61}_{+0.58}$	$^{-0.83}_{+0.79}$	$^{-0.92}_{+0.90}$
b-Quark tagging efficiency (eigenvector 1) [%]	-	-	±0.12	±0.20	±0.13	±0.12	$^{-0.13}_{+0.12}$	$^{-0.62}_{+0.60}$
b-Quark tagging efficiency (eigenvector 2) [%]	-	-	-	∓0.14	∓0.14	$^{-0.13}_{+0.14}$	∓0.12	∓0.21
b-Quark tagging efficiency (eigenvector 3) [%]	-	-	-	-	-	-	-	±0.26
b-Quark tagging efficiency (eigenvector 4) [%]	-	-	-	-	-	-	±0.11	-
b-Quark tagging efficiency (eigenvector 5) [%]	-	-	-	-	-	-	-	-
c-Quark tagging efficiency (eigenvector 0) [%]	-	-	-	∓0.14	-	-	±0.19	±0.15
c-Quark tagging efficiency (eigenvector 1) [%]	-	-	-	-	-	-	-	±0.13
c-Quark tagging efficiency (eigenvector 2) [%]	-	-	-	-	-	-	±0.12	±0.12
Light-jet tagging efficiency (eigenvector 0) [%]	-	-	$^{+0.11}_{-0.12}$	-	-	$^{+0.91}_{-0.90}$	±0.73	±1.48
Light-jet tagging efficiency (eigenvector 1) [%]	-	-	-	-	-	±0.15	±0.40	±0.80
Light-jet tagging efficiency (eigenvector 2) [%]	-	-	-	-	-	-	-	±0.19
Light-jet tagging efficiency (eigenvector 3) [%]	-	-	-	-	-	-	-	-
Light-jet tagging efficiency (eigenvector 4) [%]	-	-	-	-	-	-	-	-
Light-jet tagging efficiency (eigenvector 5) [%]	-	-	-	-	-	-	-	-
Light-jet tagging efficiency (eigenvector 6) [%]	-	-	-	-	-	-	-	-
Light-jet tagging efficiency (eigenvector 7) [%]	-	-	-	-	-	-	-	-
Light-jet tagging efficiency (eigenvector 8) [%]	-	-	-	-	-	-	-	-
Light-jet tagging efficiency (eigenvector 9) [%]	-	-	-	-	-	-	-	-
Light-jet tagging efficiency (eigenvector 10) [%]	-	-	-	-	-	-	-	-
b-Quark tagging extrapolation [%]	-	-	-	-	-	∓0.13	∓0.36	∓0.80
b-Quark tagging extrapolation from c-Quark [%]	-	-	-	-	-	-	-	-
JET JER cross calibration forward [%]	-	-	-	-	-	-	-	-
JET JER noise forward [%]	-	-	-	-	-	-	-	-
JET JER NP0 [%]	-	-	-	-	-	-	-	-
JET JER NP1 [%]	±0.26	-	$^{-0.78}_{-}$	$^{+0.46}_{-}$	∓0.68	∓0.73	∓3.99	$^{+6.65}_{-0.29}$
JET JER NP2 [%]	±0.77	∓0.96	∓0.74	$^{-0.27}_{+0.83}$	$^{+0.70}_{-2.48}$	∓1.51	$^{+0.18}_{-3.51}$	±4.71
JET JER NP3 [%]	∓0.18	±0.57	$^{-0.85}_{+0.27}$	±0.75	$^{+0.13}_{-1.41}$	-	∓1.82	±3.01
JET JER NP4 [%]	±0.55	$^{+0.12}_{-0.47}$	∓0.94	$^{+0.57}_{-0.12}$	∓1.20	∓1.07	∓2.27	±2.56
JET JER NP5 [%]	±0.19	∓0.22	∓0.90	±0.69	∓1.00	$^{-}_{-0.60}$	∓2.14	±1.81
JET JER NP6 [%]	$^{+0.23}_{-}$	$^{-0.46}_{+0.34}$	∓0.65	±0.58	$^{+0.34}_{-0.57}$	$^{+0.70}_{-0.88}$	∓1.61	±5.43
JET JER NP7 [%]	±0.34	∓0.33	∓0.91	$^{+0.47}_{-0.40}$	$^{-0.42}_{+0.37}$	$^{+1.11}_{-1.67}$	∓2.06	±3.04
JET JER NP8 [%]	-	-	-	-	-	-	-	-
QCD estimation [%]	∓0.66	±1.33	±0.50	∓1.05	∓0.99	±0.53	∓1.67	∓6.14
K-factor normalization mass [%]	-	-	-	∓0.12	-	-	-	-
K-factor normalization PDFAS [%]	-	-	∓0.13	∓0.18	∓0.10	-	-	-
K-factor normalization scale [%]	-	-	-	$^{-0.10}_{+0.16}$	-	-	-	-
Luminosity [%]	-	-	-	-	-	-	-	-
MCSignal stat. [%]	±0.76	±1.00	±1.28	±1.56	±1.90	±2.83	±4.45	±8.42
QCD stat. [%]	±0.49	±0.72	±1.18	±1.83	±2.42	±3.31	±3.43	±4.18
ISR/FSR + scale [%]	$^{-0.46}_{+0.96}$	$^{+0.15}_{-0.39}$	$^{+1.73}_{-1.18}$	∓2.45	$^{+0.24}_{-3.05}$	$^{+2.58}_{-3.80}$	$^{-2.51}_{-}$	$^{+0.93}_{-4.81}$
Alternate hard-scattering model [%]	∓7.26	∓2.95	±22.7	±30.1	±16.2	±2.30	±4.12	±8.24
Alternate parton-shower model [%]	∓6.50	±5.87	±9.43	±7.10	±8.38	∓0.63	±9.34	±0.69
Inter PDF [%]	-	-	-	-	±0.20	±0.38	±0.22	∓0.12
Intra PDF [%]	-	-	∓0.13	∓0.18	∓0.24	∓0.34	∓0.35	±0.25

TABLE D.32: Table of systematics for the normalised differential cross-section at the parton level for the $p_T^{t\bar{t}}$ observable.

Bins [Unit y^{tt}]	0–0.12	0.12–0.25	0.25–0.38	0.38–0.50	0.50–0.65	0.65–0.80	0.80–1	1–1.15	1.15–1.30	1.30–1.50	1.50–1.70	1.70–2.50
$1/\sigma \cdot d\sigma$ / dy^{tt}	$6.96 \cdot 10^{-1}$	$7.42 \cdot 10^{-1}$	$7.26 \cdot 10^{-1}$	$6.54 \cdot 10^{-1}$	$6.54 \cdot 10^{-1}$	$6.03 \cdot 10^{-1}$	$5.36 \cdot 10^{-1}$	$4.74 \cdot 10^{-1}$	$4.31 \cdot 10^{-1}$	$3.32 \cdot 10^{-1}$	$2.60 \cdot 10^{-1}$	$1.22 \cdot 10^{-1}$
Total Uncertainty [%]	+7.95 −8.79	+8.39 −8.24	+5.38 −5.79	+8.08 −8.19	+8.37 −8.06	+8.24 −8.14	+6.60 −6.23	+7.80 −7.61	+15.9 −16.1	+8.98 −9.15	+14.1 −12.8	+21.4 −21.2
Statistics [%]	±2.4	±2.2	±2.3	±2.6	±2.3	±2.6	±2.4	±3.2	±3.5	±4.0	±5.5	±7.2
Systematics [%]	+7.14 −8.07	+7.72 −7.55	+4.93 −4.70	+7.16 −7.28	+7.63 −7.30	+7.32 −7.21	+5.61 −5.17	+6.23 −5.99	+15.0 −15.2	+6.77 −6.99	+11.4 −9.86	+18.1 −17.9
Jet vertex fraction [%]	-	-	-	-	-	-	-	-	-	-	-	-
b-Tagged jet energy scale (JES) [%]	+0.44 −0.98	±0.42	∓0.23	−0.34 +0.16	+0.21 -	±0.20	±0.25	±0.22	+0.31 −1.19	+0.84 −0.55	±0.71	−2.09 +1.00
Effective detector NP set 1 (JES) [%]	∓0.74	-	−0.11 +0.75	∓0.51	+0.38 −0.26	−0.34	±0.49	±1.01	+0.51 −0.46	+0.41 −1.34	∓0.12	−0.19 +0.39
Effective mixed NP set 1 (JES) [%]	- −0.32	±0.53	−0.22 +0.48	±0.18	∓0.38	∓0.19	±0.50	+0.24 −0.18	±0.29	+0.98 −0.69	±0.36	∓1.08
Effective mixed NP set 2 (JES) [%]	∓0.29	±0.19	-	−0.45 +0.17	- +0.13	+0.11 −0.26	-	±0.37	-	−0.41 +0.67	−0.12 +0.44	+0.73 −0.88
Effective mixed NP set 3 (JES) [%]	-	-	-	-	±0.25	-	-	-	-	-	+0.11 −0.22	−0.44 -
Effective modelling NP set 1 (JES) [%]	- −3.48	−0.93 +0.57	±0.34	∓1.91	±0.49	−1.23 +0.61	±1.03	−0.36 +0.97	∓1.97	±2.01	∓1.51	±3.79
Effective modelling NP set 2 (JES) [%]	∓0.39	±0.24	−0.24 +0.19	±0.11 +0.25	- −0.25	∓0.42	±0.89	- +0.26	±0.53	+0.54 −0.50	+0.50 −0.67	∓0.60
Effective modelling NP set 3 (JES) [%]	∓0.51	+0.63 −0.21	+0.12 −0.16	−0.41 +0.14	−0.10 +0.13	-	±0.23 −0.21	±0.48	+0.39 −0.67	∓0.45	±0.67	−0.74 +0.60
Effective modelling NP set 4 (JES) [%]	∓0.15	+0.23	-	∓0.12	+0.17 −0.19	−0.39 -	±0.13	-	-	+1.05 −0.45	±0.31	−0.56 +0.11
Effective statistical NP set 1 (JES) [%]	-	-	-	-	-	-	-	-	-	-	-	-
Effective statistical NP set 2 (JES) [%]	−0.24 -	±0.20 -	+0.12 -	∓0.23	±0.21	+0.22 −0.28	- +0.28	+0.30 −0.10	±0.13	−0.47 +0.81	- +0.29	+0.12 −0.86
Effective statistical NP set 3 (JES) [%]	- −0.19	+0.31 -	±0.16	−0.26 -	-	+0.22 -	+0.16 −0.10	±0.35 -	-	±0.37	−0.18 +0.62	∓0.97
Effective statistical NP set 4 (JES) [%]	-	−0.24 +0.23	-	- −0.39	-	+0.19	-	−0.10 +0.54	−0.13 +0.28	±0.32	+0.20 −0.64	∓0.39
Effective statistical NP set 5 (JES) [%]	-	∓0.17	-	∓0.17	±0.13	-	+0.22	+0.35 −0.12	+0.15 −0.18	−0.14 +0.50	-	∓0.27
Effective statistical NP set 6 (JES) [%]	-	-	±0.11	−0.21	±0.18	+0.16	-	±0.20	+0.18	+0.55	∓0.12	∓0.57
η intercalibration model (JES) [%]	∓0.54	∓0.79	−0.53 +0.62	∓1.38	±0.39	∓1.28	+0.60 -	±1.21	+0.49 −1.43	+0.57 −2.49	+1.40 -	±2.13
high E η intercalibration non closure (JES) [%]	-	-	-	-	-	-	-	-	-	-	-	-
neg η intercalibration non closure (JES) [%]	-	-	-	-	-	-	-	-	-	-	+0.31 −0.25	-
pos η intercalibration non closure (JES) [%]	-	-	-	-	-	-	-	-	-	-	∓0.23	+0.68
η intercalibration total stat (JES) [%]	- −0.45	-	−0.26 -	−0.14 +0.21	-	−0.37 +0.13	-	±0.12	-	+0.80 −0.57	−0.21 +0.17	±0.28
Flavour composition (JES) [%]	+0.21 −0.47	-	−0.16 +0.21	∓0.54	±0.40	−0.71 +0.16	±0.53	±0.74	+0.16 −0.26	+1.02 −1.17	−0.50 +0.89	−0.84 +0.35
Flavour response (JES) [%]	∓1.51	+0.48 −0.92	+1.56 −0.34	∓1.12	+0.39 −0.14	∓1.25	+0.73 −0.16	∓0.39	−0.74 -	−1.38 +0.24	−1.42 +0.65	±3.71
Pile-up offset μ (JES) [%]	∓0.33	−0.19 +0.14	-	−0.21	-	∓0.70	+0.28 −0.46	±0.26	∓0.24 +0.22	−0.79 -	+0.18 -	±1.53
Pile-up offset N_{PV} (JES) [%]	∓1.04	−0.70	±0.35	∓0.44	∓0.57	∓0.64	+0.72 −0.14	±0.53	+0.17 -	∓0.90	±0.68	−0.81 +3.23
Pile-up offset p_T (JES) [%]	∓0.38	±0.30	+0.21 −0.16	-	∓0.15	∓0.89	±0.38	±0.16	∓0.14	±0.65	∓0.71	±1.55
Pile-up offset ρ topology (JES) [%]	∓2.38	−0.44 -	±0.50	∓1.05	±0.19	∓0.33	±0.42	−0.51 +0.55	+0.89 −1.22	∓0.89	∓1.72	±4.38
Punch-through (JES) [%]	-	-	±0.10	-	-	-	-	-	-	-	-	∓0.21
Single particle high-p_T (JES) [%]	-	-	-	-	-	-	-	-	-	-	-	-
b-Quark tagging efficiency (eigenvector 0) [%]	-	-	−0.13 +0.12	-	-	-	-	-	-	-	+0.59 −0.57	-
b-Quark tagging efficiency (eigenvector 1) [%]	-	-	-	-	-	-	-	-	-	-	-	-
b-Quark tagging efficiency (eigenvector 2) [%]	-	-	-	-	-	-	-	-	-	-	-	-
b-Quark tagging efficiency (eigenvector 3) [%]	-	-	-	-	-	-	-	-	-	-	-	-
b-Quark tagging efficiency (eigenvector 4) [%]	-	-	-	-	-	-	-	-	-	-	-	-
b-Quark tagging efficiency (eigenvector 5) [%]	-	-	-	-	-	-	-	-	-	-	-	-
c-Quark tagging efficiency (eigenvector 0) [%]	-	-	-	-	-	-	-	-	-	-	∓0.26	-
c-Quark tagging efficiency (eigenvector 1) [%]	-	-	-	-	-	-	-	-	-	-	-	-
c-Quark tagging efficiency (eigenvector 2) [%]	-	-	-	-	-	-	-	-	-	-	-	-
Light-jet tagging efficiency (eigenvector 0) [%]	-	-	-	-	+0.14 −0.16	±0.15	-	+0.23 −0.22	∓0.12	−0.24 +0.23	∓0.22	-
Light-jet tagging efficiency (eigenvector 1) [%]	-	-	-	-	-	-	-	-	-	-	-	-
Light-jet tagging efficiency (eigenvector 2) [%]	-	-	-	-	-	-	-	-	-	-	-	-
Light-jet tagging efficiency (eigenvector 3) [%]	-	-	-	-	-	-	-	-	-	-	-	-
Light-jet tagging efficiency (eigenvector 4) [%]	-	-	-	-	-	-	-	-	-	-	-	-
Light-jet tagging efficiency (eigenvector 5) [%]	-	-	-	-	-	-	-	-	-	-	-	-
Light-jet tagging efficiency (eigenvector 6) [%]	-	-	-	-	-	-	-	-	-	-	-	-
Light-jet tagging efficiency (eigenvector 7) [%]	-	-	-	-	-	-	-	-	-	-	-	-
Light-jet tagging efficiency (eigenvector 8) [%]	-	-	-	-	-	-	-	-	-	-	-	-
Light-jet tagging efficiency (eigenvector 9) [%]	-	-	-	-	-	-	-	-	-	-	-	-
Light-jet tagging efficiency (eigenvector 10) [%]	-	-	-	-	-	-	-	-	-	-	-	-
b-Quark tagging extrapolation [%]	-	-	-	-	-	-	-	-	-	-	-	-
b-Quark tagging extrapolation from c-Quark [%]	-	-	-	-	-	-	-	-	-	-	-	-
JET JER cross calibration forward [%]	-	-	-	-	-	-	-	-	-	-	-	-
JET JER noise forward [%]	-	-	-	-	-	-	-	-	-	-	-	-
JET JER NP0 [%]	-	-	-	-	-	-	-	-	-	-	-	-
JET JER NP1 [%]	-	∓0.14	−0.58	−0.83	+0.78 -	−2.22	±2.95	±0.81	∓1.64	−1.27 +0.18	±2.80	∓0.78
JET JER NP2 [%]	±1.00	∓0.18	+0.45 −0.81	∓2.15	- +1.12	∓3.00	±1.53	±3.10	∓1.55	∓2.21	−0.55 +4.06	- −0.15
JET JER NP3 [%]	−0.11 +0.45	-	+0.49 −0.61	∓1.34	±0.62	∓2.26	+1.91 −0.50	−0.64 +0.55	∓2.97	∓0.46	±1.30	±1.71
JET JER NP4 [%]	-	∓0.17	∓0.63	∓2.04	−0.34 +1.50	∓1.24	±0.77	+1.18	∓1.18	∓1.81	±2.56	±1.89
JET JER NP5 [%]	+0.32 −0.58	−0.31 +0.46	±0.17	+0.16 −0.78	±0.26	∓1.26	±1.94	∓0.34	∓2.15	∓1.02	−0.11 +2.72	∓0.32
JET JER NP6 [%]	∓0.51	−0.44 +0.25	-	+0.70 −0.35	±0.80	∓1.55	±1.08	−0.15 +0.48	−1.07	∓2.66	±1.90	±1.42
JET JER NP7 [%]	+0.19 −0.68	−0.79 +0.62	∓0.39	∓0.42	−0.35 +0.94	∓1.97	±1.34	−0.32 +0.55	∓1.15	∓1.54	±1.35	±1.45
JET JER NP8 [%]	-	-	-	-	-	-	-	-	-	-	-	-
QCD estimation [%]	±2.14	±1.83	±0.54	±1.37	∓0.67	±1.38	±0.86	∓0.45	∓2.36	±1.94	∓3.54	∓4.59
K-factor normalization mass [%]	-	-	-	-	-	-	-	-	-	-	−0.12 +0.13	∓0.17
K-factor normalization PDFAS [%]	-	-	-	-	-	-	-	-	-	-	∓0.19	∓0.25
K-factor normalization scale [%]	-	-	-	-	-	-	-	-	-	-	−0.11 +0.17	−0.14 +0.22
Luminosity [%]	-	-	-	-	-	-	-	-	-	-	-	-
MCSignal stat. [%]	±1.72	±1.67	±1.71	±1.85	±1.72	±1.88	±1.73	±2.35	±2.67	±2.88	±4.02	±5.35
QCD stat. [%]	±1.76	±1.69	±1.73	±1.89	±1.75	±1.95	±1.80	±2.43	±2.74	±3.13	±4.62	±6.87
ISR/FSR + scale [%]	±4.54	+2.08 −0.23	±3.44	∓0.84	∓2.65	+2.94 −0.11	+0.67 −0.73	±4.07	∓7.11	−1.00 +2.51	+3.18 −0.40	∓9.12
Alternate hard-scattering model [%]	±2.24	±6.21	±1.86	±3.38	∓5.78	±3.46	∓1.39	±1.67	±5.89	∓1.61	∓1.39	∓11.7
Alternate parton-shower model [%]	±2.83	±3.13	±1.76	∓4.07	∓3.06	±1.11	±1.02	±0.31	∓10.4	∓0.36	±6.96	-
Inter PDF [%]	∓0.19	∓0.18	∓0.11	-	±0.22	±0.43	±0.52	±0.43	±0.31	∓0.15	∓0.39	∓0.96
Intra PDF [%]	-	-	-	∓0.10	∓0.14	∓0.15	∓0.16	-	-	-	±0.49	±0.31

TABLE D.33: Table of systematics for the normalised differential cross-section at the parton level for the $y_{t\bar{t}}$ observable.

Appendix E

Unfolding corrections

In this Appendix, the complete set of corrections entering the unfolding procedure, introduced in Chapter 7, are presented. Particle level corrections are shown in in Section E.1, while parton level ones are presented in Section E.2.

E.1 Corrections at particle level

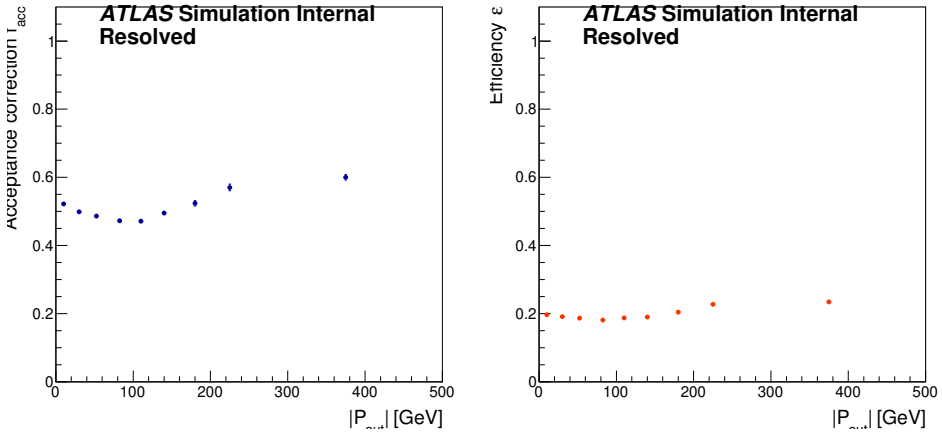

(A) (B)

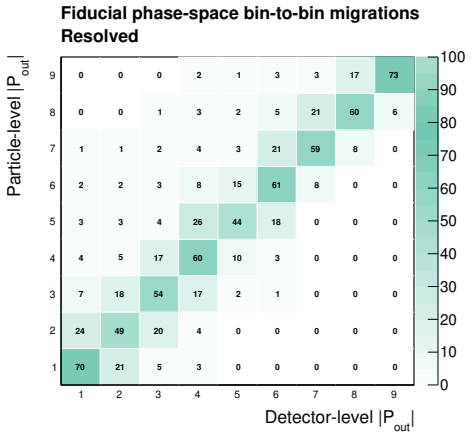

(C)

FIGURE E.1: (a) Acceptance correction,(b) efficiency and (c) reconstruction-to-particle-level migration matrix for $|P_{\text{out}}^{t\bar{t}}|$ observable.

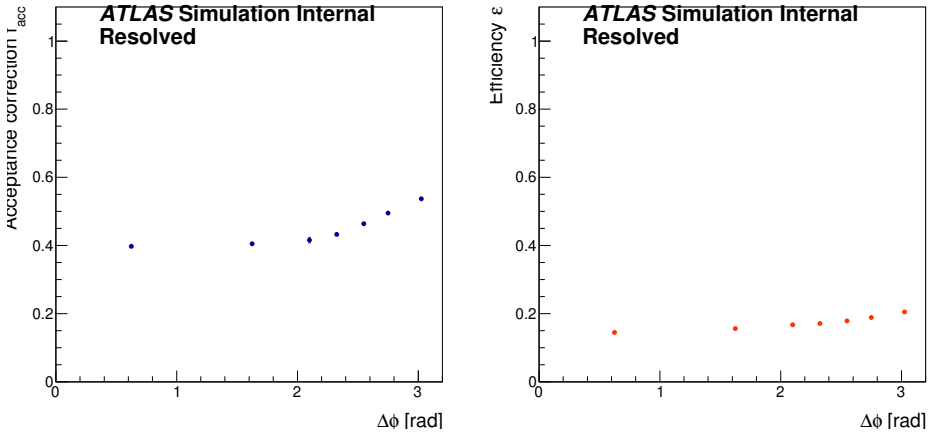

(A) (B)

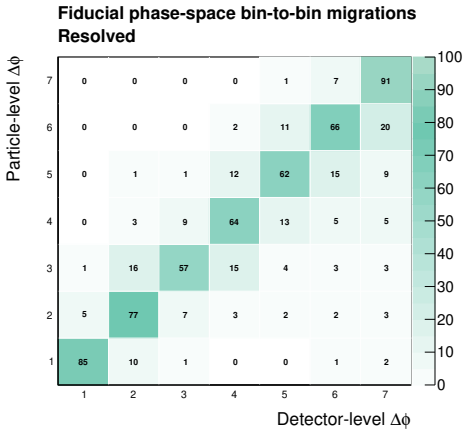

(C)

FIGURE E.2: (a) Acceptance correction,(b) efficiency and (c) reconstruction-to-particle-level migration matrix for $\Delta\phi_{t\bar{t}}$ observable.

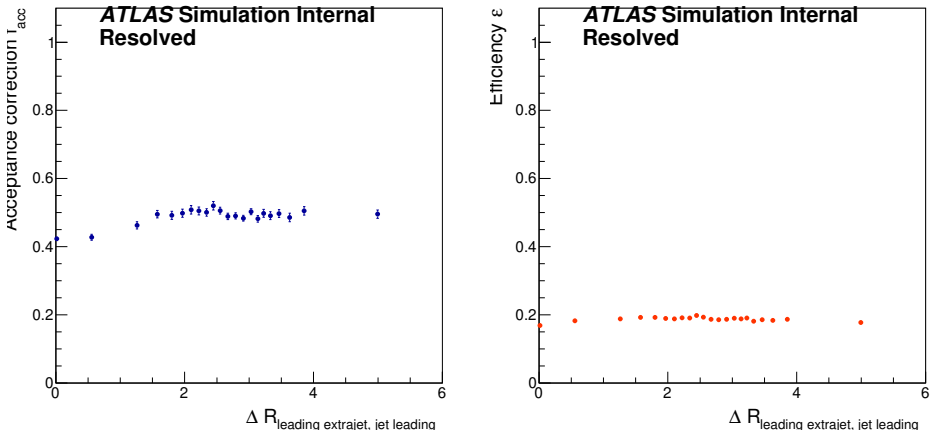

(A) (B)

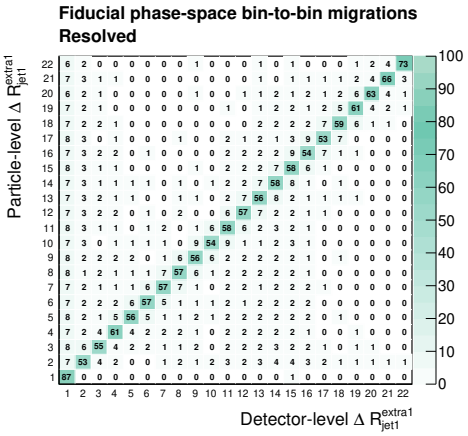

(C)

FIGURE E.3: (a) Acceptance correction,(b) efficiency and (c) reconstruction-to-particle-level migration matrix for $\Delta R_{\text{jet1}}^{\text{extra1}}$ observable.

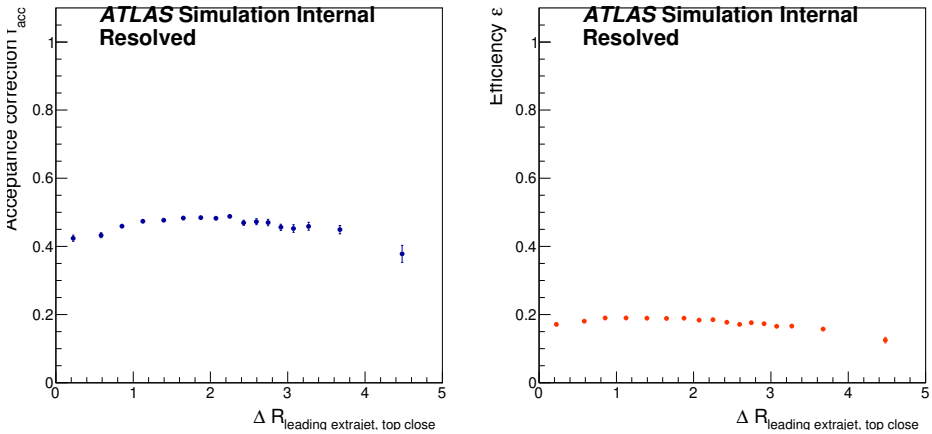

(A) (B)

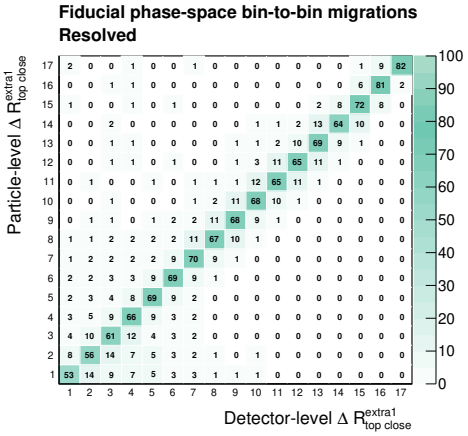

(C)

FIGURE E.4: (a) Acceptance correction,(b) efficiency and (c) reconstruction-to-particle-level migration matrix for $\Delta R^{\text{extra1}}_{\text{topclose}}$ observable.

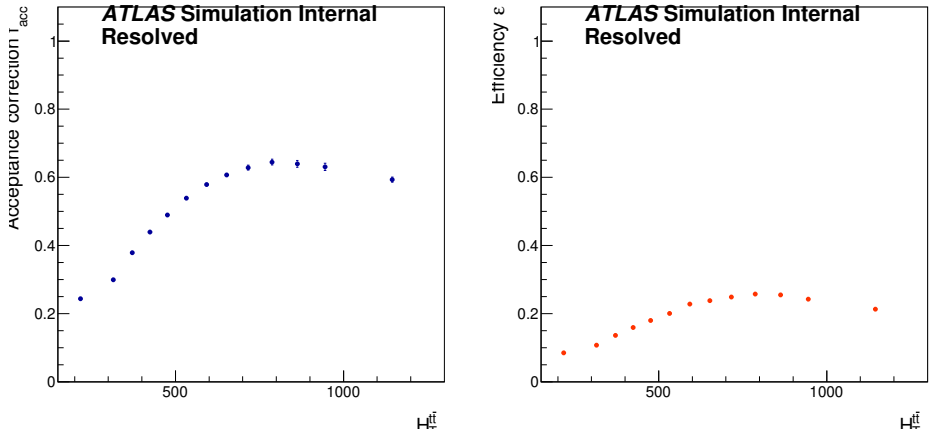

(A) (B)

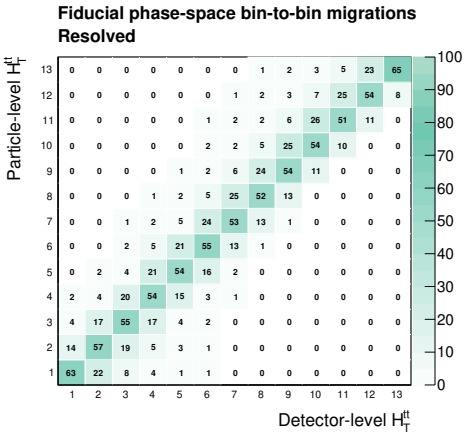

(C)

FIGURE E.5: (a) Acceptance correction,(b) efficiency and (c) reconstruction-to-particle-level migration matrix for $H_{\mathrm{T}}^{t\bar{t}}$ observable.

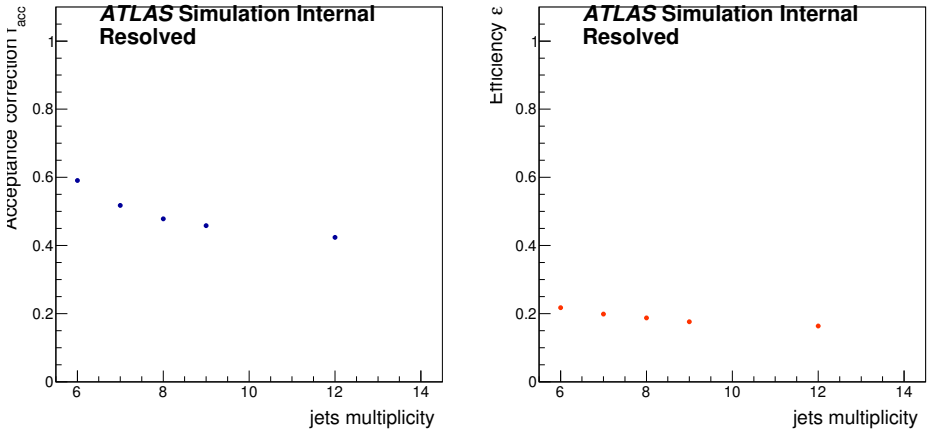

(A) (B)

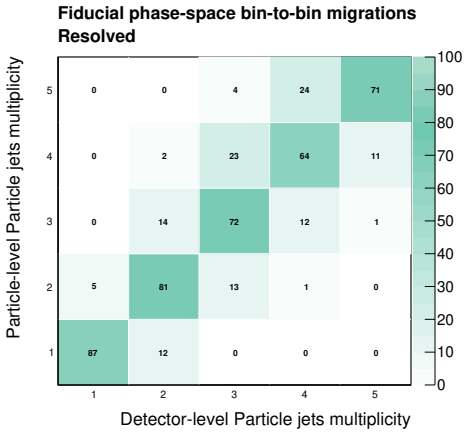

(C)

FIGURE E.6: (a) Acceptance correction,(b) efficiency and (c) reconstruction-to-particle-level migration matrix for N. jets observable.

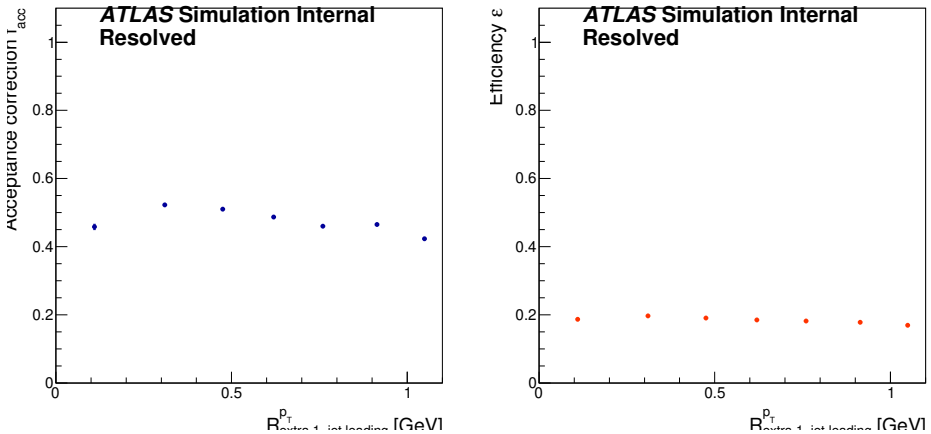

(A) (B)

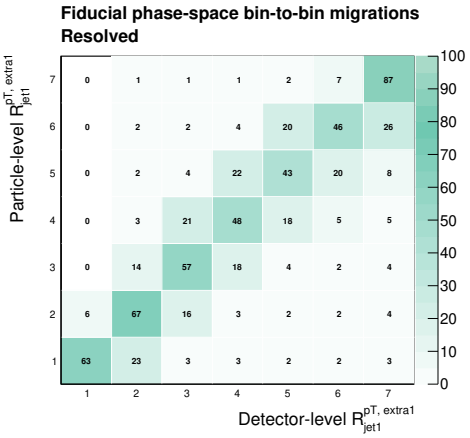

(C)

FIGURE E.7: (a) Acceptance correction,(b) efficiency and (c) reconstruction-to-particle-level migration matrix for $R^{\mathrm{extra1}}_{\mathrm{jet1}}$ observable.

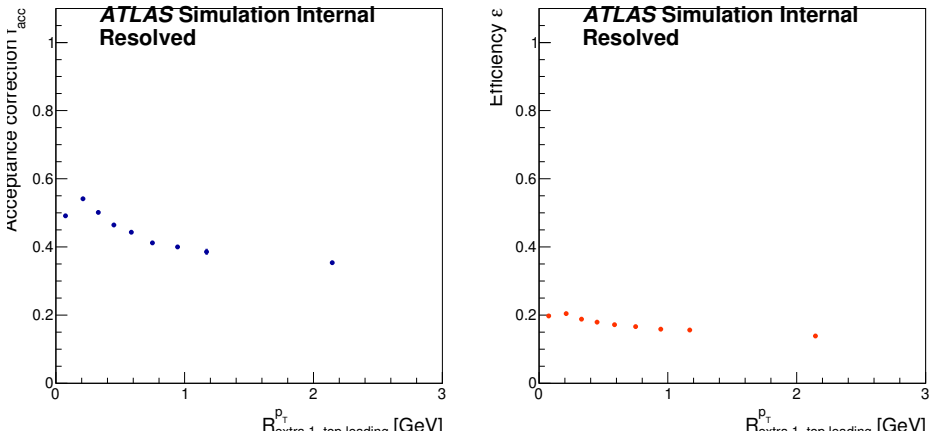

(A) (B)

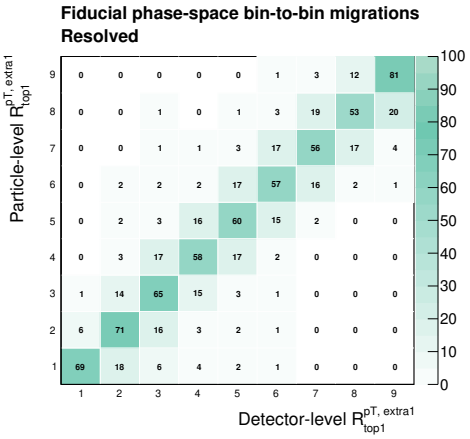

(C)

FIGURE E.8: (a) Acceptance correction,(b) efficiency and (c) reconstruction-to-particle-level migration matrix for $R^{\mathrm{extra1}}_{\mathrm{top1}}$ observable.

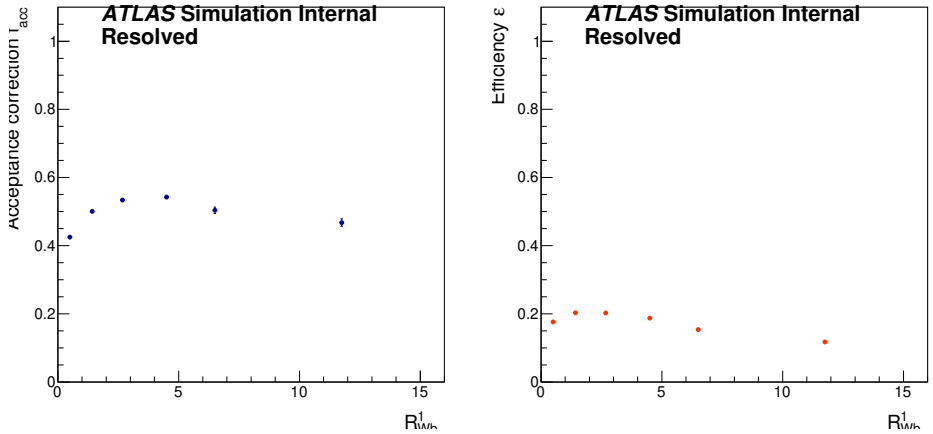

(A) (B)

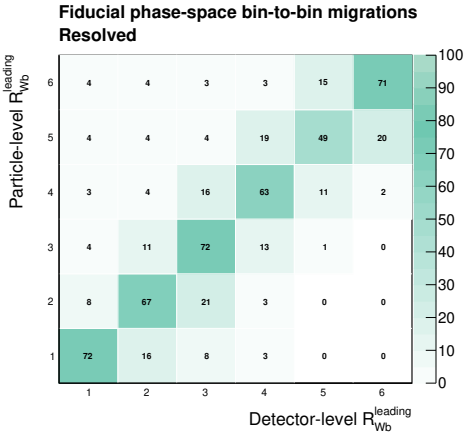

(C)

FIGURE E.9: (a) Acceptance correction,(b) efficiency and (c) reconstruction-to-particle-level migration matrix for $R^{leading}_{Wb}$ observable.

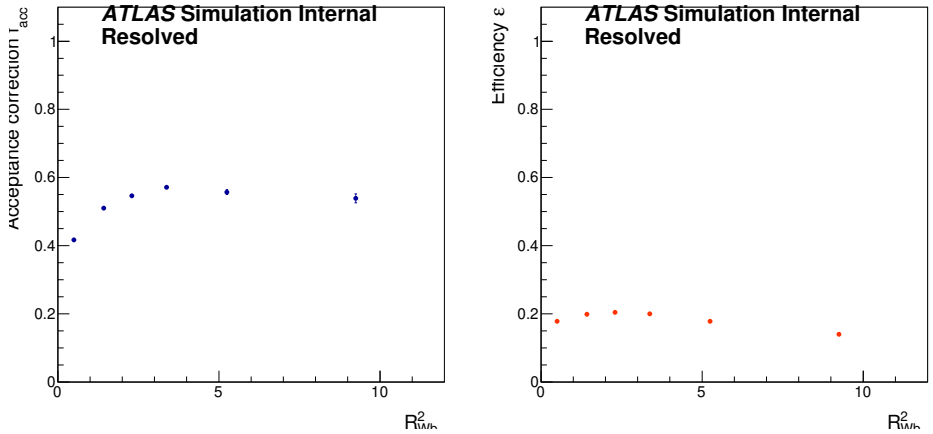

(A) (B)

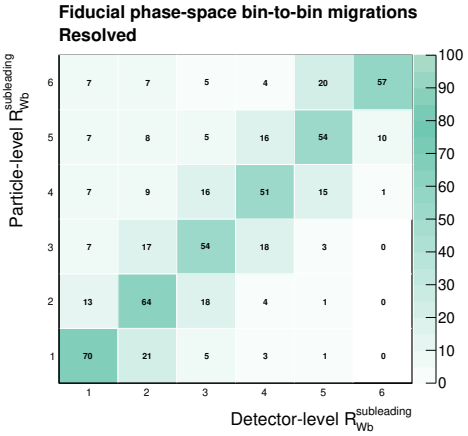

(C)

FIGURE E.10: (a) Acceptance correction, (b) efficiency and (c) reconstruction-to-particle-level migration matrix for $R^{subleading}_{Wb}$ observable.

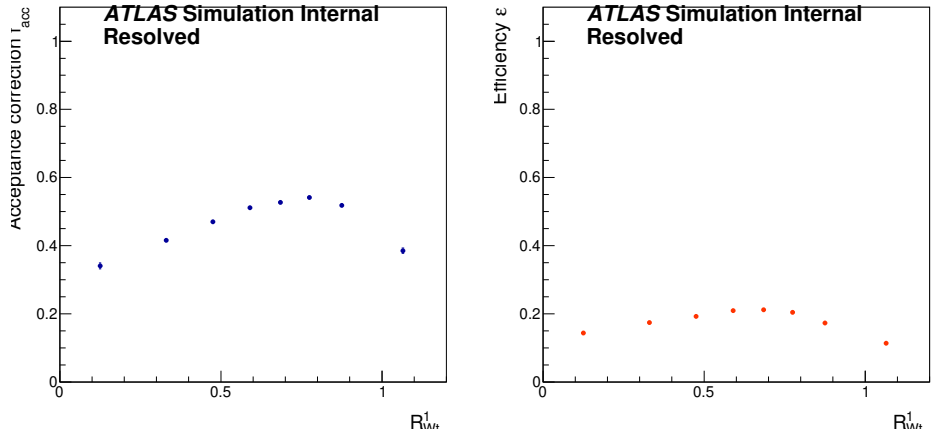

(A) (B)

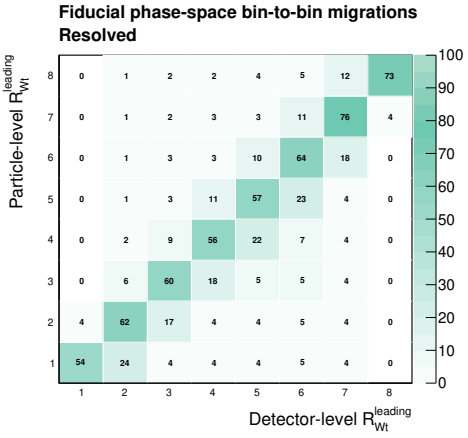

(C)

FIGURE E.11: (a) Acceptance correction,(b) efficiency and (c) reconstruction-to-particle-level migration matrix for $R^{leading}_{Wt}$ observable.

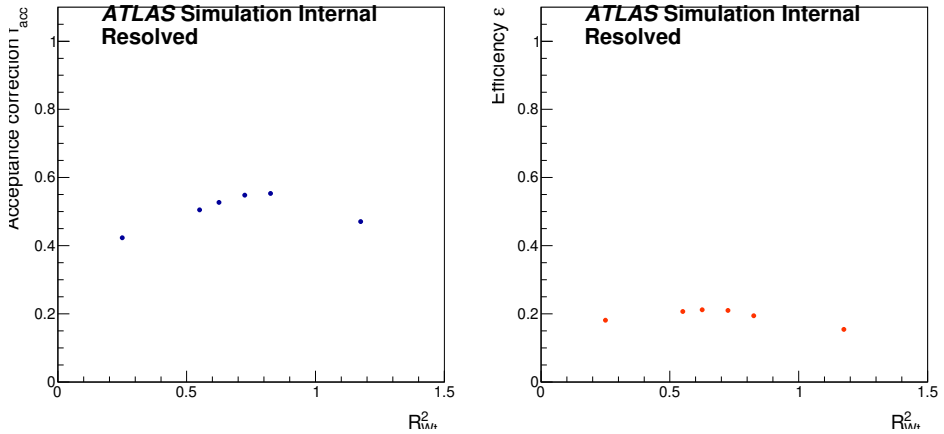

(A) (B)

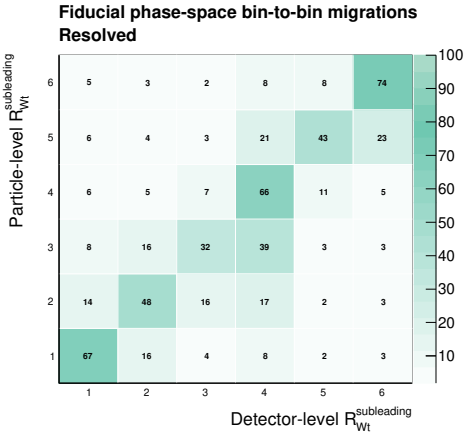

(C)

FIGURE E.12: (a) Acceptance correction,(b) efficiency and (c) reconstruction-to-particle-level migration matrix for $R^{subleading}_{Wt}$ observable.

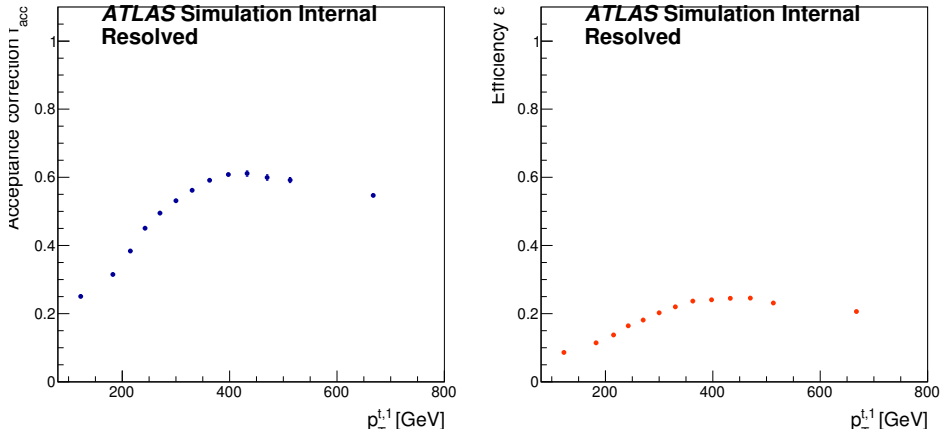

(A) (B)

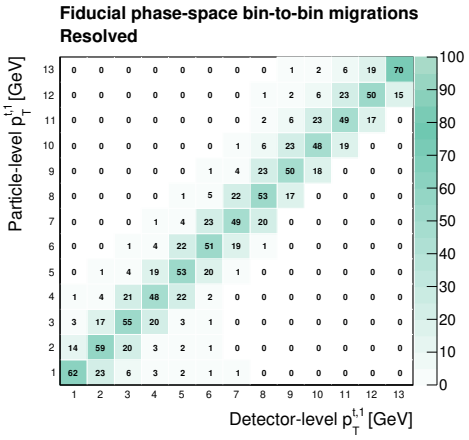

(C)

FIGURE E.13: (a) Acceptance correction,(b) efficiency and (c) reconstruction-to-particle-level migration matrix for p_T^{top1} observable.

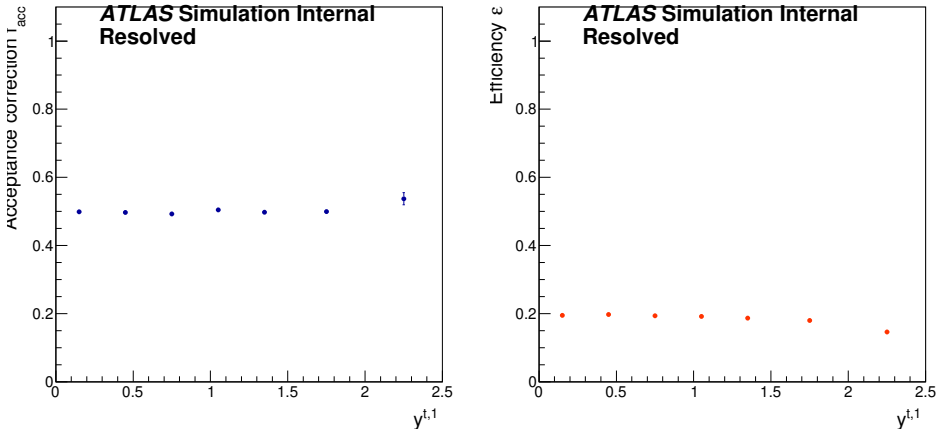

(A) (B)

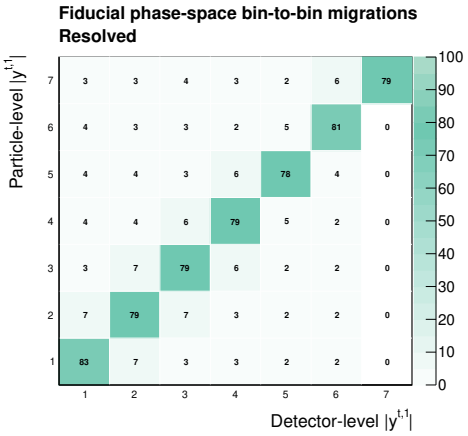

(C)

FIGURE E.14: (a) Acceptance correction,(b) efficiency and (c) reconstruction-to-particle-level migration matrix for y_{top1} observable.

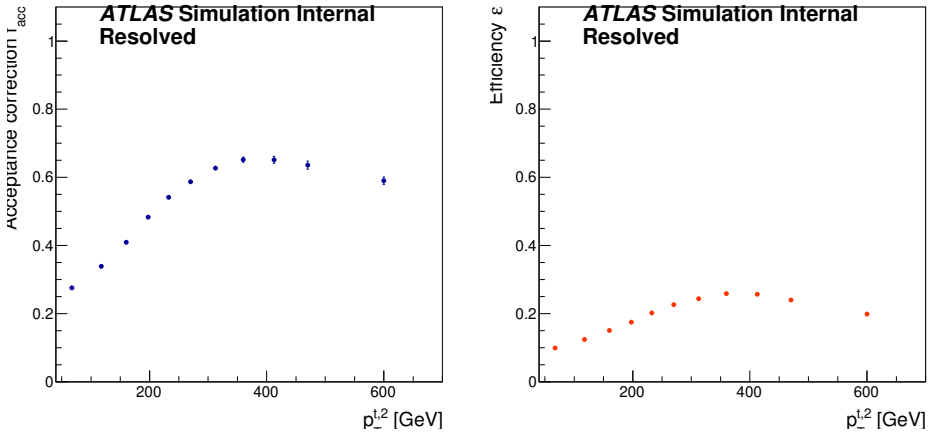

(A) (B)

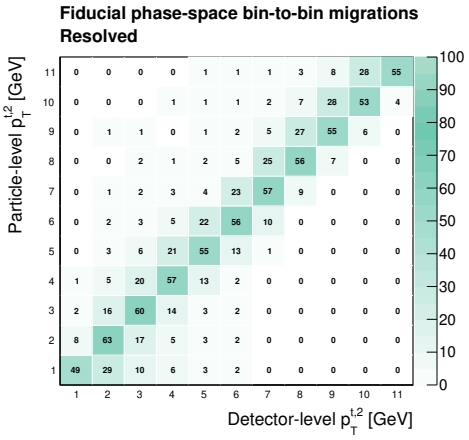

(C)

FIGURE E.15: (a) Acceptance correction,(b) efficiency and (c) reconstruction-to-particle-level migration matrix for p_T^{top2} observable.

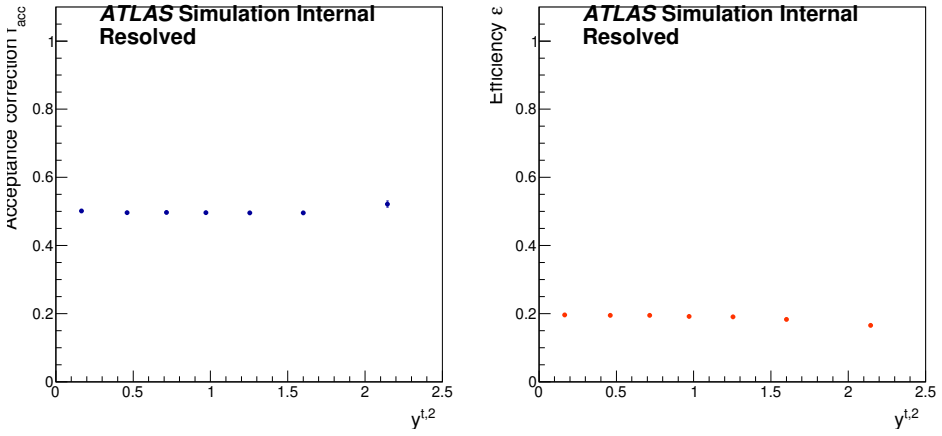

(A) (B)

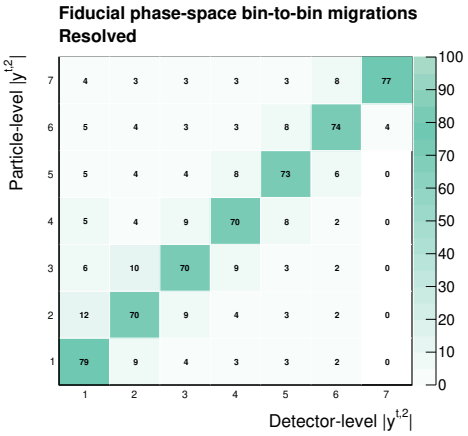

(C)

FIGURE E.16: (a) Acceptance correction,(b) efficiency and (c) reconstruction-to-particle-level migration matrix for y_{top2} observable.

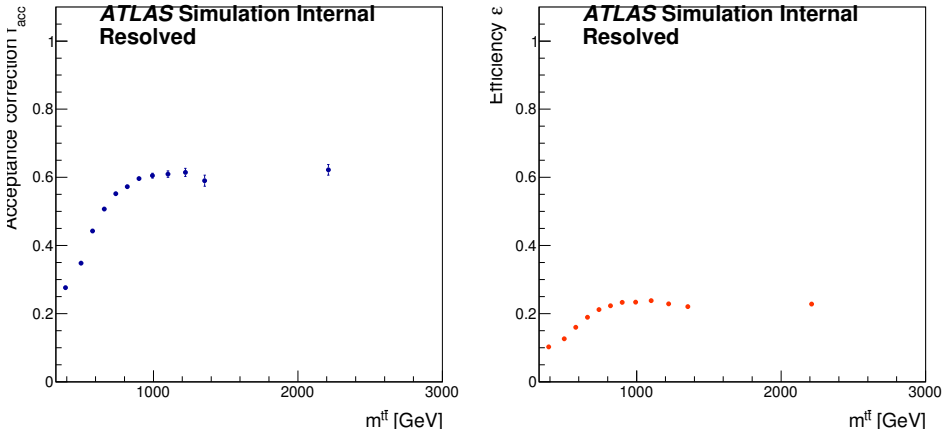

(A) (B)

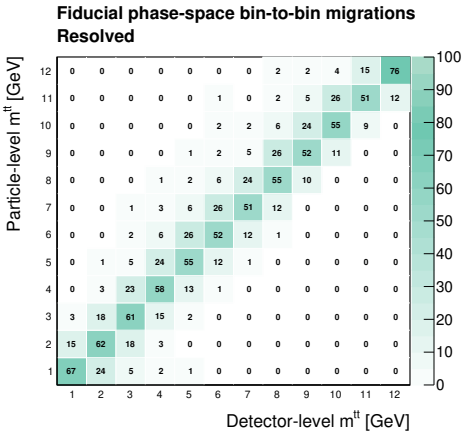

(C)

FIGURE E.17: (a) Acceptance correction,(b) efficiency and (c) reconstruction-to-particle-level migration matrix for $m_{t\bar{t}}$ observable.

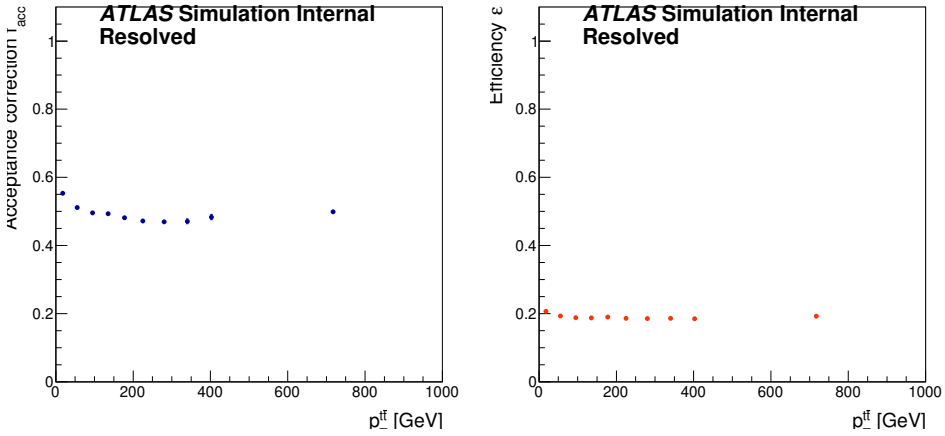

(A) (B)

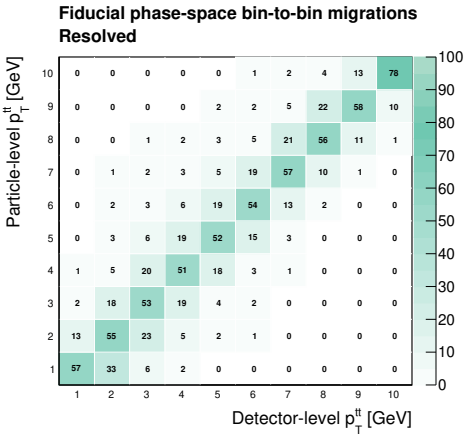

(C)

FIGURE E.18: (a) Acceptance correction,(b) efficiency and (c) reconstruction-to-particle-level migration matrix for $p_T^{t\bar{t}}$ observable.

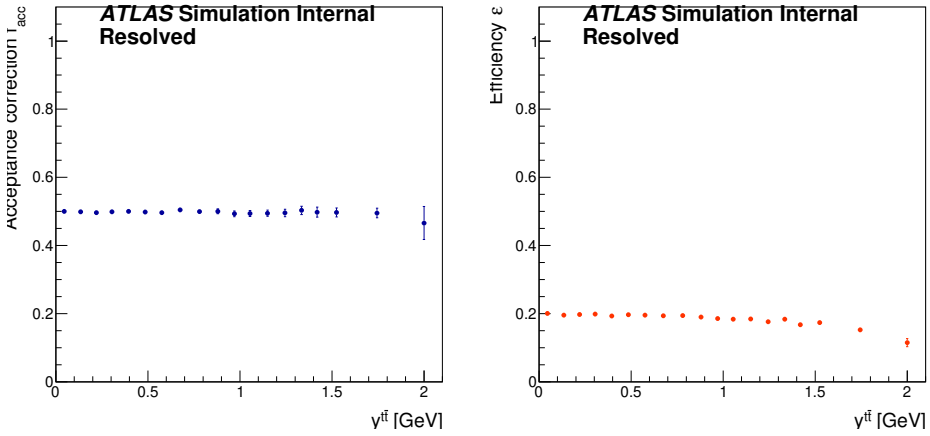

(A) (B)

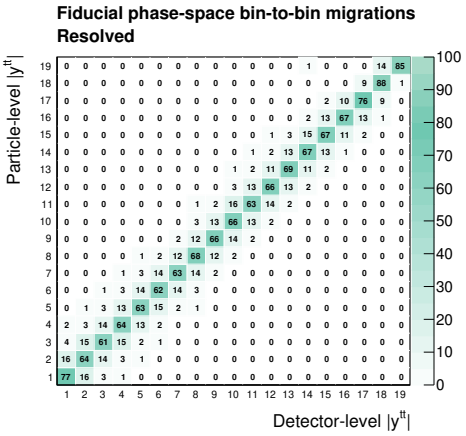

(C)

FIGURE E.19: (a) Acceptance correction,(b) efficiency and (c) reconstruction-to-particle-level migration matrix for $y_{t\bar{t}}$ observable.

E.2 Corrections at parton level

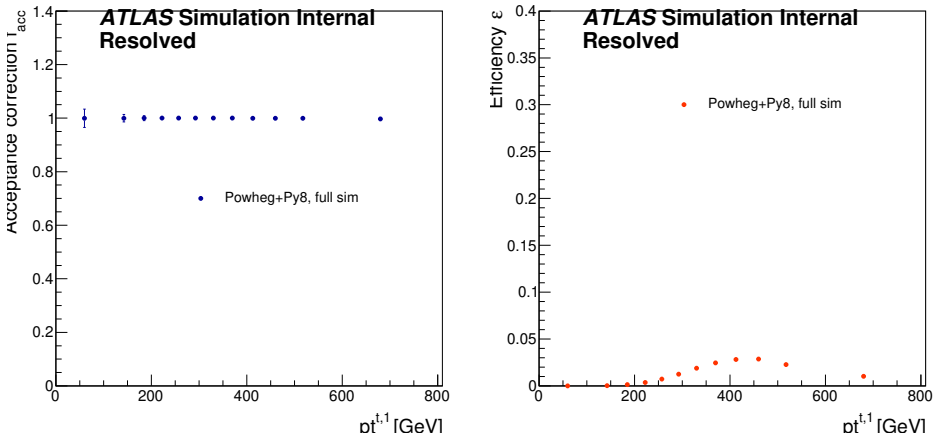

(A) (B)

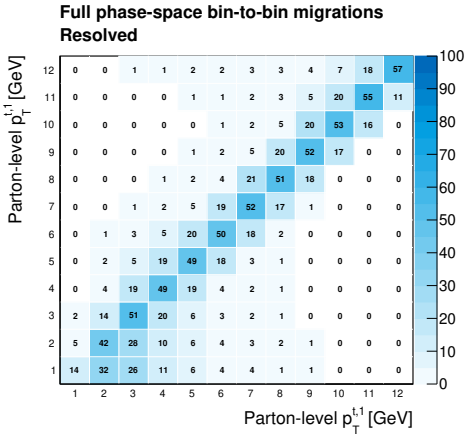

(C)

FIGURE E.20: (a) Acceptance correction,(b) efficiency and (c) reconstruction-to-parton-level migration matrix for p_T^{top1} observable.

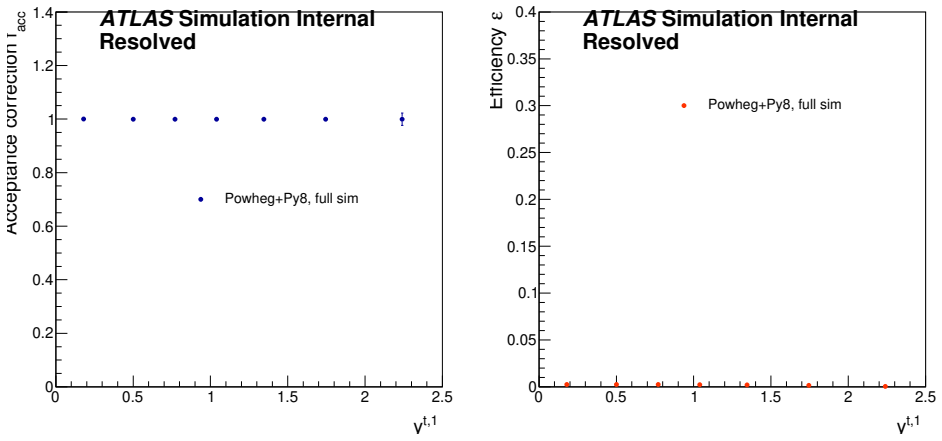

(A)

(B)

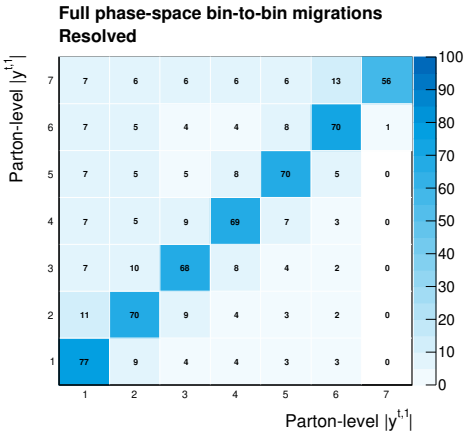

(C)

FIGURE E.21: (a) Acceptance correction,(b) efficiency and (c) reconstruction-to-parton-level migration matrix for y_{top1} observable.

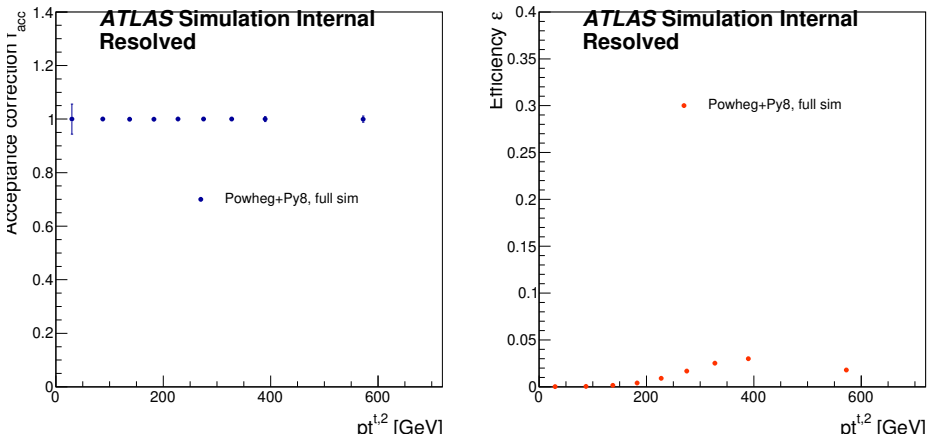

(A) (B)

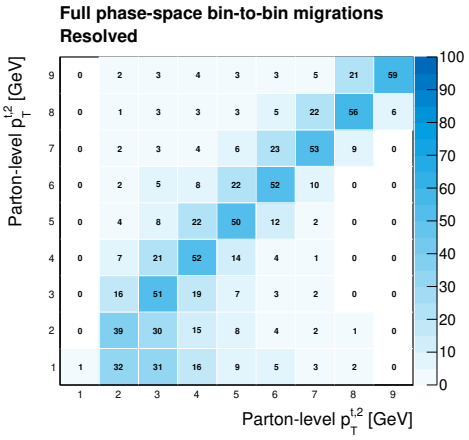

(C)

FIGURE E.22: (a) Acceptance correction,(b) efficiency and (c) reconstruction-to-parton-level migration matrix for p_T^{top2} observable.

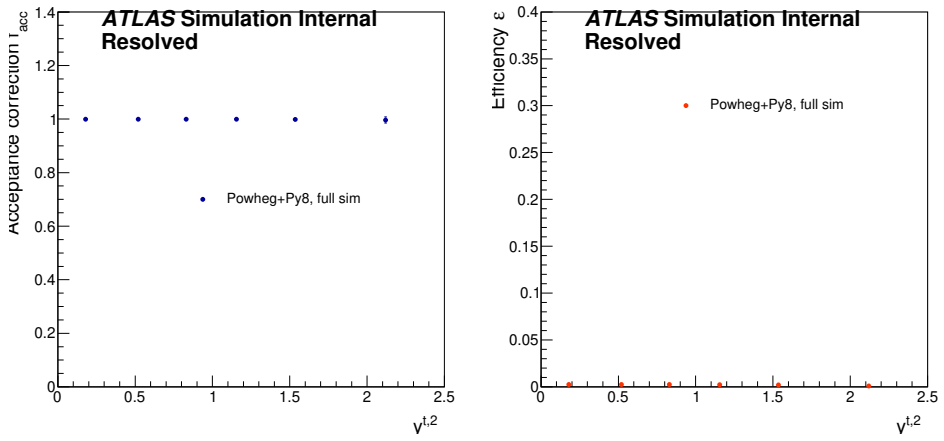

(A) (B)

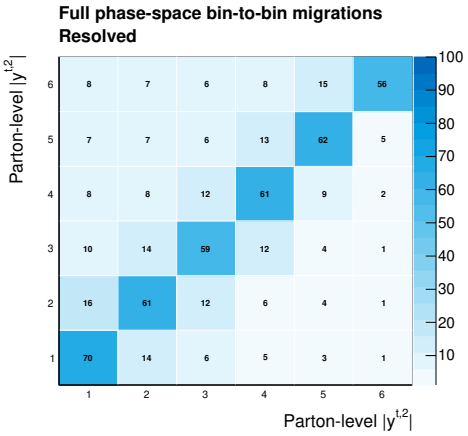

(C)

FIGURE E.23: (a) Acceptance correction,(b) efficiency and (c) reconstruction-to-parton-level migration matrix for y_{top2} observable.

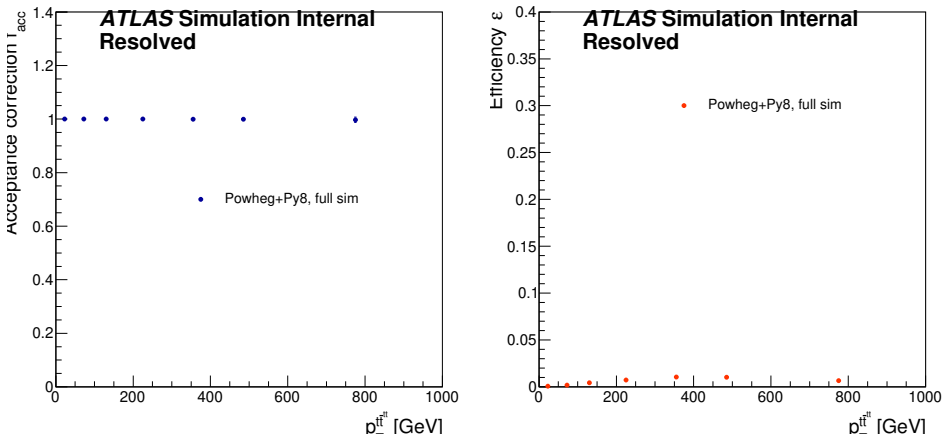

(A) (B)

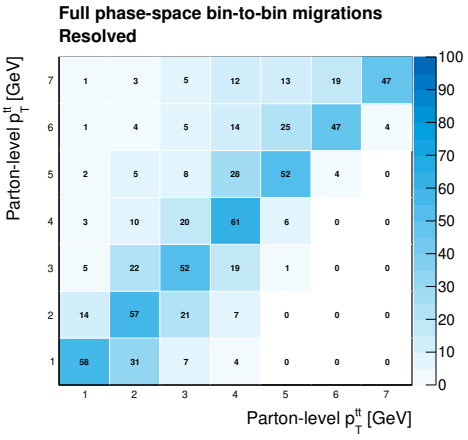

(C)

FIGURE E.24: (a) Acceptance correction,(b) efficiency and (c) reconstruction-to-parton-level migration matrix for $p_T^{t\bar{t}}$ observable.

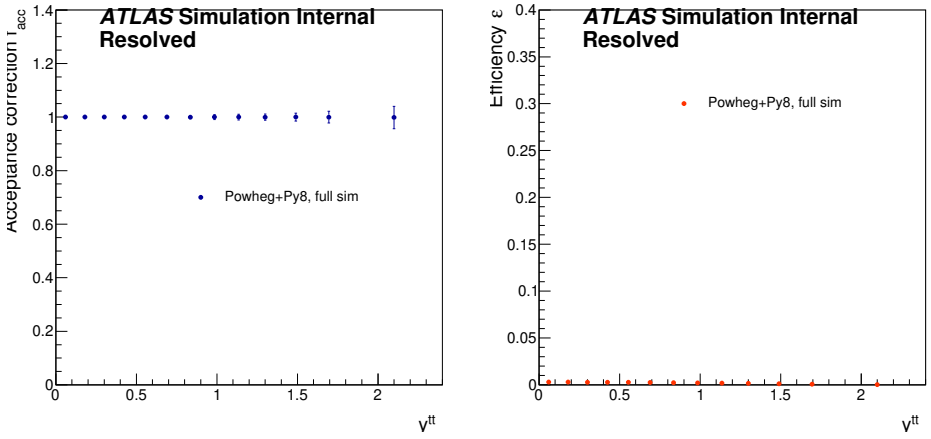

(A) (B)

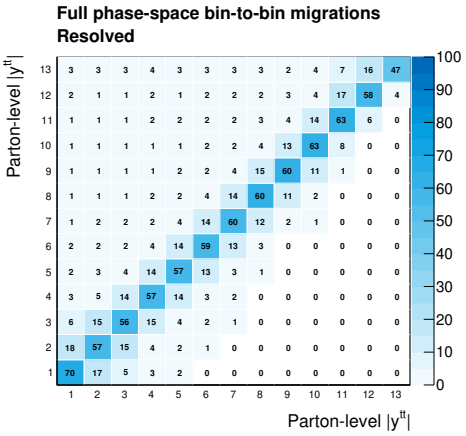

(C)

FIGURE E.25: (a) Acceptance correction,(b) efficiency and (c) reconstruction-to-parton-level migration matrix for $y_{t\bar{t}}$ observable.

Appendix F

Unfolding stability tests

F.1 Closure tests

In this section, the closure tests to validate the unfolding procedure at particle and particle level, are reported.

F.1.1 Closure, particle level

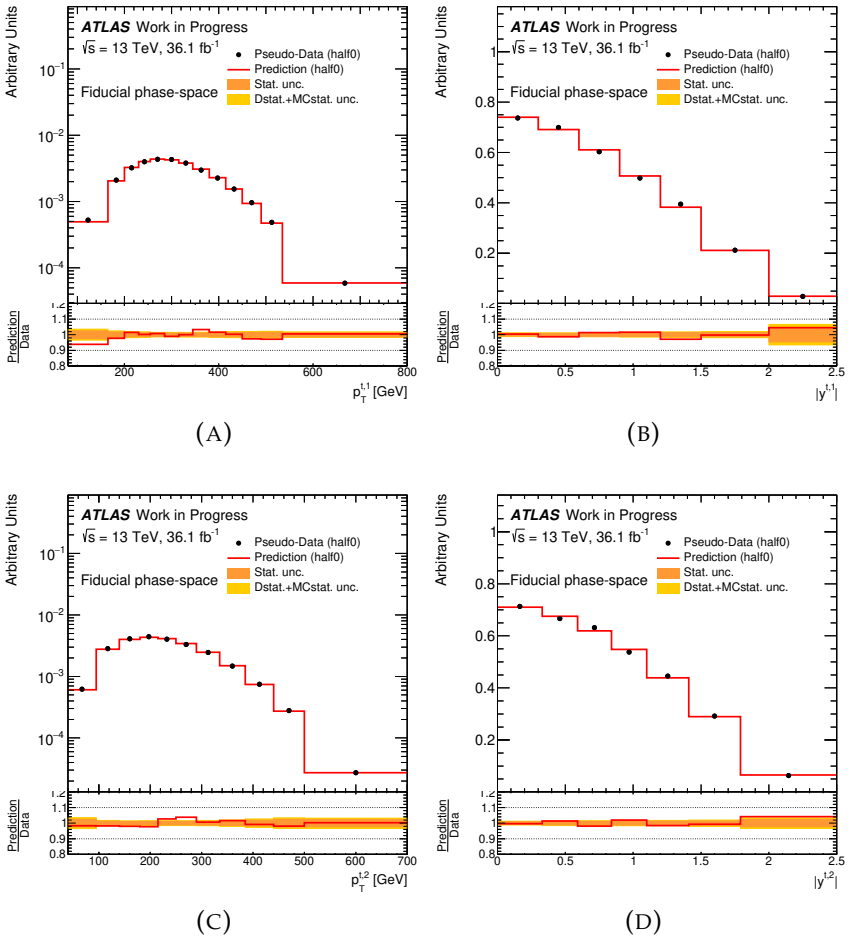

(A) (B)

(C) (D)

FIGURE F.1: Unfolding closure of a differential cross-section as a function of p_T^{top1} (a), y_{top1} (b), p_T^{top2} (c) and y_{top2} (d) observables normalised in the fiducial phase-space. The shaded area represents the statistical uncertainty.

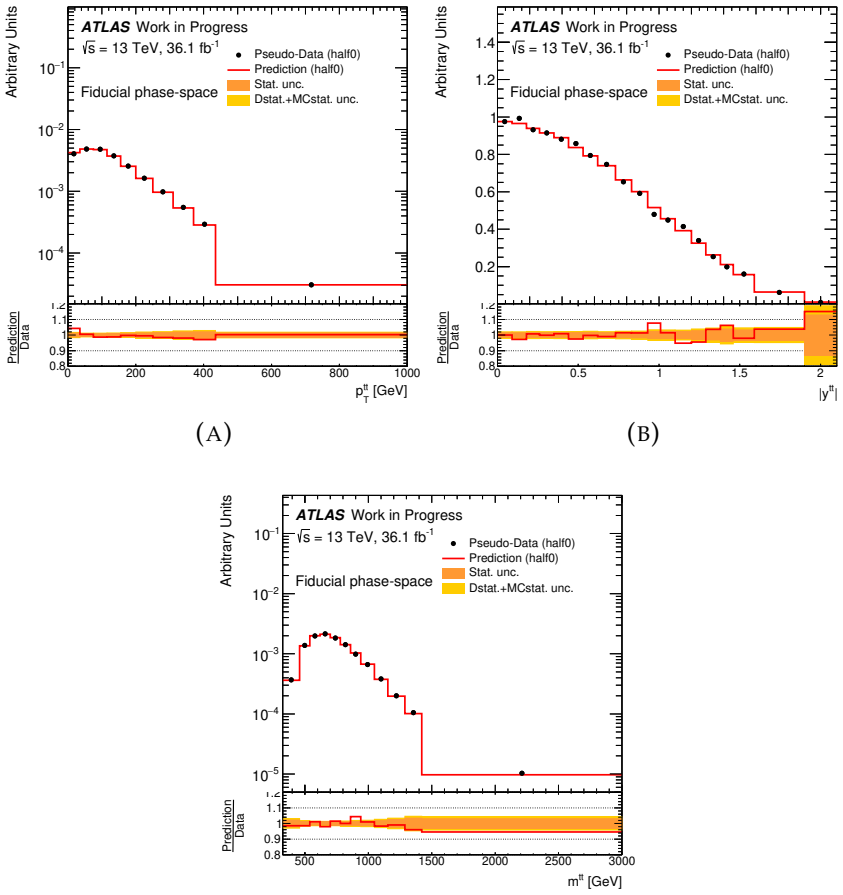

(A) (B)

(C)

FIGURE F.2: Unfolding closure of a differential cross-section as a function of $p_T^{t\bar{t}}$ (a), $y_{t\bar{t}}$ (b) and $m_{t\bar{t}}$ (c) observables normalised in the fiducial phase-space. The shaded area represents the statistical uncertainty.

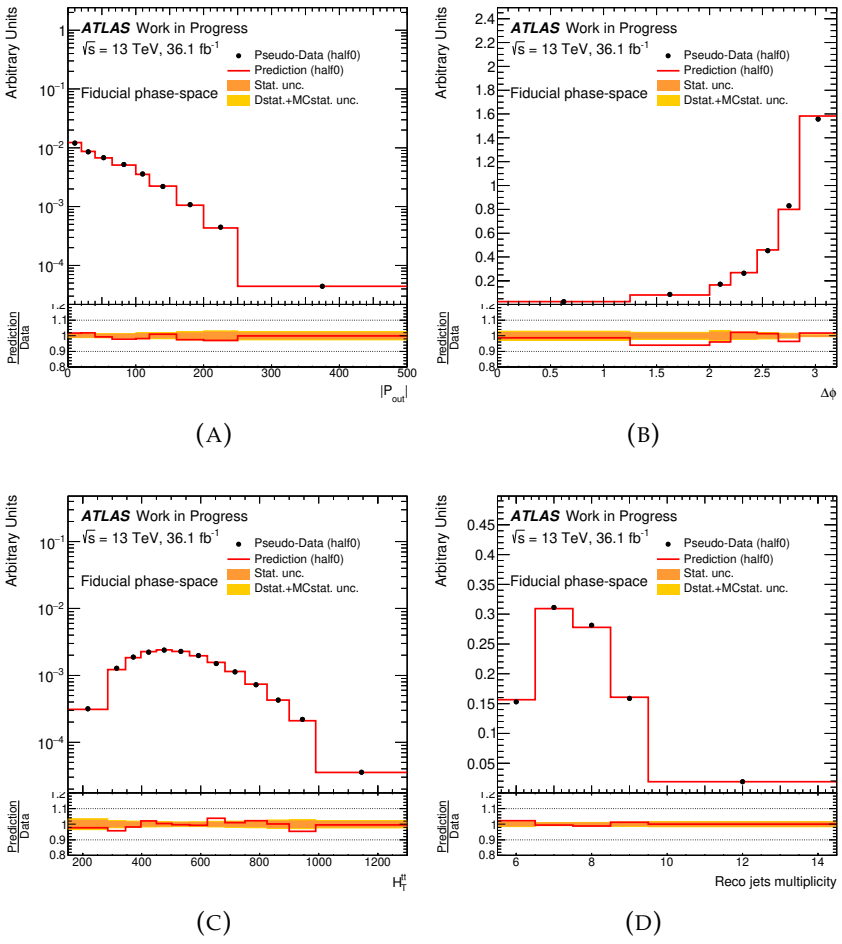

(A) (B)

(C) (D)

FIGURE F.3: Unfolding closure of a differential cross-section as a function of $|P_{\text{out}}^{t\bar{t}}|$ (a), $\Delta\phi_{t\bar{t}}$ (b), $H_{\text{T}}^{t\bar{t}}$ (c) and N_{jets} (d) observables normalised in the fiducial phase-space. The shaded area represents the statistical uncertainty.

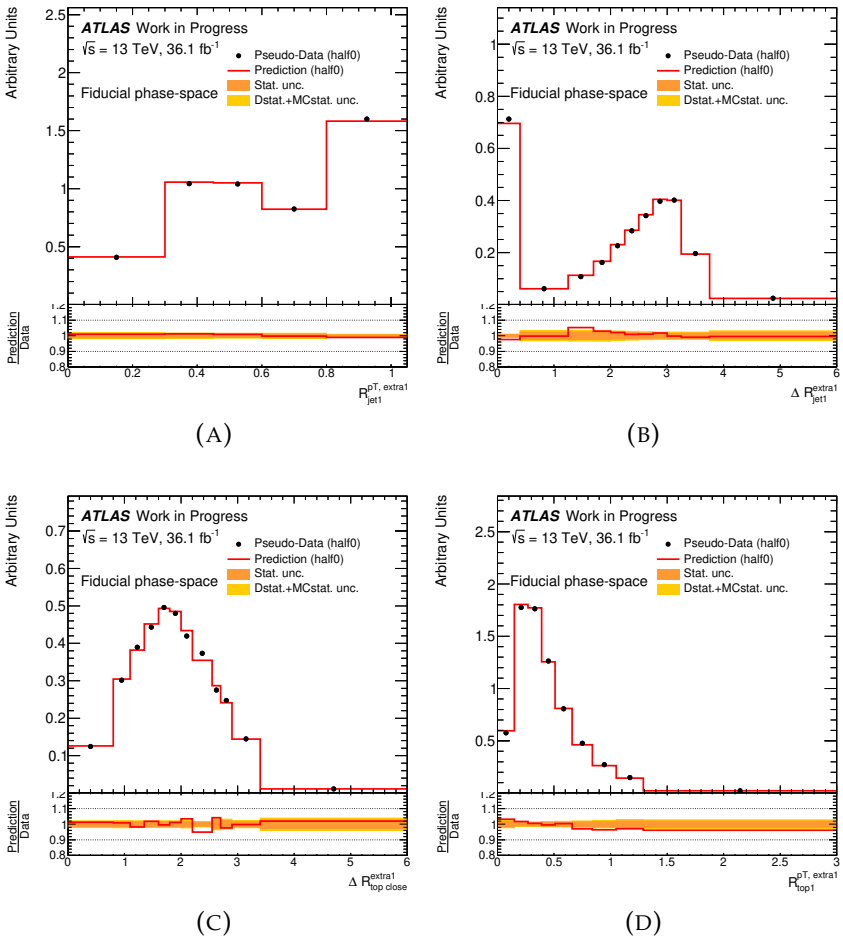

FIGURE F.4: Unfolding closure of a differential cross-section as a function of $\Delta R_{\text{jet1}}^{\text{extra1}}$ (b), $\Delta R_{\text{topclose}}^{\text{extra1}}$ (c), $R_{\text{jet1}}^{\text{extra1}}$ (a) and $R_{\text{top1}}^{\text{extra1}}$ (d) observables normalised in the fiducial phase-space. The shaded area represents the statistical uncertainty.

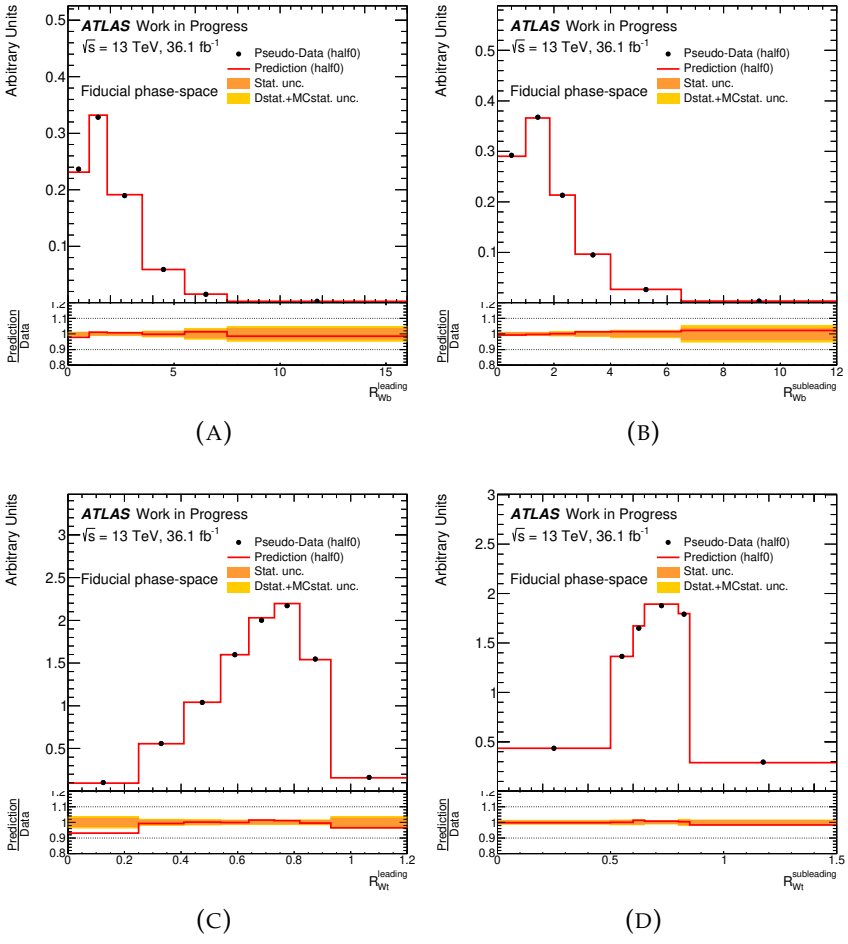

(A) (B)

(C) (D)

FIGURE F.5: Unfolding closure of a differential cross-section as a function of $R_{Wb}^{leading}$ (a), $R_{Wb}^{subleading}$ (b), $R_{Wt}^{leading}$ (c) and $R_{Wt}^{subleading}$ (d) observables normalised in the fiducial phase-space. The shaded area represents the statistical uncertainty.

F.1.2 Closure, parton level

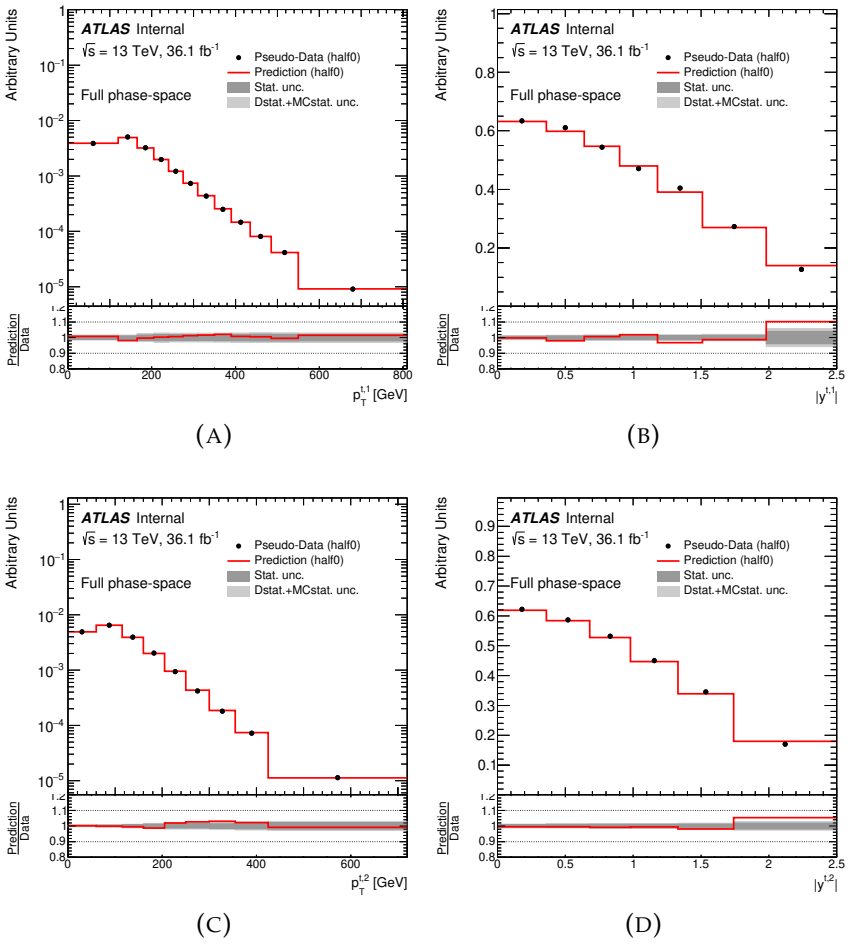

FIGURE F.6: Unfolding closure of a differential cross-section as a function of the $p_T^{t,1}$ (a), $y^{t,1}$ (b), $p_T^{t,2}$ (c) and $y^{t,2}$ (d) observables normalised in the full phase-space. The shaded area represents the statistical uncertainty.

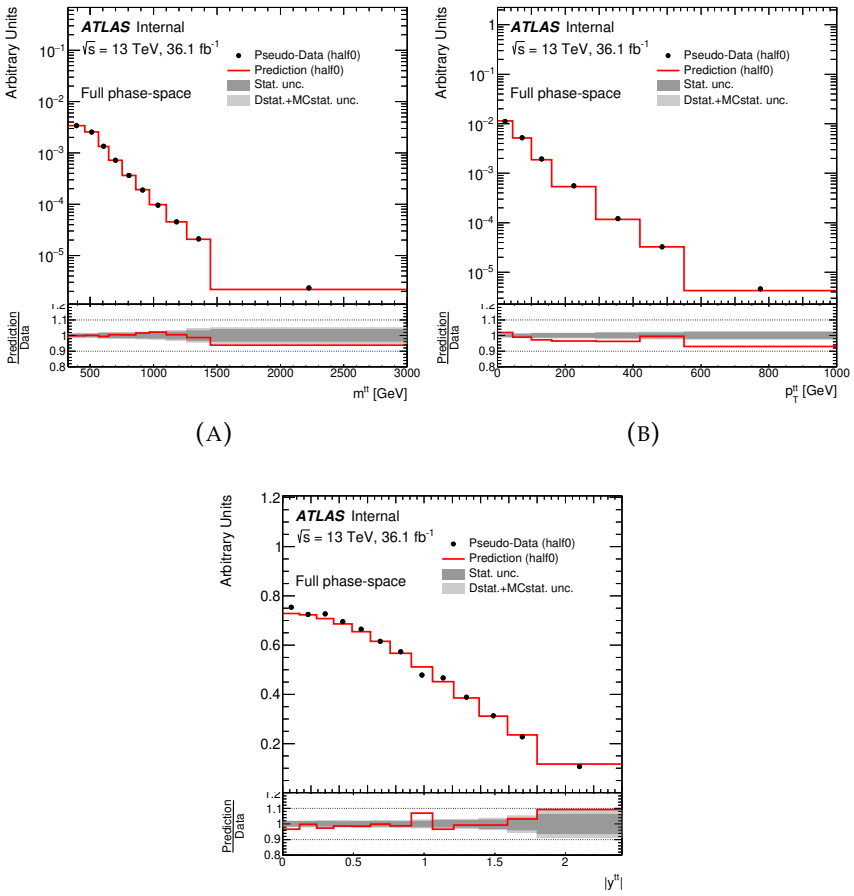

(A) (B)

(C)

FIGURE F.7: Unfolding closure of a differential cross-section as a function of the $m^{t\bar{t}}$ (a), $p_T^{t\bar{t}}$ (b) and $y^{t\bar{t}}$ (c) observable normalised in the full phase-space. The shaded area represents the statistical uncertainty.

F.2 Stress tests

F.2.1 Stress test, particle level

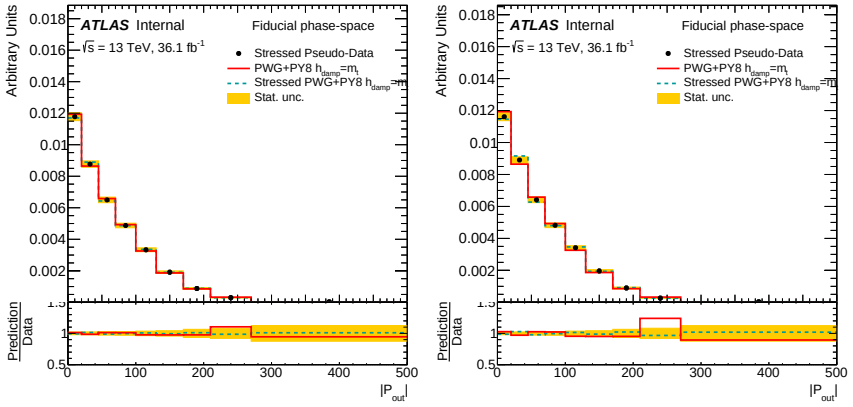

(A) (B)

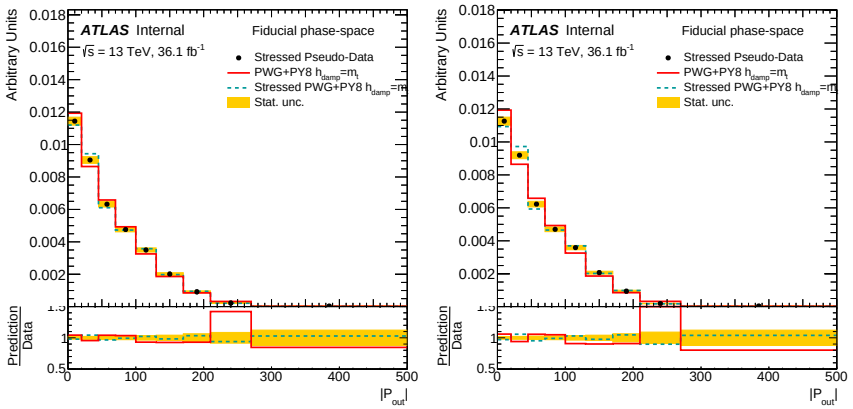

(C) (D)

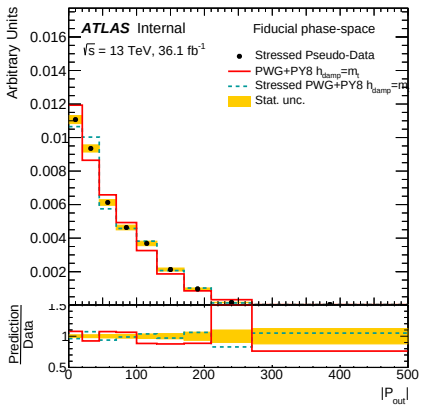

(E)

FIGURE F.8: Linearity stress test using for the normalised cross section as a function of $|P_{\text{out}}^{t\bar{t}}|$. The stress is achieve by re-weigthing the input distribution (red line) by a factor proportional to the data/MC difference. The factors are 1 (top left), 2 (top right), 3 (center left), 4 (center right), 5 (bottom). The efficiency correction has been applied.

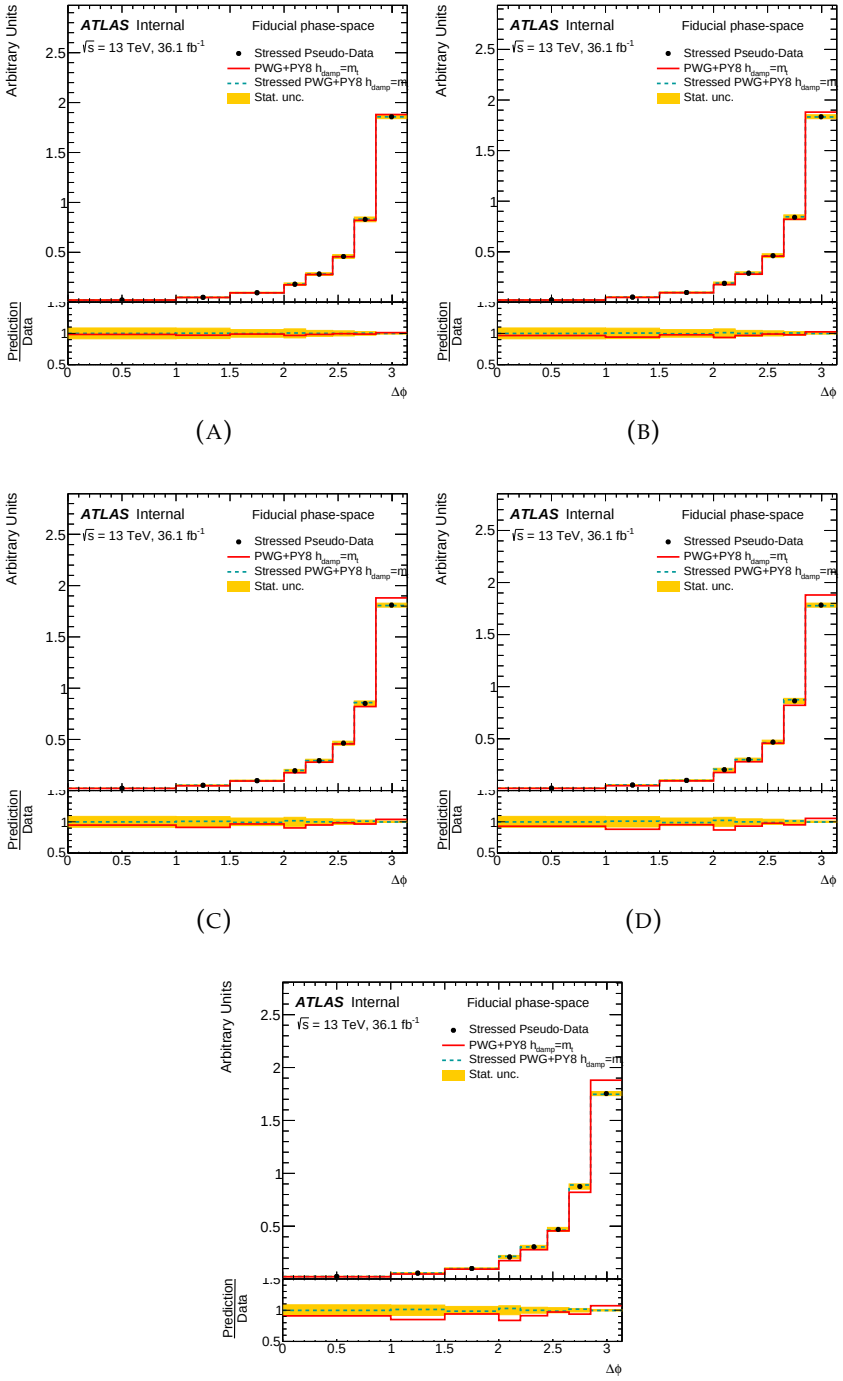

(A) (B)

(C) (D)

(E)

FIGURE F.9: Linearity stress test using for the normalised cross section as a function of $\Delta\phi_{t\bar{t}}$. The stress is achieve by re-weigthing the input distribution (red line) by a factor proportional to the data/MC difference. The factors are 1 (top left), 2 (top right), 3 (center left), 4 (center right), 5 (bottom). The efficiency correction has been applied.

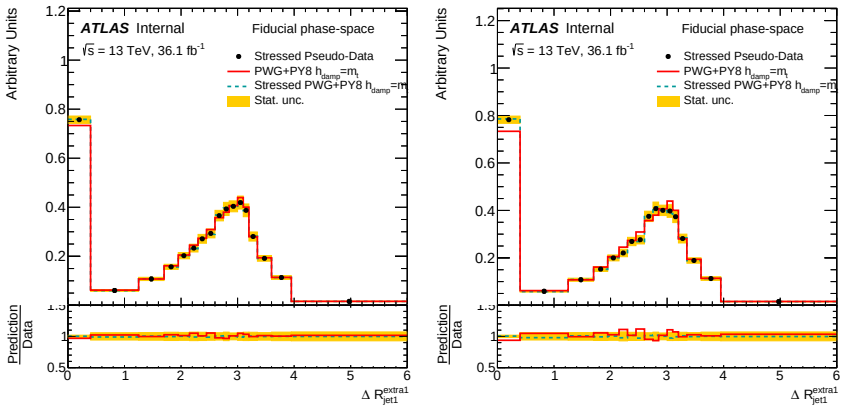

(A) (B)

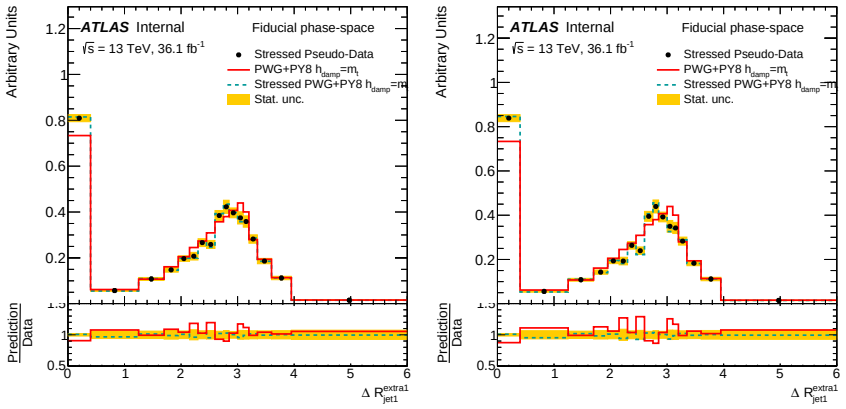

(C) (D)

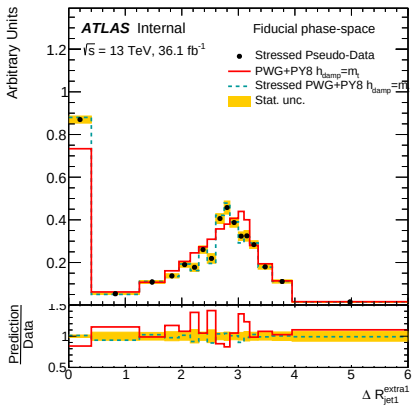

(E)

FIGURE F.10: Linearity stress test using for the normalised cross section as a function of $\Delta R_{\text{jet1}}^{\text{extra1}}$. The stress is achieve by re-weigthing the input distribution (red line) by a factor proportional to the data/MC difference. The factors are 1 (top left), 2 (top right), 3 (center left), 4 (center right), 5 (bottom). The efficiency correction has been applied.

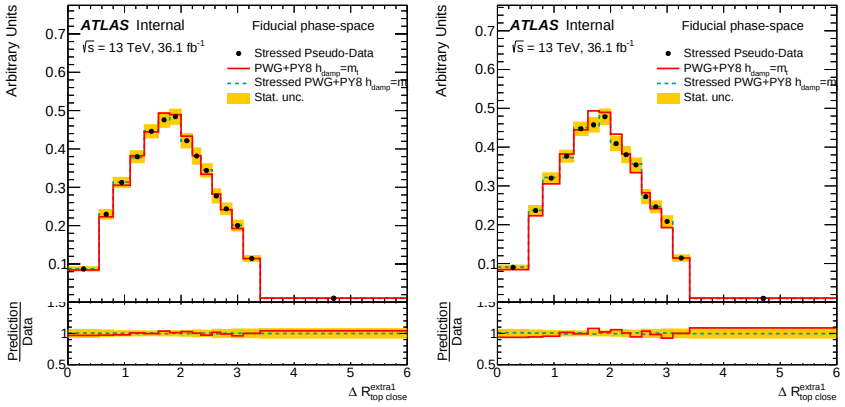

(A) (B)

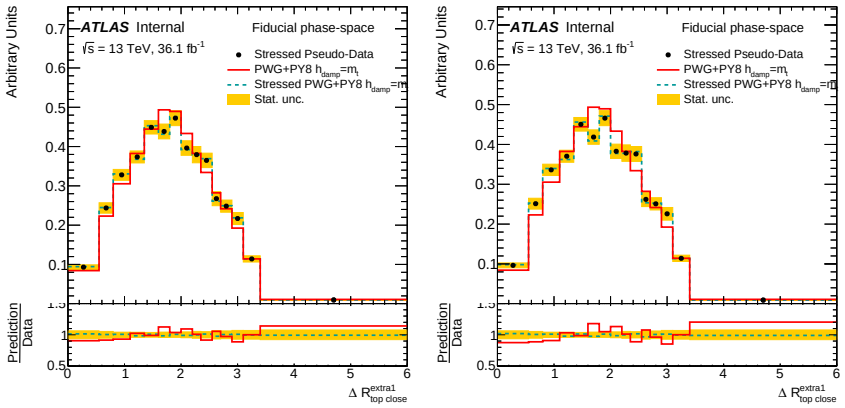

(C) (D)

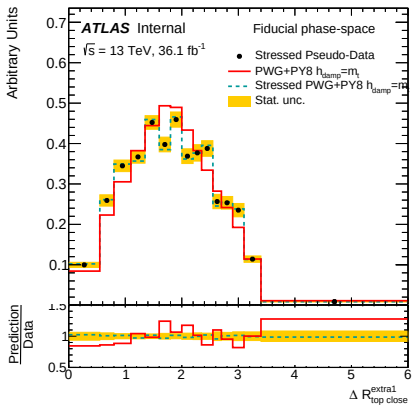

(E)

FIGURE F.11: Linearity stress test using for the normalised cross section as a function of $\Delta R^{\text{extra1}}_{\text{topclose}}$. The stress is achieve by re-weigthing the input distribution (red line) by a factor proportional to the data/MC difference. The factors are 1 (top left), 2 (top right), 3 (center left), 4 (center right), 5 (bottom). The efficiency correction has been applied.

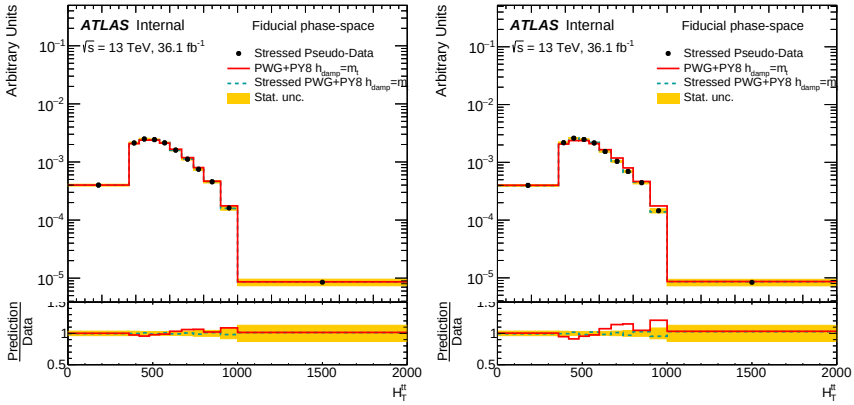

(A) (B)

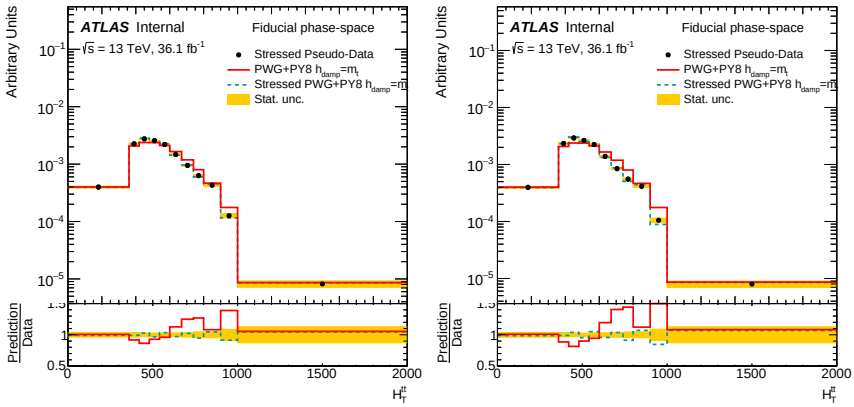

(C) (D)

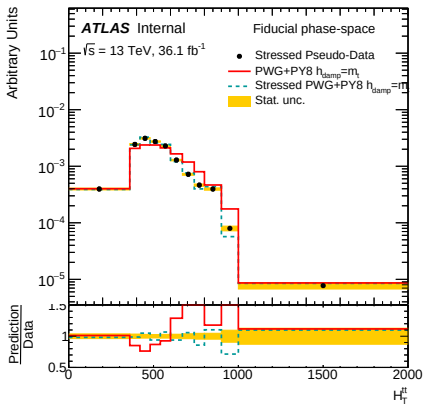

(E)

FIGURE F.12: Linearity stress test using for the normalised cross section as a function of $H_{\mathrm{T}}^{t\bar{t}}$. The stress is achieve by re-weigthing the input distribution (red line) by a factor proportional to the data/MC difference. The factors are 1 (top left), 2 (top right), 3 (center left), 4 (center right), 5 (bottom). The efficiency correction has been applied.

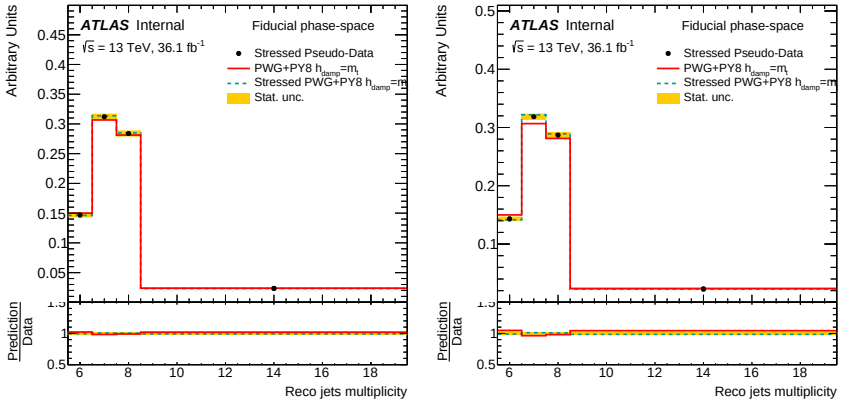

(A) (B)

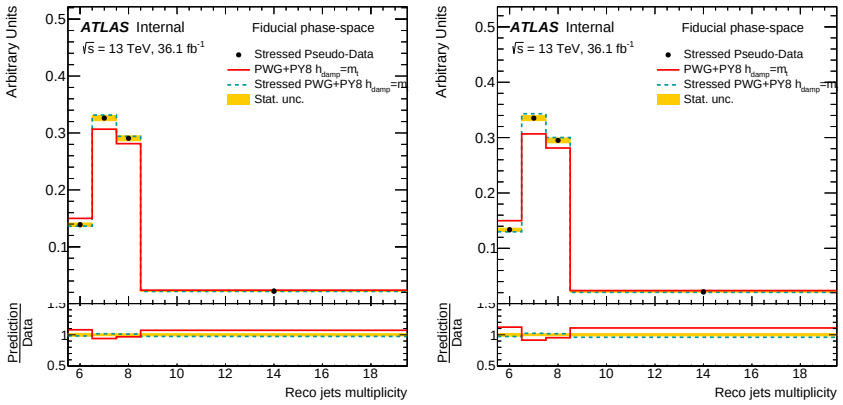

(C) (D)

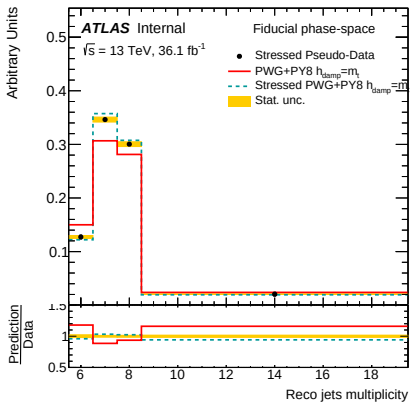

(E)

FIGURE F.13: Linearity stress test using for the normalised cross section as a function of number of jets. The stress is achieve by re-weigthing the input distribution (red line) by a factor proportional to the data/MC difference. The factors are 1 (top left), 2 (top right), 3 (center left), 4 (center right), 5 (bottom). The efficiency correction has been applied.

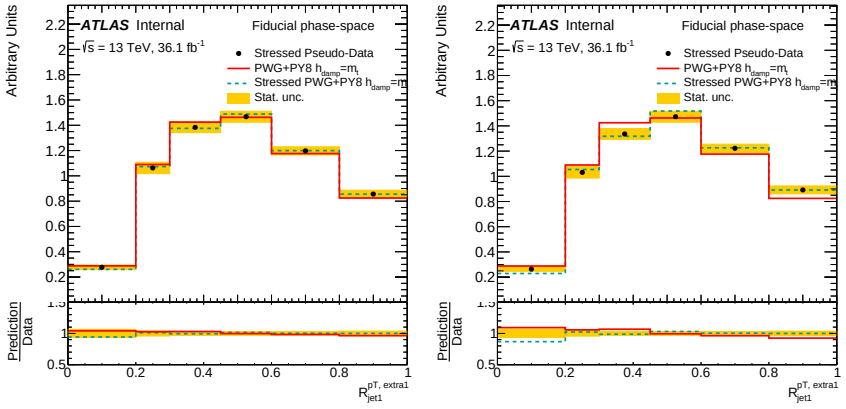

(A) (B)

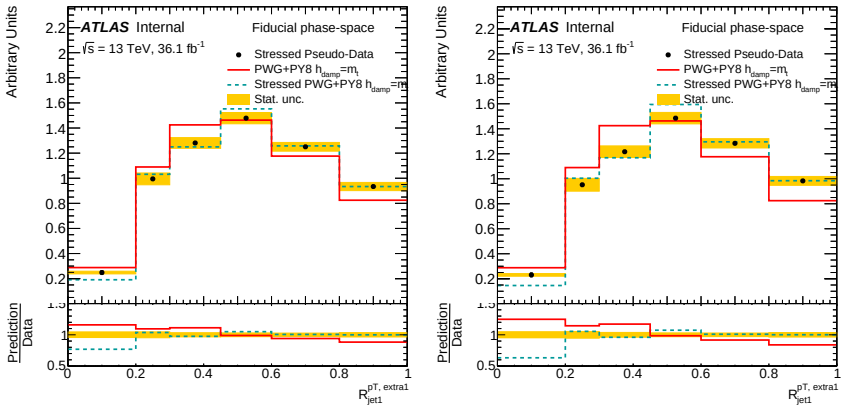

(C) (D)

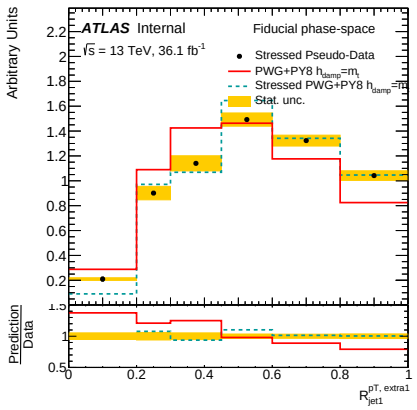

(E)

FIGURE F.14: Linearity stress test using for the normalised cross section as a function of $R_{\mathrm{jet1}}^{\mathrm{extra1}}$. The stress is achieve by re-weigthing the input distribution (red line) by a factor proportional to the data/MC difference. The factors are 1 (top left), 2 (top right), 3 (center left), 4 (center right), 5 (bottom). The efficiency correction has been applied.

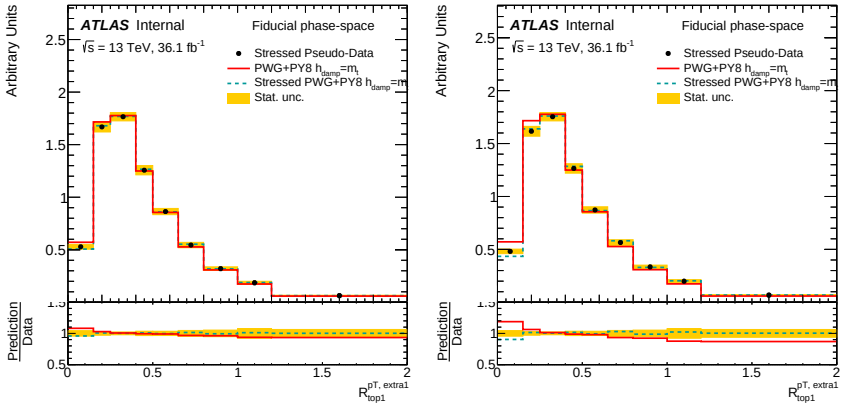

(A) (B)

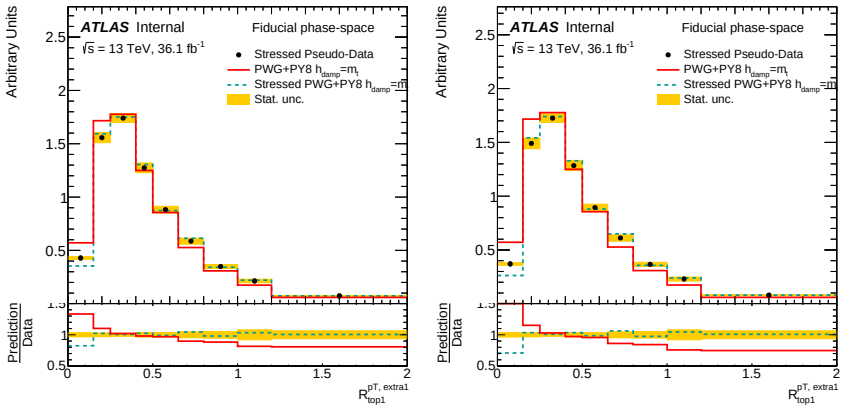

(C) (D)

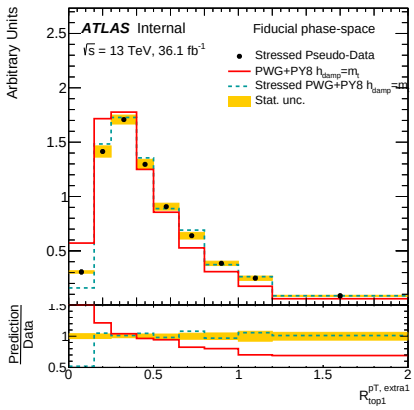

(E)

FIGURE F.15: Linearity stress test using for the normalised cross section as a function of $R_{\text{top1}}^{\text{extra1}}$. The stress is achieve by re-weigthing the input distribution (red line) by a factor proportional to the data/MC difference. The factors are 1 (top left), 2 (top right), 3 (center left), 4 (center right), 5 (bottom). The efficiency correction has been applied.

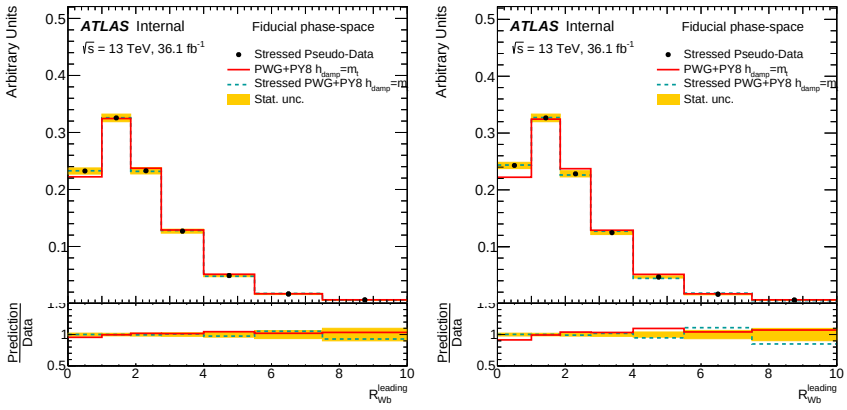

(A) (B)

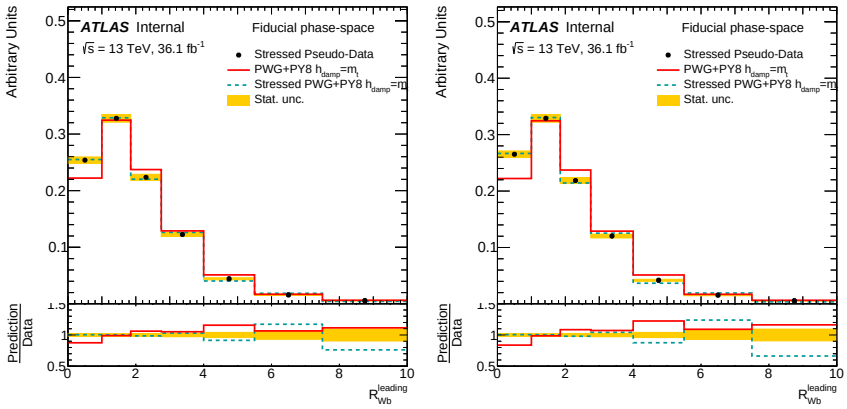

(C) (D)

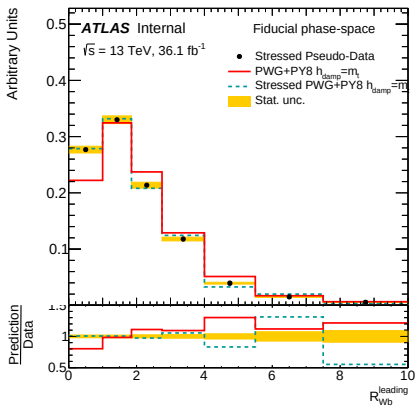

(E)

FIGURE F.16: Linearity stress test using for the normalised cross section as a function of $R_{Wb}^{leading}$. The stress is achieve by re-weigthing the input distribution (red line) by a factor proportional to the data/MC difference. The factors are 1 (top left), 2 (top right), 3 (center left), 4 (center right), 5 (bottom). The efficiency correction has been applied.

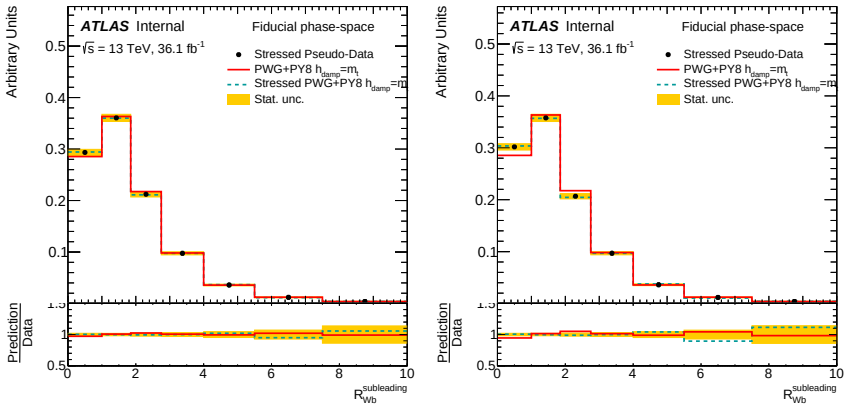

(A) (B)

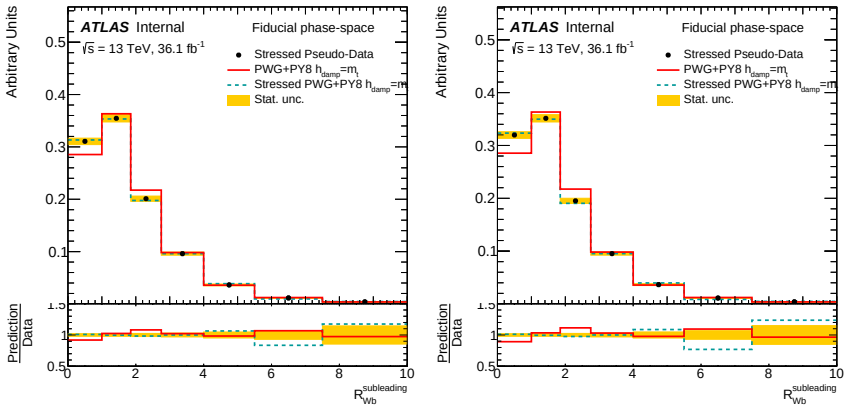

(C) (D)

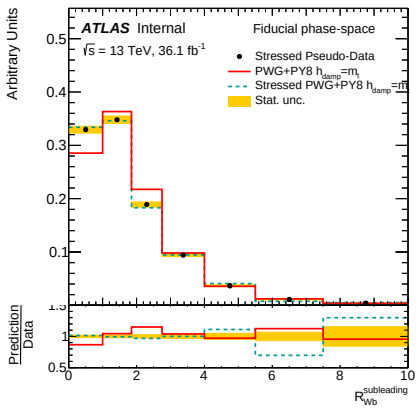

(E)

FIGURE F.17: Linearity stress test using for the normalised cross section as a function of $R_{Wb}^{subleading}$. The stress is achieve by re-weigthing the input distribution (red line) by a factor proportional to the data/MC difference. The factors are 1 (top left), 2 (top right), 3 (center left), 4 (center right), 5 (bottom). The efficiency correction has been applied.

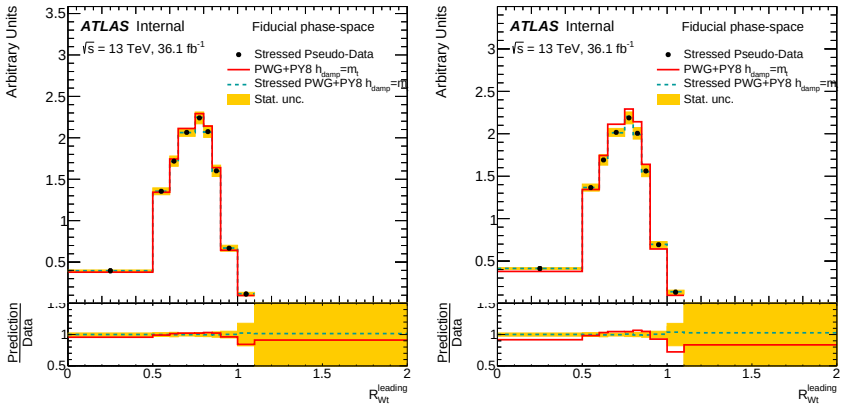

(A) (B)

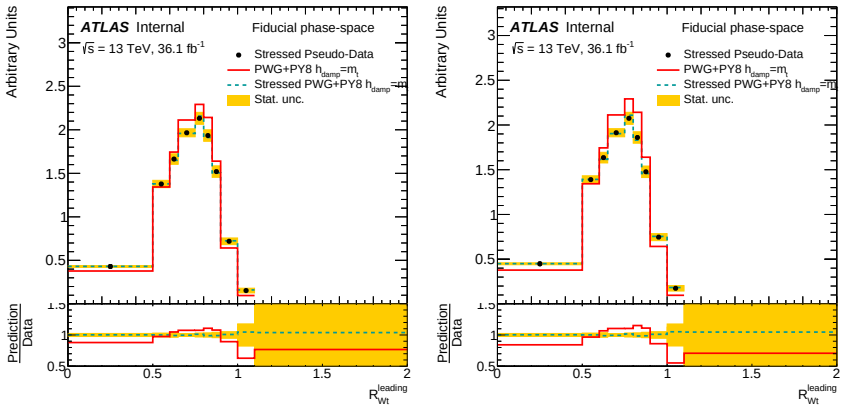

(C) (D)

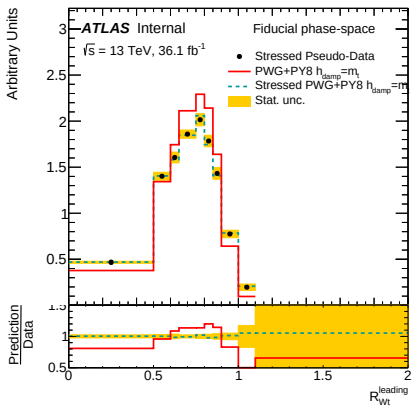

(E)

FIGURE F.18: Linearity stress test using for the normalised cross section as a function of $R_{Wt}^{leading}$. The stress is achieve by re-weigthing the input distribution (red line) by a factor proportional to the data/MC difference. The factors are 1 (top left), 2 (top right), 3 (center left), 4 (center right), 5 (bottom). The efficiency correction has been applied.

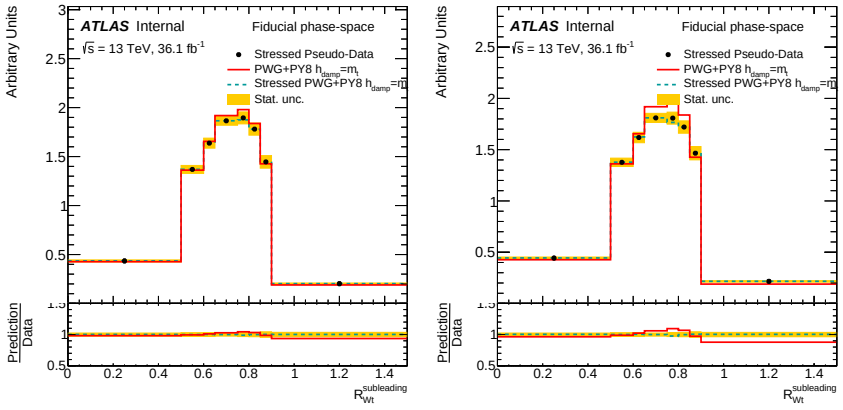

(A) (B)

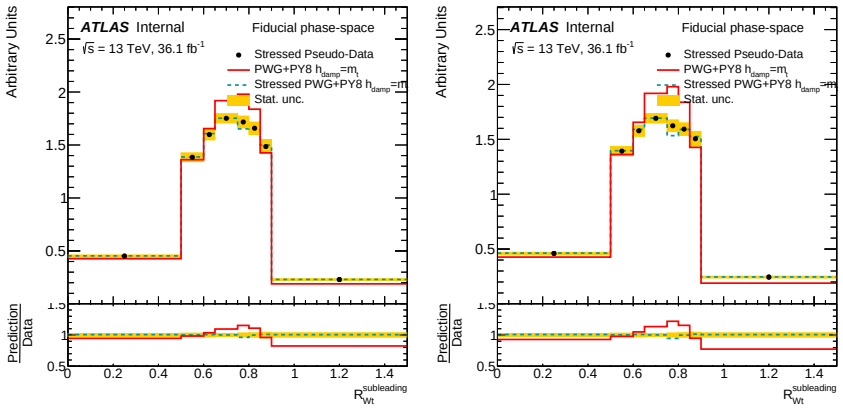

(C) (D)

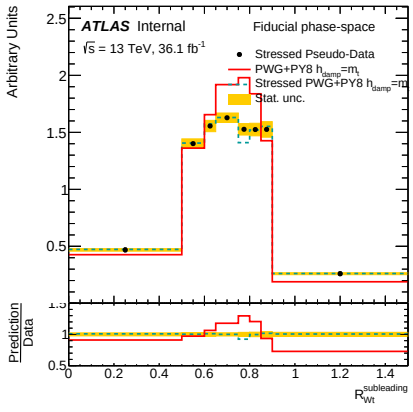

(E)

FIGURE F.19: Linearity stress test using for the normalised cross section as a function of $R_{Wt}^{subleading}$. The stress is achieve by re-weigthing the input distribution (red line) by a factor proportional to the data/MC difference. The factors are 1 (top left), 2 (top right), 3 (center left), 4 (center right), 5 (bottom). The efficiency correction has been applied.

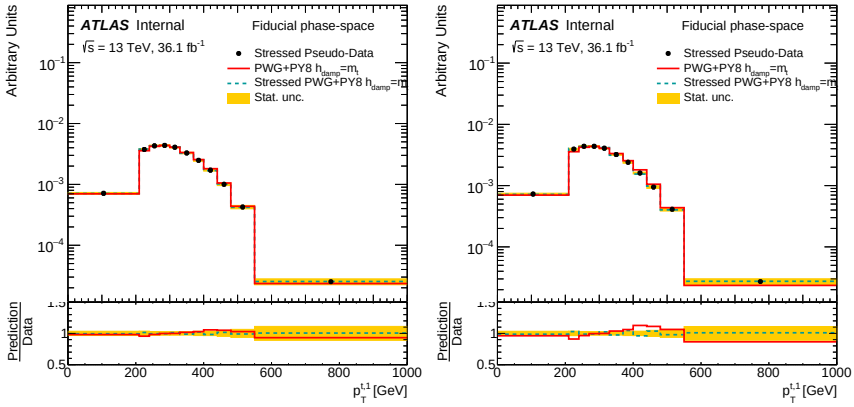

(A) (B)

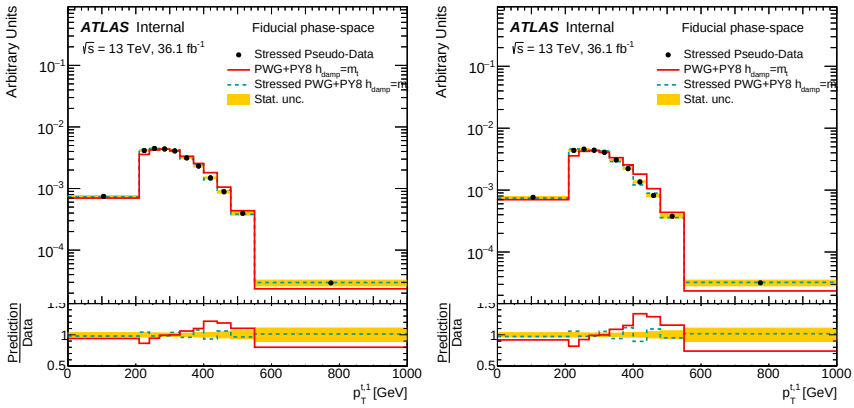

(C) (D)

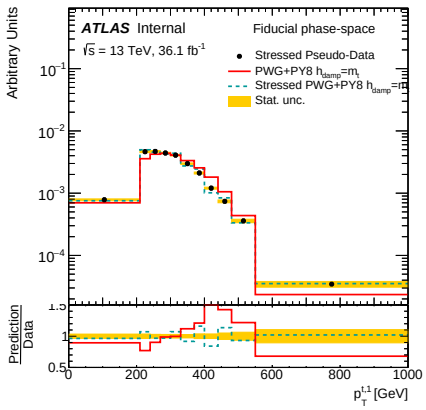

(E)

FIGURE F.20: Linearity stress test using for the normalised cross section as a function of p_T^{top1}. The stress is achieve by re-weigthing the input distribution (red line) by a factor proportional to the data/MC difference. The factors are 1 (top left), 2 (top right), 3 (center left), 4 (center right), 5 (bottom). The efficiency correction has been applied.

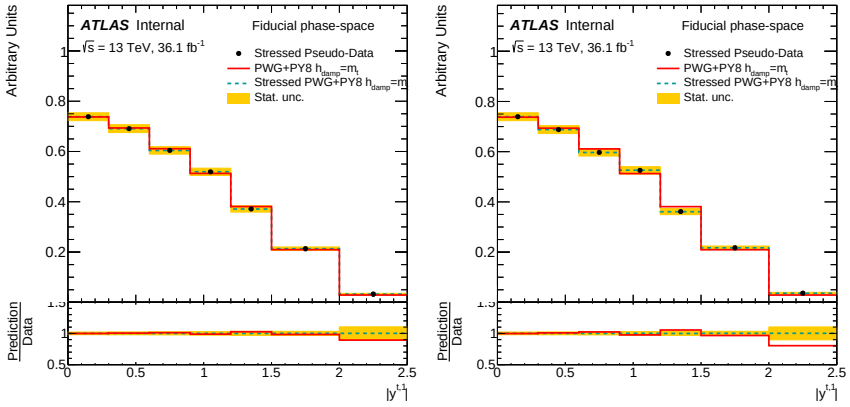

(A) (B)

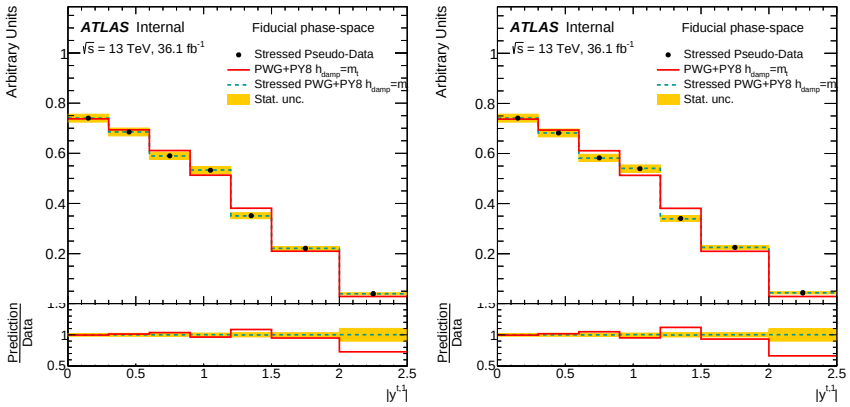

(C) (D)

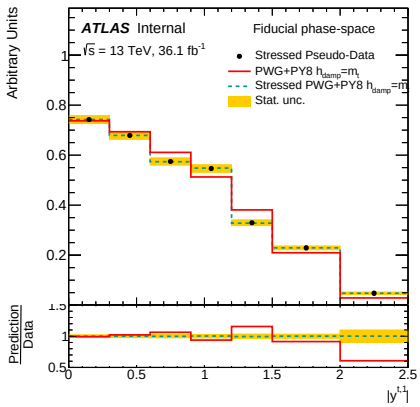

(E)

FIGURE F.21: Linearity stress test using for the normalised cross section as a function of y_{top1}. The stress is achieve by re-weigthing the input distribution (red line) by a factor proportional to the data/MC difference. The factors are 1 (top left), 2 (top right), 3 (center left), 4 (center right), 5 (bottom). The efficiency correction has been applied.

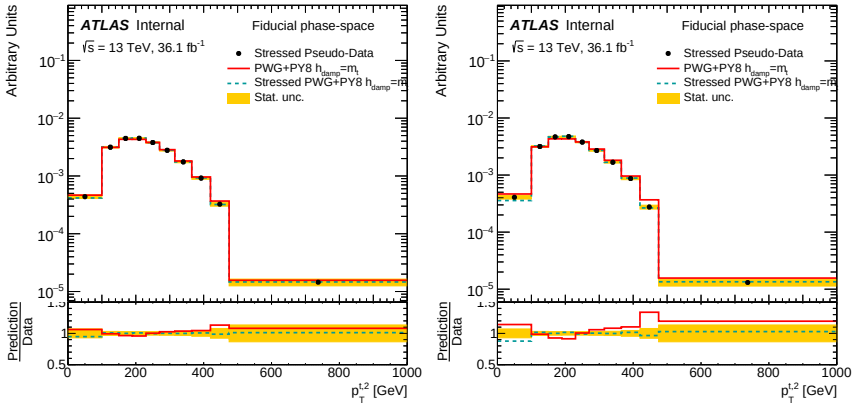

(A) (B)

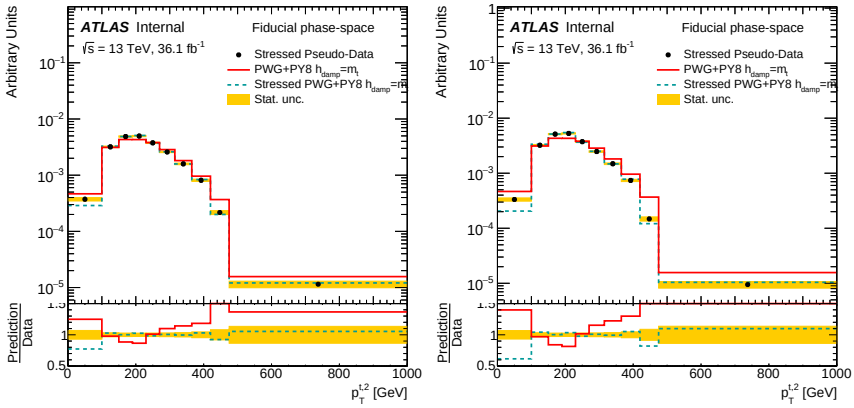

(C) (D)

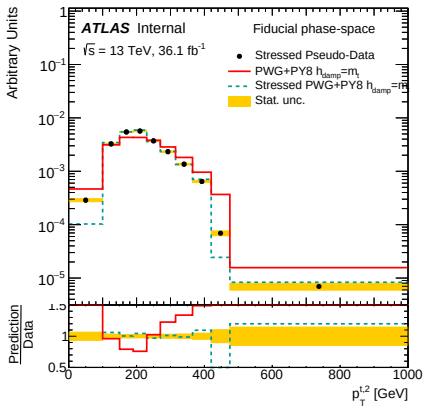

(E)

FIGURE F.22: Linearity stress test using for the normalised cross section as a function of p_T^{top2}. The stress is achieve by re-weigthing the input distribution (red line) by a factor proportional to the data/MC difference. The factors are 1 (top left), 2 (top right), 3 (center left), 4 (center right), 5 (bottom). The efficiency correction has been applied.

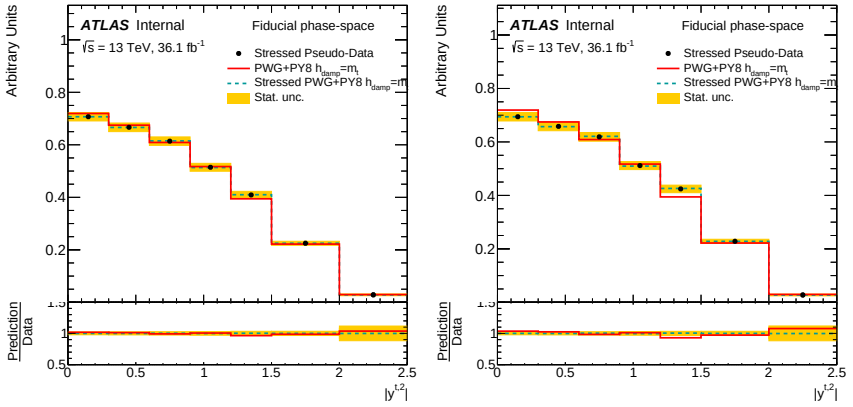

(A) (B)

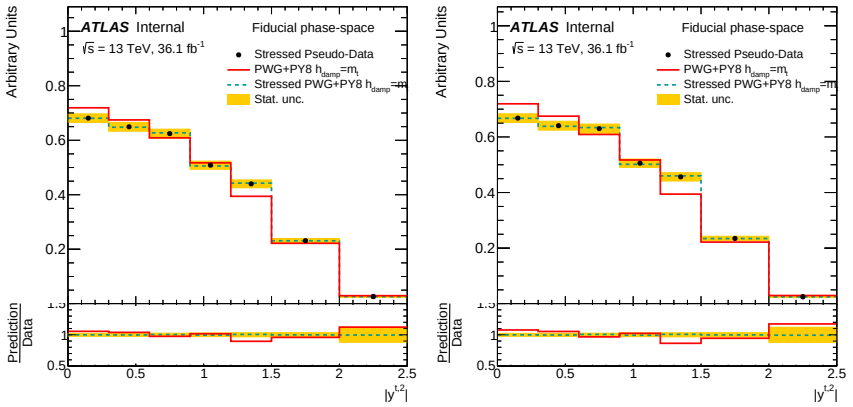

(C) (D)

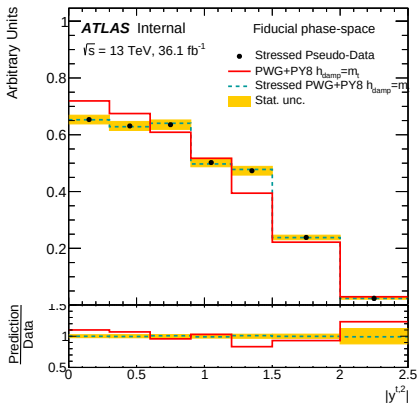

(E)

FIGURE F.23: Linearity stress test using for the normalised cross section as a function of y_{top2}. The stress is achieve by re-weigthing the input distribution (red line) by a factor proportional to the data/MC difference. The factors are 1 (top left), 2 (top right), 3 (center left), 4 (center right), 5 (bottom). The efficiency correction has been applied.

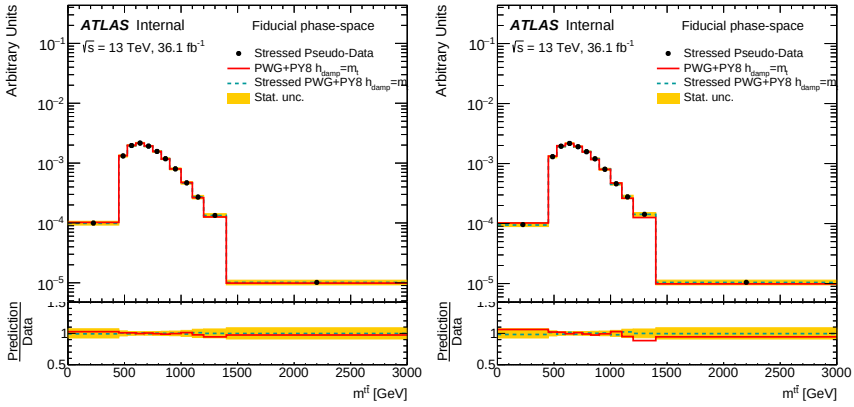

(A) (B)

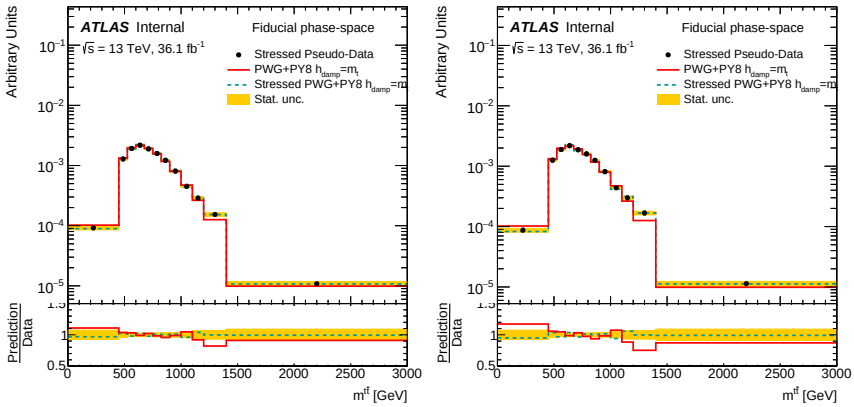

(C) (D)

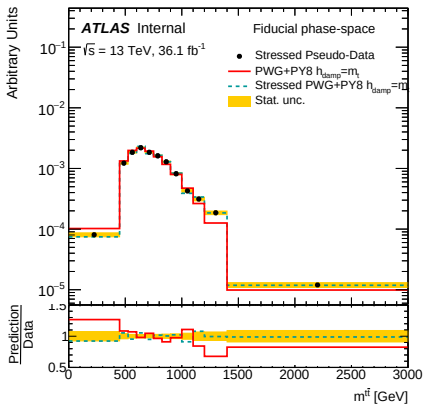

(E)

FIGURE F.24: Linearity stress test using for the normalised cross section as a function of $m_{t\bar{t}}$. The stress is achieve by re-weigthing the input distribution (red line) by a factor proportional to the data/MC difference. The factors are 1 (top left), 2 (top right), 3 (center left), 4 (center right), 5 (bottom). The efficiency correction has been applied.

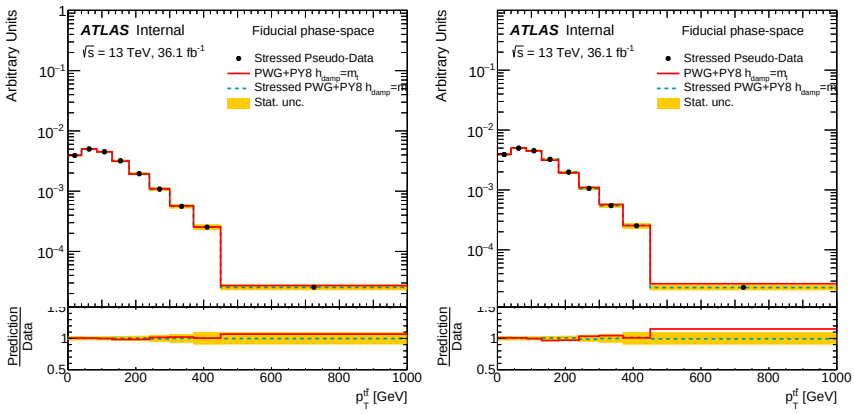

(A) (B)

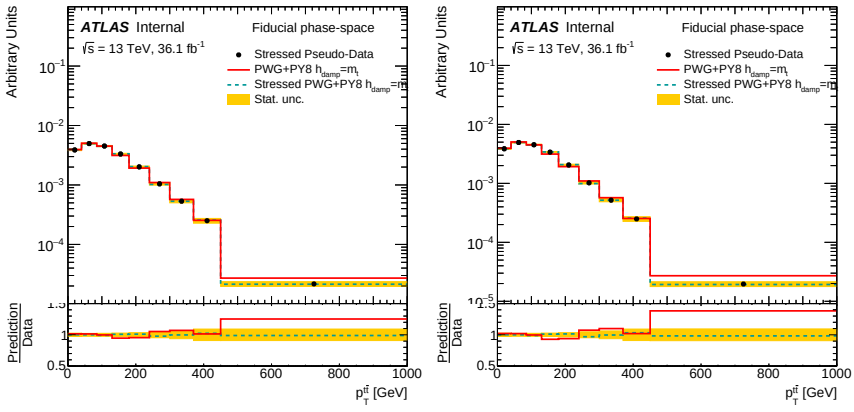

(C) (D)

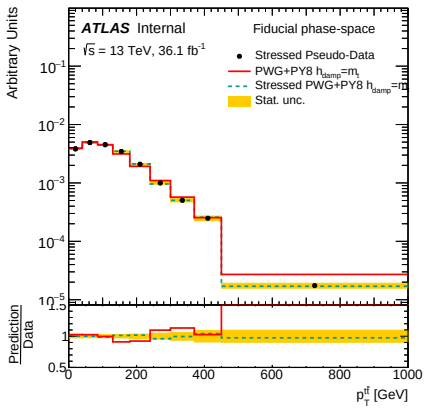

(E)

FIGURE F.25: Linearity stress test using for the normalised cross section as a function of $p_T^{t\bar{t}}$. The stress is achieve by re-weigthing the input distribution (red line) by a factor proportional to the data/MC difference. The factors are 1 (top left), 2 (top right), 3 (center left), 4 (center right), 5 (bottom). The efficiency correction has been applied.

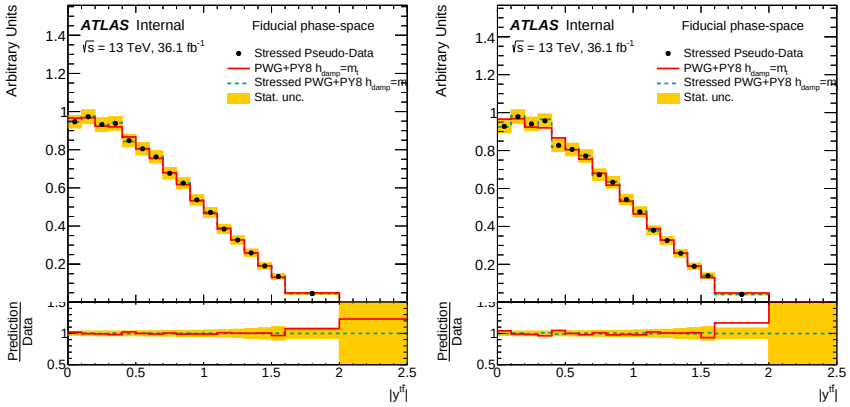

(A) (B)

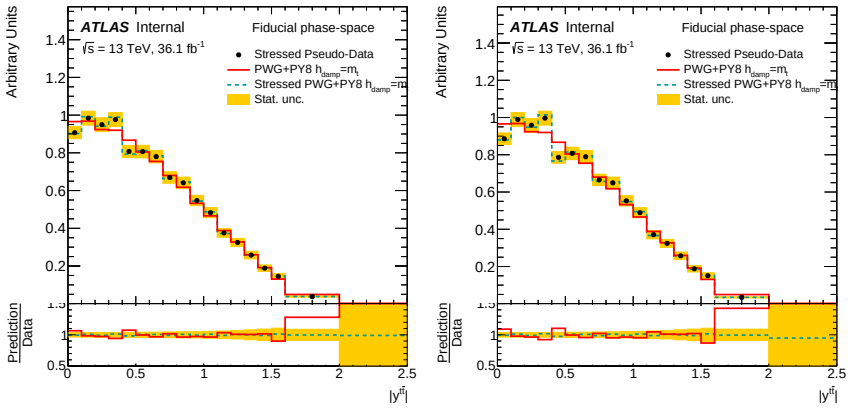

(C) (D)

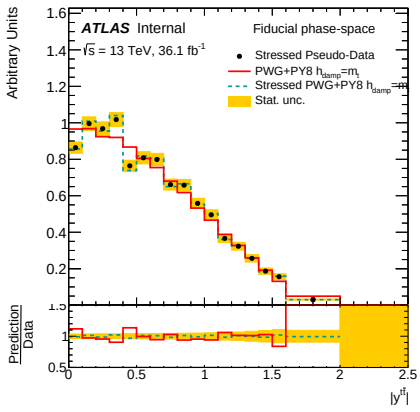

(E)

FIGURE F.26: Linearity stress test using for the normalised cross section as a function of $y_{t\bar{t}}$. The stress is achieve by re-weigthing the input distribution (red line) by a factor proportional to the data/MC difference. The factors are 1 (top left), 2 (top right), 3 (center left), 4 (center right), 5 (bottom). The efficiency correction has been applied.

F.2.2 Stress test, parton level

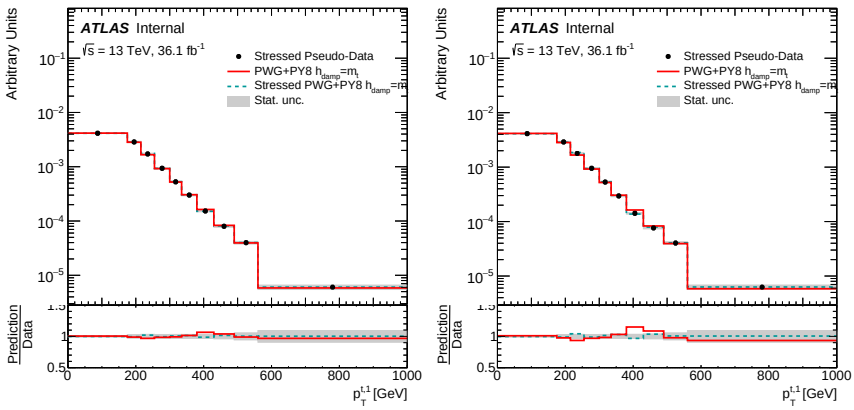

(A) (B)

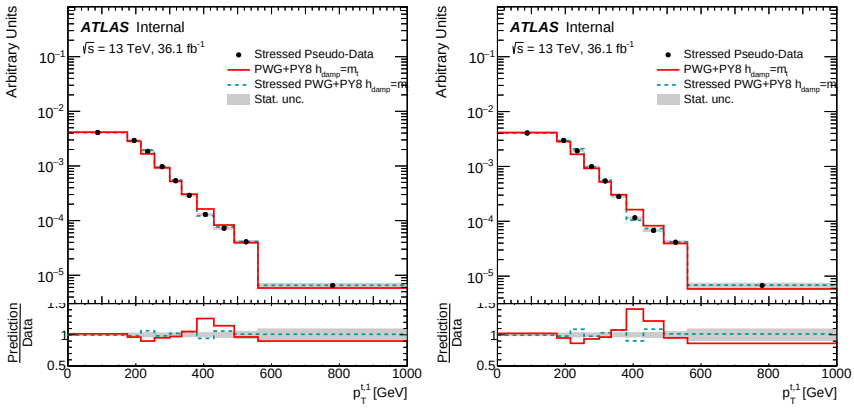

(C) (D)

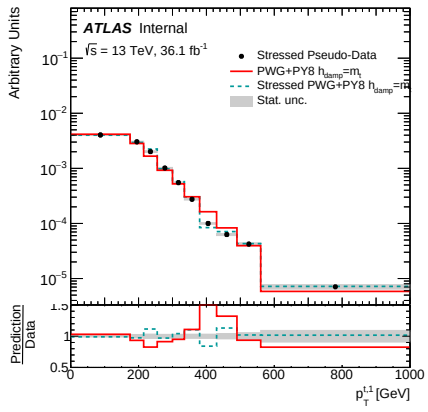

(E)

FIGURE F.27: Linearity stress test using for the normalised cross section as a function of p_T^{top1}. The stress is achieve by re-weigthing the input distribution (red line) by a factor proportional to the data/MC difference. The factors are 1 (top left), 2 (top right), 3 (center left), 4 (center right), 5 (bottom). The efficiency correction has been applied.

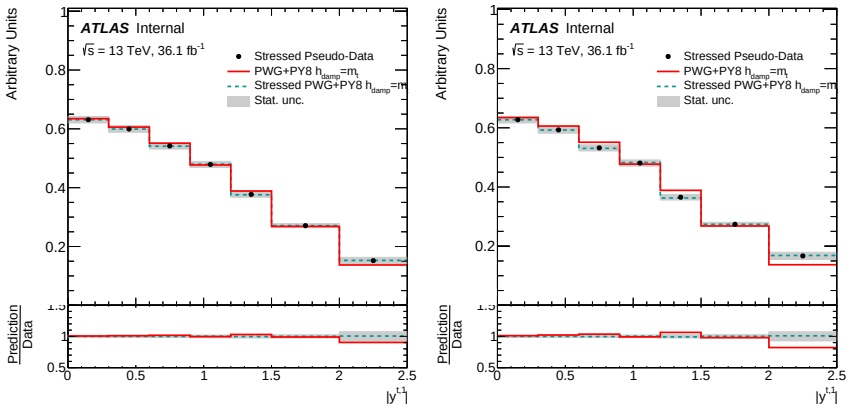

(A) (B)

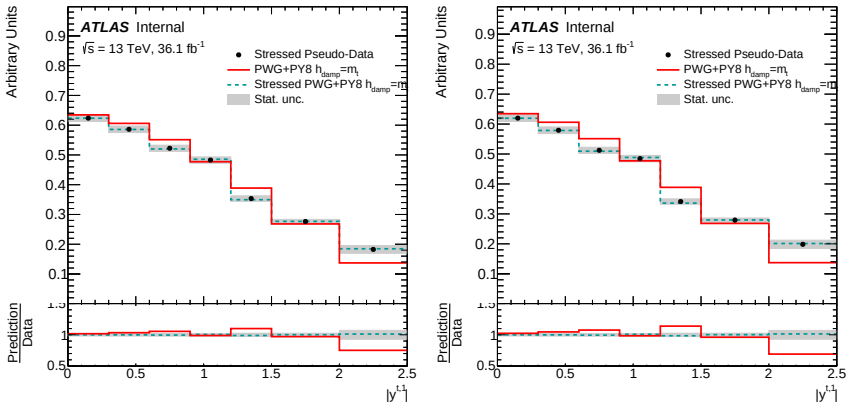

(C) (D)

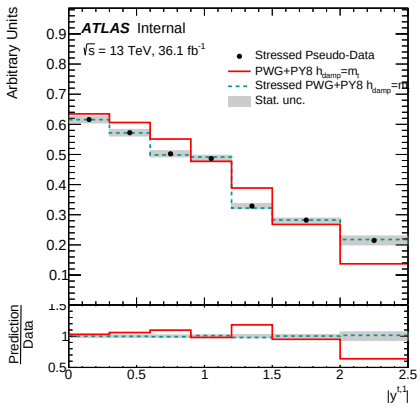

(E)

FIGURE F.28: Linearity stress test using for the normalised cross section as a function of y_{top1}. The stress is achieve by re-weigthing the input distribution (red line) by a factor proportional to the data/MC difference. The factors are 1 (top left), 2 (top right), 3 (center left), 4 (center right), 5 (bottom). The efficiency correction has been applied.

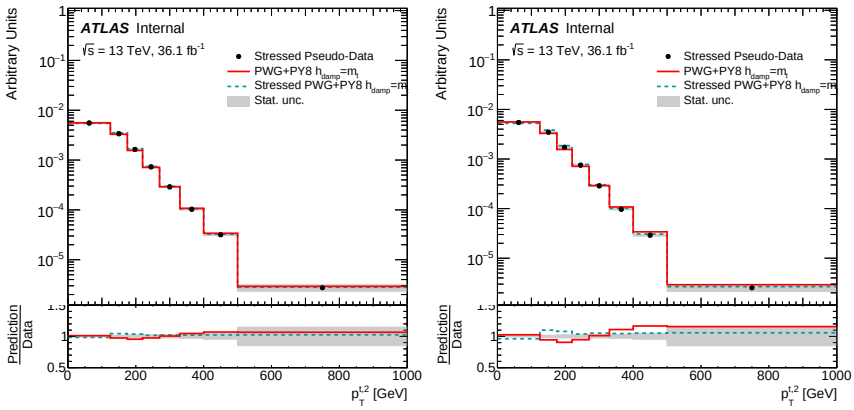

(A) (B)

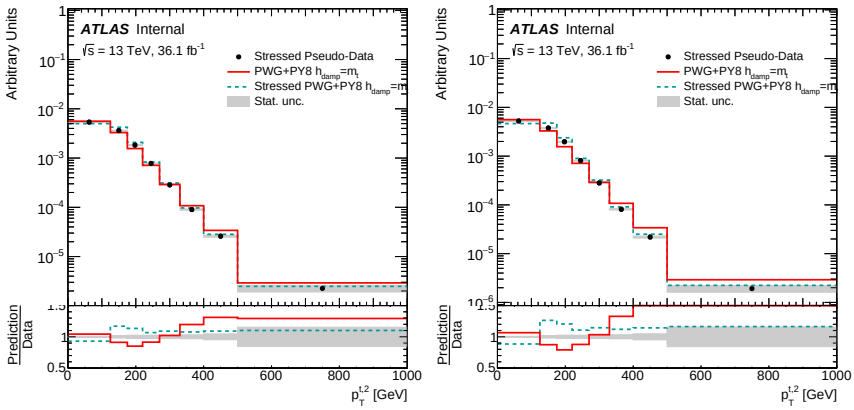

(C) (D)

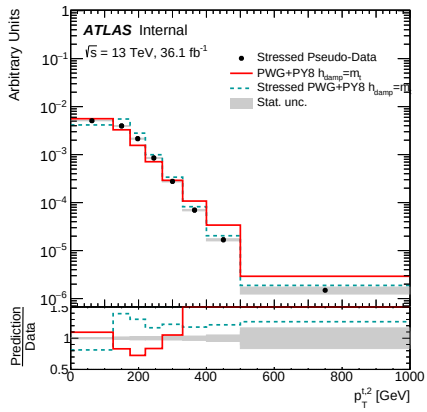

(E)

FIGURE F.29: Linearity stress test using for the normalised cross section as a function of p_T^{top2}. The stress is achieve by re-weigthing the input distribution (red line) by a factor proportional to the data/MC difference. The factors are 1 (top left), 2 (top right), 3 (center left), 4 (center right), 5 (bottom). The efficiency correction has been applied.

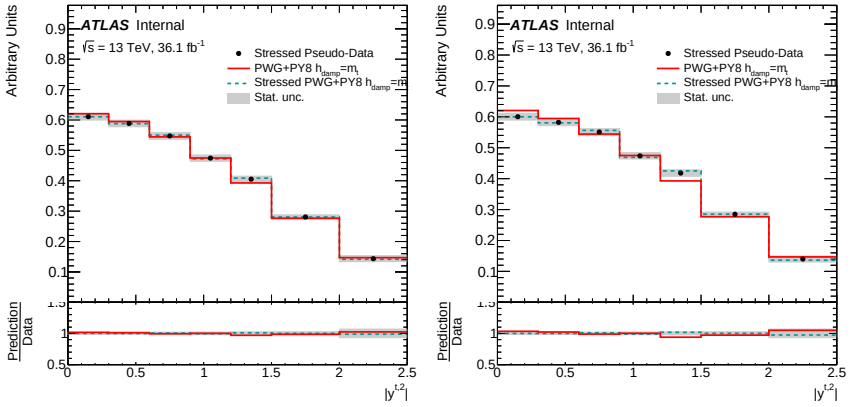

(A) (B)

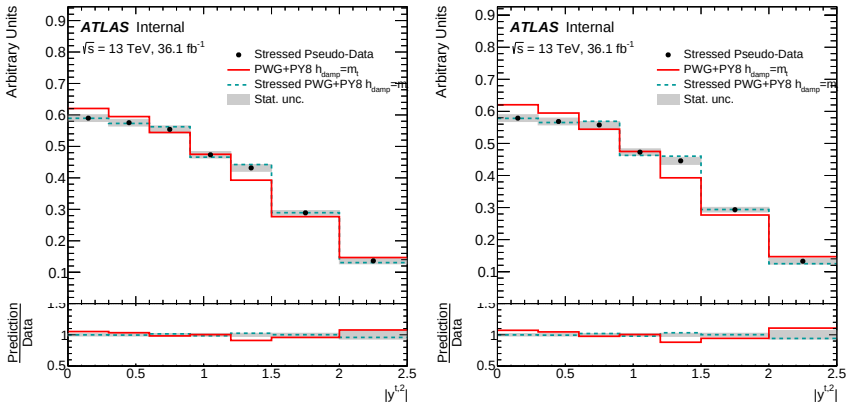

(C) (D)

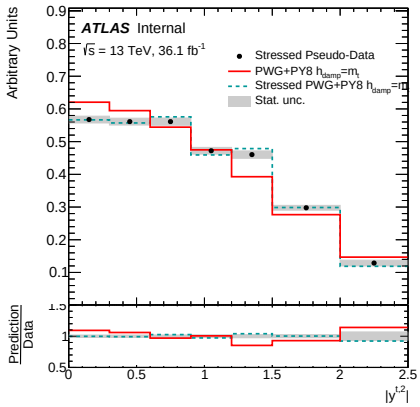

(E)

FIGURE F.30: Linearity stress test using for the normalised cross section as a function of y_{top2}. The stress is achieve by re-weigthing the input distribution (red line) by a factor proportional to the data/MC difference. The factors are 1 (top left), 2 (top right), 3 (center left), 4 (center right), 5 (bottom). The efficiency correction has been applied.

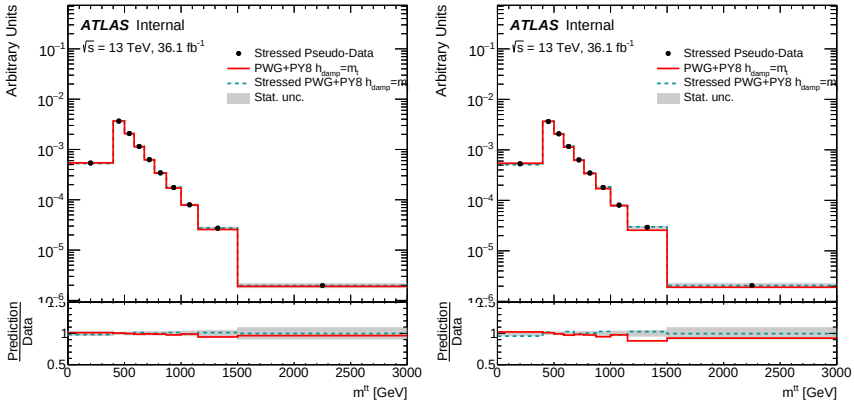

(A) (B)

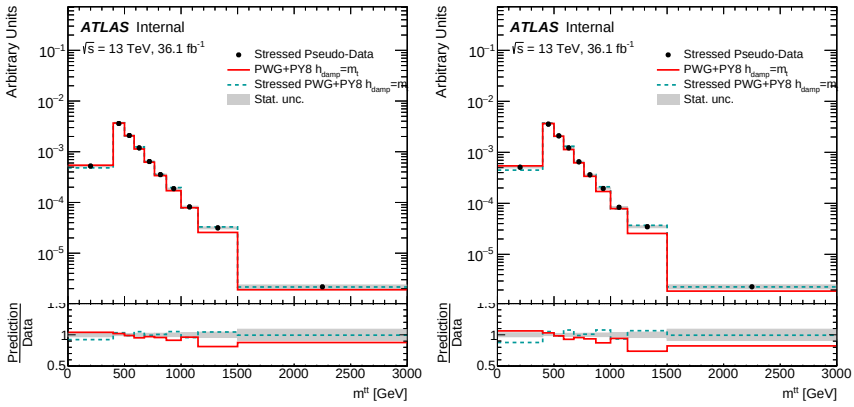

(C) (D)

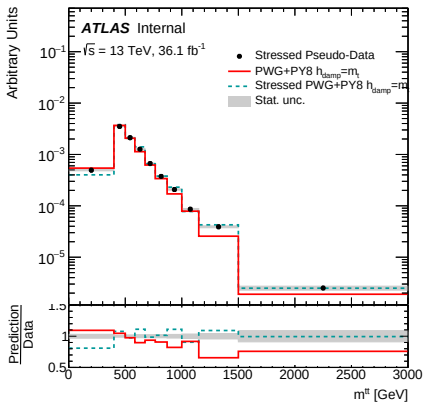

(E)

FIGURE F.31: Linearity stress test using for the normalised cross section as a function of $m_{t\bar{t}}$. The stress is achieve by re-weigthing the input distribution (red line) by a factor proportional to the data/MC difference. The factors are 1 (top left), 2 (top right), 3 (center left), 4 (center right), 5 (bottom). The efficiency correction has been applied.

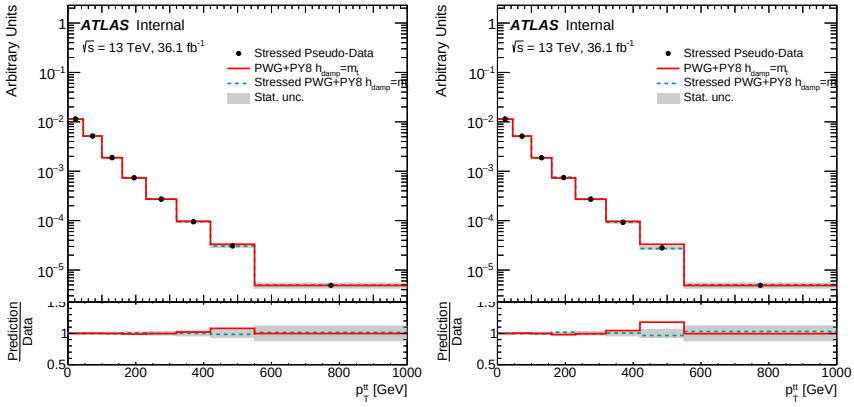

(A) (B)

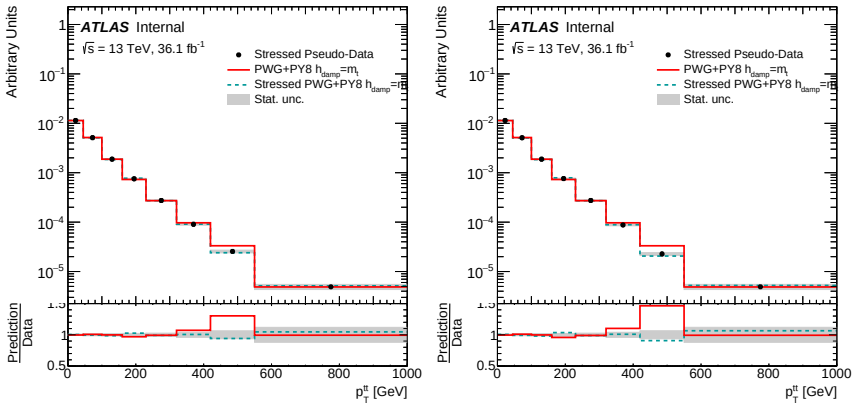

(C) (D)

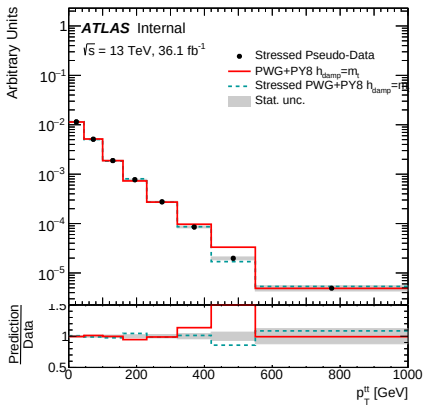

(E)

FIGURE F.32: Linearity stress test using for the normalised cross section as a function of $p_T^{t\bar{t}}$. The stress is achieve by re-weigthing the input distribution (red line) by a factor proportional to the data/MC difference. The factors are 1 (top left), 2 (top right), 3 (center left), 4 (center right), 5 (bottom). The efficiency correction has been applied.

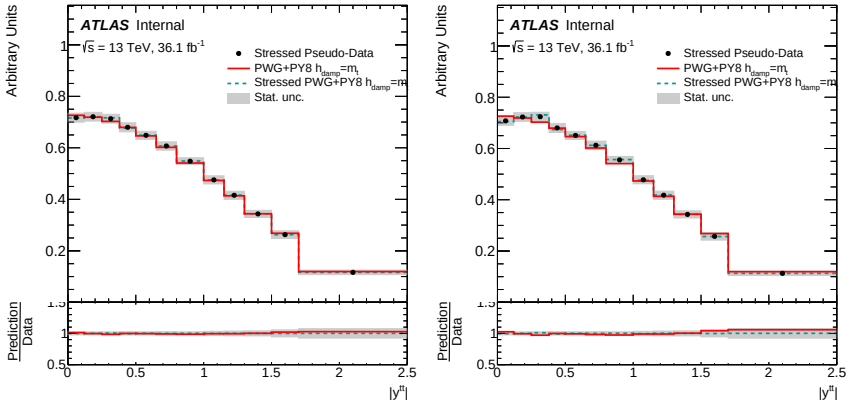

(A) (B)

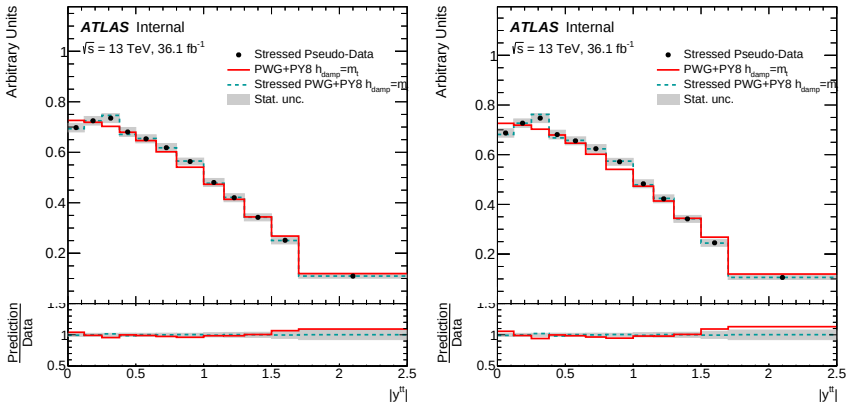

(C) (D)

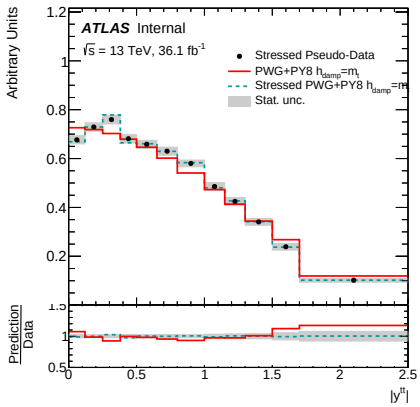

(E)

FIGURE F.33: Linearity stress test using for the normalised cross section as a function of $y_{t\bar{t}}$. The stress is achieve by re-weigthing the input distribution (red line) by a factor proportional to the data/MC difference. The factors are 1 (top left), 2 (top right), 3 (center left), 4 (center right), 5 (bottom). The efficiency correction has been applied.

F.3 Unfolding iterations stability checks

The chosen number of iterations used in the unfolding procedure is 4. However, it is important to check whether this number is suitable to be used in the unfolding procedure. In general, the higher the number of iterations, the less regularized the unfolding is; therefore, the bias should decrease with the number of iterations while the statistical uncertainty is expected to increase with the number of iterations. In this Appendix, the figures of merit for data unfolded to particle are shown.

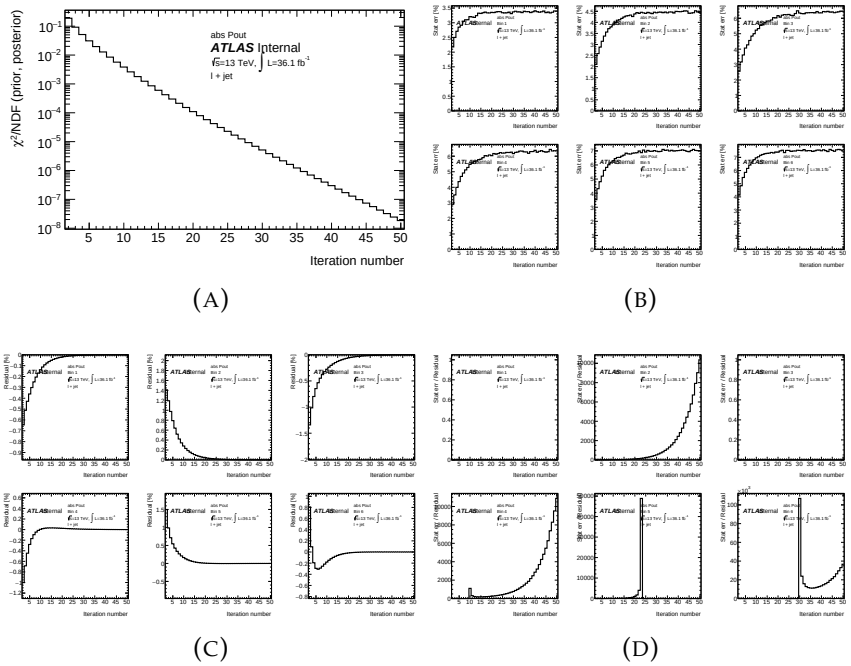

(A) (B)

(C) (D)

FIGURE F.34: χ^2 F.34a, statistical error F.34b, residuals (w.r.t. previous iteration) F.34c and statistical error over residuals ratio F.34d as a function of the N_{iter} in $|P_{\text{out}}^{t\bar{t}}|$bins in the fiducial phase-space.

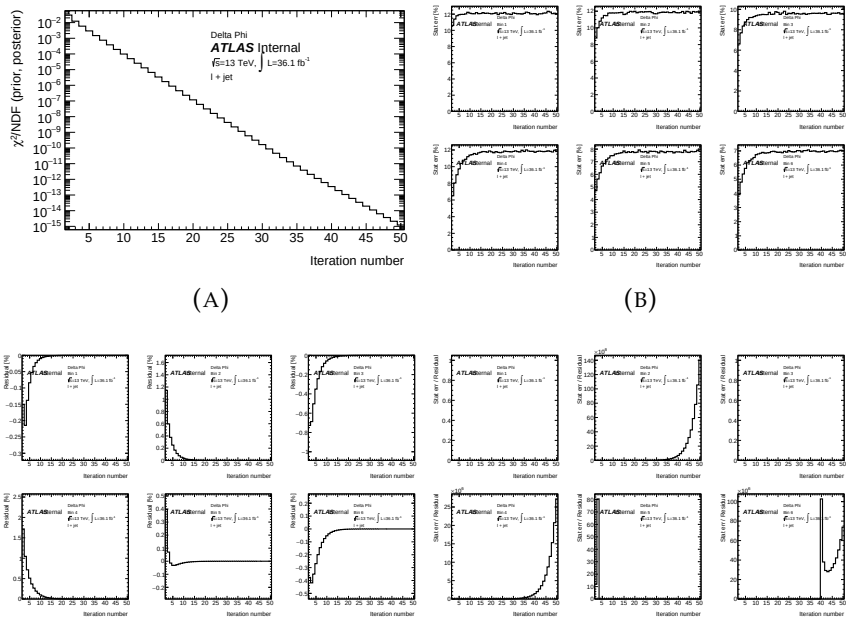

(A) (B)

(C) (D)

FIGURE F.35: χ^2 (a), statistical error (b), residuals (w.r.t. previous iteration) (c) and statistical error over residuals ratio (d) as a function of the N_{iter} in $\Delta\phi_{tt}$bins in the fiducial phase-space.

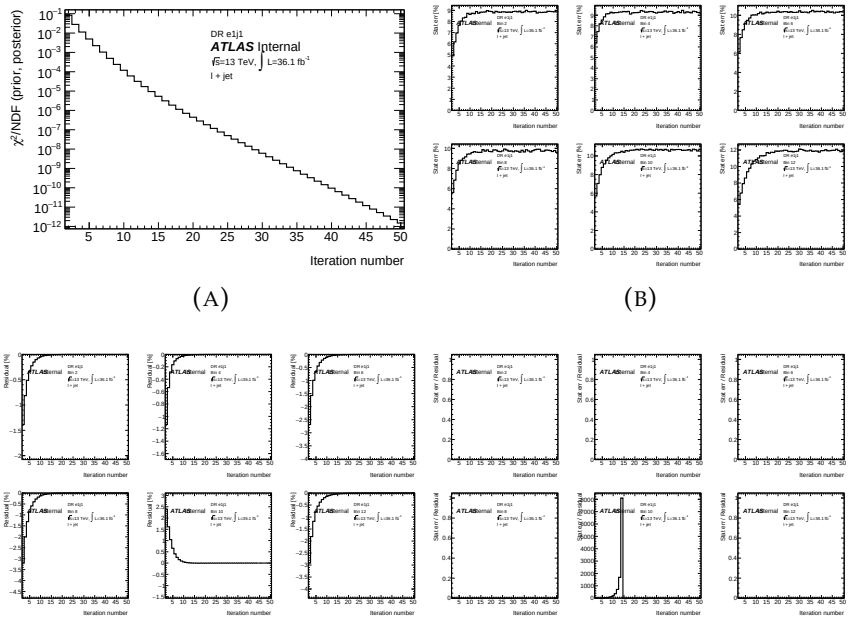

(A) (B)

(C) (D)

FIGURE F.36: χ^2 (a), statistical error (b), residuals (w.r.t. previous iteration) (c) and statistical error over residuals ratio (d) as a function of the N_{iter} in $\Delta R_{\mathrm{jet1}}^{\mathrm{extra1}}$bins in the fiducial phase-space.

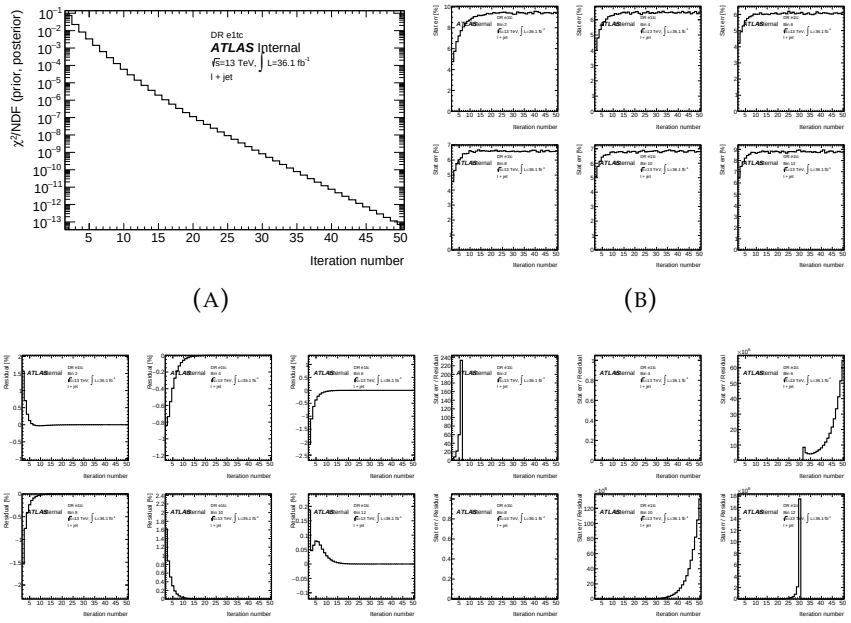

FIGURE F.37: χ^2 (a), statistical error (b), residuals (w.r.t. previous iteration) (c) and statistical error over residuals ratio (d) as a function of the N_{iter} in $\Delta R^{\text{extra1}}_{\text{topclose}}$ bins in the fiducial phase-space.

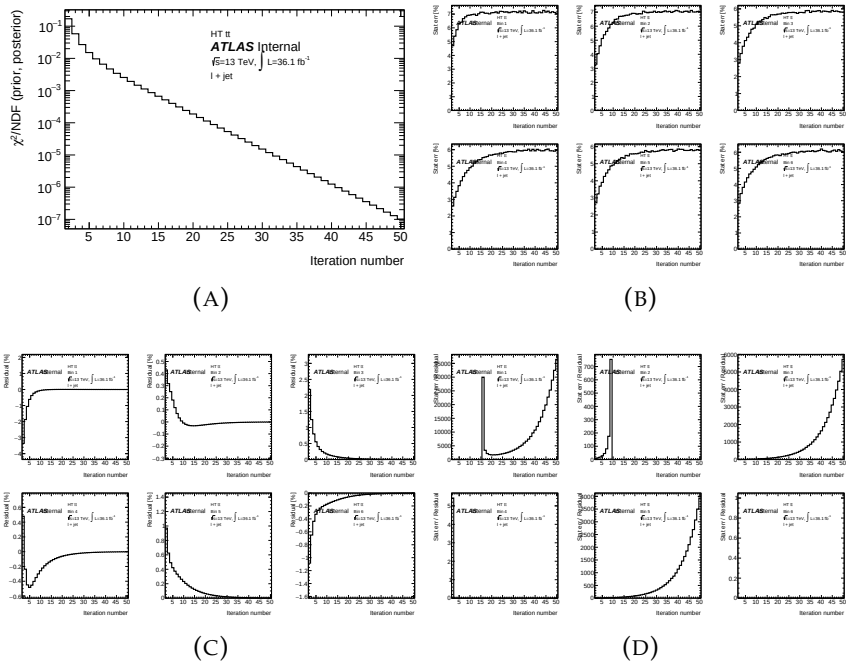

FIGURE F.38: χ^2 (a), statistical error (b), residuals (w.r.t. previous iteration) (c) and statistical error over residuals ratio (d) as a function of the N_{iter} in $H_{\text{T}}^{t\bar{t}}$ bins in the fiducial phase-space.

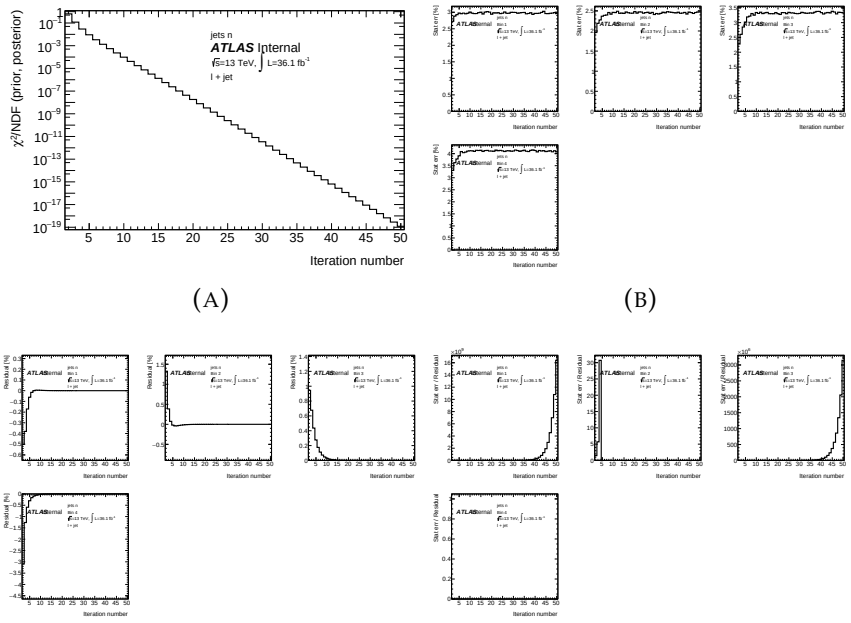

(A) (B)

(C) (D)

FIGURE F.39: χ^2 (a), statistical error (b), residuals (w.r.t. previous iteration) (c) and statistical error over residuals ratio (d) as a function of the N_{iter} in N_{jets} bins in the fiducial phase-space.

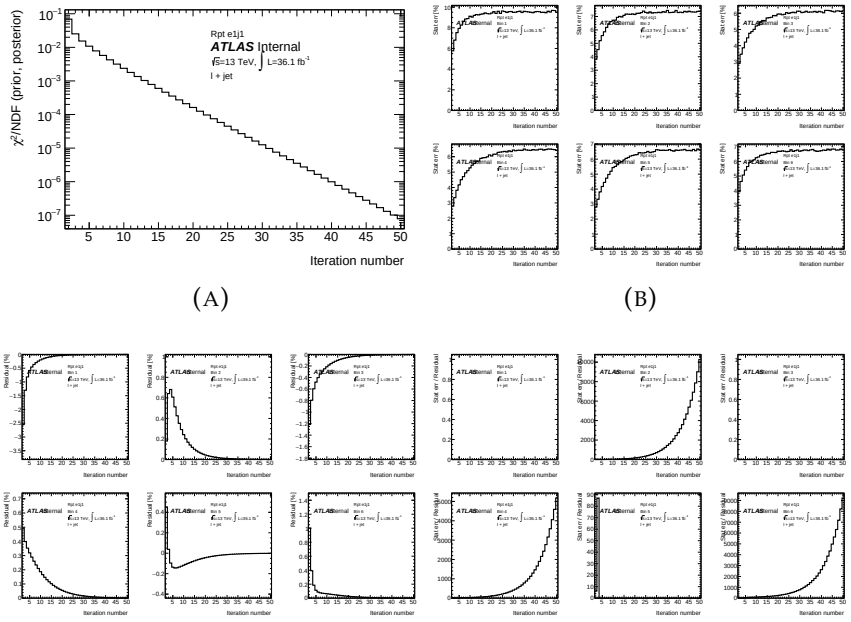

(A) (B)

(C) (D)

FIGURE F.40: χ^2 (a), statistical error (b), residuals (w.r.t. previous iteration) (c) and statistical error over residuals ratio (d) as a function of the N_{iter} in $R_{\text{jet1}}^{\text{extra1}}$bins in the fiducial phase-space.

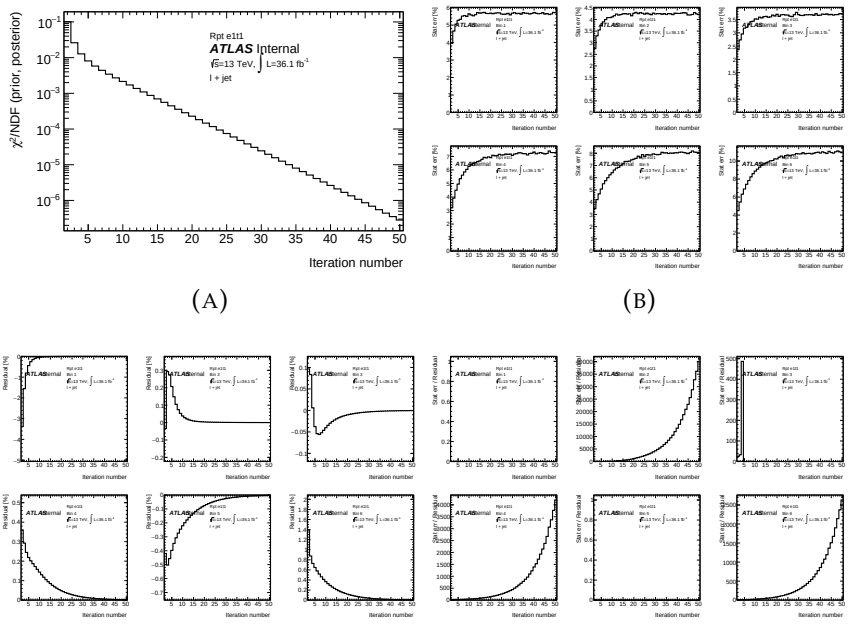

FIGURE F.41: χ^2 (a), statistical error (b), residuals (w.r.t. previous iteration) (c) and statistical error over residuals ratio (d) as a function of the N_{iter} in $R_{\mathrm{top1}}^{\mathrm{extral}}$bins in the fiducial phase-space.

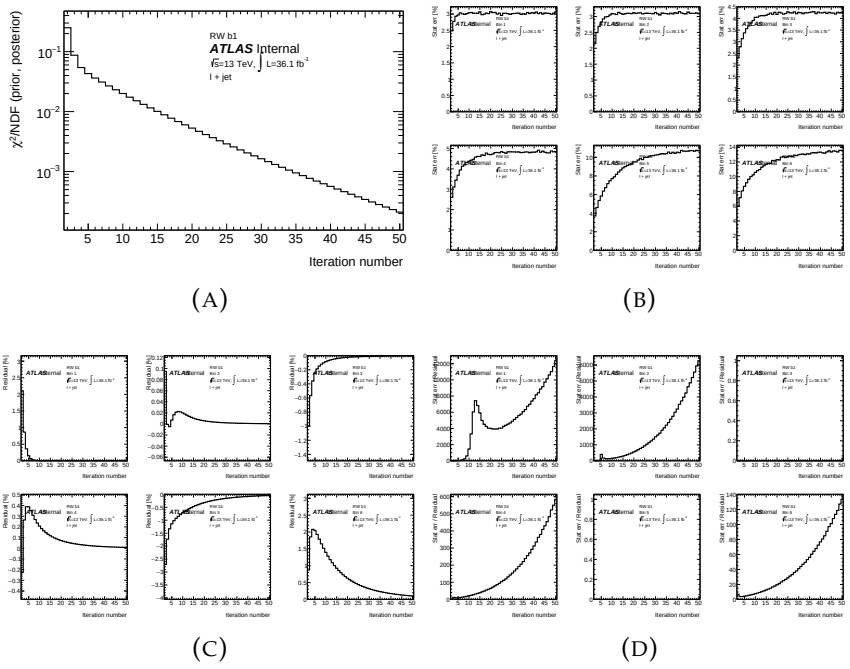

FIGURE F.42: χ^2 (a), statistical error (b), residuals (w.r.t. previous iteration) (c) and statistical error over residuals ratio (d) as a function of the N_{iter} in $R_{Wb}^{leading}$bins in the fiducial phase-space.

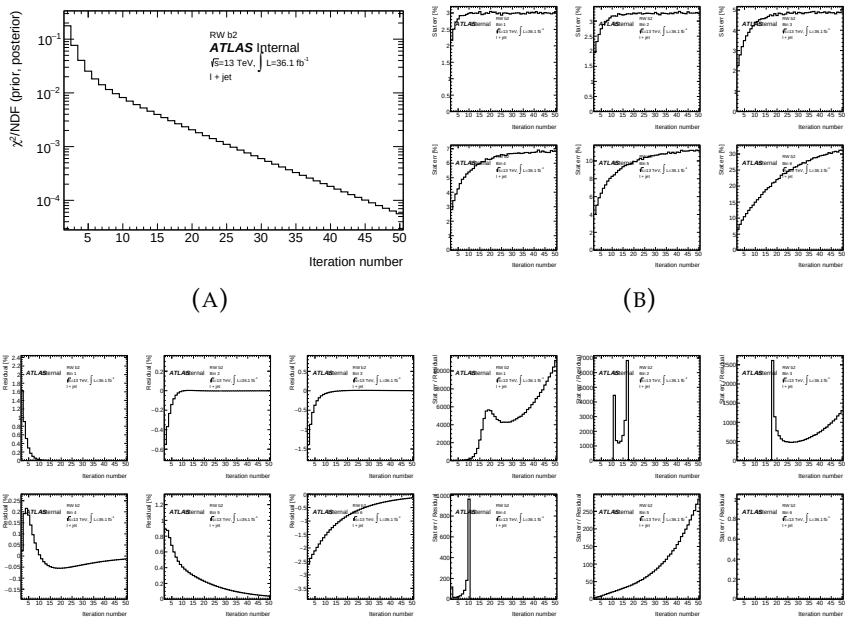

FIGURE F.43: χ^2 (a), statistical error (b), residuals (w.r.t. previous iteration) (c) and statistical error over residuals ratio (d) as a function of the N_{iter} in $R_{Wb}^{subleading}$bins in the fiducial phase-space.

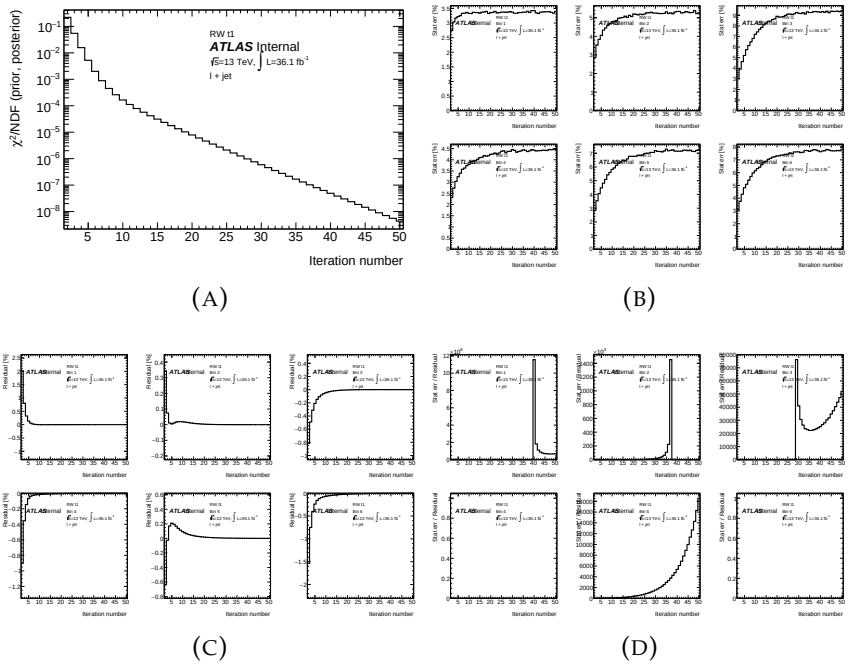

FIGURE F.44: χ^2 (a), statistical error (b), residuals (w.r.t. previous iteration) (c) and statistical error over residuals ratio (d) as a function of the N_{iter} in $R_{Wt}^{leading}$bins in the fiducial phase-space.

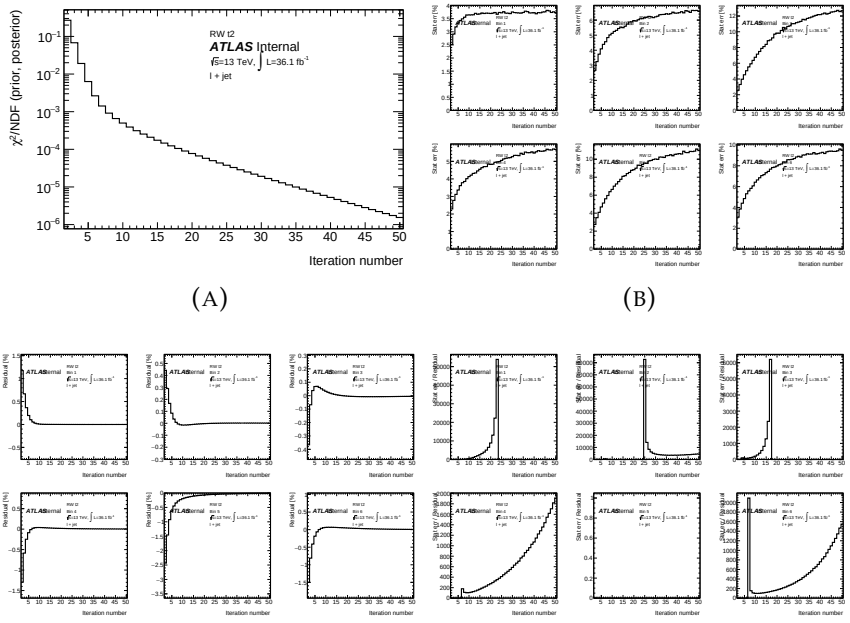

FIGURE F.45: χ^2 (a), statistical error (b), residuals (w.r.t. previous iteration) (c) and statistical error over residuals ratio (d) as a function of the N_{iter} in $R_{Wt}^{subleading}$bins in the fiducial phase-space.

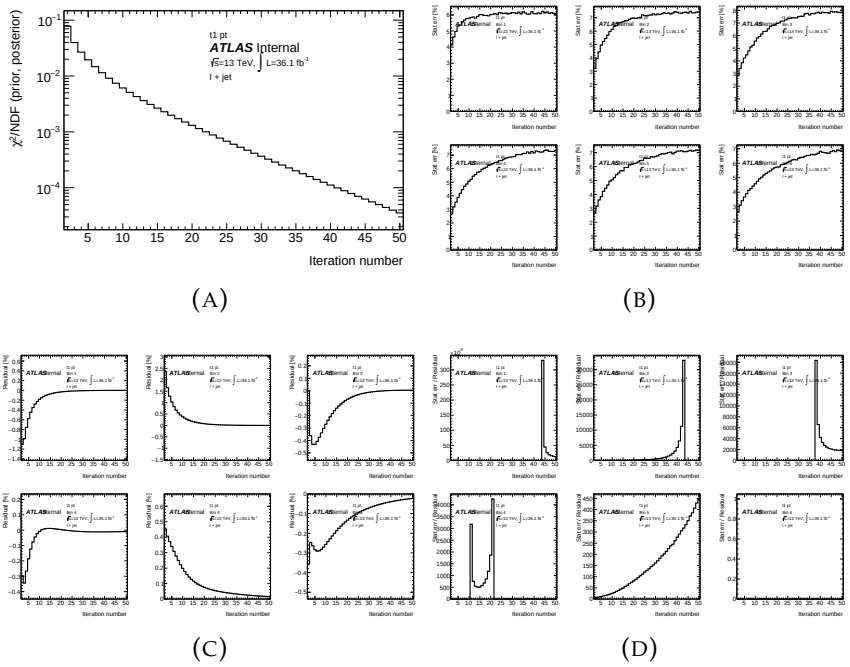

FIGURE F.46: χ^2 (a), statistical error (b), residuals (w.r.t. previous iteration) (c) and statistical error over residuals ratio (d) as a function of the N_{iter} in p_T^{top1}bins in the fiducial phase-space.

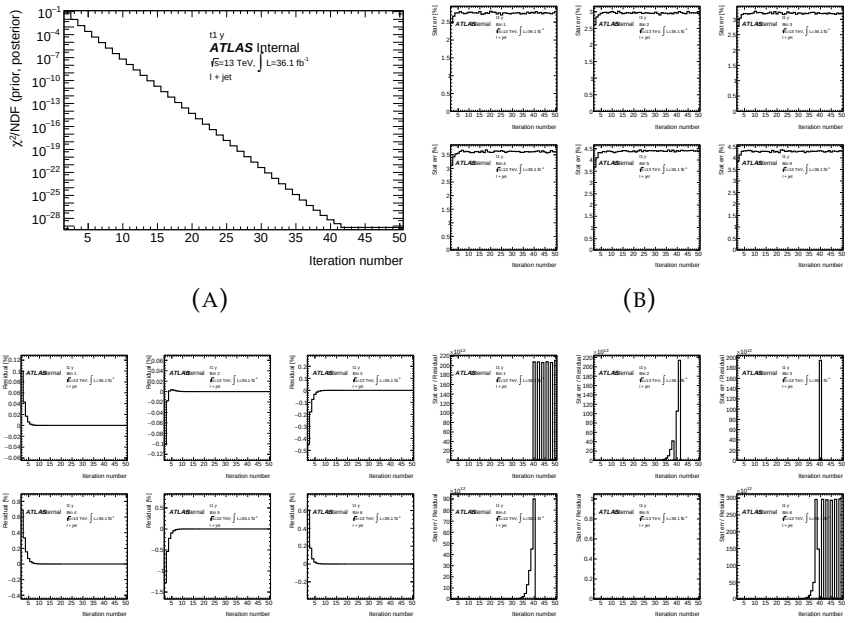

(A) (B)

(C) (D)

FIGURE F.47: χ^2 (a), statistical error (b), residuals (w.r.t. previous iteration) (c) and statistical error over residuals ratio (d) as a function of the N_{iter} in y_{top1}bins in the fiducial phase-space.

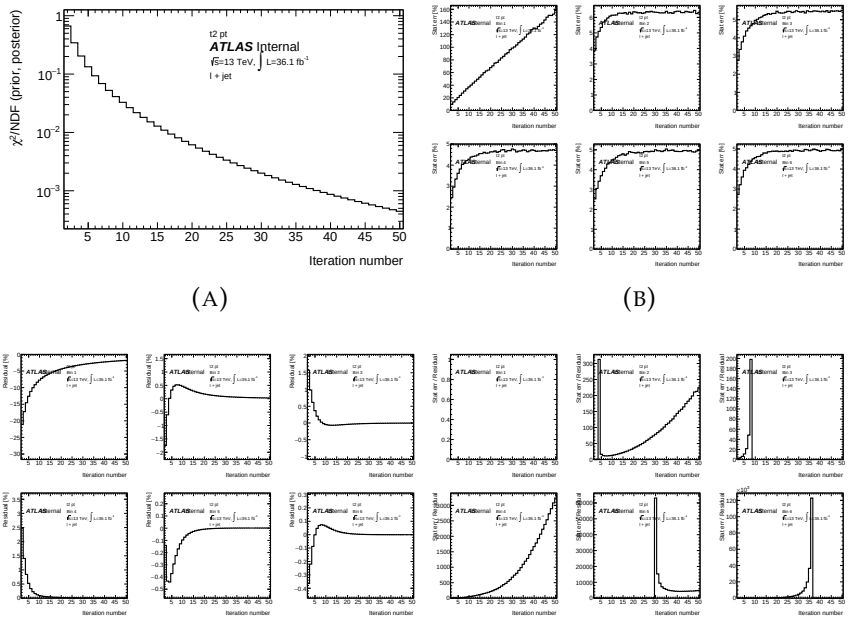

(A) (B)

(C) (D)

FIGURE F.48: χ^2 (a), statistical error (b), residuals (w.r.t. previous iteration) (c) and statistical error over residuals ratio (d) as a function of the N_{iter} in p_T^{top2}bins in the fiducial phase-space.

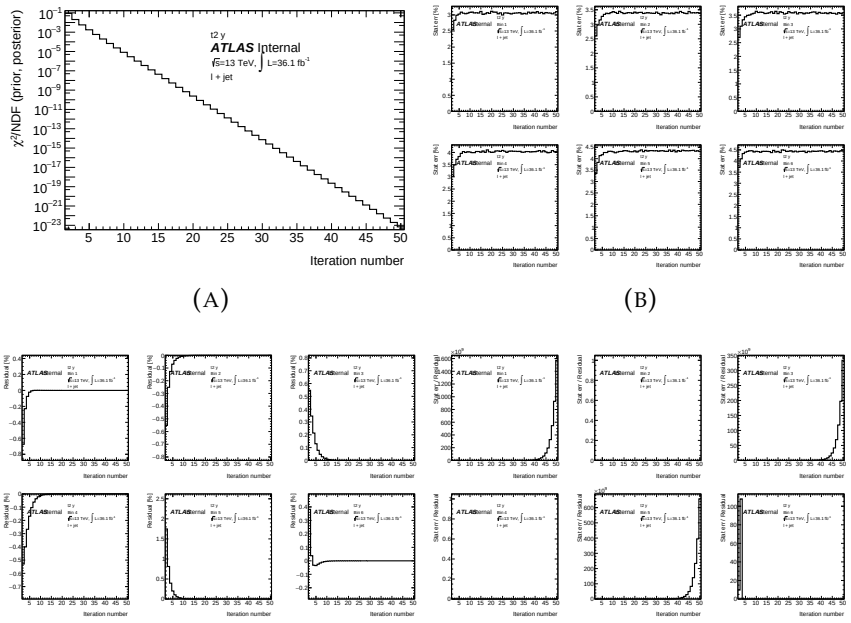

(A) (B)

(C) (D)

FIGURE F.49: χ^2 (a), statistical error (b), residuals (w.r.t. previous iteration) (c) and statistical error over residuals ratio (d) as a function of the N_{iter} in y_{top2}bins in the fiducial phase-space.

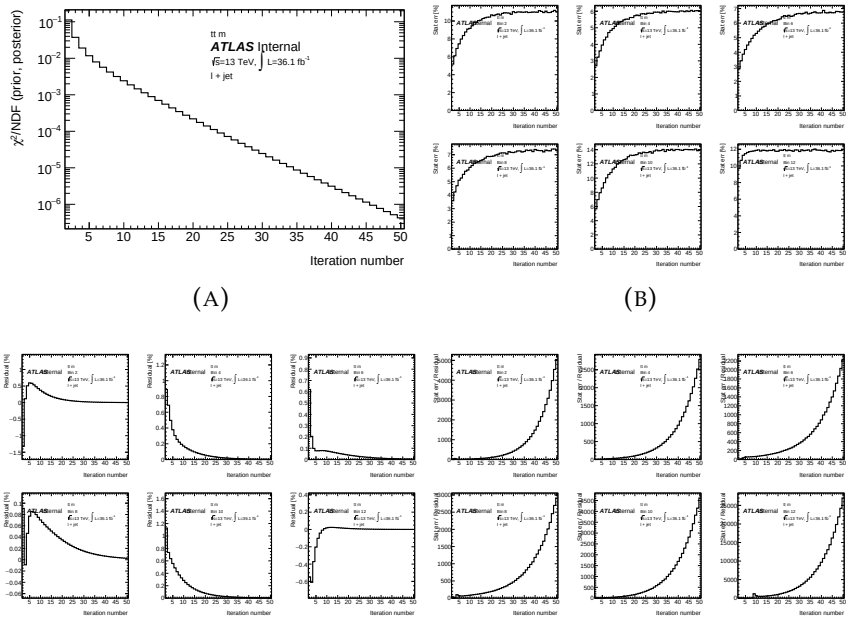

(A) (B)

(C) (D)

FIGURE F.50: χ^2 (a), statistical error (b), residuals (w.r.t. previous iteration) (c) and statistical error over residuals ratio (d) as a function of the N_{iter} in $m_{t\bar{t}}$bins in the fiducial phase-space.

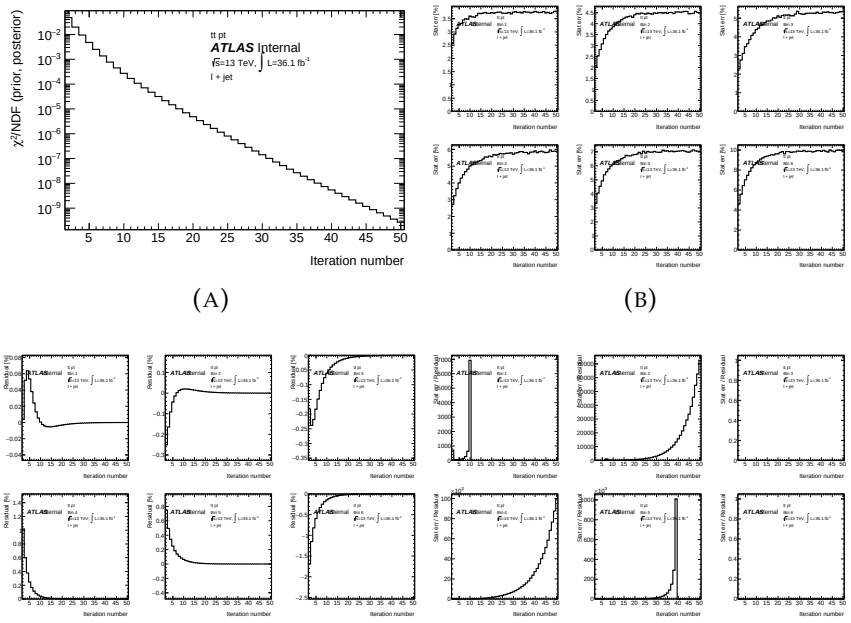

FIGURE F.51: χ^2 (a), statistical error (b), residuals (w.r.t. previous iteration) (c) and statistical error over residuals ratio (d) as a function of the N_{iter} in $p_T^{t\bar{t}}$bins in the fiducial phase-space.

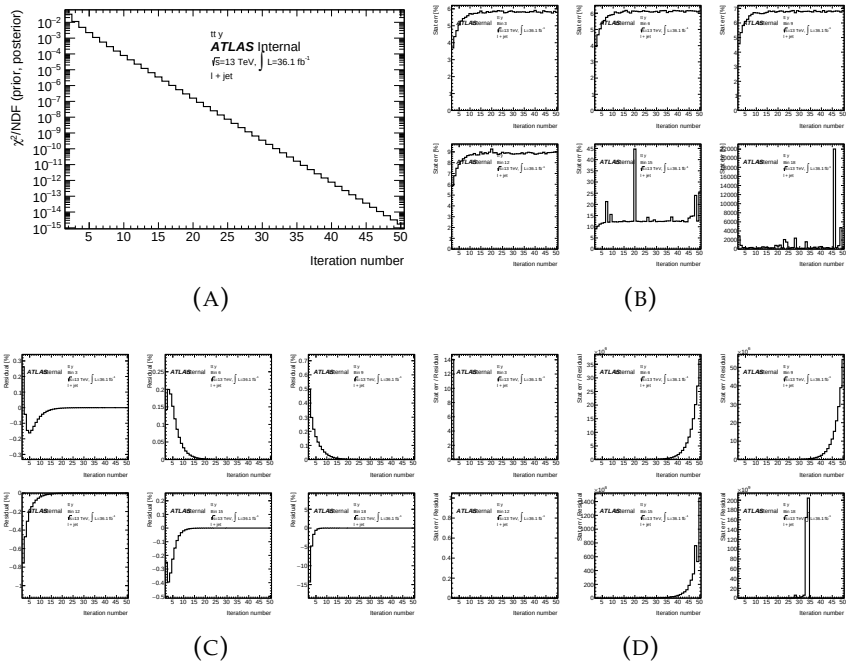

FIGURE F.52: χ^2 (a), statistical error (b), residuals (w.r.t. previous iteration) (c) and statistical error over residuals ratio (d) as a function of the N_{iter} in $y_{t\bar{t}}$bins in the fiducial phase-space.

Appendix G

Covariance matrices

In this Appendix the covariance matrices, presented in a tabular form, for all the variables unfolded variables, are presented. Tables G.1 – G.19 show the covariance matrices for the absolute distributions, while the one for the relative distributions are shown in Tables G.20 – G.38.

bin [GeV]	0-20	20-45	45-70	70-100	100-130	130-170	170-210	210-270	270-550
0-20	5.5041927925e-06	4.1857884569e-06	3.2054008024e-06	2.4070771756e-06	1.6322627126e-06	8.5230382323e-07	3.4216184576e-07	1.1447738449e-07	1.3081010855e-08
20-45	4.1857884569e-06	3.5366245176e-06	2.5925731462e-06	1.8851946520e-06	1.2977667247e-06	6.8128880128e-07	2.6380193754e-07	8.7403914464e-08	1.0236016712e-08
45-70	3.2054008024e-06	2.5925731462e-06	2.1452853427e-06	1.4635304396e-06	9.8630082601e-07	5.2671960363e-07	1.9172233240e-07	6.6299005738e-08	7.5312642021e-09
70-100	2.4070771756e-06	1.8851946520e-06	1.4635304396e-06	1.3271048527e-06	8.6393412673e-07	3.6640568918e-07	1.8858366502e-07	6.3433643379e-08	7.6821545218e-09
100-130	1.6322627126e-06	1.2977667247e-06	9.8630082601e-07	8.6393412673e-07	7.5850640748e-07	2.3169494479e-07	1.1542510216e-07	4.2128787070e-08	5.9482226375e-09
130-170	8.5230382323e-07	6.8128880128e-07	5.2671960363e-07	3.6640568918e-07	2.3169494479e-07	1.7338332826e-07	4.8750626772e-08	1.6816709221e-08	1.6436756706e-09
170-210	3.4216184576e-07	2.6380193754e-07	1.9172233240e-07	1.8858366502e-07	1.1542510216e-07	4.8750626772e-08	5.6710000246e-08	1.1590592855e-08	1.3213643897e-09
210-270	1.1447738449e-07	8.7403914464e-08	6.6299005738e-08	6.3433643379e-08	4.2128787070e-08	1.6816709221e-08	1.1590592855e-08	6.0973849142e-09	4.1782992253e-10
270-550	1.3081010855e-08	1.0236016712e-08	7.5312642021e-09	7.6821545218e-09	5.9482226375e-09	1.6436756706e-09	1.3213643897e-09	4.1782992253e-10	9.5440636268e-11

TABLE G.1: Covariance matrix of the absolute cross section as function of $|P_{\text{out}}^{t\bar{t}}|$, accounting for the statistical and systematic uncertainties.

bin [GeV]	0-1	1.0-1.5	1.5-2.0	2.0-2.2	2.2-2.5	2.5-2.6	2.6-2.9	2.9-3.2
0-1	7.0221993065e-05	7.3572797268e-05	1.3656853157e-04	3.4384414080e-04	2.4505505201e-04	4.1500942322e-04	1.1919140910e-03	1.1206173496e-03
1.0-1.5	7.3572797268e-05	2.7662378394e-04	2.8485147477e-04	6.4083290890e-04	6.8203228946e-04	1.1679612937e-03	2.6150009799e-03	2.5275265767e-03
1.5-2.0	1.3656853157e-04	2.8485147477e-04	8.4413079629e-04	1.4184349375e-03	1.3450177949e-03	2.4778353112e-03	4.8694094838e-03	6.5413680419e-03
2.0-2.2	3.4384414080e-04	6.4083290890e-04	1.4184349375e-03	4.2292409900e-03	2.6519549762e-03	4.9758190383e-03	1.0803828005e-02	1.3370917081e-02
2.2-2.5	2.4505505201e-04	6.8203228946e-04	1.3450177949e-03	2.6519549762e-03	4.8588262073e-03	6.8052021420e-03	1.0704315493e-02	1.5400035931e-02
2.5-2.6	4.1500942322e-04	1.1679612937e-03	2.4778353112e-03	4.9758190383e-03	6.8052021420e-03	1.3599424658e-02	1.8675250599e-02	2.7698762073e-02
2.6-2.9	1.1919140910e-03	2.6150009799e-03	4.8694094838e-03	1.0803828005e-02	1.0704315493e-02	1.8675250599e-02	4.2415759660e-02	4.5665830038e-02
2.9-3.2	1.1206173496e-03	2.5275265767e-03	6.5413680419e-03	1.3370917081e-02	1.5400035931e-02	2.7698762073e-02	4.5665830038e-02	8.1092397341e-02

TABLE G.2: Covariance matrix of the absolute cross section as function of $\Delta\phi_{t\bar{t}}$, accounting for the statistical and systematic uncertainties.

bin [GeV]	0.0-0.5	0.5-0.6	0.6-0.7	0.7-0.8	0.8-0.8	0.8-0.8	0.8-0.9	0.9-1.0	1-2
0.0-0.5	1.5319744155e-02	3.7127455420e-02	4.2803778544e-02	3.1938182197e-02	2.8349923081e-02	3.6052193138e-02	3.6755073296e-02	2.4967954152e-02	7.9384173666e-04
0.5-0.6	3.7127455420e-02	1.0327943607e-01	1.1290667341e-01	8.4478010945e-02	8.0159226566e-02	1.0207918993e-01	1.0792112152e-01	6.1755816853e-02	1.8522555998e-03
0.6-0.7	4.2803778544e-02	1.1290667341e-01	1.4941922747e-01	1.0565254211e-01	9.8950347392e-02	1.2242108449e-01	1.3038570196e-01	7.1754281902e-02	1.9489222133e-03
0.7-0.8	3.1938182197e-02	8.4478010945e-02	1.0565254211e-01	1.1019888406e-01	1.0224735531e-01	1.0902486164e-01	9.3952945226e-02	6.0246806853e-02	1.2517409559e-03
0.8-0.8	2.8349923081e-02	8.0159226566e-02	9.8950347392e-02	1.0224735531e-01	1.4424455676e-01	1.2359464665e-01	1.0157036174e-01	5.6973397703e-02	1.1366543376e-03
0.8-0.8	3.6052193138e-02	1.0207918993e-01	1.2242108449e-01	1.0902486164e-01	1.2359464665e-01	1.5962299510e-01	1.3729312897e-01	6.4812208933e-02	1.4278370453e-03
0.8-0.9	3.6755073296e-02	1.0792112152e-01	1.3038570196e-01	9.3952945226e-02	1.0157036174e-01	1.3729312897e-01	2.1503358266e-01	5.2714758468e-02	1.3481199167e-03
0.9-1.0	2.4967954152e-02	6.1755816853e-02	7.1754281902e-02	6.0246806853e-02	5.6973397703e-02	6.4812208933e-02	5.2714758468e-02	5.1672407827e-02	1.4310209587e-03
1-2	7.9384173666e-04	1.8522555998e-03	1.9489222133e-03	1.2517409559e-03	1.1366543376e-03	1.4278370453e-03	1.3481199167e-03	1.4310209587e-03	7.4883315931e-05

TABLE G.3: Covariance matrix of the absolute cross section as function of $R_{Wt}^{leading}$, accounting for the statistical and systematic uncertainties.

bin [GeV]	0.0-0.5	0.5-0.6	0.6-0.7	0.7-0.8	0.8-0.8	0.8-0.8	0.8-0.9	0.9-1.5
0.0-0.5	1.4778852097e-02	3.2720287215e-02	3.6184611701e-02	3.2088726773e-02	3.0168487867e-02	2.7657655083e-02	2.6708615689e-02	7.9605155600e-03
0.5-0.6	3.2720287215e-02	9.7123344748e-02	9.5700468541e-02	8.8107805812e-02	7.7234822777e-02	7.1815316033e-02	7.1421838006e-02	1.8449179690e-02
0.6-0.7	3.6184611701e-02	9.5700468541e-02	1.2190353403e-01	1.0174156257e-01	8.9103555582e-02	8.1882310435e-02	7.4576832794e-02	2.0898387457e-02
0.7-0.8	3.2088726773e-02	8.8107805812e-02	1.0174156257e-01	1.0554258214e-01	8.7182032763e-02	7.9945110625e-02	7.6316413099e-02	1.8132504847e-02
0.8-0.8	3.0168487867e-02	7.7234822777e-02	8.9103555582e-02	8.7182032763e-02	1.0119224966e-01	8.4455096034e-02	8.6573524570e-02	1.6694937575e-02
0.8-0.8	2.7657655083e-02	7.1815316033e-02	8.1882310435e-02	7.9945110625e-02	8.4455096034e-02	9.4569923490e-02	6.8934736307e-02	1.4719795754e-02
0.8-0.9	2.6708615689e-02	7.1421838006e-02	7.4576832794e-02	7.6316413099e-02	6.8573524570e-02	6.8934736307e-02	8.3368342582e-02	1.4768285649e-02
0.9-1.5	7.9605155600e-03	1.8449179690e-02	2.0898387457e-02	1.8132504847e-02	1.6694937575e-02	1.4719795754e-02	1.4768285649e-02	4.9750805212e-03

TABLE G.4: Covariance matrix of the absolute cross section as function of $R_{Wt}^{subleading}$, accounting for the statistical and systematic uncertainties.

bin [GeV]	0-1	1.0-1.9	1.9-2.8	2.8-4.0	4.0-5.5	5.5-7.5	7.5-16.0
0-1	5.2309080334e-03	4.6577081202e-03	2.2918416037e-03	1.2866872368e-03	3.8736957017e-04	1.8017641547e-04	1.1345302747e-05
1.0-1.9	4.6577081202e-03	4.9169633439e-03	2.4655457197e-03	1.4594612340e-03	4.2702375107e-04	2.0629689531e-04	4.9859590967e-05
1.9-2.8	2.2918416037e-03	2.4655457197e-03	1.6450044895e-03	7.9558720779e-04	2.7208101633e-04	1.1008639471e-04	1.8949423186e-05
2.8-4.0	1.2866872368e-03	1.4594612340e-03	7.9558720779e-04	5.8027302994e-04	1.4665570062e-04	7.6108890875e-05	2.0815554314e-05
4.0-5.5	3.8736957017e-04	4.2702375107e-04	2.7208101633e-04	1.4665570062e-04	7.7415357052e-05	2.4791157259e-05	3.6695858255e-06
5.5-7.5	1.8017641547e-04	2.0629689531e-04	1.1008639471e-04	7.6108890875e-05	2.4791157259e-05	1.8055476686e-05	3.8337024572e-06
7.5-16.0	4.1345302747e-05	4.9859590967e-05	1.8949423186e-05	2.0815554314e-05	3.6695858255e-06	3.8337024572e-06	1.8063664600e-06

TABLE G.5: Covariance matrix of the absolute cross section as function of $R_{Wb}^{leading}$, accounting for the statistical and systematic uncertainties.

bin [GeV]	0-1	1.0-1.9	1.9-2.8	2.8-4.0	4.0-5.5	5.5-7.5	7.5-12.0
0-1	7.6657651812e-03	6.0195374192e-03	2.3371801584e-03	9.4052129519e-04	4.9594222127e-04	1.1502640428e-04	1.3299585411e-05
1.0-1.9	6.0195374192e-03	5.7747798231e-03	2.3430906103e-03	9.2872306654e-04	4.5935775098e-04	1.3816046580e-04	2.1584421540e-05
1.9-2.8	2.3371801584e-03	2.3430906103e-03	1.2313117122e-03	4.4358526545e-04	2.1735167407e-04	7.2491197968e-05	1.4707509462e-05
2.8-4.0	9.4052129519e-04	9.2872306654e-04	4.4358526545e-04	2.3553157439e-04	9.3196382976e-05	2.7340152435e-05	5.3504631911e-06
4.0-5.5	4.9594222127e-04	4.5935775098e-04	2.1735167407e-04	9.3196382976e-05	9.1744368944e-05	1.5779205774e-05	3.6753969142e-06
5.5-7.5	1.1502640428e-04	1.3816046580e-04	7.2491197968e-05	2.7340152435e-05	1.5779205774e-05	8.8352342062e-06	1.5566429559e-06
7.5-12.0	1.3299585411e-05	2.1584421540e-05	1.4707509462e-05	5.3504631911e-06	3.6753969142e-06	1.5566429559e-06	8.5545733107e-07

TABLE G.6: Covariance matrix of the absolute cross section as function of $R_{Wb}^{subleading}$, accounting for the statistical and systematic uncertainties.

bin [GeV]	0-360	360-420	420-480	480-540	540-600	600-670	670-740	740-800	800-900	900-1000	1000-2000
0-360	2.1594640512e-08	2.8361711031e-08	2.1120944475e-08	2.0106276708e-08	2.1090010788e-08	1.5656078257e-08	1.3044647818e-08	8.1612972857e-09	6.5652596114e-09	2.5564013461e-09	1.7316977825e-10
360-420	2.8361711031e-08	3.1604722078e-07	2.5522987017e-07	1.9851284516e-07	2.1888528932e-07	1.2679965008e-07	8.6112650964e-08	3.7103885191e-08	3.0746418429e-08	9.9410045520e-09	7.0226282373e-10
420-480	2.1120944475e-08	2.5522987017e-07	3.0510183078e-07	2.2743129778e-07	1.9160590974e-07	1.1560481668e-07	8.1044821448e-08	4.3074675161e-08	3.6815672359e-08	1.0167211262e-08	9.3031253753e-10
480-540	2.0106278708e-08	1.9851284516e-07	2.2743129778e-07	2.0461319760e-07	1.5660056988e-07	9.3386092439e-08	6.7076032398e-08	3.7584460599e-08	3.1417122351e-08	8.8475581290e-09	7.6165862822e-10
540-600	2.1090010788e-08	2.1888528932e-07	1.9160590974e-07	1.5660056988e-07	1.8630252251e-07	9.9902018977e-08	6.7799587498e-08	3.1169454956e-08	2.5559592663e-08	8.4227883641e-09	5.3417899814e-10
600-670	1.5656078257e-08	1.2679965008e-07	1.1560481668e-07	9.3386092439e-08	9.9902018977e-08	7.0393036688e-08	4.2386709225e-08	2.0622864934e-08	1.5401701852e-08	5.4541796095e-09	3.3161151124e-10
670-740	1.3044647818e-08	8.6112650964e-08	8.1044821448e-08	6.7076032398e-08	6.7799587498e-08	4.2386709225e-08	3.7118865055e-08	1.6003157465e-08	1.2649111792e-08	4.3283970778e-09	3.1550230858e-10
740-800	8.1612972857e-09	3.7103885191e-08	4.3074675161e-08	3.7584460599e-08	3.1169454956e-08	2.0622864934e-08	1.6003157465e-08	1.5430419374e-08	7.3271424208e-09	2.5427350395e-09	2.0459052523e-10
800-900	6.5652596014e-09	3.0746418429e-08	3.6815672359e-08	3.1417122351e-08	2.5559592663e-08	1.5401701852e-08	1.2649111792e-08	7.3271424208e-09	1.1284811784e-08	2.0377815742e-09	3.1961069520e-10
900-1000	2.5564013461e-09	9.9410045520e-09	1.0167211262e-08	8.8475581290e-09	8.4227883641e-09	5.4541796095e-09	4.3283970778e-09	2.5427350395e-09	2.0377815742e-09	1.4174713120e-09	5.4111410870e-11
1000-2000	1.7316977825e-10	7.0226282373e-10	9.3031253753e-10	7.6165862822e-10	5.3417899814e-10	3.3161151124e-10	3.1550230858e-10	2.0459052523e-10	3.1961069520e-10	5.4111410870e-11	1.8314692921e-11

TABLE G.7: Covariance matrix of the absolute cross section as function of $H_{\mathrm{T}}^{t\bar{t}}$, accounting for the statistical and systematic uncertainties.

bin [GeV]	5.5-6.5	6.5-7.5	7.5-8.5	8.5-9.5	9.5-14.5
5.5-6.5	4.3546484274e-04	8.2785341273e-04	8.3266643762e-04	6.4226867408e-04	9.8813639409e-05
6.5-7.5	8.2785341273e-04	2.4325679537e-03	2.5827273800e-03	1.3961078698e-03	1.9343863145e-04
7.5-8.5	8.3266643762e-04	2.5827273800e-03	3.6466280463e-03	2.0644033543e-03	3.2221063768e-04
8.5-9.5	6.4226867408e-04	1.3961078698e-03	2.0644033543e-03	2.3005899785e-03	3.9755030876e-04
9.5-14.5	9.8813639409e-05	1.9343863145e-04	3.2221063768e-04	3.9755030876e-04	8.4433558637e-05

TABLE G.8: Covariance matrix of the absolute cross section as function of N_{jets}, accounting for the statistical and systematic uncertainties.

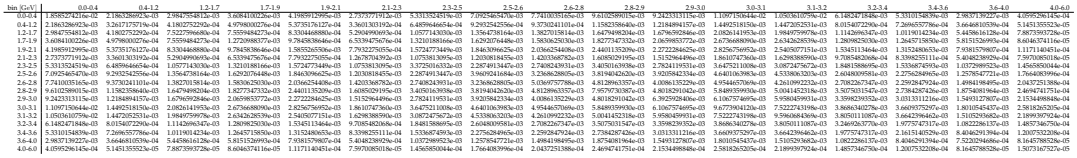

TABLE G.9: Covariance matrix of the absolute cross section as function of $\Delta R_{\text{jet1}}^{\text{extra1}}$, accounting for the statistical and systematic uncertainties.

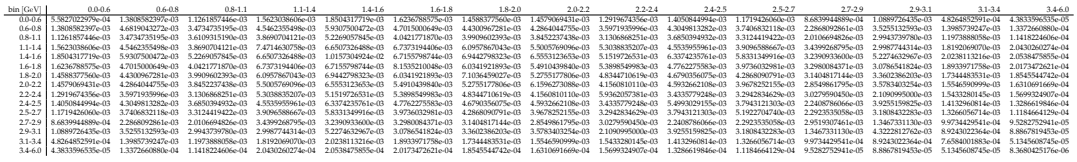

TABLE G.10: Covariance matrix of the absolute cross section as function of $\Delta R_{\text{topclose}}^{\text{extra1}}$, accounting for the statistical and systematic uncertainties.

bin [GeV]	0.0-0.2	0.2-0.3	0.3-0.5	0.5-0.6	0.6-0.8	0.8-1.1
0.0-0.2	1.5526381020e-03	4.5553728326e-03	5.1432738852e-03	5.7221022539e-03	4.6373747801e-03	8.8908988307e-03
0.2-0.3	4.5553728326e-03	2.1752415376e-02	2.0670725229e-02	2.4565403524e-02	2.1864590699e-02	3.6615734365e-02
0.3-0.5	5.1432738852e-03	2.0670725229e-02	2.6560962154e-02	2.6905913047e-02	2.1016214277e-02	4.1291804077e-02
0.5-0.6	5.7221022539e-03	2.4565403524e-02	2.6905913047e-02	3.7690885445e-02	3.3332059523e-02	5.1638334900e-02
0.6-0.8	4.6373747801e-03	2.1864590699e-02	2.1016214277e-02	3.3332059523e-02	4.2622911720e-02	5.0614188024e-02
0.8-1.1	8.8908988307e-03	3.6615734365e-02	4.1291804077e-02	5.1638334900e-02	5.0614188024e-02	8.6173185063e-02

TABLE G.11: Covariance matrix of the absolute cross section as function of $R_{\text{jet1}}^{\text{extra1}}$, accounting for the statistical and systematic uncertainties.

bin [GeV]	0.0-0.1	0.1-0.2	0.2-0.4	0.4-0.5	0.5-0.7	0.7-0.8	0.8-1.0	1.0-1.2	1.2-5.0
0.0-0.1	8.5344116375e-03	2.3189725358e-02	2.2340054628e-02	1.9634825993e-02	1.1543232075e-02	7.9259514415e-03	3.7009081304e-03	2.8625768921e-03	2.2225261958e-04
0.1-0.2	2.3189725358e-02	8.6660173476e-02	7.9067356749e-02	6.9945921029e-02	4.2778419283e-02	2.9903454487e-02	1.2606424023e-02	9.7875137169e-03	8.4106736583e-04
0.2-0.4	2.2340054628e-02	7.9067356749e-02	8.8713570794e-02	7.3396758870e-02	4.6636970058e-02	3.2028891578e-02	1.2801873974e-02	1.0203356914e-02	9.3370905640e-04
0.4-0.5	1.9634825993e-02	6.9945921029e-02	7.3396758870e-02	7.1614777440e-02	4.1608299074e-02	2.8105601476e-02	1.1453421850e-02	9.1035766601e-03	8.3517095256e-04
0.5-0.7	1.1543232075e-02	4.2778419283e-02	4.6636970058e-02	4.1608299074e-02	3.0278722415e-02	1.8489423685e-02	6.9224315741e-03	5.8229025617e-03	5.5603316895e-04
0.7-0.8	7.9259514415e-03	2.9903454487e-02	3.2028891578e-02	2.8105601476e-02	1.8489423685e-02	1.5481145998e-02	5.2057633038e-03	3.9911546494e-03	3.8627107680e-04
0.8-1.0	3.7009081304e-03	1.2606424023e-02	1.2801873974e-02	1.1453421850e-02	6.9224315741e-03	5.2057633038e-03	3.9156436442e-03	1.9910620025e-03	1.4479665878e-04
1.0-1.2	2.8625768921e-03	9.7875137169e-03	1.0203356914e-02	9.1035766601e-03	5.8229025617e-03	3.9911546494e-03	1.9910620025e-03	2.2700907879e-03	1.1590531204e-04
1.2-5.0	2.2225261958e-04	8.4106736583e-04	9.3370905640e-04	8.3517095256e-04	5.5603316895e-04	3.8627107680e-04	1.4479665878e-04	1.1590531204e-04	1.5349287428e-05

TABLE G.12: Covariance matrix of the absolute cross section as function of $R_{\text{top1}}^{\text{extra1}}$, accounting for the statistical and systematic uncertainties.

bin [GeV]	0-210	210-240	240-270	270-300	300-330	330-370	370-400	400-440	440-480	480-550	550-1000
0-210	3.7327801137e-08	1.2715510962e-07	1.0673709846e-07	1.2663022532e-07	1.0764073986e-07	7.1469075746e-08	6.2471648964e-08	4.2570007521e-08	2.7653536357e-08	1.2019637969e-08	5.3253468764e-10
210-240	1.2715510962e-07	8.9257296676e-07	7.0455513587e-07	7.7998554729e-07	6.7257937770e-07	4.2395714039e-07	3.3910888973e-07	2.3625109932e-07	1.4515786758e-07	5.6216058226e-08	2.6096119366e-09
240-270	1.0673709846e-07	7.0455513587e-07	6.9812170805e-07	7.0687373473e-07	6.5129810211e-07	4.1690036701e-07	3.2821667256e-07	2.1563445528e-07	1.2554473228e-07	5.2244742283e-08	1.8794299990e-09
270-300	1.2663022532e-07	7.7998554729e-07	7.0687373473e-07	8.8480775792e-07	6.6674295935e-07	4.0256431423e-07	3.3812778010e-07	2.5448461510e-07	1.5832734283e-07	6.5735126927e-08	3.0875514529e-09
300-330	1.0764073986e-07	6.7257937770e-07	6.5129810211e-07	6.6674295935e-07	6.7876086238e-07	3.8131932737e-07	3.2417361703e-07	1.9792453891e-07	1.3478385073e-07	5.0808130747e-08	3.7060216080e-09
330-370	7.1469075746e-08	4.2395714039e-07	3.6900036701e-07	4.0256431423e-07	3.8131932737e-07	2.8407812324e-07	2.1451243833e-07	1.2574365402e-07	8.2902213908e-08	3.2152383978e-08	2.0972522383e-09
370-400	6.2471648964e-08	3.3910888973e-07	3.2821667256e-07	3.3812778010e-07	3.2417361703e-07	2.1451243833e-07	2.2603280229e-07	1.1101387430e-07	7.3723872162e-08	2.9576189128e-08	2.5209067158e-09
400-440	4.2570007521e-08	2.3625109932e-07	2.1563445528e-07	2.5448461510e-07	1.9792453891e-07	1.2574365402e-07	1.1101387430e-07	1.0329180184e-07	5.4242256181e-08	2.2297763423e-08	1.0429229034e-09
440-480	2.7653536357e-08	1.4515786758e-07	1.2558134303e-07	1.5832734283e-07	1.3478385073e-07	8.2902213908e-08	7.3723872162e-08	5.4242256181e-08	4.6347106502e-08	1.5648641768e-08	9.1575903162e-10
480-550	1.2019637969e-08	5.6216058226e-08	5.2244742283e-08	6.5735126927e-08	5.0808130747e-08	3.2152383978e-08	2.9576189128e-08	2.2297763423e-08	1.5648641768e-08	9.2336696771e-09	3.0576718084e-10
550-1000	5.3253468764e-10	2.6096119366e-09	1.8794299990e-09	3.0875514529e-09	3.7060216080e-09	2.0972522383e-09	2.5209067158e-09	1.0429229034e-09	9.1575903162e-10	3.0576718084e-10	7.4508872027e-11

TABLE G.13: Covariance matrix of the absolute cross section as function of p_T^{top1}, accounting for the statistical and systematic uncertainties.

bin [GeV]	0.0-0.3	0.3-0.6	0.6-0.9	0.9-1.2	1.2-1.5	1.5-2.0	2.0-2.5
0.0-0.3	2.0371226791e-02	1.9035947279e-02	1.8240994972e-02	1.5371252499e-02	1.1656139478e-02	3.3178663478e-03	6.8157616435e-04
0.3-0.6	1.9035947279e-02	2.1031254119e-02	1.8416923226e-02	1.5603262344e-02	1.2069479880e-02	6.3842365326e-03	6.7285458746e-04
0.6-0.9	1.8240994972e-02	1.8416923226e-02	1.9976169214e-02	1.4639072185e-02	1.1795342442e-02	6.2559069759e-03	9.5211540903e-04
0.9-1.2	1.5371252499e-02	1.5603262344e-02	1.4639072185e-02	1.3582745538e-02	9.5832904027e-03	5.1588024992e-03	5.4919741885e-04
1.2-1.5	1.1656139478e-02	1.2069479880e-02	1.1795342442e-02	9.5832904027e-03	8.2319055724e-03	3.9994111702e-03	5.1439793831e-04
1.5-2.0	6.3178663478e-03	6.3842365326e-03	6.2559069759e-03	5.1588024992e-03	3.9994111702e-03	2.3739956970e-03	2.5919311296e-04
2.0-2.5	6.8157616435e-04	6.7285458746e-04	9.5211540903e-04	5.4919741885e-04	5.1439793831e-04	2.5919311296e-04	1.2542000793e-04

TABLE G.14: Covariance matrix of the absolute cross section as function of y_{top1}, accounting for the statistical and systematic uncertainties.

bin [GeV]	0-100	100-150	150-190	190-230	230-270	270-315	315-365	365-420	420-475	475-1000
0-100	1.0687605296e-07	2.6309756975e-07	1.3506457722e-08	-3.6608630777e-08	-5.8102630395e-09	1.5964031639e-08	9.8457181099e-09	1.5083087108e-08	8.5050383373e-09	6.5039678534e-10
100-150	2.6309756975e-07	1.0893250175e-06	5.2747606560e-07	3.5803853603e-07	2.5657720122e-07	2.4981344226e-07	9.5366069816e-08	9.4794400375e-08	5.1091438003e-08	3.8652239768e-09
150-190	1.3506457722e-08	5.2747606560e-07	1.0977983866e-06	8.9087084423e-07	5.1889297973e-07	4.3647845500e-07	1.4042048898e-07	1.1138090742e-07	6.2559576418e-08	4.6543922771e-09
190-230	-3.6608630777e-08	3.5803853603e-07	8.9087084423e-07	9.4374732656e-07	5.5145169315e-07	3.9890936763e-07	1.3253824627e-07	1.1346648247e-07	5.0087910301e-08	3.6352930302e-09
230-270	-5.8102630395e-09	2.5657720122e-07	5.1889297973e-07	5.5145169315e-07	4.0889015250e-07	2.5105612729e-07	9.1776049403e-08	8.2945013431e-08	3.0048025662e-08	2.2422113411e-09
270-315	1.5964031639e-08	2.4981344226e-07	4.3647845500e-07	3.9890936763e-07	2.5105612729e-07	2.2962868109e-07	7.1244287458e-08	5.9545813156e-08	3.0300669682e-08	2.2082448472e-09
315-365	9.8457181099e-09	9.5366069816e-08	1.4042048898e-07	1.3253824627e-07	9.1776049403e-08	7.1244287458e-08	4.5441529984e-08	2.2639281774e-08	1.0120196656e-08	7.0801532391e-10
365-420	1.5083087108e-08	9.4794400375e-08	1.1138090742e-07	1.1346648247e-07	8.2945013431e-08	5.9545813156e-08	2.2639281774e-08	3.0174235821e-08	8.6253557242e-09	6.9713900011e-10
420-475	8.5050383373e-09	5.1091438003e-08	6.2559576418e-08	5.0087910301e-08	3.0048025662e-08	3.0300669682e-08	1.0120196656e-08	8.6253557242e-09	8.2097144526e-09	4.0554602579e-10
475-1000	6.5039678534e-10	3.8652239768e-09	4.6543922771e-09	3.6352930302e-09	2.2422113411e-09	2.2082448472e-09	7.0801532391e-10	6.9713900011e-10	4.0554602579e-10	4.9194933267e-11

TABLE G.15: Covariance matrix of the absolute cross section as function of p_T^{top2}, accounting for the statistical and systematic uncertainties.

bin [GeV]	0-40	40-85	85-130	130-180	180-240	240-300	300-370	370-450	450-1100
0-40	4.9859544021e-07	7.2472725401e-07	7.1497436653e-07	4.3626039614e-07	2.8637739281e-07	1.2183363675e-07	6.2744144850e-08	3.9112502216e-08	2.2963426784e-09
40-85	7.2472725401e-07	1.2347375694e-06	1.1469788529e-06	6.9632061080e-07	4.5423923240e-07	1.9004678251e-07	1.0413844561e-07	6.1421028015e-08	3.4833595325e-09
85-130	7.1497436653e-07	1.1469788529e-06	1.3412913949e-06	6.6365215681e-07	4.8178390311e-07	1.9816426880e-07	9.6045253653e-08	7.9044509927e-08	3.6046611038e-09
130-180	4.3626039614e-07	6.9632061080e-07	6.6365215681e-07	4.6439085934e-07	2.7307799127e-07	1.1454850351e-07	6.2183969643e-08	3.4608749390e-08	2.1381713927e-09
180-240	2.8637739281e-07	4.5423923240e-07	4.8178390311e-07	2.7307799127e-07	2.3776684640e-07	8.3508166184e-08	3.9855848275e-08	2.9845262478e-08	1.5114346680e-09
240-300	1.2183363675e-07	1.9004678251e-07	1.9816426880e-07	1.1454850351e-07	8.3508166184e-08	4.8291397640e-08	1.6657568277e-08	1.1134442089e-08	6.5070120296e-10
300-370	6.2744144850e-08	1.0413844561e-07	9.6045253653e-08	6.2183969643e-08	3.9855848275e-08	1.6657568277e-08	1.7309319695e-08	4.9453937657e-09	2.8171384865e-10
370-450	3.9112502216e-08	6.1421028015e-08	7.9044509927e-08	3.4608749390e-08	2.9845262478e-08	1.1134442089e-08	4.9453937657e-09	7.7793333847e-09	1.9160639386e-10
450-1100	2.2963426784e-09	3.4833595325e-09	3.6046611038e-09	2.1381713927e-09	1.5114346680e-09	6.5070120296e-10	2.8171384865e-10	1.9160639386e-10	2.6647455395e-11

TABLE G.16: Covariance matrix of the absolute cross section as function of $p_T^{t\bar{t}}$, accounting for the statistical and systematic uncertainties.

bin [GeV]	0.0-0.1	0.1-0.2	0.2-0.3	0.3-0.4	0.4-0.5	0.5-0.6	0.6-0.7	0.7-0.8	0.8-0.9	0.9-1.0	1.0-1.1	1.1-1.2	1.2-1.3	1.3-1.4	1.4-1.5	1.5-1.6	1.6-2.5
0.0-0.1	7.2908093585e-02	6.9724562019e-02	4.0247488321e-02	4.9340097881e-02	4.0902836194e-02	4.1446020276e-02	2.9945595028e-02	3.7518747815e-02	3.5959684971e-02	2.5328844697e-02	2.3595893475e-02	1.9431085814e-02	1.9443528225e-02	1.5328447942e-02	1.3354290087e-02	7.5818584860e-03	9.5656691548e-04
0.1-0.2	6.9724562019e-02	8.6069403886e-02	3.9082133775e-02	5.0764507741e-02	3.9316633948e-02	4.6496888025e-02	2.9479258035e-02	3.7625452792e-02	3.7478590743e-02	2.5356663370e-02	2.6024836382e-02	2.0351668685e-02	2.2497736241e-02	1.5181788882e-02	1.4519188000e-02	8.4219139634e-03	1.0470265946e-03
0.2-0.3	4.0247488321e-02	3.9082133775e-02	3.8373075112e-02	3.0225244043e-02	3.2339681857e-02	3.3662471952e-02	2.1283602298e-02	2.4857496539e-02	2.1823528821e-02	2.1219936310e-02	1.5469660579e-02	1.3775663087e-02	1.2172116134e-02	1.1716902612e-02	7.4994147603e-03	4.7314567803e-03	6.4484015095e-04
0.3-0.4	4.9340097881e-02	5.0764507741e-02	3.0225244043e-02	4.0863432352e-02	3.0258818689e-02	3.0941373636e-02	2.2484421314e-02	2.7436184878e-02	2.6225246330e-02	1.9265795687e-02	1.7559988116e-02	1.4193967066e-02	1.4245123229e-02	1.1277679777e-02	9.4621862155e-03	5.5757722430e-03	6.9311663603e-04
0.4-0.5	4.0902836194e-02	3.9316633948e-02	3.2339681857e-02	3.0258818689e-02	3.6779602208e-02	3.1180363515e-02	2.0905723827e-02	2.5217545240e-02	2.1741627995e-02	2.0109628190e-02	1.4934710920e-02	1.3295480926e-02	1.1967884469e-02	1.1531924194e-02	7.3471610381e-03	4.5528144570e-03	6.0072899768e-04
0.5-0.6	4.1446020327e-02	4.6496888025e-02	3.3662471952e-02	3.0941373636e-02	3.1180363515e-02	4.3900579777e-02	2.0491563366e-02	2.3648218024e-02	2.1892814706e-02	2.1961243677e-02	1.7358333367e-02	1.5295914344e-02	1.5503127725e-02	1.1842147668e-02	8.4298387141e-03	5.7639943789e-03	7.9319534886e-04
0.6-0.7	2.9945595028e-02	2.9479258035e-02	2.1283602298e-02	2.2484421314e-02	2.0905723827e-02	2.0491563366e-02	1.8631637894e-02	1.6959219036e-02	1.5922882045e-02	1.3272113762e-02	1.0880237631e-02	9.3399277467e-03	8.6898275475e-03	7.4805261216e-03	5.6197156255e-03	3.4991673364e-03	4.4798974056e-04
0.7-0.8	3.7518747815e-02	3.7625452792e-02	2.4857496539e-02	2.7436184878e-02	2.5217545240e-02	2.3648218024e-02	1.6959219036e-02	2.5593613804e-02	1.9639707329e-02	2.2311003802e-02	1.9639707329e-02	1.7041441778e-02	1.6077115625e-02	1.3741447778e-02	1.0077115625e-02	9.1654147205e-03	6.9879313174e-03	3.7782024581e-03	4.8807545534e-04
0.8-0.9	3.5959684971e-02	3.7478590743e-02	2.1823528821e-02	2.6225246330e-02	2.1741627995e-02	2.1892814706e-02	1.5922882045e-02	1.9639707329e-02	2.2311003802e-02	1.3252239735e-02	1.1446721442e-02	9.6081437608e-03	9.1295676167e-03	7.1041441778e-03	5.1072115625e-03	3.1654147205e-03	3.9879313174e-03	3.7782024581e-03	4.8807545534e-04
0.9-1.0	2.5328844697e-02	2.5356663370e-02	2.1219893610e-02	1.9265795687e-02	2.0109628190e-02	2.1961243677e-02	1.3272113762e-02	1.5094986312e-02	1.3252239735e-02	1.6487211442e-02	9.6081437608e-03	8.8742552967e-03	8.1248751362e-03	7.4298353479e-03	4.8011416489e-03	3.2876435971e-03	4.5265867068e-04
1.0-1.1	2.3595893475e-02	2.6024836382e-02	1.5469660679e-02	1.7559988116e-02	1.4934710920e-02	1.7358333367e-02	1.0880237631e-02	1.2951676167e-02	1.1446721442e-02	1.1571220804e-02	9.6081437608e-03	7.1015405110e-03	7.6805758211e-03	5.4596973614e-03	4.7180010058e-03	3.0522895086e-03	3.8314572341e-04
1.1-1.2	1.9431085814e-02	2.0351668685e-02	1.3775663087e-02	1.4193967066e-02	1.3295480926e-02	1.5295914344e-02	9.3399277467e-03	1.0744144778e-02	1.0244585027e-02	8.8742552967e-03	7.1015405110e-03	8.5269509539e-03	6.0780384772e-03	4.9651226250e-03	3.9076880483e-03	2.5574020766e-03	3.3877364486e-04
1.2-1.3	1.9443528225e-02	2.2497736241e-02	1.2172116134e-02	1.4245123229e-02	1.1967884469e-02	1.5503127725e-02	8.6898275475e-03	1.0077115625e-02	1.0091123016e-02	8.1248751362e-03	7.6805758211e-03	6.0780384772e-03	8.9850478584e-03	4.2416889156e-03	5.8728208624e-03	2.7813483205e-03	3.4695395289e-04
1.3-1.4	1.5328447942e-02	1.5181788882e-02	1.1716902612e-02	1.1277679777e-02	1.1531924194e-02	1.1842147668e-02	7.4805261216e-03	9.1654147205e-03	6.9879313174e-03	7.4298353479e-03	5.4596973614e-03	4.9651226250e-03	4.2416889156e-03	5.8728208624e-03	2.7813483205e-03	1.6261738523e-03	2.2795109353e-04
1.4-1.5	1.3354290087e-02	1.4519088000e-02	7.4994147603e-03	9.4621862155e-03	7.3471610381e-03	8.4298387141e-03	5.6197156255e-03	6.9879313174e-03	5.0269993839e-03	4.8011416489e-03	4.7180010058e-03	3.9076880483e-03	3.9850560204e-03	2.7813483205e-03	3.8587187764e-03	1.4676454582e-03	2.0312489578e-04
1.5-1.6	7.5818584860e-03	8.4219139634e-03	4.7314856783e-03	5.5757722430e-03	4.5528144519e-03	5.7639943789e-03	3.4991673364e-03	3.7782024581e-03	4.0030477590e-03	3.2876435971e-03	3.0522895086e-03	2.5573402766e-03	2.7742824248e-03	1.6261738523e-03	1.4676454582e-03	1.9119989293e-03	1.2936179623e-04
1.6-2.5	9.5656691548e-04	1.0470265946e-03	6.4484015095e-04	6.9311663603e-04	6.0072899768e-04	7.9319534886e-04	4.4798974056e-04	4.8807545534e-04	4.9487778770e-04	4.3265686768e-04	3.8314572341e-04	3.3877364486e-04	3.4695395289e-04	2.2795109353e-04	2.0312489578e-04	1.2936179623e-04	3.1897742787e-05

TABLE G.17: Covariance matrix of the absolute cross section as function of $y_{t\bar{t}}$, accounting for the statistical and systematic uncertainties.

bin [GeV]	0.0-0.3	0.3-0.6	0.6-0.9	0.9-1.2	1.2-1.5	1.5-2.5
0.0-0.3	2.2676958315e-02	1.9649210391e-02	1.7696564475e-02	1.8883867053e-02	1.2980152899e-02	3.1946089773e-03
0.3-0.6	1.9649210391e-02	2.0679273478e-02	1.7438509289e-02	1.8038978362e-02	1.2777479246e-02	3.2068754782e-03
0.6-0.9	1.7696564475e-02	1.7438509289e-02	1.6973769576e-02	1.6298128096e-02	1.1242504131e-02	2.8381850662e-03
0.9-1.2	1.8883867053e-02	1.8038978362e-02	1.6298128096e-02	1.8176935280e-02	1.1601777337e-02	2.8727629949e-03
1.2-1.5	1.2980152899e-02	1.2777479246e-02	1.1242504131e-02	1.1601777337e-02	9.3757860335e-03	2.1662887593e-03
1.5-2.5	3.1946089773e-03	3.2068754782e-03	2.8381850662e-03	2.8727629949e-03	2.1662887593e-03	6.2285497636e-04

TABLE G.18: Covariance matrix of the absolute cross section as function of y_{top2}, accounting for the statistical and systematic uncertainties.

bin [GeV]	0-450	450-525	525-600	600-675	675-750	750-825	825-900	900-1000	1000-1100	1100-1200	1200-1400	1400-3200
0-450	2.6807599725e-09	1.5717302504e-08	1.3898558780e-08	5.4130639451e-09	2.0703498724e-09	6.2719143627e-11	1.2707321220e-09	1.6617772543e-10	2.5689762266e-10	1.4961144884e-10	3.3673468015e-11	-8.3406822114e-12
450-525	1.5717302504e-08	1.6368383793e-07	1.5406334326e-07	8.9778705978e-08	7.0941513559e-08	3.9837038749e-08	4.2474912038e-08	2.2402335850e-08	1.6318434103e-08	1.2257399767e-08	4.4940819897e-09	2.6315376563e-10
525-600	1.3898558780e-08	1.5406334326e-07	2.3025558474e-07	1.4426963428e-07	1.2170837114e-07	8.0387029969e-08	7.7427181208e-08	4.4521064433e-08	2.7897735680e-08	1.9484760801e-08	8.0692343519e-09	5.3098685059e-10
600-675	5.4130639451e-09	8.9778705978e-08	1.4426963428e-07	1.4522941002e-07	1.1594067681e-07	7.9224374939e-08	7.5484124550e-08	4.5392648667e-08	2.6727081552e-08	1.9355636315e-08	8.0122291504e-09	6.1214810058e-10
675-750	2.0703498724e-09	7.0941513559e-08	1.2170837114e-07	1.1594067681e-07	1.3141032787e-07	8.1297465545e-08	6.8290254527e-08	4.1866888583e-08	3.0362452542e-08	1.9993859196e-08	8.5556088477e-09	6.3295062074e-10
750-825	6.2719143627e-11	3.9837038749e-08	8.0387029969e-08	7.9224374939e-08	8.1297465545e-08	6.9032501537e-08	5.0329653104e-08	3.0548683236e-08	2.0195578152e-08	1.3669178847e-08	6.0071626553e-09	4.3478874422e-10
825-900	1.2707321220e-09	4.2474912038e-08	7.7427181208e-08	7.5484124550e-08	6.8290254527e-08	5.0329653104e-08	5.5427336976e-08	3.0731634350e-08	1.5152376416e-08	1.2205390951e-08	4.9509720038e-09	4.2752190048e-10
900-1000	1.6617772543e-10	2.2402335850e-08	4.4521064433e-08	4.5392648667e-08	4.1866888583e-08	3.0548683236e-08	3.0731634350e-08	2.3460648353e-08	1.5152376416e-08	9.0776832609e-09	2.7059027424e-09	3.0586023083e-09
1000-1100	2.5689762266e-10	1.6318434103e-08	2.7897735680e-08	2.6727081552e-08	3.0362452542e-08	2.0195578152e-08	1.5152376416e-08	9.0776832609e-09	1.0569413182e-08	5.5360884615e-09	2.2833034298e-09	1.6243220094e-10
1100-1200	1.4961144884e-10	1.2257399767e-08	1.9484760801e-08	1.9355636315e-08	1.9993859196e-08	1.3669178847e-08	1.2205390951e-08	7.2059027424e-09	5.5360884615e-09	5.0881872875e-09	1.5187082707e-09	1.2070835637e-10
1200-1400	3.3673468015e-11	4.4940819897e-09	8.0692343519e-09	8.0122291504e-09	8.5556088477e-09	6.0071626553e-09	4.9509720036e-09	3.0586023083e-09	2.2833034298e-09	1.5187082707e-09	9.4543068125e-10	4.5054938949e-11
1400-3200	-8.3406822114e-12	2.6315376563e-10	5.3098685059e-10	6.1214810058e-10	6.3295062074e-10	4.3478874422e-10	4.2752190048e-10	3.0586023083e-09	1.6243220094e-10	1.2070835637e-10	4.5054938949e-11	6.2711308571e-12

TABLE G.19: Covariance matrix of the absolute cross section as function of $m_{t\bar{t}}$, accounting for the statistical and systematic uncertainties.

bin [GeV]	0-20	20-45	45-70	70-100	100-130	130-170	170-210	210-270	270-550
0-20	1.4136315358e-07	3.5570268939e-08	2.4428950855e-09	3.5750747698e-08	1.0984759322e-08	2.0705933622e-08	2.3031310410e-08	5.8499733438e-09	6.9791715708e-10
20-45	3.5570268939e-08	7.9299695627e-08	1.0829128973e-08	1.7780075588e-08	8.2572952437e-09	1.4790401609e-08	1.2234489045e-08	2.6442268405e-09	5.0523316254e-10
45-70	2.4428950855e-09	1.0829128973e-08	4.9095031057e-08	1.2110708148e-08	2.8599122882e-09	7.2457471647e-09	1.4076491257e-09	6.2571180360e-10	2.2031706387e-10
70-100	3.5750747698e-08	1.7780075588e-08	1.2110708148e-08	6.1419537440e-08	1.8928309438e-08	1.2532280334e-08	1.0034992424e-08	3.1625358167e-09	5.9094342497e-10
100-130	1.0984759322e-08	8.2572952437e-09	2.8599122882e-09	1.8928309438e-08	5.3872213305e-08	5.3510064328e-09	1.2778769168e-09	1.3249561813e-09	7.0028060396e-10
130-170	2.0705933622e-08	1.4790401609e-08	7.2457471647e-09	1.2532280334e-08	5.3510064328e-09	1.6857628985e-08	4.6032037193e-09	1.3713446659e-09	2.1177911789e-10
170-210	2.3031310410e-08	1.2234489045e-08	1.4076491257e-09	1.0034992424e-08	1.2778769168e-09	4.6032037193e-09	1.2549846819e-08	1.8054789874e-09	1.6885964425e-10
210-270	5.8499733438e-09	2.6442268405e-09	6.2571180360e-10	3.1625358167e-09	1.3249561813e-09	1.3713446659e-09	1.8054789874e-09	1.2223566356e-09	5.3827361112e-11
270-550	6.9791715708e-10	5.0523316254e-10	2.2031706387e-10	5.9094342497e-10	7.0028060396e-10	2.1177911789e-10	1.6885964425e-10	5.3827361112e-11	2.7227096402e-11

TABLE G.20: Covariance matrix of the relative cross section as function of $|P_{\text{out}}^{t\bar{t}}|$, accounting for the statistical and systematic uncertainties.

bin [GeV]	0-1	1.0-1.5	1.5-2.0	2.0-2.2	2.2-2.5	2.5-2.6	2.6-2.9	2.9-3.2
0-1	1.3890867420e-05	7.2522551693e-06	4.7735921364e-06	2.6209300521e-05	3.6897403330e-05	2.3719132084e-05	1.0044451281e-04	6.5379424977e-05
1.0-1.5	7.2522551693e-06	5.2063140950e-05	9.6762889471e-06	3.2551568827e-05	8.5595193379e-05	9.5552305144e-05	2.5243856671e-04	7.5249245583e-05
1.5-2.0	4.7735921364e-06	9.6762889471e-06	7.9486329007e-05	6.5612814499e-05	7.0255228559e-05	1.1134473294e-04	1.6322711851e-04	2.1537154711e-05
2.0-2.2	2.6209300521e-05	3.2551568827e-05	6.5612814499e-05	5.2228939311e-04	2.1758118706e-04	2.9422874882e-04	5.1007996623e-04	2.6151438728e-04
2.2-2.5	3.6897403330e-05	8.5595193379e-05	7.0255228559e-05	2.1758118706e-04	6.6231056735e-04	4.8871671729e-04	9.9421040911e-04	2.5639920813e-04
2.5-2.6	2.3719132084e-05	9.5552305144e-05	1.1134473294e-04	2.9422874882e-04	4.8871671729e-04	1.2549710759e-03	1.1223251281e-03	6.3611926868e-05
2.6-2.9	1.0044451281e-04	2.5243856671e-04	1.6322711851e-04	5.1007996623e-04	9.9421040911e-04	1.1223251281e-03	3.5184417712e-03	8.7780338317e-04
2.9-3.2	6.5379424977e-05	7.5249245583e-05	2.1537154711e-05	2.6151438728e-04	2.5639920813e-04	6.3611926868e-05	8.7780338317e-04	1.2818601698e-03

TABLE G.21: Covariance matrix of the relative cross section as function of $\Delta\phi_{t\bar{t}}$, accounting for the statistical and systematic uncertainties.

bin [GeV]	0.0-0.5	0.5-0.6	0.6-0.7	0.7-0.8	0.8-0.8	0.8-0.8	0.8-0.9	0.9-1.0	1-2
0.0-0.5	8.6879016213e-04	8.1191719216e-04	-8.7427856187e-05	-2.3744247440e-03	-3.7395333487e-03	-2.2734811549e-03	-1.1353983704e-03	1.2114231258e-03	9.1217182066e-05
0.5-0.6	8.1191719216e-04	3.5957129382e-03	3.6194459190e-04	-2.1465647141e-03	-3.0763161228e-03	-1.8748329526e-03	1.6429777625e-03	1.3850425506e-03	1.4441520352e-04
0.6-0.7	-8.7427856187e-05	3.6194459190e-04	5.2389420349e-03	1.3720906851e-03	5.3074351394e-04	-6.8641761933e-04	1.9515279189e-03	-2.5970067243e-04	3.6715228962e-06
0.7-0.8	-2.3744247440e-03	-2.1465647141e-03	1.3720906851e-03	1.4759960902e-02	1.6187867699e-02	6.1697326792e-03	1.2469812791e-02	-3.5101655172e-03	-2.2937678825e-04
0.8-0.8	-3.7395333487e-03	-3.0763161228e-03	5.3074351394e-04	1.6187867699e-02	3.2178563406e-02	1.2521068115e-02	1.7095092224e-02	-5.1770078035e-03	-3.4836918492e-04
0.8-0.8	-2.2734811549e-03	-1.8748329526e-03	-6.8641761933e-04	6.1697326792e-03	1.2521068115e-02	1.3997613541e-02	7.6081907060e-03	-3.3422538781e-03	-2.0859220352e-04
0.8-0.9	-1.1353983704e-03	1.6429777625e-03	1.9515279189e-03	1.2469812791e-02	1.7095092224e-02	7.6081907060e-03	3.2326099323e-02	7.0445172626e-04	5.0162494296e-05
0.9-1.0	1.2114231258e-03	1.3850425506e-03	-2.5970067243e-04	-3.5101655172e-03	-5.1770078035e-03	-3.3422538781e-03	7.0445172626e-04	4.3062711860e-03	1.7724974613e-04
1-2	9.1217182066e-05	1.4441520352e-04	3.6715228962e-06	-2.2937678825e-04	-3.4836918492e-04	-2.0859220352e-04	5.0162494296e-05	1.7724974613e-04	1.7359202856e-05

TABLE G.22: Covariance matrix of the relative cross section as function of $R_{Wt}^{leading}$, accounting for the statistical and systematic uncertainties.

bin [GeV]	0.0-0.5	0.5-0.6	0.6-0.7	0.7-0.8	0.8-0.8	0.8-0.8	0.8-0.9	0.9-1.5
0.0-0.5	5.9016325286e-04	-2.6541645115e-04	-6.8281330846e-04	-1.4246853027e-03	-1.7347148710e-03	-1.6516871244e-03	-5.4400588454e-04	3.0106989695e-04
0.5-0.6	-2.6541645115e-04	6.0775940477e-03	2.1650381834e-03	2.7029856949e-03	2.0570859418e-03	2.3516785887e-03	2.0382135436e-03	-2.0032248177e-04
0.6-0.7	-6.8281330846e-04	2.1650381834e-03	5.0921691041e-03	3.2197985427e-03	2.3313747643e-03	3.1380918904e-03	2.6978363676e-03	-3.2559209744e-04
0.7-0.8	-1.4246853027e-03	2.7029856949e-03	3.2197985427e-03	8.4761248153e-03	5.5126713937e-03	4.8151328101e-03	2.6241112172e-03	-9.9693476355e-04
0.8-0.8	-1.7347148710e-03	2.0570859418e-03	2.3313747643e-03	5.5126713937e-03	1.2048669580e-02	8.3974895454e-03	3.8818560072e-03	-9.9558402303e-04
0.8-0.8	-1.6516871244e-03	2.3516785887e-03	3.1380918904e-03	4.8151328101e-03	8.3974895454e-03	1.2707623754e-02	5.7619538840e-03	-8.5451025552e-04
0.8-0.9	-5.4400588454e-04	2.0382135436e-03	2.6978363676e-03	2.6241112172e-03	3.8818560072e-03	5.7619538840e-03	1.0324891411e-02	1.4083578229e-04
0.9-1.5	3.0106989695e-04	-2.0032248177e-04	-3.2559209744e-04	-9.9693476355e-04	-9.9558402303e-04	-8.5451025552e-04	1.4083578229e-04	3.8489282275e-04

TABLE G.23: Covariance matrix of the relative cross section as function of $R_{Wt}^{subleading}$, accounting for the statistical and systematic uncertainties.

bin [GeV]	0-1	1.0-1.9	1.9-2.8	2.8-4.0	4.0-5.5	5.5-7.5	7.5-16.0
0-1	3.4723515620e-04	5.7209208701e-06	-1.1327342547e-04	-9.8064328594e-05	-3.6389792866e-05	-1.1280155305e-05	-2.4388017580e-06
1.0-1.9	5.7209208701e-06	5.4353098807e-05	-1.0779462438e-05	-1.0546143877e-05	-4.5138991590e-06	-2.2332034389e-06	-1.8186592261e-07
1.9-2.8	-1.1327342547e-04	-1.0779462438e-05	1.3281103687e-04	4.1172660493e-05	2.4646085276e-05	7.2552426785e-06	3.8555950360e-06
2.8-4.0	-9.8064328594e-05	-1.0546143877e-05	4.1172660493e-05	4.6928665550e-05	1.3278808969e-05	3.3158327841e-06	1.4526282478e-06
4.0-5.5	-3.6389792866e-05	-4.5138991590e-06	2.4646085276e-05	1.3278808969e-05	1.4196197359e-05	3.0911930235e-06	1.0118508851e-06
5.5-7.5	-1.1280155305e-05	-2.2332034389e-06	7.2552426785e-06	3.3158327841e-06	3.0911930235e-06	2.4411460561e-06	3.9754530645e-07
7.5-16.0	-2.4388017580e-06	-1.8186592261e-07	3.8555950360e-06	1.4526282478e-06	1.0118508851e-06	3.9754530645e-07	3.6310605631e-07

TABLE G.24: Covariance matrix of the relative cross section as function of $R_{Wb}^{leading}$, accounting for the statistical and systematic uncertainties.

bin [GeV]	0-1	1.0-1.9	1.9-2.8	2.8-4.0	4.0-5.5	5.5-7.5	7.5-12.0
0-1	4.1094665603e-04	-3.3418073731e-05	-1.2978677519e-04	-6.2008765007e-05	-1.5652543074e-05	-1.2170411446e-05	-2.6267570404e-06
1.0-1.9	-3.3418073731e-05	7.6507585120e-05	9.3403962491e-07	-6.5205784076e-06	1.4338111158e-06	5.7362481756e-07	4.7034927097e-07
1.9-2.8	-1.2978677519e-04	9.3403962491e-07	1.0765702983e-04	3.9728622437e-05	2.0695524301e-05	5.6642531986e-06	2.5560522829e-06
2.8-4.0	-6.2008765007e-05	-6.5205784076e-06	3.9728622437e-05	4.2850971025e-05	1.8288982625e-05	2.1216996764e-06	1.2680146629e-06
4.0-5.5	-1.5652543074e-05	1.4338111158e-06	2.0695524301e-05	1.8288982625e-05	1.8464257508e-05	1.8912012955e-06	8.5914856770e-07
5.5-7.5	-1.2170411446e-05	5.7362481756e-07	5.6642531986e-06	2.1216996764e-06	1.8912012955e-06	1.6985999891e-06	3.4946031774e-07
7.5-12.0	-2.6267570404e-06	4.7034927097e-07	2.5560522829e-06	1.2680146629e-06	8.5914856770e-07	3.4946031774e-07	2.6209716042e-07

TABLE G.25: Covariance matrix of the relative cross section as function of $R_{Wb}^{subleading}$, accounting for the statistical and systematic uncertainties.

bin [GeV]	0-360	360-420	420-480	480-540	540-600	600-670	670-740	740-800	800-900	900-1000	1000-2000
0-360	4.1364314129e-09	-3.8715779467e-09	-5.3768561869e-09	-4.5775483406e-09	-4.0244850265e-09	-2.0093483853e-09	-9.0784914648e-10	-1.6387237593e-11	6.2518099568e-11	1.4396471921e-10	1.0014737442e-11
360-420	-3.8715779467e-09	3.1493226113e-08	2.6919777463e-08	1.0275744125e-08	1.0589420672e-08	2.3091974614e-09	9.8307785689e-11	9.0456172195e-10	2.1742612619e-09	4.0331138992e-10	9.6705197031e-11
420-480	-5.3768561869e-09	2.6919777463e-08	3.8654274387e-08	1.4165743115e-08	1.3626831879e-08	8.3373313560e-09	2.5901411343e-09	3.8904995444e-09	5.4469238228e-09	1.3808776785e-09	2.8717114595e-09
480-540	-4.5775483406e-09	1.0275744125e-08	1.4165743115e-08	1.3997032332e-08	8.3373313560e-09	1.3817406020e-08	3.8904995444e-09	1.4952912890e-09	1.8308776785e-09	2.8717114595e-09	9.0030278712e-10
540-600	-4.0244850265e-09	1.0589420672e-08	1.3626831879e-08	8.3373313560e-09	1.3817406020e-08	2.5901411343e-09	5.4469238228e-09	1.3808776785e-09	2.8717114595e-09	9.0030278712e-10	6.5489298422e-10
600-670	-2.0093483853e-09	2.3091974614e-09	2.5901411343e-09	3.8904995444e-09	5.4469238228e-09	1.3808776785e-09	1.2317491145e-09	8.1509893837e-10	1.2317491145e-09	8.1509893837e-10	2.7338837441e-10
670-740	-9.0784914648e-10	9.8307785689e-11	5.0751347284e-10	1.0150480783e-09	1.4952912890e-09	1.3808776785e-09	2.8717114595e-09	9.0030278712e-10	6.5489298422e-10	2.4570081118e-10	1.6834226581e-11
740-800	-1.6387237593e-11	9.0456172195e-10	1.5687976469e-09	1.0670586517e-09	2.1811545409e-09	1.2317491145e-09	9.0030278712e-10	2.8989484556e-09	8.9182164136e-10	3.7502615908e-10	1.8494473513e-11
800-900	6.2518099568e-11	2.1742612619e-09	2.6758686124e-09	1.7768413365e-09	1.9088922882e-09	8.1509893837e-10	6.5489298422e-10	8.9182164136e-10	2.3972891055e-09	3.4903480499e-10	6.9189056452e-11
900-1000	1.4396471921e-10	4.0331138992e-10	5.2247001798e-10	2.1258544703e-10	5.5147608300e-10	2.7338837441e-10	2.4570081118e-10	3.7502615908e-10	3.4903480499e-10	3.3966194342e-10	9.0268564871e-12
1000-2000	1.0014737442e-11	9.6705197031e-11	7.0073139229e-11	4.2768181405e-11	1.6524077960e-11	1.1566172786e-11	1.6834226581e-11	1.8494473513e-11	6.9189056452e-11	9.0268564871e-12	5.3384716820e-12

TABLE G.26: Covariance matrix of the relative cross section as function of $H_{\mathrm{T}}^{\bar{t}t}$, accounting for the statistical and systematic uncertainties.

bin [GeV]	5.5-6.5	6.5-7.5	7.5-8.5	8.5-9.5	9.5-14.5
5.5-6.5	2.3267636129e-04	1.1948637657e-04	2.1087918696e-05	1.6220208823e-05	8.4934372402e-07
6.5-7.5	1.1948637657e-04	2.7814208576e-04	4.9544957384e-05	-1.6547998101e-04	-4.5506405846e-05
7.5-8.5	2.1087918696e-05	4.9544957384e-05	1.4895781858e-04	-2.5752401117e-05	-9.2862844634e-06
8.5-9.5	1.6220208823e-05	-1.6547998101e-04	-2.5752401117e-05	2.2083789292e-04	4.3423122123e-05
9.5-14.5	8.4934372402e-07	-4.5506405846e-05	-9.2862844634e-06	4.3423122123e-05	1.3494363925e-05

TABLE G.27: Covariance matrix of the relative cross section as function of N_{jets}, accounting for the statistical and systematic uncertainties.

bin [GeV]	0.0-0.4	0.4-1.2	1.2-1.7	1.7-1.9	1.9-2.1	2.1-2.3	2.3-2.5	2.5-2.6	2.6-2.8	2.8-2.9	2.9-3.0	3.0-3.1	3.1-3.2	3.2-3.4	3.4-3.6	3.6-4.0	4.0-6.0
0.0-0.4	4.7074409513e-04	4.1608337922e-06	-1.9617405137e-05	2.2147195899e-05	-2.5754185311e-06	-5.9339198242e-05	5.9290231138e-05	-4.1905692736e-05	-2.3568122192e-05	1.8533897104e-05	-4.7581220592e-05	8.5549010032e-05	6.3119986040e-05	-8.1127224289e-05	-2.5285888025e-05	-8.7705034527e-06	-1.4333489548e-06
0.4-1.2	4.1608337922e-06	3.5727634785e-05	2.5243684392e-05	6.5234320872e-05	1.7760253914e-05	-7.4557845010e-06	5.2416348883e-05	2.4588530958e-05	5.3946180329e-05	7.9765052408e-05	2.9489169227e-05	6.5236009701e-05	1.0041851123e-04	9.5048246975e-07	1.5401045699e-05	3.3077210344e-05	1.5903289849e-06
1.2-1.7	-1.9617405137e-05	2.5243684392e-05	9.2502147045e-05	8.6962573445e-05	5.8274446547e-05	2.5625738723e-05	9.3060524412e-05	4.7668798387e-05	5.8834832948e-05	7.8733937783e-05	4.8192000030e-05	1.0396860514e-04	1.0272916755e-04	1.6360589002e-05	3.9603294180e-05	3.9531188162e-05	5.5931874777e-06
1.7-1.9	2.2147195899e-05	6.5234320872e-05	8.6962573445e-05	4.9865143199e-04	1.2675212209e-04	2.0457646410e-04	3.1051797343e-04	1.1809898900e-04	2.2255618726e-04	2.4141236344e-04	2.0124319384e-04	3.6605538754e-04	5.1246069542e-04	5.0868080851e-05	1.7667341985e-04	9.9283932063e-05	8.8684381679e-06
1.9-2.1	-2.5754185311e-06	1.7760253914e-05	5.8274446547e-05	1.2675212209e-04	2.7776118514e-04	8.3087824346e-05	1.7461538667e-04	6.4543128876e-05	6.0828149662e-05	7.0185916341e-05	5.8483603382e-05	1.9420153840e-04	1.5880290622e-04	3.2746744615e-05	4.5305557572e-05	3.2351393751e-05	5.5943576843e-06
2.1-2.3	-5.9339198242e-05	7.4557845010e-06	2.5625738723e-05	2.0457646410e-04	8.3087824346e-05	5.4128425289e-04	1.4210390393e-04	3.1602532615e-05	5.4186681518e-05	-2.5056933525e-05	1.2171466671e-04	1.5801125666e-04	2.1819598627e-04	4.8211297550e-05	7.0344342065e-05	1.9672604621e-06	-6.4628422032e-07
2.3-2.5	5.9290231138e-05	5.2416348830e-05	9.3060524412e-05	3.1051797343e-04	1.7461538667e-04	1.4210390393e-04	7.5907578603e-04	1.0300790561e-04	1.5339164078e-04	2.4615440754e-04	1.9451063245e-04	3.1974543351e-04	4.4541942714e-04	5.6029964844e-05	1.1009135326e-04	7.1314253362e-05	8.3138029962e-06
2.5-2.6	-4.1905692736e-05	2.4588530958e-05	4.7668798387e-05	1.1809898900e-04	6.4543128876e-05	3.1602532615e-05	1.0300790561e-04	4.1964140622e-04	6.6428920600e-05	3.8898283777e-05	5.7068128502e-05	9.7887951325e-05	1.6223431345e-04	8.9281424658e-06	4.1446558555e-05	4.1125283994e-05	5.7696868708e-06
2.6-2.8	-2.3568122192e-05	5.3946180329e-05	5.8834832948e-05	2.2255618726e-04	6.0828149662e-05	5.4186681518e-05	1.5339164078e-04	6.6428920600e-05	6.3721165901e-04	2.0942057794e-04	9.3731363235e-05	2.4290884231e-04	3.5230033351e-04	-7.4288423116e-06	1.1365853984e-04	1.1365853984e-04	7.5293027721e-05
2.8-2.9	1.8533897104e-05	7.9765052408e-05	7.8733937783e-05	2.4141236344e-04	7.0185916341e-05	-2.5056933525e-05	2.4615440754e-04	3.8890283777e-05	2.0942057794e-04	1.0859618945e-03	5.7309722260e-05	6.1159119764e-04	2.1776758670e-04	2.3334136738e-04	1.5171270002e-06	8.1911084119e-05	4.1722230342e-05
3.0-3.1	-4.7581220592e-05	2.9489169227e-05	4.8192000030e-05	2.0124319384e-04	8.3483630382e-05	1.2171466671e-04	1.9451063245e-04	5.7068128502e-05	9.3731363235e-05	5.7309722260e-05	6.1159119764e-04	2.1776758670e-04	2.3334136738e-04	1.5171270002e-06	8.1911084119e-05	4.1722230342e-05	5.1362738856e-06
3.0-3.1	8.5549010032e-05	6.5236009701e-05	1.0396860514e-04	3.6605538754e-04	1.9420153840e-04	1.5801125666e-04	3.1974543351e-04	9.7887951325e-05	2.4290884231e-04	6.1159119764e-04	2.1776758670e-04	1.3704737974e-03	5.8220158967e-04	-2.3182866014e-06	1.5817899626e-04	8.0182440453e-05	1.1628067815e-05
3.1-3.2	6.3119986040e-05	1.0041851123e-04	1.0272916755e-04	5.1246069542e-04	1.5880296023e-04	2.1819598627e-04	4.4541942714e-04	1.6223431345e-04	3.5230033351e-04	2.1776758670e-04	2.3334136738e-04	5.8220158967e-04	1.5039734610e-03	4.1159076953e-05	2.2604903027e-04	1.2824754062e-04	1.1188846970e-05
3.2-3.4	-8.1127224289e-05	9.5048246975e-07	1.6360589002e-05	5.0868080851e-05	3.2746744615e-05	4.8211297550e-05	5.6029964844e-05	8.9281424658e-06	-7.4288423116e-06	4.7176229675e-05	1.5171270002e-06	-2.3182866014e-06	4.1159076953e-05	4.0431331778e-04	1.9507954135e-05	2.2572279852e-05	4.5166110619e-05
3.4-3.6	-2.5285888025e-05	1.5401045699e-05	3.9603294180e-05	1.7667341985e-04	4.5305557572e-05	7.0344342065e-05	1.1009135326e-04	4.1446558555e-05	1.1365853984e-04	8.1911084119e-05	1.5817899626e-04	2.2604903027e-04	1.9507954135e-05	2.2572279852e-05	4.5166110619e-05	1.0899331631e-04	5.1602992218e-06
3.6-4.0	-8.7705034527e-06	3.3077210344e-05	3.9531188162e-05	9.9283932063e-05	3.2351393751e-05	1.9672604621e-06	7.1314253362e-05	4.1125283994e-05	7.5293027721e-05	4.1722230342e-05	8.0182440453e-05	1.2824754062e-04	7.4205759017e-06	4.5166110619e-05	1.0899331631e-04	1.1602992218e-04	2.2657465437e-06
4.0-6.0	-1.4333489548e-06	1.5903289849e-06	5.5931874777e-06	8.8684381679e-06	5.5943576843e-06	-6.4628422032e-07	8.3138029962e-06	5.7696868708e-06	7.5293027521e-06	8.9934807499e-06	5.1362738856e-06	1.1628067815e-05	1.1188846970e-05	9.2121848808e-07	4.1468902318e-06	5.1602992218e-06	2.2657465437e-06

TABLE G.28: Covariance matrix of the relative cross section as function of $\Delta R_{\mathrm{jet1}}^{\mathrm{extra1}}$, accounting for the statistical and systematic uncertainties.

bin [GeV]	0.0-0.6	0.6-0.8	0.8-1.1	1.1-1.4	1.4-1.6	1.6-1.8	1.8-2.0	2.0-2.2	2.2-2.4	2.4-2.5	2.5-2.7	2.7-2.9	2.9-3.1	3.1-3.4	3.4-6.0
0.0-0.6	5.9964597749e-05	6.7958429012e-05	-1.3577194601e-05	4.3266638440e-05	-2.3224601886e-05	-4.1963158662e-05	-2.2901417020e-05	5.9925206463e-05	1.3611034895e-05	6.4272623562e-05	6.4909216201e-05	4.6335807928e-05	1.1270884615e-05	1.9516357359e-07
0.6-0.8	6.7958429012e-05	4.9219993233e-04	5.0177435332e-05	1.8947241851e-04	1.4225616988e-04	1.7127854136e-04	1.3794947705e-05	6.8794367608e-05	2.5897914164e-04	1.3170895777e-04	4.8538594488e-04	1.5616083377e-04	2.9429602879e-04	5.3607577427e-05	5.8083003228e-06
0.8-1.1	-1.3577194601e-05	5.0177435332e-05	3.5900618646e-04	-9.0269087157e-05	1.3309952606e-04	1.1541922311e-04	1.2747136285e-04	4.8830115623e-05	1.4237080088e-04	1.1362118197e-04	3.4276213382e-04	3.6824351541e-05	1.3668707108e-04	3.6058414861e-05	-1.5215093845e-06
1.1-1.4	4.3266638440e-05	1.8947241851e-04	-9.0269087157e-05	5.8204717004e-04	3.9395703175e-05	1.9409853766e-05	-4.8669591600e-05	-6.9123659014e-05	-1.5672853189e-05	2.2117119498e-04	1.5762224573e-04	1.0363432523e-04	1.8380103038e-04	-2.9062404400e-06	8.9003667594e-06
1.4-1.6	-2.3224601886e-05	1.4225616988e-04	1.3309952606e-04	3.9395703175e-05	7.2099403625e-04	1.6807732577e-04	1.9932526725e-04	3.8869410107e-05	1.9052928029e-04	2.0108503240e-04	5.8715418063e-04	-2.1598013611e-05	3.6072635244e-04	2.4305129478e-05	5.9824922880e-06
1.6-1.8	1.5659644358e-05	1.7127854136e-04	1.1541922311e-04	1.9409853766e-05	1.6807732577e-04	6.7510738913e-04	6.4306575757e-05	-2.2446925146e-05	2.1414738922e-04	1.8977297759e-04	5.1287884986e-04	4.6030034104e-05	3.0947875053e-04	3.9223261345e-05	1.3195798929e-06
1.8-2.0	-4.1963158662e-05	1.3794894705e-05	1.2747136285e-04	-4.8669591600e-05	1.9932526725e-04	6.4306575757e-05	6.7896244595e-04	2.9874601851e-05	1.1514639433e-04	1.2581269632e-04	4.0066221063e-04	3.6957906961e-05	1.8480881226e-04	2.4704621836e-05	1.3685615756e-06
2.0-2.2	-2.2901417020e-05	-6.8794367608e-05	4.8830115623e-05	-6.9123659014e-05	3.8869410107e-05	-2.2446925146e-05	2.9874601851e-05	6.7896244595e-04	2.7298539471e-05	1.4307623196e-05	1.1773235884e-04	3.2015474626e-05	4.3764192541e-05	-5.7866594562e-06	-1.6749956033e-06
2.2-2.4	5.9925206463e-05	2.5897914164e-04	1.4237080088e-04	1.0363432523e-04	1.9052928029e-04	2.1414738922e-04	1.1514639433e-04	-2.7298539471e-05	9.1765637338e-04	1.7733422749e-04	6.3544557195e-04	2.2891854917e-04	3.9558195811e-04	5.5419161469e-05	3.2600966819e-06
2.4-2.5	1.3611034895e-05	1.3170895777e-04	1.1362118197e-04	-1.5672853189e-05	2.0108503240e-04	1.8977297759e-04	1.2581269632e-04	1.4307623196e-05	1.7733422749e-04	5.5095516225e-04	4.3116330750e-04	4.9695918116e-05	3.0123885476e-04	7.7596941062e-04	3.8703859496e-05	-2.6536931956e-07
2.5-2.7	6.4272623562e-05	4.8538594488e-04	5.0871543522e-05	2.2117119498e-04	5.8715418063e-04	1.5126784894e-04	4.0066221063e-04	1.1773235884e-04	6.3544557195e-04	4.3116330750e-04	1.8294979604e-03	3.3914392197e-04	4.3317443863e-04	1.0749919057e-04	1.2703299362e-06
2.7-2.9	6.4909216201e-05	1.5616083377e-04	3.6824351541e-05	1.5762224573e-04	-2.1558013611e-05	4.6030034104e-05	3.6957906961e-05	3.2015474626e-05	2.2891854917e-04	1.9695918116e-05	3.3914392197e-04	5.9766626550e-04	1.4012040928e-04	4.3317443863e-05	2.0320105202e-06
2.9-3.1	4.6335807928e-05	2.9429602879e-04	1.3668707108e-04	1.8380103038e-04	3.6072635244e-04	3.0947875053e-04	1.8480881226e-04	4.3764192541e-05	3.9558195811e-04	4.9695918116e-05	3.3914392197e-04	1.4012040928e-04	7.9699407373e-04	1.0749919057e-04	1.1208262794e-04
3.1-3.4	1.1270884615e-05	5.3607577427e-05	1.3668707108e-04	-2.9062404400e-06	2.4305129478e-05	3.9223261345e-05	2.4704621836e-05	-5.7866594562e-06	5.5419161469e-05	3.8703859496e-05	4.3317443863e-05	1.4012040928e-04	4.3317443863e-05	1.0749919057e-04	1.1208262794e-04
3.4-6.0	1.9516357359e-07	5.8083003228e-06	-1.5215093845e-06	8.9003667594e-06	5.9824922880e-06	1.3195798929e-06	1.3685615756e-06	-1.6749956033e-06	3.2600966819e-06	-2.6536931956e-07	7.7960278032e-06	2.0320105202e-06	6.6446017744e-06	-7.9588033578e-07	1.1963917254e-06

TABLE G.29: Covariance matrix of the relative cross section as function of $\Delta R_{\mathrm{topclose}}^{\mathrm{extra1}}$, accounting for the statistical and systematic uncertainties.

bin [GeV]	0.0-0.2	0.2-0.3	0.3-0.5	0.5-0.6	0.6-0.8	0.8-1.1
0.0-0.2	2.4554400548e-04	2.1291453442e-04	3.1049065204e-04	1.1818239588e-04	3.7637898963e-04	-3.5408022136e-06
0.2-0.3	2.1291453442e-04	1.9434446481e-03	8.3116160001e-04	7.6793885589e-04	3.1638016966e-04	-2.0912266367e-04
0.3-0.5	3.1049065204e-04	8.3116160001e-04	2.6130713897e-03	8.7667645889e-04	1.7768909488e-03	1.6905764874e-04
0.5-0.6	1.1818239588e-04	7.6793885589e-04	8.7667645889e-04	3.1798906113e-03	2.3844924291e-04	-6.9671190627e-05
0.6-0.8	3.7637898963e-04	3.1638016966e-04	1.7768909488e-03	2.3844924291e-04	4.1273293408e-03	3.7157527959e-04
0.8-1.1	-3.5408022136e-06	-2.0912266367e-04	1.6905764874e-04	-6.9671190627e-05	3.7157527959e-04	1.4556566869e-03

TABLE G.30: Covariance matrix of the relative cross section as function of $R_{\mathrm{jet1}}^{\mathrm{extra1}}$, accounting for the statistical and systematic uncertainties.

bin [GeV]	0.0-0.1	0.1-0.2	0.2-0.4	0.4-0.5	0.5-0.7	0.7-0.8	0.8-1.0	1.0-1.2	1.2-5.0
0.0-0.1	9.9202439990e-04	7.5871881104e-04	2.4785188882e-04	1.1019539222e-04	-2.8657037530e-06	1.5625390950e-04	8.8438774756e-05	1.8765887050e-04	-3.4767655209e-06
0.1-0.2	7.5871881104e-04	4.9595607423e-03	4.5798682041e-04	-3.0970010005e-04	-4.8122358352e-04	1.6304806056e-04	1.3353973064e-04	2.2687355885e-05	-2.0240820974e-05
0.2-0.4	2.4785188882e-04	4.5798682041e-04	2.3223827308e-03	-5.8737818461e-04	-3.4204071744e-04	5.8904847172e-05	1.8906650423e-04	6.9663204761e-05	-1.1066794456e-05
0.4-0.5	1.1019539222e-04	-3.0970010005e-04	-5.8737818461e-04	2.9901180042e-03	2.5195853253e-04	7.4148920503e-05	-5.4196635496e-06	3.5865649629e-04	7.4525174752e-06
0.5-0.7	-2.8657037530e-06	-4.8122358352e-04	-3.4204071744e-04	2.5195853253e-04	1.6900802982e-03	3.8678780239e-04	1.2082203177e-04	4.3205142587e-04	1.4858762056e-05
0.7-0.8	1.5625390950e-04	1.6304806056e-04	5.8904847172e-05	7.4148920503e-05	3.8678780239e-04	1.5730949592e-03	3.4772081890e-04	3.5895255481e-04	1.5826307559e-05
0.8-1.0	8.8438774756e-05	1.3353973064e-04	1.8906650423e-04	-5.4196635496e-06	1.2082203177e-04	3.4772081890e-04	7.9612078726e-04	2.2188267299e-04	4.6611428795e-06
1.0-1.2	1.8765887050e-04	2.2687355885e-05	6.9663204761e-05	3.5865649629e-04	4.3205142587e-04	3.5895255481e-04	2.2188267299e-04	6.7674682717e-04	1.0761337761e-05
1.2-5.0	-3.4767655209e-06	-2.0240820974e-05	-1.1066794456e-05	7.4525174752e-06	1.4858762056e-05	1.5826307559e-05	4.6611428795e-06	1.0761337761e-05	2.1454207059e-06

TABLE G.31: Covariance matrix of the relative cross section as function of $R_{\mathrm{top1}}^{\mathrm{extra1}}$, accounting for the statistical and systematic uncertainties.

bin [GeV]	0-210	210-240	240-270	270-300	300-330	330-370	370-400	400-440	440-480	480-550	550-1000
0-210	3.8828487467e-09	-2.6491351535e-09	-4.1967691137e-09	-5.4395591647e-10	-3.1056865290e-09	-3.7543718101e-09	-1.1612593733e-09	-1.4869980638e-10	6.7464321820e-10	5.7244048630e-10	-9.5610740302e-13
210-240	-2.6491351535e-09	4.4999615098e-08	1.1126260904e-08	1.4087554529e-08	9.7246007177e-09	-6.2794453324e-09	-5.4054401661e-09	-2.6872586114e-09	-1.1465253248e-09	-1.1185587082e-09	-1.0071414109e-10
240-270	-4.1967691137e-09	1.1126260904e-08	3.0508502306e-08	1.2493873816e-08	6.4011333339e-09	2.4427030196e-09	2.8466319703e-10	-6.3624494658e-11	-9.3719212301e-11	-5.6964629200e-10	-3.3302240519e-11
270-300	-5.4395591647e-10	1.4087554529e-08	1.2493873816e-08	4.2300117557e-08	1.8223759030e-08	-4.8319577570e-09	3.2202831064e-09	2.3098068938e-09	3.6036327233e-09	1.2532075367e-09	1.7126923349e-10
300-330	-3.1056865290e-09	9.7246007177e-09	6.4011333339e-09	1.8223759030e-08	6.0284806380e-08	1.5500079814e-08	1.8030462998e-08	5.8549905957e-09	8.2758315700e-09	1.5794738334e-09	6.6316763880e-10
330-370	-3.7543718101e-09	-6.2794453324e-09	2.4427030196e-09	-4.8319577570e-09	1.5500079814e-08	2.4046235840e-08	1.3844902711e-08	2.9659392784e-09	3.8512065219e-09	3.3917384485e-10	3.1428635684e-10
370-400	-1.1612593733e-09	-5.4054401661e-09	2.8466319703e-10	3.2202831064e-09	1.8030462998e-08	1.3844902711e-08	2.5546276794e-08	7.5365681631e-09	6.3973456621e-09	2.0015833772e-09	4.7829194831e-10
400-440	-1.4869980638e-10	-2.6872586114e-09	-6.3624494658e-11	2.3098068938e-09	5.8549905957e-09	2.9659392784e-09	7.5365681631e-09	8.5205231106e-09	3.8480383268e-09	8.6671252859e-10	1.9320240892e-10
440-480	6.7464321820e-10	-1.1465253248e-09	-9.3719212301e-11	3.6036327233e-09	8.2758315700e-09	3.8512065219e-09	6.3973456621e-09	3.8480383268e-09	7.1673692236e-09	1.4581780422e-09	1.9386322406e-10
480-550	5.7244048630e-10	-1.1185587082e-09	-5.6964629200e-10	1.2532075367e-09	1.5794738334e-09	3.3917384485e-10	2.0015833772e-09	8.6671252859e-10	1.4581780422e-09	1.2910225343e-09	5.2302597810e-11
550-1000	-9.5610740302e-13	-1.0071414109e-10	-3.3302240519e-11	1.7126923349e-10	6.6316763880e-10	3.1428635684e-10	4.7829194831e-10	1.9320240892e-10	1.9386322406e-10	5.2302597810e-11	2.2354055909e-11

TABLE G.32: Covariance matrix of the relative cross section as function of p_T^{top1}, accounting for the statistical and systematic uncertainties.

bin [GeV]	0.0-0.3	0.3-0.6	0.6-0.9	0.9-1.2	1.2-1.5	1.5-2.0	2.0-2.5
0.0-0.3	5.3206414032e-04	1.2040768459e-04	1.8823930645e-04	-5.5499511792e-05	1.1070127207e-04	-8.7174034916e-06	6.1148230888e-05
0.3-0.6	1.2040768459e-04	3.8744318936e-04	1.0022123873e-04	-5.6917405011e-05	4.6297645490e-05	-2.2943746542e-05	3.5054070229e-05
0.6-0.9	1.8823930645e-04	1.0022123873e-04	6.7651038443e-04	2.8609440748e-05	1.9171748935e-04	2.8023879815e-05	8.2826099024e-05
0.9-1.2	-5.5499511792e-05	-5.6917405011e-05	2.8609440748e-05	2.8257562968e-04	1.7334963110e-05	3.5102340000e-07	1.4962891090e-05
1.2-1.5	1.1070127207e-04	4.6297645490e-05	1.9171748935e-04	1.7334963110e-05	3.0844722118e-04	1.0694137513e-05	4.8023315330e-05
1.5-2.0	-8.7174034916e-06	-2.2943746542e-05	2.8023879815e-05	3.5102340000e-07	1.0694137513e-05	7.0662607453e-05	5.5068219749e-06
2.0-2.5	6.1148230888e-05	3.5054070229e-05	8.2826099024e-05	1.4962891090e-05	4.8023315330e-05	5.5068219749e-06	3.4203575719e-05

TABLE G.33: Covariance matrix of the relative cross section as function of y_{top1}, accounting for the statistical and systematic uncertainties.

bin [GeV]	0-100	100-150	150-190	190-230	230-270	270-315	315-365	365-420	420-475	475-1000
0-100	2.7128256549e-08	4.9681089373e-08	-3.1416886204e-08	-4.2265265124e-08	-2.3454217065e-08	-1.4322230115e-08	-5.4860578422e-09	-7.6428600184e-10	-9.8870700736e-11	5.5397523023e-11
100-150	4.9681089373e-08	1.5191919889e-07	-5.7350614590e-08	-8.1109886875e-08	-5.3674323450e-08	-4.0539554886e-08	-2.2301517520e-08	-4.1153561871e-09	-1.0009898292e-09	2.5490862871e-10
150-190	-3.1416886204e-08	-5.7350614590e-08	9.0015734056e-08	7.1137795975e-08	4.1737838442e-08	1.8397612807e-08	6.7743575148e-09	6.2471801963e-09	1.8568824889e-09	3.6984221005e-10
190-230	-4.2265265124e-08	-8.1109886875e-08	7.1137795975e-08	1.1592690189e-07	5.0893696465e-08	2.7812288806e-08	6.9001089399e-09	7.4395883027e-09	1.8742187429e-09	2.4618188409e-10
230-270	-2.3454217065e-08	-5.3674323450e-08	4.1737838442e-08	5.0893696465e-08	5.1923395998e-08	2.1410061824e-08	1.4918035951e-08	8.7308979094e-09	2.7762457142e-09	3.0507012243e-10
270-315	-1.4322230115e-08	-4.0539554886e-08	1.8397612807e-08	2.7812288806e-08	2.1410061824e-08	2.3736328272e-08	1.0772398409e-08	4.8581015932e-09	1.6396412791e-09	7.0141898844e-11
315-365	-5.4860578422e-09	-2.2301517520e-08	6.7743575148e-09	6.9001089399e-09	1.4918035951e-08	1.0772398409e-08	1.6174979842e-08	4.4941658064e-09	1.5360110580e-09	9.8780075208e-11
365-420	-7.6428600184e-10	-4.1153561871e-09	6.2471801963e-09	7.4395883027e-09	8.7308979094e-09	4.8581015932e-09	4.4941658064e-09	6.0450849177e-09	1.3234330615e-09	1.6456868488e-10
420-475	-9.8870700736e-11	-1.0009898292e-09	1.8568824889e-09	1.8742187429e-09	2.7762457142e-09	1.6396412791e-09	1.5360110580e-09	1.3234330615e-09	1.3417050927e-09	6.1071958387e-11
475-1000	5.5397523023e-11	2.5490862871e-10	3.6984221005e-10	2.4618188409e-10	3.0507012243e-10	7.0141898844e-11	9.8780075208e-11	1.6456868488e-10	6.1071958387e-11	1.4612958058e-11

TABLE G.34: Covariance matrix of the relative cross section as function of p_T^{top2}, accounting for the statistical and systematic uncertainties.

bin [GeV]	0-40	40-85	85-130	130-180	180-240	240-300	300-370	370-450	450-1100
0-40	7.3900283469e-08	-2.6552173496e-09	4.5917433051e-08	7.0832830589e-09	4.2532566795e-09	1.2152353929e-09	3.3440067143e-09	5.7540452300e-09	5.8612076052e-11
40-85	-2.6552173496e-09	1.9035034491e-08	6.1472867760e-10	-1.9487020549e-09	-2.1250235319e-09	-1.9263285700e-09	8.6757314374e-10	1.8460773751e-11	-5.0937600113e-11
85-130	4.5917433051e-08	6.1472867760e-10	6.2500507020e-08	8.3601428278e-09	5.3677171344e-09	5.8037522953e-10	2.1870724785e-09	4.9054388203e-09	-2.9124436325e-11
130-180	7.0832830589e-09	-1.9487020549e-09	8.3601428278e-09	1.3519492074e-08	-2.5175255762e-10	-1.2026268724e-09	3.5084205225e-11	7.1273411626e-10	-2.3925651385e-11
180-240	4.2532566795e-09	-2.1250235319e-09	5.3677171344e-09	-2.5175255762e-10	1.1025791314e-08	8.1859800383e-10	-6.3256684184e-10	9.5000721383e-10	1.0683882264e-11
240-300	1.2152353929e-09	-1.9263285700e-09	5.8037522953e-10	-1.2026268724e-09	8.1859800383e-10	4.7723112422e-09	2.5429279552e-11	2.2968212293e-10	1.9973284040e-11
300-370	3.3440067143e-09	8.6757314374e-10	2.1870724785e-09	3.5084205225e-11	-6.3256684184e-10	2.5429279552e-11	2.7103561299e-09	3.2642850553e-10	-5.8600824263e-13
370-450	5.7540452300e-09	1.8460773751e-11	4.9054388203e-09	7.1273411626e-10	9.5000721383e-10	2.2968212293e-10	3.2642850553e-10	1.3369558028e-09	1.6771290815e-12
450-1100	5.8612076052e-11	-5.0937600113e-11	-2.9124436325e-11	-2.3925651385e-11	1.0683882264e-11	1.9973284040e-11	-5.8600824263e-13	1.6771290815e-12	5.0580092064e-12

TABLE G.35: Covariance matrix of the relative cross section as function of $p_T^{t\bar{t}}$, accounting for the statistical and systematic uncertainties.

bin [GeV]	0.0-0.1	0.1-0.2	0.2-0.3	0.3-0.4	0.4-0.5	0.5-0.6	0.6-0.7	0.7-0.8	0.8-0.9	0.9-1.0	1.0-1.1	1.1-1.2	1.2-1.3	1.3-1.4	1.4-1.5	1.5-1.6	1.6-2.5
0.0-0.1	3.9808676668e-03	2.8507674708e-03	9.8108482638e-04	5.4831470763e-04	1.2667125991e-03	1.0395214867e-03	-2.4584991851e-04	4.1294854907e-04	5.0112751797e-04	4.3595848857e-04	1.1505065312e-04	8.7810130469e-04	1.4425334507e-03	4.0386306703e-04	5.1101188338e-04	6.5040953776e-05	-8.1480504436e-08
0.1-0.2	2.8507674708e-03	7.9200336477e-03	1.9732869058e-03	1.3230944003e-03	1.7714256896e-03	3.0547972197e-03	6.4417954553e-04	7.4183995588e-04	9.8764435668e-04	1.1608803095e-03	1.1946084864e-03	1.7885731840e-03	2.7163191449e-03	5.1263808511e-04	8.9472158000e-04	3.3107456949e-04	3.0829514196e-05
0.2-0.3	9.8108482638e-04	1.9735286958e-03	2.4284490121e-03	3.1514572114e-04	5.4148679283e-04	8.7419236931e-04	3.4796632578e-04	1.1094225304e-05	4.5726675734e-04	5.5203446218e-04	3.7105443163e-04	8.4529965586e-04	1.0803298866e-03	9.6485032213e-05	3.6879367818e-04	1.8142710320e-04	1.5623054833e-05
0.3-0.4	5.4831470763e-04	1.3230944003e-03	3.1514572114e-04	1.8463676552e-03	2.0465018740e-04	3.4280606861e-04	3.3011907098e-04	1.3124973083e-04	2.7548288136e-04	1.8260604421e-04	3.4226127162e-04	3.2574441845e-04	6.1529087007e-04	-1.0097812600e-05	1.3464312769e-04	6.4169522103e-05	5.6781941900e-06
0.4-0.5	1.2667125991e-03	1.7714256896e-03	5.4148679283e-04	2.0465018740e-04	1.9783515132e-03	4.1204724103e-04	-1.4204253656e-05	1.8606144832e-04	3.1764835898e-04	2.3935320979e-04	1.2344809597e-04	5.4813120728e-04	8.7711685418e-04	1.4591301184e-04	2.6748661859e-04	9.2354442936e-05	-2.8970850413e-06
0.5-0.6	1.0395214867e-03	3.0547972197e-03	8.7419236931e-04	3.4280606861e-04	4.1204724103e-04	3.9588244773e-03	1.0824881592e-04	-3.0937353122e-05	9.8993808571e-06	7.6087865257e-04	8.7720870743e-04	9.4806939535e-04	1.4768156948e-03	2.7224201733e-04	4.4325661446e-04	3.2873266268e-04	4.8982880641e-05
0.6-0.7	-2.4584991851e-04	6.4417954553e-04	3.4796610278e-04	3.3011907098e-04	-1.4204253656e-05	1.0824881592e-04	1.6588625793e-03	-2.4431515894e-04	1.3374837887e-04	1.3020454407e-04	3.5696383297e-04	3.2242809986e-04	4.1754143694e-04	-1.6699429216e-04	6.7087244805e-05	1.2336801527e-04	1.9464303120e-05
0.7-0.8	4.1294854907e-04	7.4183995588e-04	1.1094225304e-05	1.3124973083e-04	1.8606144832e-04	-3.0937353122e-05	-2.4431515894e-04	1.3672714266e-03	-1.3918713449e-06	-1.4978093289e-04	2.2197206735e-05	-7.7997144584e-05	5.5676748411e-05	5.0051536175e-05	3.3469781199e-05	-1.1219089144e-04	-1.2888910020e-05
0.8-0.9	5.0112751797e-04	9.8764435668e-04	4.5726675734e-04	2.7548288136e-04	3.1764835898e-04	9.8993808571e-06	1.3374837887e-04	-1.3918713449e-06	1.2330584990e-03	2.9755664733e-05	3.7258208619e-05	3.1446126294e-04	4.0395037788e-04	3.5588958271e-05	1.5489374392e-04	2.0036539032e-05	-3.4192336197e-06
0.9-1.0	4.3595848857e-04	1.1608803095e-03	5.5203446218e-04	1.8260604421e-04	2.3935320979e-04	7.6087865257e-04	1.3020454407e-04	-1.4978093289e-04	2.9755664733e-05	1.2405024025e-03	1.5824496998e-04	4.8363550101e-04	4.2027423944e-04	1.4162374232e-03	9.3156778591e-04	1.5824957403e-04	1.5080149624e-05
1.0-1.1	1.1505065312e-04	1.1946084864e-03	3.7105443163e-04	3.4226127162e-04	1.2344809597e-04	8.7720870743e-04	3.5696383297e-04	2.2197206735e-05	3.7258208619e-05	1.5824496998e-04	1.2163023120e-03	2.4377623444e-04	5.3270470403e-04	-3.9623150973e-05	1.1892277742e-04	1.4994059038e-04	2.1753162686e-05
1.1-1.2	8.7810130469e-04	1.7885731840e-03	8.4542996558e-04	3.2574441845e-04	5.4813120728e-04	1.4768156948e-03	3.2242809986e-04	-7.7997144584e-05	3.1446126294e-04	4.8363550101e-04	2.4377623444e-04	1.4162374232e-03	9.5136778591e-04	1.1161508279e-04	5.5592409977e-04	2.0997133176e-04	2.2929101250e-05
1.2-1.3	1.4425334507e-03	2.7163191449e-03	1.0803298866e-03	6.1529087007e-04	8.7711685418e-04	4.0395037788e-04	4.1754143694e-04	5.5676748411e-05	4.0395037788e-04	4.2027423944e-04	5.3270470403e-04	9.5136778591e-04	2.0121591227e-03	1.2413812530e-04	4.2369091384e-04	2.9017723471e-04	2.6134612386e-05
1.3-1.4	4.0386306703e-04	5.1263808511e-04	9.6485032213e-05	-1.0097812600e-05	1.4591301184e-04	2.7224201733e-04	-1.6699429216e-04	5.0051536175e-05	3.5588958271e-05	8.6910896735e-05	-3.9623150973e-05	1.1161508279e-04	1.2413812530e-04	5.7353016030e-04	5.5152797820e-05	-2.6700869539e-05	-3.0914248017e-06
1.4-1.5	5.1101188338e-04	8.9472158000e-04	3.6879367818e-04	1.3464312769e-04	2.6748661859e-04	4.4325661446e-04	6.7087244805e-05	3.3469781199e-05	1.5489374392e-04	1.9502600263e-04	1.1892277742e-04	5.5592409977e-04	4.2369091384e-04	5.5152797820e-05	4.8743827108e-04	1.9362125543e-05	6.3229653117e-06
1.5-1.6	6.5040953776e-05	3.3107456949e-04	1.8142710320e-04	6.4169522103e-05	9.2354442936e-05	3.2873266268e-04	1.2336801527e-04	-1.1219089144e-04	2.0036539032e-05	1.2196190206e-04	1.4994059038e-04	2.0997133176e-04	2.9017723471e-04	-2.6700869539e-05	1.9362125543e-05	3.2140920060e-04	6.6612800759e-06
1.6-2.5	-8.1480504436e-08	3.0829514196e-05	1.5623054833e-05	5.6781941900e-06	-2.8970850413e-06	4.8982880641e-05	1.9464303120e-05	-1.2888910020e-05	-3.4192336197e-06	1.5080149624e-05	2.1753162686e-05	2.2929101250e-05	2.6134612386e-05	-3.0914248017e-06	6.3229653117e-06	6.6612800759e-06	5.8044972300e-06

TABLE G.36: Covariance matrix of the relative cross section as function of $y_{t\bar{t}}$, accounting for the statistical and systematic uncertainties.

bin [GeV]	0.0-0.3	0.3-0.6	0.6-0.9	0.9-1.2	1.2-1.5	1.5-2.5
0.0-0.3	8.3466188942e-04	-7.2596536143e-05	-4.8462278437e-05	9.2143329586e-05	4.7817540462e-04	5.9476996184e-05
0.3-0.6	-7.2596536143e-05	3.0390668844e-04	-6.7146794647e-05	-4.4770842015e-05	-1.6627985413e-05	-9.5618641962e-06
0.6-0.9	-4.8462278437e-05	-6.7146794647e-05	3.2735470080e-04	1.1849495123e-05	-2.5563910225e-05	-1.0559228360e-05
0.9-1.2	9.2143329586e-05	-4.4770842015e-05	1.1849495123e-05	5.9231485125e-04	3.3730340203e-04	-2.6928886533e-07
1.2-1.5	4.7817540462e-04	-1.6627985413e-05	-2.5563910225e-05	3.3730340203e-04	1.0357296280e-03	6.1682032550e-05
1.5-2.5	5.9476996184e-05	-9.5618641962e-06	-1.0559228360e-05	-2.6928886533e-07	6.1682032550e-05	2.8215492736e-05

TABLE G.37: Covariance matrix of the relative cross section as function of y_{top2}, accounting for the statistical and systematic uncertainties.

bin [GeV]	0-450	450-525	525-600	600-675	675-750	750-825	825-900	900-1000	1000-1100	1100-1200	1200-1400	1400-3200
0-450	6.5886341945e-10	2.7893541722e-09	1.3166600597e-09	-7.9956154949e-10	-1.5787341829e-09	-1.6007226463e-09	-9.8666617548e-10	-8.1615419250e-10	-4.3804021267e-10	-2.8198727089e-10	-1.3828103702e-10	-1.2517287521e-11
450-525	2.7893541722e-09	2.2840500709e-08	8.3347829628e-09	-2.9349031316e-09	-7.3153641528e-09	-8.3725940552e-09	-4.2926409387e-09	-3.4461075553e-09	-1.8349751535e-09	-6.8117830029e-10	-4.5739979154e-10	-4.6041439091e-11
525-600	1.3166600597e-09	8.3347829628e-09	1.3052583371e-08	-2.5599581548e-09	-5.0615353783e-09	-5.6873542471e-09	-2.2382815203e-09	-1.9354356918e-09	-1.2417532396e-09	-4.9403957633e-10	-2.3079505349e-10	-2.5651449032e-11
600-675	-7.9956154949e-10	-2.9349031316e-09	-2.5599581548e-09	1.0031832125e-08	3.2862958094e-09	2.4664170899e-09	2.4567018716e-09	1.9227062366e-09	1.2696009365e-09	1.5355398665e-09	4.7292847065e-10	4.2381361782e-11
675-750	-1.5787341829e-09	-7.3153641528e-09	-5.0615353783e-09	3.2862958094e-09	9.7534698486e-09	4.5117219172e-09	3.1645230592e-09	3.0956196643e-09	2.2783260763e-09	1.3502457742e-09	8.3822720088e-10	6.1982282534e-11
750-825	-1.6007226463e-09	-8.3725940552e-09	-5.6873542471e-09	2.4664170899e-09	4.5117219172e-09	8.5810945080e-09	2.4562953526e-09	2.1974216330e-09	1.5260150984e-09	9.4048249076e-10	4.6066085417e-10	2.8912581053e-11
825-900	-9.8666617548e-10	-4.2926409387e-09	-2.2382815203e-09	2.4567018716e-09	3.1645230592e-09	2.4562953526e-09	4.8267768242e-09	2.3599159239e-09	1.2383403969e-09	1.1542207789e-09	5.8004674068e-10	5.0649284345e-11
900-1000	-8.1615419250e-10	-3.4461075553e-09	-1.9354356918e-09	1.9227062366e-09	3.0956196643e-09	2.1974216330e-09	2.3599159239e-09	3.3450218641e-09	1.3347917504e-09	8.2981765096e-10	5.9568695854e-10	4.1572965516e-11
1000-1100	-4.3804021267e-10	-1.8349751535e-09	-1.2417532396e-09	1.2696009365e-09	2.2783260763e-09	1.5260150984e-09	1.2383403969e-09	1.3347917504e-09	1.6033518164e-09	5.8700078577e-10	4.2032464702e-10	2.7140574750e-11
1100-1200	-2.8198727089e-10	-6.8117830029e-10	-4.9403957633e-10	1.5355398665e-09	1.3502457742e-09	9.4048249076e-10	1.1542207789e-09	8.2981765096e-10	5.8700078577e-10	8.8333919534e-10	2.1523574716e-10	1.9375452357e-11
1200-1400	-1.3828103702e-10	-4.5739979154e-10	-2.3079505349e-10	4.7292847065e-10	8.3822720088e-10	4.6066085417e-10	5.8004674068e-10	5.9568695854e-10	4.2032464702e-10	2.1523574716e-10	2.8268330654e-10	1.0387631111e-11
1400-3200	-1.2517287521e-11	-4.6041439091e-11	-2.5651449032e-11	4.2381361782e-11	6.1982282534e-11	2.8912581053e-11	5.0649284345e-11	4.1572965516e-11	2.7140574750e-11	1.9375452357e-11	1.0387631111e-11	1.4954934683e-12

TABLE G.38: Covariance matrix of the relative cross section as function of $m_{t\bar{t}}$, accounting for the statistical and systematic uncertainties.

Bibliography

[1] T. Muta. *Foundations Of Quantum Chromodynamics: An Introduction to Perturbative Methods in Gauge Theories*. 3rd ed. World Scientific Lecture Notes in Physics. World Scientific Publishing Company, 2009. ISBN: 9812793542.

[2] Guido Altarelli. *Collider Physics within the Standard Model: a Primer*. 2013. arXiv: 1303.2842 [hep-ph].

[3] Günther Dissertori, Ian G. Knowles, and Michael Schmelling. *Quantum Chromodynamics: High Energy Experiments and Theory (International Series of Monographs on Physics)*. Oxford University Press, 2009. ISBN: 0199566410.

[4] R. K. Ellis, W. J. Stirling, and B. R. Webber. *QCD and Collider Physics (Cambridge Monographs on Particle Physics, Nuclear Physics and Cosmology)*. Cambridge University Press, 2003.

[5] Steven Weinberg. "The Making of the standard model". In: *Eur. Phys. J.* C34 (2004). DOI: 10.1142/9789812567147_0005, 10.1140/epjc/s2004-01761-1. arXiv: hep-ph/0401010 [hep-ph].

[6] F. Pisano and N. O. Reis. "Natural units, numbers and numerical clusters". In: (2001). arXiv: hep-ph/0112097 [hep-ph].

[7] Robert N. Cahn and Gerson Goldhaber. *The Experimental Foundations of Particle Physics*. Cambridge University Press, 2009. ISBN: 0521521475.

[8] Lyndon Evans and Philip Bryant. "LHC Machine". In: *JINST* 3 (2008), S08001. DOI: 10.1088/1748-0221/3/08/S08001.

[9] C. Patrignani et al. "Review of Particle Physics". In: *Chin. Phys.* C40.10 (2016), p. 100001. DOI: 10.1088/1674-1137/40/10/100001.

[10] Y. Fukuda et al. "Evidence for oscillation of atmospheric neutrinos". In: *Phys. Rev. Lett.* 81 (1998), pp. 1562–1567. DOI: 10.1103/PhysRevLett.81.1562. arXiv: hep-ex/9807003 [hep-ex].

[11] F. Englert and R. Brout. "Broken Symmetry and the Mass of Gauge Vector Mesons". In: *Physical Review Letters* 13 (Aug. 1964), pp. 321–323. DOI: 10.1103/PhysRevLett.13.321.

[12] P. W. Higgs. "Broken Symmetries and the Masses of Gauge Bosons". In: *Physical Review Letters* 13 (Oct. 1964), pp. 508–509. DOI: 10.1103/PhysRevLett.13.508.

[13] Murray Gell-Mann. "Symmetries of Baryons and Mesons". In: *Phys. Rev.* 125 (3 1962), pp. 1067–1084. DOI: 10.1103/PhysRev.125.1067. URL: https://link.aps.org/doi/10.1103/PhysRev.125.1067.

[14] Franz Mandl and Graham Shaw. *Quantum Field Theory*. Wiley, 2010. ISBN: 0471496847.

[15] A. Ali, E. Pietarinen, and W.J. Stirling. "Transverse energy-energy correlations: A test of perturbative QCD for the proton-antiproton collider". In: *Physics Letters B* 141.5 (1984), pp. 447 –454. ISSN: 0370-2693. DOI: https://doi.org/10.1016/0370-2693(84)90283-1. URL: http://www.sciencedirect.com/science/article/pii/0370269384902831.

[16] Morad Aaboud et al. "Determination of the strong coupling constant α_s from transverse energy–energy correlations in multijet events at $\sqrt{s} = 8$ TeV using the ATLAS detector". In: *Eur. Phys. J.* C77.12 (2017), p. 872. DOI: 10.1140/epjc/s10052-017-5442-0. arXiv: 1707.02562 [hep-ex].

[17] Sheldon L. Glashow. "Partial-symmetries of weak interactions". In: *Nuclear Physics* 22.4 (1961), pp. 579 –588. ISSN: 0029-5582. DOI: https://doi.org/10.1016/0029-5582(61)90469-2. URL: http://www.sciencedirect.com/science/article/pii/0029558261904692.

[18] Steven Weinberg. "A Model of Leptons". In: *Phys. Rev. Lett.* 19 (21 1967), pp. 1264–1266. DOI: 10.1103/PhysRevLett.19.1264. URL: https://link.aps.org/doi/10.1103/PhysRevLett.19.1264.

[19] Abdus Salam. "Weak and Electromagnetic Interactions". In: *Conf. Proc.* C680519 (1968), pp. 367–377.

[20] F. J. Hasert et al. "Observation of Neutrino Like Interactions Without Muon Or Electron in the Gargamelle Neutrino Experiment". In: *Phys. Lett.* B46 (1973). [,5.15(1973)], pp. 138–140. DOI: 10.1016/0370-2693(73)90499-1.

[21] J. Alcaraz et al. "A Combination of preliminary electroweak measurements and constraints on the standard model". In: (2006). arXiv: hep-ex/0612034 [hep-ex].

[22] The ATLAS collaboration. "Observation of a new particle in the search for the Standard Model Higgs boson with the ATLAS detector at the LHC". In: *Phys. Lett.* (2012). DOI: 10.1016/j.physletb.2012.08.020.

[23] The CMS collaboration. "Observation of a new boson at a mass of 125 GeV with the CMS experiment at the LHC". In: *Phys. Lett.* (2012). DOI: 10.1016/j.physletb.2012.08.021.

[24] The ATLAS collaboration. "Measurements of the Higgs boson production and decay rates and constraints on its couplings from a combined ATLAS and CMS analysis of the LHC pp collision data at $\sqrt{s} =$ 7 and 8 TeV". In: *JHEP* (2016). DOI: 10.1007/JHEP08(2016)045.

[25] Enrico Fermi. *Nuclear Physics: A Course Given by Enrico Fermi at the University of Chicago*. University of Chicago Press, 1974. ISBN: 0226243656.

[26] John C. Collins, Davison E. Soper, and George F. Sterman. "Factorization of Hard Processes in QCD". In: *Adv. Ser. Direct. High Energy Phys.* 5 (1989), pp. 1–91. DOI: 10.1142/9789814503266_0001. arXiv: hep-ph/0409313 [hep-ph].

[27] Guido Altarelli and G. Parisi. "Asymptotic Freedom in Parton Language". In: *Nucl. Phys.* B126 (1977), pp. 298–318. DOI: 10.1016/0550-3213(77)90384-4.

[28] L. A. Harland-Lang et al. "Parton distributions in the LHC era: MMHT 2014 PDFs". In: *Eur. Phys. J.* C75.5 (2015), p. 204. DOI: 10.1140/epjc/s10052-015-3397-6. arXiv: 1412.3989 [hep-ph].

[29] Sayipjamal Dulat et al. "New parton distribution functions from a global analysis of quantum chromodynamics". In: *Phys. Rev.* D93.3 (2016), p. 033006. DOI: 10.1103/PhysRevD.93.033006. arXiv: 1506.07443 [hep-ph].

[30] Richard D. Ball et al. "Parton distributions for the LHC Run II". In: *JHEP* 04 (2015), p. 040. DOI: 10.1007/JHEP04(2015)040. arXiv: 1410.8849 [hep-ph].

[31] H. Abramowicz et al. "Combination of measurements of inclusive deep inelastic $e^{\pm}p$ scattering cross sections and QCD analysis of HERA data". In: *Eur. Phys. J.* C75.12 (2015), p. 580. DOI: 10.1140/epjc/s10052-015-3710-4. arXiv: 1506.06042 [hep-ex].

[32] S. Alekhin, J. Blumlein, and S. Moch. "The ABM parton distributions tuned to LHC data". In: *Phys. Rev.* D89.5 (2014), p. 054028. DOI: 10.1103/PhysRevD.89.054028. arXiv: 1310.3059 [hep-ph].

[33] Pedro Jimenez-Delgado and Ewald Reya. "Delineating parton distributions and the strong coupling". In: *Phys. Rev.* D89.7 (2014), p. 074049. DOI: 10.1103/PhysRevD.89.074049. arXiv: 1403.1852 [hep-ph].

[34] J. F. Owens, A. Accardi, and W. Melnitchouk. "Global parton distributions with nuclear and finite-Q^2 corrections". In: *Phys. Rev.* D87.9 (2013), p. 094012. DOI: 10.1103/PhysRevD.87.094012. arXiv: 1212.1702 [hep-ph].

[35] Jon Butterworth et al. "PDF4LHC recommendations for LHC Run II". In: *J. Phys.* G43 (2016), p. 023001. DOI: 10.1088/0954-3899/43/2/023001. arXiv: 1510.03865 [hep-ph].

[36] Oliver Sim Brüning et al. *LHC Design Report*. CERN Yellow Reports: Monographs. Geneva: CERN, 2004. URL: https://cds.cern.ch/record/782076.

[37] F. Abe et al. "Observation of top quark production in $\bar{p}p$ collisions". In: *Phys. Rev. Lett.* 74 (1995), pp. 2626–2631. DOI: 10.1103/PhysRevLett.74.2626. arXiv: hep-ex/9503002 [hep-ex].

[38] S. Abachi et al. "Observation of the top quark". In: *Phys. Rev. Lett.* 74 (1995), pp. 2632–2637. DOI: 10.1103/PhysRevLett.74.2632. arXiv: hep-ex/9503003 [hep-ex].

[39] S. W. Herb et al. "Observation of a Dimuon Resonance at 9.5 GeV in 400-GeV Proton-Nucleus Collisions". In: *Phys. Rev. Lett.* 39 (5 1977), pp. 252–255. DOI: 10.1103/PhysRevLett.39.252. URL: https://link.aps.org/doi/10.1103/PhysRevLett.39.252.

[40] The CDF Collaboration. "Lower limit on the top-quark mass from events with two leptons in $p\bar{p}$ collisions at $\sqrt{s}$ =1.8 TeV". In: *Phys. Rev. Lett.* 68 (4 1992), pp. 447–451. DOI: 10.1103/PhysRevLett.68.

447. URL: https://link.aps.org/doi/10.1103/PhysRevLett.68.447.

[41] *LHC Top Physics Working Group*. https://twiki.cern.ch/twiki/bin/view/LHCPhysics/LHCTopWG. Accessed: 08-08-2018.

[42] S. Alekhin, A. Djouadi, and S. Moch. "The top quark and Higgs boson masses and the stability of the electroweak vacuum". In: *Phys. Lett.* B716 (2012), pp. 214–219. DOI: 10.1016/j.physletb.2012.08.024. arXiv: 1207.0980 [hep-ph].

[43] "First combination of Tevatron and LHC measurements of the top-quark mass". In: (2014). arXiv: 1403.4427 [hep-ex].

[44] Jun Gao, Chong Sheng Li, and Hua Xing Zhu. "Top-Quark Decay at Next-to-Next-to-Leading Order in QCD". In: *Phys. Rev. Lett.* 110 (4 2013), p. 042001. DOI: 10.1103/PhysRevLett.110.042001. URL: https://link.aps.org/doi/10.1103/PhysRevLett.110.042001.

[45] Andrzej Czarnecki, Jurgen G. Korner, and Jan H. Piclum. "Helicity fractions of W bosons from top quark decays at NNLO in QCD". In: *Phys. Rev.* D81 (2010), p. 111503. DOI: 10.1103/PhysRevD.81.111503. arXiv: 1005.2625 [hep-ph].

[46] Michal Czakon, Paul Fiedler, and Alexander Mitov. "Total Top-Quark Pair-Production Cross Section at Hadron Colliders Through $O(\alpha_S^4)$". In: *Phys. Rev. Lett.* 110 (2013), p. 252004. DOI: 10.1103/PhysRevLett.110.252004. arXiv: 1303.6254 [hep-ph].

[47] The ATLAS Collaboration. "Measurement of the $t\bar{t}$ production cross-section using eμ events with b-tagged jets in pp collisions at s=13TeV with the ATLAS detector". In: *Physics Letters B* 761 (2016), pp. 136–157. ISSN: 0370-2693. DOI: https://doi.org/10.1016/j.physletb.2016.08.019. URL: http://www.sciencedirect.com/science/article/pii/S0370269316304397.

[48] Vardan Khachatryan et al. "Measurement of the $t\bar{t}$ production cross section using events in the eμ final state in pp collisions at $\sqrt{s} =$ 13 TeV". In: *Eur. Phys. J.* C77 (2017), p. 172. DOI: 10.1140/epjc/s10052-017-4718-8. arXiv: 1611.04040 [hep-ex].

[49] Werner Bernreuther and Zong-Guo Si. "Top quark and leptonic charge asymmetries for the Tevatron and LHC". In: *Phys. Rev.* D86 (2012), p. 034026. DOI: 10.1103/PhysRevD.86.034026. arXiv: 1205.6580 [hep-ph].

[50] Georges Aad et al. "Measurements of the charge asymmetry in top-quark pair production in the dilepton final state at $\sqrt{s} = 8$ TeV with the ATLAS detector". In: *Phys. Rev.* D94.3 (2016), p. 032006. DOI: 10.1103/PhysRevD.94.032006. arXiv: 1604.05538 [hep-ex].

[51] Vardan Khachatryan et al. "Measurements of $t\bar{t}$ charge asymmetry using dilepton final states in pp collisions at $\sqrt{s} = 8$ TeV". In: *Phys. Lett.* B760 (2016), pp. 365–386. DOI: 10.1016/j.physletb.2016.07.006. arXiv: 1603.06221 [hep-ex].

[52] G. Bachy et al. "The LEP collider". In: *Part. Accel.* 26 (1990), pp. 19–32.

[53] The ATLAS Collaboration. *LuminosityPublicResults*. https://twiki.cern.ch/twiki/bin/view/AtlasPublic/LuminosityPublicResults. Accessed: 17-09-2018.

[54] The ATLAS Collaboration. *LuminosityPublicResultsRun2*. https://twiki.cern.ch/twiki/bin/view/AtlasPublic/LuminosityPublicResultsRu Accessed: 17-09-2018.

[55] Esma Mobs. "The CERN accelerator complex - August 2018. Complexe des accélérateurs du CERN - Août 2018". In: (2018). General Photo. URL: https://cds.cern.ch/record/2636343.

[56] The ALICE collaboration. "The ALICE experiment at the CERN LHC". In: *JINST* 3 (2008). DOI: 10.1088/1748-0221/3/08/S08002.

[57] The ATLAS collaboration. "The ATLAS Experiment at the CERN Large Hadron Collider". In: *JINST* 3 (2008). DOI: 10.1088/1748-0221/3/08/S08003.

[58] The CMS collaboration. "The CMS Experiment at the CERN LHC". In: *JINST* 3 (2008). DOI: 10.1088/1748-0221/3/08/S08004.

[59] The LHCb collaboration. "The LHCb Detector at the LHC". In: *JINST* 3 (2008). DOI: 10.1088/1748-0221/3/08/S08005.

[60] The LHCf collaboration. "The LHCf detector at the CERN Large Hadron Collider". In: *JINST* 3 (2008). DOI: 10.1088/1748-0221/3/08/S08006.

[61] The TOTEM collaboration. "The TOTEM experiment at the CERN Large Hadron Collider". In: *JINST* 3 (2008). DOI: 10.1088/1748-0221/3/08/S08007.

[62] The MoEDAL collaboration. "The MoEDAL Experiment at the LHC - a New Light on the Terascale Frontier". In: *J. Phys. Conf. Ser.* 631.1 (2015). DOI: 10.1088/1742-6596/631/1/012014.

[63] I Bird et al. *Update of the Computing Models of the WLCG and the LHC Experiments*. Tech. rep. CERN-LHCC-2014-014. LCG-TDR-002. 2014. URL: https://cds.cern.ch/record/1695401.

[64] "Legal Service: Memorandum of Understanding for collaboration in the deployment and exploitation of the Worldwide LHC Computing Grid between the European Organization for Nuclear Research and all the Institutions participating in the provision of the Worldwide LHC Computing Grid - Participation of the University of Malaya". URL: https://cds.cern.ch/record/2020763.

[65] The WLCG Project. *WLCG Document repository*. http://wlcg-docs.web.cern.ch/wlcg-docs/. Accessed: 17-09-2018.

[66] Jean-Luc Caron. "ATLAS detector in A4 format with English captions.. Détecteur ATLAS format A4 avec légende et caractéristiques en anglais." AC Collection. Legacy of AC. Pictures from 1992 to 2002. 1998. URL: https://cds.cern.ch/record/841458.

[67] Ketevi Assamagan. "A Hierarchical Software Identifier Scheme for the ATLAS Muon Spectrometer". In: (Nov. 2018).

[68] *ATLAS magnet system: Technical Design Report, 1*. Technical Design Report ATLAS. Geneva: CERN, 1997. URL: https://cds.cern.ch/record/338080.

[69] *Track Reconstruction Performance of the ATLAS Inner Detector at* $\sqrt{s} = 13$ *TeV*. Tech. rep. ATL-PHYS-PUB-2015-018. Geneva: CERN, 2015. URL: http://cds.cern.ch/record/2037683.

[70] M Capeans et al. *ATLAS Insertable B-Layer Technical Design Report*. Tech. rep. CERN-LHCC-2010-013. ATLAS-TDR-19. 2010. URL: https://cds.cern.ch/record/1291633.

[71] The ATLAS Collaboration. *TDAQPublicResults*. https://twiki.cern.ch/twiki/bin/view/AtlasPublic/ApprovedPlotsDAQ. Accessed: 17-09-2018.

[72] Morad Aaboud et al. "Performance of the ATLAS Trigger System in 2015". In: *Eur. Phys. J.* C77.5 (2017), p. 317. DOI: 10.1140/epjc/s10052-017-4852-3. arXiv: 1611.09661 [hep-ex].

[73] *ATLAS Phase-II Upgrade Scoping Document*. Tech. rep. CERN-LHCC-2015-020. LHCC-G-166. Geneva: CERN, 2015. URL: http://cds.cern.ch/record/2055248.

[74] *Letter of Intent for the Phase-I Upgrade of the ATLAS Experiment*. Tech. rep. CERN-LHCC-2011-012. LHCC-I-020. Geneva: CERN, 2011. URL: https://cds.cern.ch/record/1402470.

[75] T Kawamoto et al. *New Small Wheel Technical Design Report*. Tech. rep. CERN-LHCC-2013-006. ATLAS-TDR-020. ATLAS New Small Wheel Technical Design Report. 2013. URL: http://cds.cern.ch/record/1552862.

[76] M (CERN) Aleksa et al. *ATLAS Liquid Argon Calorimeter Phase-I Upgrade Technical Design Report*. Tech. rep. CERN-LHCC-2013-017. ATLAS-TDR-022. Final version presented to December 2013 LHCC. 2013. URL: http://cds.cern.ch/record/1602230.

[77] M Shochet et al. *Fast TracKer (FTK) Technical Design Report*. Tech. rep. CERN-LHCC-2013-007. ATLAS-TDR-021. ATLAS Fast Tracker Technical Design Report. 2013. URL: http://cds.cern.ch/record/1552953.

[78] The ATLAS Collaboration. *Technical Design Report for the Phase-I Upgrade of the ATLAS TDAQ System*. Tech. rep. CERN-LHCC-2013-018. ATLAS-TDR-023. Final version presented to December 2013 LHCC. 2013. URL: http://cds.cern.ch/record/1602235.

[79] ATLAS Collaboration. *Technical Design Report for the ATLAS Inner Tracker Strip Detector*. Tech. rep. CERN-LHCC-2017-005. ATLAS-TDR-025. Geneva: CERN, 2017. URL: http://cds.cern.ch/record/2257755.

[80] ATLAS Collaboration. *Technical Design Report for the ATLAS Inner Tracker Pixel Detector*. Tech. rep. CERN-LHCC-2017-021. ATLAS-TDR-030. Geneva: CERN, 2017. URL: https://cds.cern.ch/record/2285585.

[81] ATLAS Collaboration. *Technical Design Report for the Phase-II Upgrade of the ATLAS Tile Calorimeter*. Tech. rep. CERN-LHCC-2017-019. ATLAS-TDR-028. Geneva: CERN, 2017. URL: http://cds.cern.ch/record/2285583.

[82] ATLAS Collaboration. *Technical Design Report for the Phase-II Upgrade of the ATLAS LAr Calorimeter*. Tech. rep. CERN-LHCC-2017-018. ATLAS-TDR-027. Geneva: CERN, 2017. URL: http://cds.cern.ch/record/2285582.

[83] ATLAS Collaboration. *Technical Proposal: A High-Granularity Timing Detector for the ATLAS Phase-II Upgrade*. Tech. rep. CERN-LHCC-2018-023. LHCC-P-012. Geneva: CERN, 2018. URL: http://cds.cern.ch/record/2623663.

[84] ATLAS Collaboration. *Technical Design Report for the Phase-II Upgrade of the ATLAS Muon Spectrometer*. Tech. rep. CERN-LHCC-2017-017. ATLAS-TDR-026. Geneva: CERN, 2017. URL: http://cds.cern.ch/record/2285580.

[85] ATLAS Collaboration. *Technical Design Report for the Phase-II Upgrade of the ATLAS TDAQ System*. Tech. rep. CERN-LHCC-2017-020. ATLAS-TDR-029. Geneva: CERN, 2017. URL: https://cds.cern.ch/record/2285584.

[86] S. Agostinelli et al. "Geant4—a simulation toolkit". In: *Nuclear Instruments and Methods in Physics Research Section A: Accelerators, Spectrometers, Detectors and Associated Equipment* 506.3 (2003), pp. 250 –303. ISSN: 0168-9002. DOI: https://doi.org/10.1016/S0168-9002(03)01368-8. URL: http://www.sciencedirect.com/science/article/pii/S0168900203013688.

[87] M. Aaboud et al. "Reconstruction of primary vertices at the ATLAS experiment in Run 1 proton–proton collisions at the LHC". In: *The European Physical Journal C* 77.5 (2017), p. 332. ISSN: 1434-6052. DOI: 10.1140/epjc/s10052-017-4887-5. URL: https://doi.org/10.1140/epjc/s10052-017-4887-5.

[88] E. Bouhova-Thacker et al. "Vertex reconstruction in the ATLAS experiment at the LHC". In: *2008 IEEE Nuclear Science Symposium Conference Record*. 2008, pp. 1720–1727. DOI: 10.1109/NSSMIC.2008.4774734.

[89] G. Aad et al. "Performance of pile-up mitigation techniques for jets in $$pp$$ppcollisions at $\sqrt{s} = 8$ TeV using the ATLAS detector". In: *The European Physical Journal C* 76.11 (2016), p. 581. ISSN: 1434-6052. DOI: 10.1140/epjc/s10052-016-4395-z. URL: https://doi.org/10.1140/epjc/s10052-016-4395-z.

[90] Atlas Collaboration et al. "Jet energy measurement and its systematic uncertainty in proton–proton collisions at $\sqrt{s} = 7$ TeV with the ATLAS detector". In: *The European Physical Journal C* 75.1 (2015), p. 17. ISSN: 1434-6052. DOI: 10.1140/epjc/s10052-014-3190-y. URL: https://doi.org/10.1140/epjc/s10052-014-3190-y.

[91] Matteo Cacciari, Gavin P. Salam, and Gregory Soyez. "FastJet User Manual". In: *Eur. Phys. J.* C72 (2012), p. 1896. DOI: 10.1140/epjc/s10052-012-1896-2. arXiv: 1111.6097 [hep-ph].

[92] Stefan Weinzierl. "Introduction to Monte Carlo methods". In: (2000). arXiv: hep-ph/0006269 [hep-ph].

[93] Stefan Hoche. "Introduction to parton-shower event generators". In: *Proceedings, Theoretical Advanced Study Institute in Elementary Particle Physics: Journeys Through the Precision Frontier: Amplitudes for Colliders (TASI 2014): Boulder, Colorado, June 2-27, 2014*. 2015, pp. 235–295. DOI: 10.1142/9789814678766_0005. arXiv: 1411.4085 [hep-ph].

[94] Andy Buckley et al. "General-purpose event generators for LHC physics". In: *Phys. Rept.* 504 (2011), pp. 145–233. DOI: 10.1016/j.physrep.2011.03.005. arXiv: 1101.2599 [hep-ph].

[95] Ronald Kleiss and Roberto Pittau. "Weight optimization in multichannel Monte Carlo". In: *Comput. Phys. Commun.* 83 (1994), pp. 141–146. DOI: 10.1016/0010-4655(94)90043-4. arXiv: hep-ph/9405257 [hep-ph].

[96] John M. Campbell and R. Keith Ellis. "An Update on vector boson pair production at hadron colliders". In: *Phys. Rev.* D60 (1999), p. 113006. DOI: 10.1103/PhysRevD.60.113006. arXiv: hep-ph/9905386 [hep-ph].

[97] Stefano Frixione and Bryan R. Webber. "Matching NLO QCD computations and parton shower simulations". In: *Journal of High Energy Physics* 2002.06 (2002), p. 029. URL: http://stacks.iop.org/1126-6708/2002/i=06/a=029.

[98] T. Gleisberg et al. "Event generation with SHERPA 1.1". In: *JHEP* 02 (2009), p. 007. DOI: 10.1088/1126-6708/2009/02/007. arXiv: 0811.4622 [hep-ph].

[99] John C. Collins. "Sudakov form-factors". In: *Adv. Ser. Direct. High Energy Phys.* 5 (1989), pp. 573–614. DOI: 10.1142/9789814503266_0006. arXiv: hep-ph/0312336 [hep-ph].

[100] G. Marchesini and B. R. Webber. "Monte Carlo Simulation of General Hard Processes with Coherent QCD Radiation". In: *Nucl. Phys.* B310 (1988), pp. 461–526. DOI: 10.1016/0550-3213(88)90089-2.

[101] Torbjorn Sjostrand. "A Model for Initial State Parton Showers". In: *Phys. Lett.* 157B (1985), pp. 321–325. DOI: 10.1016/0370-2693(85)90674-4.

[102] Gosta Gustafson and Ulf Pettersson. "Dipole Formulation of QCD Cascades". In: *Nucl. Phys.* B306 (1988), pp. 746–758. DOI: 10.1016/0550-3213(88)90441-5.

[103] Torbjorn Sjostrand et al. "An Introduction to PYTHIA 8.2". In: *Comput. Phys. Commun.* 191 (2015), pp. 159–177. DOI: 10.1016/j.cpc.2015.01.024. arXiv: 1410.3012 [hep-ph].

[104] Johannes Bellm et al. "Herwig 7.0/Herwig++ 3.0 release note". In: *Eur. Phys. J.* C76.4 (2016), p. 196. DOI: 10.1140/epjc/s10052-016-4018-8. arXiv: 1512.01178 [hep-ph].

[105] Bo Andersson. *The Lund Model*. Cambridge Monographs on Particle Physics, Nuclear Physics and Cosmology. Cambridge University Press, 1998. DOI: 10.1017/CBO9780511524363.

[106] Bo Andersson et al. "Parton Fragmentation and String Dynamics". In: *Phys. Rept.* 97 (1983), pp. 31–145. DOI: 10.1016/0370-1573(83)90080-7.

[107] Bo Andersson, G. Gustafson, and B. Soderberg. "A General Model for Jet Fragmentation". In: *Z. Phys.* C20 (1983), p. 317. DOI: 10.1007/BF01407824.

[108] Torbjorn Sjostrand. "Jet Fragmentation of Nearby Partons". In: *Nucl. Phys.* B248 (1984), pp. 469–502. DOI: 10.1016/0550-3213(84)90607-2.

[109] D. Amati and G. Veneziano. "Preconfinement as a Property of Perturbative QCD". In: *Phys. Lett.* 83B (1979), pp. 87–92. DOI: 10.1016/0370-2693(79)90896-7.

[110] A. Bassetto, M. Ciafaloni, and G. Marchesini. "Color Singlet Distributions and Mass Damping in Perturbative QCD". In: *Phys. Lett.* 83B (1979), pp. 207–212. DOI: 10.1016/0370-2693(79)90687-7.

[111] Stephen Wolfram. "Parton and Hadron Production in e^+e^- Annihilation". In: *ELEMENTARY CONSTITUENTS AND HADRONIC STRUCTURE. PROCEEDINGS, 15TH RENCONTRES DE MORIOND, LES ARCS, FRANCE, MARCH 9-21, 1980. VOL. 1*. 1980, pp. 549–588. URL: http://www.stephenwolfram.com/publications/articles/particle/80-parton.

[112] Torbjörn Sjöstrand and Maria van Zijl. "A multiple-interaction model for the event structure in hadron collisions". In: *Phys. Rev. D* 36 (7 1987), pp. 2019–2041. DOI: 10.1103/PhysRevD.36.2019. URL: https://link.aps.org/doi/10.1103/PhysRevD.36.2019.

[113] Peter Zeiler Skands. "Tuning Monte Carlo Generators: The Perugia Tunes". In: *Phys. Rev.* D82 (2010), p. 074018. DOI: 10.1103/PhysRevD.82.074018. arXiv: 1005.3457 [hep-ph].

[114] R. Corke and T. Sjöstrand. "Multiparton interactions and rescattering". In: *Journal of High Energy Physics* 2010.1 (2010), p. 35. ISSN: 1029-8479. DOI: 10.1007/JHEP01(2010)035. URL: https://doi.org/10.1007/JHEP01(2010)035.

[115] Peter Z. Skands and Daniel Wicke. "Non-perturbative QCD effects and the top mass at the Tevatron". In: *Eur. Phys. J.* C52 (2007), pp. 133–140. DOI: 10.1140/epjc/s10052-007-0352-1. arXiv: hep-ph/0703081 [HEP-PH].

[116] B. R. Webber. "Color reconnection and Bose-Einstein effects". In: *J. Phys.* G24 (1998), pp. 287–296. DOI: 10.1088/0954-3899/24/2/003. arXiv: hep-ph/9708463 [hep-ph].

[117] G. Aad et al. "The ATLAS Simulation Infrastructure". In: *Eur. Phys. J.* C70 (2010), pp. 823–874. DOI: 10.1140/epjc/s10052-010-1429-9. arXiv: 1005.4568 [physics.ins-det].

[118] *ATLAS Computing: technical design report*. Technical Design Report ATLAS. Geneva: CERN, 2005. URL: https://cds.cern.ch/record/837738.

[119] Matt Dobbs and Jorgen Beck Hansen. "The HepMC C++ Monte Carlo event record for High Energy Physics". In: *Comput. Phys. Commun.* 134 (2001), pp. 41–46. DOI: 10.1016/S0010-4655(00)00189-2.

[120] Geant4 Working Group. *Geant4 Public Gallery*. https://geant4.web.cern.ch/gallery. Accessed: 17-09-2018.

[121] E. Barberio et al. "The Geant4-Based ATLAS Fast Electromagnetic Shower Simulation". In: *Astroparticle, particle and space physics, detectors and medical physics applications. Proceedings, 10th Conference, ICATPP 2007, Como, Italy, October 8-12, 2007*. 2008, pp. 802–806. DOI: 10.1142/9789812819093_0133. URL: http://cdsweb.cern.ch/record/1064665/files/soft-conf-2007-002.pdf.

[122] E Barberio et al. "Fast shower simulation in the ATLAS calorimeter". In: *Journal of Physics: Conference Series* 119.3 (2008), p. 032008. URL: http://stacks.iop.org/1742-6596/119/i=3/a=032008.

[123] K. Edmonds et al. "The fast ATLAS track simulation (FATRAS)". In: (2008).

[124] Coll ATLAS et al. *The simulation principle and performance of the ATLAS fast calorimeter simulation FastCaloSim*. Tech. rep. ATL-PHYS-PUB-2010-013. Geneva: CERN, 2010. URL: https://cds.cern.ch/record/1300517.

[125] R. Brun and F. Rademakers. "ROOT: An object oriented data analysis framework". In: *Nucl. Instrum. Meth.* A389 (1997), pp. 81–86. DOI: 10.1016/S0168-9002(97)00048-X.

[126] ATLAS Collaboration. "Luminosity determination in pp collisions at $\sqrt{s}$ = 8 TeV using the ATLAS detector at the LHC". In: *ArXiv e-prints* (Aug. 2016). arXiv: 1608.03953 [hep-ex].

[127] The ATLAS collaboration. *Measurement of the luminosity with the new LUCID-2 detector in 2015*. Tech. rep. ATL-COM-FWD-2016-008. CERN, 2016. URL: https://cds.cern.ch/record/2154368.

[128] Stefano Frixione, Paolo Nason, and Carlo Oleari. "Matching NLO QCD computations with Parton Shower simulations: the POWHEG method". In: *JHEP* 11 (2007), p. 070. DOI: 10.1088/1126-6708/2007/11/070. arXiv: 0709.2092 [hep-ph].

[129] Stefano Carrazza et al. "An unbiased Hessian representation for Monte Carlo PDFs". In: *The European Physical Journal C* 75.8 (2015), p. 369. ISSN: 1434-6052. DOI: 10.1140/epjc/s10052-015-3590-7. URL: https://doi.org/10.1140/epjc/s10052-015-3590-7.

[130] Torbjörn Sjöstrand et al. "An introduction to PYTHIA 8.2". In: *Computer Physics Communications* 191 (2015), pp. 159 –177. ISSN: 0010-4655. DOI: https://doi.org/10.1016/j.cpc.2015.01.024. URL: http://www.sciencedirect.com/science/article/pii/S0010465515000442.

[131] *ATLAS Run 1 Pythia8 tunes*. Tech. rep. ATL-PHYS-PUB-2014-021. Geneva: CERN, 2014. URL: https://cds.cern.ch/record/1966419.

[132] Richard D. Ball et al. "Parton distributions with LHC data". In: *Nucl. Phys.* B867 (2013), pp. 244–289. DOI: 10.1016/j.nuclphysb.2012.10.003. arXiv: 1207.1303 [hep-ph].

[133] M. Bahr et al. "Herwig++ Physics and Manual". In: *Eur. Phys. J.* C58 (2008), pp. 639–707. DOI: 10.1140/epjc/s10052-008-0798-9. arXiv: 0803.0883 [hep-ph].

[134] J. Alwall et al. "The automated computation of tree-level and next-to-leading order differential cross sections, and their matching to parton shower simulations". In: *JHEP* 07 (2014), p. 079. DOI: 10.1007/JHEP07(2014)079. arXiv: 1405.0301 [hep-ph].

[135] Hung-Liang Lai et al. "New parton distributions for collider physics". In: *Phys. Rev.* D 82 (2010). DOI: 10.1103/PhysRevD.82.074024.

[136] Edmond L. Berger et al. "NNLO QCD Corrections to t-channel Single Top-Quark Production and Decay". In: *Phys. Rev.* D94.7 (2016), p. 071501. DOI: 10.1103/PhysRevD.94.071501. arXiv: 1606.08463 [hep-ph].

[137] Nikolaos Kidonakis. "Theoretical results for electroweak-boson and single-top production". In: *PoS* DIS2015 (2015), p. 170. DOI: 10.22323/1.247.0170. arXiv: 1506.04072 [hep-ph].

[138] M. Aaboud et al. "Performance of the ATLAS Track Reconstruction Algorithms in Dense Environments in LHC Run 2". In: *Eur. Phys. J.* C77.10 (2017), p. 673. DOI: 10.1140/epjc/s10052-017-5225-7. arXiv: 1704.07983 [hep-ex].

[139] Azriel Rosenfeld and John L. Pfaltz. "Sequential Operations in Digital Picture Processing". In: *J. ACM* 13.4 (Oct. 1966), pp. 471–494. ISSN: 0004-5411. DOI: 10.1145/321356.321357. URL: http://doi.acm.org/10.1145/321356.321357.

[140] R. Fruhwirth. "Application of Kalman filtering to track and vertex fitting". In: *Nucl. Instrum. Meth.* A262 (1987), pp. 444–450. DOI: 10.1016/0168-9002(87)90887-4.

[141] Georges Aad et al. "A neural network clustering algorithm for the ATLAS silicon pixel detector". In: *JINST* 9 (2014), P09009. DOI: 10.1088/1748-0221/9/09/P09009. arXiv: 1406.7690 [hep-ex].

[142] *Performance of the ATLAS Inner Detector Track and Vertex Reconstruction in the High Pile-Up LHC Environment*. Tech. rep. ATLAS-CONF-2012-042. Geneva: CERN, 2012. URL: https://cds.cern.ch/record/1435196.

[143] Morad Aaboud et al. "Charged-particle distributions at low transverse momentum in $\sqrt{s} = 13$ TeV pp interactions measured with the ATLAS detector at the LHC". In: *Eur. Phys. J.* C76.9 (2016), p. 502. DOI: 10.1140/epjc/s10052-016-4335-y. arXiv: 1606.01133 [hep-ex].

[144] Morad Aaboud et al. "Reconstruction of primary vertices at the ATLAS experiment in Run 1 proton–proton collisions at the LHC". In: *Eur. Phys. J.* C77.5 (2017), p. 332. DOI: 10.1140/epjc/s10052-017-4887-5. arXiv: 1611.10235 [physics.ins-det].

[145] G. Aad et al. "Charged-particle multiplicities in pp interactions measured with the ATLAS detector at the LHC". In: *New J. Phys.* 13 (2011), p. 053033. DOI: 10.1088/1367-2630/13/5/053033. arXiv: 1012.5104 [hep-ex].

[146] S. Boutle et al. "Primary vertex reconstruction at the ATLAS experiment". In: *J. Phys. Conf. Ser.* 898.4 (2017), p. 042056. DOI: 10.1088/1742-6596/898/4/042056.

[147] Tim Robertson and J. D. Cryer. "An Iterative Procedure for Estimating the Mode". In: *Journal of the American Statistical Association* 69.348 (1974), pp. 1012–1016. ISSN: 01621459. URL: http://www.jstor.org/stable/2286181.

[148] R Fruhwirth, Wolfgang Waltenberger, and Pascal Vanlaer. *Adaptive Vertex Fitting*. Tech. rep. CMS-NOTE-2007-008. Geneva: CERN, 2007. URL: https://cds.cern.ch/record/1027031.

[149] Morad Aaboud et al. "Measurement of the photon identification efficiencies with the ATLAS detector using LHC Run 2 data collected in 2015 and 2016". In: *Submitted to: Eur. Phys. J.* (2018). arXiv: 1810.05087 [hep-ex].

[150] Morad Aaboud et al. "Measurement of the photon identification efficiencies with the ATLAS detector using LHC Run-1 data". In: *Eur. Phys. J.* C76.12 (2016), p. 666. DOI: 10.1140/epjc/s10052-016-4507-9. arXiv: 1606.01813 [hep-ex].

[151] W Lampl et al. *Calorimeter Clustering Algorithms: Description and Performance*. Tech. rep. ATL-LARG-PUB-2008-002. ATL-COM-LARG-2008-003. Geneva: CERN, 2008. URL: https://cds.cern.ch/record/1099735.

[152] T Cornelissen et al. *Concepts, Design and Implementation of the ATLAS New Tracking (NEWT)*. Tech. rep. ATL-SOFT-PUB-2007-007. ATL-COM-SOFT-2007-002. Geneva: CERN, 2007. URL: https://cds.cern.ch/record/1020106.

[153] Thijs G. Cornelissen et al. "The global chi**2 track fitter in ATLAS". In: *J. Phys. Conf. Ser.* 119 (2008), p. 032013. DOI: 10.1088/1742-6596/119/3/032013.

[154] *Improved electron reconstruction in ATLAS using the Gaussian Sum Filter-based model for bremsstrahlung*. Tech. rep. ATLAS-CONF-2012-047. Geneva: CERN, 2012. URL: https://cds.cern.ch/record/1449796.

[155] *Electron and photon energy calibration with the ATLAS detector using data collected in 2015 at* $\sqrt{s} = 13$ TeV. Tech. rep. ATL-PHYS-PUB-2016-015. Geneva: CERN, 2016. URL: https://cds.cern.ch/record/2203514.

[156] James Saxon and Hugh H Williams. "Discovery of the Higgs Boson, Measurements of its Production, and a Search for Higgs Boson Pair Production". Presented 13 06 2014. 2014. URL: https://cds.cern.ch/record/1746004.

[157] Matteo Cacciari, Gavin P. Salam, and Gregory Soyez. "The Catchment Area of Jets". In: *JHEP* 04 (2008), p. 005. DOI: 10.1088/1126-6708/2008/04/005. arXiv: 0802.1188 [hep-ph].

[158] Matteo Cacciari, Gavin P. Salam, and Sebastian Sapeta. "On the characterisation of the underlying event". In: *JHEP* 04 (2010), p. 065. DOI: 10.1007/JHEP04(2010)065. arXiv: 0912.4926 [hep-ph].

[159] Matteo Cacciari and Gavin P. Salam. "Pileup subtraction using jet areas". In: *Phys. Lett.* B659 (2008), pp. 119–126. DOI: 10.1016/j.physletb.2007.09.077. arXiv: 0707.1378 [hep-ph].

[160] Andrea Valassi and Roberto Chierici. "Information and treatment of unknown correlations in the combination of measurements using the BLUE method". In: *Eur. Phys. J.* C74 (2014), p. 2717. DOI: 10.1140/epjc/s10052-014-2717-6. arXiv: 1307.4003 [physics.data-an].

[161] *Electron efficiency measurements with the ATLAS detector using the 2015 LHC proton-proton collision data*. Tech. rep. ATLAS-CONF-2016-024. Geneva: CERN, 2016. URL: http://cds.cern.ch/record/2157687.

[162] *Electron efficiency measurements with the ATLAS detector using the 2012 LHC proton-proton collision data*. Tech. rep. ATLAS-CONF-2014-032. Geneva: CERN, 2014. URL: http://cds.cern.ch/record/1706245.

[163] Georges Aad et al. "Electron and photon energy calibration with the ATLAS detector using LHC Run 1 data". In: *Eur. Phys. J.* C74.10 (2014), p. 3071. DOI: 10.1140/epjc/s10052-014-3071-4. arXiv: 1407.5063 [hep-ex].

[164] Georges Aad et al. "Muon reconstruction performance of the ATLAS detector in proton–proton collision data at $\sqrt{s}$ =13 TeV". In: *Eur. Phys. J.* C76.5 (2016), p. 292. DOI: 10.1140/epjc/s10052-016-4120-y. arXiv: 1603.05598 [hep-ex].

[165] J. Illingworth and J. Kittler. "A survey of the hough transform". In: *Computer Vision, Graphics, and Image Processing* 44.1 (1988), pp. 87 – 116. ISSN: 0734-189X. DOI: https://doi.org/10.1016/S0734-189X(88)80033-1. URL: http://www.sciencedirect.com/science/article/pii/S0734189X88800331.

[166] Georges Aad et al. "Measurement of the muon reconstruction performance of the ATLAS detector using 2011 and 2012 LHC proton–proton collision data". In: *Eur. Phys. J.* C74.11 (2014), p. 3130. DOI: 10.1140/epjc/s10052-014-3130-x. arXiv: 1407.3935 [hep-ex].

[167] *Measurement of the tau lepton reconstruction and identification performance in the ATLAS experiment using pp collisions at* $\sqrt{s} = 13$ TeV. Tech. rep. ATLAS-CONF-2017-029. Geneva: CERN, 2017. URL: http://cds.cern.ch/record/2261772.

[168] Matteo Cacciari, Gavin P. Salam, and Gregory Soyez. "The Anti-k(t) jet clustering algorithm". In: *JHEP* 04 (2008). DOI: 10.1088/1126-6708/2008/04/063.

[169] G. Aad et al. "Topological cell clustering in the ATLAS calorimeters and its performance in LHC Run 1". In: *The European Physical Journal C* 77.7 (2017), p. 490. ISSN: 1434-6052. DOI: 10.1140/epjc/s10052-017-5004-5. URL: https://doi.org/10.1140/epjc/s10052-017-5004-5.

[170] T Barillari et al. *Local Hadronic Calibration*. Tech. rep. ATL-LARG-PUB-2009-001-2. ATL-COM-LARG-2008-006. ATL-LARG-PUB-2009-001. Due to a report-number conflict with another document, the report-number ATL-LARG-PUB-2009-001-2 has been assigned. Geneva: CERN, 2008. URL: https://cds.cern.ch/record/1112035.

[171] Leo Breiman. *Classification and Regression Trees*. New York: Routledge, 1984.

[172] Yoav Freund and Robert E Schapire. "A Decision-Theoretic Generalization of On-Line Learning and an Application to Boosting". In: *J. Comput. Syst. Sci.* 55.1 (Aug. 1997), pp. 119–139. ISSN: 0022-0000. DOI: 10.1006/jcss.1997.1504. URL: http://dx.doi.org/10.1006/jcss.1997.1504.

[173] Georges Aad et al. "Identification and energy calibration of hadronically decaying tau leptons with the ATLAS experiment in pp collisions at $\sqrt{s}$=8 TeV". In: *Eur. Phys. J.* C75.7 (2015), p. 303. DOI: 10.1140/epjc/s10052-015-3500-z. arXiv: 1412.7086 [hep-ex].

[174] M. Aaboud et al. "Jet energy scale measurements and their systematic uncertainties in proton-proton collisions at $\sqrt{s} = 13$ TeV with the ATLAS detector". In: *Phys. Rev.* D96.7 (2017), p. 072002. DOI: 10.1103/PhysRevD.96.072002. arXiv: 1703.09665 [hep-ex].

[175] Georges Aad et al. "Jet energy measurement with the ATLAS detector in proton-proton collisions at $\sqrt{s} = 7$ TeV". In: *Eur. Phys. J.* C73.3 (2013), p. 2304. DOI: 10.1140/epjc/s10052-013-2304-2. arXiv: 1112.6426 [hep-ex].

[176] Stephen D. Ellis and Davison E. Soper. "Successive combination jet algorithm for hadron collisions". In: *Phys. Rev.* D48 (1993), pp. 3160–3166. DOI: 10.1103/PhysRevD.48.3160. arXiv: hep-ph/9305266 [hep-ph].

[177] Morad Aaboud et al. "A measurement of the calorimeter response to single hadrons and determination of the jet energy scale uncertainty using LHC Run-1 pp-collision data with the ATLAS detector". In: *Eur. Phys. J.* C77.1 (2017), p. 26. DOI: 10.1140/epjc/s10052-016-4580-0. arXiv: 1607.08842 [hep-ex].

[178] Georges Aad et al. "Performance of b-Jet Identification in the ATLAS Experiment". In: *JINST* 11.04 (2016), P04008. DOI: 10.1088/1748-0221/11/04/P04008. arXiv: 1512.01094 [hep-ex].

[179] Morad Aaboud et al. "Measurements of b-jet tagging efficiency with the ATLAS detector using $t\bar{t}$ events at $\sqrt{s} = 13$ TeV". In: *JHEP* 08 (2018), p. 089. DOI: 10.1007/JHEP08(2018)089. arXiv: 1805.01845 [hep-ex].

[180] *Optimisation of the ATLAS b-tagging performance for the 2016 LHC Run*. Tech. rep. ATL-PHYS-PUB-2016-012. Geneva: CERN, 2016. URL: https://cds.cern.ch/record/2160731.

[181] Georges Aad et al. "Performance of Missing Transverse Momentum Reconstruction in Proton-Proton Collisions at 7 TeV with ATLAS". In: *Eur. Phys. J.* C72 (2012), p. 1844. DOI: 10.1140/epjc/s10052-011-1844-6. arXiv: 1108.5602 [hep-ex].

[182] Morad Aaboud et al. "Performance of missing transverse momentum reconstruction with the ATLAS detector using proton-proton collisions at $\sqrt{s}$ = 13 TeV". In: (2018). arXiv: 1802.08168 [hep-ex].

[183] The ATLAS collaboration. "Performance of pile-up mitigation techniques for jets in pp collisions at $\sqrt{s} = 8$ TeV using the ATLAS detector". In: *Eur. Phys. J.* C76 (2016). DOI: 10.1140/epjc/s10052-016-4395-z.

[184] A. Hoecker et al. "TMVA - Toolkit for Multivariate Data Analysis". In: *ArXiv Physics e-prints* (Mar. 2007). eprint: physics/0703039.

[185] M. Aaboud et al. "Identification and rejection of pile-up jets at high pseudorapidity with the ATLAS detector". In: *The European Physical Journal C* 77.9 (2017), p. 580. DOI: 10.1140/epjc/s10052-017-5081-5. URL: https://doi.org/10.1140/epjc/s10052-017-5081-5.

[186] Morad Aaboud et al. "Jet reconstruction and performance using particle flow with the ATLAS Detector". In: *Eur. Phys. J.* C77.7 (2017), p. 466. DOI: 10.1140/epjc/s10052-017-5031-2. arXiv: 1703.10485 [hep-ex].

[187] *E_T^{miss} performance in the ATLAS detector using 2015-2016 LHC p-p collisions*. Tech. rep. ATLAS-CONF-2018-023. Geneva: CERN, 2018. URL: http://cds.cern.ch/record/2625233.

[188] Morad Aaboud et al. "Measurements of top-quark pair differential cross-sections in the $e\mu$ channel in pp collisions at $\sqrt{s} = 13$ TeV using the ATLAS detector". In: *Eur. Phys. J.* C77.5 (2017), p. 292. DOI: 10.1140/epjc/s10052-017-4821-x. arXiv: 1612.05220 [hep-ex].

[189] M. Aaboud et al. "Measurements of top-quark pair differential cross-sections in the lepton+jets channel in pp collisions at $\sqrt{s} = 13$ TeV using the ATLAS detector". In: *JHEP* 11 (2017), p. 191. DOI: 10.1007/JHEP11(2017)191. arXiv: 1708.00727 [hep-ex].

[190] Morad Aaboud et al. "Measurements of differential cross sections of top quark pair production in association with jets in pp collisions at $\sqrt{s} = 13$ TeV using the ATLAS detector". In: *JHEP* 10 (2018), p. 159. DOI: 10.1007/JHEP10(2018)159. arXiv: 1802.06572 [hep-ex].

[191] Morad Aaboud et al. "Measurements of $t\bar{t}$ differential cross-sections of highly boosted top quarks decaying to all-hadronic final states in pp collisions at $\sqrt{s} = 13$ TeV using the ATLAS detector". In: *Phys. Rev.* D98.1 (2018), p. 012003. DOI: 10.1103/PhysRevD.98.012003. arXiv: 1801.02052 [hep-ex].

[192] Vardan Khachatryan et al. "Measurement of the $\mathrm{t\bar{t}}$ production cross section in the all-jets final state in pp collisions at $\sqrt{s} = 8$ TeV". In: *Eur. Phys. J.* C76.3 (2016), p. 128. DOI: 10.1140/epjc/s10052-016-3956-5. arXiv: 1509.06076 [hep-ex].

[193] CMS Collaboration. "Measurement of the $\mathrm{t\bar{t}}$ production cross section at 13 TeV in the all-jets final state". In: (2016).

[194] L. Apanasevich et al. "Evidence for Parton k_T Effects in High- p_T Particle Production". In: *Phys. Rev. Lett.* 81 (13 1998), pp. 2642–2645. DOI: 10.1103/PhysRevLett.81.2642. URL: https://link.aps.org/doi/10.1103/PhysRevLett.81.2642.

[195] Georges Aad et al. "Search for New Phenomena in Dijet Angular Distributions in Proton-Proton Collisions at $\sqrt{s} = 8$ TeV Measured with the ATLAS Detector". In: *Phys. Rev. Lett.* 114.22 (2015), p. 221802. DOI: 10.1103/PhysRevLett.114.221802. arXiv: 1504.00357 [hep-ex].

[196] A. Denner et al. "NLO QCD corrections to WWbb production at hadron colliders". In: *Phys. Rev. Lett.* 106 (2011), p. 052001. DOI: 10.1103/PhysRevLett.106.052001. arXiv: 1012.3975 [hep-ph].

[197] Giuseppe Bevilacqua et al. "Complete off-shell effects in top quark pair hadroproduction with leptonic decay at next-to-leading order". In: *JHEP* 02 (2011), p. 083. DOI: 10.1007/JHEP02(2011)083. arXiv: 1012.4230 [hep-ph].

[198] *Selection of jets produced in 13TeV proton-proton collisions with the ATLAS detector*. Tech. rep. ATLAS-CONF-2015-029. Geneva: CERN, 2015. URL: https://cds.cern.ch/record/2037702.

[199] G. Aad et al. "Readiness of the ATLAS Liquid Argon Calorimeter for LHC Collisions". In: *Eur. Phys. J.* C70 (2010), pp. 723–753. DOI: 10.1140/epjc/s10052-010-1354-y. arXiv: 0912.2642 [physics.ins-det].

[200] M Verducci. "ATLAS conditions database experience with the LCG COOL conditions database project". In: *Journal of Physics: Conference Series* 119.4 (2008), p. 042031. URL: http://stacks.iop.org/1742-6596/119/i=4/a=042031.

[201] T. Golling et al. "The ATLAS Data Quality Defect Database System". In: *Eur. Phys. J.* C72 (2012), p. 1960. DOI: 10.1140/epjc/s10052-012-1960-y. arXiv: 1110.6119 [physics.ins-det].

[202] Georges Aad et al. "Measurement of the inclusive jet cross-section in proton-proton collisions at $\sqrt{s} = 7$ TeV using 4.5 fb^{-1} of data with the ATLAS detector". In: *JHEP* 02 (2015). [Erratum: JHEP09,141(2015)], p. 153. DOI: 10.1007/JHEP02(2015)153, 10.1007/JHEP09(2015)141. arXiv: 1410.8857 [hep-ex].

[203] Georges Aad et al. "ATLAS Measurements of the Properties of Jets for Boosted Particle Searches". In: *Phys. Rev.* D86 (2012), p. 072006. DOI: 10.1103/PhysRevD.86.072006. arXiv: 1206.5369 [hep-ex].

[204] Morad Aaboud et al. "Top-quark mass measurement in the all-hadronic $t\bar{t}$ decay channel at $\sqrt{s}$ = 8 TeV with the ATLAS detector. Top-quark mass measurement in the all-hadronic $t\bar{t}$ decay channel at $\sqrt{s}$ = 8 TeV with the ATLAS detector". In: *JHEP* 09.CERN-EP-2016-264 (2017). 39 pages in total, author list starting page 23, 6 figures, 4 tables, submitted to JHEP, All figures including auxiliary figures are available at https://atlas.web.cern.ch/Atlas/GROUPS/PHYSICS/PAPERS/TOPQ-2015-03/, 118. 39 p. URL: https://cds.cern.ch/record/2253316.

[205] Georges Aad et al. "Search for resonances decaying into top-quark pairs using fully hadronic decays in pp collisions with ATLAS at $\sqrt{s} =$ 7 TeV". In: *JHEP* 01 (2013), p. 116. DOI: 10.1007/JHEP01(2013)116. arXiv: 1211.2202 [hep-ex].

[206] Volker Blobel. "An Unfolding method for high-energy physics experiments". In: *Advanced Statistical Techniques in Particle Physics. Proceedings, Conference, Durham, UK, March 18-22, 2002*. 2002, pp. 258–267. arXiv: hep-ex/0208022 [hep-ex]. URL: http://www.ippp.dur.ac.uk/Workshops/02/statistics/proceedings//blobel2.pdf.

[207] Stefan Schmitt. "Data Unfolding Methods in High Energy Physics". In: *EPJ Web Conf.* 137 (2017), p. 11008. DOI: 10.1051/epjconf/201713711008. arXiv: 1611.01927 [physics.data-an].

[208] Andreas Hocker and Vakhtang Kartvelishvili. "SVD approach to data unfolding". In: *Nucl. Instrum. Meth.* A372 (1996), pp. 469–481. DOI: 10.1016/0168-9002(95)01478-0. arXiv: hep-ph/9509307 [hep-ph].

[209] G. D'Agostini. "A multidimensional unfolding method based on Bayes' theorem". In: *Nuclear Instruments and Methods in Physics Research Section A: Accelerators, Spectrometers, Detectors and Associated Equipment* 362.2 (1995). DOI: https://doi.org/10.1016/0168-9002(95)00274-X.

[210] Francesco Spano. "Unfolding in particle physics: a window on solving inverse problems". In: *EPJ Web Conf.* 55 (2013), p. 03002. DOI: 10.1051/epjconf/20135503002.

[211] Michael Schmelling. "The method of reduced cross-entropy A general approach to unfold probability distributions". In: *Nuclear Instruments and Methods in Physics Research Section A: Accelerators, Spectrometers, Detectors and Associated Equipment* 340.2 (1994), pp. 400 –412. ISSN: 0168-9002. DOI: https://doi.org/10.1016/0168-9002(94)90119-8. URL: http://www.sciencedirect.com/science/article/pii/0168900294901198.

[212] V. Blobel. "Unfolding Methods in High-energy Physics Experiments". In: *Proceedings, CERN School of Computing: Aiguablava, Spain, September 9-22 1984*. 1984.

[213] Tim Adye. "Unfolding algorithms and tests using RooUnfold". In: arXiv:1105.1160 (2011). Comments: 6 pages, 5 figures, presented at PHYSTAT 2011, CERN, Geneva, Switzerland, January 2011, to be published in a CERN Yellow Report, 313–318. 6 p. URL: https://cds.cern.ch/record/1349242.

[214] *Data-driven determination of the energy scale and resolution of jets reconstructed in the ATLAS calorimeters using dijet and multijet events at* $\sqrt{s} = 8\ TeV$. Tech. rep. ATLAS-CONF-2015-017. Geneva: CERN, 2015. URL: http://cds.cern.ch/record/2008678.

[215] Michal Czakon and Alexander Mitov. "Top++: A Program for the Calculation of the Top-Pair Cross-Section at Hadron Colliders". In: *Comput. Phys. Commun.* 185 (2014). DOI: 10.1016/j.cpc.2014.06.021.